Dynamics and energetics relevant to multiphoton excitation via Rydberg and Ion-pair molecular and atomic states

Mengxu Jiang

Faculty of Physical Sciences
School of Engineering and Natural Sciences
University of Iceland
2022

Dynamics and energetics relevant to multiphoton excitation via Rydberg and Ion-pair molecular and atomic states

Mengxu Jiang

Dissertation submitted in partial fulfillment of a
Philosophiae Doctor degree in chemistry

Advisor
Ágúst Kvaran

Co-Advisor
Huasheng Wang

PhD Committee
Jingming Long
Gísli Hólmar Jóhannesson
Sveinn Ólafsson

Opponents
Peter Rakitzis
Egill Antonsson

Faculty of Physical Sciences
School of Engineering and Natural Sciences
University of Iceland
Reykjavik, December 2022

Dynamics and energetics relevant to multiphoton excitation via Rydberg and Ion-pair molecular and atomic states

Dynamics & energetics of excited states
Dissertation submitted in partial fulfillment of a *Philosophiae Doctor* degree in chemistry

Faculty of Natural Sciences
School of Engineering and Natural Sciences
University of Iceland
Dunhagi 3
107, Reykjavik
Iceland

Telephone: 525 4000

Bibliographic information:
Mengxu Jiang, 2022, *Dynamics and energetics relevant to multiphoton excitation via Rydberg and Ion-pair molecular and atomic states*, PhD dissertation, Faculty of Natural Sciences, University of Iceland.

Author ORCID: 0000-0003-1989-908X

ISNB: 978-9935-9697-2-9

Printing: Háskólaprent ehf, Fálkagata 2, 107 Reykjavík.
Reykjavik, Iceland, December 2022

Abstract

The research focused on the multiphoton dynamics and energetics for the HI, CH_3I, CH_3Br, and C_2H_2 molecules by using one- and two-color mass-resolved (MR) resonance enhanced multiphoton ionization (REMPI) and/or velocity map imaging (VMI) in association with REMPI.

MR-REMPI experiments for HI revealed new Rydberg and ion-pair states as well as perturbation cases due to interactions between electronic states, which appeared as line-shift (LS), line-intensity (LI), and line-width (LW) alternations in REMPI spectra.

CH_3I multiphoton dynamic studies by VMI-REMPI revealed the formation of excited Rydberg states of iodine atoms (I**) along with $CH_3(X)$ to be the significant formation channel in the two-photon excitation region of 55 700 to 70 000 cm^{-1}. Rather unusual observation, this was found to occur via three-photon excitation to superexcited molecular states ($CH_3I^{\#}$).

Iodine atomic lines in REMPI spectra for I^+ signals in the two-photon excitation region of 76 680 -82 620 cm^{-1} for CH_3I and HI revealed autoionization of superexcited iodine atoms ($I^{\#}$). Several new spectral peaks were assigned, and the autoionization mechanisms were identified.

Two-color MR-REMPI / pump and probe experiments were designed and developed to perform photofragmentation experiments and spectra analysis of fragment species. The technique was successfully applied for CH_3Br. Further work is in preparation.

Multiphoton breakdown of acetylene (C_2H_2) was studied by VMI-REMPI via molecular Rydberg states. The number of photofragmentation channels, involving the formation of ground and excited state fragments for two-, three- and four-photon excitations prior to photoionization, were identified.

Útdráttur

Rannsóknirnar fjölluðu um ljósrof og orkueiginleika sameindanna HI, CH_3I, CH_3Br og C_2H_2. Ýmist var notast við einn eða tvo lasergeisla við ljósörvanir og fleiri en ein ljóseind nýttust til að rjúfa og/eða jóna sameindirnar eða sameindabrot þeirra. Annars vegar var notast við massagreiningu jóna (aðferð MR-REMPI), hins vegar við myndgreiningu jónadreifinga (VMI-REMPI).

MR-REMPI mælingar HI leiddu til auðkenningar nýrra orkuástanda sameindarinnar sem og orkuvíxlverkana innan sameindarinnar. Orkuvíxlverkanir birtast í formi bjögunar/óreglu á mældum litrófum (REMPI-litróf).

VMI-REMPI mælingar á CH_3I leiddu í ljós ýmsa roferla. Einn, fremur óvenjulegur, var þó yfirgnæfandi. Hann fólst í myndun orkuríkra joðatóma (I**) og sameindabrotsins CH_3 í kjölfar myndunar óstöðugra ofurorkuríkra sameinda ($CH_3I^{\#}$) við þriggja ljóseinda örvun.

Joð-atóm litrófslínur í REMPI rófum fyrir CH_3I og HI báru með sér að sjálfjónun (e. autoionization) óstöðugra ofurorkuríkra atóma ($I^{\#}$) ætti sér stað. Ýmsar nýjar joðatóm litrófslínur voru auðkenndar.

Aðstaða til að framkvæma rannsóknir á rofferlum og orkueiginleikum sameindabrota með tvílita ljósörvun (MR-REMPI) var hönnuð og þróuð. Aðferðin var notum með jákvæðum árangri við mælingar á CH_3Br. Frekari vinnsla er enn í gangi.

Fjölljóseindarof acetylene (C_2H_2) sameindarinnar var rannsakað með VMI-REMPI aðferðinni. Fjölmargir rofferlar, í kjölfar tveggja-, þriggja- og fjögurra- ljóseinda örvana, sem leiddu til myndunar ýmissa sameindabrota og frekari jónunnar fundust og voru auðkenndir.

For past, for now, for future

Table of Contents

List of Figures

List of Tables

Abbreviations

LIF − Laser induced fluorescence

PE − Photoelectron

iPEPICO − Imaging photoelectron photoion coincidence

cipp − coincident Ion-pair production

REMPI − Resonance enhanced multiphoton ionization

MR-TOF − Mass resolved time-of-flight

VMI − Velocity map imaging

HI – Hydrogen iodide

CH_3I – Iodomethane

CH_3Br – bromomethane

C_2H_2 – Acetylene

LCAO – Linear combination of atom orbitals

FCFs – Franck-Condon factors

CG – Clebsch-Gordon

LI – Line-Intensity

LS – Line-Shift

LW – Line-Width

SHG – Second harmonic generator

Nd:YAG – Neodymium-doped yttrium aluminum garnet or $Nd:Y_3Al_5O_{12}$

PC – pockels cell

BBO – Beta Barium Borate or β-BaB_2O_4

KDP – Potassium dihydrogen phosphate or KH_2PO_4

MCP – Microchannel plates

CCD – Charge-couple Device

Acknowledgements

I am very grateful to my supervisor, Prof. Ágúst Kvaran, for providing me Ph.D. position, supporting my study in the research field, and guiding me in writing and revising the manuscript. He always gave me good new insight and essential knowledge for some complicated problems we encountered during the study.

My Co-Advisor, Viktor Huasheng Wang, provided me with a lot of technical support at the beginning of my Ph.D. study and life assistance during my study. I will never forget the delicious food his family made at the spring festival each year, which gave me a good feeling like living in China with my family.

Dr. Jingming Long introduced me to this group for the first time and provided me with technical support for the program. Dr. Arnar Hafliðason and Kristján Matthíasson assisted me with some basic knowledge of the research field.

The partner Ioannis C. Giannakidis and supervisor Dr. Petros C. Samartzis, in the exchanged study in FORTH, Crete of Greece, provided me with experimental assistance and guidance on the VMI technique.

The doctor committee, Gísli Hólmar Jóhannesson, and Sveinn Ólafsson gave me a positive evaluation of the study stages.

My family and friends gave me backup for challenging the difficulty.

The financial support from the Icelandic Science Foundation (RANNÍS) and Aðalsteinn Kristjánsson's memorial fund for the promotion of natural sciences and chemistry, is acknowledged.

1 Introduction

The universe's evolution involves the exchange of energy and matter in various forms, both reversibly and irreversibly. The exchange between the light (radiomagnetic waves/photons) and the matter is among the critical processes in this respect.[1-3] Thus, exchanges of photons and matter can drive transitions of electrons to higher (absorption) or lower (emission) energies. For more than a century, scientists focused on experimental and theoretical research work relevant to the exchange between light and matter based on quantum mechanics. Basic information provides a comprehensive understanding relevant to various necessary research fields such as atmospheric chemistry[4-6], photochemistry[7-9], and astrochemistry.[10-12]

Laser spectroscopy is a powerful technique to explore the fundamental properties of molecules and atoms and the exchange between light and matter. Several different spectroscopic techniques have been used for that purpose, such as traditional absorption spectroscopy,[13-15] laser-induced fluorescence (LIF) spectroscopy,[16] photoelectron spectroscopy (PE),[17-18] imaging photoelectron photoion coincidence spectroscopy(iPEPICO),[19] coincident Ion-pair production spectroscopy(cipp),[20] resonance enhanced multiphoton ionization (REMPI) spectroscopy,[21-25] to name but few. The mass-resolved time-of-flight (MR-TOF) REMPI technique is useful for deriving high-resolution atom and molecular spectra due to transitions to electronically excited states. [23-25] Furthermore, it allows the determination of photofragmentation (photodissociation and photoionization) processes[26-28] and the characterization of state interactions.[29-31] For a molecule, it, typically, involves initial resonance photoexcitation by n-photons to an excited state followed by a further photoexcitation of the excited molecule or its fragments (in the case of photodissociation) by m-photons to form ions and electrons (photoionization).

In recent years, our research group has studied Rydberg states of halogen-containing molecules using the MR-TOF REMPI technique. The emphasis has been on observations and characterizations of new excited states, state-to-state interactions as well as photofragmentation processes. Small diatomic and polyatomic molecules have been emphasized. Furthermore, more recently, in a collaboration work,[32-36] a use of the velocity map imaging (VMI) technique in combination with REMPI (VMI-REMPI) has been utilized for more detailed characterization/determination of the photofragmentation processes involved. The technique involves the determination of ion and/or electron speed distributions from recorded images on a position-sensitive detector followed by comparison with calculated energy thresholds for fragments or information.[37]

My Ph.D. work can be grouped into three main categories: i) One color MR-REMPI;ii) VMI-REMPI; iii)Development and use of two-color MR-REMPI. For both halogen-containing molecules (HI(i), CH_3I(i,ii), CH_3Br(iii)) and an organic molecule (acetylene/C_2H_2 (ii)) for studies relevant to spectroscopic characterization (HI, CH_3I, CH_3Br), state interactions (HI) and photofragmentation processes (HI, CH_3I, CH_3Br). The derived results and conclusions are relevant to the fundamental understanding of exchange between light and matter, processes in atmospheric chemistry (e.g. photofragmentation of halogen-containing molecules) as well as astrochemistry (e.g.photofragmentation of acetylene to form organic

building block fragments). This research aims to add to our understanding of the properties of highly excited molecular states and state interactions in the Rydberg state energy region, both in terms of state energetics and dynamics. Such fundamental information is vital for possible applications in related fields, such as photochemical synthesis and plasma chemistry, and/or for understanding processes in fields, such as atmospheric chemistry and astrochemistry. This aim follows the fundamental importance of academic research, which can be phrased in this context as "understanding the properties and behavior of matter is a vital prerequisite for its usefulness".

1.1 HI

The spectroscopy of the HI molecule has been studied extensively.[38-47] Number of valence and Rydberg states have been identified in absorption spectra, lower in energy than 74 400 cm^{-1}, by Tilford, Ginter, and Bass.[38-40] The first REMPI studies of HI were reported in 1994 by Wright et al. for the two-photon excitation energy region of 64 600 – 71 000 cm^{-1}.[41] Spectra due to transitions to Rydberg states show perturbation effects as irregular rotational structure due to state interactions. Recently Hróðmarsson et al. reported a detailed REMPI work on HI for the two-photon excitation region 69 600 cm^{-1} – 74 600 cm^{-1} about the identification of new states as well as interactions between Rydberg and ion-pair states, based on observations of line-shifts, line-intensity, and line-width alterations.[45-47] An overall scheme of vibrational-dependent state interactions was proposed.

Relevant work on HI, presented here, can be found in papers no. 1, 3, and 5 (see below) using the MR-REMPI technique. We extended the exploration region for two-photon resonant transitions to Rydberg and ion-pair states and relevant interactions to the high energy excitation region of 74 000 – 80 300 cm^{-1}. H^+, I^+, and HI^+ REMPI spectra were recorded and analyzed. The data allow the identification of new Rydberg and ion-pair vibrational states as well as state interactions. Clear homogeneous couplings as non-degenerate level-to-level interactions/mixing and heterogeneous couplings as near-degenerate level-to-level interactions/mixing between Rydberg and ion-pair states, were identified and characterized.

1.2 CH_3I

The UV/Vis spectroscopy of CH_3I, involving transitions to repulsive valence states (A-band) and higher energy Rydberg states, has been recorded before and assigned thoroughly by use of either standard absorption[48–53] or REMPI.[54–59] A vast amount of both experimental[58,60–69] and theoretical[70-73]studies on the photodissociation of the molecule for the A-band have made CH_3I a prototype for studying photofragmentation processes in polyatomic molecules. Fewer studies have been on the photodissociation of the molecule for excitations to Rydberg state. [54,56,67,73-77]

Relevant work on CH_3I, present here, is to be found in paper no. 2 (see below) by use of the VMI-REMPI technique. We present multiphoton ionization studies of CH_3I for resonant excitations to the Rydberg states in the two-photon excitation region of 55 000–70 000 cm^{-1} based on analysis of ion and photoelectron images. The analyses shed light on the

multiphoton dynamics of the molecule concerning both the photodissociation and photoionization mechanisms involved.

1.3 $I^{\#}$

Superexcited Rydberg states ($I^{\#}$) exist in the high energy region above the first ionization limit for the iodine atom (i.e.above $I^{+}(^{3}P_2)$). Berkowitz et al. reported an observation of a series of superexcited states of I ($I^{\#}$) corresponding to s and d Rydberg electrons and the atom-ion cores $^{3}P_0$, $^{3}P_1$, $^{1}D_2$, and $^{1}S_0$ in photoionization spectra.[78] Jung et al. applied photoelectron spectroscopy and recorded photoelectron images for the photolysis of CH_3I in the A-band followed by probing the iodine atoms by (2 + 1) REMPI.[79] Hu et al. reported spectral peaks due to two-photon transitions from I to Rydberg states (I**) and from spin-orbit excited I atoms (I*) to $I^{\#}$.[80] The latter group of peaks (for $I^{\#}$) was found to be particularly broad.[80] By use of the photoelectron imaging technique coupled with (2 + 1) REMPI via p Rydberg atomic states (I**). Shen et al. characterized iodine atom Rydberg substrates as well as state interactions between I** and $I^{\#}$.[81a]

Relevant work on $I^{\#}$, present here, is to be found in paper no. 4. We present I^{+} REMPI signals of mass-resolved REMPI data for CH_3I and HI in the high energy two-photon excitation region of 76 680–82 620 cm^{-1} and laser power dependence of signals for HI. The data reveal iodine atomic lines due to (2 + 1) REMPI of I via I** and $I^{\#}$ as well as due to two-photon resonant excitation of I* to $I^{\#}$ followed by autoionization to form excited atom-ions (I^{+}*).

1.4 CH_3Br

Methyl bromide (CH_3Br) has been of interest in spectroscopic and photofragmentation studies, both experimentally[82-92] and theoretically.[93] Our group has focused on the effect of two-photon excitation via CH_3Br Rydberg states in the region of 66 000 – 80 000 cm-1 by MR- and VMI-REMPI.[35-36,94] The MR-REMPI analysis reveals that the primary ion signal intensities changed as $CH_3^{+} > CH_2^{+} > CH^{+} > C^{+}$, while very weak signals are detected for Br^{+}, CBr^{+}, H^{+} and CH_xBr+ (x=1,2,3). [94] Characteristic ion intensities were observed. The relative ion intensities, I (M^{+})/I (CH_3^{+}), for $M^{+} = CH_2^{+}$, CH^{+}, and Br^{+} reached maxima near the ion-pair threshold. Hafliðason et al. observed the formation of CH_3** along with Br/Br* by three-photon dissociation followed by one-photon ionization of CH_3** to form CH_3^{+} in the analysis of CH_3^{+} ion and photoelectron kinetic energy release spectra (KERs) derived from slice images by use of one-color excitations.[35] Furthermore, predissociation channels following two-photon resonant excitations and non-resonant photodissociation to form ground state CH_3(X) and Br/Br* were identified and characterized by the use of the two-color pump and probe slice imaging experiments.[36]

Relevant work on CH_3Br is presented here in combination with developing of the two-color MR-REMPI technique (see below). REMPI spectra of the CH_3 fragment due to transitions to vibrational Rydberg states (CH_3**(v_i)) were recorded.

1.5 C_2H_2

Photodissociation of C_2H_2 has been studied experimentally by single-[95-99], two-[100-101], and three-[102-103] photon excitations. Due to either ungerade (u) or gerade (g) symmetries of molecular Rydberg states (C_2H_2**) and relevant selection rules[95-104] photoexcitation and corresponding photodissociation processes differ for odd and even numbers of photons used for resonant excitations. Laser-induced fluorescence (LIF) studies reveal the formation of several neutral excited state fragment species by photodissociation, such as C_2H* (B'), C_2*(C, d), H*, CH*.[103] Based on REMPI analysis Tsuji et al.[100]concluded that the fragment ion formations are dominantly due to ionization of neutral molecular fragments after predissociation. Recently Jiang [104-105] an evidence for strong fragment fluorescence from C_2* due to the $d^3\Pi_g \rightarrow a^3\Pi_u$ (swan band) and the $C^1\Pi_g \rightarrow A^1\Pi_u$ transitions in dispersed fluorescence experiments by using one-color (212-220 nm) multiphoton resonant enhanced excitation at the one-photon level of the acetylene S1-S0 transition. They proposed a mechanism that involved predissociation of C_2H_2** in forming C_2H*(B') followed by one-photon excitation of the C_2H*(B') intermediate fragment to form C_2*(C, d).

Relevant work on C_2H_2, presented here, is in paper no. 6 (to be published). The work is a continuation of an MR-REMPI work by Matthíasson et al.[107] We primarily present multiphoton fragmentation studies of C_2H_2 by VMI-REMPI of electrons and number of fragment ions for two-photon resonant excitations to molecular Rydberg states in the excitation region of 73 969 – 83 006 cm^{-1}. Analysis of ion mass resolved REMPI spectra, kinetic energy release data for electrons and ions, and angular distributions of images allow us to derive a picture of the multiphoton breakdown of the molecule into reactive fragments, both radicals and ions.

2 Theoretical considerations

2.1 The Born-Oppenheimer approximation

In order to simplify the Schrödinger equation for molecules, the Born-Oppenheimer approximation is applied. It is based on a separation of the motion of the atom nuclei and the electrons due to the significant difference in masses, hence the movement speeds. Thus, for the electron motions, to a first approximation, the nuclei can be considered to be static. The approximation allows the determination of potential energy as a function of the molecule geometry. Thus, the Hamiltonian of a diatomic molecule can be written as a sum of separate terms:

$$\widehat{H} = H^{el}(R) + T^{N}(R) + H^{rot} + H^{so} \tag{1}$$

where H^{el} (R) describes the term for the potential energy curve as a function of the internuclear distance (R) and T^{N} (R) represents the vibrational motion as a function of R. H^{rot} is a variable that defines the rotational motion, and H^{so} describes the spin-orbit interaction.

The total energy E_{tot} of the molecule can be expressed as:

$$E_{tot} = T_e + G(v) + F_v(J) \tag{2}$$

where T_e , $G(v)$ and $F_v(J)$ are the electronic-vibrational- and rotational energies, respectively.[108]

The electronic energy, T_e, of Rydberg states, can be derived from the modified Rydberg equation,

$$T_e = \ IE - \frac{\mathcal{R}}{(n-\delta)^2} \tag{3}$$

where *IE* is the ionization energy, $\mathcal{R}$ is the Rydberg constant, n is the principal quantum number and δ is the quantum defects that depend on the Rydberg electron orbital. The quantum defect value depends on the shielding effect of the core electrons of the molecule.

The vibrational energy, $G(v)$, in wavenumbers, can be expressed as,

$$G(v) = \omega_e\left(v + {}^1/_2\right) - \omega_e x_e\left(v + {}^1/_2\right)^2 + \omega_e y_e\left(v + {}^1/_2\right)^3 + \cdots \tag{4}$$

where, v is the vibrational quantum number (v = 0, 1, 2 …), ω_e is, to a first approximation, the harmonic oscillator vibrational wavenumber, and the $\omega_e x_e$ and $\omega_e y_e$ terms are the

anharmonicity constants that describe the deviation from the simple harmonic oscillator approximation.

The rotational energy, $F_v(J)$, in wavenumbers, is expressed as,

$$F_v(J) = B_v J(J+1) - D_v J^2(J+1)^2 + \cdots \quad (5)$$

$$B_v = B_e - \alpha_e\left(v + {}^1/_2\right) \quad (6)$$

$$D_v = D_e - \beta_e\left(v + {}^1/_2\right) \quad (7)$$

where B_v and D_v are the rotational and the centrifugal distortion constants for the vibrational state v, respectively. B_e and D_e are the vibrationally unaffected rotational and centrifugal distortion constants of individual electronic states. α_e and β_e are vibrational-rotational coupling constants that describe the impact of increasing vibrational energy.

2.2 Term symbols and Hund's cases; diatomic molecules

2.2.1 Term symbols

In general, linear combination of atom orbitals (LCAO) are applied to describe the diatomic molecular orbital. Table 1 shows the relationship between atomic and molecular orbitals.

Table 2.1 *Relationship between atomic orbitals and molecular bonding orbitals.*

Atomic orbital (*l*)	Molecular bonding orbitals (λ)
s	$s\,\sigma$
p	$p\,\sigma$, $p\,\pi$
d	$d\,\sigma$, $d\,\pi$, $d\,\delta$
f	$f\,\sigma$, $f\,\pi$, $f\,\delta$, $f\,\phi$

Electronic term symbol for a molecule is in the form,

$$^{2S+1}\Lambda_\Omega \quad (8)$$

where S is the electron spin angular momentum quantum number. The projection vector of the spin angular momentum vector, $\boldsymbol{S}$ on the molecular axis is labeled as $\boldsymbol{\Sigma}$. $\boldsymbol{\Lambda}$ is the projection vector of the electronic orbital angular momentum vector, $\boldsymbol{L}$ on the molecular

axis. Symbols Σ, Π, Δ… are used to represent the $\Lambda=0,1,2,\ldots$.Ω is the electronic total angular momentum quantum number corresponding to the $\boldsymbol{\Omega}$ vector along the molecular axis),

$$\boldsymbol{\Omega} = \boldsymbol{\Sigma} + \boldsymbol{\Lambda} \tag{9}$$

2.2.2 Hund's cases a and c

Hund's cases[109] is about coupling(interactions) arrangements of the various electron angular momenta within molecules. The total angular momentum without nuclear spin, ***J***, is a combination of the electron orbital angular momentum ***L***, the electron spin angular momentum ***S*** and the nuclear rotation angular momentum ***R***.

For Hund's case (a) in diatomic molecules, the bond axis (z-axis) electric field of the nucleus is strong. In Hund's case (a) ***L*** is strongly (electrostatically) coupled to the internuclear axis and ***S*** is coupled to ***L*** magnetically, by spin-orbit coupling. Then ***S*** and ***L*** have well-defined axial components ($\boldsymbol{\Sigma}$ and $\boldsymbol{\Lambda}$, respectively) which give $\boldsymbol{\Omega}$ ($\boldsymbol{\Omega} = \boldsymbol{\Sigma} + \boldsymbol{\Lambda}$) in the direction of the bond axis. Hund's case (a) is adapted to states of $\boldsymbol{\Lambda} \neq 0$, for short internuclear distances.

For Hund's case (c), the bond axis/z-axis electric field between the nucleus is relatively weak, so the spin-orbit coupling between ***S*** and ***L*** is stronger than the individual couplings of the internuclear axis. As a result, the $\boldsymbol{\Lambda}$ and $\boldsymbol{\Sigma}$ vectors are not well defined. Instead, ***S*** and ***L*** combine to form $\boldsymbol{J_a}$, which has a well-defined projection along the internuclear axis, $\boldsymbol{\Omega}$. Hund's case (c) is more common in molecules of heavy atoms.

The coupling between the electron spin and orbital motions and the nuclear rotation motion is weak. The nuclear rotation angular momentum vector, ***R,*** is perpendicular to the z-axis. The total angular momentum ***J***, for both Hund cases (a and c), is given by,

$$\boldsymbol{J} = \boldsymbol{\Omega} + \boldsymbol{R} \tag{10}$$

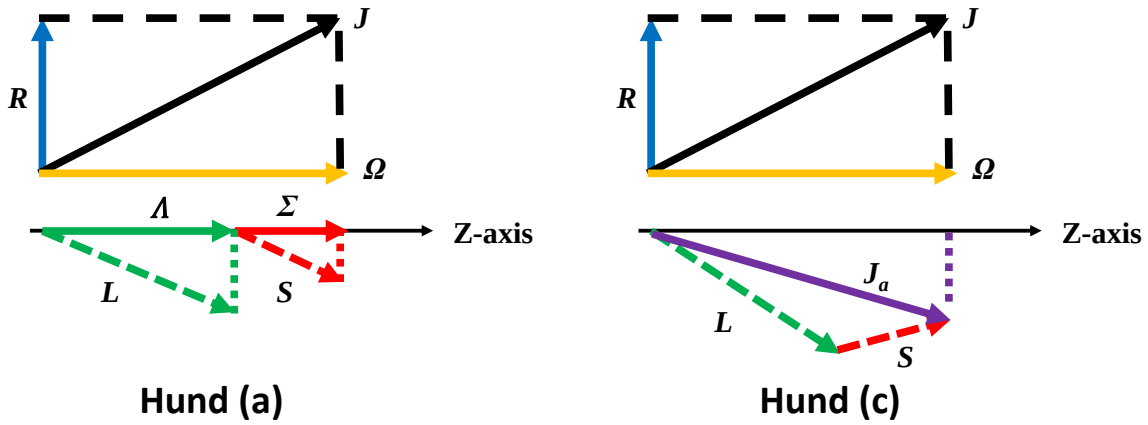

Figure 2.1 *Schematic representation of the angular momenta in a diatomic molecule for Hund's cases (a) and (c).*

2.3 One- and two- photon selection rules for molecules

When a molecule absorbs a photon/photons, the change in the total angular momentum (J) is restricted. For a linear or diatomic molecule, the selection rule for a one-photon excitation is,

$$\Delta J = \pm 1, for\ \Lambda = 0 \quad (11)$$

$$\Delta J = 0, \pm 1, for\ \Lambda \neq 0 \quad (12)$$

For a two-photon excitation, the one-photon selection rule is effectively applied two times to give,

$$\Delta J = 0, \pm 2, for\ \Lambda = 0 \quad (13)$$

$$\Delta J = 0, \pm 1, \pm 2, for\ \Lambda \neq 0 \quad (14)$$

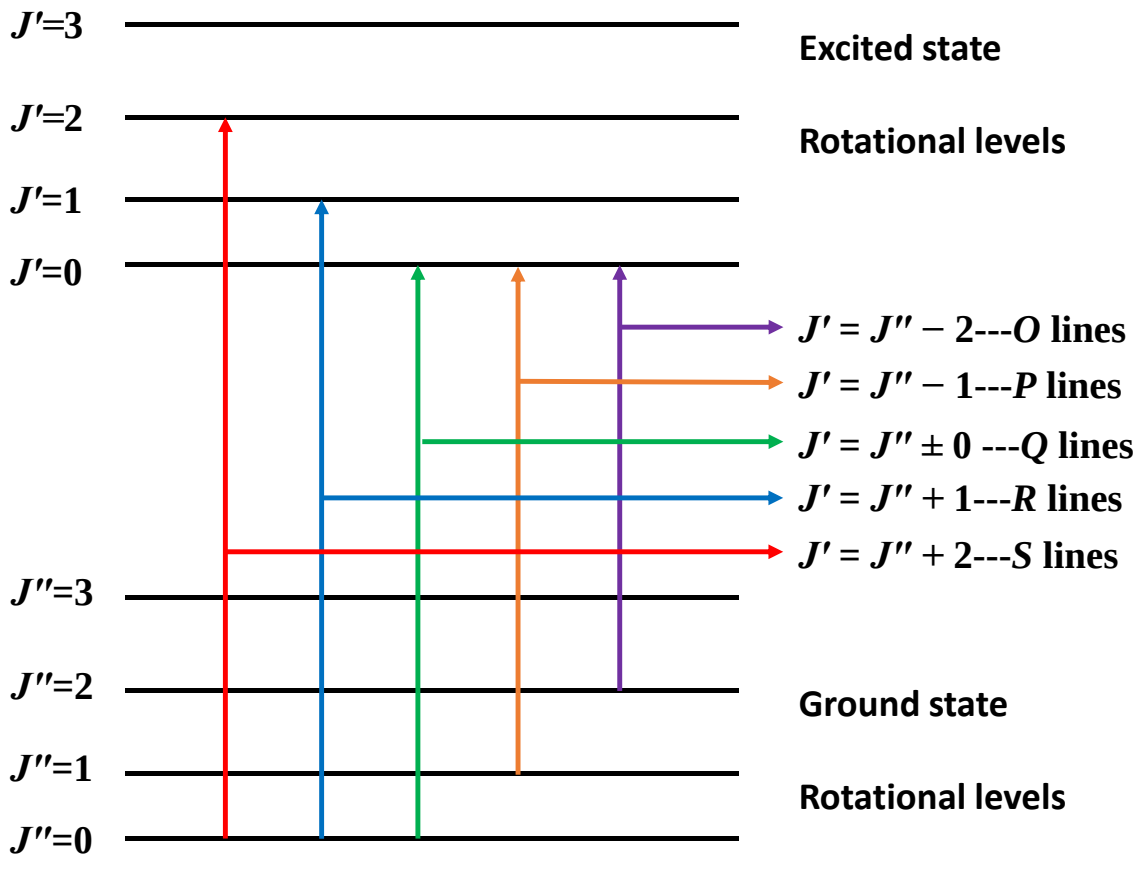

Figure 2.2 *Schematic diagram for of the O, P, Q, R, and S line transitions.*

2.4 Line strengths; Diatomic molecules

2.4.1 Franck-Condon principle

According to the Born-Oppenheimer approximation (see above), internuclear distances / chemical bonds are virtually unchanged during electron transfers due to photon excitations within molecules. This leads to the Franck-Condon principle, which states that "vertical transition" between potential surfaces/curves are most probable. In other words, due to the zero vibrational speed and long resident time at turning points of vibrational levels and potential energy curves, hence unchanged speed of nuclear motions, these are the most probable transitions (Fig. 2.3). This criterion allows evaluation of Franck-Condon factors (FCFs), ***q***, which give relative transition probabilities, depending on the two vibronic wavefunctions ψ^1 and ψ^0 involved as,

$$q = \langle \psi^1 | \mu | \psi^0 \rangle^2 \tag{15}$$

where μ is the transition dipole moment operator.

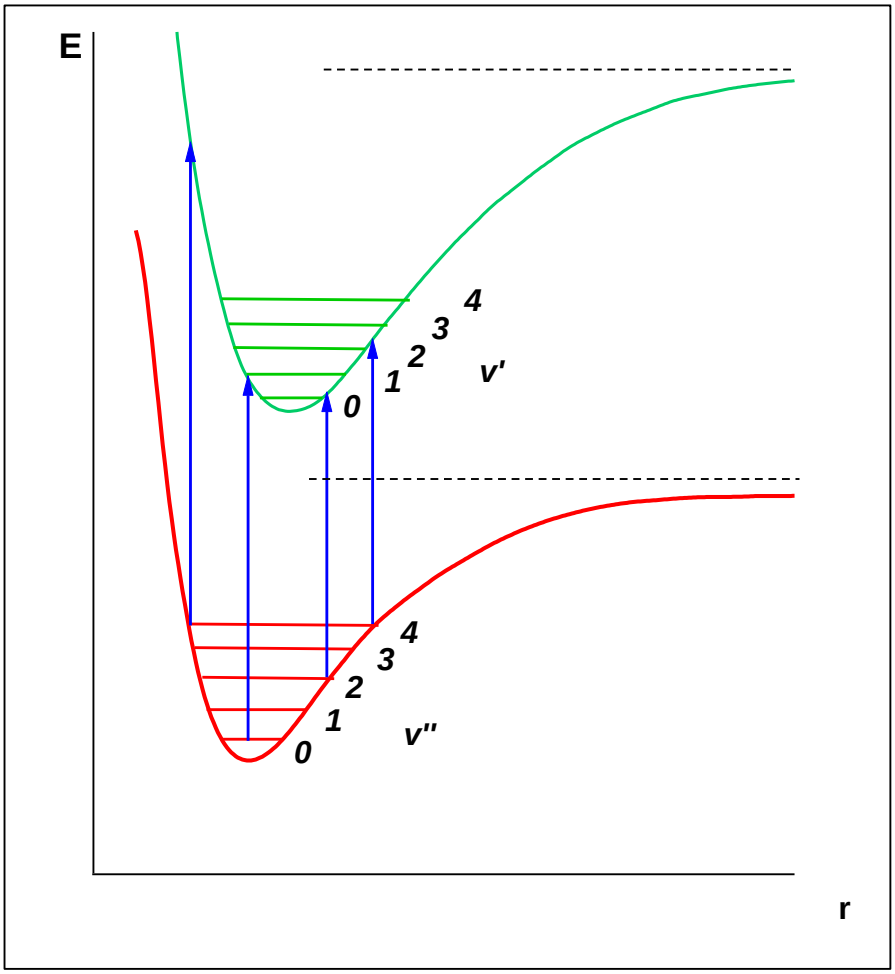

Figure 2.3 *Most probable electronic transitions according to the Franck-Condon principle.*

2.4.2 Boltzmann distribution

The intensity of rotational lines depends on the population in J'' levels, which is assumed to be according to the Boltzmann equation,

$$N_{J'',V''} = N_0 e^{\left(\frac{-E_{J'',V''}}{k_B T}\right)}(2J''+1) \quad (16)$$

Where N_0 is the total number of molecules in the ground state, $(2J''+1)$ is the degeneracy, $E_{J'',v''}$ is the rotational energy, k_B is the Boltzmann constant, and T is the temperature in K.

2.4.3 Transition strengths

Transition strengths are also important factors to determine the intensity of rotational lines. Two-photon transition strengths, $S(\Delta\Omega, J', J'')$ for diatomic molecules as a function of J', J'', Ω' and $\Omega''$is,

$$S(\Delta\Omega, J', J'') = s_0\mu_0^2 + s_2\mu_2^2 \quad (17)$$

where s_0 and s_2 are zeroth order and second order Clebsch-Gordon (CG) coefficients, respectively. μ_0^2 and μ_2^2 are sum and product functions of transition dipole moments.[110-111]

Table 2.2 *Two-photon transition strengths for transitions from a Σ state (Ω″ = 0).*

	$\Omega' = 0$ (Σ)		$\Omega' = 1$ (Π)	$\Omega' = 2$ (Δ)
	s_0	s_2	s_2	s_2
O	0	$\frac{1\,J(J-1)}{30(2J-1)}$	$\frac{1\,J(J-1)}{15(2J-1)}$	$\frac{1\,(J-2)\,(J-3)}{30(2J-1)}$
P	0	$J''\geq 2; J'\geq 0$ 0	$J''\geq 3; J'\geq 1$ $\frac{1}{30}(J+1)$	$J''\geq 4; J'\geq 2$ $\frac{1}{15}(J-2)$
Q	$\frac{1}{9}(2J+1)$	$\frac{1\,(J+1)(2J+1)}{45(2J-1)(2J+3)}$	$J''\geq 2; J'\geq 1$ $\frac{1\,(2J+1)}{10(2J-1)(2J+3)}$	$J''\geq 3; J'\geq 2$ $\frac{1\,(J+1)(J-1)(2J+1)}{5(2J-1)(2J+3)}$
R	$J''\geq 0; J'\geq 0$ 0	$J''\geq 1; J'\geq 1$ 0	$J''\geq 1; J'\geq 1$ $\frac{1}{3}J$	$J''\geq 2; J'\geq 2$ $\frac{1}{15}(J+3)$
S	0	$\frac{1\,(J+1)(J+2)}{30(2J+3)}$	$J''\geq 0; J'\geq 1$ $\frac{1\,(J+1)(J+3)}{15(2J+3)}$	$J''\geq 1; J'\geq 2$ $\frac{1\,(J+3)(J+4)}{30(2J+3)}$
		$J''\geq 0; J'\geq 2$	$J''\geq 0; J'\geq 2$	$J''\geq 0; J'\geq 2$

2.4.4 Relative rotational line strength

By combining the various factors (see above) which affect rotational line strengths the following expression is derived for the relative line intensities:

$$I_{rel} = C(v',\ v'')S(\Delta\Omega, J', J'')N_{J'',\,v''} \tag{18}$$

where $C(v',\ v'')$ is a factor, independent of *J'* and *J''*, which can be further expressed as:

$$C(v',\ v'') = Kq(v',\ v'')P^n \tag{19}$$

where *K* depends on the electron configuration of the molecule, *P* is the laser power and *n* is the number of photons involved in the excitation process.

2.5 State interactions; Diatomic molecules

2.5.1 State interactions and perturbations

State to state interactions are shown as the spectra perturbations, such as line-shifts (LS-effect), line-intensity (LI-effect), and/or line-width (LW-effect) alterations. The interactions are classified as electrostatic, vibrational, rotational, and spin-orbit interactions or couplings. Selection rules are listed in Table 3.

Table 2.3 *State interactions and selection rules.*

Operator	Interactions	Selection rules including ΔJ = 0			
		ΔΛ	ΔΣ	ΔS	ΔΩ
$\mathbf{H}^{el}$	Electronic (homogeneous)	0	0	0	0
$\mathbf{T}^{N}$	Vibrational (homogeneous)	0	0	0	0
$\mathbf{H}^{so}$	Spin-orbit (homogeneous)	0, ±1	0, ±1	0, ±1	0
$-\frac{\mathbf{1}}{\mathbf{2\mu R^2}}\mathbf{JL}$	L-uncoupling (heterogeneous)	±1	0	0	±1
$-\frac{\mathbf{1}}{\mathbf{2\mu R^2}}\mathbf{JS}$	S-uncoupling (heterogeneous)	0	±1	0	±1

2.5.2 Line shifts / LS-effect

Interactions between states typically show irregularities in rotational line positions due to rotational energy level shifts (LS-effects).[45] This is demonstrated in Fig. 2.4:

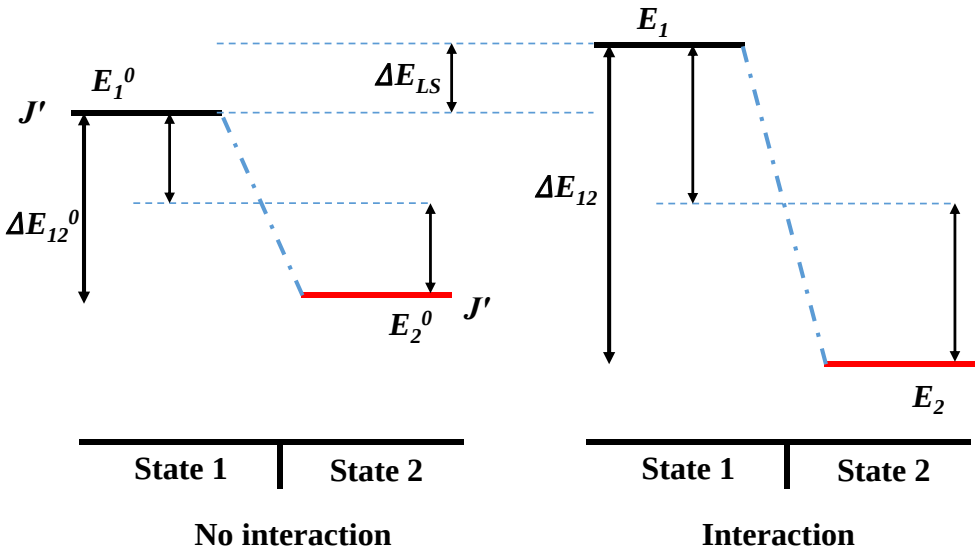

Figure 2.4 *Schematic diagram of line shifts due to two state interaction*

The interaction strength for two states (1) and (2) (W_{12}) can be evaluated from (see Fig. 2.4),

$$\Delta E_{LS} = \frac{1}{2}(\Delta E_{12} - \sqrt{(\Delta E_{12}) - 4|W_2|^2}) \tag{20}$$

2.5.3 Line intensity / LI-effect

Line intensities[45] for two-state (1 and 2) interactions are based on the corresponding perturbed wavefunctions ψ_1 and ψ_2, which depend on the unperturbed wavefunctions $\psi_1{}^0$ and $\psi_2{}^0$ as,

$$|\psi_1\rangle = c_1|\psi_1{}^0\rangle - c_2|\psi_2{}^0\rangle \tag{21}$$

$$|\psi_2\rangle = c_1|\psi_1{}^0\rangle + c_2|\psi_2{}^0\rangle \tag{22}$$

for the weight factors (see Fig. 2.4)

$$c_i{}^2 = \frac{1}{2} \pm \frac{\sqrt{|\Delta E_{12}|^2 - 4|W_2|^2}}{2|\Delta E_{12}|} \tag{23}$$

For the hydrogen halides (HX, X = Cl, Br, I), the X^+ intensities in REMPI via Rydberg states (HX**), which are interacting with ion-pair states (H^+X^-) are found to be proportional to the fraction of *HX*** molecules in the state mixing,

$$I(X^+) = \alpha_2 c_1{}^2 + \beta_1 c_2{}^2 \tag{24}$$

and the HX^+ intensity is,

$$I(HX^+) = \alpha_1 c_1{}^2 + \beta_2 c_2{}^2 \tag{25}$$

where $c_1{}^2 + c_1{}^2 = 1$. For $\alpha = \alpha_2/\alpha_1$; $\gamma = \beta_1/\alpha_2$; $\delta = 1 - (\beta_2/\alpha_1)$, the intensities ratio can be simplified as:

$$\frac{I(X^+)}{I(HX^+)} = \alpha \frac{(\gamma + c_2{}^2(1-\gamma)}{1-\delta c_2{}^2} \tag{26}$$

where the α factor measures the relative rate of the main formation channel of X^+ from states 2 (α_2) to state 1 (α_1), and the multiplicative factor $\alpha\gamma = \beta_1/\alpha_1$, measures the relative contributions to the X^+ formation and HX^+ formation from state 1.

2.5.4 Line width /LW-effect

Line widths (LI-effects)[45], can be related to lifetimes, which are strongly influenced by state-to-state interactions. In these cases the lower limit of lifetimes (τ_{min}) can be derived from the line-widths (Γ):

$$\tau_{min}(ps) = 5.3/\Gamma(cm^{-1}) \tag{27}$$

3 Experimental and analyses methods

Our two-color REMPI-TOF system includes two pump-laser sources, two dye lasers, two second harmonic generators (SHG), a pulse generator, a gas injecting system, a vacuum chamber with an MCP detector, and a storage oscilloscope. A schematic figure is shown in Figure 3.1.

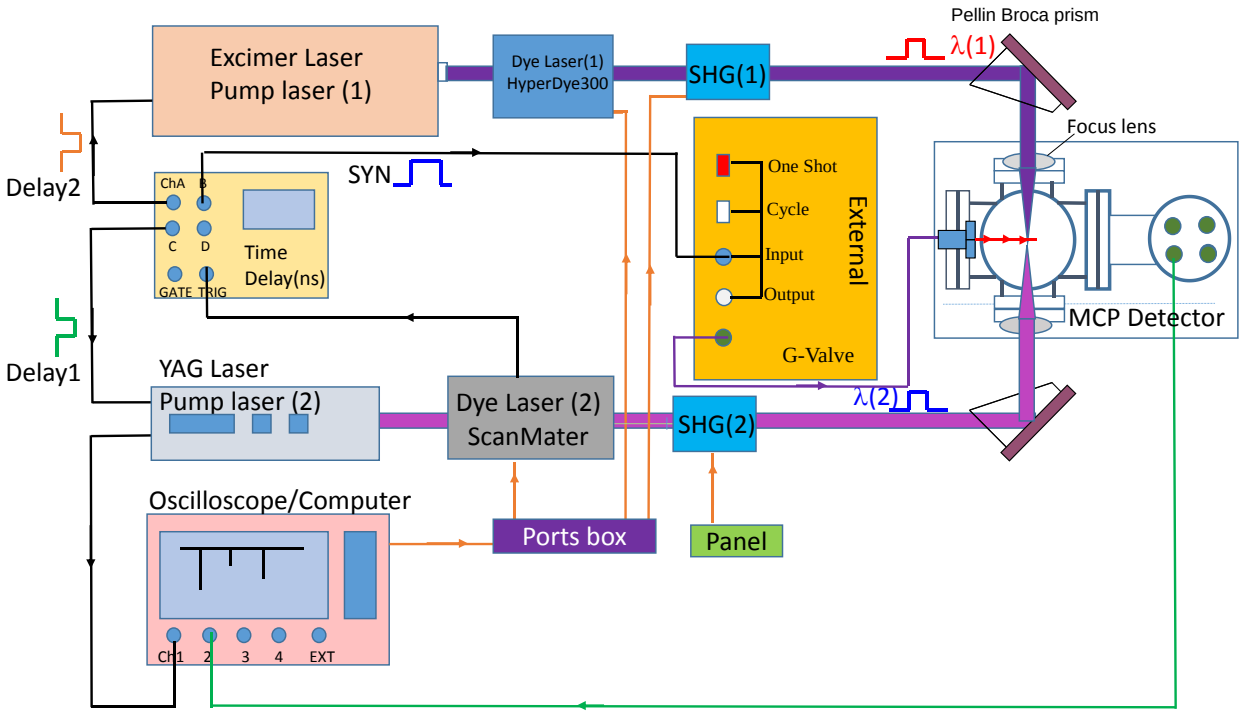

Figure 3.1 *Schematic figure of our two color REMPI−TOF system.*

3.1 Laser systems

Ultraviolet and visible laser beams were generated by pumped dye lasers and focused into SHG to create frequency-doubled radiation. The lasers and relevant parameters are listed in Table 3.1

Table 3.1 *Lasers and relevant parameters*

	Pump lasers		Dye lasers	
Name	Compex 205	NL300Serise	Scanmatepro	HyperDYE-300
Manufacturer	Lambda Physics	Nd:YAG EKSPLA	Lambda Physics	Lumonics

Wavelength(nm)	308	1064/532/355	320-1100	320-950
Repetition (Hz)	10	10	10	10
Bandwidth(cm^{-1})	-	-	0.095	0.06
Max.Pulse energy(mJ)	400	800/380/250	250	-
Resolution(cm^{-1})	-	-	0.1	0.1
Pulse duration (ns)	20	3-6	2-50	2 less than pump pulse

3.1.1 Excimer laser

The laser beam from an excimer laser originates from an excimer[110-113] (shortening for "excited dimer"): The excited state of an excimer, AB, is a bound state, while the ground state is a dissociative/repulsive state. A schematic representation of relevant energetics and energy transitions is shown in Figure 3.2.

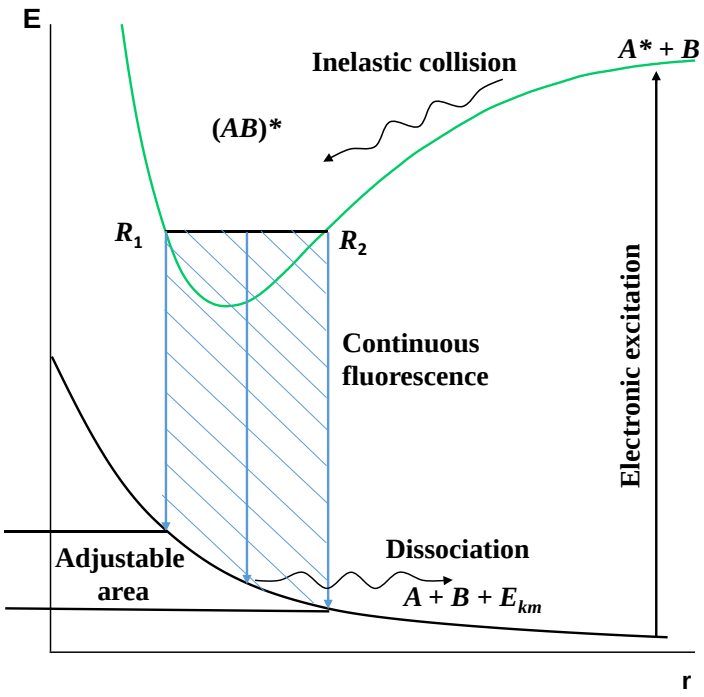

Figure 3.2 *Schematic figure of excimer energies and energy transfers.*

In the case of the XeCl excimer laser (which we used), the laser cavity contains a gas mixture of Xe, HCl, He, and Ne. The major excimer (XeCl*) formation reactions occurring are the following;

$$Xe + e^- \rightarrow Xe^* + e^- \text{ or } Xe^+ + 2e^- \quad (28)$$

$$Xe^* + Cl_2 \rightarrow XeCl^* + Cl \quad (29)$$

$$Xe^* + HCl \rightarrow XeCl^* + H \quad (30)$$

$$Xe^{+} + Cl^{-} + M \rightarrow XeCl^{*} + M \quad (31)$$

Followed by stimulated emission to give laser pulses of about 10^{-8}~10^{-9} s (1 – 10 ns)

3.1.2 Nd:YAG laser

Nd:YAG[114-115](neodymium-doped yttrium aluminum garnet; Nd:$Y_3Al_5O_{12}$) is a solid crystal used as a laser medium. The dopant, triply ionized neodymium, Nd(III) plays an essential role in providing the laser activity in the crystal, typically providing a laser beam of the wavelength 1064 nm.

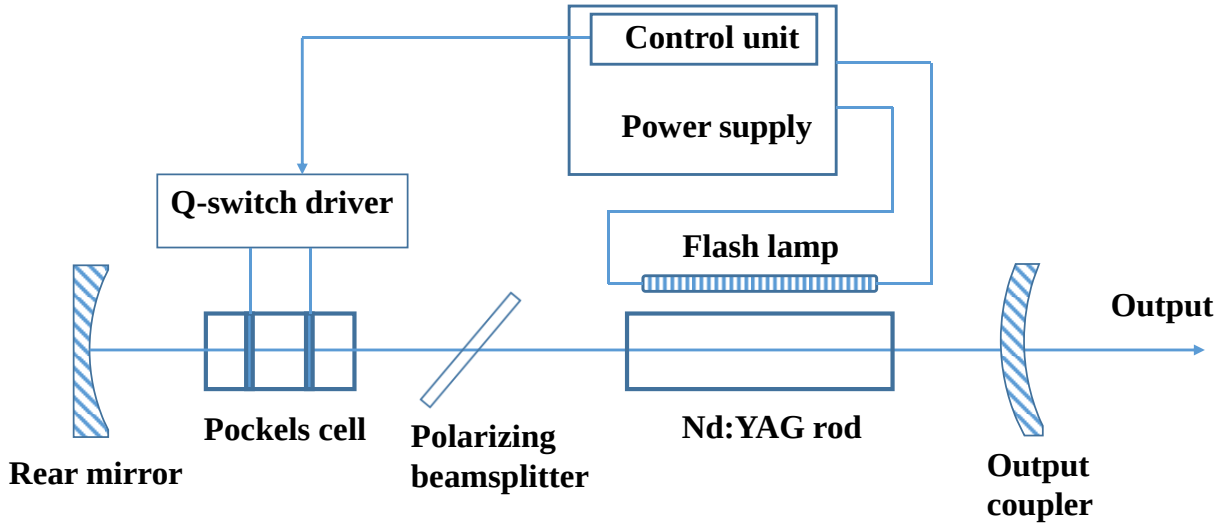

Figure 3.3 *Schematic figure of the NL300 series laser head.*

Q-switching is performed by a pockels cell (PC, voltage-controlled wave plates) to induce considerable steady losses in the resonator. While high PC voltage is present, $t < t_0$, Q-switching is closed, and no generation occurs. When the high voltage is off, $t > t_0$, losses in the resonator are minimized to generate a laser pulse.

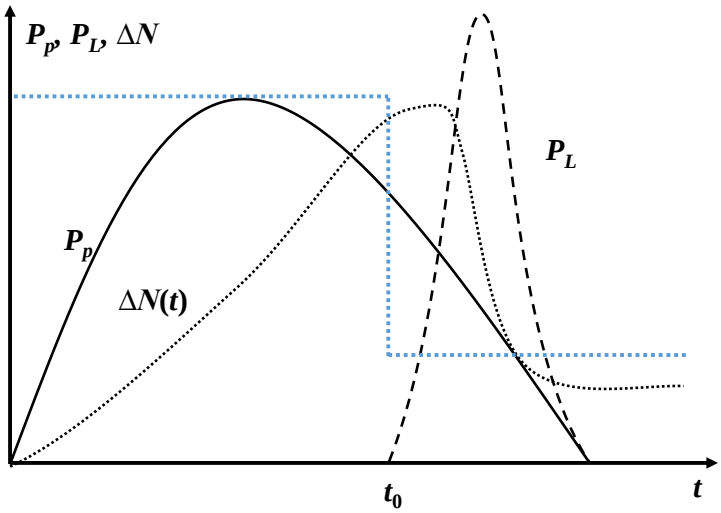

Figure 3.4 *Relationship between the pump power $P_p(t)$, inversed population density $\Delta N(t)$ and laser output power $P_L(t)$ for a Q-switched Nd:YAG laser.*

3.1.3 Dye laser

The dye lasers use liquid solutions of organic dyes as the lasing media to produce tunable laser beams for a wide range of wavelengths. Typically, a dye laser is pumped by a pump laser source to create radiate from dye within its fluorescence spectral region.

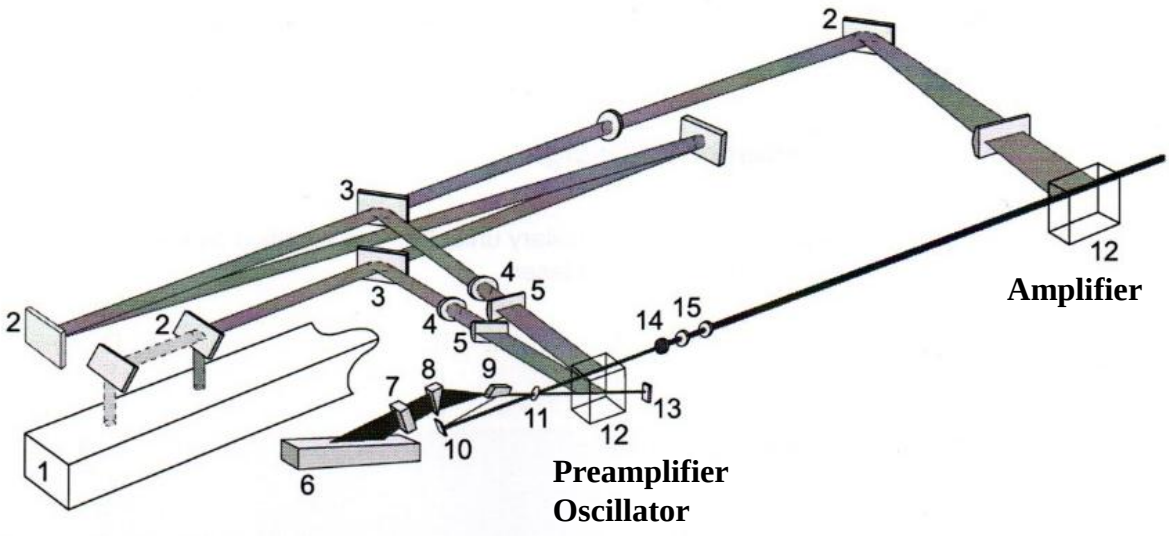

Figure 3.5 *Optical layout of the pumped ScanMate Pro dye laser: 1, Nd:YAG laser; 2, Mirror; 3,Beamsplitter; 4, Cylindrical lens (expansion); 5, Cylindrical lens (focusing); 6,Grating; 7,Intracavity etalon; 8,Beam expander; 9,Lambda Super Pure outcoupling; 10,folding mirror; 11,Brewster window; 12,Dye cell; 13,End Mirror; 14,Pinhole; 15,Telescope.*

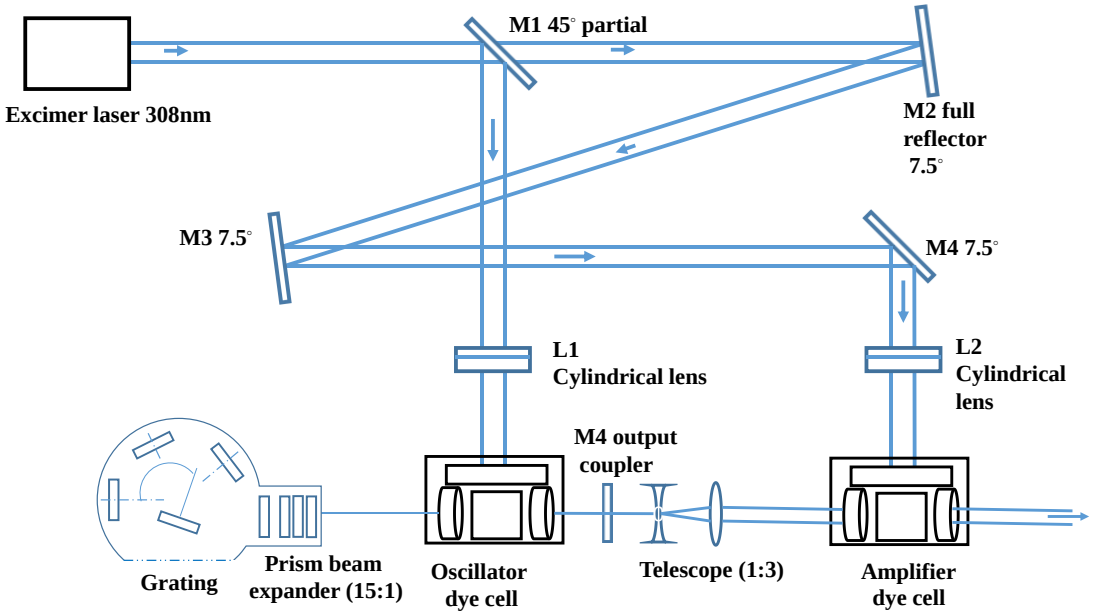

Figure 3.6 *Schematic figure of the excimer laser pumped Hyperdye-300 dye laser*

3.1.4 Second harmonic generator (SHG)

The frequency conversion / second harmonic generation (SHG) is a nonlinear process. A schematic description of a harmonic generator is shown in Figure 3.7. Briefly, a polarized laser beam from a dye laser enters a nonlinear crystal (BBO or KDP crystals; see Table 3.1) which produces an additional polarized beam, twice the frequency / half the wavelength of the original one. After that, suitable optical components are used to improve beam's quality and separate the two beams.

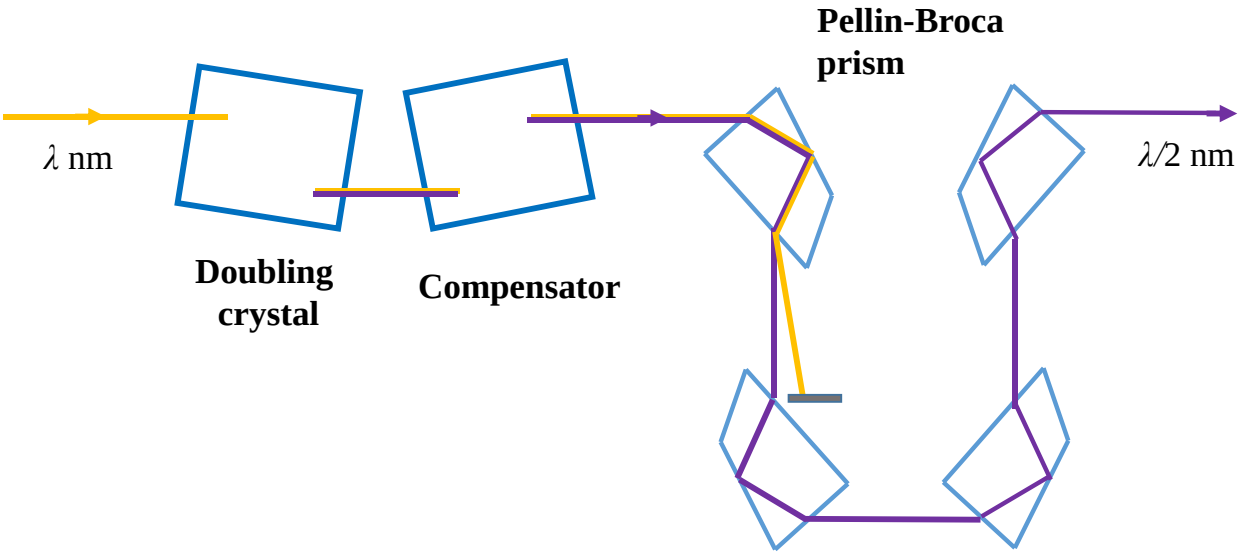

Figure 3.7 *Optical scheme of a SHG. The compensator is used to compensate the angle and the linear shift of the frequency-doubled beam. Pellin-Broca prisms are used to separate the frequency-doubled and original beams and to compensate the angle and the linear shift of the frequency-doubled beam.*

Table 3.2 *Crystals used for frequency doubling by a SHG in our laboratory: Beta Barium Borate Crystal (BBO) and Potassium dideuterium phosphate (KDP) crystals.*

Name	Material	Cut angle	Use
SHG-280	BBO	34°	SHG 280-450nm
SHG-215	BBO	57.4°	SHG 215-280nm
KDP	KDP	-	SHG 260-400nm

3.2 MR-REMPI

The mass-resolved REMPI (MR-REMPI) experiments involved 1) sample/molecular beam preparation by use of a pulsed nozzle, 2) multiphoton-fragmentation by focused laser pulses (one- or two-colors/laser beams), 3) ion-separation by acceleration and time-of-flight

separation and 4) detection by microchannel plates (MCPs) in a vacuum system (see Fig. 3.8).

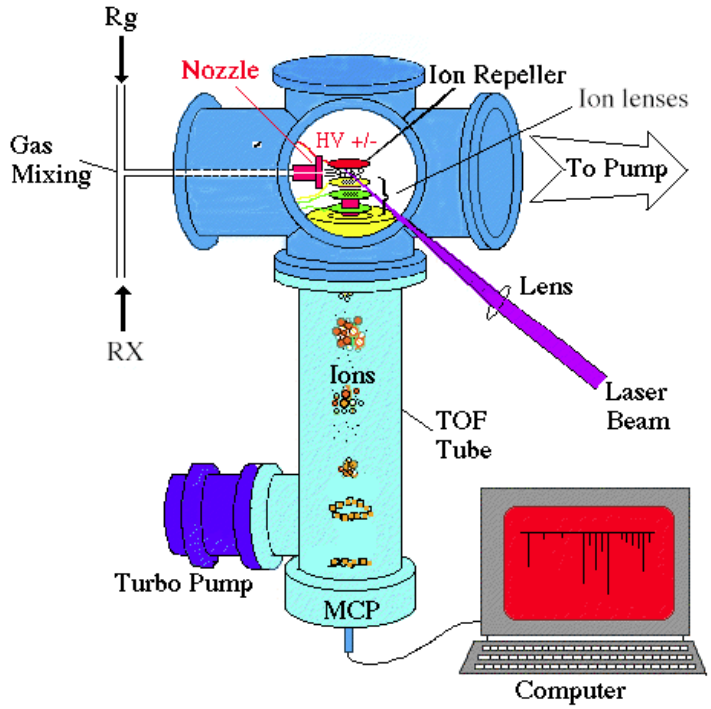

Figure 3.8 *Schematic configuration of the MR-detector system for one-color experiments.*

3.2.1 Ion acceleration

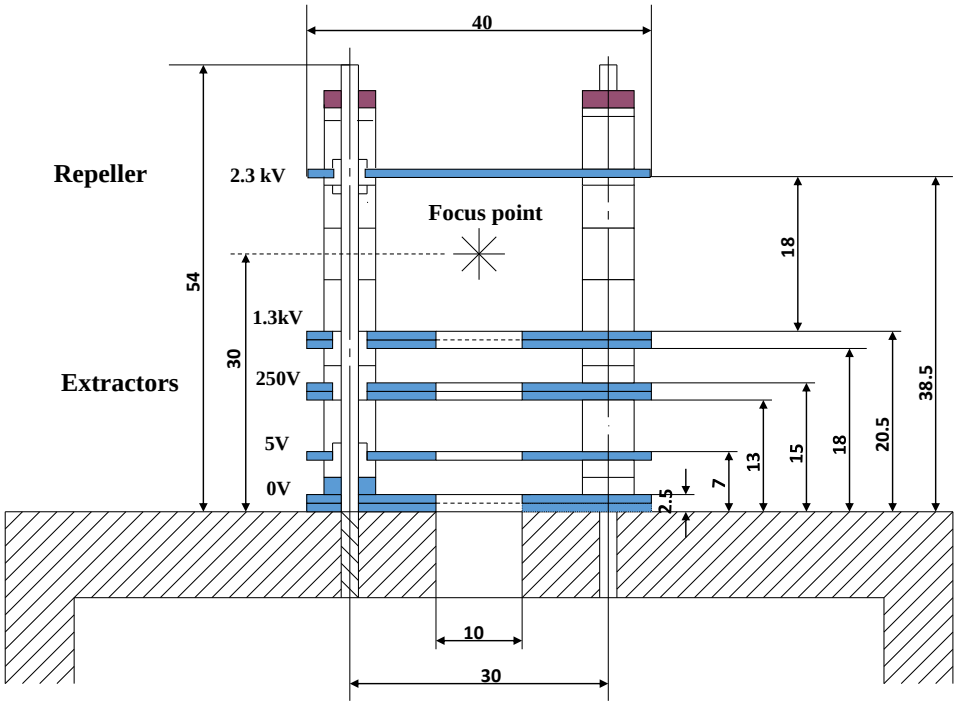

Figure 3.9 *Schematic diagram of the electrodes in the ion acceleration region*

A repeller at a high positive voltage and a series of extractors and electronic lenses at lower voltages (see Fig. 3.9) were used to direct e ions into a time-of-flight mass spectrometer onto the MCP detector.

3.2.2 Sample preparation

An electromagnetic pulse nozzle was used to create gas pulses (see Fig. 3.10). The nozzle diameter used is about 500 μm. The backing pressure of the gas sample was typically about 2 bar. Laser pulses were typically delayed about 450 - 550 μs refers to the gas pulse to guarantee maximum signals. The repetition rate of the gas and laser pulses was typically kept at 10 Hz.

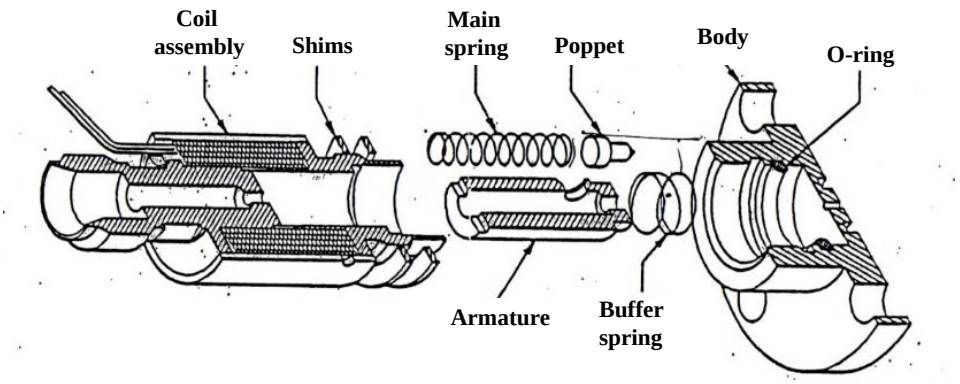

Figure 3.10 *Schematic diagram of the electromagnetic pulse nozzle, dis-assembled (Parker Hannifin corporation, General valve division)*

3.2.3 Microchannel Plate (MCP) detector

The MCP[116] detector is an open detector with two microchannel plates and a single metal anode (see Fig. 3.11). The microchannel surface has a significant secondary emission coefficient for electrons. Typically, for an electric field of 500V/mm, the magnification factor is about 10^3. For two tandem plates, the magnification factor could become about10^6.

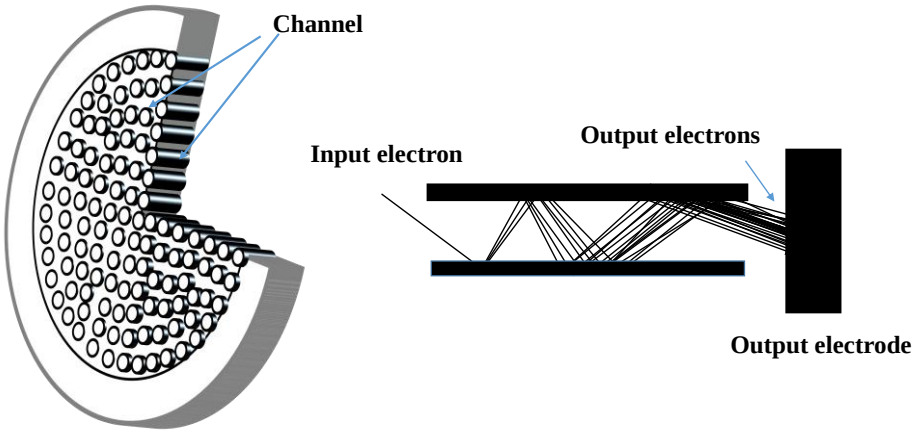

Figure 3.11 *Schematic figures relevant to the MCP detector.*

3.2.4 Time-of-flight (TOF) mass spectrometer (MS).

Our TOF-MS consisted of a 75 cm long vacuum-pumped, field-free steel tube. The flight time of ions in the TOF tube is proportional to the square root of the ion masses. Thus, the ion masses (Mw) were determined by the approximated expression:

$$t_{TOF} = a\sqrt{M_w} + b \tag{32}$$

for constants a and b.

3.3 Equipment control pulse sequences

During experiments, the devices are controlled by a sequence of electric pulses starting by triggering pulses from the dye laser (Scanmate pro) (see Fig. 3.12) using the LabVIEW program.

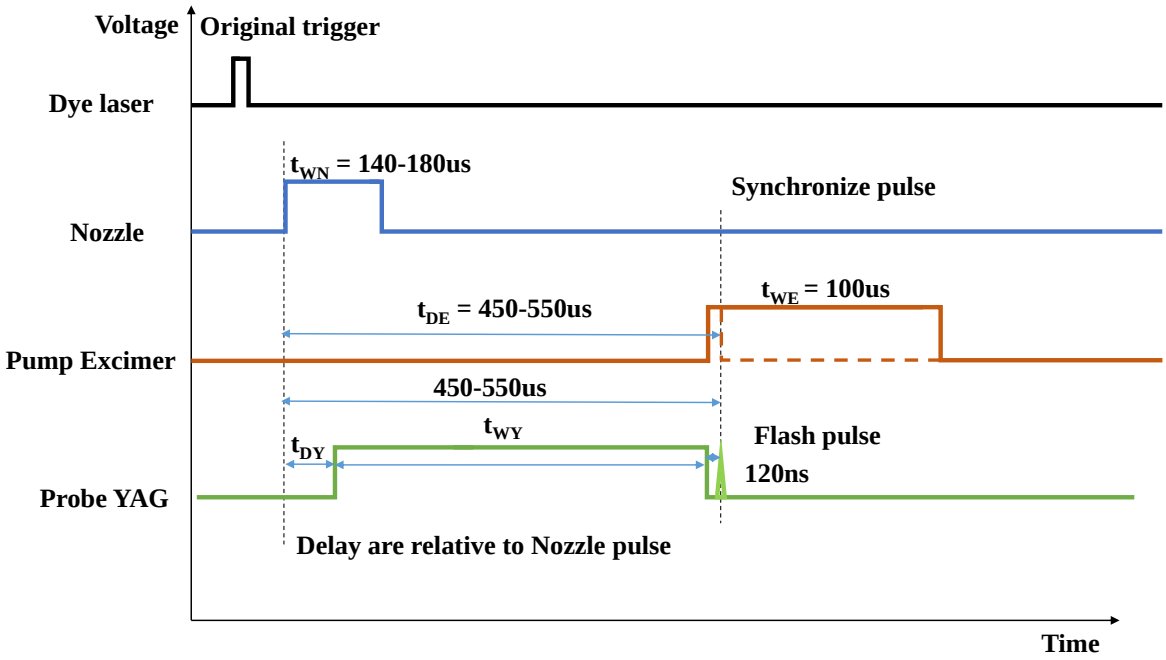

Figure 3.12 *The equipment control pulse sequence.*

At the beginning of a sequence, a command is sent to the dye laser to create a trigger pule. The trigger pulse is fed into a pulse generator which distributes pulses into different channels for the nozzle, the excimer laser, and the YAG laser. A pulse $\mathbf{t_{WN}}$ controls the nozzle opening duration, typically about 140-180 us. The delay time ($\mathbf{t_{DE}}$) for the excimer laser pulse was about 450-550 us after the nozzle pulse. $\mathbf{t_{WE}}$ is the duration of the excimer laser pulse. The duration ($\mathbf{t_{WY}}$) of the Nd:YAG laser control pulse is designated to control the output energy of the laser beam. The Nd:YAG laser pulse typically appeared about 120ns after the end of

the control pulse. Thus, the delay time (t_{DY}) of Nd:YAG laser pulse relative to the nozzle pulse is also determined by Nd:YAG laser's pulse duration (t_{WY}). The sum of t_{DY}, t_{WY}, and the additional 120 ns equals t_{DE}.

3.4 Data analysis

In one-color REMPI, photoexcitation and ionization of molecules occur by the same laser wavelength, whereas by adding a delayed second laser wavelength, two-color REMPI allows the detection of specific fragment species (see Fig. 3.13). This system is often called pump-probe detection, where the pump laser creates causes photodissociation and the probe laser ionizes fragment species.

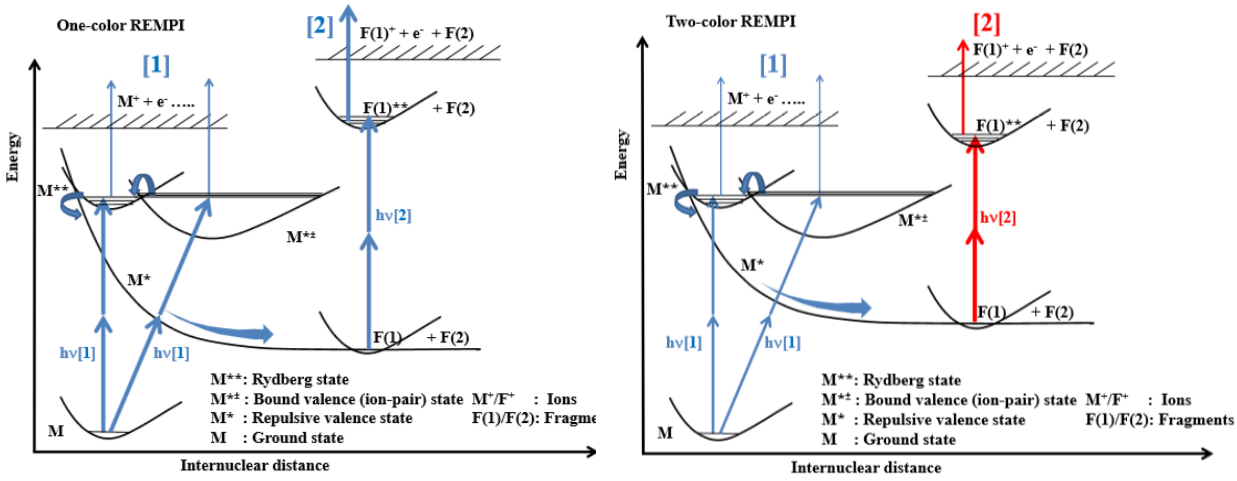

Figure 3.13 *Schematic representation of the energetics and excitation processes for one- (left) and two- (right) color REMPI.*

Ion signals were recorded by a LeCroy 44MXs-A 400 MHz digital oscilloscope. Mass and REMPI spectra were derived from the raw data by using the Igor Pro.v.6[117]data analysis software and REMPI spectra simulations were performed by use of the PGOPHER v9.0[118] program.

3.4.1 Mass and REMPI spectra

A mass spectrum shows ion intensities as a function of the mass (M/z Units: amu) as determined by the equation given in section 3.2.4. Figure 3. 14 shows mass spectra derived for CH_3Br for two-color REMPI (two-photon pump wavenumber 72 944 cm^{-1} / probe wavenumber 74 991.4 cm^{-1}). REMPI spectra of particular ions show ion intensities as a function of either the pump or the probe excitation wavenumber. Figure 3.15 shows the CH_3^+ REMPI spectrum created by pumping CH_3Br by the wavelength 240 nm (41 666 cm^{-1}) and by scanning the probe laser over the two-photon excitation region of 59 706 to 60 159 cm^{-1} to give a CH_3 REMPI spectrum due to the two-photon resonant excitation from $CH_3(X)$ to the CH_3 ($3p^2A_2''$ (000)) Rydberg state (two-color REMPI). Figure 3.16 shows mass-resolved REMPI spectra of the HI molecule for two-photon resonant excitations in the region of 74 640 – 74 940 cm^{-1} (one color REMPI).

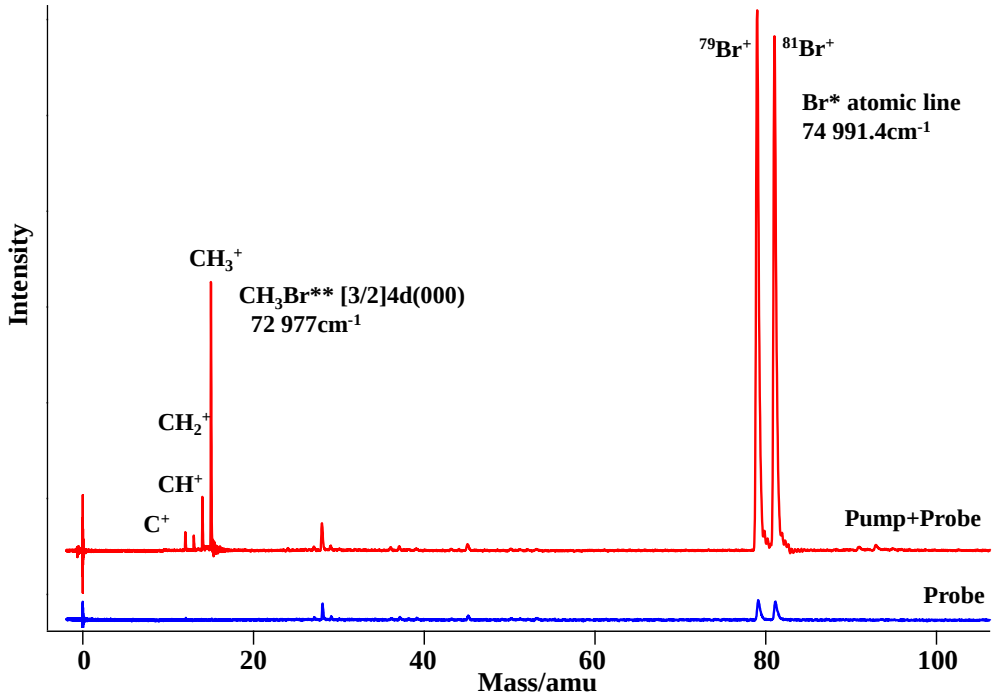

Figure 3.14 *CH_3Br: Mass spectra for two-photon 72 944cm^{-1}pumping laser and two-photon 74 991.4 cm^{-1} resonant probing of Br* atom(red)and two-photon 74 991.4 cm^{-1} probing of Br* only (blue).*

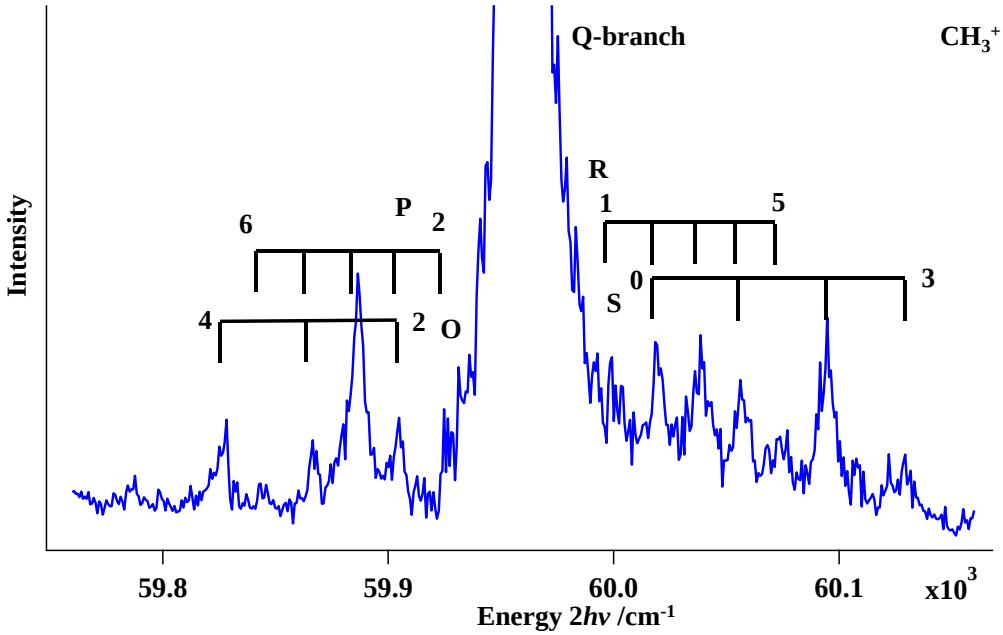

Figure 3.15 *CH_3Br: CH_3^+ REMPI spectrum due to two-photon resonant transition of $CH_3(X)$ to the CH_3 $3p^2A_2''$ (000) Rydberg state (pump: 240 nm; probe laser scanning).*

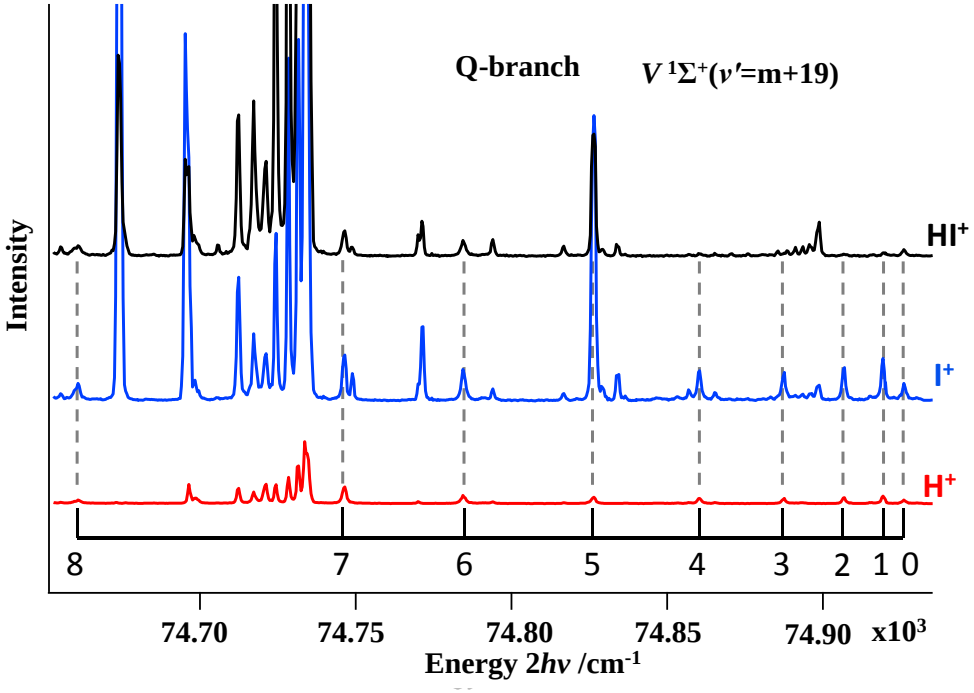

Figure 3.16 *MR-REMPI spectra for HI due to two-photon resonant transitions in the region of 74 640 – 74 940 cm^{-1}. HI$^+$ ions (top; black), I$^+$ ions (middle; blue), H$^+$ ions (bottom; red) H$^+$ ion. Spectra due to transitions from HI(X) to the V$^1\Sigma^+$(v′=m+19) ion-pair state is seen.*

3.4.2 Spectra simulations

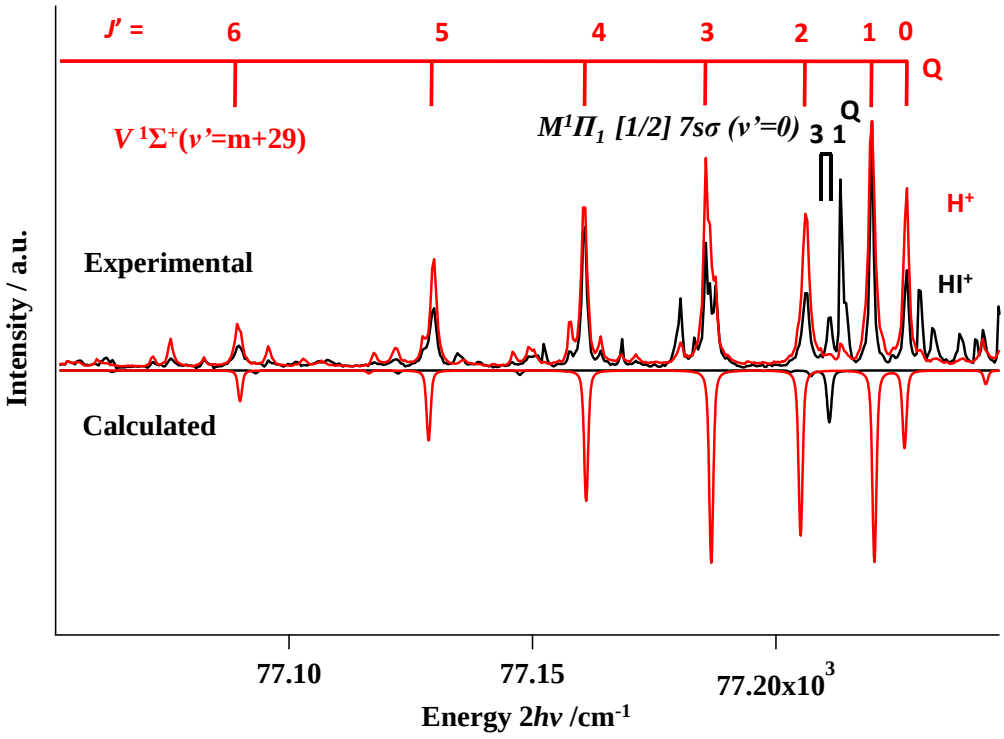

Figure 3.17 *Spectral simulation: Simulation by PGOPHER of a REMPI spectra due to two-photon resonant excitation to the $M^1\Pi_1$ [1/2] 7sσ (v′=0) Rydberg state and V $^1\Sigma^+$(v′=m+29) ion-pair state of HI.*

Simulations of REMPI spectra were performed by using the PGOPHER v9.0 program.[117] The simulations typically allow the determination of band origins, first- and second-order rotational constants (B and D, respectively), and spin-orbit and lambda doubling constants for excited states of linear molecules. A deviation from regular patterns of spectra structures, i.e., a spectral perturbation, indicates state interaction. An example of a simulation of a spectrum showing the effects of near-degenerate perturbation (see definition above; from paper no.5) is shown in Figure 3.17: Perturbation due to state interaction between the $M^1\Pi_1$ [1/2] 7sσ (v'=0) Rydberg state and the V $^1\Sigma^+$(v'= m + 29) ion-pair state of HI shows irregular line intensities for transitions to rotational level J′= 3. Perturbation analysis of such spectra can reveal state interaction strengths (see above) (from paper No.5).

3.5 Velocity map Imaging (VMI)

By using a charge-coupled device (CCD) camera behind MCP plates coupled with a position-sensitive detector, images showing spatial ion intensities distributions around spheres can be recorded (i.e., velocity map imaging (VMI)). These can be useful for further understanding molecular photofragmentation processes.

A schematic figure relevant to VMI in association with REMPI (VMI-REMPI) is shown in Figure 3.18. The significant differences to that in MR-REMPI characteristics are 1) the supersonic molecular beam is directed toward the detector, and 2) the laser beam polarization is in a plane parallel to the detector plane. The detector used here is constructed of MCP plates coupled with a phosphor screen followed by a CCD camera.

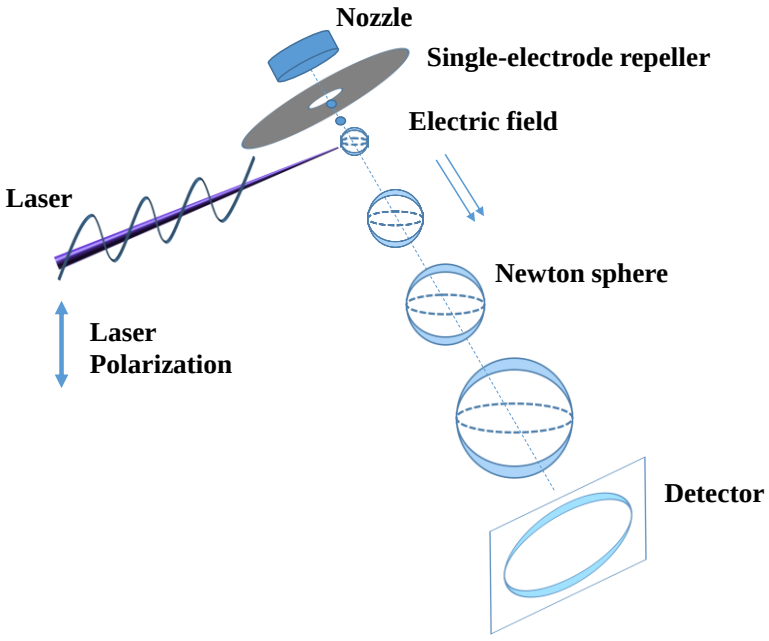

Figure 3.18 *Schematic representation of a VMI-REMPI apparatus.*

Raw images are processed to derive intensity distributions as a function of the distance from the detector center (Abel transformation) (see Fig. 3.19). From the processed images, the following can be derived: 1) kinetic energy release (KER) of ions corresponding to detected photo-fragments (see Fig. 3.20 (a)) and 2) angular distributions, which describes the spatial distribution of ions relative to the polarization direction of the laser beam (see Fig. 3.20 (b)).

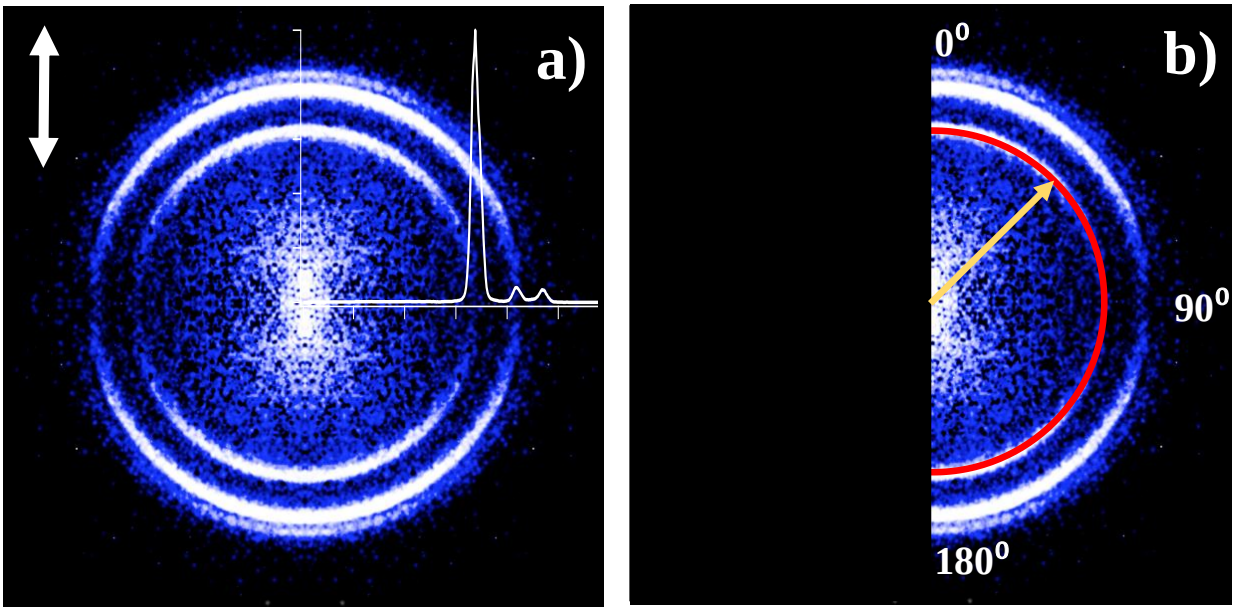

Figure 3.19 *VMI-REMPI of CH_3I: a) Velocity map image for the CH_3^+ ion following CH_3I two-photon excitation at 69 783 cm^{-1}(from paper No.5). Ion intensity increases from blue to white. b) Half image of CH_3^+. The red line indicates ions formed with same recoil velocities, i.e. for the same radius from the centre of the image. The double headed arrow in (a) indicates the linear polarization of the laser.*

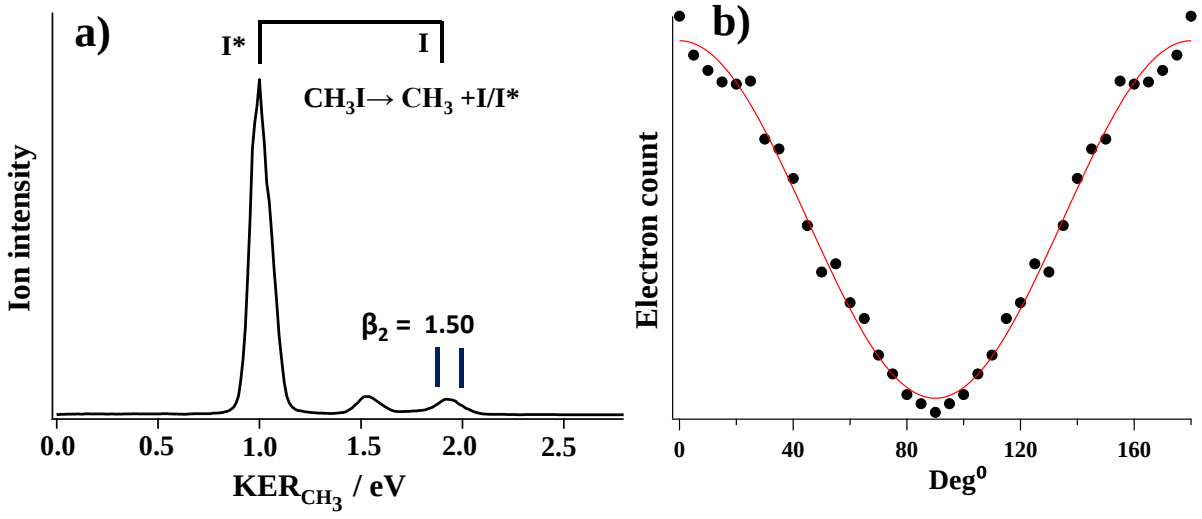

Figure 3.20 *Data derived from VMI-REMPI; CH_3I: a) KER spectrum for two-photon excitation 69 783 cm^{-1}. Assignments for KER peaks are labeled on top. b) Angular distribution for the ring which corresponds to the KER peak near 2.0 eV in (a). The KER*

range for the angular distribution in (b) and the anisotropy parameter β_2 derived are indicated in fig. (a).

KER spectra extracted from images are initially stored as functions of pixels (pix) / integer numbers (KER (pix)) which are converted to electron volts (eV) to give KER (eV) according to the relationship,

$$KER(eV) = KER(pix)^2 * f \tag{36}$$

where *f* is a calibration factor depending on the TOF distance.

Information about dissociation energies relevant to different photodissociation channels of molecules is important to be able to assign KER spectra. Thus, for instance, in Figure 3.20 (a), the one-photon dissociation of CH_3I to create the CH_3+I/I* is identified from the relationship:

$$KER(CH_3 + I/I^*) = h\nu - D_0(CH_3I) - E(CH_3) - E(I/I^*) \tag{37}$$

where $h\nu$ is the photon energy, $D_0(CH_3I)$ is the bond energy for CH_3-I and $E(CH_3)$, and $E(I/I^*)$ are the internal energies of the fragments, respectively.

The angular distributions are extracted from the ion images over an angle range (typically from θ = 0° to 180°) for a specified radius range (see Fig. 3.20 (a) and (b)). The following expression is fitted to the angular distributions to derive anisotropy parameters,

$$P(\theta) = A[1 + \beta_2 P_2(\cos(\theta) + \beta_4 P_4(\cos(\theta) + \beta_6 P_6(\cos(\theta)] \tag{38}$$

where A is a normalizing constant, β_2, β_4, β_6 are the anisotropy parameters and P_2, P_4, P_6 are Legendre polynomials. The acquired β_2 parameters are in the range +2 (solely parallel transition) and -1 (solely perpendicular transition). β_2 = 0 corresponds to isotropic distribution.

4 Included papers

1. Arnar Hafliðason, Meng-Xu Jiang and Ágúst Kvaran, *High energy Rydberg and ion-pair states, state mixing and excitation dynamics of HI, Phys. Chem. Chem. Phys* (PCCP), **21,** p: 23154 - 23161, **(2019).**
1.1. Supporting information

2. Kristján Matthíasson, Greta Koumrianou, Meng-Xu Jiang, Pavle Glodic, Peter C. Samartzis and Ágúst Kvaran, *Formation of highly excited iodine atoms from multiphoton excitation of CH_3I, Phys. Chem. Chem. Phys* (PCCP), **22**, p: 4984 - 4992, **(2020)**.
2.1. Supporting information

3. Meng-Xu Jiang, Arnar Hafliðason and Ágúst Kvaran, *Addition to and revision of the HI Rydberg states energy region*, *J. Molecular Spectroscopy*, **372**C, p:111329, **(2020**).
3.1. Supporting information

4. Arnar Hafliðason, Meng-Xu Jiang and Ágúst Kvaran, *Photo and autoionization processes of superexcited iodine atoms in MPI of CH_3I and HI, Chem. Phys*, **541**, p: 111016, **(2021)**.
4.1. Supporting information

5. Meng-Xu Jiang and Ágúst Kvaran, *High energy state interactions, energetics and multiphoto-fragmentation processes of HI, Phys. Chem. Chem. Phys* (PCCP)**, 24**, 6676 - 6689, (**2022**).
5.1. Supporting information

6. Meng-Xu Jiang, Giannis Giannakidis, Peter C. Samartzis and Ágúst Kvaran, *Multiphoton breakdown of acetylene; Formation of organic building block fragments (**Accepted for publication in PCCP**)*
6.1. Supporting information

4.1 Paper 1

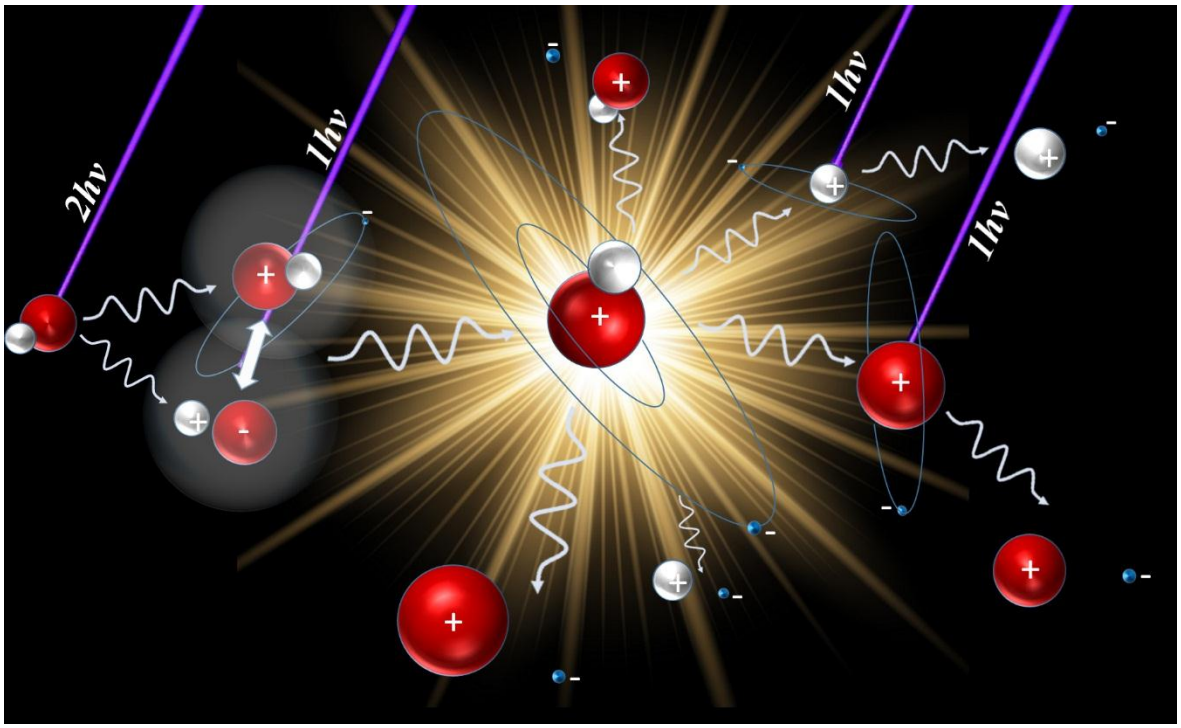

Arnar Hafliðason, Meng-Xu Jiang and Ágúst Kvaran, *High energy Rydberg and ion-pair states, state mixing and excitation dynamics of HI*, Physical Chemistry *Chem.Phys* (PCCP), **21,** p: 23154 - 23161, **(2019).**

DOI: 10.1039/C9CP04872C

PCCP

PAPER

Cite this: *Phys. Chem. Chem. Phys.*, 2019, **21**, 23154

High energy Rydberg and ion-pair states, state mixing and excitation dynamics of HI†

Arnar Hafliðason, ‡ Meng-Xu Jiang ‡ and Ágúst Kvaran *

Received 2nd September 2019,
Accepted 8th October 2019

DOI: 10.1039/c9cp04872c

rsc.li/pccp

Mass resolved multiphoton ionization data for two-photon resonant excitations (REMPI) in the region of 74 000–75 000 cm^{-1} were recorded for HI. Spectra structures of fragment and molecular ions derived from the data were analyzed to derive information relevant to the energetics and state mixing of ion-pair and Rydberg resonance states as well as for the excitation dynamics. Four new ion-pair vibrational states ($V^1\Sigma^+(v' = m + i)$; i = 16–19) and two Rydberg states ($j^3\Sigma^-(0^+; v' = 1)$ and $N^1\Pi_1(v' = 2)$) were identified and characterized. Spectral perturbations allowed characterization and quantization of both homogeneous and heterogeneous state interactions and mixing of the Rydberg states and ion-pair states. Intensity alterations, with respect to energy level excitations and ion masses, are found to be clear indications of state mixing as well as branching into different fragmentation (both photodissociation and photoionization) channels.

I. Introduction

It is convenient to divide molecular energy into three major regions depending on the characteristics of the dominant electronic states involved, *i.e.* the ground, valence and Rydberg state regions. The density of states increases with energy to allow gradual enhancement in state interactions and, therefore, richer excitation dynamics. The Rydberg state region characteristically involves interactions between Rydberg and valence states as well as between different Rydberg states to allow intersystem crossing and/or (pre)dissociation processes to occur. Such processes are relevant to selective formation of reactive fragment species useful in photochemical synthesis, the understanding of atmospheric and interstellar photochemical reactions and mechanisms of plasma chemistry. High energy state interactions can be seen as spectral perturbations in the form of spectra line shifts and/or intensity anomalies. The hydrogen halides are ideal candidates for exploring such effects due to their heavy (halogen atoms) *vs.* light (hydrogen) fragment particle (hence low reduced mass) combination which generally results in easily resolvable rotational spectra structures and, therefore, relatively clear distinction between different perturbation effects.

Although less explored than the lower energy regions, significant amount of data has been collected relevant to the Rydberg state region of hydrogen iodide (HI). Large number of Rydberg states and ion-pair vibrational states (levels) have been characterized and assigned in absorption[1–3] and REMPI[4–10] for the excitation energy region of about 66 000–74 000 cm^{-1}. Photofragmentation processes have been explored by REMPI,[4–10] photoelectron spectra[11–15] and velocity map imaging (VMI)[16,17] studies. Rydberg to ion-pair state interactions have been seen as line shift and/or line intensity effects within rotational line series.[6–10] These effects have been interpreted as being due to energy level-to-level state interactions and mixing to a different degree, either due to strong homogeneous ($\Delta\Omega = 0$) or weak heterogeneous ($\Delta\Omega \neq 0$) state couplings. Such data as well as mass dependent intensity alterations in REMPI spectra have been found to be informative about photofragmentation processes.[9,10,18–22]

In this paper we extend the exploration region of Rydberg and ion-pair states and relevant interactions for HI to the energy-rich photoexcitation region of about 74 000–75 000 cm^{-1} for two-photon resonant excitations followed by photofragmentation (both photodissociation and photoionization) processes to form the fragment ions (H^+ and I^+) as well as the parent molecular ion (HI^+). The data allow identification of new Rydberg and ion-pair states and vibrational levels as well as a characterization of particularly clear homogeneous couplings as non-degenerate level interactions/mixing and heterogeneous couplings as near-degenerate level interactions/mixing between Rydberg and ion-pair states. State mixing is found to play an important role in excitation processes. Furthermore, we emphasize to demonstrate the usefulness of perturbation effects and signal intensities in understanding molecular excitation dynamics.

II. Experimental

The experimental apparatus and equipment parameters resemble that described in previous publications.[10,23,24] Mass resolved

Science Institute, University of Iceland, Dunhagi 3, 107 Reykjavík, Iceland. E-mail: arnarhaf@hi.is, mej7@hi.is, agust@hi.is; Fax: +354-552-8911; Tel: +354-525-4800

† Electronic supplementary information (ESI) available. See DOI: 10.1039/c9cp04872c

‡ Co-authors.

REMPI data for HI molecular beam were collected. A molecular beam was created by jet expansion of a diluted gas mixture of HI and argon (HI : Ar ~ 1 : 2) through a 500 μm pulsed nozzle with backing pressure of about 2.0–2.5 bar. Pressure inside the ionization chamber was about 10^{-6} mbar during experiments. The pulsed nozzle was kept open for about 140 μs and a laser excitation beam was typically fired 460 μs after its opening. The excitation radiation was generated by a Nd:YAG laser (EKSPLA NL300 Series, 355 nm) pumped Coherent ScanMatePro dye laser (C-540A dye) followed by a frequency doubling with a BBO crystal. The laser beam was focused on the molecular beam by a 200 mm quartz focal lens between a repeller and extractor plates. Ions were directed into a 70 cm long time-of-flight (TOF) tube and detected by a microchannel plate (MCP) detector to record the ion yield as a function of mass and laser radiation energy. Signals were fed into a LeCroy WaveSurfer 44 MXs-A, 400 MHz storage oscilloscope and recorded. To prevent saturation effects and power broadening the laser power was minimized. Laser calibration was based on observed atomic lines of iodine (2+1) REMPI peaks. Accuracy of calibration was typically found to be about ± 2.0 cm^{-1} on the two-photon wavenumber scale.

III. Results and analysis

Mass resolved REMPI data were collected for the two-photon excitation region of about 74 000–75 000 cm^{-1} for HI.[25] REMPI spectra for HI^+, I^+ and H^+ were derived from the data (see Fig. 1 and 2 and ref. 25).

The I^+ REMPI spectra show number of iodine atomic lines, which are due to (2+1) REMPI of I(3/2) (herby named I) and I(1/2) (hereby named I*) *via* resonant excitation to atomic Rydberg states (I**). The I and I* atoms are believed to be mostly formed by one-photon non-resonant excitation of HI *via* the repulsive valence states (HI*; A-band) which correlate with H + I/I*. In addition, a number of molecular spectral lines, due to two-photon resonant excitations to ion-pair and Rydberg states followed by further photoexcitation and fragmentation processes were observed in all the REMPI spectra. The position and relative intensities of the molecular spectral lines were used to assign excited states (levels) as well as to determine photo-fragmentation processes involved. Four vibrational states (levels) of the ion-pair state ($V^1\Sigma^+$) and two Rydberg vibrational states were identified and assigned in the spectral region. Spectral perturbations, appearing as line shifts and intensity anomalies are indicative of both homogeneous and heterogeneous couplings between the Rydberg states and the ion-pair state. Corresponding interaction strengths and state mixings were quantified. Photodissociation and photoionization processes, following the resonant excitations, are discussed in Section IV.

A. Ion-pair vibrational states

Fig. 1 shows REMPI spectra due to two-photon resonant transitions from the ground molecular state of HI ($X^1\Sigma^+(v'' = 0)$) to four

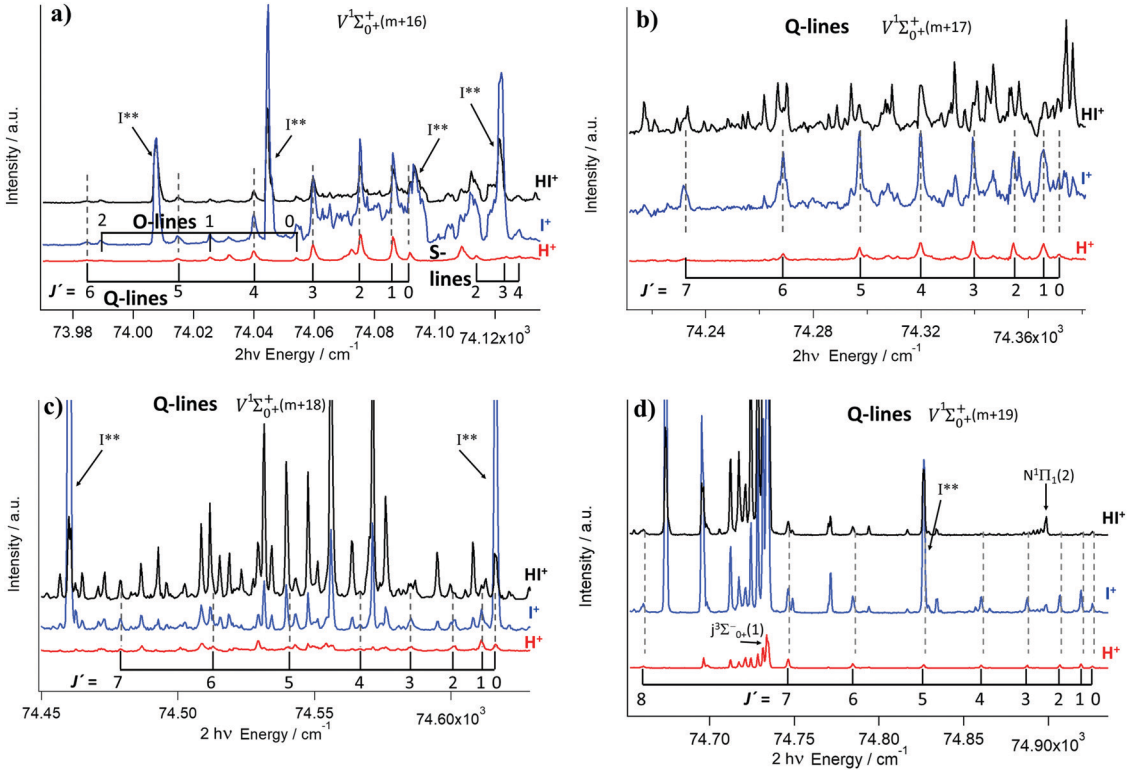

Fig. 1 Mass resolved (H^+(red), I^+(blue) and HI^+(black) ions) (2+n) REMPI spectra as a function of two-photon excitation wavenumber for HI. Rotational line assignments for two-photon resonant transitions from the ground state $X^1\Sigma^+(v'' = 0)$ to the ion-pair vibrational levels $V^1\Sigma^+(v' = m + i)$ for i = 16 (a), 17 (b), 18 (c) and 19 (d) (m is an unknown integer; see main text) are indicated. Iodine atomic lines due to two-photon resonant transitions from ground state iodine atoms to atomic Rydberg states (I**) are also indicated. Spectra due to transitions from ground molecular state to the $j^3\Sigma^-(\Omega = 0^+; v' = 1)$ and $N^1\Pi$ ($\Omega = 1$; $v' = 2$) Rydberg states are also marked (d).

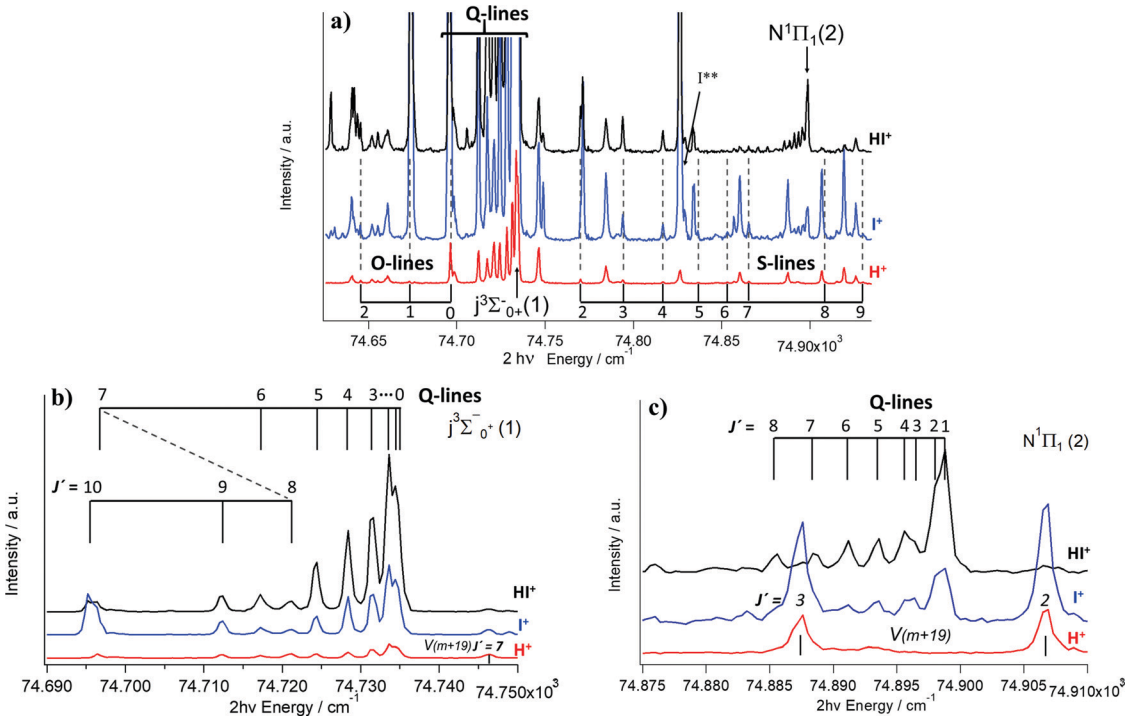

Fig. 2 Mass resolved (H^+(red), I^+(blue) and HI^+(black) ions) (2+n) REMPI spectra as a function of two-photon excitation wavenumber for HI. Rotational line assignments for two-photon resonant transitions from the ground state $X^1\Sigma^+(v'' = 0)$ to the Rydberg states $j^3\Sigma^-(\Omega = 0^+; v' = 1)$, O and S lines (a), $j^3\Sigma^-(\Omega = 0^+; v' = 1)$, Q lines (b) and $N^1\Pi$ ($\Omega = 1; v' = 2$), Q lines (c) are indicated. Q rotational lines for two-photon resonant transitions from the ground state to the ion-pair vibrational states (levels) $V^1\Sigma^+(v' = m + 19)$, $J' = 7$ (b) and $J' = 2$ and 3 (c) are indicated. Iodine atomic line due to two-photon resonant transitions from the ground state to an atomic Rydberg state (I**) is indicated in (a).

vibrational states (levels) of the ion-pair electronic state ($V^1\Sigma^+(v' = m + i)$), where m is an uncertain integer number[8] and i = 16, 17, 18 and 19 (hereby named V(m + i)). The lowest energy vibrational state (level) (i = 16) has been observed before in absorption[8] where it was assigned as V(m + 14). More recent analysis of previously unobserved vibrational states (levels),[7,9] lower in energy, however, allow it to be reassigned as V(m + 16). Whereas, O, Q and S lines were identified for V(m + 16), only Q lines were observed for V(m + i); i = 17–19. Peak positions are listed in Table 1. Analysis of the peak positions by a traditional line fitting, allowed determination of relevant spectroscopic constants (see Table 2). The spectrum for the V(m + 19) state (level) shows severe irregularities in the peak positions as well as line intensities due to state interaction (see below). Spectral simulations[26] by assuming the effect of interaction with a Rydberg state, close in energy (see below) allowed determination of corresponding deperturbed spectroscopic constants (see Section IIIC and Table 2). Signal strengths (intensities) for the ions (H^+, I^+ and HI^+), behave as $I(I^+) \geq I(H^+) \sim I(HI^+)$, for all the four ion-pair spectra, virtually independent of J' for V(m + i) for i = 16, 17 and 18 but J'-dependent for i = 19 (see more detailed analysis below).

B. Rydberg states

Fig. 2 shows REMPI spectra due to resonant transitions from the ground molecular state of HI ($X^1\Sigma^+(v'' = 0)$) to two Rydberg states with band origins of 74 735 and 74 899 cm^{-1} (Table 2).

The 74 735 cm^{-1} spectra show O, Q and S lines for $J' \geq 0$ (Table 1), relatively strong in intensity, indicative of an $\Omega' = 0$ (Σ) state. This assignment is further supported by an observed non-degenerate interaction and mixing with the $V^1\Sigma^+(m + 19)$ ion-pair state (level) of an intermediate strength (see more detailed analysis below). The state can neither be a vibrationally excited $E^1\Sigma^+((\sigma^2\pi^3)6p\pi)$ nor $H^1\Sigma^+((\sigma^2\pi^3)5d\pi)$ state, since it does not fit into the corresponding vibrational state series. Energetically it fits the first vibrationally excited state of $j^3\Sigma^-(\Omega = 0^+)$ with the electronic configuration $(\sigma^2\pi^3)5d\pi$. We, therefore, assign the 74 735 cm^{-1} band to the transition from the ground state to the $j^3\Sigma^-$ ($\Omega = 0^+; v' = 1$), $(\sigma^2\pi^3)5d\pi$ state (hereby named j(1)). The signal intensities vary as $I(HI^+) > I(I^+) > I(H^+)$. Spectral simulation obtained by assuming the effect of interaction between the 74 735 cm^{-1} ($j^3\Sigma^-(\Omega = 0^+; v' = 1)$) state and $V^1\Sigma^+(\Omega = 0^+; v' = m + 19)$, close in energy (see below) allowed determination of corresponding deperturbed spectroscopic constants (Table 2).

The spectra at 74 899 cm^{-1} show weak Q lines, only, with small perturbation effects as line shifts due to interactions with the $V^1\Sigma^+(m + 19)$ ion-pair state (level), close in energy, suggesting that it is due to a heterogeneous coupling ($\Delta\Omega \neq 0$), hence $\Omega' \neq 0$. The spectral structure resembles what to expect for an absorption to an $\Omega' = 1$ (Π) state and fits, energetically, the second vibrationally excited state of the $N^1\Pi_1$ state with the electronic configuration $(\sigma^2\pi^3)5d\sigma$. We, therefore, assign the 74 899 cm^{-1} band to the transition from the ground state to the $N^1\Pi_1$ ($\Omega' = 1; v' = 2$), $(\sigma^2\pi^3)5d\sigma$ state (hereby named N(2)).

Table 1 Rotational lines for HI due to two-photon resonant transitions to four vibrational levels, $v' = (m + i)$; i = 16, 17, 18 and 19 of the $V^1\Sigma^+$ ion-pair state and to the $j^3\Sigma^-_{0+}$ (v' = 1) and $N^1\Pi_1$(v' = 2) Rydberg states. $J = J'$. (a) Wavenumbers for measured REMPI transitions in HI for $V^1\Sigma^+ \leftarrow\leftarrow X^1\Sigma^+$ ($m + i$, 0). (b) Wavenumbers for measured REMPI transitions in HI for $j^3\Sigma^-_{0+} \leftarrow\leftarrow X^1\Sigma^+$ (1,0). (c) Wavenumbers for measured REMPI transitions in HI for $N^1\Pi_1 \leftarrow\leftarrow X^1\Sigma^+$ (2,0)

(a)

	i: 16	16	16	17	18	19
J	O(J)	Q(J)	S(J)	Q(J)	Q(J)	Q(J)
0	74054.0	74091.7		74371.2	74616.4	74926.0
1	74025.2	74086.1		74365.6	74611.2	74919.3
2	73988.8	74075.2	74113.7	74354.4	74600.8	74906.9
3		74059.6	74123.7	74339.2	74585.3	74887.6
4		74040.0	74128.1	74320.0	74566.4	74860.4
5		74014.5		74297.2	74540.4	74826.5
6		73984.4		74268.8	74512.9	74784.4
7				74231.7	74478.8	74746.1
8						74660.8

(b)

J	O(J)	P(J)	Q(J)	R(J)	S(J)
0	74698.8		74735.2		
1	74672.9		74734.6		
2	74645.6		74733.7		74794.0
3			74731.6		74770.4
4			74728.4		74836.5
5			74724.1		74816.8
6			74717.2		74865.2
7			74699.2		74853.2
8			74721.2		74930.0
9			74712.0		74908.9
10			74698.4		

(c)

J	O(J)	P(J)	Q(J)	R(J)	S(J)
0					
1			74898.8		
2			74898.2		
3			74896.5		
4			74895.6		
5			74893.6		
6			74891.3		
7			74888.5		
8			74885.4		

The signal intensities vary as $I(HI^+) > I(I^+)$; $I(H^+)$ negligible. Analysis of peak positions by a traditional line fitting and a simulation, allowed determination of relevant spectroscopic constants (see Table 2).

C. State interactions

Clear irregularities in rotational line positions are observed both for the V(m + 19) (Fig. 1d) and j(1) (Fig. 2a and b) spectra. This appears, in particular, as enhanced gaps between the J' = 7 and 8 peaks in the Q line series for V(m + 19) (Fig. 1d) and in the S line series for j(1) (Fig. 2a) as well as a severe rearrangement of the Q rotational lines for j(1) (J' = 5–10) (Fig. 2b). The rotational energy levels ($E_{J'}$) of the excited states were derived from the line positions for given (known) energy levels of the ground state.[27,28] These are shown in Fig. 3a for the V(m + 19) and j(1)

Table 2 Band origin (ν^0) and rotational constants (B' and D') attained by traditional line fitting and simulation[26]/deperturbation (see main text).[b,c] (a) $V^1\Sigma^+$ ion-pair vibrational states/levels. (b) Rydberg states

(a)

		ν^0/cm^{-1}		B'/cm^{-1}		D$'$ × 10^3/cm^{-1}	
State	i ($v' = m + i$)	Our	Others	Our	Others	Our	Others
$V^1\Sigma^+$	16	74 091.0	74 090[a]	3.71	3.724[a]	2.26	0.588[a]
$V^1\Sigma^+$	17	74 372.0		3.90		0.42	
$V^1\Sigma^+$	18	74 615.4		3.76		3.67	
$V^1\Sigma^+$	19	74 926.0		3.18		7.65	
$V^1\Sigma^+$	19	74 924.0[b]		3.05[b]		3.83[b]	

(b)

		ν^0/cm^{-1}		B'/cm^{-1}		D' × 10^3/cm^{-1}	
State	v'	Our	Others	Our	Others	Our	Others
$j^3\Sigma^-_{0+}$	1	74735.2		6.05		1.12	
$j^3\Sigma^-_{0+}$	1	74738.0[c]		6.10 [c]		1.48[c]	
$N^1\Pi_1$	2	74899.2		6.16		0.39	
$N^1\Pi_1$	2	74899.1[c]		6.17[c]		0.62[c]	

[a] Assigned as V(m + 14) in ref. 2. [b] Deperturbed values derived by taking account of interaction with $j^3\Sigma^-(\Omega = 0^+; v' = 1)$. [c] Deperturbed values derived by taking account of interaction with $V^1\Sigma^+(\Omega = 0^+; v' = m + 19)$.

states (levels) as well as for the N(2) state. The observed spectral perturbations are due to level-to-level interactions between the V(m + 19) and j(1) states, which appear as repulsions between energy levels of same J' values, which increase with decreasing energy difference between the levels ($\Delta E_{J'}$) to reach maxima for the closest to degenerate (near-degenerate) levels of J' = 7–8. Spectral simulation (see above) allowed determination of the zero order (unperturbed) energy levels ($E^0_{J'}$) (Fig. 3a) and the corresponding spectroscopic constants ($B^{0'}$ and $D^{0'}$) for both states,

$$E^0_{J'} = \nu^0 + B^{0'}J'(J'+1) - D^{0'}J'^2(J'+1)^2 \qquad (1)$$

Fig. 3b shows the energy mismatch of the perturbed and unperturbed levels ($E_{J'} - E^0_{J'}$) as a function of J' (reduced term plots). The plots show a characteristic ''near-mirror image'' effect, such that an increase in $E_{J'} - E^0_{J'}$, for one of the states, results in a decrease in the corresponding value for the other state and *vice versa*. Thus, a gradual increase in $E_{J'} - E^0_{J'}$ is observed for the V(m + 19) state (level) (decrease for j(1)) as J' increases from 0 to 7 followed by a reversed behavior for higher J's. The repulsion effect is largest for J' = 7. Furthermore, an interaction strength of W_{12} = 22.3 cm^{-1} was derived from the perturbed and deperturbed energy levels of both states based on,[10]

$$E_{J'}(i) = \frac{1}{2}\left(E^0_{J'}(1) + E^0_{J'}(2)\right) \pm \frac{1}{2}\left[4|W_{12}|^2 + \left(E^0_{J'}(1) - E^0_{J'}(2)\right)^2\right]^{1/2} \qquad (2)$$

where the numbers 1, and 2 refer to the two states, j(1) and V(m + 19), respectively. Based on this value and the energy difference for the J' levels of the interacting states

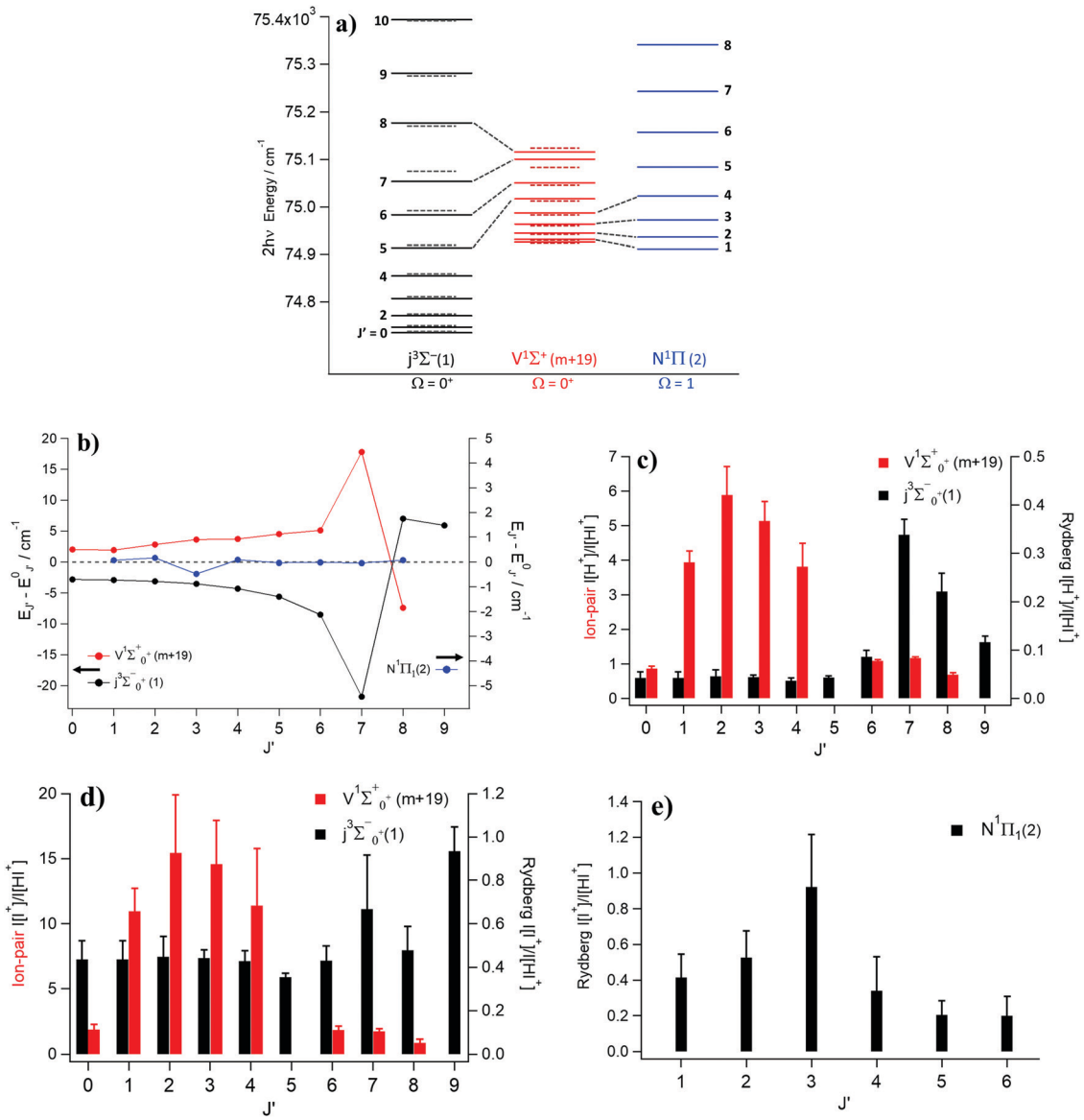

Fig. 3 Effects of state interactions. (a) Rotational energy levels of the $j^3\Sigma^-(\Omega = 0^+; v' = 1)$, $V^1\Sigma^+(\Omega = 0^+; v' = m + 19)$ and $N^1\Pi$ ($\Omega = 1$; $v' = 2$) states, derived from the REMPI spectra (solid lines) and derived by deperturbation calculations (zero order energy levels; broken horizontal lines). Major level-to-level state interactions are indicated by broken leaning lines. (b) Difference between perturbed (experimental; $E_{J'}$) and unperturbed (zero order; $E^0_{J'}$) energy levels ($E_{J'} - E^0_{J'}$) as a function of J' (reduced term plots) for the $j^3\Sigma^-(\Omega = 0^+; v' = 1)$, $V^1\Sigma^+(\Omega = 0^+; v' = m + 19)$ and $N^1\Pi$ ($\Omega = 1$; $v' = 2$) states. Notice that the *y*-axis scale for the N(2) state (right) is expanded by a factor of four. (c and d) Relative ion-signal intensities ($I(H^+)/I(HI^+)$ (c) and $I(I^+)/I(HI^+)$ (d)) *vs.* J' derived from the Q-rotational lines for the j(1) and V(m + 19) spectra. (e) Relative ion-signal intensities ($I(I^+)/I(HI^+)$) *vs.* J' derived from the Q-rotational lines for the N(2) spectrum.

($\Delta E_{J'} = E_{J'}(1) - E_{J'}(2)$) the fractional state mixing (c_1^2 and c_2^2) could also be evaluated from (see Table 3),

$$c_2^2 = \frac{1}{2} \pm \frac{\sqrt{|\Delta E_{J'}|^2 - 4|W_{12}|^2}}{2|\Delta E_{J'}|}$$

$$c_1^2 = 1 - c_2^2 \qquad (3)$$

The effect of this state interaction also appears as line-intensity alterations as a function of J'. Thus the ratios of fragment ion intensities ($I(H^+)$ and $I(I^+)$) to the parent molecular ion intensities ($I(HI^+)$) for the Q lines of the j(1) spectrum is found to rise as J' gets closer to the near-degenerate energy levels to reach a maximum for $J' = 7$ (Fig. 3c and d). This is particularly evident for $I(H^+)/I(HI^+)$. In a corresponding way these ratios drop for J's closest to the resonant energy levels ($J' = 5$–8) by comparison with the values for the lower J's ($J' = 1$–4) in the case of V(m + 19). This is due to an enhanced state mixing as J' gets closer to the near-resonant levels, reaching a maximum for J' of about 7. Thus, as the ion-pair character of the j(1) state increases, channels for fragment ion formations are enhanced over those for forming HI^+ or, correspondingly, as the Rydberg state character of the V(m + 19) state (level) increases, channels for fragment ion formations diminish compared to those for HI^+.

Table 3 Rydberg to ion-pair state interactions. (a) j(1) *vs.* V(m + 19)/homogeneous ($\Delta\Omega$ = 0) coupling: parameters derived from deperturbation analysis of the j(1) Rydberg state (state labelled 1 in table) and V(m + 19) ion-pair state (level) (state labelled 2 in table) spectra. J' level proximity ($\Delta E_{J'} = E_{J'}(1) - E_{J'}(2)/\mathrm{cm}^{-1}$), interaction strength (W_{12}/cm^{-1}) and fractional state mixing (c_1^2, c_2^2). (b) N(2) *vs.* V(m + 19)/heterogeneous ($\Delta\Omega \neq 0$) coupling: parameters derived from deperturbation analysis of the N(2) Rydberg state (state labelled 1) and V(m + 19) ion-pair state (state labelled 2) spectra. J' level proximity ($\Delta E_{J'} = E_{J'}(1) - E_{J'}(2)/\mathrm{cm}^{-1}$), interaction strength ($W_{12} = 0.75(J'(J'+1))^{1/2}/\mathrm{cm}^{-1}$) and fractional state mixing (c_1^2, c_2^2)

(a)

J'	$\Delta E_{J'}$	W_{12}	c_1^2	c_2^2
0	−190.8	22.3	0.986	0.014
1	−184.7	22.3	0.985	0.015
2	−173.5	22.3	0.983	0.017
3	−156.2	22.3	0.979	0.021
4	−132.0	22.3	0.971	0.029
5	−102.4	22.3	0.950	0.050
6	−67.2	22.3	0.875	0.125
7	−47.3	22.3	0.669	0.331
8	60.4	22.3	0.838	0.162

(b)

J'	$\Delta E_{J'}$	W_{12}	c_1^2	c_2^2
1	−20.5	1.06	0.997	0.003
2	−9.0	1.84	0.953	0.047
3	8.5	2.60	0.906	0.094
4	35.2	3.35	0.991	0.009
5	67.1	4.11	0.996	0.004
6	106.9	4.86	0.998	0.002

The spectral simulation/deperturbation analysis revealed lowering in the rotational constant (B') for the V(m + 19) ion-pair state (level) (3.05 cm^{-1} instead of 3.18 cm^{-1}) but increase in the B' constant for the j(1) state (6.10 cm^{-1} instead of 6.05 cm^{-1}). This is in agreement with expectations, since the interaction appears as a compression of energy levels for the Rydberg state but as an expansion of levels for the ion-pair state.[6]

Small localized line shifts are evident from the Q(2) and Q(3) lines of the N(2) spectra (Fig. 2c). Energy level shifts derived from analysis of the data reveal a weak near-degenerate interaction of N(2) with the V(m + 19) state (level) for J' = 2 and 3 (see Fig. 3a and b). The interaction strength (W_{12}), which is assumed to vary with J' for a heterogeneous ($\Delta\Omega \neq 0$) interaction, as,[10,29]

$$W_{12} = W'_{12}\sqrt{J'(J'+1)};\ W'_{12} \quad \text{constant} \qquad (4)$$

was found to be about 2 cm^{-1} for J' = 2–3 and to give the largest state mixing of about 0.91 (Rydberg state): 0.09 (ion-pair state) for J' = 3 (Table 3b).[25] Furthermore, the ratio of iodine ion intensities ($I(I^+)$) to the parent molecular ion intensities ($I(HI^+)$) for the Q lines of the N(2) spectrum is found to rise as J' approaches the near-degenerate energy levels to reach a maximum for J' = 3 (Fig. 3e).

IV. Discussion

A. State energetics

The energies of the states and levels observed and characterized here are shown in Fig. 4 along with other known and predicted ion-pair and Rydberg states (levels). Fig. 4c shows the vibrational

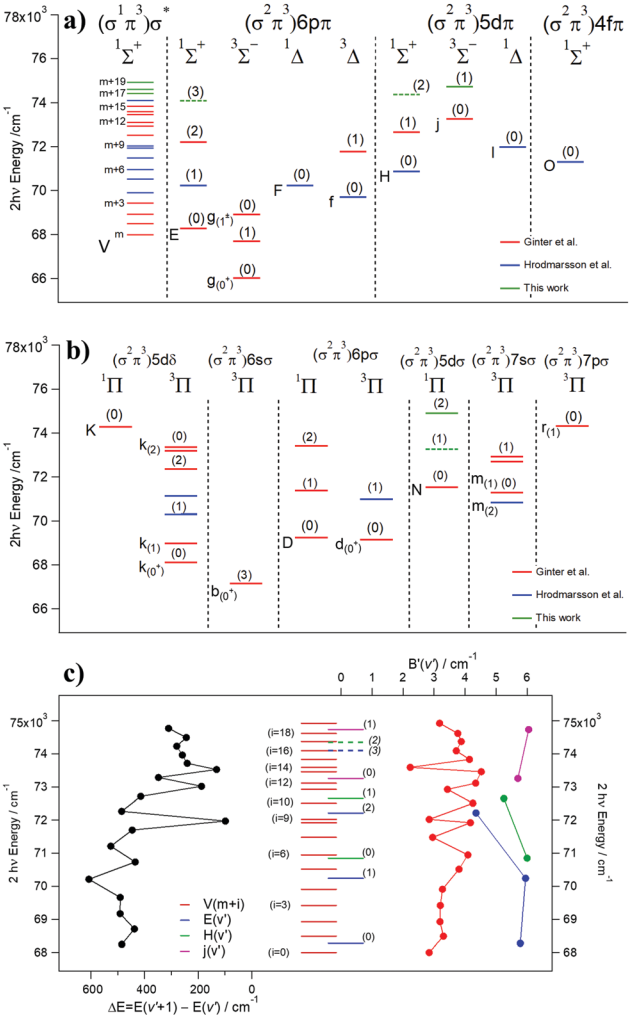

Fig. 4 Energetics of ion-pair and Rydberg states for HI. (a) Energies of the ion-pair and the $^{1,3}\Sigma$ and $^{1,3}\Delta$ Rydberg states with π Rydberg electrons. (b) The $^{1,3}\Pi$ Rydberg states with σ and δ Rydberg electrons. Red and blue lines correspond to previous observations,[2,7–9] whereas green lines are our present observations (solid lines) and predictions (broken lines). Vibrational level numberings are shown in parenthesis on top of every line for the Rydberg states. Vibrational levels for the V ion-pair state are labeled as $v' = m + i$; i = 0, 1, 2,... (see main text). (c) Vibrational energy levels for the $E^1\Sigma^+$ (blue), $H^1\Sigma^+$ (green), $j^3\Sigma^-$ (purple) and $V^1\Sigma^+$ (red) states (in middle) as well as vibrational energy level spacing ($\Delta E(v'+1, v')$) for the $V^1\Sigma^+$ ion-pair state (black curve tilted to the left) and rotational constants ($B'(v')$) (tilted to the right).

states of the V ion-pair state and some Ω' = 0 Rydberg states along with plots of energy spacing between adjacent levels (tilted to the left) and rotational constants (tilted to the right).

Whereas, the overall spacing between levels for the ion-pair state decreases with energy (higher v'), as might be expected for an unperturbed state, large variation in the values is observed. The corresponding rotational constants ($B'(v')$), which might be expected to decrease with v', also vary largely. These observations can be attributed to level-to-level interactions of the V state with Rydberg states, near in energy,[6,28] of which homogeneous ($\Delta\Omega$ = 0) couplings are the strongest. Such interactions appear as enhanced energy gaps between the vibrational levels of the V

state above and below those of the interacting $\Omega' = 0$ Rydberg states as well as expansions of the corresponding rotational levels, hence, increase in $B'(v')$ values. Thus, the enhanced energy gaps between the V(m + 18) and V(m + 19) levels (Fig. 4c), compared to the adjacent energy gaps and the corresponding increase in the $B'(v')$ value for V(m +18) must be due to the interaction with the j(1) state, analogous to similar effects observed for interactions between j(0) and V(m + 10)/V(m + 11). Whereas, these state interactions cause the effective rotational constants for the ion-pair vibrational states to increase, an opposite effect, of decreasing rotational constants, is found for the corresponding Rydberg states. The apparently smaller rotational constant for j(0) than for j(1) suggests that j(0) interacts stronger with the ion-pair state than j(1), which in turn causes the rotational constant for the V states (levels) close to j(0) to be significantly larger than those neighboring the j(1) state. An apparently enhanced energy gap observed between V(m +16) and V(m + 17) (Fig. 4c) could be due to interactions of either one or both of the H(2) and E(3), $\Omega' = 0$, states, which are hidden, but expected to be close in energy.

B. Photofragmentation processes

Variations in relative spectral line intensities with J' quantum numbers and/or ion masses are informative regarding photofragmentation processes, which are involved. Based on the perturbation analysis due to the j(1) and N(2) *vs.* V(m + 19) state interactions (see Section IIIC, above; Fig. 3c–e) an ion-pair character of mixed states (at long internuclear distance range) favors fragment ion formation, whereas a Rydberg character (at short internuclear distance range) favors the parent molecular ion formation. This can also be seen from the observed relative line intensities of the ion-pair state spectra ($I(I^+) \geq I(H^+) \sim I(HI^+)$) on the one hand and the Rydberg state spectra ($I(HI^+) > I(I^+) > I(H^+)$ for j(1) and $I(HI^+) > I(I^+)$; $I(H^+) \sim 0$ for N(2)) on the other hand (see Sections IIIA and IIIB). These observation are in agreement with general findings for the hydrogen halides.[9,10,18–22]

It has been argued[10,16] that the major channels responsible for the ion formations following two-photon resonant excitations to HI**(Rydberg and ion-pair states) in the region of about 72 650–73 260 cm^{-1} follow a further third-photon excitation to a superexcited state ($HI^{\#}$). $HI^{\#}$ lies above the molecular ion ground states (*i.e.* the energy threshold for $H(n = 1) + I^+(^3P_2)$ formation) and belongs to a Rydberg series that converges to the $A^2\Sigma^+$ state (*i.e.* $[A^2\Sigma^+]5d\pi$). The relevant fragmentation and/or photofragmentation processes as summarized schematically in Fig. 5 (see channels 3a–3d and 4). There is a reason to believe that the same ionization processes are active in the higher energy region, below the $A^2\Sigma^+$ state, studied here. Furthermore, formation of H^+ by dissociation of $HI^{\#}$ to form the ion-pair fragments $H^+ + I^-$ is also energetically feasible (channel 3e in Fig. 5).

Such a process would involve a cross over from the superexcited Rydberg state ($HI^{\#}$) to the ion-pair state above its dissociation limit. This is likely to occur by analogy to the many crossovers (interactions) from Rydberg states to the bound region of the ion-pair state which have been observed after two-photon resonant excitations. Furthermore, observations of analogous channels in

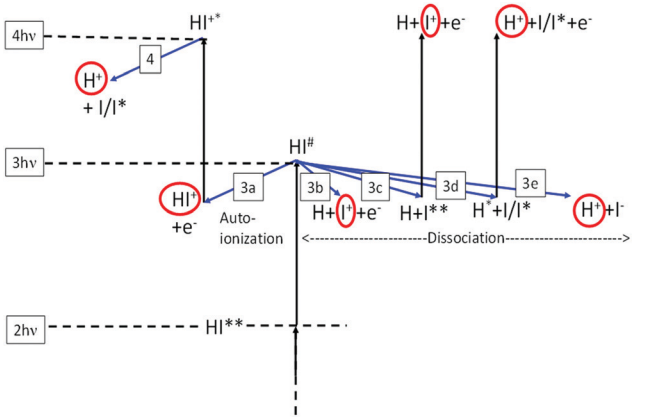

Fig. 5 Schematic energy diagram for excitation processes of HI in the two-photon energy region of 74 000–75 000 cm^{-1}. Vertical black arrows denote photon absorption. Blue arrows denote fragmentation (autoionization (3a) and dissociation (3b, 3c, 3d, 3e, 4)) processes. The numbers inside boxes are the number of photons absorbed prior to the fragmentation processes. HI** and $HI^{\#}$ are resonant and superexcited neutral molecular states, respectively. HI^+ and HI^{+}* are ground and excited ion states, respectively. I, I* and I** are ground, spin–orbit excited and Rydberg states of iodine atoms, respectively. Ions detected are highlighted by red circles.

related compounds, HCl,[30] CH_3Br[31] and CH_3I,[32] makes it a likely channel to be involved. Channel 3a is believed to form HI^+ primarily in low vibrational (v^+) levels without significant further photodissociation (channel 4) in the cases of short range (dominating Rydberg character) excitations, whereas high v^+ levels are populated, followed by significant photodissociation for long range (dominating ion-pair character) excitations. Channel 3b for, formation of I^+, *via* autoionization of an atomic iodine Rydberg state (I**), has been found to be important both for short range (Rydberg character) and long range (ion-pair character) excitations. The fragmentation channels 3c and 3d for formation of the excited I (I**) and H (H*($n = 2$)) atoms, prior to photoionization, are believed to occur primarily for long range (ion-pair character) excitations. Based on the relative ion signal intensities observed for the ion-pair states ($I(I^+) \geq I(H^+) \sim I(HI^+)$), the largely mixed Rydberg state, j(1) ($I(HI^+) > I(I^+) > I(H^+)$) and the weakly mixed Rydberg state N(2) ($I(HI^+) > I(I^+)$; $I(H^+) \sim 0$) the following conclusions are made:

(i) Formation of HI^+ (low v^+) by channel 3a is the dominant channel *via* a Rydberg state (short range) excitation.

(ii) The fragment channels 3b and/or 3c leading to I^+ formation are the dominant channels *via* an ion-pair state (long range) excitation.

(iii) The channels 3a/4, 3d and 3e leading to H^+ formation are negligible for Rydberg state (short range) excitations.

V. Summary and conclusions

Mass resolved multiphoton ionization (MR-MPI) data for HI were collected for the two-photon resonant excitation region of 74 000–75 000 cm^{-1}. HI^+, I^+ and H^+ signals as a function of excitation wavenumber (MPI spectra) were derived from the data. All spectra show peak structure due to two-photon resonant transitions to

Rydberg and ion-pair states (levels) followed by further fragmentation and/or ionization processes, *i.e.* (2+*n*) molecular REMPI. In addition, the I^+ spectrum shows atomic lines due to (2+1) REMPI of ground state iodine atoms formed after one-photon non-resonant excitation *via* the A-band. The molecular REMPI spectra show irregular structure, to a large extent, which is due to a large density of states and/or state mixing within the molecule in the resonant energy region. Four new ion-pair vibrational states (levels) and two new Rydberg states could be identified and characterized. Spectral perturbations in the form of line shifts and line intensity alterations allowed characterization and quantization of both strong homogeneous (non-degenerate level-to-level interactions) and weak heterogeneous (near-degenerate level-to-level interactions) state couplings between the Rydberg states and the ion-pair state. Relative signal intensities, with respect to different ions and excitations, were interpreted in terms of varying photofragmentation (photodissociation and photoionization) processes following the resonant excitations. Channels of fragment ion (H^+, I^+) formations are found to dominate for excitations *via* the ion-pair states (long internuclear distance excitations) whereas parent ion (HI^+) formation dominates for excitations *via* the Rydberg states (short internuclear distance excitations), in agreement with observations for lower energy excitations. Thus, intensity ratios of fragment ion signals over parent ion signals as a function of quantum energy levels (J') are good indicators of ion-pair to Rydberg state mixing.

The results of this paper add important information to the energetics and fragmentation processes of the hydrogen halides. It will hopefully render further theoretical interpretation of the characteristics involved. The paper is of importance to shed light on the effect of various competing channels and excited Rydberg and valence (ion-pair) states and state mixing on the photoexcitation dynamics of molecules in general.

Conflicts of interest

There are no conflicts to declare.

Acknowledgements

The financial support of the University Research Fund, University of Iceland (2019) and the Icelandic Research Fund (Grant No. 184693-051) is gratefully acknowledged. We would like to thank Huasheng Wang and Jingming Long for useful help prior to the experiments.

References

1 S. G. Tilford, M. L. Ginter and A. M. Bass, *J. Mol. Spectrosc.*, 1970, **34**, 327–340.
2 D. S. Ginter, M. L. Ginter and S. G. Tilford, *J. Mol. Spectrosc.*, 1982, **92**, 40–54.
3 D. S. Ginter, M. L. Ginter, S. G. Tilford and A. M. Bass, *J. Mol. Spectrosc.*, 1982, **92**, 55–66.
4 S. A. Wright and J. D. McDonald, *J. Chem. Phys.*, 1994, **101**, 238–245.
5 S. T. Pratt and M. L. Ginter, *J. Chem. Phys.*, 1995, **102**, 1882–1888.
6 Á. Kvaran, Á. Logadóttir and H. Wang, *J. Chem. Phys.*, 1998, **109**, 5856–5867.
7 H. R. Hrodmarsson, H. S. Wang and Á. Kvaran, *J. Mol. Spectrosc.*, 2013, **290**, 5–12.
8 H. R. Hródmarsson, H. Wang and Á. Kvaran, *J. Chem. Phys.*, 2014, **140**, 244304.
9 H. R. Hrodmarsson, H. Wang and Á. Kvaran, *J. Chem. Phys.*, 2015, **142**, 244312.
10 H. R. Hródmarsson and Á. Kvaran, *Phys. Chem. Chem. Phys.*, 2015, **17**, 32517.
11 T. A. Carlson, P. Gerard, M. O. Krause, G. V. Wald, J. W. Taylor and F. A. Grimm, *J. Chem. Phys.*, 1986, **84**, 4755–4759.
12 D. J. Hart and J. W. Hepburn, *Chem. Phys.*, 1989, **129**, 51–64.
13 S. T. Pratt, *J. Chem. Phys.*, 1994, **101**, 8302–8309.
14 A. J. Yencha, P. Baltzer, A. J. Cormack, Y. Li, H.-P. Liebermann, A. B. Alekseyev and R. J. Buenker, *J. Chem. Phys.*, 2003, **119**, 5943–5948.
15 Y. Hikosaka and K. Mitsuke, *J. Chem. Phys.*, 2004, **121**, 792–799.
16 P. M. Regan, D. Ascenzi, E. Wrede, P. A. Cook, M. N. R. Ashfold and A. J. Orr-Ewing, *Phys. Chem. Chem. Phys.*, 2000, **2**, 5364–5374.
17 H. P. Loock, B. L. Bakker and D. H. Parker, *Can. J. Phys.*, 2001, **79**, 211–227.
18 Á. Kvaran, K. Matthíasson, H. Wang, A. Bodi and E. Jonsson, *J. Chem. Phys.*, 2008, **129**, 164313.
19 Á. Kvaran, K. Matthiasson and H. Wang, *J. Chem. Phys.*, 2009, **131**, 044324.
20 K. Matthiasson, J. Long, H. Wang and Á. Kvaran, *J. Chem. Phys.*, 2011, **134**, 164302.
21 J. Long, H. R. Hrodmarsson, H. Wang and Á. Kvaran, *J. Chem. Phys.*, 2012, **136**, 214315.
22 J. Long, H. Wang and Á. Kvaran, *J. Chem. Phys.*, 2013, **138**, 044308.
23 A. Hafliðason, H. S. Wang and Á. Kvaran, *Phys. Chem. Chem. Phys.*, 2016, **18**, 1797–1806.
24 A. Hafliðason, H. Wang and Á. Kvaran, *J. Mol. Spectrosc.*, 2017, **341**, 1–9.
25 See ESI†.
26 C. M. Western, a Program for Simulating Rotational Sturcture, C. M. Western, University of Bristol, 10.1.180 ed., University of Bristol, 2003–2018, http://pgopher.chm.bris.ac.uk/.
27 NIST Chemistry WebBook – (National Institute of Standards and Technology) https://webbook.nist.gov/chemistry/name-ser/.
28 Á. Kvaran, H. Wang and Á. Logadóttir, *J. Chem. Phys.*, 2000, **112**, 10811–10820.
29 H. Lefebvre-Brion and R. W. Field, *Perturbations in the Spectra of Diatomic Molecules*, Academic Press, Inc., London, 1986.
30 A. J. Yencha, D. Kaur, R. J. Donovan, Á. Kvaran, A. Hopkirk, H. Lefebvre-Brion and F. Keller, *J. Chem. Phys.*, 1993, **99**, 4986–4992.
31 A. Hafliðason, P. Glodic, G. Koumarianou, P. C. Samartzis and Á. Kvaran, *Phys. Chem. Chem. Phys.*, 2019, **21**, 10391–10401.
32 K. Matthíasson, G. Koumarianou, M. Jiang, P. Glodic, P. C. Samartzis and Á. Kvaran, to be published.

4.1.1 Supporting information

High energy Rydberg and ion-pair states, state mixing and excitation dynamics of HI

Arnar Hafliðason, Meng-Xu Jiang and Ágúst Kvaran*

Science Institute, University of Iceland, Dunhagi 3, 107 Reykjavík, Iceland.

Supplementary material

Content: **pages:**

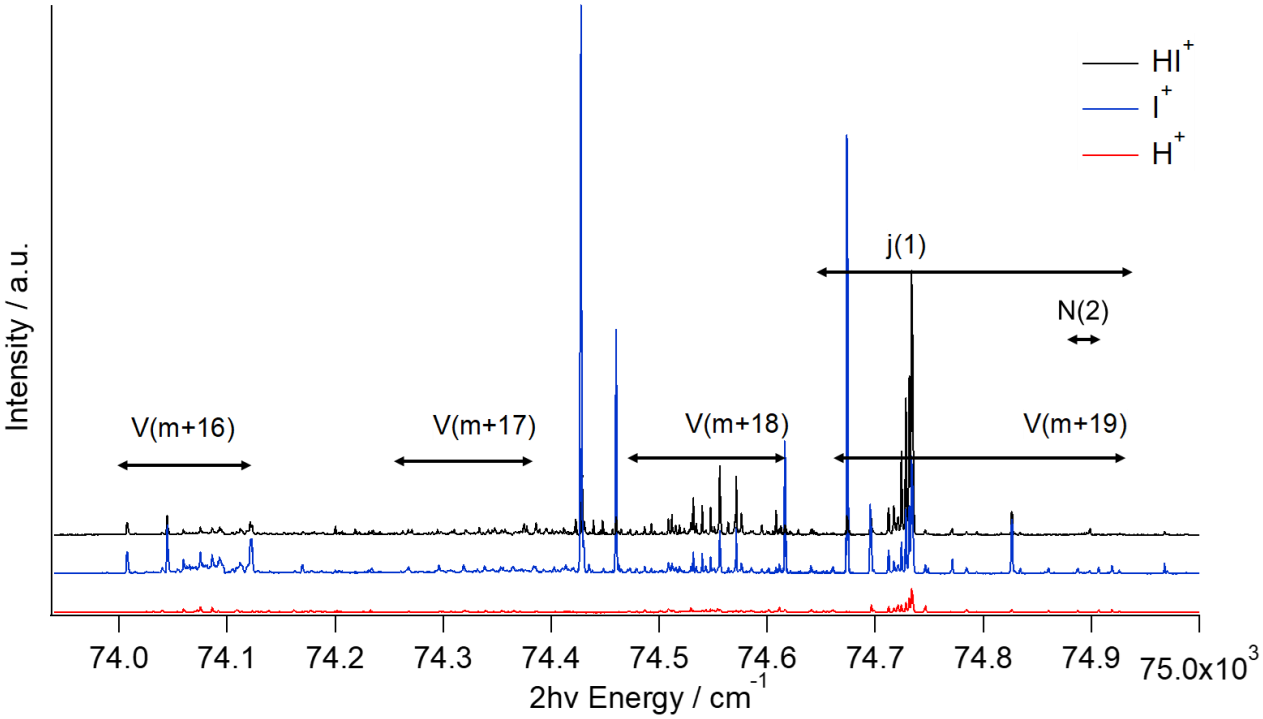

Fig. S1 Overall REMPI spectra of the ions H^+(red), I^+(blue) and HI^+(black) for the two-photon (2hv) excitation region of 73 980 – 75 000 cm^{-1}. States identified are indicated. Horizional double arrows cover the energy region of individual spectra.

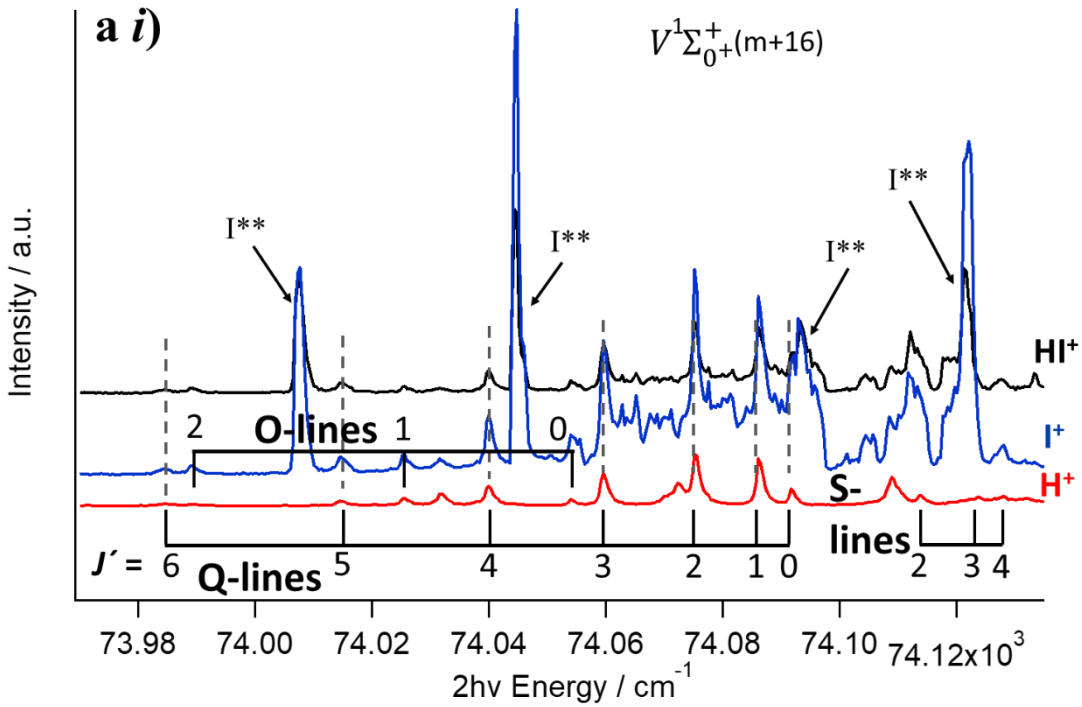

Fig. S2 a i) REMPI spectra of H^+(red), I^+(blue) and HI^+(black) for the two-photon (2hν) excitation region of 73 970 – 74 125 cm^{-1}. Rotational lines are labeled (J´) and indicated by vertical lines for the V(m+16) ion-pair state spectra, for the O, Q and S line series. I** indicate atomic lines.

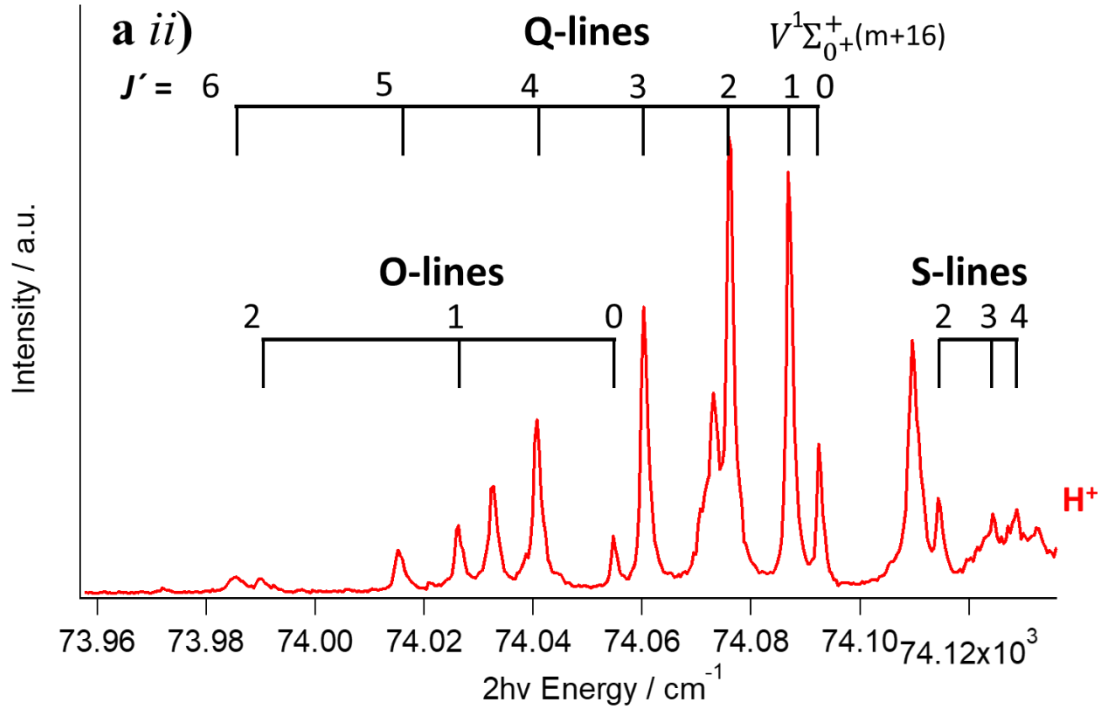

Fig. S2 a ii) REMPI spectrum of H^+(red) for the two-photon (2hν) excitation region of 73 960 – 74 125 cm^{-1}. Rotational lines are labeled (J´) and indicated by vertical lines for the V(m+16) ion-pair state spectrum, for the O, Q and S line series.

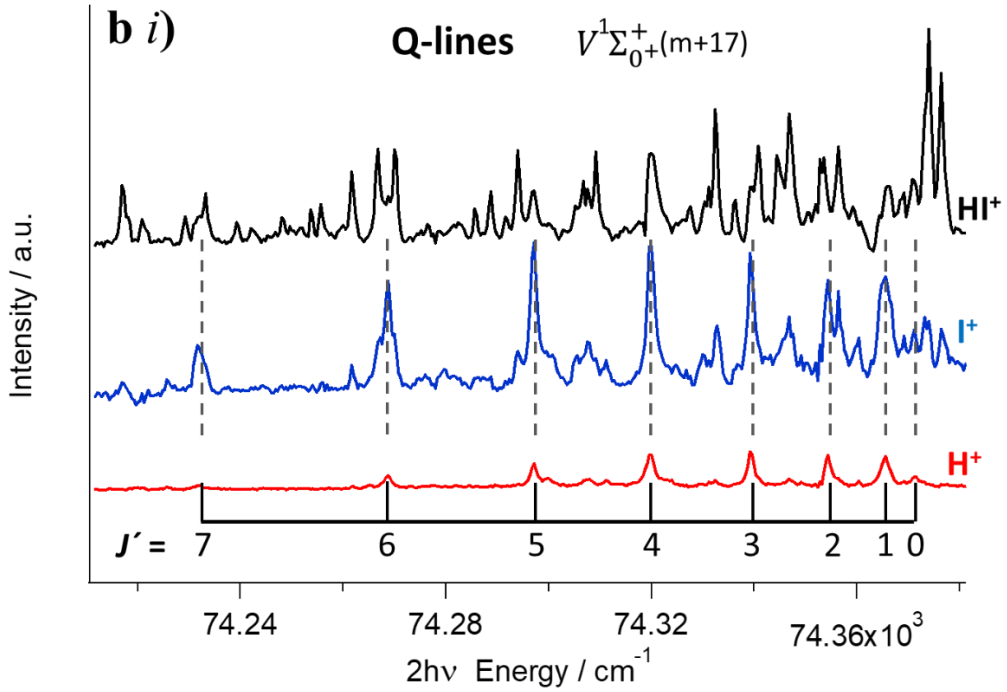

Fig. S2 b i) REMPI spectra of H^+(red), I^+(blue) and HI^+(black) for the two-photon (2hν) excitation region of 74 215 – 74 380 cm^{-1}. Rotational Q-lines are labeled (J´) and indicated by vertical lines for the V(m+17) ion-pair state spectra.

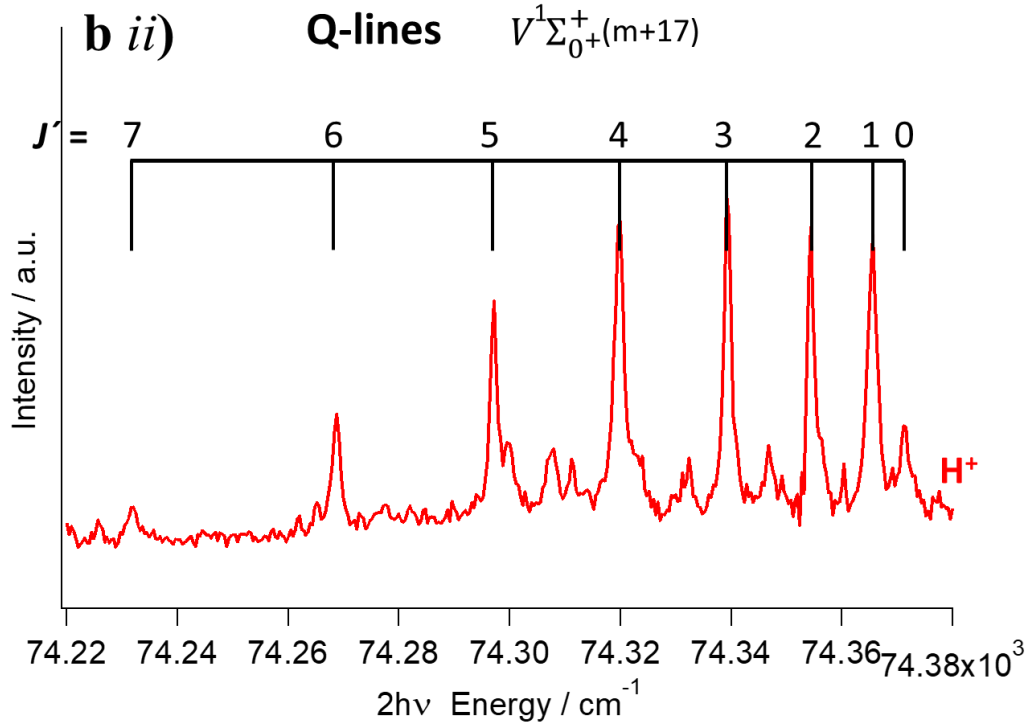

Fig. S2 b ii) REMPI spectrum of H^+(red) for the two-photon (2hν) excitation region of 74 220 – 74 380 cm^{-1}. Rotational Q-lines are labeled (J´) and indicated by vertical lines for the V(m+17) ion-pair state spectrum.

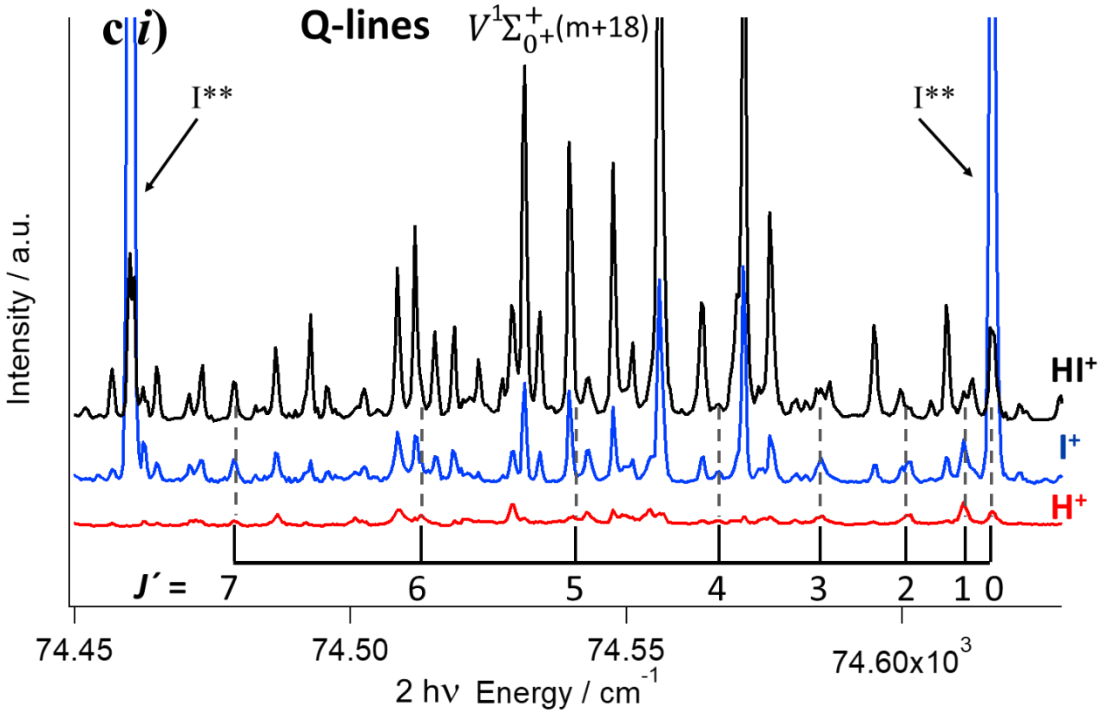

Fig. S2 c i) REMPI spectra of H^+(red), I^+(blue) and HI^+(black) for the two-photon (2hν) excitation region of 74 450 – 74 650 cm^{-1}. Rotational Q-lines are labeled (J´) and indicated by vertical lines for the V(m+18) ion-pair state spectra. I** indicate atomic lines.

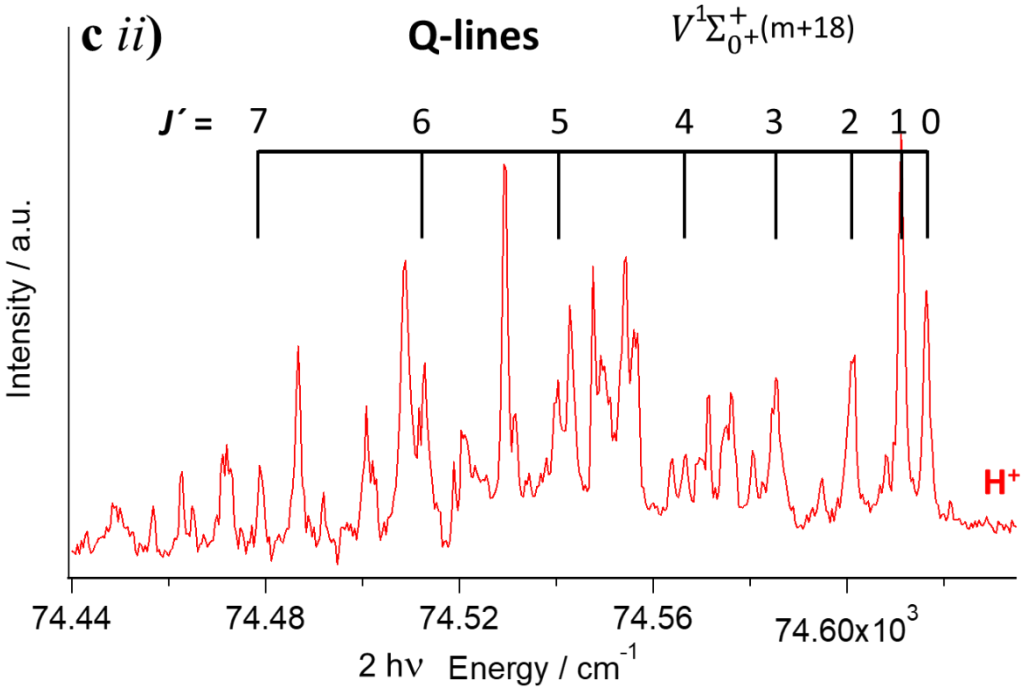

Fig. S2 c ii) REMPI spectrum of H^+(red) for the two-photon (2hν) excitation region of 74 220 – 74 380 cm^{-1}. Rotational Q-lines are labeled (J´) and indicated by vertical lines for the V(m+18) ion-pair state spectrum.

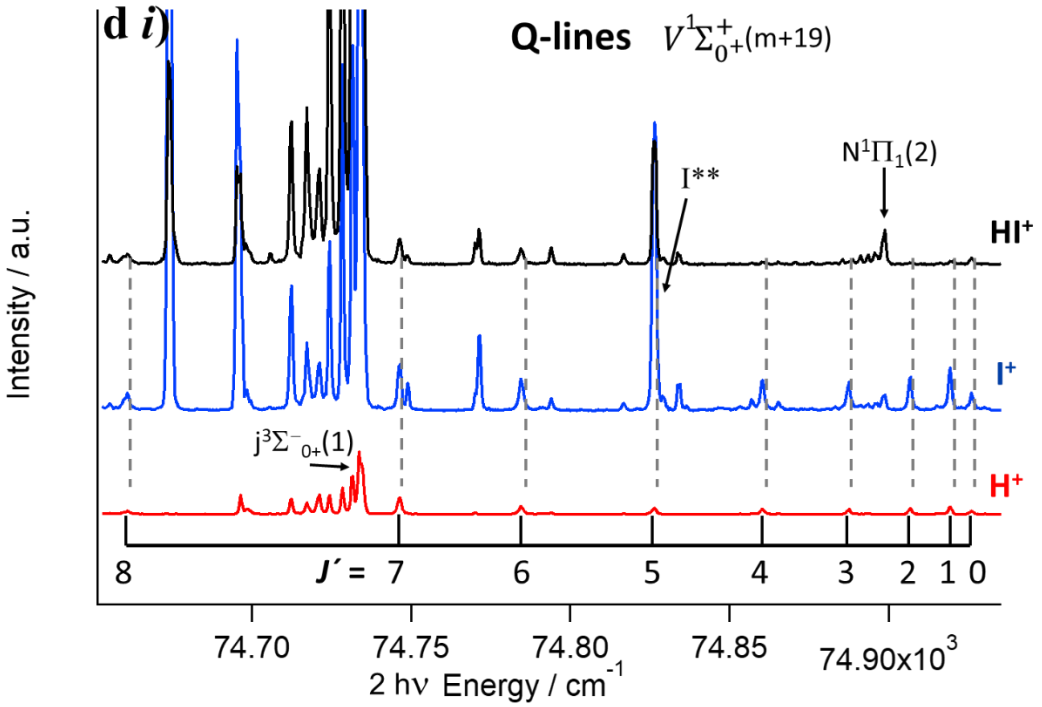

Fig. S2 d i) REMPI spectra of H^+(red), I^+(blue) and HI^+(black) for the two-photon (2hν) excitation region of 74 650 – 74 950 cm^{-1}. Rotational Q-lines are labeled (J´) and indicated by vertical lines for the V(m+19) ion-pair state spectra. I** indicates a atomic line. Spectra of the $j^3\Sigma^-_{0+}(1)$ and $N^1\Pi_1(2)$ Rydberg states are observed at 74 735 cm^{-1} and 74 900 cm^{-1}, respectively.

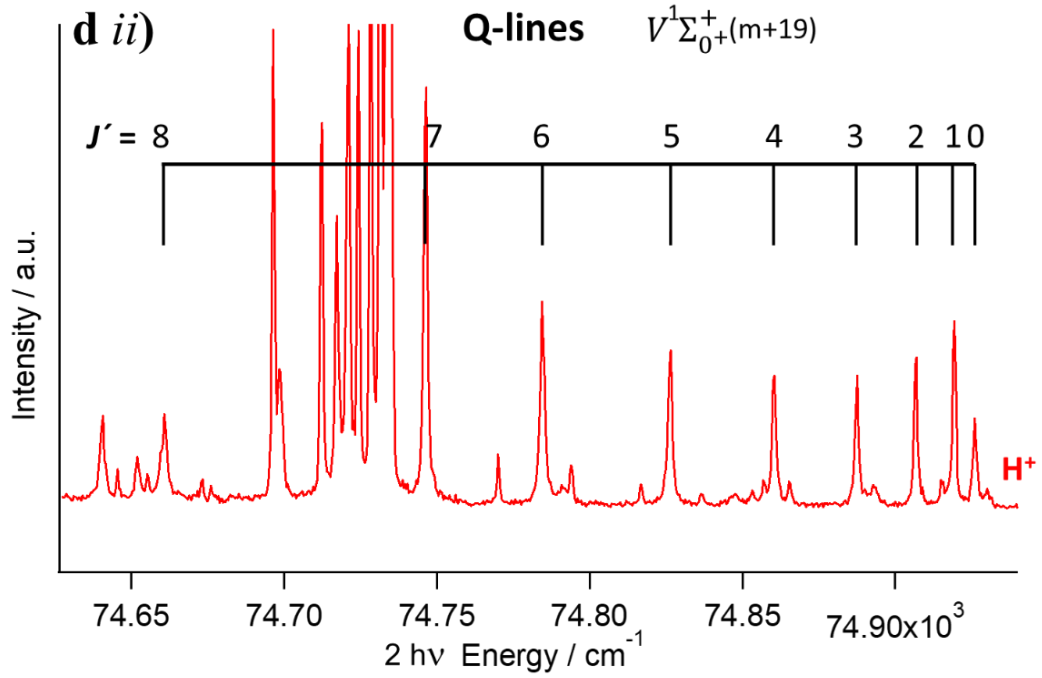

Fig. S2 d ii) REMPI spectrum of H^+(red) for the two-photon (2hν) excitation region of 74 640 – 74 940 cm^{-1}. Rotational Q-lines are labeled (J´) and indicated by vertical lines for the V(m+19) ion-pair state spectrum.

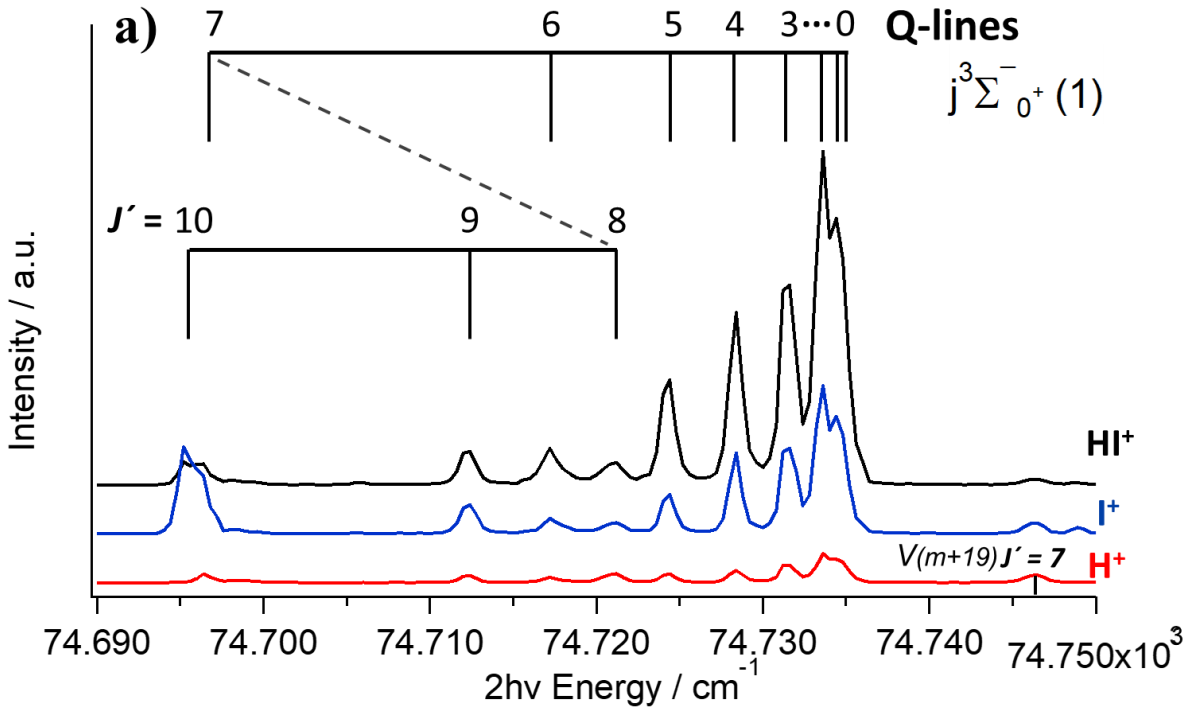

Fig. S3 a) REMPI spectra of H^+(red), I^+(blue) and HI^+(black) for the s two-photon (2hν) eexcitation region of 74 690 – 74 750 cm^{-1}. Rotational Q-lines are labeled (*J'*) and indicated by vertical lines for the j(1) Rydberg state spectra. The *J'=7*, Q line, for V(m+19) is to be seen at 74 747 cm^{-1}.

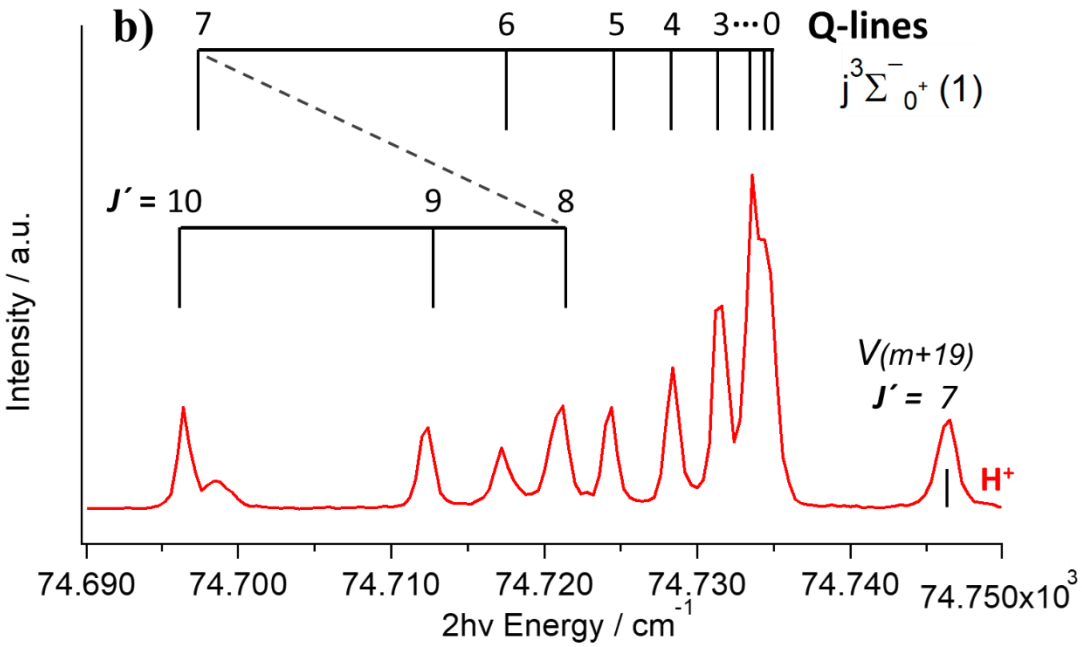

Fig. S3 b) REMPI spectrum of H^+(red) for the two-photon (2hν) excitation region of 74 690 – 74 750 cm^{-1}. Rotational Q-lines are labeled (*J'*) and indicated by vertical lines for the j(1) Rydberg state spectrum. The *J'=7*, Q line, for V(m+19) is to be seen at 74 747 cm^{-1}.

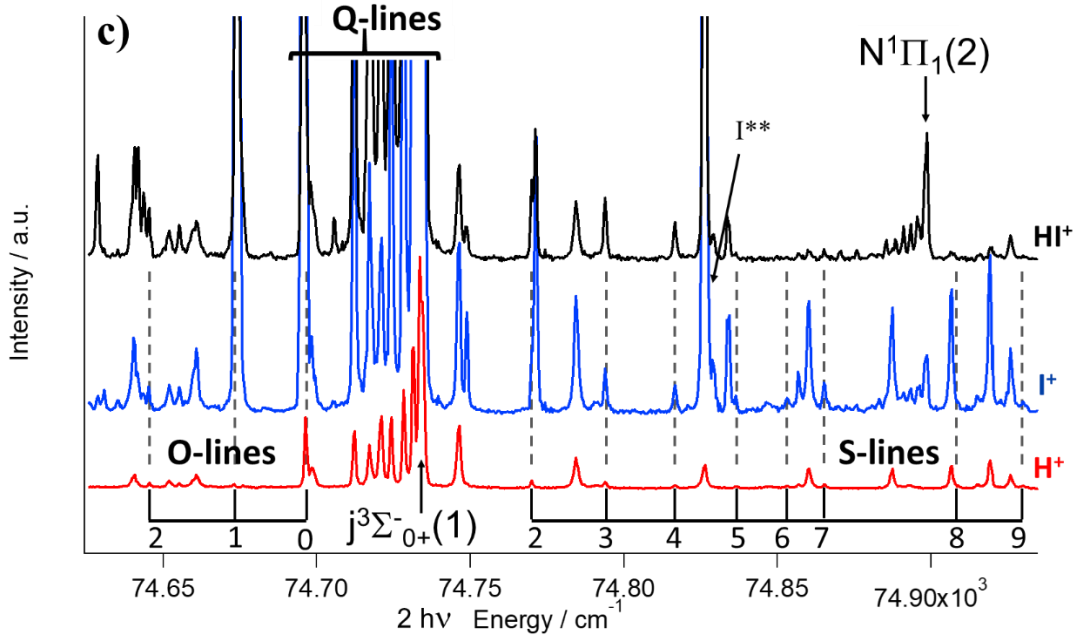

Fig. S3 c) REMPI spectra of H^+(red), I^+(blue) and HI^+(black) for the two-photon (2hν) excitation region of 74 690 – 74 750 cm^{-1}. Rotational O- and S-lines are labeled (J') and indicated by vertical lines for the j(1) Rydberg state spectra. I** indicates an iodine atomic line. Spectrum of the Rydberg state $N^1\Pi_1(2)$ is at 74 900 cm^{-1}.

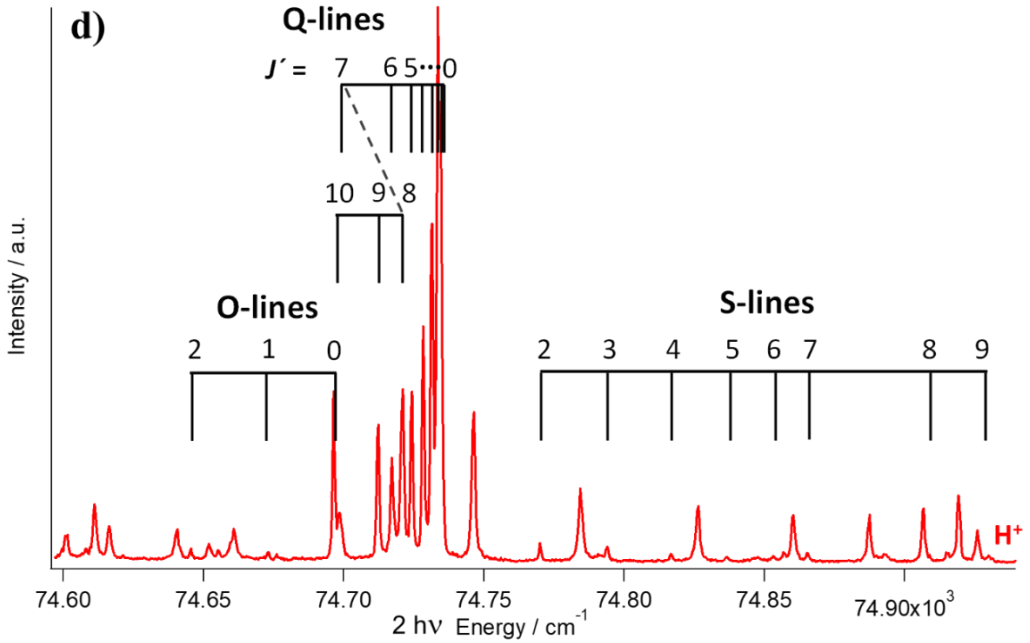

Fig. S3 d) REMPI spectrum of H^+(red) for the two-photon (2hν) excitation region of 74 600 – 74 950 cm^{-1}. Rotational Q- Rotational O-, Q- and S-lines are labeled (J') and indicated by vertical lines for the j(1) Rydberg state spectrum.

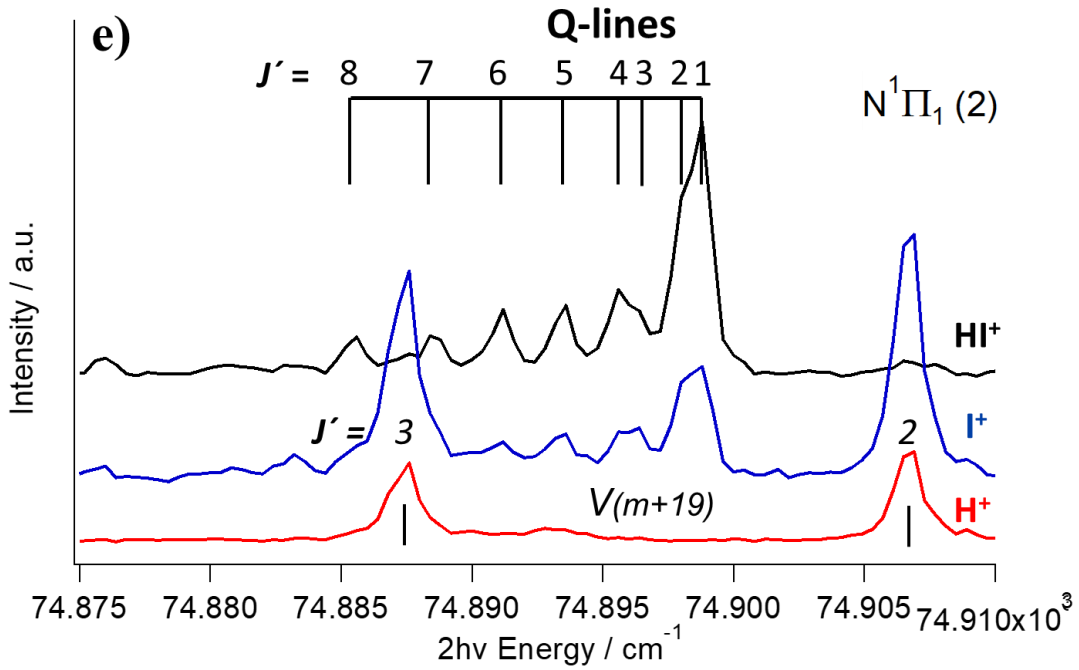

Fig. S3 e) REMPI spectra of H^+(red), I^+(blue) and HI^+(black) for the two-photon (2hν) excitation region of 74 690 – 74 750 cm^{-1}. Rotational Q-lines are labeled (*J'*) and indicated by vertical lines for the N(2) Rydberg state spectra. *J'=2* and *3*, Q lines, for V(m+19) are also labeled.

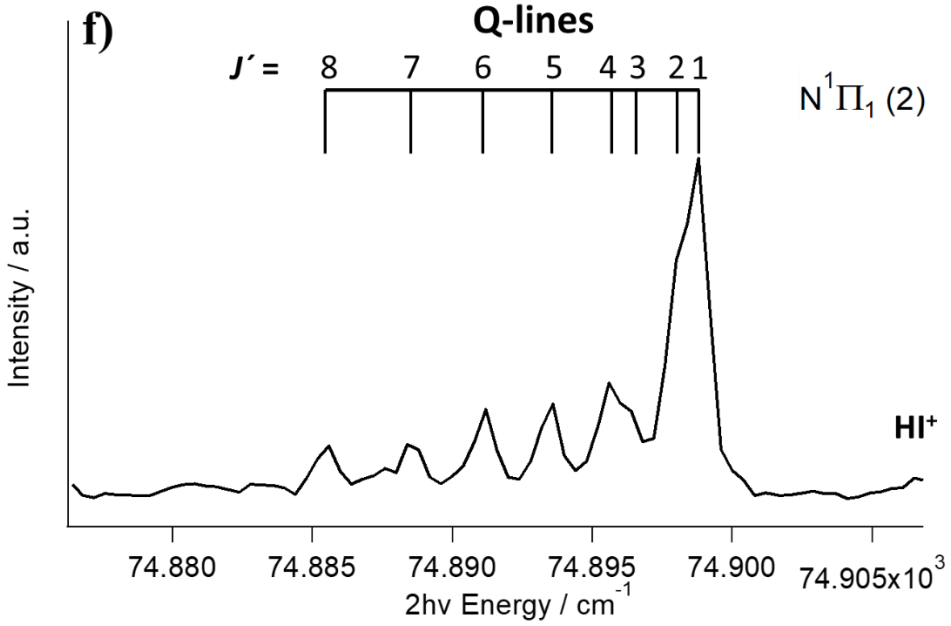

Fig. S3 f) REMPI spectra of HI^+(black) for the two-photon (2hν) excitation region of 74 875 – 74 905 cm^{-1}. Rotational Q-lines are labeled (*J'*) and indicated by vertical lines for the N(2) Rydberg state spectrum.

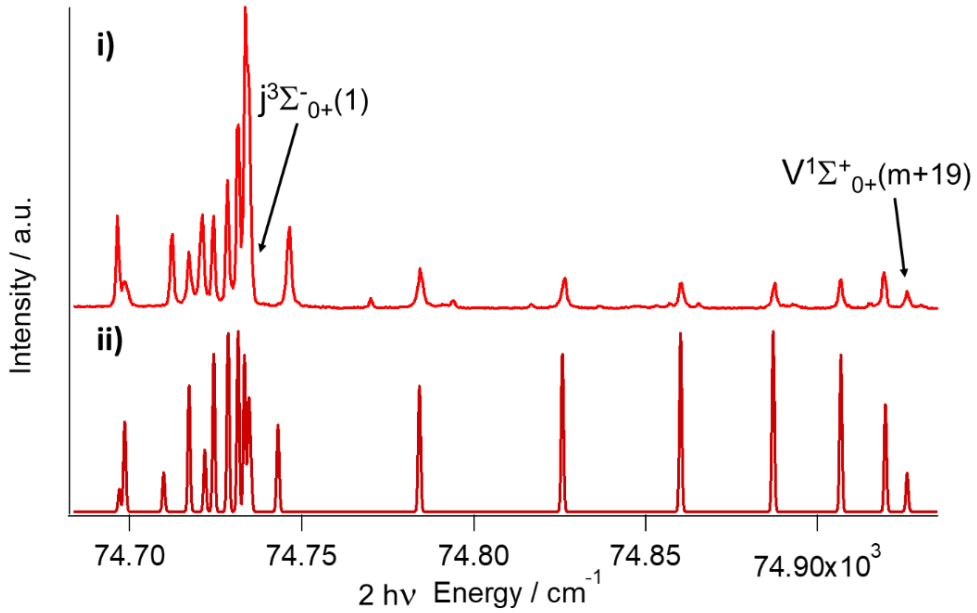

Fig. S4 Simulation: Comparison of the experimental spectra for j(1) and V(m+19) and corresponding calculated two-photon absorption spectra. Black arrows indicate the band origin for the two states. **i)** Two-photon REMPI spectrum of HI for the H^+ ion. **ii)** Calculated two-photon absorption spectrum[1].(*See Fig. S2 d ii) and S3 b) for assignment*)

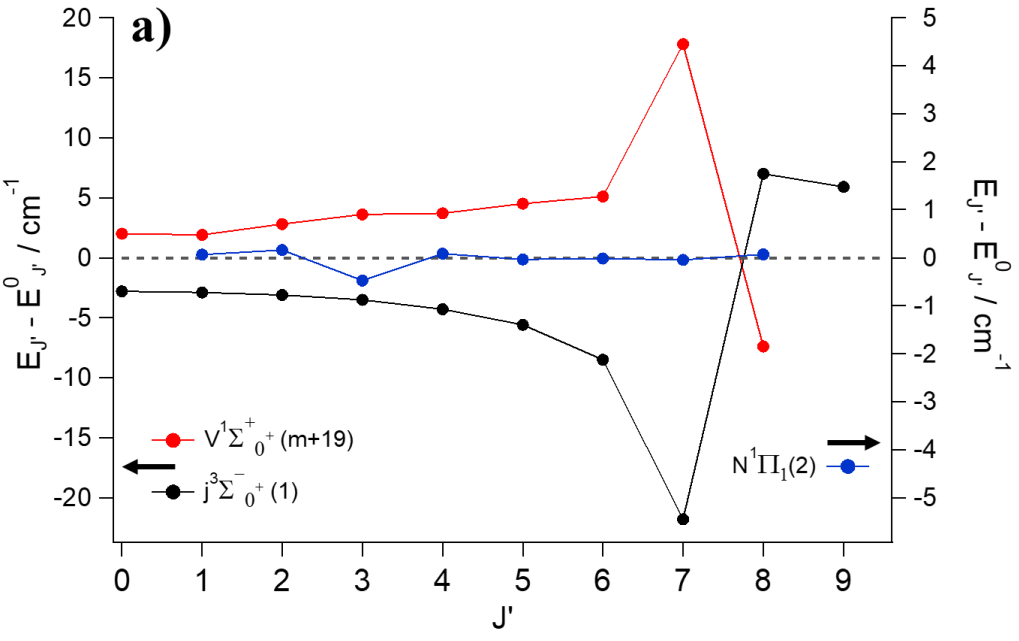

Fig. S5 a) Reduced term value plots for the V(m+19), j(1) and N(2) states: Deperturbed energy level values subtracted from experimental energy level values. Homogenous coupling between the j(1) and V(m+19) states appears as gradual changes in the energy differences for J´= 0 – 6 (i.e. non-degenerate interaction), whereas a near-degenerate interaction is seen for J´= 7 – 8. Small deviations of the energies from deperturbed values were observed for J´= 2 and J´= 3 for N(2) (and V(m+19)) (near-degenerate interactions) due to heterogenous coupling. Deperturbation calculations were performed by assuming independent **two-state interactions**.

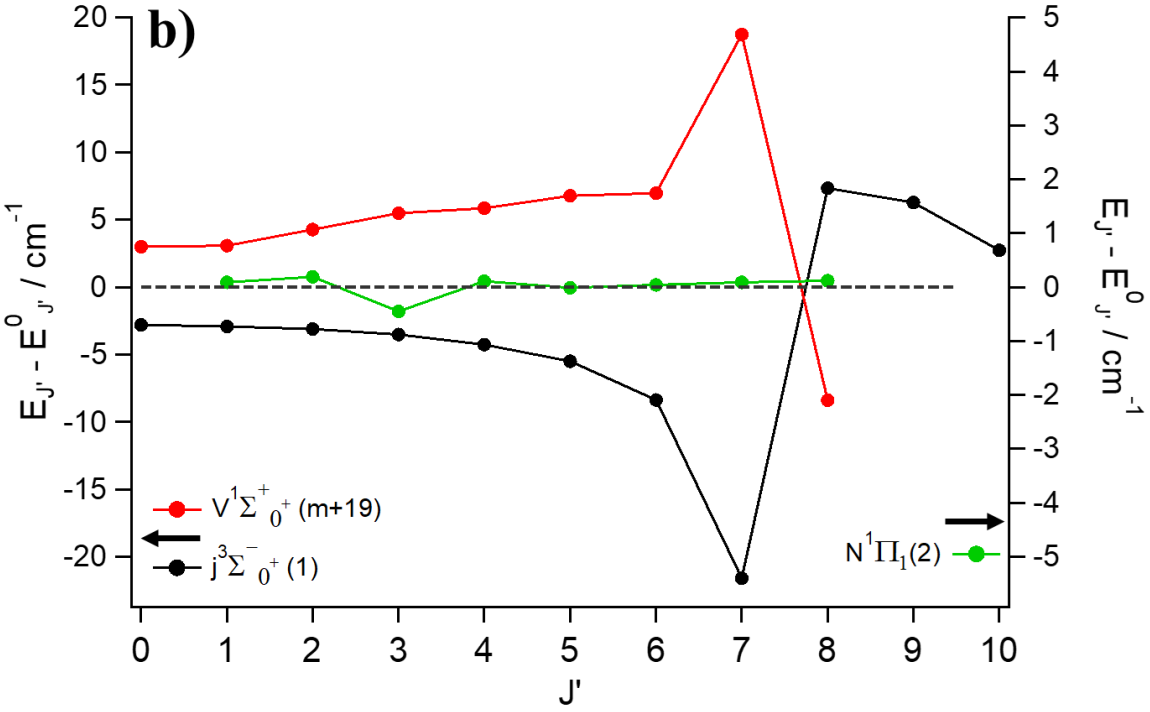

Fig. S5 b) Reduced term value plots for the V(m+19), j(1) and N(2) states: Deperturbed energy level values subtracted from experimental energy level values. Homogenous coupling between the j(1) and V(m+19) states appears as gradual changes in the energy differences for J´= 0 – 6 (i.e. non-degenerate interaction), whereas a near-degenerate interaction is seen for J´= 7 – 8. Small deviations of the energies from deperturbed values were observed for J´= 2 and J´= 3 for N(2) (and V(m+19)) (near-degenerate interactions) due to heterogenous coupling. Deperturbation calculations were performed by assuming **three-state interaction**.

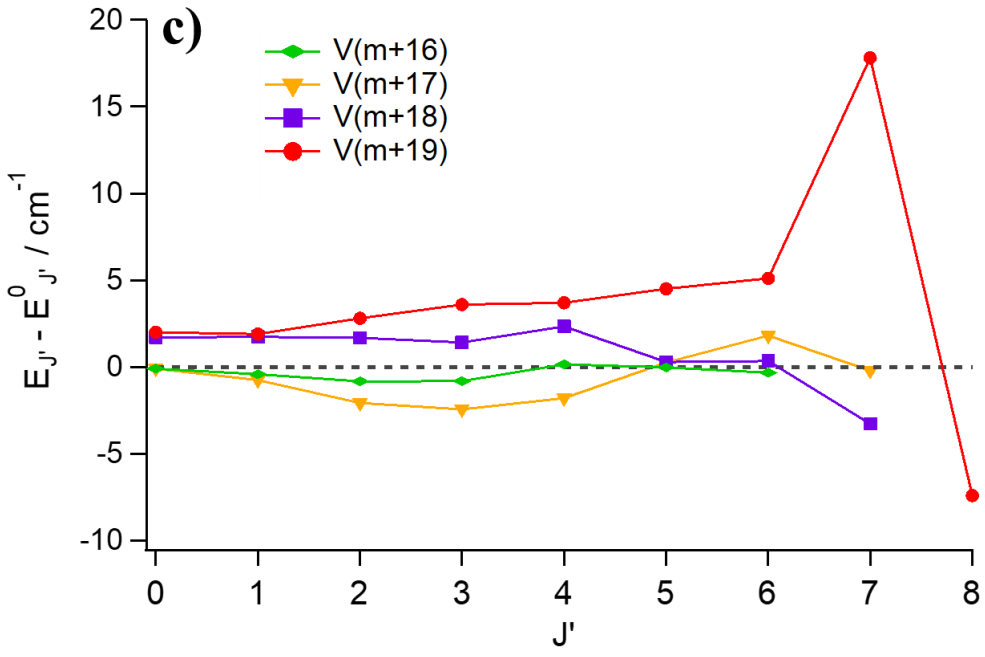

Fig. S5 c) Reduced term value plots for V(m + i); i = 16 - 19. All states show indications of interaction with neighboring Rydberg states.

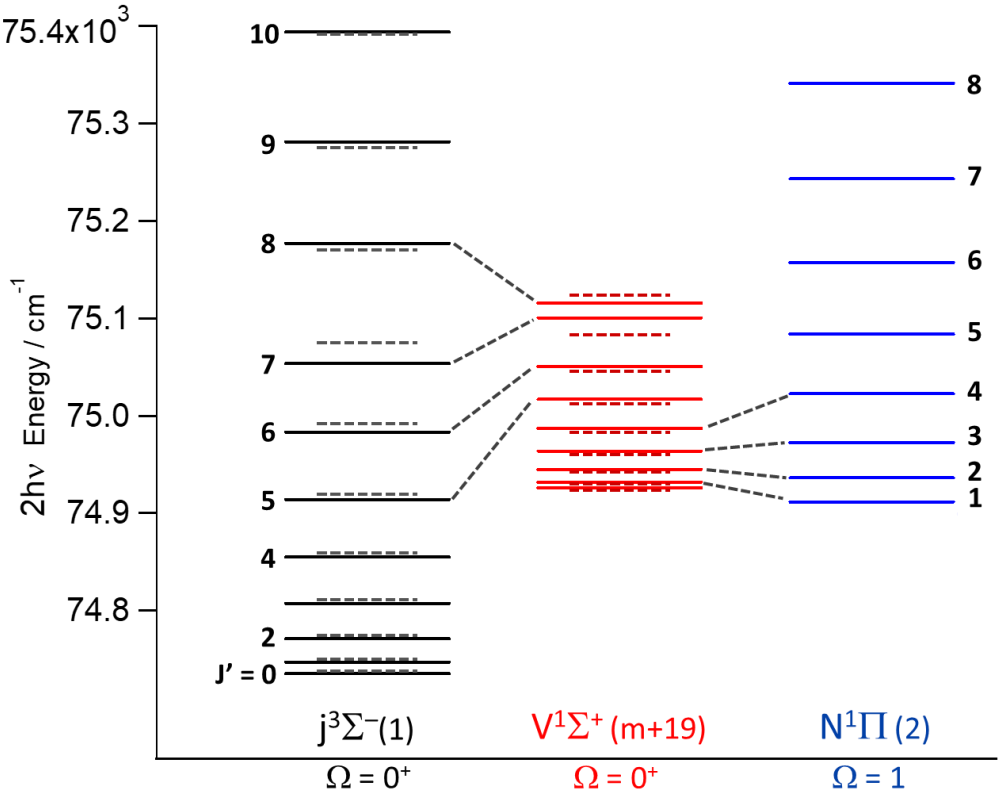

Fig. S6 Rotational energy levels derived from spectral peak positions for states j(1), V(m+19) and N(2) (solid lines). Energy levels derived from deperturbation analysis (broken lines). Close to degenerate interactions are indicated by broken leaned lines connecting energy levels of sane J' values.

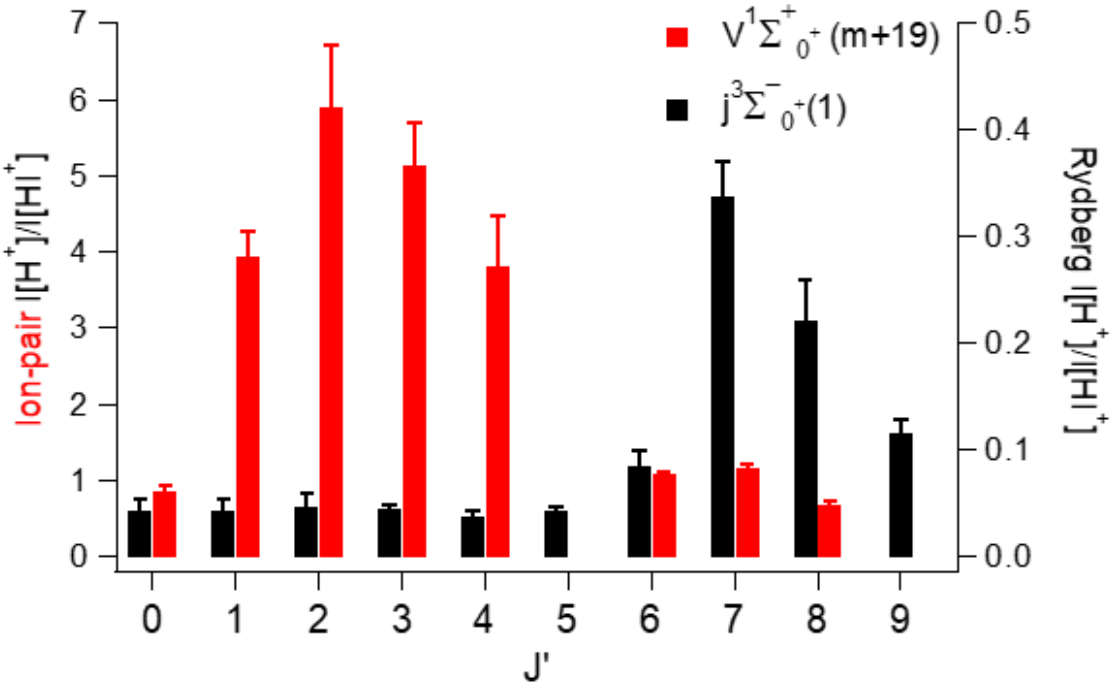

Fig. S7 a) Relative ion-signal intensities (I(H+)/I(HI+) vs. J´ derived from the Q-rotational lines for the j(1) and V(m + 19) spectra.

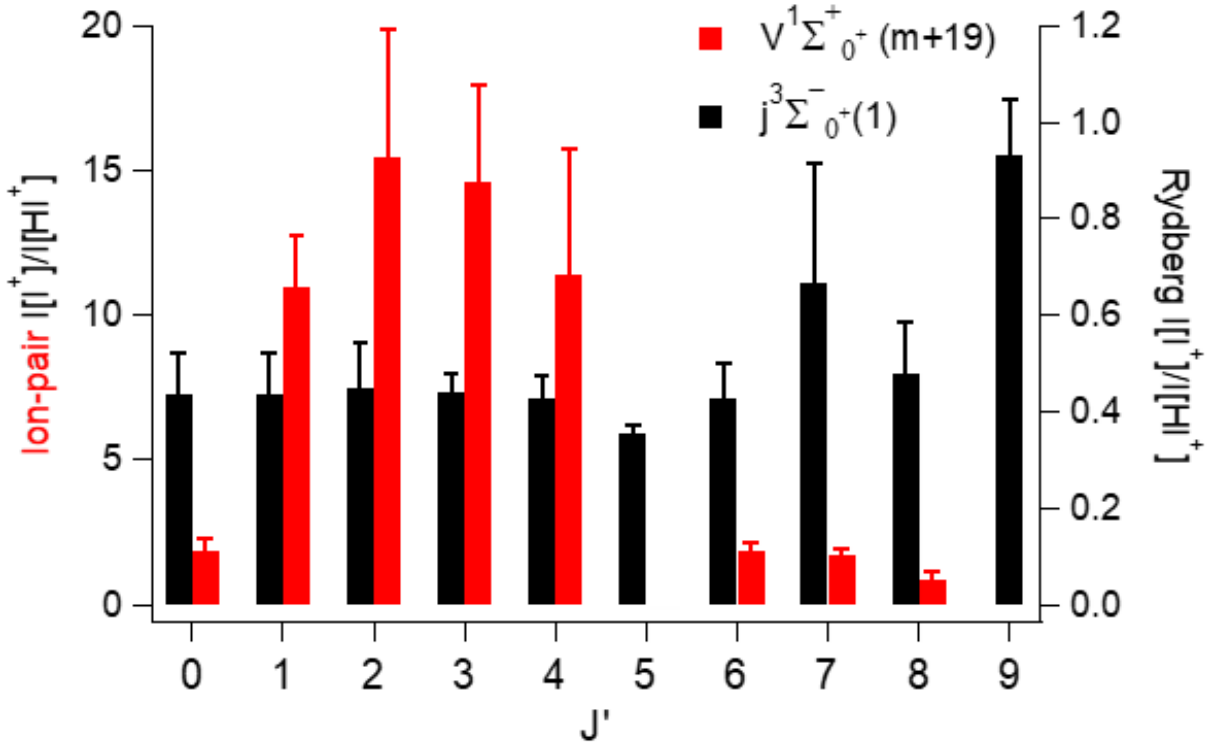

Fig. S7 b) Relative ion-signal intensities $I(I^+)/I(HI^+)$ vs. J´ derived from the Q-rotational lines for the j(1) and V(m + 19) spectra.

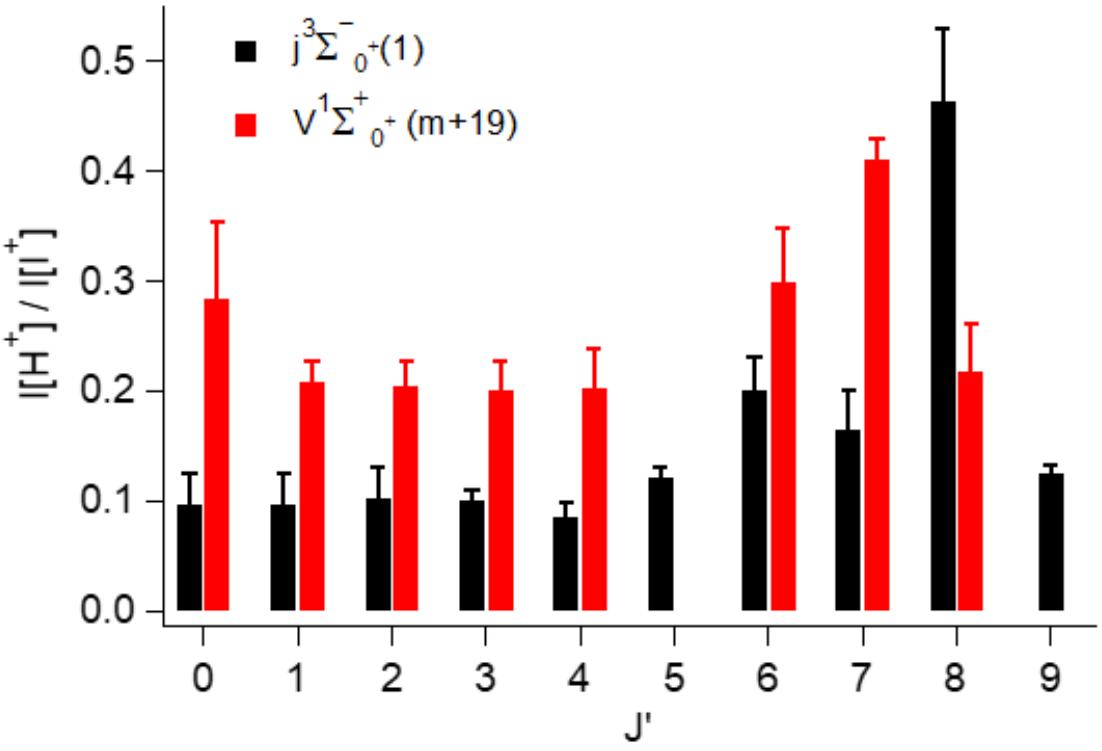

Fig. S7 c) Relative ion-signal intensities $(I(H^+)/I(I^+)$ vs. J´ derived from the Q-rotational lines for the j(1) and V(m + 19) spectra.

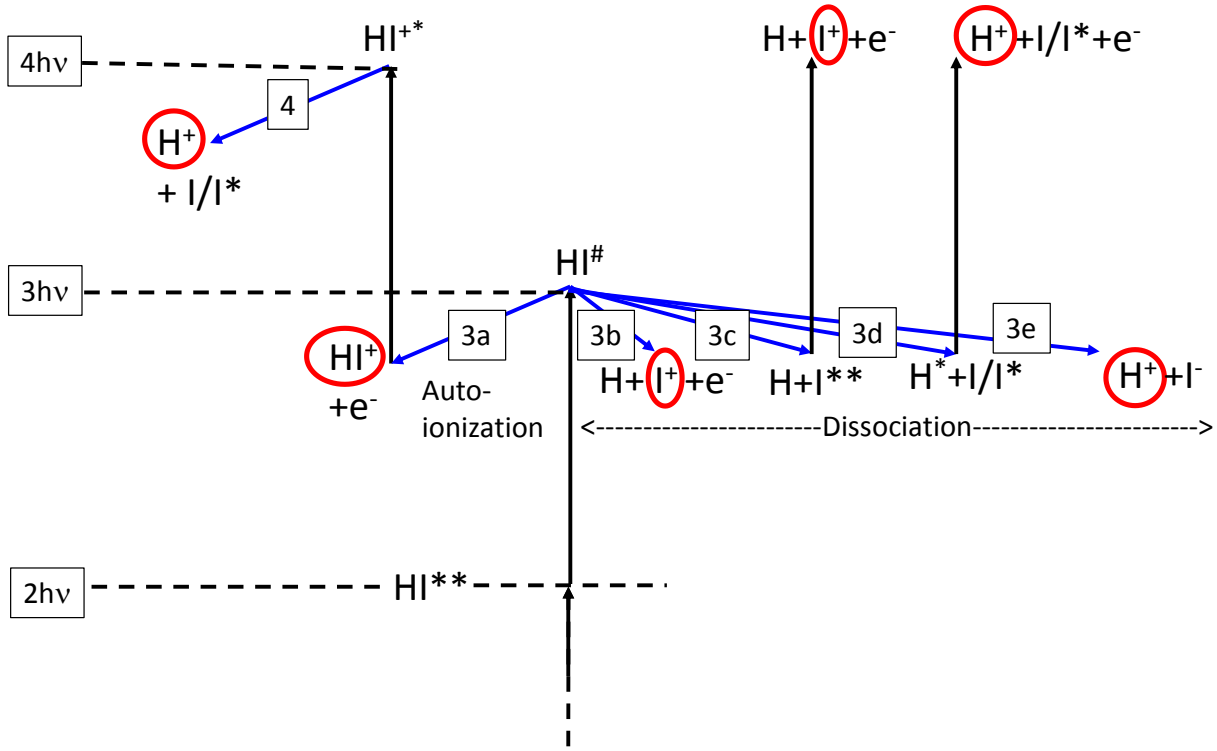

Fig. S8 Schematic energy diagram for excitation processes of HI in the two-photon energy region of 74 000 – 75 000 cm^{-1}. Vertical black arrows denote photon absorption. Blue arrows denote fragmentation (autoionization (3a) and dissociation (3b,3c,3d,3e,4)) processes. The numbers in inside boxes are the number of photons absorbed prior to the fragmentation processes. HI**, and $HI^{\#}$ are resonant and superexcited neutral molecular states, respectively. HI^{+} and HI^{+}* are ground and excited ion states, respectively. I, I* and I** are ground, spin-orbit excited and Rydberg states of iodine atoms, respectively. Ions detected are highlighted by red circles.

Table S1. Rotational lines for HI due to two-photon resonant transitions to four vibrational levels (v' = m + i); i = 16, 17, 18 and 19 of the $V^1\Sigma^+$ ion-pair state and to the $j^3\Sigma^-$ (v' = 1) and $N^1\Pi$(v' = 2) Rydberg states. J = J´

Table 1a. Wavenumbers for measured REMPI transitions in HI for $V^1\Sigma^+ \leftarrow\leftarrow X^1\Sigma^+$ (m + i,0)

J	**i:**	***16***		***17***	***18***	***19***
	O(J)	Q(J)	S(J)	Q(J)	Q(J)	Q(J)
0	74054.0	74091.7		74371.2	74616.4	74926.0
1	74025.2	74086.1		74365.6	74611.2	74919.3
2	73988.8	74075.2	74113.7	74354.4	74600.8	74906.9
3		74059.6	74123.7	74339.2	74585.3	74887.6
4		74040.0	74128.1	74320.0	74566.4	74860.4
5		74014.5		74297.2	74540.4	74826.5
6		73984.4		74268.8	74512.9	74784.4
7				74231.7	74478.8	74746.1
8						74660.8

Table 1b. Wavenumbers for measured REMPI transitions in HI for $j^3\Sigma^-_{0+} \leftarrow\leftarrow X^1\Sigma^+$ (1,0)

J	**O (J)**	**P (J)**	**Q (J)**	**R (J)**	**S (J)**
0	74698.8		74735.2		
1	74672.9		74734.6		
2	74645.6		74733.7		74794.0
3			74731.6		74770.4
4			74728.4		74836.5
5			74724.1		74816.8
6			74717.2		74865.2
7			74699.2		74853.2
8			74721.2		74930.0
9			74712.0		74908.9
10			74698.4		

60

Table 1c. Wavenumbers for measured REMPI transitions in HI for $N^1\Pi_1 \leftarrow\leftarrow X^1\Sigma^+$ (2,0)

J	O (J)	P (J)	Q (J)	R (J)	S (J)
0					
1			74898.8		
2			74898.2		
3			74896.5		
4			74895.6		
5			74893.6		
6			74891.3		
7			74888.5		
8			74885.4		

Table S2. Deperturbation analysis

Hamiltonian matrices, used to derive interaction strengths (W, W') and zero order state energies (E^0) by diagonalization for **a)** two- and **b)** three-state interactions. W is an interaction strength for homogenous interaction and W' stands for heterogenous interaction strength. States of concern are E_1^0=V(m+19), E_2^0=j(1) and E_3^0=N(2):

a) Two state interaction matrices:

$$\begin{matrix} E_1^0 & \boldsymbol{W} \\ \boldsymbol{W} & E_2^0 \end{matrix} \quad \textit{and} \quad \begin{matrix} E_1^0 & \boldsymbol{W'} \\ \boldsymbol{W'} & E_3^0 \end{matrix}$$

b) Three state interaction matrix:

$$\begin{matrix} E_1^0 & \boldsymbol{W} & \boldsymbol{W'} \\ \boldsymbol{W} & E_2^0 & 0 \\ \boldsymbol{W'} & 0 & E_3^0 \end{matrix}$$

Table S3. Band origin (ν^0) and rotational constants (B' and D') attained by traditional line fitting and simulation / deperturbation.

a) $V^1\Sigma^+$ ion-pair vibrational states; Fit analysis

		ν^0/cm^{-1}		B´/cm^{-1}		D´x 10^3/ cm^{-1}		H´x 10^6/ cm^{-1}
State	v´	Our	Others´	Our	Others´	Our	Others´	
$V^1\Sigma^+$	16	74 091.0	74 090 [a]	3.714	3.724 [a]	2.262	0.588 [a]	0
$V^1\Sigma^+$	17	74 372.0		3.896		0.418		0
$V^1\Sigma^+$	18	74 615.4		3.763		3.670		0
$V^1\Sigma^+$	19	74 926.0		3.177		7.650		1.50

a. *Ginter et al. (assigned as V(m+14))*[2]

b) Rydberg states; Fit analysis

		ν^0		B´/cm^{-1}		D´x 10^3/ cm^{-1}		H´x 10^6/ cm^{-1}
State	v´	Our	Others´	Our	Others´	Our	Others´	
$j^3\Sigma^-$	1	74 735.2		6.053		1.115		2.40
$N^1\Pi_1$	2	74 899.2		6.1605		0.390		0

c) Deperturbation analysis

i. Values derived by assuming two state interactions at a time: Homogenous coupling between j(1) ↔ V(m+19) and heterogenous coupling between N(2) ↔ V(m+19).

		ν^0 /cm^{-1}		B$^{0\prime}$/cm^{-1}		D$^{0\prime}$x 10^3/ cm^{-1}		Ω
State	v´	Our	±	Our	±	Our	±	
$V^1\Sigma^+$	19	74 924.0	1	3.049	0.048	3.83	0.86	0+
$j^3\Sigma^-$	1	74 738.0	1	6.102	0.031	1.48	0.28	0+
$N^1\Pi_1$	2	74899.1	1	6.171	0.015	0.62	0.26	1

ii. Values derived by assuming three state interactions: j(1) ↔ V(m+19) ↔ N(2) for homogenous coupling between j(1) ↔ V(m+19) and heterogenous coupling obetween V(m+19) ↔ N(2).

		ν^0 /cm^{-1}		$B^{0'}$/cm^{-1}		$D^{0'}$x 10^3/ cm^{-1}		Ω
State	v´	Our	±	Our	±	Our	±	
$V\,^1\Sigma^+$	19	74 923	3	2.958	0.123	2.17	1.46	0+
$j\,^3\Sigma^-$	1	74 738	1	6.101	0.021	1.51	0.20	0+
$N\,^1\Pi_1$	2	74899	3	6.171	0.205	0.54	3.01	1

Table S4. Rydberg to ion-pair state interactions.

a) **j(1) vs. V(m + 19)** / Homogeneous ($\Delta\Omega = 0$) coupling: Parameters derived from deperturbation analysis of the j(1) Rydberg state (state labelled 1 in table)) and V(m + 19) ion-pair state (state labelled 2 in table) spectra. J' level proximity ($\Delta E_{J'} = E_{J'}(1) - E_{J'}(2)$ / cm^{-1}), interaction strength (W_{12} / cm^{-1}) and fractional state mixing (c_1^2, c_2^2).

J'	$\Delta E_{J'}$	W_{12}	c_1^2	c_2^2
0	-190.8	22.3	0.986	0.014
1	-184.7	22.3	0.985	0.015
2	-173.5	22.3	0.983	0.017
3	-156.2	22.3	0.979	0.021
4	-132.0	22.3	0.971	0.029
5	-102.4	22.3	0.950	0.050
6	-67.2	22.3	0.875	0.125
7	-47.3	22.3	0.669	0.331
8	60.4	22.3	0.838	0.162

b) **N(2) vs. V(m + 19)** / Heterogeneous ($\Delta\Omega \neq 0$) coupling: Parameters derived from deperturbation analysis of the N(2) Rydberg state (state labelled 1)) and V(m + 19) ion-pair state (state labelled 2) spectra. J' level proximity ($\Delta E_{J'} = E_{J'}(1) - E_{J'}(2)$ / cm^{-1}), interaction strength ($W_{12} = 0.75(J'(J'+1))^{1/2}$ / cm^{-1}) and fractional state mixing (c_1^2, c_2^2).

J'	$\Delta E_{J'}$	W_{12}	c_1^2	c_2^2
1	-20.5	1.06	0.997	0.003
2	-9.0	1.84	0.953	0.047
3	8.5	2.60	0.906	0.094
4	35.2	3.35	0.991	0.009
5	67.1	4.11	0.996	0.004
6	106.9	4.86	0.998	0.002

Reference

1. C. M. Western, *PGOPHER, a Program for Simulating Rotational Structure, C. M. Western, University of Bristol*, http://pgopher.chm.bris.ac.uk University of Bristol 9.0.116 edn., 2003-2015.
2. D. S. Ginter, M. L. Ginter and S. G. Tilford, *J. Mol. Spectrosc.*, 1982, **92**, 40.

4.2 Paper 2

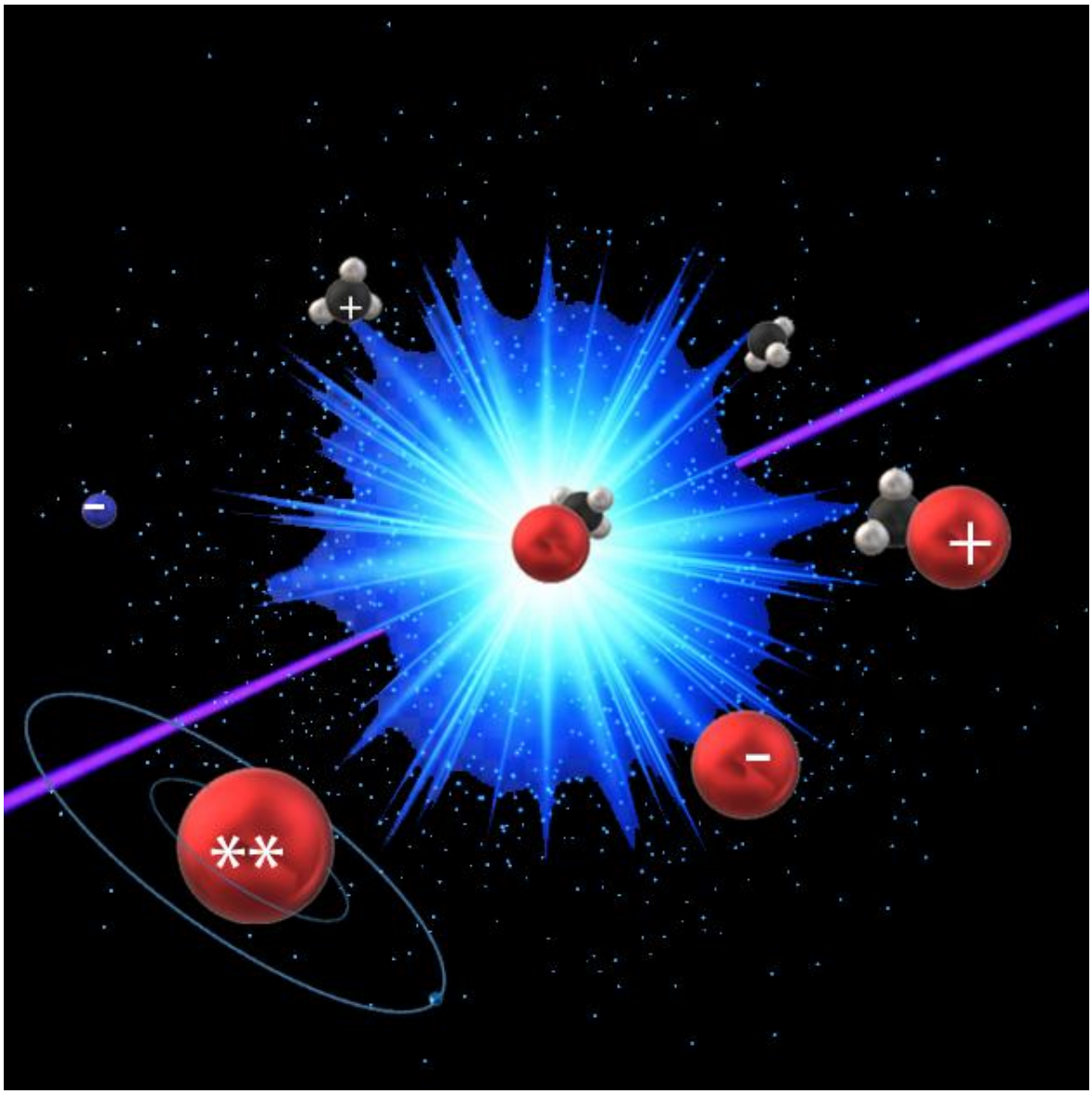

Kristján Matthíasson, Greta Koumrianou, Meng-Xu Jiang, Pavle Glodic, Peter C. Samartzis and Ágúst Kvaran, *Formation of highly excited iodine atoms from multiphoton excitation of CH_3I*, Physical Chemistry *Chem.Phys* (PCCP), **22**, p: 4984 - 4992, **(2020)**.

DOI: 10.1039/C9CP06242D

PCCP

ROYAL SOCIETY OF CHEMISTRY

PAPER

Cite this: *Phys. Chem. Chem. Phys.*, 2020, **22**, 4984

Formation of highly excited iodine atoms from multiphoton excitation of CH_3I†

Kristján Matthíasson, [a] Greta Koumarianou, [b] Meng-Xu Jiang, [a] Pavle Glodic, [b] Peter C. Samartzis *[b] and Ágúst Kvaran *[a]

Received 18th November 2019,
Accepted 7th February 2020

DOI: 10.1039/c9cp06242d

rsc.li/pccp

Mass resolved REMPI spectra, as well as CH_3^+ and I^+ ion and photoelectron images, were recorded for two-photon resonant excitations of CH_3I *via* s, p and d Rydberg states (CH_3I^{**}) in the excitation region of 55 700 to 70 000 cm^{-1}. Photoelectron (PE) and ion kinetic energy release spectra (KERs) were derived from the images. The data revealed that after the two-photon resonant excitation, an additional photon is absorbed to form one or more superexcited state(s) ($CH_3I^{\#}$), followed by branching into three pathways. The major one is the dissociation of $CH_3I^{\#}$ to form excited Rydberg states of iodine atoms (I**) along with CH_3(X), a phenomenon not commonly observed in methyl halides. The second (minor) pathway involves autoionization of $CH_3I^{\#}$ towards CH_3I^+(X), which absorbs another photon to form CH_3^+ along with I/I* and the third one (minor) is $CH_3I^{\#}$ dissociation towards the ion pair, $CH_3^+ + I^-$, prior to I^- electron ejection. Furthermore, one-photon non-resonant dissociation of CH_3I to form CH_3(X) and I/I* prior to three-photon ionization of the fragments is also detected.

I. Introduction

The UV/vis spectroscopy of CH_3I, involving transitions to repulsive valence states (A-band) and higher energy Rydberg states, has previously been recorded and assigned quite thoroughly either by standard absorption[1–5] or REMPI.[6–11] A vast amount of both experimental[10,12–21] and theoretical[22–25] studies on the photodissociation of the molecule in the A-band have made CH_3I a prototype for studying photofragmentation processes in polyatomic molecules. Less, but significant, studies on the photodissociation of the molecule for Rydberg state excitations have also been performed.[6,8,19,26–30] In addition to being of fundamental interest in the fields of molecular spectroscopy and photofragmentation studies, CH_3I has been of interest as a source of atmospheric iodine atoms. Efficient photodissociation of the molecule by UV solar radiation makes it a potentially significant source of iodine atom radicals, and hence a possible agent of ozone depletion.[31–33]

The A-band involves transitions to three different repulsive valence states ($^3Q_0$, $^1Q_1$ and $^3Q_1$) which correlate with CH_3 in its ground electronic state (CH_3(X)) and iodine atoms either in the ground ($I(^2P_{3/2})$) or in the spin–orbit excited ($I^*(^2P_{1/2})$) states (hereby named I and I*, respectively).[17,19] It appears in the wavenumber range of about 28 600–47 600 cm^{-1} (350–210 nm) as a weak, broad, band peaking at about 38 500 cm^{-1} (260 nm) in absorption (see Fig. 1a).[4,34] Photofragmentation studies reveal formation of the I and I* fragments in different proportions depending on the excitation wavenumber.[16,17,19,20] Absorption[4,5] and REMPI photoelectron spectroscopy[7] studies of CH_3I show a series of sharp peaks due to transitions to a large number of states in the excitation region of about 49 600–83 000 cm^{-1} (6.15–10.3 eV). These features have been found to be Rydberg states of s, p and d Rydberg electrons, which converge to the ground ($\Omega = 3/2$) and spin–orbit excited ($\Omega = 1/2$) molecular ion states. Limited photofragmentation studies upon excitation in the Rydberg state region, mainly for the lowest energy 6s Rydberg state, reveal the formation of the ground state fragments CH_3(X) and I/I* by predissociation.[6,8,27–29]

In this paper, we present multiphoton ionization studies of CH_3I, involving two-photon ($2h\nu$: 55 000–70 000 cm^{-1}; see Fig. 1a and b) resonant excitation to intermediate energy ns, np and nd Rydberg states, by mass resolved detection and ion and photoelectron imaging. The analysis sheds light on multiphoton dynamics of the molecule with respect to both photodissociation and photoionization mechanisms involved. Whereas no such data have been presented for CH_3I, comparable studies have been performed on CH_3Br recently.[35–37] The analysis presented here shows a striking difference in the multiphoton-fragmentation dynamics of these two molecules.

[a] *Science Institute, University of Iceland, Dunhagi 3, 107 Reykjavík, Iceland. E-mail: agust@hi.is, kristjm@hi.is, gkoumarianou@ucsb.edu, mej7@hi.is, glodic.pavle@gmail.com; Web: https://notendur.hi.is/agust/; Tel: +354-525-4800*

[b] *Institute of Electronic Structure and Laser, Foundation for Research and Technology-Hellas, Vassilika Vouton, 71110 Heraklion, Greece. E-mail: sama@iesl.forth.gr; Fax: +30-2810-391305; Tel: +30-2810-391467*

† Electronic supplementary information (ESI) available. See DOI: 10.1039/c9cp06242d

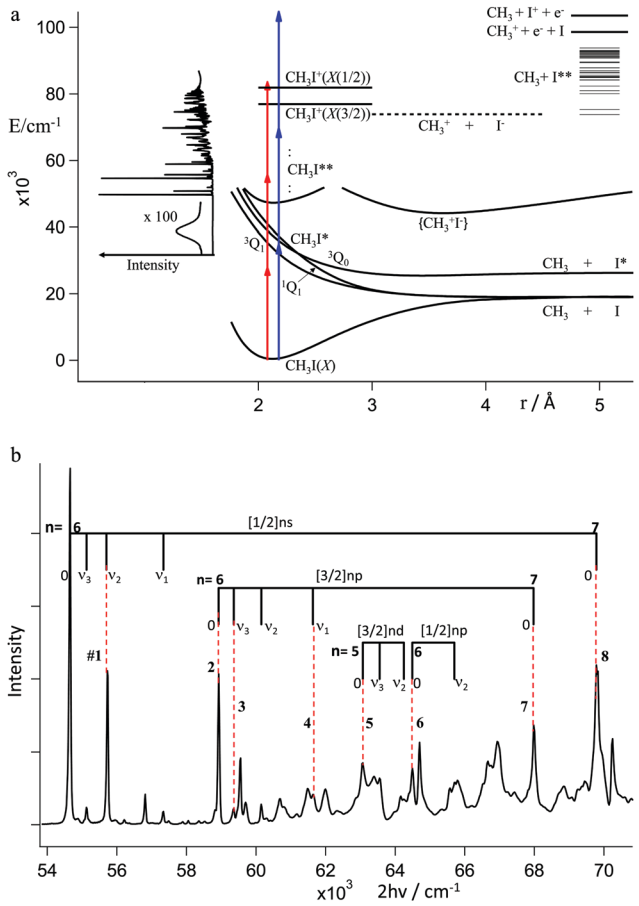

Fig. 1 Energetics and excitations *vs.* absorption spectra for CH_3I: (a) shows potential energy curves for the ground state ($CH_3I(X)$), A-band repulsive states (CH_3I^*: $^3Q_1$, $^1Q_1$, $^3Q_0$), the lowest energy Rydberg state (CH_3I^{**}) and an ion-pair state ($CH_3^+I^-$) derived from ref. 24 and energy thresholds. Arrows indicate the smallest ($2h\nu$ = 55 700 cm^{-1}, red color) and the largest ($2h\nu$ = 69 783 cm^{-1}, blue color) energy photons used (excitations no. 1 and 8 in Table 1). The absorption spectrum for CH_3I from ref. 4 is inserted and rotated to the left. (b) shows the CH_3I absorption spectrum from ref. 4 in the excitation region of about 54 000–70 000 cm^{-1} along with the assignment of selected Rydberg states. The two-photon resonant Rydberg state excitations involved in the slice imaging//REMPI studies, in this work, are marked by dashed, red lines and the numbers in Table 1.

II. Experimental

The slice imaging setup used in this work has been described in detail before.[38,39] Hence, only a brief description will be given here. A supersonic molecular beam, typically a mixture of 20% CH_3I in He, was formed by expansion through a home-made piezoelectrically-actuated nozzle valve (∅ 1 mm orifice) and skimmed (∅ 1.5 mm, Beam Dynamics) prior to entering the interaction region of the slice imaging setup. A stagnation pressure of $P_0 \sim 1$ bar was used. The excitation laser beam was focused (f = 30 cm) on the geometric focal point of a single-electrode repeller-extractor plate arrangement where it intersected the collimated molecular beam at right angles. The laser beam (typically 1.5 mJ per pulse) was generated by a pulsed Nd^{3+}:YAG laser (Spectra Physics Quanta Ray Pro 250) pumping a master oscillator – power oscillator system (Spectra Physics MOPO 730-10) set at the appropriate wavelength.

For the slicing experiments reported here, the repeller is pulsed ON at the appropriate time delay (~300 ns) following the photolysis/ionization. The charged photofragments traverse a field-free time-of-flight region (45 cm) and a gated, position-sensitive detector (dual, imaging-quality MCP array coupled to a phosphor screen) images the center slice of the photofragment sphere. The image frame is recorded asynchronously every second (~10 laser shots) by a CCD camera and several thousand frames are averaged to form images such as those shown in Fig. 2. Each final image is integrated from its center over angle to extract the speed and over radius to extract the angular distributions of the corresponding fragments. For photoelectrons, the repeller is negatively charged and both the repeller electrode and the detector are not gated (*i.e.*, they are always ON).

III. Results and analysis

A. Mass resolved MPI

Mass resolved multiphoton ionization (MR-MPI) data were collected for CH_3I by the use of low laser power (typically 0.2 mJ pulse energy) in the two-photon excitation region of 62 800–70 000 cm^{-1}. REMPI spectra of the CH_3^+ and I^+ ions were derived from the data (see ESI†[40]). Of immediate interest was the prevalence of strong iodine atomic lines due to two-photon resonant excitations from the ground (I) and spin–orbit excited (I*) atoms to atomic Rydberg states (I**)[41] followed by one-photon ionization, *i.e.* I/I* (2 + 1) REMPI. Weak background signals (continua) of fragment ions I^+ and CH_3^+, were also detected in the region with $I^+ \gg CH_3^+$, virtually independent of the excitation energy. Weak I_2^+ ion signals were also detected, decreasing in intensity with buffer gas dilution. Noticeably no signals for the parent molecular ion (CH_3I^+) were detected. These observations can be interpreted in the following way.

The majority of the signals observed for I^+ and CH_3^+ stem from initial one-photon dissociation *via* repulsive valence states of CH_3I (CH_3I^*; A-band) to form CH_3 in its ground electronic state, possibly vibrationally excited, ($CH_3(X,\nu_1\nu_2\nu_3\nu_4)$) along with I/I*, followed by ionization. The iodine atomic line peaks appear in the cases of resonant excitations to I**, whereas, the weaker "background" signal (continuum) must be due to three-photon non-resonant ionization of I/I*. The CH_3^+ ion signals must, equivalently, be due to three-photon non-resonant ionization of ($CH_3(X,\nu_1\nu_2\nu_3\nu_4)$),

$$CH_3I + 1h\nu \rightarrow CH_3I^*; \quad \text{one-photon excitation} \tag{1a}$$

$$CH_3I^* \rightarrow CH_3(X,\nu_1\nu_2\nu_3\nu_4) + I/I^*; \quad \text{dissociation} \tag{1b}$$

$$CH_3(X,\nu_1\nu_2\nu_3\nu_4) + 3h\nu \rightarrow CH_3^+ + e^-; \quad \text{three-photon non-resonant ionization} \tag{1c}$$

$$I/I^* + 3h\nu \rightarrow I^+ + e^-; \quad \text{three-photon non-resonant ionization} \tag{1d}$$

$$I/I^* + 2h\nu \rightarrow I^{**}; I^{**} + 1h\nu \rightarrow I^+ + e^-; \quad I/I^* \text{ (2 + 1) REMPI} \tag{1e}$$

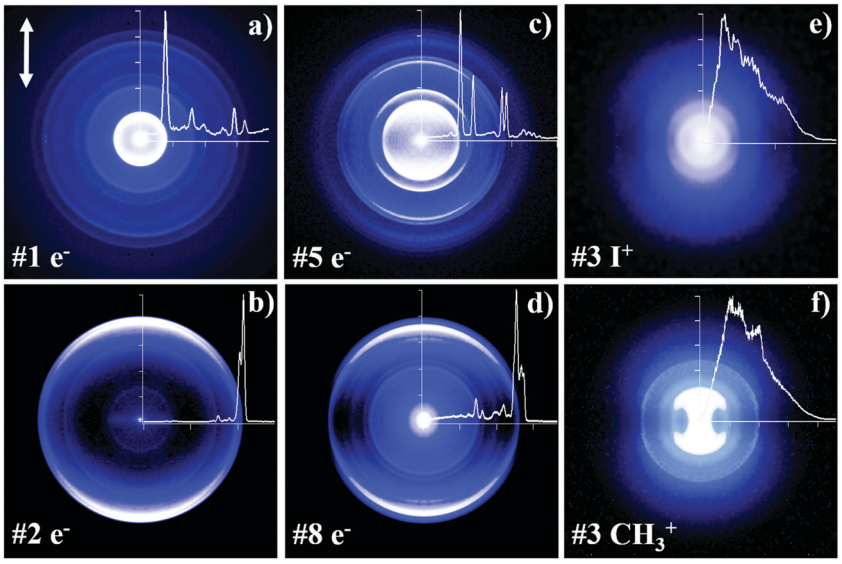

Fig. 2 Ion and photoelectron (PE) slice images and corresponding kinetic energy release spectra (KERs) recorded for the two-photon resonant excitations (see Table 1) at (a) 55 700 cm^{-1} (no. 1; PE), (b) 58 926 cm^{-1} (no. 2; PE), (c) 63 067 cm^{-1} (no. 5; PE), (d) 69 783 cm^{-1} (no. 8; PE), (e) 59 362 cm^{-1} (no. 3; I^+) and (f) 59 362 cm^{-1} (no. 3; CH_3^+). The image intensity scale has been adjusted to show all major features. The KERs are normalized to the strongest peak in each spectrum. The laser polarization is indicated by the double arrow in panel (a).

Thus, the "structureless" spectra of the I^+ and CH_3^+ ion fragments (apart from the I/I* atomic REMPI spectra) can be attributed to an overall non-resonant photolysis process through the repulsive valence states (A-band) and negligible contributions involving an initial two-photon resonant excitation of CH_3I. The I_2^+ mass signals most probably are associated with CH_3I cluster ($(CH_3I)_n$) formation, not to be dealt with here.[42]

B. Ion and photoelectron images

I^+ and CH_3^+ ion and photoelectron images were recorded for two-photon resonant excitation of CH_3I to a total of eight known Rydberg states in the excitation region of 55 000–70 000 cm^{-1}. These states belong to the Rydberg series which converge to either of the two spin–orbit components of the ground ionic CH_3I^+ states $X(^2\Pi_{3/2})$ and $X(^2\Pi_{1/2})$ for ns, np and nd Rydberg electrons.[4] The transitions and the Rydberg states are listed in Table 1 and marked in Fig. 1b. Ion and photoelectron (PE) kinetic energy release spectra (KERs) were derived from the images. Selected ion/photoelectron images and corresponding KERs are shown in Fig. 2.

Photoelectrons; KERs. Fig. 3 shows the photoelectron (PE) KERs derived from the images (see also Table 1 and Fig. 1b). All the spectra (images) show clear peaks (rings) varying in number and position (KER) depending on the excitation energy.

In Fig. 3a the spectra have been shifted by the one-photon energy difference ($\Delta(1h\nu) = |1h\nu_i - 1h\nu_0|$) with respect to the spectrum derived for the highest energy excitation (*i.e.* the "reference spectrum" for the one-photon excitation of $1h\nu_0$ = 34 892 cm^{-1}/two-photon excitation of $2h\nu_0$ = 69 783 cm^{-1}; image no. 8 in Table 1).[35–37] This way, spectral features due to one-photon ionization of the same species will match. Similarly, in Fig. 3b selected spectra have been shifted by the three-photon energy difference ($\Delta(3h\nu) = |3h\nu_i - 3h\nu_0|$) with respect to the same reference spectrum to allow comparison of

Table 1 Transitions (no. 1–8) used to obtain slice images for CH_3^+, I^+ and photoelectron (PE) images reported in this paper

# (number)	Two-photon excitation energy/cm^{-1}	CH_3I Rydberg states $[\Omega]nl$; $(\nu_1,\nu_2,\nu_3)^a$
1	55 700	[1/2]6s; (0,1,0)
2	58 926	[3/2]6p; (0,0,0)
3	59 362	[3/2]6p; (0,0,1)
4	61 632	[3/2]6p; (1,0,0)
5	63 067	[3/2]5d; (0,0,0)
6	64 484	[1/2]6p; (0,0,0)
7	67 984	[3/2]7p; (0,0,0)
8	69 783	[1/2]7s; (0,0,0)

[a] $[\Omega_c]$: total angular momentum quantum number for the core ion. n: principal quantum number for the Rydberg electron. l: Rydberg electron orbital (s, p, d). (ν_1,ν_2,ν_3): vibrational quantum numbers referring to the selected vibrational modes, ν_1 (CH_3 symmetric stretch), ν_2 (umbrella) and ν_3 (C–I stretch).

common spectral features due to three-photon ionization processes (see also ESI† [40]). Calculated threshold energies (*i.e.*, maxima of kinetic energy release) for various ionization processes are also marked in the figures.

In Fig. 3a we show thresholds corresponding to one-photon ionization of iodine atomic Rydberg states (I**), *i.e.*

$$I^{**} + 1h\nu \rightarrow I^+ + e^-; \quad \text{one-photon ionization} \qquad (2)$$

Each grid line in the figure represents an energy threshold corresponding to the kinetic energy release of an electron expelled by one photon from a specific Rydberg state as depicted in the figure and specified more precisely in Table 2. As can be seen, these energy thresholds match many observed peaks in all the spectra, which suggests that multiple I** Rydberg states are formed after a given excitation energy (multiple exit channels). Weak, broad peaks observed in spectra no. 4–8, for kinetic energy release of about 1.2 eV for the reference spectrum, could

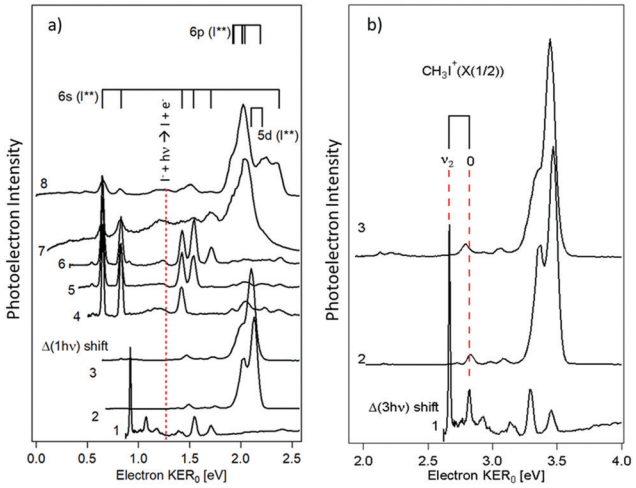

Fig. 3 Photoelectron KERs: (a) derived from images 1–8 (see Table 1) shifted by a one-photon energy difference ($\Delta(1h\nu) = |1h\nu_i - 1h\nu_0|$) with respect to the spectrum for the highest energy excitation (*i.e.* reference spectrum, no. 8), (b) derived from images 1–3 shifted by a three-photon energy difference ($\Delta(3h\nu) = |3h\nu_i - 3h\nu_0|$) with respect to the spectrum for the highest energy excitation recorded. Energy thresholds (energy maxima) (a) for one-photon ionization of Rydberg iodine atoms (I**) and (b) auto-ionization of superexcited CH_3I ($CH_3I^{\#}$), formed by three-photon excitation, are indicated by sticks above the KERs. The threshold for I^- one-photon electron ejection is indicated in (a) by a dashed red line. The spectra are plotted as a function of the electron KER for the reference spectra (KER_0). The spectra are normalized to the strongest peak in each spectrum.

not be assigned to a one-photon ionization of I**. These are found to match an energy threshold corresponding to a one-photon electron ejection of I^- (see also ref. 40), *i.e.*

$$I^- + 1h\nu \rightarrow I + e^-; \quad \text{one-photon ejection} \qquad (3)$$

indicating an ion-pair ($CH_3^+ + I^-$) formation.

In Fig. 3b we show thresholds corresponding to possible autoionization of super-excited CH_3I state(s) ($CH_3I^{\#}$) which could be formed as,

$$CH_3I + 2h\nu \rightarrow CH_3I^{**}; \quad \text{two-photon resonant excitation} \qquad (4a)$$

$$CH_3I^{**} + 1h\nu \rightarrow CH_3I^{\#}; \quad \text{one-photon excitation} \qquad (4b)$$

$$CH_3I^{\#} \rightarrow CH_3I^+(X) + e^-; \quad \text{autoionization} \qquad (4c)$$

where CH_3I^{**} is a molecular Rydberg state. The grid lines (thresholds), shown, are energy thresholds for formation of specific vibrational states of $CH_3I^+(X(1/2))$, which are found to match peaks in spectra no. 1–3, only.

I^+ and CH_3^+ ions; KERs. Fig. 4 shows the ion KERs derived from all the images (see also Table 1 and Fig. 1b). Fig. 4a shows those derived from the I^+ images and Fig. 4b and c those for CH_3^+. The I^+ KERs can be divided into two major observations. First, at relatively low kinetic energies (<4 eV), all the spectra show peaks and/or shoulders. Those for the low energy excitations no. 2 and 3 seem to consist of at least two overlapping contributions. Second, very broad peaks or shoulders at high energies are seen in some of the spectra (see no. 1, 4, 5 and 6 in Fig. 4a). All the CH_3^+ spectra (Fig. 4b and c), except for excitation no. 8, show low kinetic energy contributions, as broad peaks, without resolved vibrational structure except for no. 3. The spectrum for excitation no. 8 is the only one that displays sharp peaks. In Fig. 4a and b the spectra have been shifted by a three-photon energy difference ($\Delta(3h\nu) = |3h\nu_i - 3h\nu_0|$), similar to Fig. 3b, with respect to the spectrum derived for the highest energy excitation (*i.e.* the "reference spectrum" for the two-photon excitation of $2h\nu_0$ = 69 783 cm^{-1}/three-photon excitation of 104 675 cm^{-1}; image no. 8) to allow comparison of common spectral features due to three-photon dissociation processes.[35–37]

Table 2 Assignment of peaks observed in the photoelectron spectra no. 1–8 (see Table 1). Table entries are photoelectron kinetic energy release values in eV

	Excitation[a,b]							
	1	2	3	4	5	6	7	8
# Rydberg states	[1/2]6s,ν_2	[3/2]6p,0	[3/2]6p,ν_3	[3/2]6p,ν_1	[3/2]5d,0	[1/2]6p,0	[3/2]7p,0	[1/2]7s,0
e^- donators/formation:								
$I^{**}(6s,^2D_{5/2})^c$				0.143	0.232	0.320	0.537	0.648
$I^{**}(6s,^2D_{3/2})^c$			1.525	0.324	0.413	0.501	0.718	0.829
$I^{**}(6s,^2S_{1/2})^c$	0.552			0.920	1.009	1.097	1.313	1.425
$I^{**}(6s,^2P_{3/2})^c$	0.666				1.123	1.211	1.428	1.539
$I^{**}(6s,^2P_{1/2})^c$	0.835					1.591	1.597	1.709
$I^{**}(6p,^2D_{5/2})^c$							1.811	1.922
$I^{**}(6p,^2D_{3/2})^c$							1.821	1.932
$I^{**}(6p,^2F_{7/2})^c$		1.341	1.368				1.902	2.013
$I^{**}(6p,^2F_{5/2})^c$		1.343	1.371				1.905	2.017
$I^{**}(6p,^2P_{1/2})^c$		1.367	1.394				1.948	2.060
$I^{**}(5d,^2P_{3/2})^c$		1.429	1.455				1.990	2.101
$I^{**}(6p,^2P_{3/2})^c$								2.189
$I^{**}(5d,^2P_{1/2})^c$								2.219
$I^{**}(6s,^2D_{5/2})^c$								2.374
I^{-d}				0.762	0.851	0.939	1.156	1.267
$CH_3I^{\#} \rightarrow CH_3I^+(X(1/2); \nu_i = 0) + e^{-e}$	0.199	0.799	0.880					
$CH_3I^{\#} \rightarrow CH_3I^+(X(1/2); \nu_2 = 1) + e^{-e}$	0.043							

[a] See Table 1. [b] ν_i refers to relevant mode of vibration as labeled by NIST.[41] (*e.g.* ν_2 = vibrational mode no. 2; 0 refers to $\nu_i = 0$). [c] e^- formation by one-photon ionization: $I^{**} + 1h\nu \rightarrow I^+ + e^-$; see Fig. 3a. [d] e^- formation by $I^- + 1h\nu \rightarrow I + e^-$; see Fig. 3a. [e] e^- formation by autoionization; see Fig. 3b.

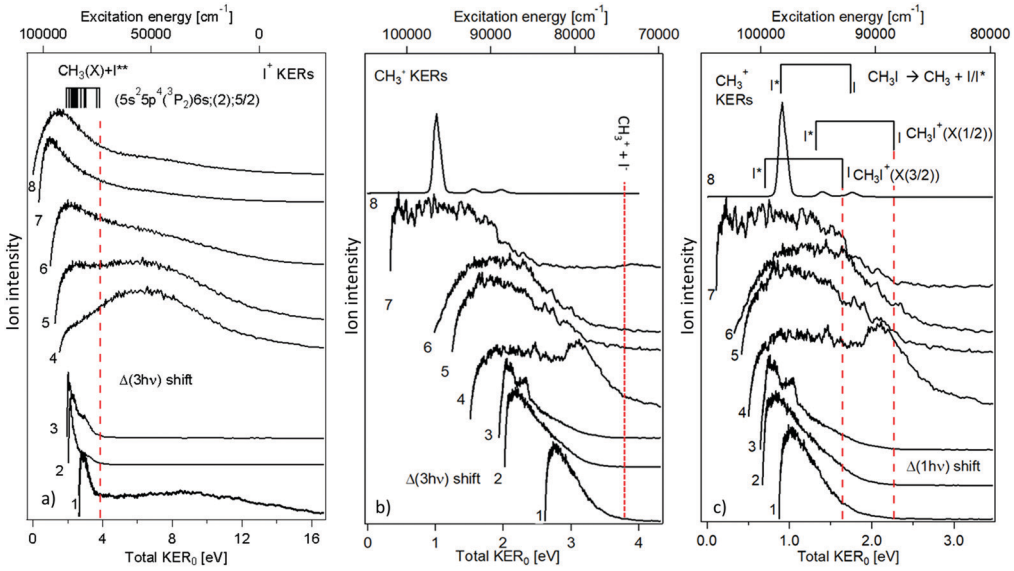

Fig. 4 Ion kinetic energy release spectra (KERs) derived from images no. 1–8 (see Table 1). (a) I^+ KERs shifted by the three-photon energy difference ($\Delta(3h\nu) = |3h\nu_i - 3h\nu_0|$) with respect to the spectrum derived for the highest energy excitation (*i.e.* reference spectrum no. 8). (b) CH_3^+ KERs shifted as in (a). (c) CH_3^+ KERs shifted by the one-photon energy difference ($\Delta(1h\nu) = |1h\nu_i - 1h\nu_0|$) with respect to the spectrum derived for the highest energy excitation. Energy thresholds (energy maxima) for three-photon dissociation of CH_3I to form (a) Rydberg iodine atoms (I**) along with $CH_3(X)$ and (b) ion-pairs ($CH_3^+ + I^-$) are indicated. Energy thresholds (energy maxima) for one-photon dissociation of CH_3I to form $CH_3(X)$ along with I/I* as well as for one-photon dissociation of $CH_3I^+(X)$ to form $CH_3^+(X)$ along with I/I* are indicated in (c). The spectra are plotted as a function of the total KER for the reference spectra (Total KER_0). The top scales show the photoexcitation energies in cm^{-1}. The spectra are normalized to the strongest peak in each spectrum.

Similarly, in Fig. 4c the spectra have been shifted by the one-photon energy difference ($\Delta(1h\nu) = |1h\nu_i - 1h\nu_0|$) with respect to the same reference spectrum to allow comparison of common spectral features due to one-photon dissociation processes. Calculated maxima of kinetic energy release (*i.e.* threshold energies) for the various ionization processes relevant to the discussion in the previous section are also shown in the figures. Broad spectral features with tails towards high kinetic energy release, lower than the thresholds (*i.e.* max KER), (*i.e.* all except the CH_3^+ KER for no. 8), could, in principle, correspond to the processes indicated in Fig. 4a–c, in which case the lower kinetic energy release corresponds to internal excitation of the CH_3 co-fragment.[36]

In Fig. 4a (I^+ KERs), we show thresholds corresponding to three-photon dissociation of CH_3I, including excitations (4a) and (4b), to form iodine atoms in Rydberg states (I**) along with $CH_3(X)$ for the lowest energy I** states, according to,

$$CH_3I^{\#} \rightarrow CH_3(X) + I^{**}; \quad \text{dissociation} \tag{5}$$

These thresholds match quite well with the observed low kinetic energy contributions mentioned above. Thus, the lowest energy I** + CH_3 thresholds (highest kinetic energy release), corresponding to the formation of the $I^{**}(6s\ ^2D_{5/2,3/2})$ fragments are found to match the high energy edges of those contributions for excitations no. 1–3. This agrees with the observation of I** ionization photoelectrons discussed in the previous section. The broad peaks or shoulders at higher energies are of unknown origin. These might be associated with formation and ionization of I/I* following multiple ($nh\nu$; $n > 3$) photon excitation and/or cluster formation (see Section III(A)).

In Fig. 4b (CH_3^+ KERs) the threshold corresponding to three-photon dissociation of CH_3I, including excitations (4a) and (4b), to form the ion-pairs is shown, *i.e.*,

$$CH_3I^{\#} \rightarrow CH_3^+ + I^-; \quad \text{dissociation} \tag{6}$$

The threshold is either found to be reasonably close to the high energy edges of the KERs or in the high energy slopes of apparently overlapping spectral contributions for the KERs no. 1–6. Considering the observation of a one-photon electron ejection of I^- for excitations no. 4–7, as mentioned above, there is reason to believe that the observed CH_3^+ signals could partly be due to dissociation channel (6). In this respect, it is worth noting that the KERs no. 1–3 differ significantly in structure from those no. 4–7, suggesting that the major CH_3^+ formations may, indeed, differ for these two groups (no. 1–3 *vs.* no. 4–7) of excitations (see next paragraph).

In Fig. 4c thresholds are shown corresponding to one-photon dissociation of $CH_3I^+(X(^2\Pi_{3/2}))$ and $CH_3I^+(X(^2\Pi_{1/2}))$ in its ground vibrational states to form CH_3^+ along with I and I*, *i.e.*

$$CH_3I^+(X(3/2,1/2)) + 1h\nu \rightarrow CH_3^+ + I/I^*; \quad \text{photodissociation} \tag{7}$$

The highest energy threshold of these, for photodissociation of $CH_3I^+(X(^2\Pi_{1/2}))$ to form CH_3^+ and I, matches the high energy edges of the KERs no. 1–3, which supports the previous statement relevant to the autoionization process identified from the PES's for the same excitations (eqn (4)).

The CH_3^+ KER spectrum for excitation no. 8, showing dramatically different structures to those for lower energy excitations,

requires special attention (Fig. 4b and c). Whereas all the other KERs (both for CH_3^+ and I^+), which have been assigned, show broad spectral features peaking at relatively low kinetic energies, the CH_3^+ KER spectrum for no. 8 shows sharp peaks. This is indicative of photodissociation processes where limited energy has redistributed among the molecule's internal degrees of freedom, prior to dissociation, as to be expected for direct, non-delayed, photodissociation.[36] The sharp peaks are, indeed, found to match energy thresholds for direct one-photon non-resonant photodissociation processes through the A-band, mentioned in Section III(A), as shown in Fig. 4c. Based on the signal intensities for the formation of CH_3(X,0000) along with I and I* the branching fraction for the I/I*formation is found to be $I/(I + I^*) \approx 0.04$.

C. Angular distributions

All the ion images recorded exhibit angular distributions corresponding to overall parallel transitions (see Fig. 2) of a degree which varies with kinetic energy release (KER). Angular distributions of selected KER ranges in the form of signal intensities as a function of the angle from 0 to 180° were fitted by the expression corresponding to a one-step, direct (non-resonant) photodissociation[35,36]

$$P(\theta) = A\left[1 + \sum_n \beta_{2n} P_{2n}(\cos(\theta))\right] \quad (8)$$

to derive anisotropy parameters β_{2n} (n = 1–3). n is the number of photons involved in the photolysis, P_{2n} is the $2n$-th order Legendre polynomial and A is a scaling factor. β_{2n} is the weighting coefficient of the corresponding P_{2n} polynomials. β_{2n} parameters derived from the data are presented in ref. 40 and Table 3.

As mentioned above, all ions, except for the CH_3^+ ions formed by excitation no. 8, are believed to be formed by channels that involve, at least, three or four-photon excitations *via* resonant transitions as well as energy redistribution among the molecule's internal degrees of freedom. These can, therefore, not be easily interpreted by standard one-step angular distribution analysis (see also discussion in Section IV and Fig. 5). The CH_3^+ ions formed by excitation no. 8, on the other hand, are created by a direct one-photon non-resonant dissociation. The values for β_2, for no. 8, of about 1.3–1.8 (Table 3) are indicative of dominating parallel transitions prior to dissociation.

IV. Discussion

Based on the results described above, four processes are responsible for our observations (see Fig. 5 and Table 4; labels **1**, **3a**, **3b** and **3c**, **4**, where the numbers refer to the number of photons involved):

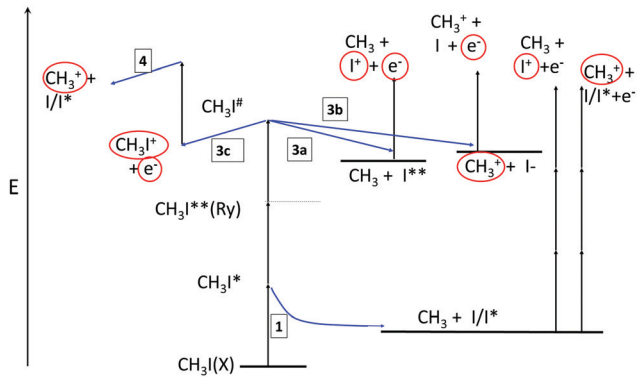

Fig. 5 Schematic energy diagram for excitation processes of CH_3I observed in this work. Vertical black arrows denote photon absorption. Blue arrows denote fragmentation (dissociation and autoionization) processes after the photoexcitations. Photofragmentation processes observed in this work are marked by numbers of photons required for the excitations (and letters) inside boxes (**1**, **3a**, **3b**, **3c**, **4**; see also main text). CH_3I(X), CH_3I*, CH_3I**(Ry) and $CH_3I^\#$ are CH_3I ground, repulsive valence (A-band states), Rydberg and superexcited states, respectively. CH_3I^+ is the molecular ion ground state and I** denotes iodine atom Rydberg states. Charged particles (ions, electrons) detected are highlighted by red circles.

1 (CH_3 and I/I* formation)

One-photon dissociation, *via* repulsive valence states (CH_3I*; the A band), to form CH_3(X) and I/I* followed by three-photon ionization of the fragment species (see eqn (1)). The mass resolved REMPI data form the major evidence for the existence of this process in the excitation region of concern (55 000–70 000 cm^{-1}). In the slice images, only CH_3^+ data of excitation no. 8 features this channel. This does not mean, however, that the channel does not exist for other excitations. It is just evidence that other processes involving three-photon excitations (**3a** in particular; see below) are more efficient.

3a (I** formation)

Three-photon dissociation of CH_3I, (two-photon resonant transition to molecular Rydberg states (CH_3I**) plus one-photon excitation to one or more superexcited state(s) ($CH_3I^\#$)), resulting in atomic iodine Rydberg states, I** (54 000–68 000 cm^{-1}) and CH_3(X), followed by one-photon ionization of I** (eqn (4a), (4b), (5) and (2)). This is the major channel observed.

3b (ion-pair formation)

Three-photon dissociation of CH_3I (*via* two-photon resonant transition to CH_3I** and one-photon excitation to $CH_3I^\#$), resulting in CH_3^+ and I^-, followed by a further detachment of I^- to form I and e^- (eqn (4a), (4b), (6) and (3)).

Table 3 β_{2n} (n = 1, 2, 3) parameters derived from angular distributions of rings (peaks in KER) for the CH_3^+ ion image of excitation no. 8 (Table 1), due to formation of $CH_3(X,v_1v_2v_3v_4)$ + I/I* by one-photon non-resonant excitation in the A-band

$CH_3(X,v_1v_2v_3v_4)$ + I/I*	KER (eV)	β_2	β_4	β_6
CH_3(X,0000) + I*	0.91	1.76 ± 0.06	−0.08 ± 0.05	0.04 ± 0.05
CH_3(X,1000) + I/CH_3(X,0010) + I	1.40	1.31 ± 0.23	−0.35 ± 0.22	−0.16 ± 0.23
CH_3(X,0000) + I	1.77	1.50 ± 0.11	−0.18 ± 0.10	−0.23 ± 0.12

Table 4 Photofragmentation channels (**1**, **3a**, **3b**, **3c**, **4**; see main text and Fig. 5) observed in this work for excitations 1–8 (see Table 1) *vs.* detection techniques

# Excitation	1	2	3	4	5	6	7	8
Rydberg states	[1/2]6s,ν_2	[3/2]6p,0	[3/2]6p,ν_3	[3/2]6p,ν_1	[3/2]5d,0	[1/2]6p,0	[3/2]7p,0	[1/2]7s,0
MR-REMPI[a]					**1**	**1**	**1**	**1**
PE-KERs[b]	**3a**	**3a**	**3a**	**3a**	**3a**	**3a**	**3a**	**3a**
	3c	**3c**	**3c**	**3b**	**3b**	**3b**	**3b**	**3b**
I^+ KERs[c]	**3a**	**3a**	**3a**	**3a**	**3a**	**3a**	**3a**	**3a**
CH_3^+ KERs[c]	**3c, 4**	**3c, 4**	**3c, 4**	**3b**	**3b**	**3b**	**3b**	**1**

[a] The mass resolved (MR) REMPI data form the major evidence for the existence of process 1 in the total excitation region of concern. [b] The photoelectron (PE) KERs serve as conclusive evidence for the existence of the ionization processes. [c] The ion KERs serve as conclusive evidence for the existence of the photoexcitation processes.

3c, **4** (autoionization and ion photolysis)

Three-photon excitation of CH_3I, (two-photon resonant transition to CH_3I^{**} and one-photon excitation to $CH_3I^{\#}$), followed by autoionization ($CH_3I^+(X)$ formation) and absorption of an additional photon (fourth photon) leading CH_3I^+ to a dissociative state and formation of CH_3^+ and I/I* (eqn (4a), (4b), (4c) and (7)).

The I** formation pathway (**3a**) is found to be the major channel according to all the PE images, except for the excitation $2h\nu$ = 55 700 cm^{-1}, *via* the Rydberg state ([1/2]6s,ν_2) (no. 1), where **3c** (autoionization) dominates. This is in striking contrast with observations for methyl bromide (CH_3Br) in cases of three-photon excitations *via* resonant p and d molecular Rydberg states.[36,37] In CH_3Br, dissociation of a superexcited $CH_3Br^{\#}$ state(s) forms excited CH_3 (Rydberg) states (CH_3^{**}) along with $Br(^2P_{3/2})$ or $Br^*(^2P_{1/2})$, *i.e.* the excitation energy is mainly channeled into CH_3, whereas Br acts mostly as a spectator. In the CH_3I case, on the other hand, the excitation energy is channeled into the iodine atom (I**), whereas CH_3 is formed in its ground state with rovibrational excitation only. In both cases, the formation of CH_3^{**} as well as excited (Rydberg) halogen atoms (I** or Br**) is energetically possible.[41,43] The relative energies of comparable formation thresholds differ, however, in favour of CH_3^{**} formation for CH_3Br but I** for CH_3I. Thus, for example, the formation of the lowest energy Br**(5s) is higher in energy than the formation of $CH_3^{**}(3p\ ^2A_2)$ for CH_3Br, opposite to what holds for the lowest energy I**(6s) for CH_3I. The different outcomes must be due to a difference in the structure of the potential energy surfaces on which the dissociations occur.

Comparing the photoelectron and ion results at different excitation energies, there are characteristic differences in the photofragmentation processes with excitation energy (see Table 4 and Fig. 3, 5). According to the photoelectron data for the lowest energy excitations (no. 1–3), the relative contribution of channel **3a** (I** formation) increases as channel **3c** ($CH_3I^+(X)$ formation) decreases with energy. This suggests that there is a competition between the I** and $CH_3I^+(X)$ formation channels at the $CH_3I^{\#}$ level after the three-photon excitation. This might be associated with a decreasing probability of autoionization, which is to be expected as the energy difference between $CH_3I^{\#}$ and $CH_3I^+(X)$ increases. Despite being energetically accessible (see Fig. 1a), no ion-pair formation is observed for these excitations (see more details in next paragraph). For the higher energy excitations (no. 4–8), where channel **3c** ($CH_3I^+(X)$ formation) is not detected, the formation of I**, according to channel **3a**, shifts from low energy I** states to higher energy states with excitation energy, suggesting that the branching into the various energy states is chiefly energetic in nature.

As the excitation energy increases, the CH_3I^+ formation propensity decreases (excitations no. 1–3), whereas the ion-pair channel **3b** opens up (for excitation no. >3) (see Tables 2 and 4). The formation of CH_3^+ along with I^- for the higher energy excitations (no. 4–8; channel **3b** (ion-pair formation)) must be associated with an increasing coupling between Rydberg states/superexcited states and ion-pair states as the excitation energy increases. The ion-pair formation *via* excitation to $CH_3I^{\#}$ in this energy region must involve ion-pair character (*i.e.* coupling) of a mixed excited state prior to dissociation. This will be dominant for the case of a close approach between the two diabatic potential curves (for the $CH_3I^{\#}$ and ion-pair states) above the dissociation limit for CH_3^+ and I^- formation or at a curve crossing located in the region of the repulsive portion of the potentials. The ion-pair character could also be acquired in the excitation process at the two-photon resonant step *via* mixing of the resonant Rydberg state (CH_3I^{**}) with the ion-pair state in its bound region. Such mixing of Rydberg and ion-pair states has been found to exist in CH_3I[44] as well as in other methyl halides.[37,45]

As mentioned before in Section III, the characteristic CH_3^+ KER signal of sharp peaks observed by excitation no. 8, is due to channel **1** (one-photon non-resonant dissociation). It sticks out from a very weak and broad "background signal", which is likely to be due to CH_3^+ formed by **3b** (ion-pair formation; see above). A relatively large proportion of a signal due to channel **1**, for excitation no. 8, compared to the other excitations (no. <8) is understandable, since it corresponds to a one-photon absorption in the low energy edge of the A-band of largest cross-section (see Fig. 1a).

No clear correlation is observed between the nature of the intermediate resonant molecular Rydberg states, whether being s, p or d states, and the ion products formed. In this respect the following should be emphasized, however. The lowest (no. 1) and highest (no. 8) energy excitations, which correspond to two-photon resonant excitations to s Rydberg states, differ from the rest (no. 2–7), which involve resonant excitations to p or d Rydberg states. Thus, excitation no. 1 involves the largest contribution of

CH_3I^+ formation by channel **3c** (autoionization) and no. 8 gives the highest fraction of CH_3^+ formed by channel **1** (one-photon dissociation). These observations have been interpreted primarily on an energetic basis (see above). However, the selectivity effect of different intermediate Rydberg states (s *vs.* p/d states), to some extent, cannot be ruled out. For comparison it is worth noticing that photofragmentation processes in REMPI of CH_3Br have been found to differ for resonant excitations *via* s Rydberg states and p/d Rydberg states, by forming primarily CH_3Br^+ for excitations *via* s states and CH_3^{**} for p/d states.[35,37]

Results based on the CH_3^+ ion image and the corresponding KER spectrum no. 8 due to the one-photon (34 892 cm^{-1}/286.60 nm) non-resonant dissociation (Fig. 4c) can be compared with photodissociation studies in the A-band.[16,17,19,20] Thus, the branching ratio (I/(I + I*)) of about 0.04 (see above, Section III(C)) is found to be very close to predicted and observed values for a similar excitation energy (286.16 nm). Furthermore, the angular distributions of the image signals, corresponding to dominant parallel transitions (see Table 3), also resemble observations for excitations close in energy.[17] The observations have been interpreted as being due to a dominant parallel transition from the ground state to the $^3Q_0$ state followed by a dissociation along the diabatic curve to form CH_3(X) and I* and by a crossing to the $^1Q_1$ curve to form CH_3(X) and I.

V. Summary and conclusions

CH_3^+ and I^+ ions as well as photoelectron (PE) slice images were recorded for multiphoton excitation of CH_3I involving two-photon resonant transitions to a total of eight ns, np and nd molecular Rydberg states and different vibrational states (ν_1,ν_2,ν_3) (CH_3I^{**}(Ry; $\nu_1\nu_2\nu_3$)) between 55 700 and 70 000 cm^{-1} (Table 1). Ion and photoelectron kinetic energy release spectra (KERs) were derived from the images. The photoelectron data were clearly indicative of iodine atom Rydberg states (I**) as well as, to a lesser extent, I^- formations, prior to one-photon ionization and electron ejection, respectively. Furthermore, CH_3I^+ formation, by autoionization, after three-photon excitations, was also evident. The ion KERs suggest that all these species were formed after three-photon excitations to superexcited state(s) ($CH_3I^{\#}$) *via* the two-photon resonant molecular Rydberg states. In combination, the following major photofragmentation channels were observed (see Fig. 5 and Table 4):

$CH_3I^{\#}$ was created by three photons *via* resonant excitation followed by,

(a) dissociation to form I** along with CH_3(X), and further one-photon ionization of I** (channels **3a**; major channel)

(b) dissociation to form the ion pair CH_3^+ and I^- and further one-photon electron ejection from I^- (channels **3b**)

(c) autoionization to form CH_3I^+(X) (channel **3c**) and further one-photon dissociation to form CH_3^+ along with I or I* (channel **4**)

The excited I** formation (channel **3a**) dominates and is observed for all the excitations (no. 1–8; Table 4). Ion pair formation (channel **3b**) is observed for the higher energy excitations (no. 4–8; Table 4) whereas the autoionization channel (channel **3c**) is mainly observed for the lowest energy excitation (no. 1; Table 4) and decreases with excitation energy as no. 1 > 2 > 3. The branching into the different fragment species seems to be mainly governed by the nature of the $CH_3I^{\#}$ state(s) at the three-photon energy excitation level, whereas, the involvement of the lower energy resonant molecular Rydberg states in the overall fragmentation process cannot be ruled out. In particular an involvement of Rydberg to ion-pair state interactions at that level might be important as found for the CH_3Br counterpart.[36] On the other hand, the dominant channel of I^+ formation by three-photon dissociation to form I** prior to its ionization in REMPI of CH_3I, *via* p and d molecular Rydberg states, is in a dramatic contrast with analogous REMPI of CH_3Br, where CH_3^+ formation by three-photon dissociation to form Rydberg states of CH_3 (CH_3^{**}), prior to its ionization, is found to dominate.

Low power I^+ multiphoton ionization (MPI and REMPI) spectra show iodine atomic lines and weak featureless I^+ background signal. This indicates ionization contribution from a one-photon non-resonant dissociation, *via* the repulsive valence states of the A-band, prior to I and I* REMPI (channel **1**; Fig. 5 and Table 4). The CH_3^+ image and the KER spectrum for excitation no. 8 are indicative of CH_3(X,$\nu_1\nu_2\nu_3\nu_4$) and I/I* formation, with branching fractions for the I/I* formations and angular distributions in close agreement with earlier observations.

The results of this paper represent a significant contribution to the knowledge of the energetics and fragmentation processes of the methyl halides. It is hoped that our work will prompt further theoretical investigations which might aid in clarifying the nature and interpretations proposed here. In particular, it shows the effect of high energy photo-excitations and involvement of neutral molecular states in the formation of highly excited iodine atoms (I**). Furthermore, the paper is of importance to shed light on the effect of various competing channels and Rydberg states on the photoexcitation dynamics of molecules in general.

Conflicts of interest

There are no conflicts to declare.

Acknowledgements

The financial support of the University Research Fund, University of Iceland and the Icelandic Research Fund (Grant No. 184693-051) is gratefully acknowledged. The imaging part of the reported results was carried out at the Ultraviolet Laser Facility at IESL-FORTH, supported in part by the European Union's Horizon 2020 research and innovation programme LASERLAB-EUROPE (Grant Agreement No. 654148) and in part by HELLAS-CH (MIS 5002735) implemented under "Action for Strengthening Research and Innovation Infrastructures," funded by the Operational Programme "Competitiveness, Entrepreneurship and Innovation" (NSRF 2014–2020) and co-financed by Greece and the European Union (European Regional Development Fund).

References

1 W. C. Price, *J. Chem. Phys.*, 1936, **4**, 539–547.
2 A. Gedanken and M. D. Rowe, *Chem. Phys. Lett.*, 1975, **34**, 39–43.
3 S. Felps, P. Hochmann, P. Brint and S. P. McGlynn, *J. Mol. Spectrosc.*, 1976, **59**, 355–379.
4 S. Eden, P. Limao-Vieira, S. V. Hoffmann and N. J. Mason, *Chem. Phys.*, 2007, **331**, 232–244.
5 R. Locht, B. Leyh, H. W. Jochims and H. Baumgartel, *Chem. Phys.*, 2009, **365**, 109–128.
6 S. P. Sapers and D. J. Donaldson, *Chem. Phys. Lett.*, 1990, **173**, 257–264.
7 M. R. Dobber, W. J. Buma and C. A. D. Lange, *J. Chem. Phys.*, 1993, **99**, 836–853.
8 Z. Min, T. Ridley, K. P. Lawley and R. J. Donovan, *J. Photochem. Photobiol., A*, 1996, **100**, 9–14.
9 N. A. Macleod, S. Wang, J. Hennessy, T. Ridley, K. P. Lawley and R. J. Donovan, *J. Chem. Soc., Faraday Trans.*, 1998, **94**, 2689–2694.
10 H. Shen, L. Q. Hua, C. J. Hu and B. Zhang, *J. Mol. Spectrosc.*, 2009, **257**, 200–204.
11 A. Wakai, K. Tsuchida, T. Fukumura and K. Suzuki, *Chem. Phys. Lett.*, 2011, **516**, 23–28.
12 S. J. Riley and K. R. Wilson, *Faraday Discuss. Chem. Soc.*, 1972, **53**, 132–146.
13 R. O. Loo, G. E. Hall, H. P. Haerri and P. L. Houston, *J. Phys. Chem.*, 1988, **92**, 5–8.
14 R. O. Loo, H. P. Haerri, G. E. Hall and P. L. Houston, *J. Chem. Phys.*, 1989, **90**, 4222–4236.
15 D. W. Chandler, J. W. T. Jr., M. H. M. Janssen and D. H. Parker, *Chem. Phys. Lett.*, 1989, **156**, 151–158.
16 Y. J. Jung, Y. S. Kim, W. K. Kang and K.-H. Jung, *J. Chem. Phys.*, 1997, **107**, 7187–7193.
17 L. Rubio-Lago, A. Garcia-Vela, A. Arregui, G. A. Amaral and L. Banares, *J. Chem. Phys.*, 2009, **131**, 174309–174316.
18 D. Jo Scardino, M. D. McDowell, J. D. Graham and N. I. Hammer, *J. At. Mol. Sci.*, 2011, **2**, 93–98.
19 M. G. González, J. D. Rodríguez, L. Rubio-Lago, A. García-Vela and L. Bañares, *Phys. Chem. Chem. Phys.*, 2011, **13**, 16404–16415.
20 L. Rubio-Lago, J. D. Rodríguez, A. García-Vela, M. G. González, G. A. Amaral and L. Bañares, *Phys. Chem. Chem. Phys.*, 2011, **13**, 8186–8194.
21 M. Poullain Sonia, V. Chicharro David, L. Rubio-Lago, A. García-Vela and L. Bañares, *Philos. Trans. R. Soc. London, Ser. A*, 2017, **375**, 20160205.
22 Y. Amatatsu, S. Yabushita and K. Morokuma, *J. Chem. Phys.*, 1996, **104**, 9783–9794.
23 D. Xie, H. Guo, Y. Amatatsu and R. Kosloff, *J. Phys. Chem. A*, 2000, **104**, 1009–1019.
24 A. B. Alekseyev, H.-P. Liebermann, R. J. Buenker and S. N. Yurchenko, *J. Chem. Phys.*, 2007, **126**, 234102.
25 A. B. Alekseyev, H.-P. Liebermann and R. J. Buenker, *J. Chem. Phys.*, 2007, **126**, 234103.
26 D. H. Parker and R. B. Bernstein, *J. Phys. Chem.*, 1982, **86**, 60–66.
27 N. Thiré, R. Cireasa, D. Staedter, V. Blanchet and S. T. Pratt, *Phys. Chem. Chem. Phys.*, 2011, **13**, 18485–18496.
28 M. G. Gonzalez, J. D. Rodriguez, L. Rubio-Lago and L. Banares, *J. Chem. Phys.*, 2011, **135**, 021102.
29 S. Marggi Poullain, M. G. González, P. C. Samartzis, T. N. Kitsopoulos, L. Rubio-Lago and L. Bañares, *Phys. Chem. Chem. Phys.*, 2015, **17**, 29958–29968.
30 S. Marggi Poullain, D. V. Chicharro, A. Zanchet, M. G. González, L. Rubio-Lago, M. L. Senent, A. García-Vela and L. Bañares, *Phys. Chem. Chem. Phys.*, 2016, **18**, 17054–17061.
31 M. R. Bassford, G. Nickless, P. G. Simmonds, A. C. Lewis, M. J. Pilling and M. J. Evans, *Atmos. Environ.*, 1999, **33**, 2373–2383.
32 R. Vogt, R. Sander, R. Von Glasow and P. J. Crutzen, *J. Atmos. Chem.*, 1999, **32**, 375–395.
33 N. Bell, L. Hsu, D. J. Jacob, M. G. Schultz, D. R. Blake, J. H. Butler, D. B. King, J. M. Lobert and E. Maier-Reimer, *J. Geophys. Res.: Atmos.*, 2002, **107**, 1–12.
34 O. V. Rattigan, D. E. Shallcross and R. Anthony Cox, *J. Chem. Soc., Faraday Trans.*, 1997, **93**, 2839–2846.
35 F. Wang, M. L. Lipciuc, X. Yang and T. N. Kitsopoulos, *Phys. Chem. Chem. Phys.*, 2009, **11**, 2234–2240.
36 A. Hafliðason, P. Glodic, G. Koumarianou, P. C. Samartzis and Á. Kvaran, *Phys. Chem. Chem. Phys.*, 2018, **20**, 17423–17433.
37 A. Hafliðason, P. Glodic, G. Koumarianou, P. C. Samartzis and Á. Kvaran, *Phys. Chem. Chem. Phys.*, 2019, **21**, 10391–10401.
38 C. R. Gebhardt, T. P. Rakitzis, P. C. Samartzis, V. Ladopoulos and T. N. Kitsopoulos, *Rev. Sci. Instrum.*, 2001, **72**, 3848.
39 V. Papadakis and T. N. Kitsopoulos, *Rev. Sci. Instrum.*, 2006, **77**, 5.
40 See ESI†.
41 NIST Chemistry WebBook, National Institute of Standards and Technology, https://webbook.nist.gov/chemistry/name-ser/.
42 A. Kartakoullis, P. C. Samartzis, T. N. Kitsopoulos and D. H. Parker, *J. Phys. Chem. C*, 2013, **117**, 22383–22390.
43 NIST atomic energy levels, https://www.nist.gov/pml/atomic-spectra-database.
44 R. J. Donovan, J. T. Hennessy, K. P. Lawley and T. Ridley, *J. Chem. Phys.*, 2013, **138**, 234102.
45 T. Ridley, J. T. Hennessy, R. J. Donovan, K. P. Lawley, S. Wang, P. Brint and E. Lane, *J. Phys. Chem. A*, 2008, **112**, 7170–7176.

4.2.1 Supporting information

Formation of highly excited iodine atoms from multiphoton excitation of CH_3I

Kristján Matthíasson[1#], Greta Koumarianou[2#] , Meng-Xu Jiang [1#], Pavle Glodic [2#]
Peter C. Samartzis[2]* and Ágúst Kvaran[1]*

1. *Science Institute, University of Iceland, Dunhagi 3, 107 Reykjavík, Iceland.*
2. *Institute of Electronic Structure and Laser, Foundation for Research and Technology-Hellas, Vassilika Vouton, 71110 Heraklion, Greece.*

Supplementary material

Content: pages:

Fig. S1

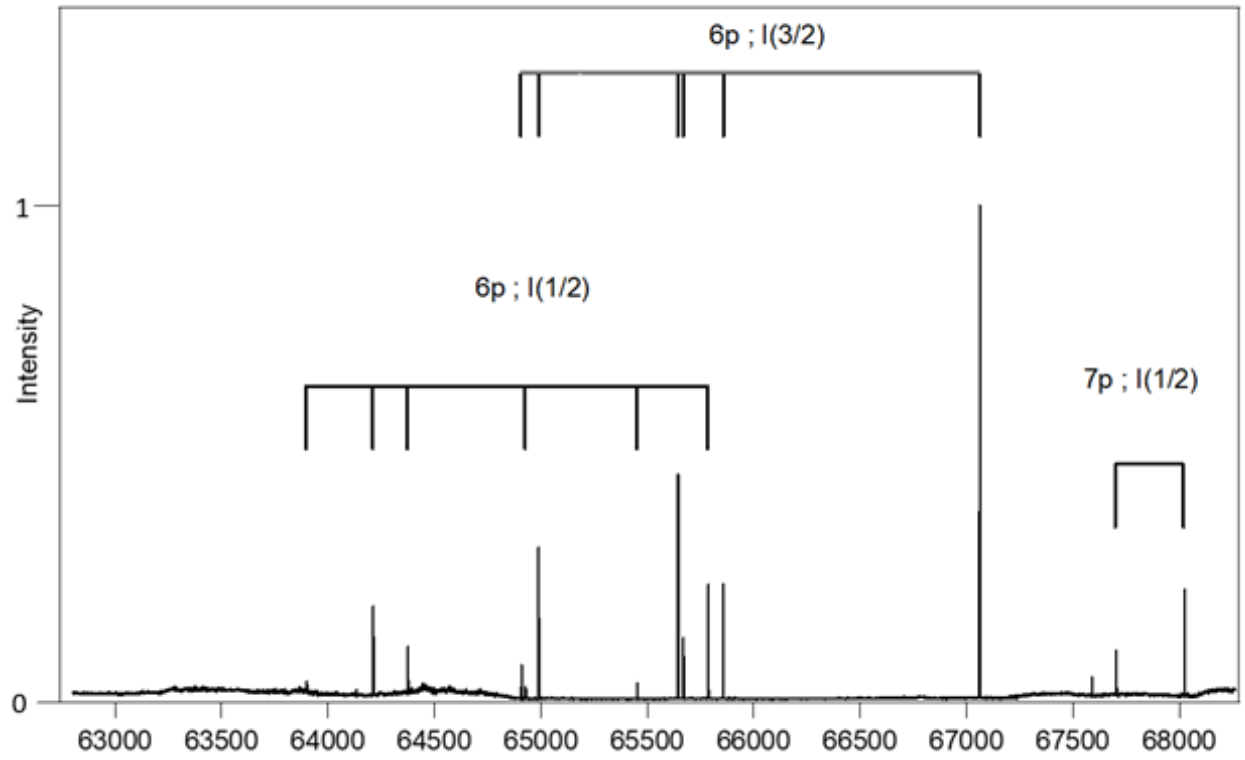

Fig. S1: *Figure shows REMPI spectra for I^+ ion in the energy region of 65 000 cm^{-1} to 70 000 cm^{1}. Grid shows iodine atomic lines according to NIST. Atomic lines originate from either iodine atoms in the ground (I(3/2)) or the spin-orbit excited (I(1/2)) state.*

Fig. S2

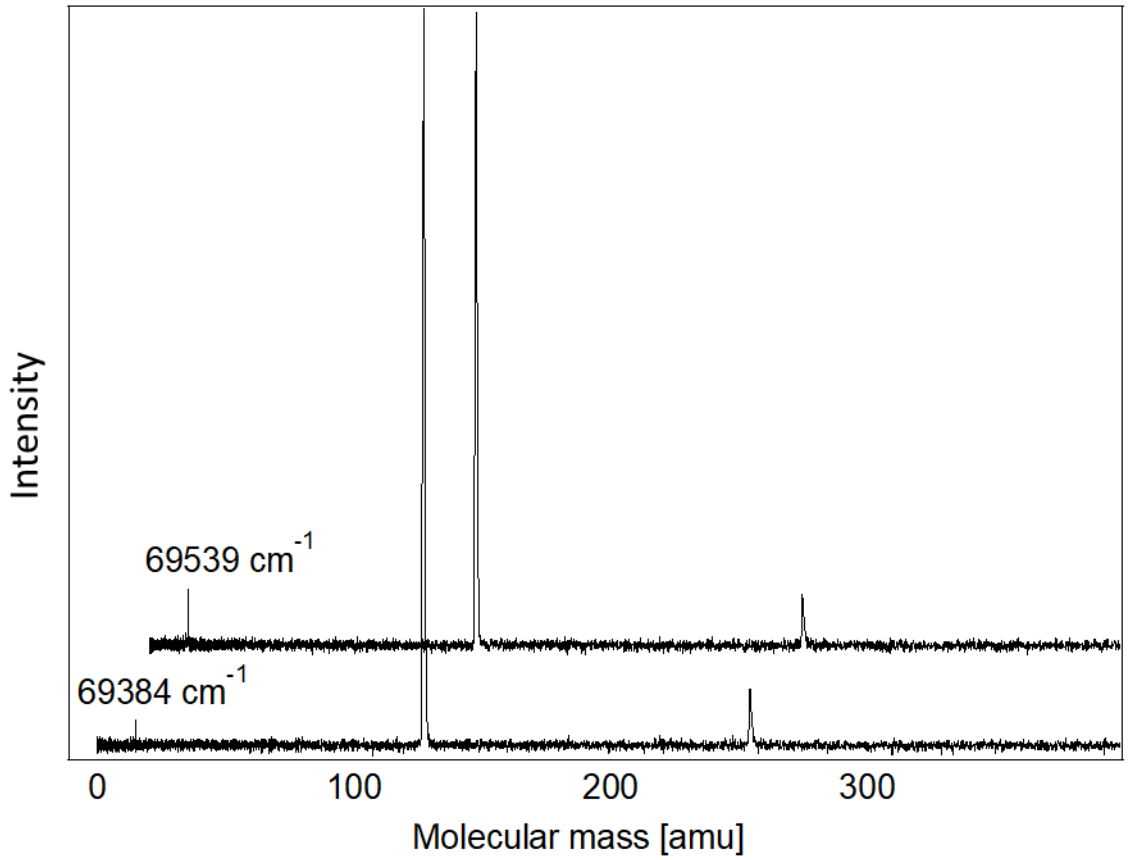

Fig. S2*: Figure shows mass spectra at non-resonant frequencies of 69 384 cm^{-1} and 69 539 cm^{-1}. CH_3^+, I^+ and I_2^+ mass peaks are observed due to non-resonance excitation and ionization.*

Fig. S3

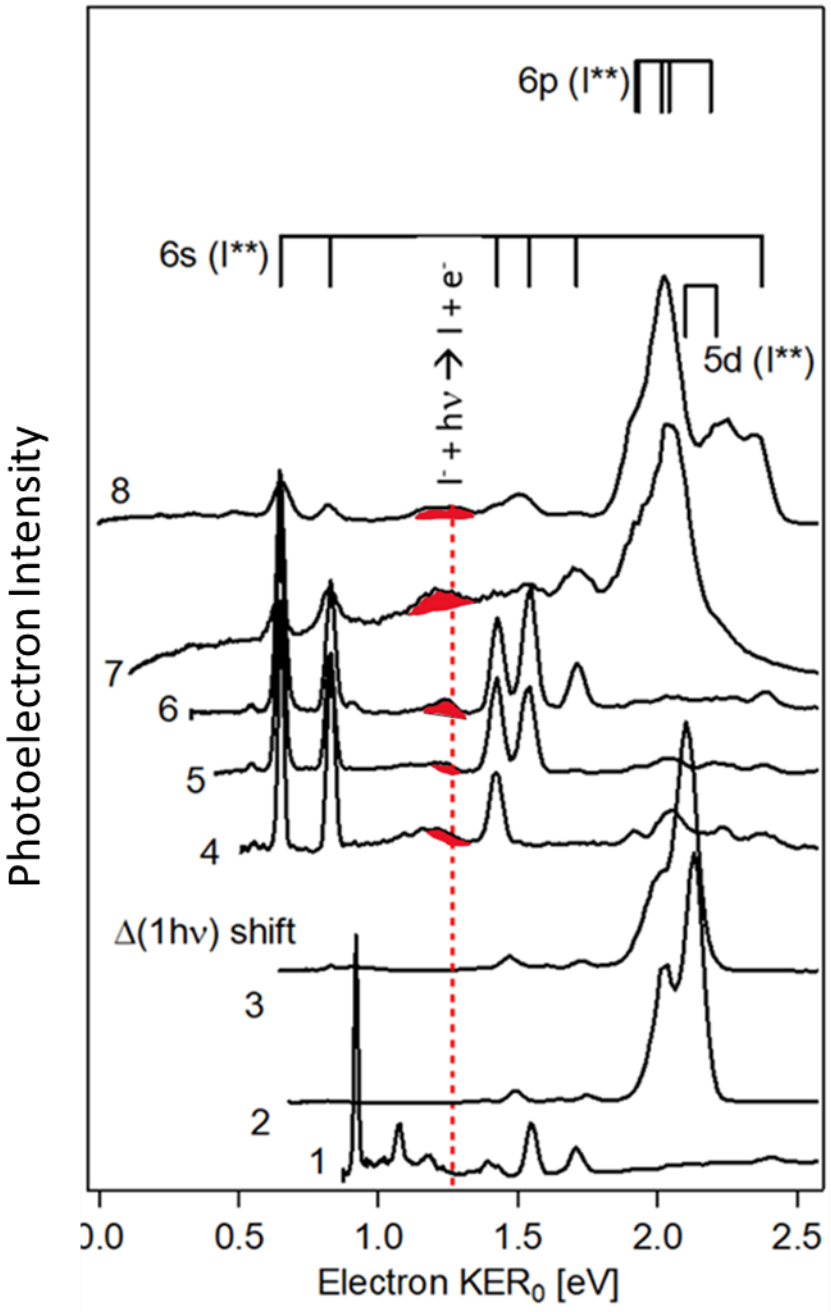

***Fig. S3a**: Photoelectron KERs derived from images no. 1 – 8 (see paper main text) shifted by a one-photon energy difference (Δ(1hν) = /1hν$_i$ - 1hν$_0$/) with respect to the spectrum for the highest energy excitation (i.e. reference spectrum, no. 8). Common energy thresholds (energy maxima) for one-photon ionization of Rydberg iodine atoms (I**) are indicated by sticks above the KERs. The threshold for electron ejection of I⁻ is indicated by a red broken line and the corresponding peaks(shoulders) are highlighted in red. The spectra are normalized to the strongest peak in each spectrum.*

Fig. S3

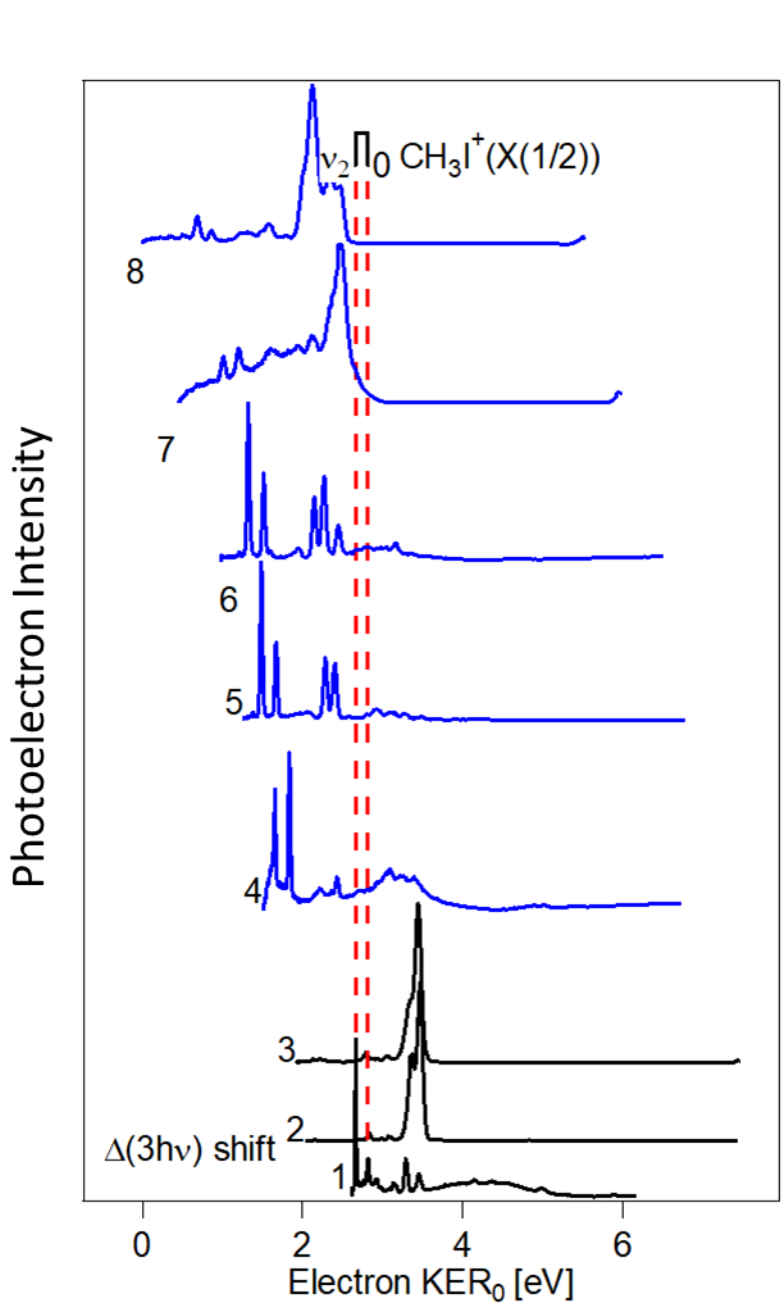

***Fig. S3b**: Photoelectron KERs derived from images 1 – 8 (see paper main text) shifted by a three-photon energy difference ($\Delta(3h\nu) = |3h\nu_i - 3h\nu_0|$) with respect to the spectrum for the highest energy excitation (i.e. reference spectrum, no. 8). Common energy thresholds (energy maxima) for autoionization of superexcited CH_3I ($CH_3I^{\#}$) are indicated by sticks above the KERs. The spectra are plotted as a function of the electron KER for the reference spectra (KER_0). The spectra are normalized to the strongest peak in each spectrum.*

Fig. S3

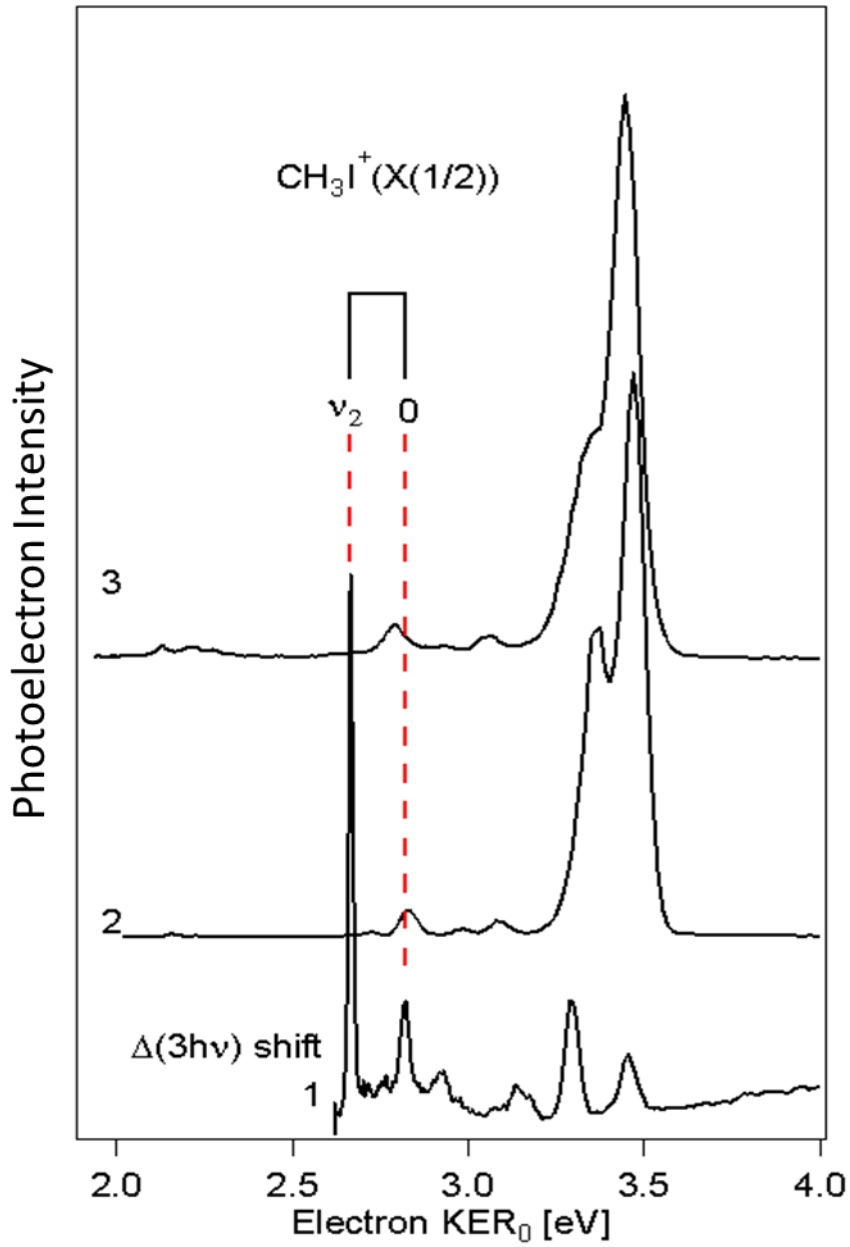

***Fig. S3c**: Photoelectron KERs derived from images 1 – 3 (see paper main text) shifted by a three-photon energy difference ($\Delta(3h\nu) = |3h\nu_i - 3h\nu_0|$) with respect to the spectrum for the highest energy excitation recorded (i.e. reference spectrum, no. 8). Common energy thresholds (energy maxima) for autoionization of superexcited CH_3I ($CH_3I^{\#}$) are indicated by sticks above the KERs. The spectra are plotted as a function of the electron KER for the reference spectra (KER_0). The spectra are normalized to the strongest peak in each spectrum.*

Fig. S4.

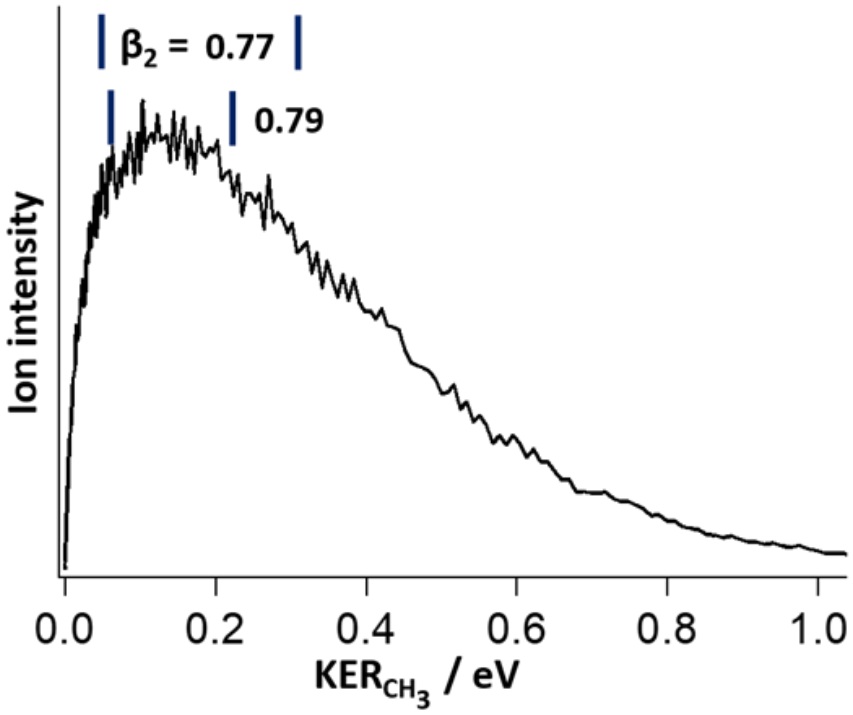

Fig. S4-a: *CH_3^+ KER spectrum and anisotropy, β_2 values. 2hv = 55700 cm^{-1}.*

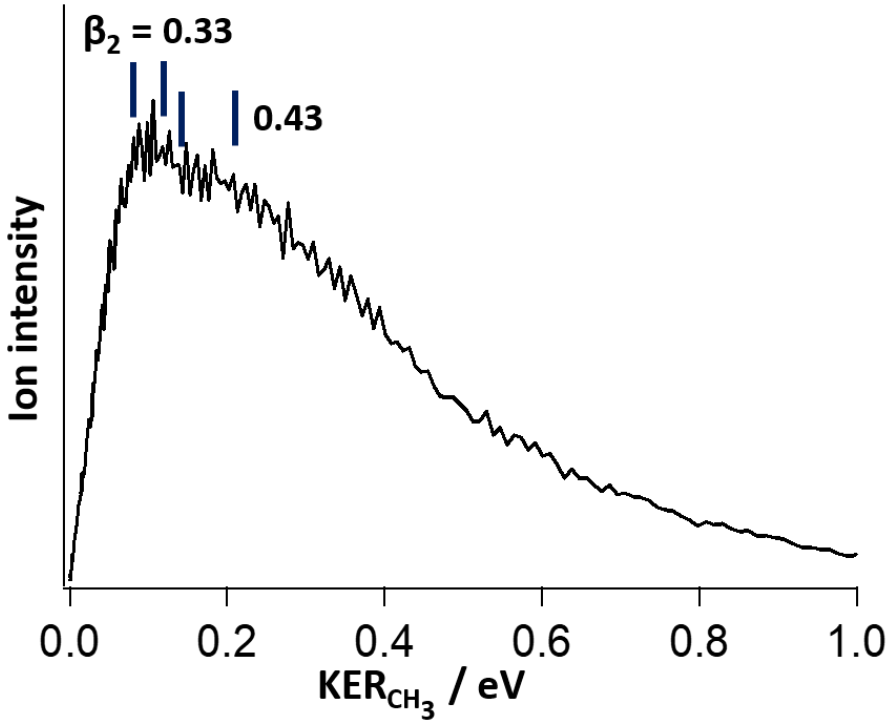

Fig. S4-b: *CH_3^+ KER spectrum and anisotropy, β_2 values. 2hv = 58926 cm^{-1}.*

Fig. S4.

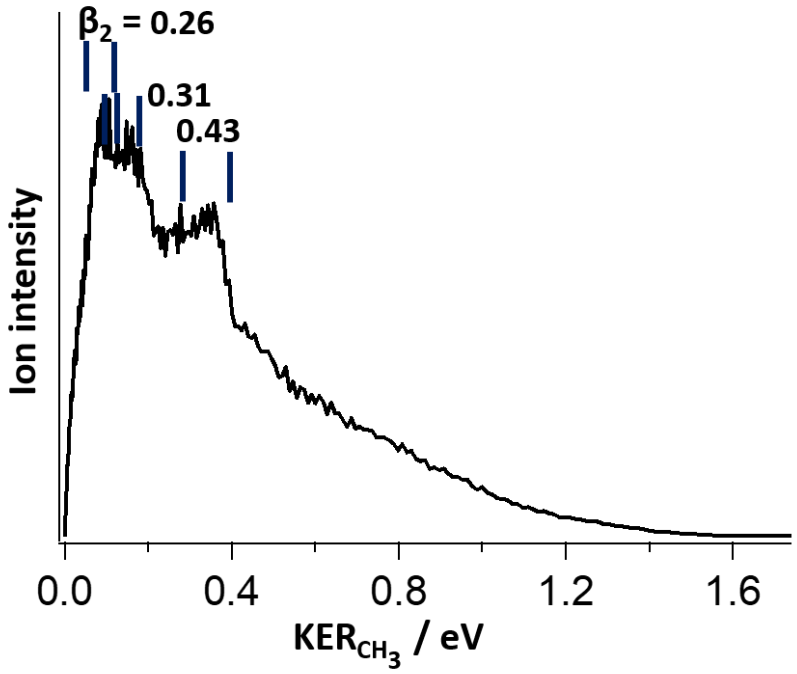

Fig. S4-c: *CH_3^+ KER spectrum and anisotropy, β_2 values. 2hv = 59362 cm^{-1}.*

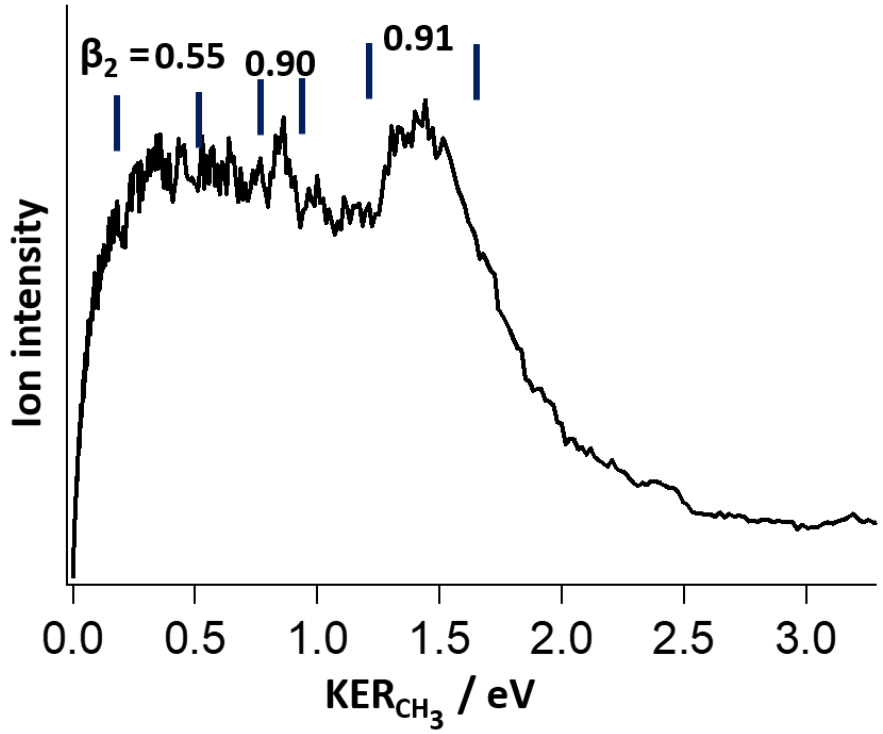

Fig. S4-d: *CH_3^+ KER spectrum and anisotropy, β_2 values. 2hv = 61632 cm^{-1}.*

Fig. S4.

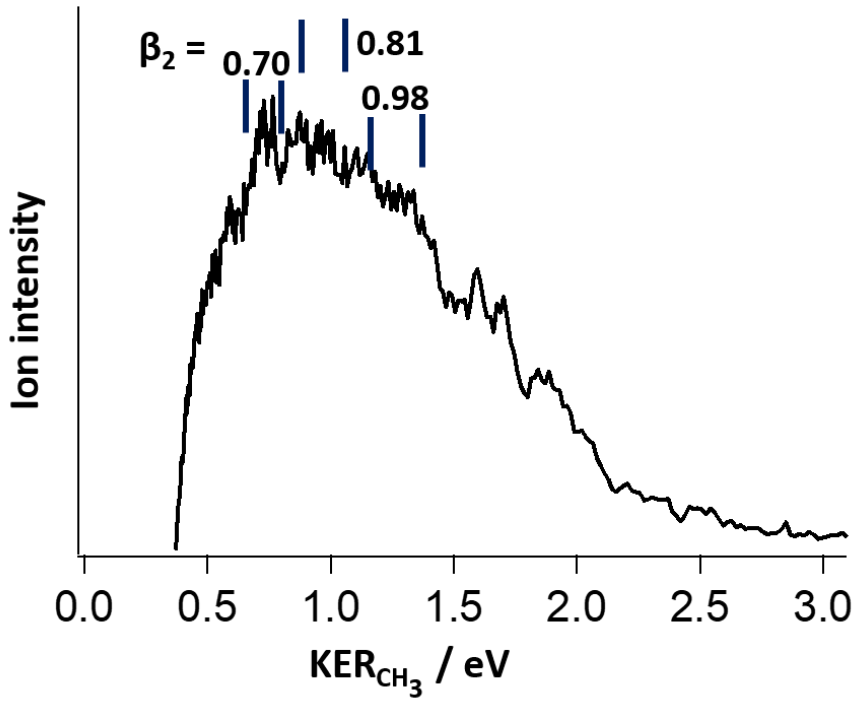

Fig. S4-e: *CH_3^+ KER spectrum and anisotropy, β_2 values. 2hν = 63067 cm^{-1}.*

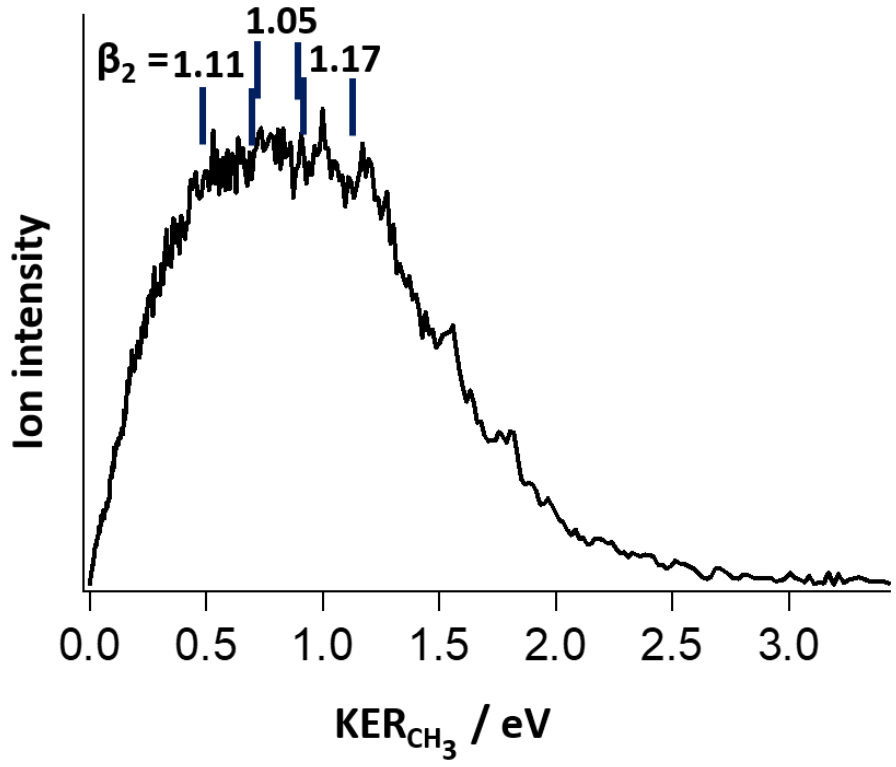

Fig. S4-f: *CH_3^+ KER spectrum and anisotropy, β_2 values. 2hν = 64484 cm^{-1}.*

Fig. S4.

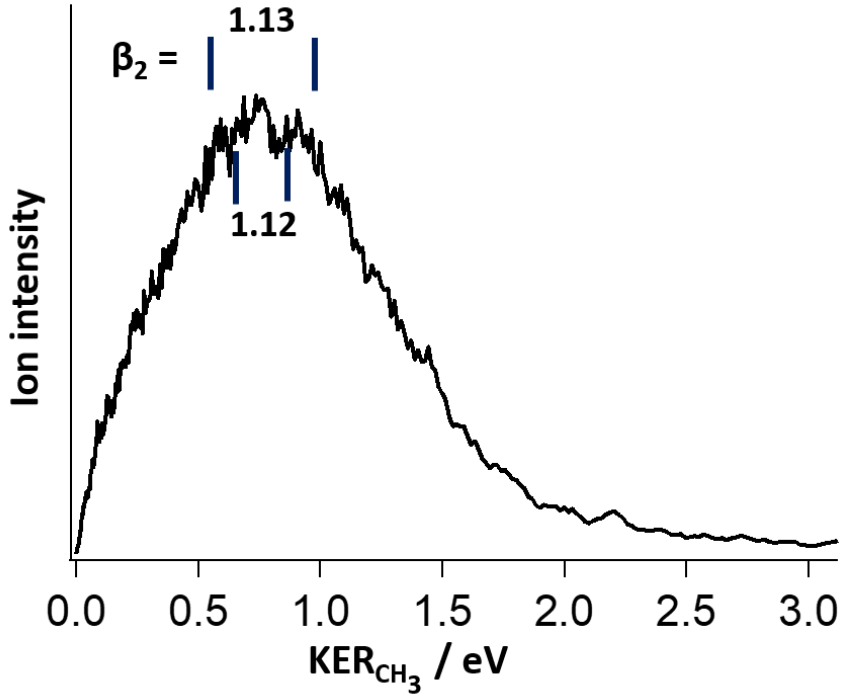

Fig. S4-g: *CH_3^+ KER spectrum and anisotropy, β_2 values. 2hν = 67984 cm^{-1}.*

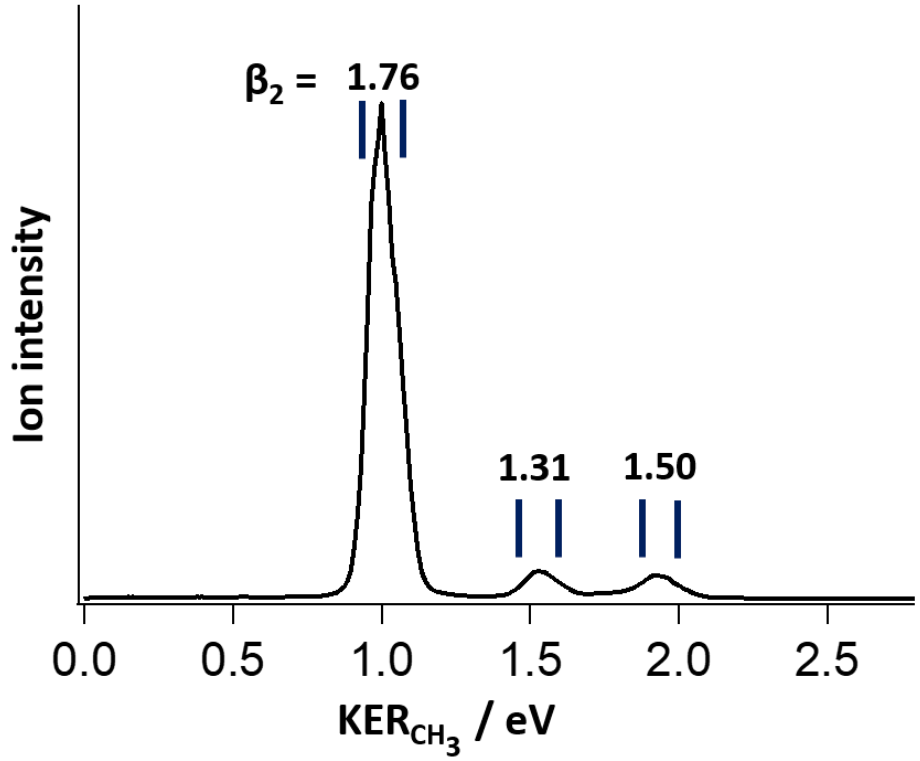

Fig. S4-h: *CH_3^+ KER spectrum and anisotropy, β_2 values. 2hν = 69783 cm^{-1}.*

Fig. S5.

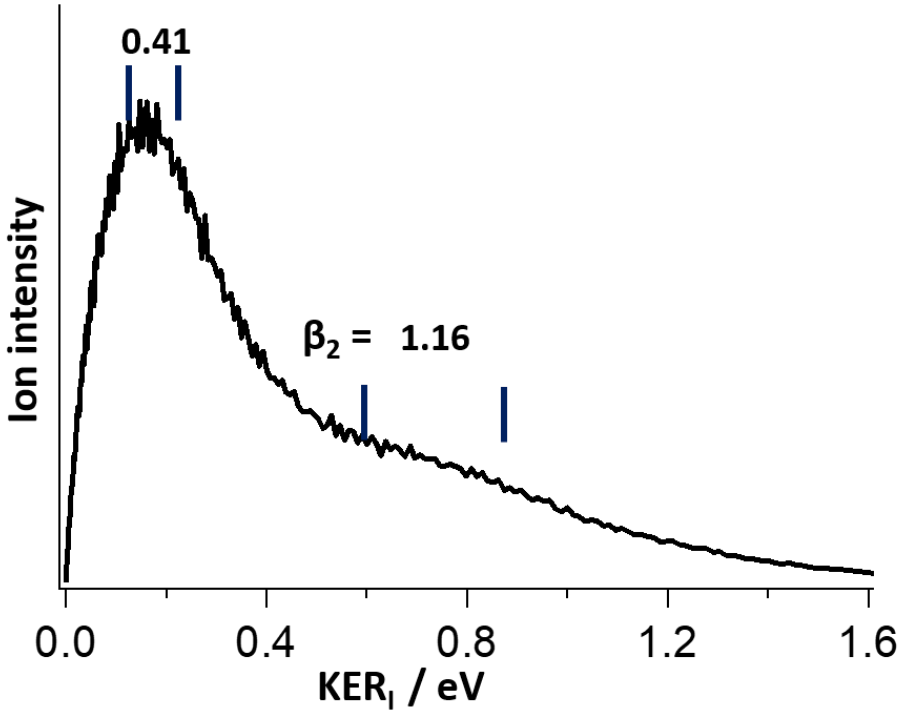

Fig. S5-a: *I^+ KER spectrum and anisotropic β_2 values. 2hν = 55700 cm^{-1}.*

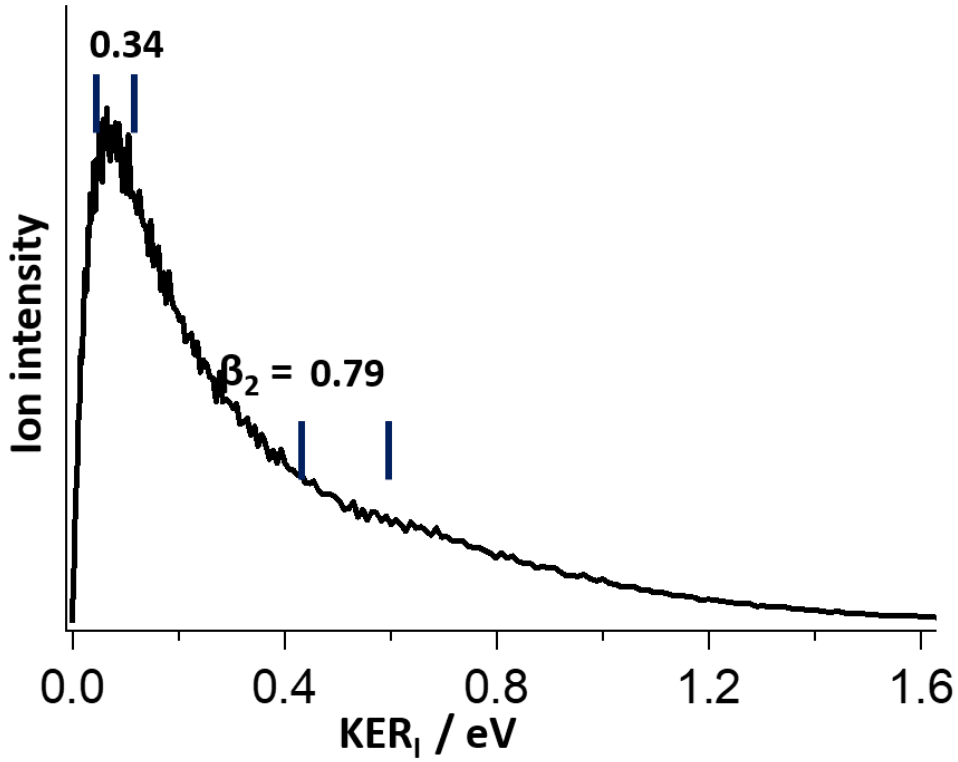

Fig. S5-b: *I^+ KER spectrum and anisotropic β_2 values. 2hν = 58926 cm^{-1}.*

Fig. S5.

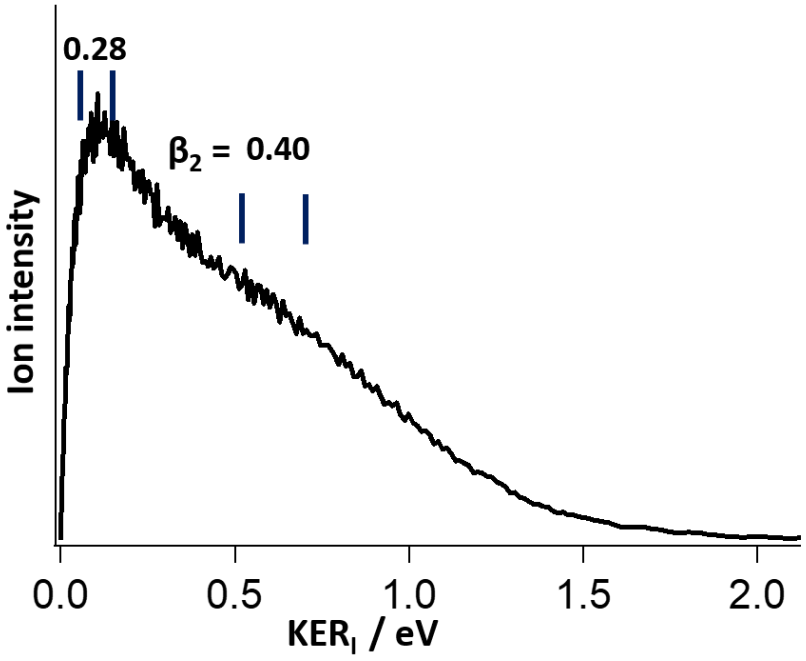

Fig. S5-c: *I^+ KER spectrum and anisotropic β_2 values. 2hv = 59362 cm^{-1}.*

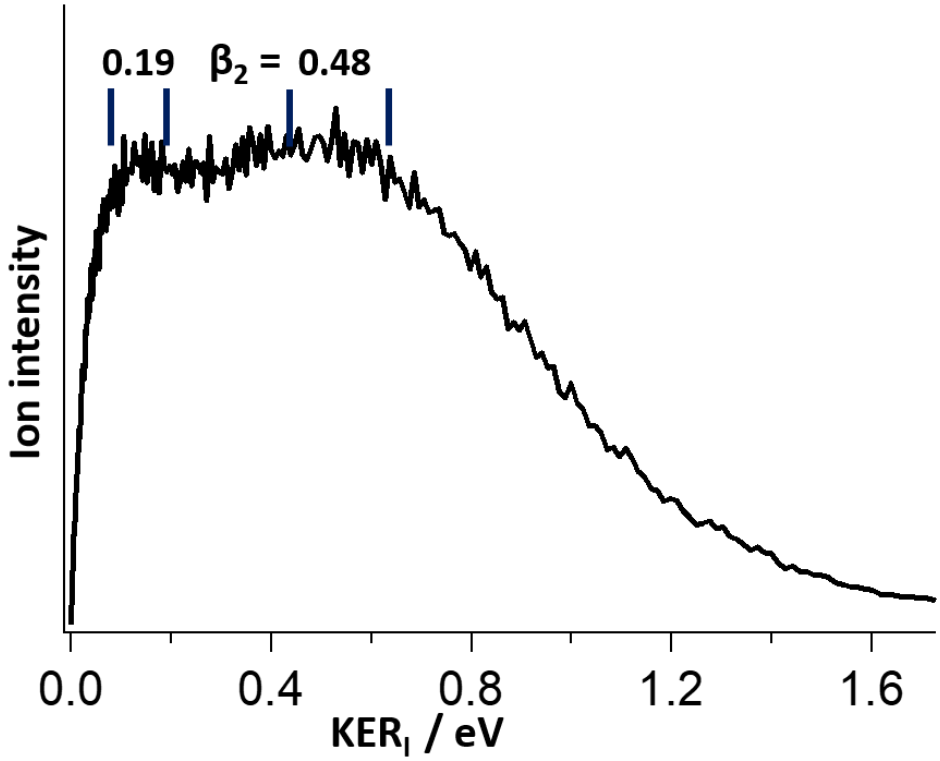

Fig. S5-d: *I^+ KER spectrum and anisotropic β_2 values. 2hv = 61632 cm^{-1}.*

Fig. S5.

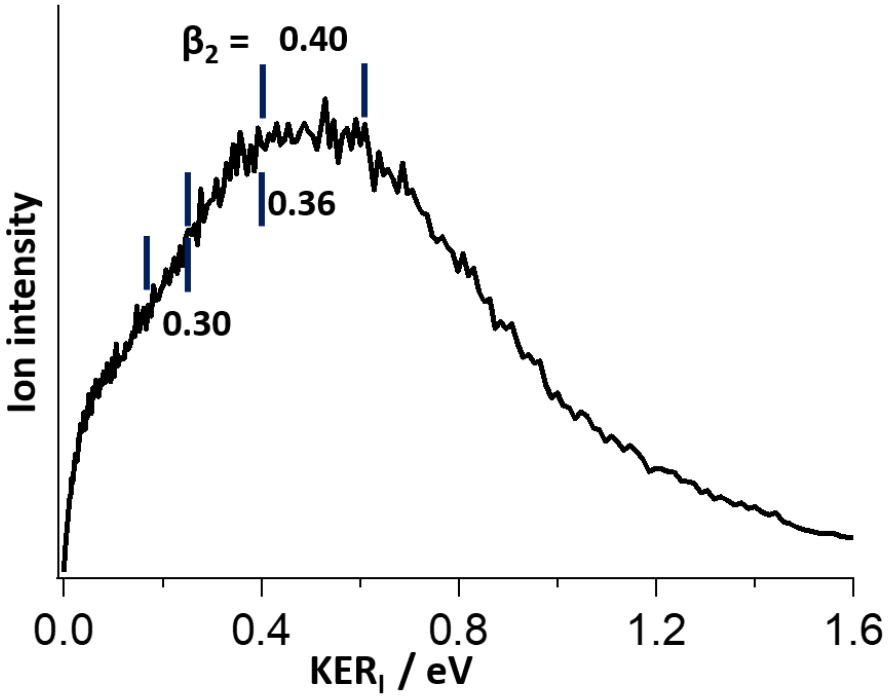

Fig. S5-e: *I^+ KER spectrum and anisotropic β_2 values. 2hν = 63067 cm^{-1}.*

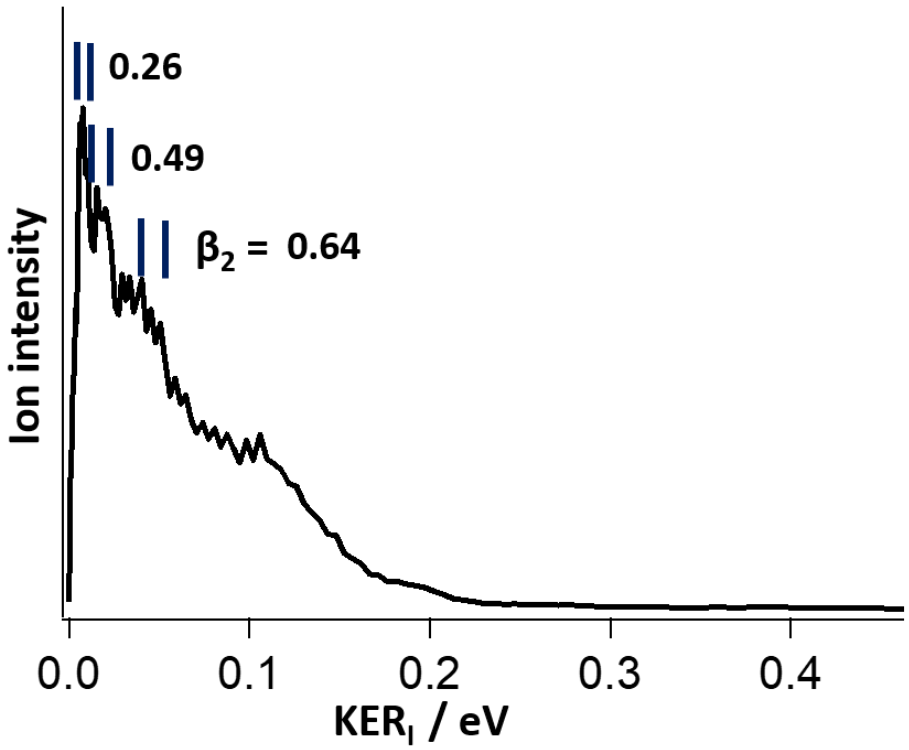

Fig. S5-f: *I^+ KER spectrum and anisotropic β_2 values. 2hν = 64484 cm^{-1}.*

Fig. S5.

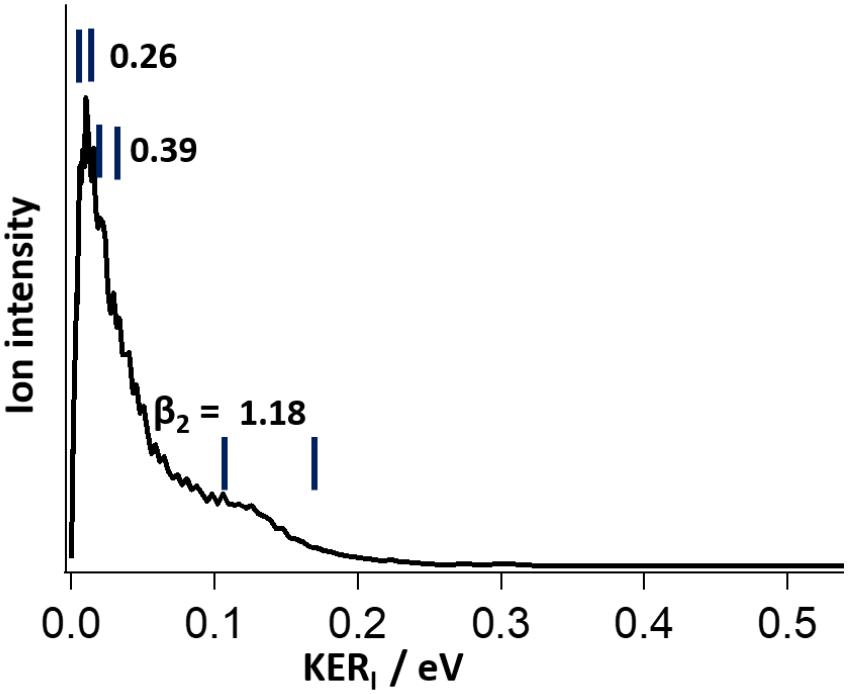

Fig. S5-g: *I^+ KER spectrum and anisotropic β_2 values. 2hv = 67984 cm^{-1}.*

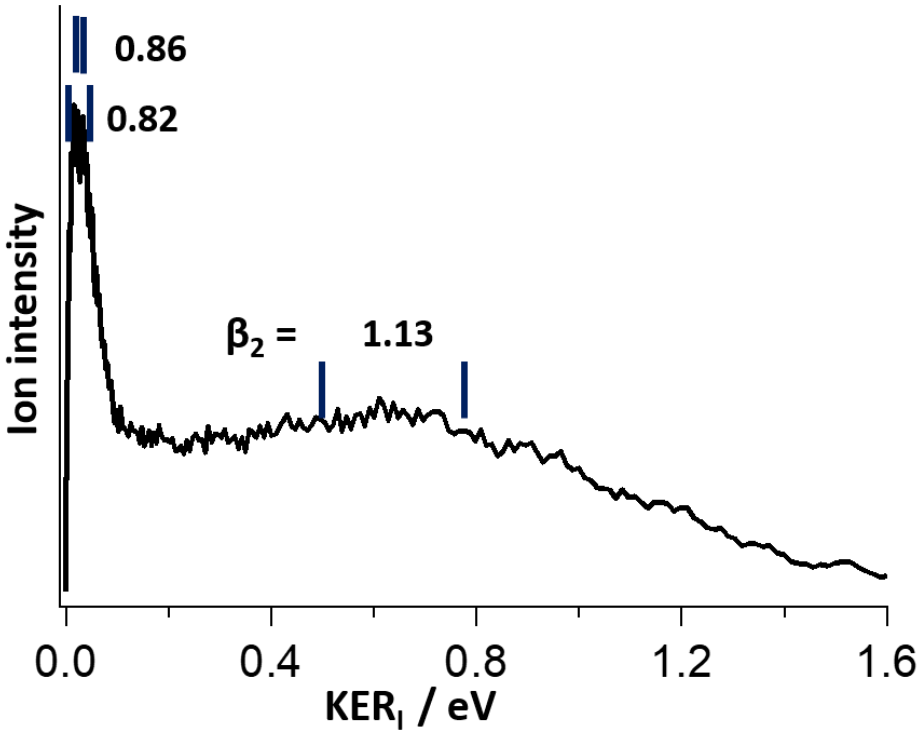

Fig. S5-h: *I^+ KER spectrum and anisotropic β_2 values. 2hv = 69783 cm^{-1}.*

Table.S1*: Anisotropy parameters (β) from figures S4a-h (CH_3^+ images / KERs) and major fragmentation channels (see paper main text).*

Figure	$2h\nu$ /cm^{-1}	KER / eV	Major Channels	β_2	Δ	β_4	Δ	β_6	Δ
S3-a	55700	0.05−0.22	3c,4	0.77	±0.01	−0.08	±0.1	−0.01	±0.01
		0.03−0.34		0.79	±0.01	−0.08	±0.1	−0.01	±0.01
S3-b	58926	0.07−0.11	3c,4	0.33	±0.01	0.07	±0.01	−0.05	±0.01
		0.13−0.23		0.43	±0.01	−0.06	±0.01	−0.04	±0.01
S3-c	59362	0.07−0.11	3c,4	0.26	±0.01	0.05	±0.01	−0.07	±0.02
		0.13−0.18		0.31	±0.01	−0.06	±0.01	0.01	±0.01
		0.28−0.38		0.43	±0.02	−0.07	±0.02	−0.08	±0.02
S3-d	61632	0.22−0.50	3b	0.55	±0.04	0.1	±0.05	−0.07	±0.05
		0.79−0.95		0.90	±0.06	0.04	±0.07	−0.18	±0.07
		1.13−1.69		0.91	±0.12	0.08	±0.13	−0.42	±0.14
S3-e	63067	90−110	3b	0.70	±0.05	−0.09	±0.05	−0.12	±0.06
		120−140		0.81	±0.06	−0.13	±0.07	−0.15	±0.07
		150−170		0.98	±0.09	−0.22	±0.10	−0.14	±0.10
S3-f	64484	120−140	3b	1.11	±0.06	−0.03	±0.05	−0.18	±0.06
		140−160		1.05	±0.09	−0.09	±0.09	−0.08	±0.10
		160−180		1.17	±0.08	−0.02	±0.08	−0.11	±0.09
S3-g	67984	140−160	3b	1.13	±0.02	−0.13	±0.04	0.01	±0.05
		130−170		1.12	±0.02	−0.19	±0.02	−0.00	±0.03
S3-h	69783	0.93−1.03	1	1.76	±0.06	−0.08	±0.05	0.04	±0.05
		1.43−1.55		1.31	±0.23	−0.35	±0.22	−0.16	±0.23
		1.82−1.95		1.50	±0.11	−0.18	±0.10	−0.23	±0.120

Table.S2*: Anisotropy parameters (β) from figures S5a-h (I^+ images / KERs) and major fragmentation channels (see paper main text).*

Figure	$2h\nu$ /cm^{-1}	KER / eV	Major Channels	β_2	Δ	β_4	Δ	β_6	Δ
S5-a	55700	0.014−0.032	3c,4	0.86	±0.01	−0.07	±0.01	−0.03	±0.01
		0.007−0.030		0.82	±0.01	−0.11	±0.01	−0.03	±0.01
		0.504−0.788		1.13	±0.03	0.03	±0.04	0.00	±0.04
S5-b	58926	0.007−0.014	3c,4	0.26	±0.02	−0.02	±0.00	−0.01	±0.00
		0.014−0.027		0.39	±0.01	−0.06	±0.01	0.00	±0.01
		0.106−0.148		1.18	±0.06	−0.20	±0.10	0.21	±0.10
S5-c	59362	0.005−0.011	3c,4	0.26	±0.00	−0.05	±0.00	−0.00	±0.00
		0.014−0.024		0.49	±0.01	−0.06	±0.01	0.03	±0.01
		0.040−0.051		0.64	±0.02	−0.12	±0.02	0.09	±0.02
S5-d	61632	0.172−0.284	3b	0.30	±0.01	0.00	±0.01	0.01	±0.01
		0.284−0.424		0.36	±0.01	0.00	±0.02	0.01	±0.02
		0.424−0.592		0.40	±0.01	0.05	±0.02	0.02	±0.02
S5-e	63067	0.059−0.197	3b	0.19	±0.01	0.03	±0.01	0.02	±0.01
		0.424−0.592		0.48	±0.01	0.02	±0.02	−0.01	±0.02
S5-f	64484	0.065−0.130	3b	0.28	±0.00	0.01	±0.01	−0.01	±0.01
		0.504−0.686		0.40	±0.01	-0.01	±0.01	0.02	±0.01
S5-g	67984	0.043−0.106	3b	0.34	±0.00	0.03	±0.00	−0.01	±0.00
		0.424−0.592		0.79	±0.02	0.11	±0.02	−0.01	±0.02
S5-h	69783	0.139−0.187	1	0.41	±0.00	0.02	±0.00	0.00	±0.00
		0.592−0.788		1.16	±0.01	0.09	±0.01	0.00	±0.01

4.3 Paper 3

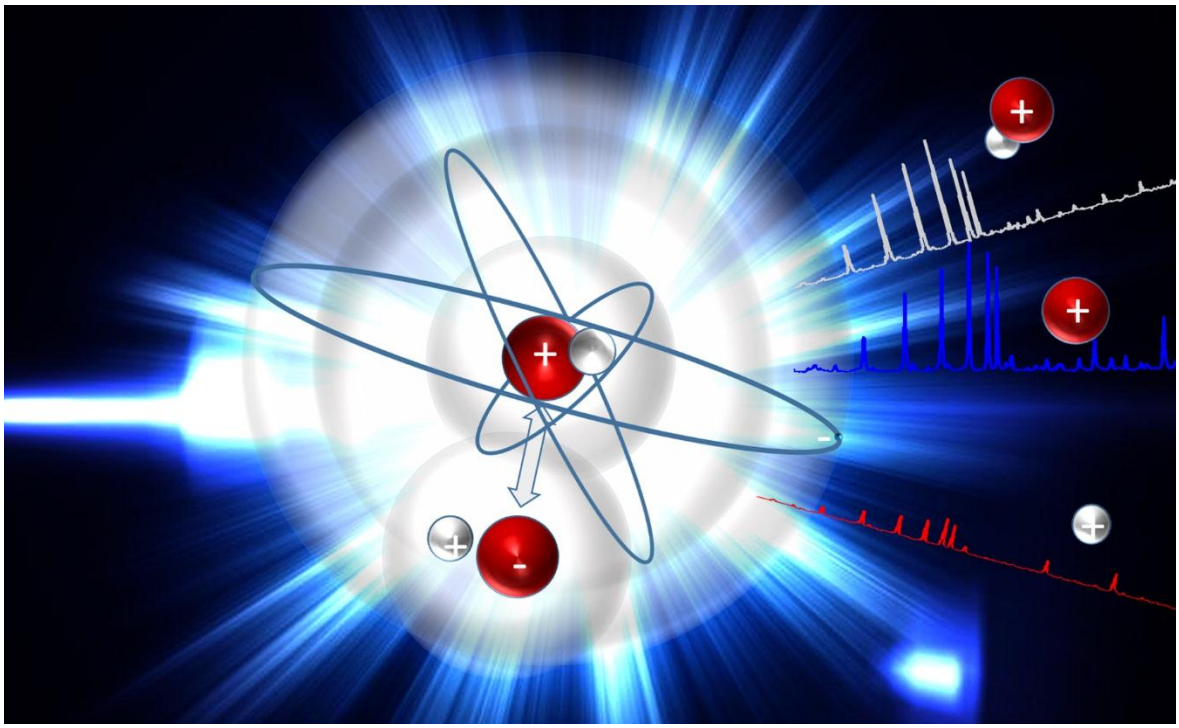

Meng-Xu Jiang, Arnar Hafliðason and Ágúst Kvaran, *Addition to and revision of the HI Rydberg states energy region*, J. Molecular Spectroscopy, **372**C, p:111329, **(2020)**.

DOI: 10.1016/j.jms.2020.111329

Journal of Molecular Spectroscopy 372 (2020) 111329

Contents lists available at ScienceDirect

Journal of Molecular Spectroscopy

journal homepage: www.elsevier.com/locate/jms

Addition to and revision of the HI Rydberg states energy region

Meng-Xu Jiang, Arnar Hafliðason, Ágúst Kvaran *

Science Institute, University of Iceland, Dunhagi 3, 107 Reykjavík, Iceland

ARTICLE INFO

Article history:
Received 4 May 2020
In revised form 22 June 2020
Accepted 29 June 2020
Available online 10 July 2020

Keywords:
Resonance enhanced multiphoton ionization
Rydberg states
Ion-pair states
Photofragmentation
Laser spectroscopy
State interactions

ABSTRACT

Mass resolved REMPI data was recorded for jet cooled HI(g) for two-photon excitation in the region of 74 200 – 80 300 cm^{-1}. REMPI spectra of the ions (HI^+, I^+ and H^+) were derived from the data. The spectra revealed dense and overlapping rotational peak structure due to two-photon resonant transitions to number of Rydberg and ion-pair molecular vibrational states as well as iodine atom (2 + 1) REMPI peaks. A total of 16 Rydberg state spectra and 9 ion-pair state spectra were identified and simulated to derive spectroscopic constants (band origin (ν^0) and 1st and 2nd order rotational constants (B′, D′)) for the excited states. Further analysis of the results for the Rydberg states and inspection of the spectral structure allowed more thorough characterization of the states as well as reassignment of some previously reported spectra. Detailed quantum defect analyses were particularly useful in that respect. The states could be specified by term symbols, ion core symmetries, Rydberg electron principal quantum numbers and configurations as well as vibrational quantum numbers. An attempt was made to assign the ion-pair spectra to vibrational quantum numbers. Relevant results on Rydberg and ion-pair states of HI, from the literature are summarized in the paper.

1. Introduction

Molecular spectroscopy corresponding to transitions of valence electrons to higher lying orbitals can be divided into two major spectroscopic regions, i.e. the valence and the Rydberg states regions, depending on the nature of the main electronically excited states and orbitals involved. The valence states region deals with transitions to excited states / orbitals corresponding to combination of atomic valence states, whereas the Rydberg states region, higher in energy, mainly corresponds to transitions to Rydberg states. There are notably more studies available in the literature for the valence states region, than for the Rydberg states region. This is partly due to easier accessibility, in terms of excitation techniques, but also due to greater complexity of spectra in the Rydberg states region, which is associated with increasing density of states and state interactions as the energy increases. Those properties, on the other hand, open up a large variety of dynamical processes as well as quantum energy level dependent selectivity of fragment and excited state formation. Such processes are relevant to selective formation of reactive fragment species useful in photochemical synthesis and understanding of atmospheric and interstellar photochemical reactions. The hydrogen iodide molecule is ideal for exploring such effects due to its heavy (iodine atom) vs. light (hydrogen) fragment particle (hence low reduced mass) combination which results in easily resolvable rotational spectra structures and, therefore, relatively clear distinction between different fragmentation processes.

The hydrogen halides HX (X = Cl, Br, I) [1–53], in general, have proven to be particularly valuable compounds for spectroscopic and photofragmentation studies in the Rydberg states region. Large number of both singlet and triplet Rydberg states of Σ - Φ symmetries (Hunds case a [48]) / Ω = 0 – 3 (Hunds case c [48]) as well as Σ / Ω = 0 ion-pair (valence) vibrational states have been identified in traditional absorption / one-photon excitation (HCl [2,4,6], HBr [5,29–30,32] and HI [36–38,41]) and resonance enhanced multiphoton ionization (REMPI) studies (HCl [7,8–13,15,16,23–28], HBr [15–17,22,28,31,33–35] and HI [39,40,49–52]). State interactions (or state mixing) between Rydberg and ion-pair states or between Rydberg states have been seen as spectral perturbations either in the form of line shifts or intensity anomalies [24,26–28, 34,35,42–47,51,52]. This has been interpreted in the form of level-to-level repulsion interactions between levels of same J, either between few / 2 – 3 levels, close in energy (weak near-degenerate interactions) or between large range of levels (stronger non-degenerate interactions) [24,26–28,34,35,42–47,51–53]. Largest perturbation effects / state interactions are seen in $^1\Sigma$ state spectra, both for Rydberg and ion-pair vibrational states, due to homogeneous ($\Delta\Omega = 0$), $^1\Sigma$ -$^1\Sigma$ state interactions [28,34,51]. Quantum energy level dependent velocity map images have also been

* Corresponding author.
E-mail address: agust@hi.is (Á. Kvaran).

https://doi.org/10.1016/j.jms.2020.111329
0022-2852/

found to reveal state mixing [44–47,49,54–56]. Ratio of fragment to parent ion formation in REMPI has been found to be indicative of the Rydberg or ion-pair nature of the resonant state, hence state mixing [26,27,33,35,50–53]. Thus, parent molecular ion formation is found to dominate for resonant excitation via Rydberg states, whereas fragment ion formation is characteristic of ion-pair resonant excitation. A distinction between different ion formation, however, becomes less clear as the size of the halogen atom increases, i.e. as Cl > Br > I. Wealth of relevant information on HCl and HBr are available in the literature, whereas less data, somewhat scattered around in the literature [36–41,49–53], is available for HI.

In this paper we present an extensive analysis of Rydberg and ion-pair states of HI for the yet unexplored two-photon resonant excitation region of 74 200 – 80 300 cm^{-1}. Spectral simulations, reveal rotational line assignments, spectroscopic parameters and symmetries of the excited states. Further assignments, with respect to vibrational and principal quantum numbers, were sought by exploring trends in line intensities, level energies and/or by performing detailed quantum defect analysis. Characteristic perturbation effects due to state interactions, mentioned above, also turned out to be useful in the assignment procedure. A total of 16 Σ (9) and Δ (7) new Rydberg states, both singlet (10) and triplet (6) states as well as 9 ion-pair vibrational states were identified (see also supplementary material [57]). This data, along with corresponding observations for lower energy of the Rydberg states region is summarized in the paper.

2. Experimental

The experimental apparatus and equipment parameters resemble that described in previous publications [50–53]. Mass resolved REMPI data for a HI molecular beam was collected. A molecular beam was created by jet expansion of a diluted gas mixture of HI and argon (HI:Ar ~ 1:3) through a 500 μm pulsed nozzle with backing pressure of about 2.0 – 2.5 bar. Pressure inside the ionization chamber was about 10^{-6} mbar during experiments. The pulsed nozzle was kept open for about 150 μs and a laser excitation beam was typically fired 460 μs after its opening. The excitation radiation was generated by a Nd:YAG laser (EKSPLA NL300 Series, 355 nm) pumped Coherent ScanMatePro dye laser (C-503A dye) followed by a frequency doubling with a BBO crystal. The laser beam was focused on the molecular beam by a 200 mm quartz focal lens between a repeller and extractor plates. Ions were directed into a 70 cm long time-of-flight (TOF) tube and detected by a microchannel plates (MCP) detector to record the ion yield as a function of mass and laser radiation energy. Signals were fed into a LeCroy WaveSurfer 44 MXs-A, 400 MHz storage oscilloscope and recorded. To prevent saturation effects and power broadening the laser power was minimized. Experimental conditions (sample dilutions and pressures) were chosen to minimize I_2^+ signals due to HI cluster formation. Laser calibration was based on observed atomic lines of iodine (2 + 1) REMPI peaks. Accuracy of calibration was typically found to be about ± 2.0 cm^{-1} on the two-photon wavenumber scale.

3. Results and analysis

REMPI data for HI was collected in the form of ion intensities as a function of excitation wavenumber for the two-photon excitation region of 74 200 – 80 300 cm^{-1}. REMPI spectra of the fragment (H^+ and I^+) and molecular (HI^+) ions were derived from the mass resolved REMPI data in the form of ion intensities as a function of two-photon excitation wavenumber (see examples in Fig. 1

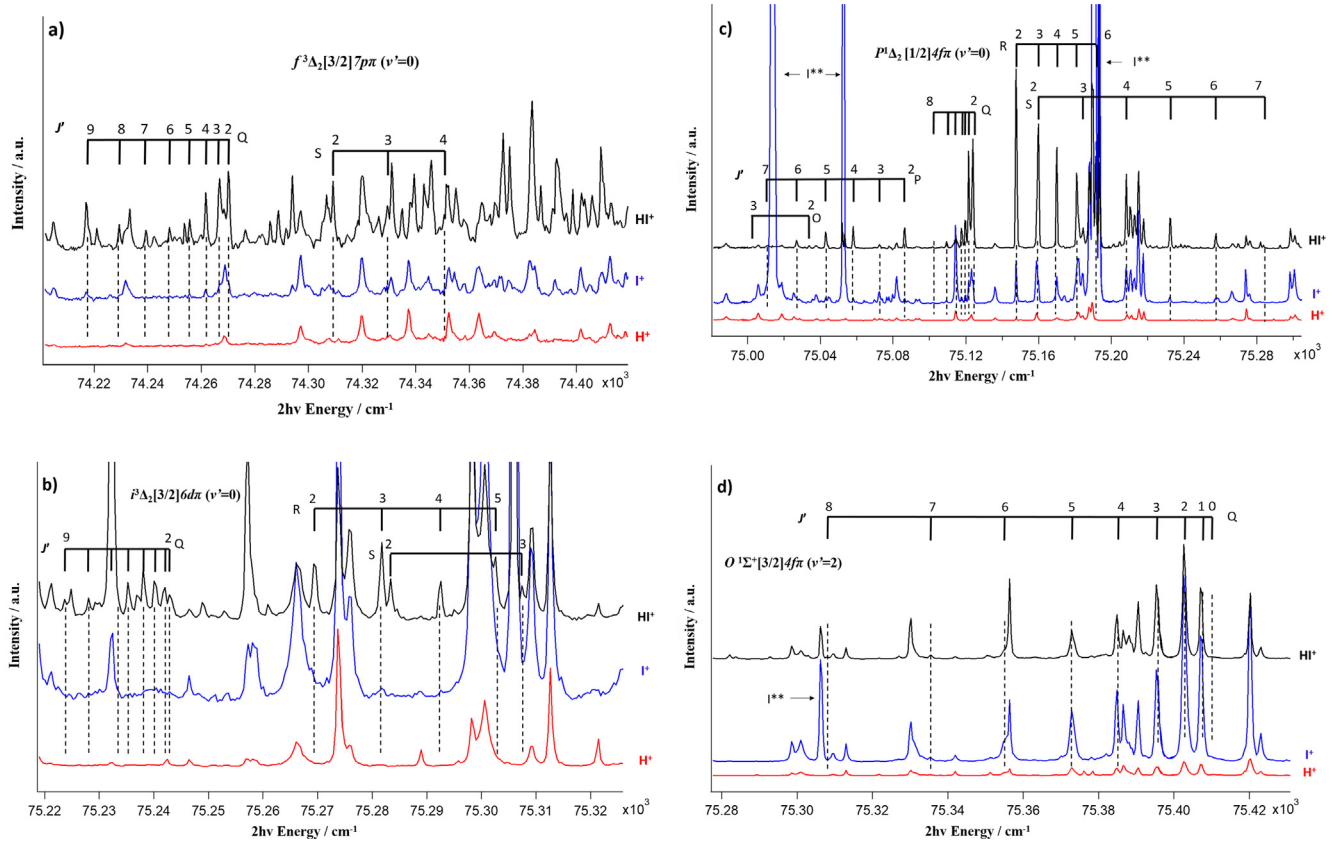

Fig. 1. REMPI spectra of HI for H^+, I^+, and HI^+ and J' assignments of rotational peaks corresponding to two-photon resonant excitations to $f\,^3\Delta_2$ [3/2]$7p\pi$ (v' = 0) (a), $i\,^3\Delta_2$[3/2]$6d\pi$ (v' = 0) (b), $P^1\Delta_2$ [1/2]$4f\pi$ (v' = 0) (c), $O^1\Sigma^+$ [3/2]$4f\pi$ (v' = 2) (d), $V^1\Sigma^+$ (v' = m + 29) (e).

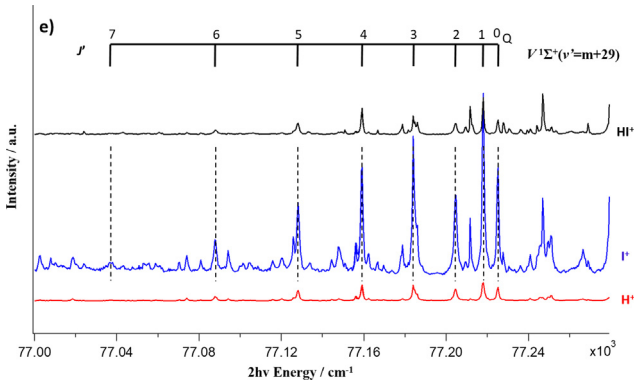

and total collection of spectra in ref. [57]). All the spectra show peak structure due to two-photon resonant transitions between rotational levels in the molecular ground state and excited Rydberg and ion-pair vibrational states, prior to ionization. Relative intensities of the spectral peaks vary significantly with ions as well as excitation energies depending on the states involved. In addition, atomic iodine lines due to (2 + 1) REMPI of I(3/2) and I*(1/2) for resonant excitations to Rydberg states (I**) were detected.

The molecular spectra were analyzed by spectral simulations, using the PGOPHER software package [58]. The simulation was based on imitations of the ion REMPI spectra contributions due to resonant transitions to specific Rydberg or ion-pair vibrational states by corresponding calculated two-photon absorption spectra. Satisfactory comparison of the experimental and calculated spectra structure, with respect to rotational line positions (see tables in ref. [57]) and intensities, was sought by variation of spectroscopic parameters (band origin (ν^0) and first (B′) and second (D′) order rotational constants) and the rotational temperature. Known spectroscopic constants were used for the ground molecular state $X^1\Sigma^+$ (B′ = 6.43 cm^{-1} and D′ = 2.05*10^{-4} cm^{-1} for v′ = 0. [37]) The simulations allowed,

(i) assignment of rotational lines in terms of rotational transitions, J′← J″ (see ref. [57])

(ii) determination of state symmetries. The excited state symmetries, whether Σ(Ω = 0) or Δ(Ω = 2) (no Π(Ω = 1) states were observed), were judged from the spectral structure in terms of relative intensities of line series and/or the absence (Σ) or appearance (Δ) of P and/or R lines.

(iii) evaluation of spectroscopic parameters ν^0, B′ and D′ (see Table 1). These are effective spectroscopic parameters, which may differ from zero order (deperturbed) values due to state interactions [50–53].

The data revealed number of new, not previously observed, spectra of Rydberg and ion-pair vibrational states.

Further characterization of the states involved to,

(iv) distinguish between $^1\Sigma$ (Ω = 0) Rydberg and ion-pair states. This was achieved, firstly, by comparison of B′ constants, which are generally found to be significantly lower for ion-pair vibrational states ($V^1\Sigma^+(v')$) than for $^1\Sigma$ Rydberg states [36–41,50–53] and, secondly, by considering that relative ion-intensities, which typically differ for the ion-pair and Rydberg states as $I(I^+) \geq I(H^+) \sim I(HI^+)$ (ion-pair states) and $I(HI^+) > I(I^+) > I(H^+)$(Rydberg states) [53].

(v) determine electron orbital configurations, spin multiplicities (singlet / triplet) and vibrational quantum numbers (v′) for the Rydberg states. Known or estimated vibrational frequencies of the Rydberg states sometimes allowed determination of the v′s in a vibrational ladder, whereas detailed quantum defect analyses were particularly useful in this context. It allowed assignments with respect to different principal quantum numbers, previously unobserved configurations as well as some reassignments. The procedure was as follows:

Band origin (ν^0) of a Rydberg state (HI^{**}) spectrum can, to a first approximation, be expressed as,

$$\upsilon^0(HI^{**}[\Omega_c, \upsilon]nl\lambda) = IE([\Omega_c, \upsilon]) - \frac{R_\infty}{(n-\delta(l))^2}; \quad (1)$$

where $HI^{**}[\Omega_c, \upsilon]nl\lambda$ refers to a Rydberg state which converges to either of the two spin–orbit components ($\Omega_c = 3/2, 1/2$) of the ground ionic state $HI^+(X\ ^2\Pi)$ in vibrational level υ, for a Rydberg electron with principal quantum number n, in a molecular orbital

Table 1
New HI Rydberg states: Rydberg state specifications ($Ry\ ^{2\Sigma+1}X_\Omega[\Omega_c]nl\lambda$) (see main text), vibrational quantum numbers (v′), band origin (ν^0), rotational parameters (B′,D′), relative intensities, quantum defect values (δ) and indications relevant to the spectral structure (line series, perturbations and relative ion intensities observed) derived from Rydberg state spectra.

State specifications	v′	ν^0 /cm^{-1}	B′/cm^{-1}	D′*10^4 / cm^{-1}	Int.	Quantum defect δ	Line seriesobserved	Perturb. Interact.	Relative ion int.
Rydberg states									
$[\Omega_c]np\pi$ (n = 6,7)									
$E\ ^1\Sigma^+[1/2]6p\pi$	3	75 982.3	4.10	−30	vw	3.61	Q	X	$I(I^+) > I(HI^+) \geq I(H^+)$
$f\ ^3\Delta_2[3/2]7p\pi$	0	74 272.8	5.93	77	w	3.60	Q,S		$I(HI^+) \gg I(I^+) \sim I(H^+) \sim 0$
$g\ ^3\Sigma_{0+}[3/2]7p\pi$	1	76 364.4	4.36	−38	m	3.61	O,Q,S	X	$I(I^+) > I(HI^+) > I(H^+)$
$g\ ^3\Sigma_1^-[1/2]7p\pi$	0	79 145.1	5.77	25.9	s	3.68	Q	X	$I(I^+) > I(HI^+) > I(H^+)$
$F^1\Delta_2[1/2]7p\pi$	0	79 923.5	6.74	10	w	3.54	O,P,Q,R,S		$I(HI^+) \geq I(I^+) > I(H^+) \sim 0$
$[\Omega_c]nd\pi$ (n = 5,6)									
$I\ ^1\Delta_2[1/2]5d\pi$	2	76 080.8	5.82	9	m	2.47	O,P,Q,R,S		$I(HI^+) > I(I^+) > I(H^+)$
$I\ ^1\Delta_2[1/2]5d\pi$	3	77 954.1	5.55	−2.6	w	2.48	O,P,Q,R,S		$I(HI^+) > I(I^+) > I(H^+)$
$j\ ^3\Sigma_{0+}[1/2]5d\pi$	2	77 346.0	5.09	−79	s	2.37	(O),Q,(S)	X	$I(I^+) > I(HI^+) \gg I(H^+)$
$i^3\Delta_2[3/2]6d\pi$	0	75 246.1	6.14	5	vw	2.42	Q,R,S		$I(HI^+) \gg I(I^+) > I(H^+) \sim 0$
$H^1\Sigma^+[3/2]6d\pi$	0	75 546.6	5.86	151	vs	2.35	Q	X	$I(I^+) > I(HI^+) \gg I(H^+)$
$H^1\Sigma^+[3/2]6d\pi$	1	77 615.4	5.56	90	vw	2.36	Q	X	$I(I^+) > I(HI^+) \gg I(H^+)$
$[\Omega_c]nf\pi$ (n = 4,5)									
$P^1\Delta_2[1/2]4f\pi$	0	75 124.6	6.15	8	ms	1.20	O,P,Q,R,S	X	$I(HI^+) > I(I^+) > I(H^+)$
$P^1\Delta_2[1/2]4f\pi$	2	78 502.6	5.67	−52	m	1.27	O,P,Q,R,S		$I(HI^+) > I(I^+) > I(H^+)$
$O^1\Sigma^+[3/2]4f\pi$	2	75 410.1	5.19	38	s	1.04	Q	X	$I(I^+) > I(HI^+) > I(H^+)$
$O^1\Sigma^+[3/2]4f\pi$	3	77 448.2	4.56	−51	m	1.03	Q	X	$I(I^+) > I(HI^+) > I(H^+)$
$q^3\Sigma_{0+}[1/2]4f\pi$	0	76 234.4	5.50	160	m	1.08	Q	X	$I(I^+) > I(HI^+) > I(H^+)$

λ, corresponding to an iodine atom orbital *l*. $IE([\Omega_c, v])$ is the ionization energy of HI($X\ ^1\Sigma^+(v'' = 0, J'' = 0)$) to form $HI^+([\Omega_c, v])$ [59]. R_∞ is the Rydberg constant suitable for HI** (109 737 cm^{-1}) and $\delta(l)$ is the quantum defect value, which depends on *l*. By matching derived band origins (Table 1) of Rydberg state spectra and corresponding values calculated by equation (1) for known ionization energies [59] and given *n*, the $\delta(l)$ were derived. Since values of $\delta(l)$ are characteristic for Rydberg state series states of common electron configurations could be identified from similarities in $\delta(l)$ values (see Table 1, Fig. 2 and ref. [57]).

The overall spectral analysis and the interpretations, (i) – (v), mentioned above, revealed identification and characterization of 16 new (not previously observed) Rydberg and 9 new ion-pair vibrational states. Furthermore, it resulted in reassignment of some previously observed spectra. Arguments for the spectra assignments and state characterizations will now be given in more details with reference to Tables 1 and 2.

3.1. Reassignment of Rydberg state spectra

3.1.1. E $^1\Sigma^+[1/2]6p\pi$ and $H^1\Sigma^+[3/2]5d\pi$

There is some discrepancy in the literature concerning assignment of spectra of $^1\Sigma^+$ Rydberg states. Ginter et al. [37] assigned the v^0 = 70 850.5 cm^{-1} and 72 650.8 cm^{-1} bands to the $E\ ^1\Sigma^+[1/2]6p\pi$, v′ = 0 and 1 Rydberg states, respectively and the v^0 = 68 277.3 cm^{-1}, 70 242.1 cm^{-1} and 72 217.6 cm^{-1} bands to the $H^1\Sigma^+[3/2]5d\pi$, v′ = 0, 1, and 2 Rydberg states, respectively, without clear arguments. Hróðmarsson et al. [50] changed the assignments, by switching the *E* and *H* labeling, based on energetic and perturbation arguments. Our detailed quantum defect analysis of these bands, as described above, convincingly show that the original assignments [50] are correct. Thus, for the former band series (v^0 = 70 850.5 cm^{-1} and 72 650.8 cm^{-1}), quantum defect parameters of δ = 3.55 and 3.57 are obtained for the $E\ ^1\Sigma^+[1/2]6p\pi$, v′ = 0 and 1 Rydberg states, respectively. This is in close agreement with values obtained for other $6p\pi$ molecular Rydberg states [37,39,50] (see Fig. 2 and Tables 1 and 2; *g*, *F* and *f* states) as well as for iodine atomic *np* Rydberg states [60]. In the latter band series (v^0 = 68 277.3 cm^{-1}, 70 242.1 cm^{-1} and 72 217.6 cm^{-1}), quantum defect parameters of δ = 2.34, 2.36 and 2.36 are obtained for the $H^1\Sigma^+[3/2]5d\pi$, v′ = 0, 1, and 2 Rydberg states, respectively, in good agreement with δ -values obtained for other $5d\pi$ molecular Rydberg states[37,49,50] (see Fig. 2 and Tables 1 and 2; *j*, *I* and *i* states) as well as for iodine atomic *nd* Rydberg states [60]. We, therefore, use the assignments relevant to the $^1\Sigma^+$ Rydberg states as given in ref. [37].

3.1.2. g $^3\Sigma^-_{0+}$ [3/2]7pπ (v′ = 0)

Strong O, Q and S lines for $I(HI^+) > I(I^+) > I(H^+)$ have been observed for a spectrum of band origin v^0 = 74 735.2 cm^{-1} and for rotational constant of B′ = 6.05 cm^{-1} [53]. The spectrum shows perturbations in the form of line shifts indicative of interaction and mixing with the ion-pair state of an intermediate strength. Based on the spectral structure and evaluated vibrational frequencies the spectrum was assigned to the $j\ ^3\Sigma^-_{0+}$ [1/2]$5d\pi$ (v″ = 1) Rydberg state. Detailed quantum defect analysis, on the other hand, favors a different assignment. A quantum defect parameter of δ = 3.52 is obtained for the v′ = 0 level of the $g\ ^3\Sigma^-_{0+}$ [3/2]$7p\pi$ state in close agreement with those obtained for the v′ = 0 (δ = 3.51) and v′ = 1 (δ = 3.54) levels of its counterpart state $g\ ^3\Sigma^-_{0+}$ [3/2]$6p\pi$. We, therefore, reassign the v^0 = 74 735.2 cm^{-1} band to the $g\ ^3\Sigma^-_{0+}$ [3/2]$7p\pi$ (v′ = 0) state.

3.1.3. $p^3\Delta_2$[3/2]4fπ (v′ = 0)

Weak Q lines for $I(HI^+) > I(I^+) > I(H^+) \sim 0$, J′ > 2, have been observed for a spectrum of band origin v^0 = 73 081.7 cm^{-1} and for rotational constant of B′ = 6.35 cm^{-1} [52]. The spectrum was assigned to the $P^1\Delta_2[1/2]4f\pi$ (v′= 0) state, mainly based on arguments relevant to the spectral structure and vibrational frequencies. We favor a different assignment for the following reasons. First, the very weak signal and absence of O, P, R and S lines disfavor a $^1\Delta$ (v′ =0) Rydberg state, by comparison with related spectra, such as for the $F\ ^1\Delta_2[1/2]6p\pi$ (v′= 0) and $I\ ^1\Delta_2[1/2]5d\pi$ (v′= 0) states [30], which show strong signals and clear O,P, Q, R and S lines. Second, our quantum defect analysis reveal a value of δ = 0.80 for v′ = 0 of the $p^3\Delta_2[3/2]4f\pi$ state, close to what might be expected for a $nf\pi$ Rydberg state [51].

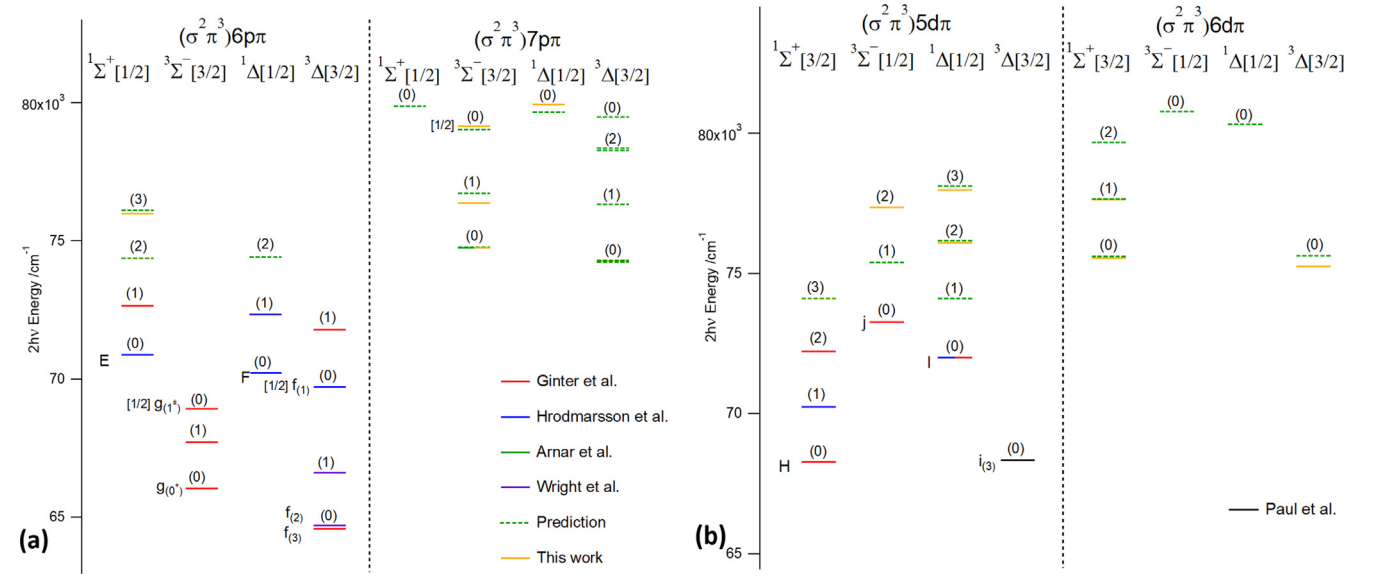

Fig. 2. Energy level diagram of known Rydberg states for HI converging to the ground ionic states $X\ ^2\Pi[3/2,1/2]$ as well as some predicted states (see main text). The $^{1,3}\Sigma$ and $^{1,3}\Delta$, $[\Omega_c]np\pi$ (*n* = 6, 7) Rydberg states are presented in (a). The $^{1,3}\Sigma$ and $^{1,3}\Delta$, $[\Omega_c]nd\pi$ (*n* = 5, 6) Rydberg states are presented in (b). The $^{1,3}\Sigma$ and $^{1,3}\Delta$, $[\Omega_c]nd\pi$ (*n* = 4, 5) Rydberg states are presented in (c). Solid lines (different colors) correspond to previously detected bands [36–39,49,50,52,53] and present work (orange lines), as specified in the figures (see also main text). Green dotted lines correspond to predicted states according to quantum defect analyses. Vibrational quantum numbers are shown in parenthesis.

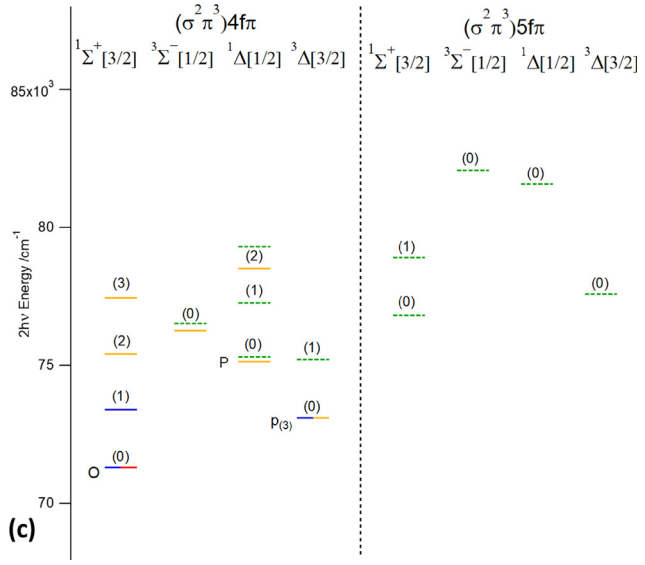

Fig. 2 (*continued*)

3.2. New Rydberg states

3.2.1. $[\Omega_c]np\pi$ (n = 6,7) Rydberg states

A total of five spectra were assigned to transitions to $(\sigma^2\pi^3)6p\pi$ and $(\sigma^2\pi^3)7p\pi$ vibrational Rydberg states, i.e. the $E\ ^1\Sigma^+[1/2]6p\pi(v'=3)(\nu^0 = 75\,982.3\ cm^{-1})$, $f\ ^3\Delta_2[3/2]7p\pi\ (v'=0)(\nu^0 = 74\,272.8\ cm^{-1})$, $g\ ^3\Sigma^-_{0+}[3/2]7p\pi\ (v'=1)(\nu^0 = 76\,364.4\ cm^{-1})$, $g^3\Sigma^-_{1\pm}[1/2]7p\pi\ (v'=0)$ $(\nu^0 = 79\,145.0\ cm^{-1})$ and $F^1\Delta_2[1/2]7p\pi(v'=0)(\nu^0 = 79\,923.5\ cm^{-1})$ states (Table 1).

3.2.1.1. $E\ ^1\Sigma^+[1/2]6p\pi(v'=3)$. Very weak (vw) Q lines of relative signal intensities as $I(I^+) > I(HI^+) \geq I(H^+)$ were observed for ν^0 = 75 982.3 cm^{-1}. The spectral structure / intensities and relatively low B′ value of 4.10 cm^{-1} derived from the simulation suggests that this corresponds to an Ω = 0 Rydberg state strongly interacting with the ion-pair state. Quantum defect analysis, as described above, as well as comparison with known lower energy vibrational states [37] suggests that this could be v′ = 3 of the $E\ ^1\Sigma^+[1/2]\ (6p\pi)$ state with δ = 3.61, which can be compared with δ = 3.55 and 3.57 for v' = 0, 1, respectively. Very low spectral intensity also favours high v′(v′ = 3). A decrease in B′ values with v′ from B′ = 5.94 to 4.10 cm^{-1} from v′ = 0 to v′ = 3, as observed, is also what might be expected [37].

3.2.1.2. $f\ ^3\Delta_2[3/2]7p\pi\ (v'=0)$. Weak (w) Q and S lines of $I(HI^+) \gg I(I^+) \sim I(H^+) \sim 0$ were observed for ν^0 = 74 272.8 cm^{-1} (see Fig. 1a). A spectrum with same band origin (74 271 cm^{-1}) was observed but left unassigned by Ginter et al. [37] in absorption. The structure of the two-photon spectrum, with respect to relative intensities of the Q lines and absence of J′ = 0 and 1 rotational lines suggests that the excited state is a Δ state. Relatively high B′ value (5.93 cm^{-1}) and dominant HI^+ signal both suggest that interaction between the Rydberg state and the ion-pair state is negligible. A quantum defect value of δ = 3.60 is obtained by assuming that the Rydberg state is the v′ = 0 level of the $f\ ^3\Delta_2[3/2]7p\pi\ \pi$ state, in close agreement with that derived for the $f\ ^3\Delta_2[3/2]6p\pi(v'=0)$ (δ = 3.60) state.

3.2.1.3. $g^3\Sigma^-_{0+}[3/2]7p\pi\ (v'=1)$. Medium (m) O, Q and S lines of I $(I^+) > I(HI^+) > I(H^+)$ were observed for ν^0 = 76 364.4 cm^{-1}. The spectral structure / intensities and relatively low B′ value of 4.36 cm^{-1} suggests that this corresponds to an Ω = 0 Rydberg state interacting strongly with the ion-pair state. Quantum defect analysis suggest that this state could be v′ = 1 of the $g^3\Sigma^-_{0+}$ [3/2]7pπ state with δ = 3.61 in a reasonable agreement with that derived for $g^3\Sigma^-_{0+}[3/2]6p\pi(v'=1)$ of δ = 3.54. Further support is gained from energy considerations. Thus, the energy difference between this state and the v′ = 0 level [52] of 1629.2 cm^{-1} is found to be close to the value of 1681.8 cm^{-1} for the corresponding v′ levels for $g^3\Sigma^-_{0+}[3/2]6p\pi$ [37].

3.2.1.4. $g\ ^3\Sigma^-_{1\pm}[1/2]7p\pi\ (v'=0)$. Strong (s) Q lines of $I(I^+) > I(HI^+) > I(H^+)$ were observed in a complicated region of many overlapping peaks for ν^0 = 79 145.0 cm^{-1}. The relatively high I^+ intensity suggest that the state is mixed with the ion-pair state whereas the relatively high rotational constant of B′ = 5.77 cm^{-1} indicates that the coupling is heterogeneous ($\Delta\Omega > 0$) rather than homogeneous ($\Delta\Omega = 0$) in nature. An indication of a perturbation, due to near-degenerate interaction, showing as line shift of the Q (J′ = 4) peak, further supports this [37]. A quantum defect value of δ = 3.68 is obtained by assuming that the Rydberg state is the v′ = 0 level of the $g^3\Sigma^-_{1\pm}$ [1/2]7pπ state in close agreement with the $g^3\Sigma^-_{1\pm}$ [1/2] $6p\pi(v'=0)$ state (δ = 3.67).

3.2.1.5. $F^1\Delta_2\ [1/2]7p\pi(v'=0)$. Weak (w) O,P,Q, R and S lines of relative signal intensities as $I(HI^+) \geq I(I^+) > I(H^+) \sim 0$ were observed for ν^0 = 79 923.5 cm^{-1}. The spectral structure is indicative of a Δ state with B′ of 6.74 cm^{-1}, which is larger than for the ground state. Although the I^+ signal intensity is relatively high, negligible H^+ signal suggests that interaction with the ion-pair state is minor. A quantum defect value of δ = 3.54 is obtained by assuming that the Rydberg state is the v′ = 0 level of the $F^1\Delta_2$ [1/2]7pπ state in close agreement with the $F^1\Delta_2$ [1/2]6pπ (v′ = 0) state (δ = 3.59).

3.2.2. $[\Omega_c]nd\pi$ (n = 5,6) Rydberg states

A total of six spectra were assigned to transitions to $(\sigma^2\pi^3)5d\pi$ and $(\sigma^2\pi^3)6d\pi$ vibrational Rydberg states, i.e. the $I^1\Delta_2[1/2]5d\pi(v'=$

Table 2
New ion-pair vibrational states: State specifications (Term symbol, and electron configuration), vibrational quantum numbers (v′)[a], band origin (ν^0), rotational parameters (B′, D′) and specifications relevant to the spectral structure (intensities, perturbations and relative ion intensities).

State specification	v′ [a]	ν^0 /cm^{-1}	B′/cm^{-1}	D′*10⁴ /cm^{-1}	Int.	Perturb. Interaction	Relative ion int.
$V\ ^1\Sigma^+_{0+}\ (\sigma\pi^4)\sigma^*$	m + 20	75 025.4	3.02	−33	w		$I(I^+) > I(H^+) > I(HI^+)$
	m + 21	75 189.5	2.41	1423	ms		$I(I^+) > I(H^+) > I(HI^+)$
	m + 23	75 822.0	2.79	63	w	X	$I(I^+) > I(H^+) \sim I(HI^+)$
	m + 24	75 919.1	3.16	−27	vw	X	$I(I^+) > I(H^+) \sim I(HI^+)$
	m + 26	76 479.9	2.67	−31	w		$I(I^+) > I(H^+) > I(HI^+)$
	m + 29	77 226.8	3.13	14	m	X	$I(I^+) > I(H^+) \sim I(HI^+)$
	m + 31	77 795.6	3.01	28	w		$I(I^+) \gg I(H^+) > I(HI^+)$
	m + 32	77 934.8	2.80	11	vw		$I(I^+) \gg I(HI^+) > I(H^+)$
	m + 35	78 585.1	2.61	−54	s	X	$I(I^+) > I(H^+) > I(HI^+)$

[a] Spectra of band origins higher in energy than 75 189.5 cm^{-1} have been assigned to i-values (for $v'' = m + i$; see main text) by guessing the number and approximate positions of yet unobserved bands, based on an assumption of a realistic continuation of the vibrational energy ladder (see Fig. 3). The i's for v′ ($m + i$); $i > 21$ should be considered to be approximation values.

2) (ν^0 = 76 080.8 cm^{-1}, $I^1\Delta_2[1/2]5d\pi(v' = 3)$ (ν^0 = 77 954.1 cm^{-1}), $j^3\Sigma_{0+}^-[1/2]5d\pi(v' = 2)$ (ν^0 = 77 349.7 cm^{-1}), $i^3\Delta_3[3/2]6d\pi(v' = 0)$ (ν^0 = 75 246.1 cm^{-1}), $H^1\Sigma^+[3/2]6d\pi$ ($v' = 0$) (ν^0 = 75 546.6 cm^{-1}) and $H^1\Sigma^+[3/2]6d\pi$ ($v' = 1$) (ν^0 = 77 615.0 cm^{-1}) states (Table 1).

3.2.2.1. $I\,^1\Delta_2[1/2]5d\pi(v' = 2, 3)$. Medium (m) and weak (w) O, P, Q, R and S lines of relative signal intensities as $I(HI^+) > I(I^+) > I(H^+)$ were observed for ν^0 = 76 080.8 cm^{-1} and 77 954.1 cm^{-1}, respectively. The spectral structures are indicative of Δ states with B′s of 5.82 cm^{-1} (ν^0 = 76 080.8 cm^{-1}) and 5.55 cm^{-1}(ν^0 = 77 954.1 cm^{-1}). Quantum defect values of δ = 2.47 and 2.48 were obtained by assuming that the Rydberg states are the v' = 2 (ν^0 = 76 080.8 cm^{-1}) and 3 (ν^0 = 77 954.1 cm^{-1}) levels, respectively, of $I^1\Delta_2$ [1/2]$5d\pi$ in close agreement with the $I^1\Delta_2$ [1/2]$5d\pi$ ($v' = 0$) state (δ = 2.47). A gradual decrease in B′ values with v′ from B′ = 6.31 cm^{-1} for v′ = 0 [37,50], as observed, is also what might be expected.

3.2.2.2. $j^3\Sigma_{0+}^-[1/2]5d\pi(v'=2)$. Strong (s) (O), Q (and S) lines of $I(I^+) > I(HI^+) \gg I(H^+)$ were observed for ν^0 = 77 349.7 cm^{-1}. The spectral structure, with respect to relative line intensities and absence of P and R lines, suggests that this is due to a Σ / Ω = 0 state interacting strongly with the ion-pair state. A rather low value of B′ = 5.09 cm^{-1} as well as an indication of line shifts for J′ ~ 5, 6, due to a state interaction further supports this. A quantum defect value of δ = 2.37 is obtained by assuming that the Rydberg state is the v′ = 2 level of the $j^3\Sigma_{0+}^-[1/2]5d\pi$ state in agreement with the $j^3\Sigma_{0+}^-[1/2]5d\pi$ ($v' = 0$) state (δ = 2.37).

3.2.2.3. $i^3\Delta_2[3/2]6d\pi(v'= 0)$. Very weak (vw) Q, R and S lines of relative signal intensities as $I(HI^+) \gg I(I^+) > I(H^+) \sim 0$ were observed for ν^0 = 75 246.1 cm^{-1}(Fig. 1b). The absence of rotational lines for J′< 2 and appearance of R lines suggest that this is due to a Δ state. Large B′ value of 6.14 cm^{-1} and dominant HI^+ signals suggest that its interaction with the ion-pair state is negligible. A quantum defect value of δ = 3.42 is obtained by assuming that this is the v' = 0 level of the $i^3\Delta_2[3/2]6d\pi$ state, close to that derived for $i^3\Delta_3[3/2]5d\pi(v'= 0)$ (δ = 3.34) [49].

3.2.2.4. $H^1\Sigma^+[3/2]6d\pi$ ($v'= 0, 1$). Very strong (vs) and very weak (vw) Q lines of $I(I^+) > I(HI^+) \gg I(H^+)$ were observed for ν^0 = 75 546.6 cm^{-1} and ν^0 = 77 615.0 cm^{-1}, respectively. The relative ion signal intensities suggest that these are due to Σ / Ω = 0 states interacting strongly with the ion-pair state. Although the B′ values of 5.86 cm^{-1} (ν^0 = 75 546.6 cm^{-1}) and 5.56 cm^{-1} (ν^0 = 77 615.0 cm^{-1}) are relatively large there is an indication of a perturbation, in the ν^0 = 75 546.6 cm^{-1} system, showing as line shifts for J′ > 5. Quantum defect values of δ = 2.35 and 2.36 were obtained by assuming that the Rydberg states correspond to the v′ = 0 (ν^0 = 75 546.6 cm^{-1}) and 1 (ν^0 = 77 615.0 cm^{-1}) levels, respectively, of $H^1\Sigma^+[3/2]6d\pi$, in very close agreement with the $H^1\Sigma^+[3/2]6d\pi$ ($v' = 0$) (δ = 2.34) and ($v' = 1$) (δ = 2.36) states. The observed decrease in the B′ values with v′ as v′ = 0 > v′ = 1 is also what might be expected.

3.2.3. $[\Omega_c]nf\pi$ (n = 4,5) Rydberg states

A total of five spectra were assigned to transitions to $(\sigma^2\pi^3)4f\pi$ vibrational Rydberg states, i.e. the $P^1\Delta_2$ [1/2]$4f\pi$ ($v' = 0$)(ν^0 = 75 124.6 cm^{-1}), $P^1\Delta_2$ [1/2]$4f\pi$ ($v' = 2$)(ν^0 = 78 502.6 cm^{-1}), $O^1\Sigma^+[3/2]4f\pi$ ($v' = 2$)(ν^0 = 75 410.1 cm^{-1}), $O^1\Sigma^+[3/2]4f\pi$ ($v' = 3$) (ν^0 = 77 448.2 cm^{-1}) and $q^3\Sigma_{0+}^-[1/2]4f\pi$ ($v' = 0$)(ν^0 = 76 234.4 cm^{-1}) states (Table 1).

3.2.3.1. $P^1\Delta_2$ [1/2]$4f\pi$ ($v' = 0, 2$). Medium-to-strong (ms) O, P,Q, R and S lines and medium intense (m) P, Q, R and S lines of relative signal intensities as $I(HI^+) > I(I^+) > I(H^+)$ were observed for ν^0 = 75 124.6 cm^{-1} (Fig. 1c) and ν^0 = 78 502.6 cm^{-1}, respectively. The spectral structures, in a wide respect, indicate Δ upper states with medium-large B′s of 6.15 cm^{-1} (ν^0 = 75 124.6 cm^{-1}) and 5.67 cm^{-1} (ν^0 = 78 502.6 cm^{-1}). There is an indication of some line shifts for low J′s (J′ = 2 – 3) for the ν^0 = 75 124.6 cm^{-1} system, suggesting that a near-degenerate interaction with the ion-pair state is involved. No clear indication of spectral perturbations, due to state interaction, for the ν^0 = 78 502.6 cm^{-1} system is seen. Quantum defect values of δ = 1.20 and 1.27 were obtained by assuming that the states are v′ = 0 (ν^0 = 75 124.6 cm^{-1}) and 2 (ν^0 = 78 502.6 cm^{-1}) of the $P^1\Delta_2$ [1/2]$4f\pi$. These values can be expected for $f\pi$ states. For comparison, δ = 1.04, is derived for the $O\,^1\Sigma^+[3/2]4f\pi(v' = 0)$ state (see also $q^3\Sigma_{0+}^-[1/2]4f\pi$ (δ = 1.08) below). A gradual decrease in B′ values with v′ as observed is also what might be expected.

3.2.3.2. $O^1\Sigma^+[3/2]4f\pi$ ($v'= 2, 3$). Strong (s) and medium (m) Q lines of $I(I^+) > I(HI^+) > I(H^+)$ were observed for ν^0 = 75 410.1 cm^{-1} (Fig. 1d) and ν^0 = 77 448.2 cm^{-1}, respectively. The spectral structures, in a wide respect, indicate Σ / Ω = 0 states, which are interacting strongly with the ion-pair state with a relatively low B′s of 5.19 cm^{-1} (ν^0 = 75 410.1 cm^{-1}) and 4.56 cm^{-1} (ν^0 = 77 448.2 cm^{-1}). Quantum defect values of δ = 1.04 and δ = 1.03 were obtained by assuming that these are the v′ = 2 (ν^0 = 75 410.1 cm^{-1}) and v′ = 3 (ν^0 = 77 448.2 cm^{-1}) levels, respectively of $O^1\Sigma^+[3/2]4f\pi$ in perfect agreement with the $O^1\Sigma^+[3/2]4f\pi$ ($v'= 0$) (δ = 1.04) and $O^1\Sigma^+[3/2]4f\pi$ ($v'= 1$) (δ = 1.04) states.

3.2.3.3. $q^3\Sigma_{0+}^-[1/2]4f\pi(v' = 0)$. Medium intense (m) Q lines of $I(I^+) > I(HI^+) > I(H^+)$ were observed for ν^0 = 76 234.4 cm^{-1}. The spectral structure, with respect to relative line intensities, apparent line shifts and intensity anomalies for J′ = 2–3 suggests that this is due to a Σ / Ω = 0 state interacting strongly with the ion-pair state. Furthermore, the B′ is relatively low (5.50 cm^{-1}) as to be expected in case of such state interaction. An expectable value for the quantum defect parameter δ of 1.08 is obtained for v′ = 0 of the $q^3\Sigma_{0+}^-[1/2]4f\pi$ state (see above for comparison).

3.3. Ion-pair states

Total of nine spectral bands were assigned to transitions to vibrational ion-pair states, $V\,^1\Sigma_{0+}^+$ $(\sigma\pi^4)$ $\sigma^*(v')$, ranging from ν^0 = 75 025.4 cm^{-1} to 78 585.1 cm^{-1} (see Table 2 and Fig. 1e). These bands all show the following characteristics, which are typical for ion-pair spectra [36–41,50–53]:

a) The spectra show Q lines only, widely spread on the excitation scale, degrading to the red, typically of weak intensity.
b) The spectra show larger fragment ion signals than molecular ion signals, typically as $I(I^+) > I(H^+) \geq I(HI^+)$.
c) Simulation analysis give B′ values significantly lower than those derived from the Rydberg state spectra, ranging between 2.4 and 3.2 cm^{-1}.

Furthermore, spectral perturbations in the form of line shifts and/or intensity anomalies are seen in many of the spectra. This is typical for ion-pair spectra and has been interpreted as being due to interactions with Rydberg states close in energy [28,34,51–53].

Assignments of the spectra with respect to vibrational quantum numbers, v′, are uncertain. Vibrational quantum numbers have been marked as $v' = m + i$ for positive integer numbers of i ranging from zero for the lowest vibrational level observed [37] to 19 [53] and for m an unknown positive integer. The new vibrational ion-pair states observed here correspond to i > 19. Because of relatively weak spectra signals and complexity of the spectral structure in our observation region we cannot exclude that some vibrational

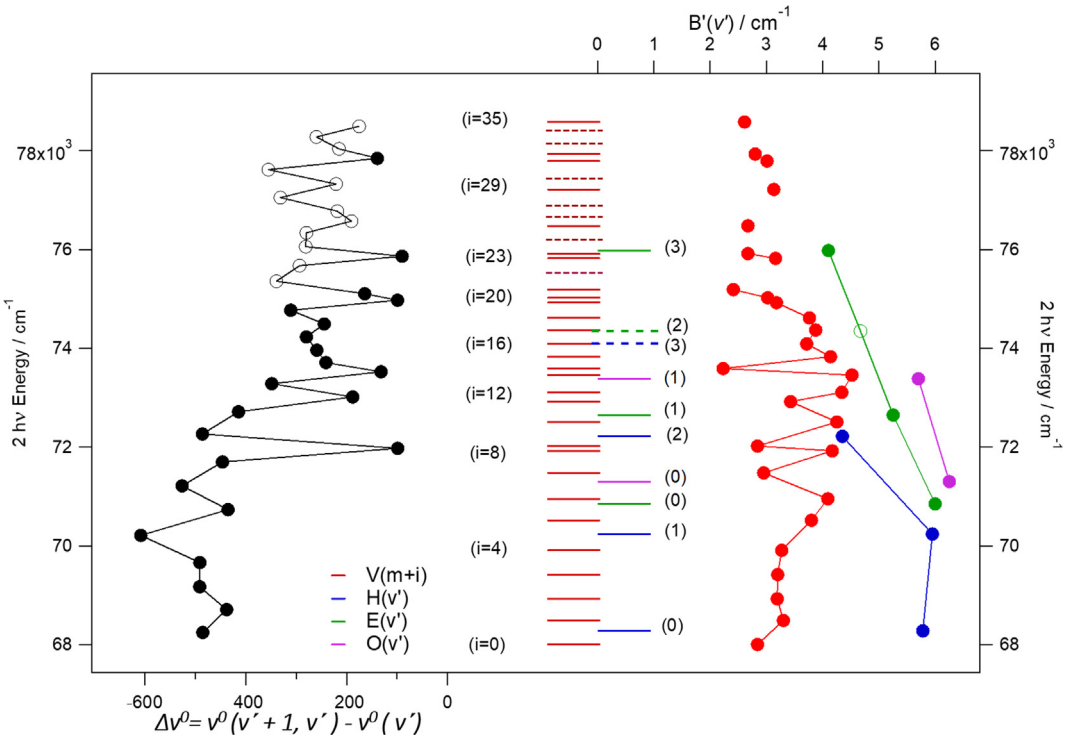

Fig. 3. Vibrational energy levels for the $E\ ^1\Sigma^+[1/2]6p\pi$ (green), $H^1\Sigma^+[3/2]6d\pi$ (blue), $O^1\Sigma^+[3/2]4f\pi$ (purple) Rydberg states and the $V\ ^1\Sigma^+_{0+}(\sigma\pi^4)\sigma^*$ (red) ion-pair state as well as vibrational energy level spacing ($\Delta v^0(v'+1, v') = v^0(v'+1, v') - v^0(v')$) for the $V^1\Sigma^+$ ion-pair state (black curve rotated to the left) and rotational constants (B′(v′)) (rotated to the right) (● – observed, ○–predicted or guessed (see main text)).

bands are yet undetected and missing in the ion-pair vibrational ladder for $i > 19$. In Table 2 we have labeled the bands at $v^0 = 75\,025.4$ and $75\,189.5\ cm^{-1}$, convincingly, as $v' = m + 20$ and $m + 21$, respectively. Spectra of higher energy band origin have been assigned to i-values by guessing the number and approximate positions of yet unobserved bands. The guesses are based on what we feel is a realistic continuation of the vibrational energy ladder (see Fig. 3). The i's for v′ ($m + i$) levels of $i > 21$ should be considered to be approximation values.

4. Discussion

4.1. Rydberg states

In Table 3 we have gathered together from number of publications relevant spectroscopic information for all Rydberg states of HI identified prior to this work. Reassignment of some of the states, as mentioned above (Section III), has been taken account of. Fig. 2 shows energies (band origin) of all these states as well as for the new ones presented in this work (Table 1). Furthermore, some predicted values based on the quantum defect calculations described above have been added. The following characteristics and interpretations can be deduced from this survey and our new data:

Intensities: Typically relative ion intensities vary as $I(I^+) > I(HI^+) > I(H^+)$ for Σ / $\Omega = 0$ states, but as $I(HI^+) > I(I^+) > I(H^+)$ for Δ / $\Omega > 0$ states. This is a consequence of a mixing with the ion-pair state, which enhances fragment ion formation over parent molecular ion formation for $\Omega = 0$ states in particular [51–53]. Normally intensities of spectra due to transitions to $v' = 0$ are the largest in series of spectra of vibrational ladders. This is what might be expected if the ion formation is primarily determined by the Franck-Condon factor of the two-photon resonant transitions.

B′(Rotational constants): There is a large variation in the B′ values depending on states. There is a tendency towards higher B′ values depending on the symmetry as $\Sigma < \Delta$, as well as with increasing Ω and multiplicity (Singles < Triplet). Most likely this is due to different strength of interactions between the Rydberg states and the ion-pair state governed by selection rules. Furthermore, there is a tendency towards decreasing B′s with vibrational quantum numbers. This is what to be expected since B′ will decrease with internuclear distance, which increases with vibrational energy.

δ (Quantum defect parameters): Good consistency is found in the quantum defect values (δ) for Rydberg states which converge to the same type of Rydberg orbitals. The values are virtually independent of state symmetry, multiplicity, total electronic quantum number (Ω and Ω_c) as well as principal quantum number (n). This makes the δ-values particularly useful in the spectral assignment procedure. δ-values for the newly observed $np\pi$ (n = 6,7), $nd\pi$ (n = 5, 6) and $4f\pi$ Rydberg states are found to be in the ranges of 3.54 – 3.68, 2.35 – 2.48 and 1.03 – 1.27, respectively.

All the new spectra presented in this paper are assigned to $\lambda = \pi$ molecular Rydberg states, for l corresponding to p, d and f iodine atomic orbitals (Table 1) to give either Σ or Δ states (Ω = 0,1,2). No spectra due to transitions to Π state, which correspond either to σ or δ molecular Rydberg states were identified. Π states are rarely observed in two-photon resonant excitation, whereas, these are more clearly seen in one-photon (absorption) or odd-number photon excitations (See Table 3). This is due to different transition probabilities and different restrictions made by selection rules. It can not be ruled out though that some of yet unassigned and complicated spectral structure seen in this spectral region could be assigned to Π Rydberg states. By the identification of $7p\pi$ and $6d\pi$ Rydberg states in this work (Table 1), now for the first time $p\pi$ and $d\pi$ Rydberg states of higher principal quantum numbers than n = 6 and 5, respectively, have been observed.

4.2. Ion-pair states

In Table 4 we have gathered together from the literature relevant spectroscopic information for all ion-pair vibrational states

Table 3
Summary of Rydberg states and spectra, previously observed and reassigned[a]. Rydberg state specifications ($Ry\ ^{2\Sigma+1}X_{\Omega}[\Omega_c]nl\lambda$), vibrational quantum numbers (v′), band origin (ν^0), rotational parameters (B′, D′), quantum defect values (δ) and references of previous observations.

State specifications	v'	ν^0 /cm^{-1}	B′ /cm^{-1}	D′*10^4 /cm^{-1}	Quantum defect δ	Refs.
$[\Omega_c]ns\sigma$ (n = 6,7)						
$b\ ^3\Pi_2[3/2]6s\sigma$	0	55 833.1	6.348	–	4.02	[36]
	1	58 040.5	6.173	–	4.02	[36]
$b\ ^3\Pi_1[3/2]6s\sigma$	0	56 738.3	6.427	–	3.99	[36]
	1	58 937 ± 20	–	–	3.98	[36]
$b\ ^3\Pi_0^{\pm}[1/2]6s\sigma$	0	60 857.9	6.426	–	4.03	[36]
	1	63 064.0	6.245	–	4.03	[36]
	3	67 150.3	5.693	2.3	4.02	[38]
$C\ ^1\Pi_1[1/2]6s\sigma$	0	62 325 ± 10	–	–	3.97	[36]
	1	64 508 ± 10	–	–	3.89	[36]
$m\ ^3\Pi_2[3/2]7s\sigma$	0	70 837.6/70 841.5	6.11/ 6.21 ± 0.04	1.94/ 12 ± 5	4.09	[37]/ [50]
	1	72 697.2	6.014	2.30	4.12	[37]
$m\ ^3\Pi_1[3/2]7s\sigma$	0	71 287.3	6.254	3.18	4.04	[37]
	1	72 924.8/72 945.0	6.205/6.16	4.6/−16	4.09	[37]/[52]
$[\Omega_c]np\sigma$ (n = 6,7)						
$d\ ^3\Pi_2[3/2]6p\sigma$	0	63 854.9	6.065	1.7	3.65	[38]
	1	66 009.4	5.926	1.5	3.65	[38]
$d\ ^3\Pi_1[3/2]6p\sigma$	0	63 883	–	–	–	[38]
$d\ ^3\Pi_0^+[1/2]6p\sigma$	0	69 157	6.117	2.1	3.65	[38]
	1	70 988.2	5.79 ± 0.12	−290 ± 40	3.67	[50]
$D^1\Pi_1[1/2]6p\sigma$	0	69 244.5	6.198	2.1	3.65	[38,37]
	1	71 382.4	6.052	1.92	3.65	[37]
	2	73 412.3	5.937	12.6	3.65	[37]
$r\ ^3\Pi_1[3/2]7p\sigma$	0	74 320	6.040	−4.48	3.59	[37]
$[\Omega_c]np\pi$ (n = 6,7)						
$E\ ^1\Sigma^+[1/2]6p\pi$	0	70 850.5/70 866.3[a]	6.00/ 5.94 ± 0.17	128/ −11 ± 21	3.55	[37]/[50]
	1	72 650.8/ 72 654.3[a]	5.29/5.19	4.63/−16	3.57	[37]/[50]
$f\ ^3\Delta_3[3/2]6p\pi$	0	64 572.6	5.715	−7.6	3.61	[38]
$f\ ^3\Delta_2[3/2]6p\pi$	0	64 693.9/64 691	6.737/6.80 ± 0.03	10.6/2.9 ± 1.2	3.60	[37]/[39]
	1	66 610	6.17 ± 0.01	15 ± 3	3.62	[39,40]
$f\ ^3\Delta_1[1/2]6p\pi$	0	69 687.0/69 699.9	6.135/6.31 ± 0.02	1.92/4.6 ± 1.0	3.62	[38,37]/[50]
	1	71 780.5	5.957	9.73	3.62	[37]
$F\ ^1\Delta_2[1/2]6p\pi$	0	70 228.3/70 223.6	6.30/ 6.32 ± 0.01	1.2/ 2.6 ± 0.6	3.59	[38,37]/[50]
	1	72 324.0	6.13	0.0003	3.59	[52]
$g\ ^3\Sigma_{0+}^-[3/2]6p\pi$	0	66 022.6	6.110	2.5	3.51	[37]
	1	67 704.4	5.62	28	3.54	[37]
$g\ ^3\Sigma_1^{-\pm}[1/2]6p\pi$	0	68 908.8	6.06	1.7	3.67	[37]
$g\ ^3\Sigma_{0+}^-[3/2]7p\pi$	0	74 735.2[a]	6.10	14.8	2.42	[53]
$[\Omega_c]nd\sigma$ (n = 5)						
$N\ ^1\Pi_1[1/2]5d\sigma$	0	71 526.2	6.163	1.74	2.50	[37]
	2	74 899.2	6.17	6.2	2.56	[53]
$[\Omega_c]nd\pi$ (n = 5)						
$H\ ^1\Sigma^+[3/2]5d\pi$	0	68 277.3[a]	5.78	5.0	2.34	[37]
	1	70 242.1/70 236.1[a]	5.95/6.34 ± 0.01	125/1100 ± 20	2.36	[37]/[50]
	2	72 217.6[a]	4.35	24.2	2.36	[37]
$i\ ^3\Delta_3[3/2]5d\pi$	0	68 326.2	6.21	−25	2.34	[49]
$I\ ^1\Delta_2[1/2]5d\pi$	0	71 990/71 989.4	6.312/ 6.31 ± 0.01	2.7/ 2.4 ± 0.1	2.47	[40]/[50]
$j\ ^3\Sigma_{0+}^-[1/2]5d\pi$	0	73 254.9/73 252.0	5.71/5.63	47.5/46	2.37	[52]
	1	74 735.2	6.10	14.8	2.42	[53]
$[\Omega_c]nd\delta$ (n = 5)						
$k\ ^3\Pi_0^{\pm}[3/2]5d\delta$	0	68 110.7	6.24	3	2.35	[37]
	1	70 320.4/70 310.8	5.058/5.13 ± 0.03	−21/ −4 ± 9	2.35	[37]/ [50]
	2	72 353.1/72 355.6	5.650/5.86	−5.49/42	2.35	[37]
$k\ ^3\Pi_1[3/2]5d\delta$	0	68 991.8	6.459	3.3	2.28	[37]
	1	71 125.0/71 126.4	6.30/6.22 ± 0.02	4.82/−2.6 ± 1.6	2.27	[37]/ [50]
	2	73 180.7/73 176.7	6.034/6.13	8.72/23	2.27	[37]
$k\ ^3\Pi_2[1/2]5d\delta$	0	73 360.9	6.403	6.123	2.36	[37]
$K\ ^1\Pi_1[1/2]5d\delta$	0	74 282.1	6.255	6.09	2.28	[37]
$[\Omega_c]nf\pi$ (n = 4)						
$O\ ^1\Sigma^+[3/2]4f\pi$	0	71 301.9/71 294.7	5.82/ 6.25 ± 0.22	–/ 33 ± 26	1.04	[40]/[50]
	1	73 383.6/73 384.2	5.819/5.70	4.46/0	1.04	[37,40]/[52]
$p\ ^3\Delta_2[3/2]4f\pi$	0	73 081.7[a]	6.35	2.0	0.8	[52]

[a] Spectra reassigned in this work.

of HI identified prior to this work. Fig. 3 shows energies (band origins) of all these states as well as for the new ones presented in this work (Table 2) and some guess values (see Section III). In addition, Fig. 3 shows energy levels (band origin) for several $^1\Sigma^+$ $6p\pi$, $5d\pi$ and $4f\pi$ vibrational Rydberg states as well as plots of energy level spacing between adjacent vibrational levels ($\Delta E_{v',v'+1}$) and for rotational constants (B′) as a function of energy. The following is evident from this data collection:

Large scatter is observed both in the $\Delta E_{v',v'+1}$ and B′ plots for the ion-pair state (Fig. 3). This is attributed to perturbation effects due to interactions between the ion-pair state and Rydberg states. The largest interactions will be between states of equivalent term symbols, i.e. between $^1\Sigma^+$ states. This appears, firstly, as an enhancement in $\Delta E_{v',v'+1}$, for ion-pair vibrational levels (v', v'+1) closest in energy to interacting $^1\Sigma^+$ (v′) Rydberg states and, secondly, as an increase in the B′s for the corresponding ion-pair vibrational states

Table 4
Summary of ion-pair states and spectra, previously observed. State specifications, vibrational quantum numbers (v′ = *m* + *i*; *m* unknown integer), band origin (ν^0), rotational parameters (B′, D′) and references.

State specification	v′[a]	ν^0 /cm^{-1}	B′ /cm^{-1}	D′*10^4 /cm^{-1}	Refs.
$V\,^1\Sigma^+_{0+}(\sigma\pi^4)\sigma^*$	m	68 004.4	2.84	2.0	[38,37]
	m + 1	68 489.4	3.3	–	[38,37]
	m + 2	68 927.3	3.19	−1.1	[38,37]
	m + 3	69 418.5	3.25	–	[38,37]
	m + 4	69 909.9/69 903.3	3.273/ 2.94 ± 0.18	6.54/ 10 ± 40	[38,37]/ [50]
	m + 5	70 512.1/70 511.0	3.800/ 3.66 ± 0.02	−70.2/ 83 ± 4	[37]/ [50]
	m + 6	70 948.6/70 952.3	4.09/3.56 ± 0.10	44/ 24 ± 10	[37]/ [50]
	m + 7	71 478.4	2.95 ± 0.10	−4 ± 5	[50]
	m + 8	71 920.3/71 924.4	3.97/4.17 ± 0.17	158/ 270 ± 70	[37]/ [50]
	m + 9	72 022.4/72 023.2	2.792/2.84 ± 0.03	−4.61/ 1 ± 4	[37]/ [50]
	m + 10	72 506.0/72 508.8	4.106/4.25	14.7/80	[37]/ [52]
	m + 11	72 923.0	3.43	19	[52]
	m + 12	73 110.8	4.34	10	[52]
	m + 13	73 457.8/73 459.1	3.177/4.52	−23.7/89	[37]/ [52]
	m + 14	73 589.5/73 590.8	2.294/2.23	−11.5/0.0	[37]/ [52]
	m + 15	73 822.7/73 831.8	3.679/4.14	−2.25/90	[37]/ [52]
	m + 16	74 090.0/74 091.0	3.724/3.71	5.8/22.6	[37]/ [53]
	m + 17	74 372.0	3.9	4.2	[53]
	m + 18	74 615.4	3.76	3.67	[53]
	m + 19	74 924.0	3.05	3.83	[53]

[a] Vibrational quantum numbers are marked as v′ = *m* + *i* for positive integer numbers of *i* ranging from zero for the lowest vibrational level observed and *m* as an unknown positive integer.

(Fig. 3). On the other hand, the opposite effect, on the B′s (i.e. decrease in the values), is observed for the interacting $^1\Sigma^+(v')$ Rydberg states.

5. Summary and conclusions

One-color REMPI data of HI, in the form of mass resolved ion signals as a function of wavenumber excitation, were recorded for the two-photon excitation region of 74 200 – 80 300 cm^{-1}. REMPI spectra of the HI^+, I^+ and H^+ ions as a function of two-photon excitation wavenumber were derived from the data. The spectra show line structure due to two-photon resonant transitions from rotational levels in the ground state, $X^1\Sigma^+$, to molecular Rydberg and ion-pair vibrational states of intensities which vary with ions, rotational line series as well as excited vibrational states. In addition, iodine atomic lines due to (2 + 1) REMPI of I(3/2) and I* (1/2) are observed. Molecular spectra were analyzed by spectral simulations which allowed (J′,J′) assignment of rotational lines and determination of spectroscopic parameters for total of 25 new excited molecular states. The ion-pair and Rydberg state spectra could be distinguished based on characteristic differences in the spectral structure and rotational constants. Observations of widely spread Q lines only, to give low B′ was typical for the ion-pair states, whereas richer line structure and larger B′s typically were found for the Rydberg states. 16 new Rydberg vibrational states and 9 new ion-pair vibrational states were identified.

The Rydberg state spectra were further assigned to state properties by considering,

(i) the nature of the spectral structure with respect to relative intensities of line series and appearance or absence of rotational lines,
(ii) relative and absolute ion intensities,
(iii) magnitude of rotational constants,
(iv) perturbation effects, which show as line shifts and/or intensity alterations in the spectra,
(v) by performing detailed quantum defect analysis of the states energetics (band origins).

These considerations (i – v) allowed characterization of state symmetries, term symbols, ion core symmetries, Rydberg electron principal quantum numbers and configurations as well as vibrational quantum numbers. The thorough and systematic assignment procedure revealed some discrepancies in earlier spectra assignments, which resulted in several reassignments.

The ion-pair state spectra show clear perturbation effects in the form of rotational line and vibrational band shifts as well as line intensity alterations. This is due to interactions with number of Rydberg states of which homogeneous couplings ($\Delta\Omega$ = 0) with states of same symmetry ($^1\Sigma$) are the strongest. Large variation in B′ values as a function of vibrational energies also indicates such effect. The spectra could not be assigned to absolute vibrational quantum numbers due to an uncertainty in the value for the lowest energy vibrational band which has been observed. An attempt was made, however, to guess relative quantum number values in the continuing vibrational energy level ladder. This left some gaps of yet unobserved vibrational bands.

It should be emphasized that since the state energies and, therefore, the spectra are clearly affected by state interactions the spectral analysis result in effective spectroscopic parameters which may differ from zero order parameters of unmixed states. Determination of those will need a thorough deperturbation analysis of the states which have been characterized, already, as well as more unobserved ones. Until then we hope that the data and interpretations presented here will render further theoretical interpretation of the characteristic state interactions involved.

CRediT authorship contribution statement

Meng-Xu Jiang: Data curation, Investigation, Writing - original draft. **Ágúst Kvaran:** Supervision, Writing - review & editing.

Declaration of Competing Interest

The authors declare that they have no known competing financial interests or personal relationships that could have appeared to influence the work reported in this paper.

Acknowledgements

The financial support of the University Research Fund, University of Iceland and the Icelandic Research Fund (Grant No. 184693-051) is gratefully acknowledged. We would like to thank

Huasheng Wang and Jingming Long for useful help with the experiments.

References

[1] W.C. Price, Proc. Roy. Soc. Ser. A 167 (1938) 216.
[2] S.G. Tilford, M.L. Ginter, J.T. Vanderslice, J. Mol. Spectrosc. 33 (1970) 505–519.
[3] S.G. Tilford, M.L. Ginter, J. Mol. Spectrosc. 40 (1971) 568–579.
[4] D.S. Ginter, M.L. Ginter, J. Mol. Spectrosc. 90 (1981) 177–196.
[5] D.S. Ginter, M.L. Ginter, S.G. Tilford, J. Mol. Spectrosc. 90 (1981) 152.
[6] J.B. Nee, M. Suto, L.C. Lee, J. Chem. Phys. 85 (1986) 719–724.
[7] T.A. Spiglanin, D.W. Chandler, D.H. Parker, Chem. Phys. Letters 137 (1987) 414–420.
[8] D.S. Green, G.A. Bickel, S.C. Wallace, J. Mol. Spectrosc. 150 (1991) 303–353.
[9] D.S. Green, G.A. Bickel, S.C. Wallace, J. Mol. Spectrosc. 150 (1991) 354–387.
[10] D.S. Green, G.A. Bickel, S.C. Wallace, J. Mol. Spectrosc. 150 (1991) 388–469.
[11] D.S. Green, S.C. Wallace, J. Chem. Phys. 96 (1992) 5857–5877.
[12] E.d. Beer, B.G. Koenders, M.P. Koopmans, C.A.d. Lange, J.Chem. Soc. Faraday Trans. 86 (1990) 2035–2041.
[13] Y. Xie, P.T.A. Reilly, S. Chilukuri, R.J. Gordon, J. Chem. Phys. 95 (1991) 854–864.
[14] E.d. Beer, W.J. Buma, C.A. deLange, J. Chem. Phys. 99 (1993) 3252–3261.
[15] Á. Kvaran, Á. Logadóttir, H. Wang, J. Chem. Phys. 109 (1998) 5856–5867.
[16] Á. Kvaran, H. Wang, Á. Logadóttir, Recent Res. Devel. in Physical Chem., Transworld Research, Network (1998) 233–244.
[17] Á. Kvaran, H. Wang, Á. Logadóttir, J. Chem. Phys. 112 (2000) 10811–10820.
[18] Á. Kvaran, H. Wang, B.G. Waage, Can. J. Physics 79 (2001) 197–210.
[19] H. Wang, Á. Kvaran, J. Mol. Struct. 563–564 (2001) 235–239.
[20] Á. Kvaran, H. Wang, Mol. Phys. 100 (2002) 3513–3519.
[21] Á. Kvaran, H. Wang, J. Mol. Spectrosc. 228 (2004) 143–151.
[22] D. Ascenzi, S. Langford, M. Ashfold, A. Orr-Ewing, Phys. Chem. Chem. Phys. 3 (2001) 29–43.
[23] R. Liyanage, R.J. Gordon, R.W. Field, J. Chem. Phys. 109 (1998) 8374–8387.
[24] Á. Kvaran, H.S. Wang, K. Matthiasson, A. Bodi, E. Jonsson, J. Chem. Phys. 129 (2008) 164313.
[25] K. Matthiasson, H.S. Wang, A. Kvaran, J. Mol. Spectrosc. 255 (2009) 1–5.
[26] Á. Kvaran, K. Matthiasson, H.S. Wang, J. Chem. Phys. 131 (2009) 044324.
[27] K. Matthiasson, J.M. Long, H.S. Wang, A. Kvaran, J. Chem. Phys. 134 (2011) 164302.
[28] J. Long, H. Wang, Á. Kvaran, J. Chem. Phys. 138 (2013) 044308.
[29] R.F. Barrow, J.G. Stamper, Proc. Roy. Soc. Ser. A. 263 (1961) 277–288.
[30] R.F. Barrow, J.G. Stamper, Proc. Roy. Soc. Ser. A. 263 (1961) 259–276.
[31] R. Callaghan, R.J. Gordon, J. Chem. Phys. 93 (1990) 4624–4636.
[32] J.B. Nee, M. Suto, L.C. Lee, J. Chem. Phys. 85 (1986) 4919.
[33] J. Long, H. Wang, Á. Kvaran, J. Mol. Spectrosc. 282 (2012) 20–22.
[34] J. Long, H.R. Hródmarsson, H. Wang, Á. Kvaran, J. Chem. Phys. 136 (2012).
[35] Á. Kvaran, B.G. Waage, H. Wang, J. Chem. Phys. 113 (2000) 1755–1761.
[36] S.G. Tilford, M.L. Ginter, A.M. Bass, J. Mol. Spectrosc. 34 (1970) 327.
[37] D.S. Ginter, M.L. Ginter, S.G. Tilford, J. Mol. Spectrosc. 92 (1982) 40.
[38] M.L. Ginter, S.G. Tilford, A.M. Bass, J. Mol. Spectrosc. 57 (1975) 271.
[39] S.A. Wright, J.D. McDonald, J. Chem. Phys. 101 (1994) 238–245.
[40] S.T. Pratt, M.L. Ginter, J. Chem. Phys. 102 (1995) 1882–1888.
[41] D.S. Ginter, M.L. Ginter, S.G. Tilford, A.M. Bass, J. Mol. Spectrosc. 92 (1982) 55.
[42] A.I. Chichinin, C. Maul, K.H. Gericke, J. Chem. Phys. 124 (2006) 224324.
[43] A.I. Chichinin, P.S. Shternin, N.G.e. al., J. Chem. Phys. 125 (2006) 034310.
[44] S. Kauczok, C. Maul, A.I. Chichinin, K.H. Gericke, J. Chem. Phys. 133 (2010) 024301.
[45] C. Romanescu, S. Manzhos, D. Boldovsky, J. Clarke, H. Loock, J. Chem. Phys. 120 (2004) 767.
[46] H.P.L.C. Romanescu, J. Chem. Phys. 127 (2007) 124304.
[47] C. Romanescu, H.P. Loock, Phys. Chem. Chem. Phys. 8 (2006) 2940–2949.
[48] G. Herzberg, Molecular Spectra and Molecular Structure: Spectra of Diatomic Molecules, 2nd edn., Van Nostrand Reinhold Company, New York, 1950.
[49] P.M. Regan, D. Ascenzi, E. Wrede, P.A. Cook, M.N.R. Ashfold, A.J. Orr-Ewing, Phys. Chem. Chem. Phys. 2 (2000) 23.
[50] H.R. Hródmarsson, H. Wang, Á. Kvaran, J. Mol. Spectrosc. 5 (2013) 290.
[51] H.R. Hródmarsson, H. Wang, Á. Kvaran, J. Chem. Phys. 140 (2014) 244304.
[52] H.R. Hródmarsson, H. Wang, Á. Kvaran, J. Chem. Phys. 142 (2015) 244312.
[53] A. Hafliðason, M.X. Jiang, A. Kvaran, Phys. Chem. Chem. Phys. 21 (2019) 23154.
[54] P. Glodic, D. Zaouris, P.C. Samartzis, A. Hafliðason, Á. Kvaran, Phys. Chem. Chem. Phys. 18 (2016) 26291.
[55] H.R. Hródmarsson, A. Kartakoullis, D. Zaouris, P. Glodic, H. Wang, P.C. Samartzis, Á. Kvaran, Phys. Chem. Chem. Phys. 19 (2017) 11354.
[56] D. Zaouris, A. Kartakoullis, P. Glodic, P.C. Samartzis, H.R. Hródmarsson, Á. Kvaran, Phys. Chem. Chem. Phys. 17 (2015) 10468.
[57] See Supplementary material.
[58] C. M Western, University of Bristol, 10.1.180 ed., University of Bristol 2003-2019., Colin Western.
[59] A.J. Cormack, A.J. Yencha, R.J. Donovan, K.P. Lawley, A. Hopkirk, G.C. King, Chem. Phys. 221 (1997) 175.
[60] NIST Chemistry WebBook, NIST (National Institute of Standards and Technology) Chemistry WebBook.

4.3.1 Supporting information

Addition to and revision of the HI Rydberg states energy region

Meng-Xu Jiang, Arnar Hafliðason and Ágúst Kvaran*

Science Institute, University of Iceland, Dunhagi 3, 107 Reykjavík, Iceland.

Supplementary material

Content: **pages:**

Table S1:

	HCl[a]			HBr[b]			HI[c]	
Upper state	v^0 [cm^{-1}]	$\delta_{i(3/2)}$	$\delta_{i(1/2)}$	v^0 [cm^{-1}]	$\delta_{i(3/2)}$	$\delta_{i(1/2)}$	v^0 [cm^{-1}]	$\delta_{i(3/2)}$
$E\ ^1\Sigma^+(v'=0)$	83780.2[d]		1.64	77940.0 [d]		2.59	70850.5 [d]	
	/83780.0[e]			/77939.5 [f]			/70866.3[g]	
$H\ ^1\Sigma^+(v'=0)$	88684.5 [d]	0.21		79646.0 [d]	1.25		68277.3 [d]	2.34
	/88685.2 [e]			/79645.5 [f]				

a. For HCl, IE (3/2) = 102818.7 cm^{-1}; IE (1/2) = 103466.9 cm^{-1};

b. For HBr, IE (3/2) = 94124.1 cm^{-1}; IE (1/2) = 96776.9 cm^{-1};

c. For HBr, IE (3/2) = 83784.8 cm^{-1}; IE (1/2) = 89087.1 cm^{-1};

d. D. S. GINTER, M. L. GINTER, AND S. G. TILFORD, J. Mol. Spectrosc. 92, 40-54 (1982).

e. D.S. GREEN, G. A. BICKPL, AND S. C. WALLACE, J. Mol. Spectrosc. 150, 303-353 (1991).

f. R. Callaghan and R. G. Gordon, J. Chem. Phys. 93, 7(1990).

g. H. R. Hróðmarsson, H. Wang, and Á. Kvaran, J. Mol. Spectrosc. 290,5 (2013)

Tables S2: Rotational lines

Table 1. Measured transition wavenumbers for the HI $f^3\Delta_2\,[3/2]7p\pi - X\,^1\Sigma^+$ (0,0)

J'	***O***	***P***	***Q***	***R***	***S***
0					
1					
2			74270.2		74309.3
3			74266.7		74329.3
4			74261.8		74350.5
5			74255.7		
6			74248.1		
7			74239.3		
8			74229.3		

Table 2. Measured transition wavenumbers for the HI $P^1\Delta_2\,[1/2]4f\pi - X\,^1\Sigma^+$ (0,0)

J'	***O***	***P***	***Q***	***R***	***S***
0					
1					
2	75033.8	75086.3	75123.8	75147.6	75159.9
3	75005.8	75072.5	75121.4	75159.8	75184.4
4		75058.1	75119.4	75169.9	75208.4
5		75042.9	75117.4	75181.0	75232.6
6		75026.8	75114.6	75191.3	75257.6
7		75011	75109.4		75282.1
8			75101.7		

Table 3. Measured transition wavenumbers for the HI $i^3\Delta_2[3/2]6d\pi - X\ ^1\Sigma^+$ (0,0)

J'	***O***	***P***	***Q***	***R***	***S***
0					
1					
2			75243.2	75269.9	75283.7
3			75242.4	75282.1	75307.8
4			75240.4	75292.8	
5			75238.4	75302.9	
6			75235.6		
7			75232.6		
8			75228.4		
			75224.0		

Table 4. Measured transition wavenumbers for the HI $O^1\Sigma^+[3/2]4f\pi - X\ ^1\Sigma^+$(2,0)

J'	***O***	***P***	***Q***	***R***	***S***
0			75410.4		
1			75407.4		
2			75402.9		
3			75395.3		
4			75384.9		
5			75372.8		
6			75354.8		
7			75335.5		
8			75307.8		

Table 5. Measured transition wavenumbers for the HI $H^1\Sigma^+[3/2]6d\pi - X\ ^1\Sigma^+$(0,0)

J'	***O***	***P***	***Q***	***R***	***S***
0	75507.9		75546.2		
1	75477.4		75545.1		
2	75452.7		75542.7		
3	75423.1		75538.2		
4			75530.5		
5			75518.3		
6			75499.7		

Table 6. Measured transition wavenumbers for the HI $E\,^1\Sigma^+[1/2]6p\pi - X\,^1\Sigma^+$ (3,0)

J'	***O***	***P***	***Q***	***R***	***S***
0			75982.9		
1			75976.9		
2			75970.0		
3			75956.7		
4			75937.9		
5			75919.1		
6			75895.9		

Table 7. Measured transition wavenumbers for the HI $I\,^1\Delta_2[1/2]5d\pi - X\,^1\Sigma^+$ (2,0)

J'	***O***	***P***	***Q***	***R***	***S***
0					
1					
2	75987.3	76038.2	76077.2	76038.9	76118.8
3	75960.4	76022.3	76074.4	76022.9	76140.8
4	75929.0	76006.1	76070.0	76006.7	76162.2
5		75989.3	76064.8	75989.9	76180.5
6		75971.2	76057.6	75971.8	76199.6
7			76043.6	75948.9	

Table 8. Measured transition wavenumbers for the HI $q^3\Sigma^-_{0+}[1/2]4f\pi - X\,^1\Sigma^+$ (0,0)

J'	***O***	***P***	***Q***	***R***	***S***
0			76234.4		
1			76231.6		
2			76226.8		
3			76222.0		
4			76209.1		
5			76195.1		
6			79169.8		

Table 9. Measured transition wavenumbers for the HI $g\,^3\Sigma^-_{0+}\,[3/2]7p\pi - X\,^1\Sigma^+$ (1,0)

J'	*O*	*P*	*Q*	*R*	*S*
0	76327.0		76364.4		76393.4
1	76299.1		76363.2		
2	76266.5		76354.7		
3			76343.5		
4			76328.2		
5			76311.2		
6			76290.5		
7			76262.9		

Table 10. Measured transition wavenumbers for the HI $j\,^3\Sigma^-_{0+}[1/2]5d\pi - X\,^1\Sigma^+$ (2,0)

J'	*O*	*P*	*Q*	*R*	*S*
0	77307.8		77346.0		77376.8
1			77343.6		
2			77338.8		
3			77332.2		
4			77325.0		
5			77318.9		
6			77313.5		

Table 11. Measured transition wavenumbers for the HI $O^1\Sigma^+[3/2]4f\pi - X\,^1\Sigma^+$ (3,0)

J'	*O*	*P*	*Q*	*R*	*S*
0			77448.2		
1			77444.6		
2			77437.6		
3			77426.8		
4			77414.4		
5			77399.9		
6			77382.5		
7			77360.4		

Table 12. Measured transition wavenumbers for the HI $H^1\Sigma^+[3/2]6d\pi - X\ ^1\Sigma^+$ (1,0)

J'	***O***	***P***	***Q***	***R***	***S***
0			77615.4		
1			77613.0		
2			77609.9		
3			77603.6		
4			77596.6		
5			77585.0		
6			77564.3		
7			77543.8		

Table 13. Measured transition wavenumbers for the HI $I\ ^1\Delta_2[1/2]5d\pi - X\ ^1\Sigma^+$ (3,0)

J'	***O***	***P***	***Q***	***R***	***S***
0					
1					
2	77858.0	77911.8	77947.5	77973.2	77985.6
3		77894.1	77942.7	77980.4	78006.0
4		77874.9	77936.3	77986.8	78024.8
5		77853.2	77928.6	77992.4	78043.7
6			77919.4	77997.6	

Table 14. Measured transition wavenumbers for the HI $P^1\Delta_2\,[1/2]4f\pi - X\ ^1\Sigma^+$ (2,0)

J'	***O***	***P***	***Q***	***R***	***S***
0					
1					
2		78461.2	78499.7	78524.9	78536.5
3		78444.4	78496.4	78533.7	78556.9
4			78492.4	78545.8	78578.3
5			78488.8	78551.8	
6			78485.2		
7			78481.6		

Table 15. Measured transition wavenumbers for the HI $g\ ^3\Sigma^-{}_1{}^{\pm}\,[1/2]7p\pi - X\ ^1\Sigma^+$ (0,0)

J'	*O*	*P*	*Q*	*R*	*S*
0			79145.1		
1			79143.5		
2			79141.9		
3			79137.5		
4			79132.6		
5			79126.2		

Table 16. Measured transition wavenumbers for the HI $F^1\Delta_2\,[1/2]7p\pi - X\,^1\Sigma^+$ (0,0)

J'	*O*	*P*	*Q*	*R*	*S*
0					
1					
2	79836.8	79886.7	79926.4	79952.4	79964.6
3	79813.9	79875.5	79928.2	79966.7	79990.1
4		79865.5	79930.6	79981.6	80015.8
5		79855.0	79933.0	79996.9	80042.9
6		79845.2	79934.6	80011.6	
7		79834.8		80025.3	

Table 17. Measured transition wavenumbers for the HI $V^1\Sigma^+ - X\,^1\Sigma^+$ (m+20,0)

J'	*O*	*P*	*Q*	*R*	*S*
0			75025.2		
1			75020.8		
2			75005.6		75044.4
3			74988.5		
4			74959.6		
5			74930.0		

Table 18. Measured transition wavenumbers for the HI $V^1\Sigma^+ - X\ ^1\Sigma^+$ (m+21,0))

J'	*O*	*P*	*Q*	*R*	*S*
0			75189.5		
1			75181.9		
2			75158.9		
3			75122.9		
4			75053.7		

Table 19. Measured transition wavenumbers for the HI $V^1\Sigma^+ - X\ ^1\Sigma^+$ (m+23,0)

J'	*O*	*P*	*Q*	*R*	*S*
0			75822.0		75837.7
1			75814.8		
2			75799.6		
3			75775.4		
4			75741.9		

Table 20. Measured transition wavenumbers for the HI $V^1\Sigma^+ - X\ ^1\Sigma^+$ (m+24,0)

J'	*O*	*P*	*Q*	*R*	*S*
0			75919.1		
1			75911.6		
2			75903.7		
3			75885.2		
4			75862.1		
5			75819.2		
6			75786.9		
7			75752.9		
8			75708.8		
9			75655.5		

Table 21. Measured transition wavenumbers for the HI $V^1\Sigma^+ - X\ ^1\Sigma^+$ (m+26,0)

J'	*O*	*P*	*Q*	*R*	*S*
0					
1					
2					
3			76436.0		
4			76407.1		
5			76372.7		
6			76331.4		

Table 22. Measured transition wavenumbers for the HI $V^1\Sigma^+ - X\ ^1\Sigma^+$ (m+29,0)

J'	*O*	*P*	*Q*	*R*	*S*
0			77226.8		
1			77219.6		
2			77206.1		
3			77185.8		
4			77160.6		
5			77129.6		
6			77089.1		
7			77038.6		

Table 23. Measured transition wavenumbers for the HI $V\Sigma^+ - X\ ^1\Sigma^+$ (m+31,0)

J'	*O*	*P*	*Q*	*R*	*S*
0	77756.5		77795.6		77813.4
1			77788.7		77818.1
2			77774.5		
3			77754.1		
4			77727.8		
5			77693.2		
6			77650.2		

Table 24. Measured transition wavenumbers for the HI $V\Sigma^+ - X\,^1\Sigma^+$ (m+32,0)

J'	***O***	***P***	***Q***	***R***	***S***
0			77934.8		
1			77927.8		
2			77914.2		
3			77892.5		
4			77862.8		
5			77828.0		
6					

Table 25. Measured transition wavenumbers for the HI $V\Sigma^+ - X\,^1\Sigma^+$ (m+35,0)

J'	***O***	***P***	***Q***	***R***	***S***
0			78585.1		
1			78577.5		
2			78563.2		
3			78540.5		
4			78512.9		
5			78478.0		
6			78424.7		
7			78367.7		
8			78301.2		

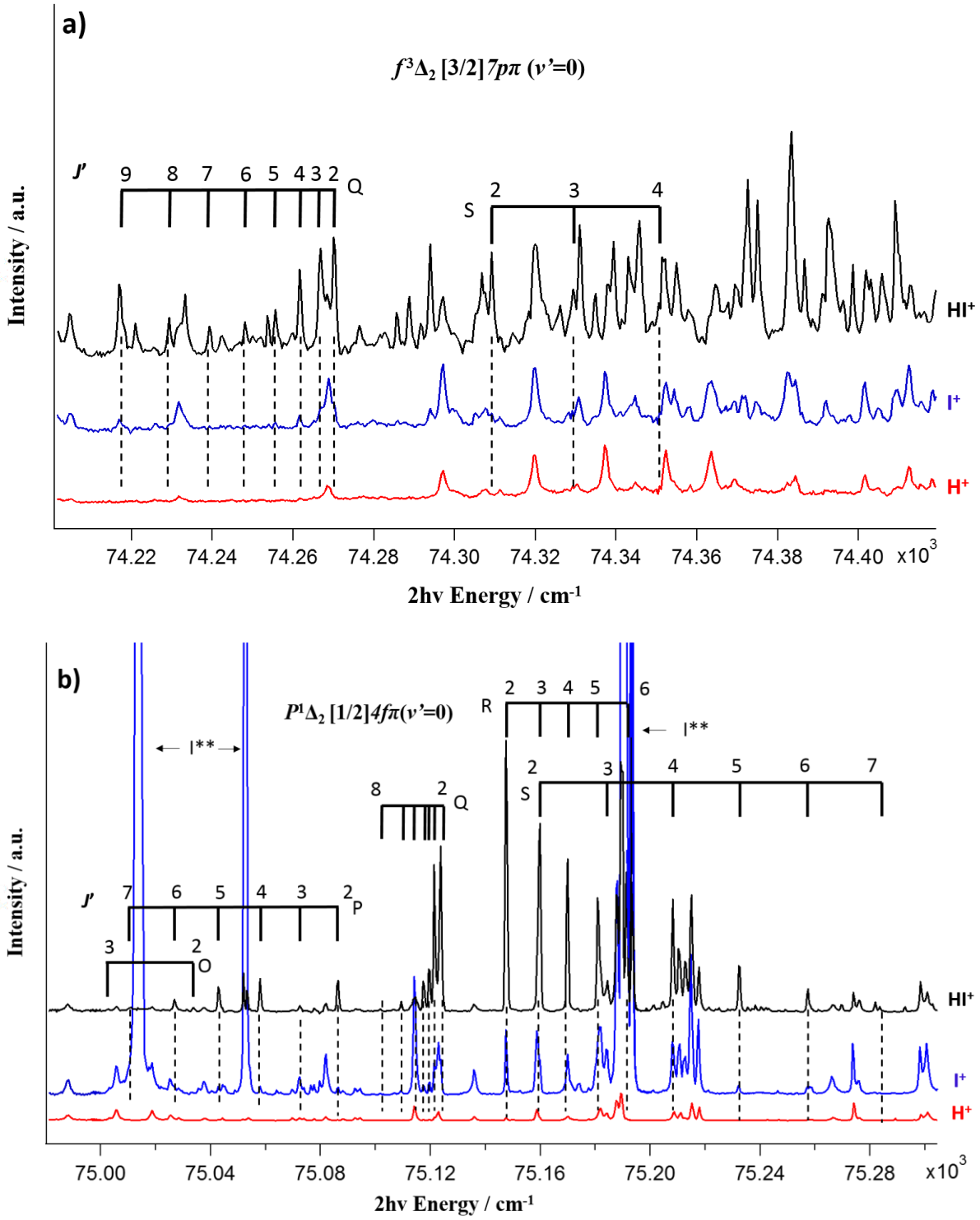
a)
$f^3\Delta_2$ [3/2] 7pπ (v'=0)
J'
9 8 7 6 5 4 3 2 Q
2 3 4 S
Intensity / a.u.
HI+
I+
H+
74.22 74.24 74.26 74.28 74.30 74.32 74.34 74.36 74.38 74.40 x10^3
2hv Energy / cm-1
b)
$P^1\Delta_2$ [1/2] 4fπ(v'=0)
I**
I**
2 3 4 5 6 R
2 3 4 5 6 7 S
8 2 Q
J'
7 6 5 4 3 2 P
3 2 O
Intensity / a.u.
HI+
I+
H+
75.00 75.04 75.08 75.12 75.16 75.20 75.24 75.28 x10^3
2hv Energy / cm-1

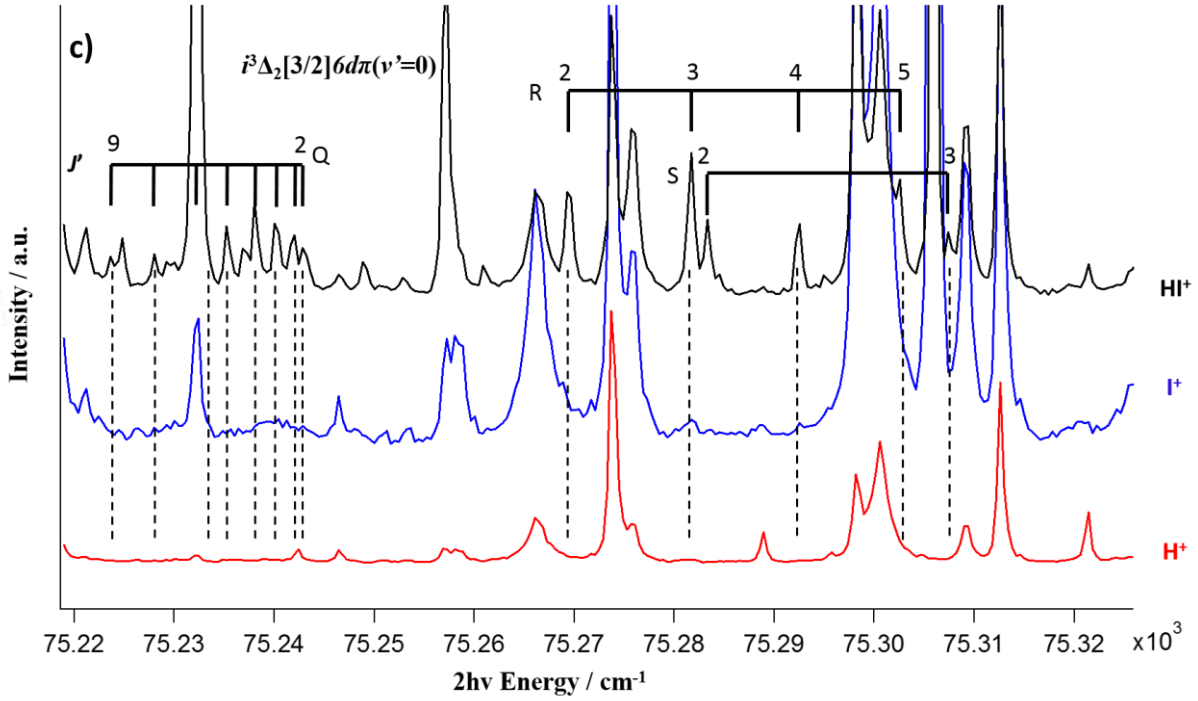
c)
$i^3\Delta_2[3/2]6d\pi(v'=0)$
J'
9
2
Q
R
2
3
4
5
S
2
3
HI+
I+
H+
Intensity / a.u.
75.22
75.23
75.24
75.25
75.26
75.27
75.28
75.29
75.30
75.31
75.32
x10^3
2hv Energy / cm-1

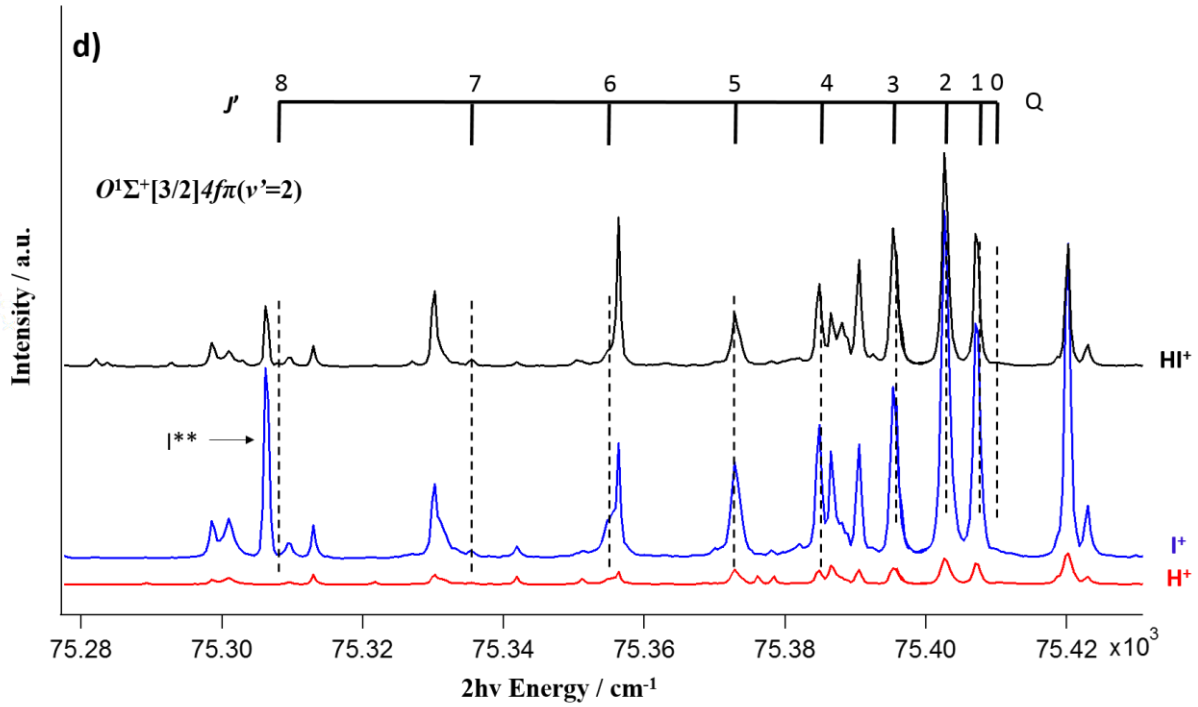
d)
J'
8
7
6
5
4
3
2
1
0
Q
$O^1\Sigma^+[3/2]4f\pi(v'=2)$
HI+
I**
I+
H+
Intensity / a.u.
75.28
75.30
75.32
75.34
75.36
75.38
75.40
75.42
x10^3
2hv Energy / cm-1

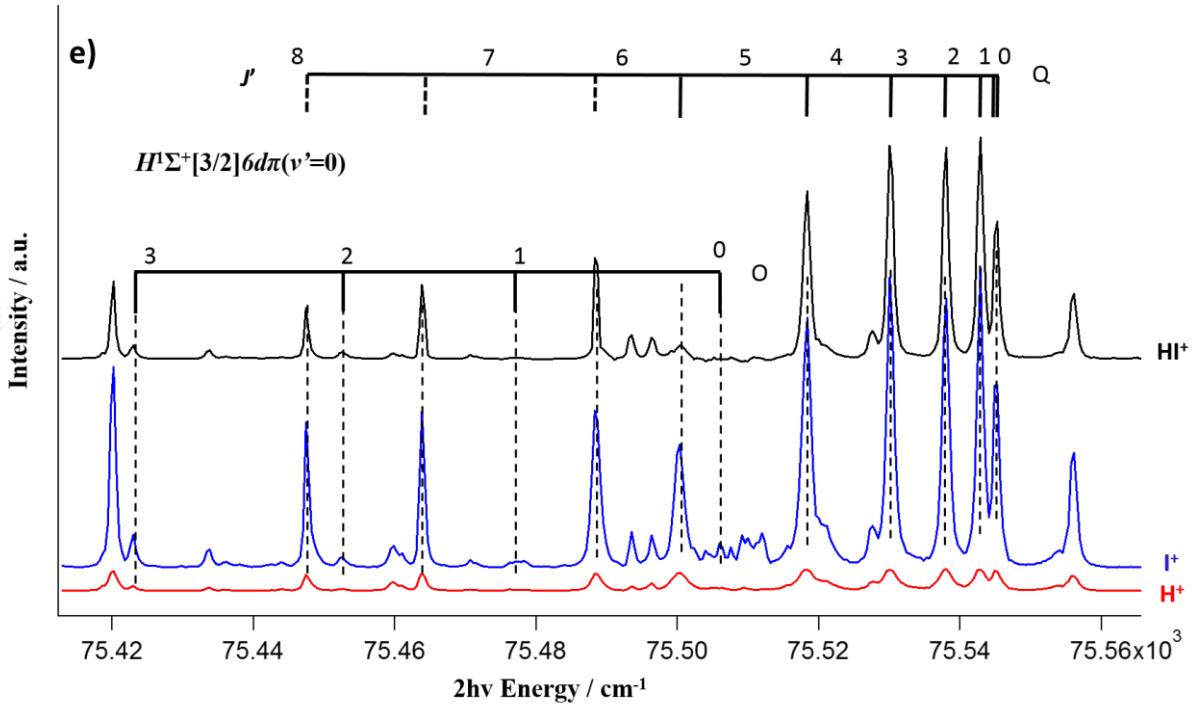
e)
J'
8
7
6
5
4
3
2
1
0
Q
H¹Σ⁺[3/2]6dπ(v'=0)
3
2
1
0
O
HI⁺
I⁺
H⁺
Intensity / a.u.
75.42
75.44
75.46
75.48
75.50
75.52
75.54
75.56x10³
2hv Energy / cm⁻¹

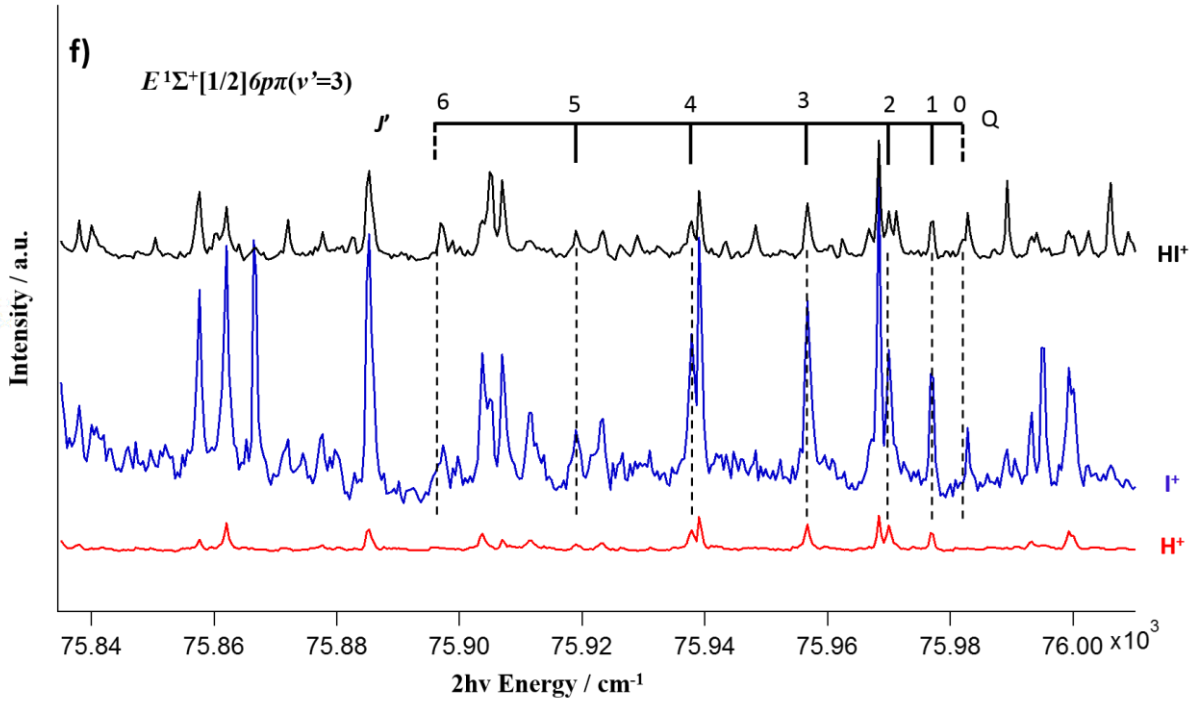
f)
E ¹Σ⁺[1/2]6pπ(v'=3)
J'
6
5
4
3
2
1
0
Q
HI⁺
I⁺
H⁺
Intensity / a.u.
75.84
75.86
75.88
75.90
75.92
75.94
75.96
75.98
76.00 x10³
2hv Energy / cm⁻¹

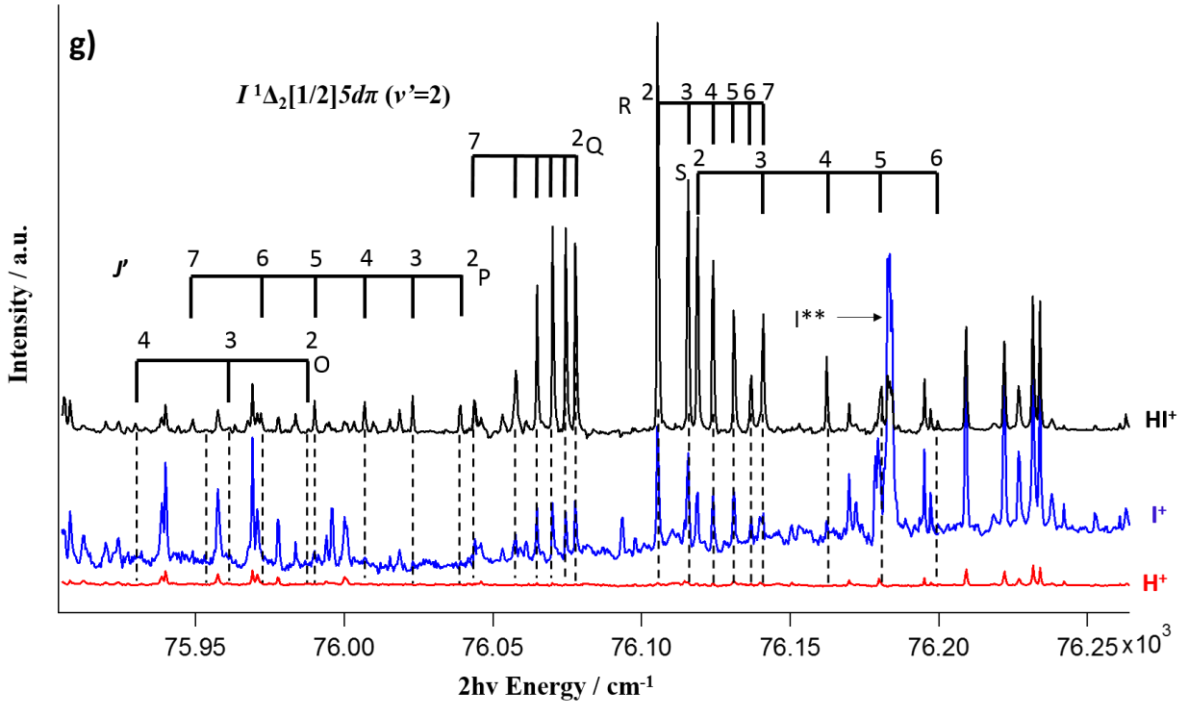
g)
$I\,^1\Delta_2[1/2]5d\pi$ (v'=2)
J'
R
S
P
Q
O
I**
HI+
I+
H+
Intensity / a.u.
75.95
76.00
76.05
76.10
76.15
76.20
76.25
x10^3
2hv Energy / cm-1

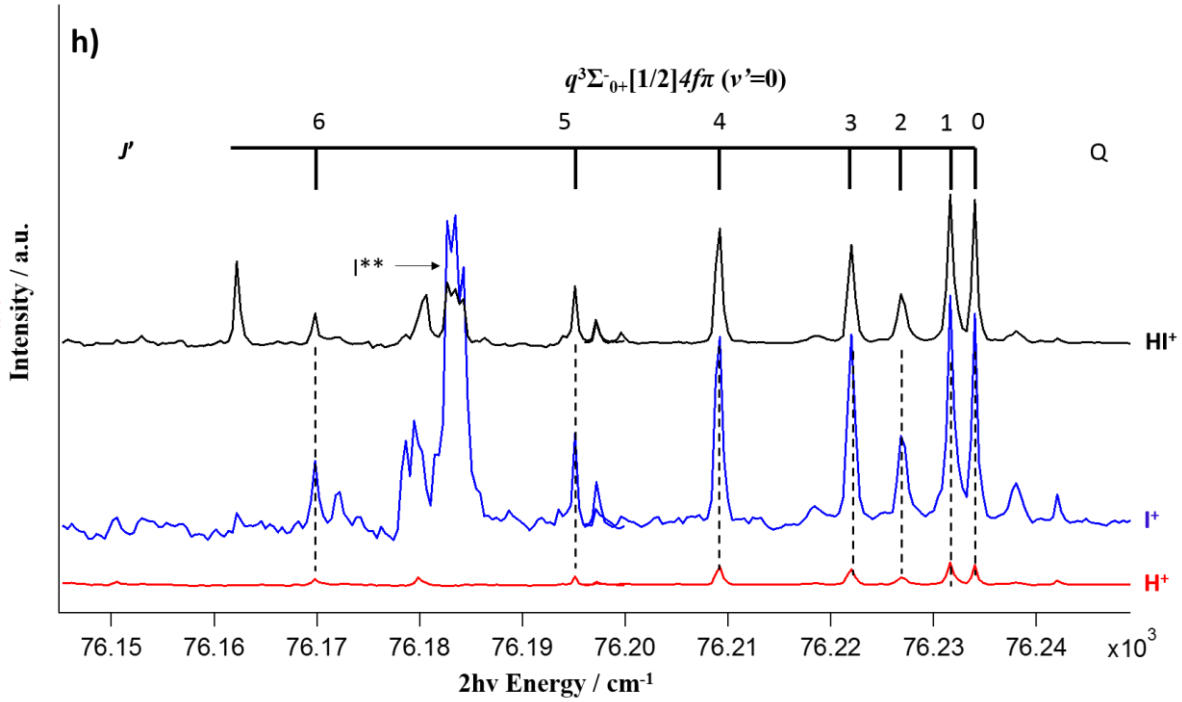
h)
$q^3\Sigma^-_{0+}[1/2]4f\pi$ (v'=0)
J'
Q
I**
HI+
I+
H+
Intensity / a.u.
76.15
76.16
76.17
76.18
76.19
76.20
76.21
76.22
76.23
76.24
x10^3
2hv Energy / cm-1

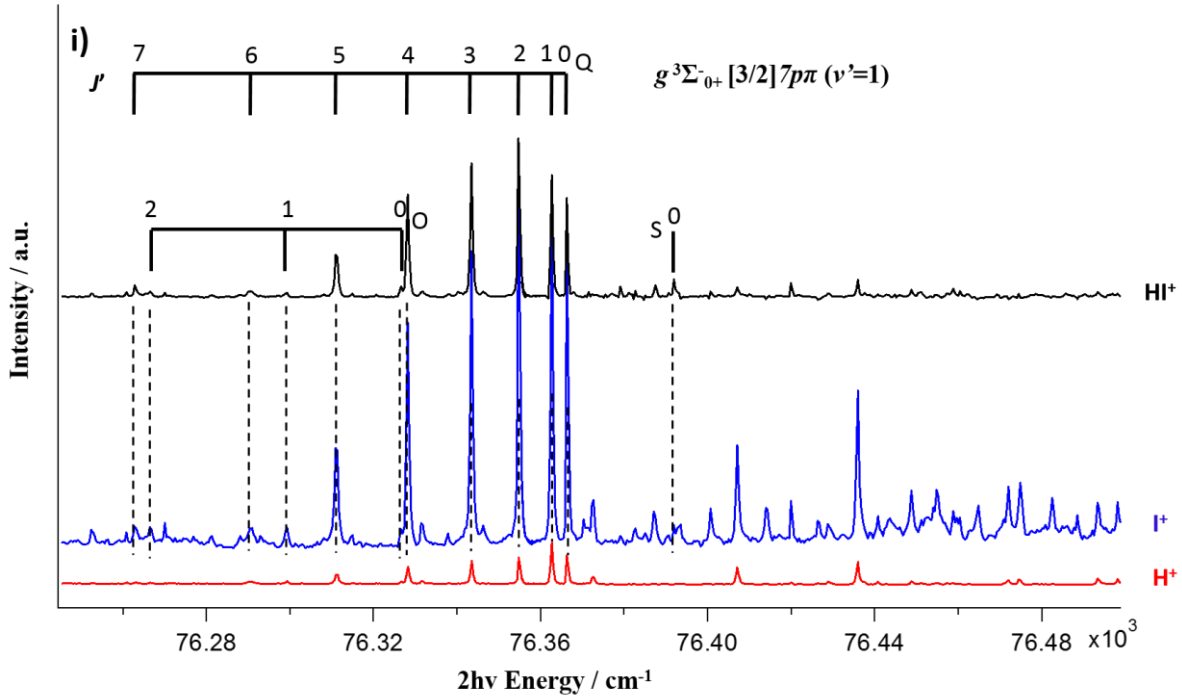
i)
J'
7 6 5 4 3 2 1 0 Q
g ³Σ⁻0+ [3/2] 7pπ (v'=1)
2 1 0 O
S 0
HI+
I+
H+
Intensity / a.u.
76.28 76.32 76.36 76.40 76.44 76.48 x10³
2hv Energy / cm⁻¹

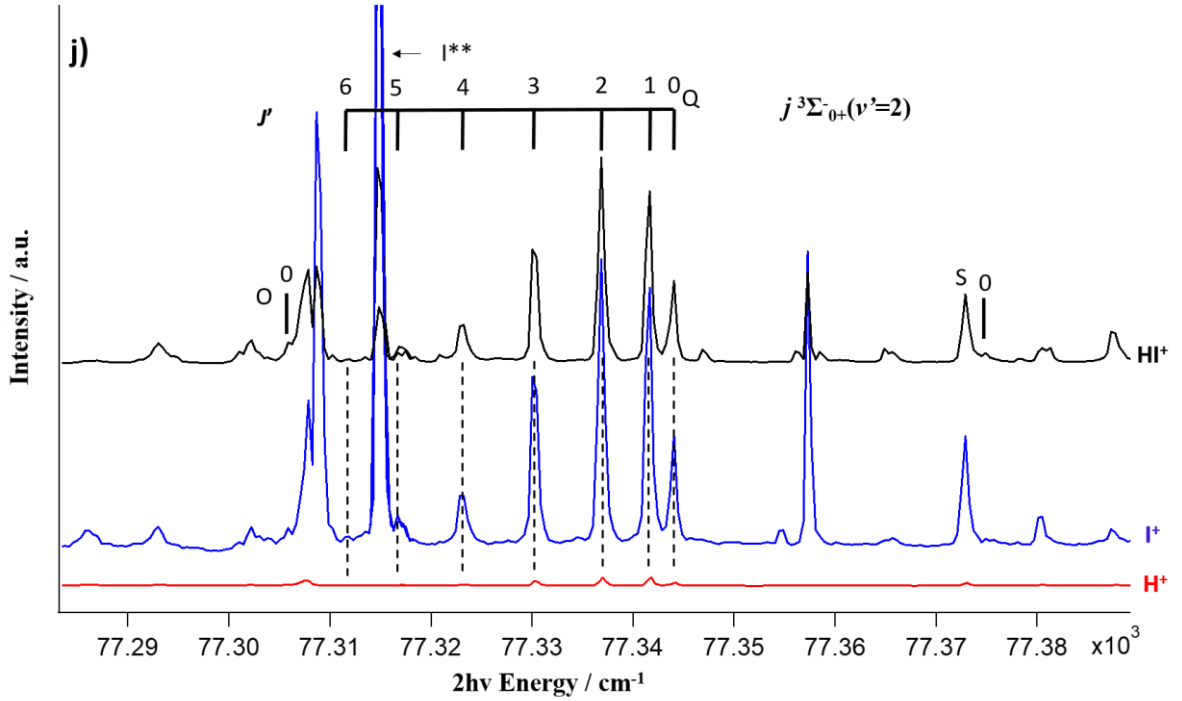
j)
I**
J'
6 5 4 3 2 1 0 Q
j ³Σ⁻0+(v'=2)
O 0
S 0
HI+
I+
H+
Intensity / a.u.
77.29 77.30 77.31 77.32 77.33 77.34 77.35 77.36 77.37 77.38 x10³
2hv Energy / cm⁻¹

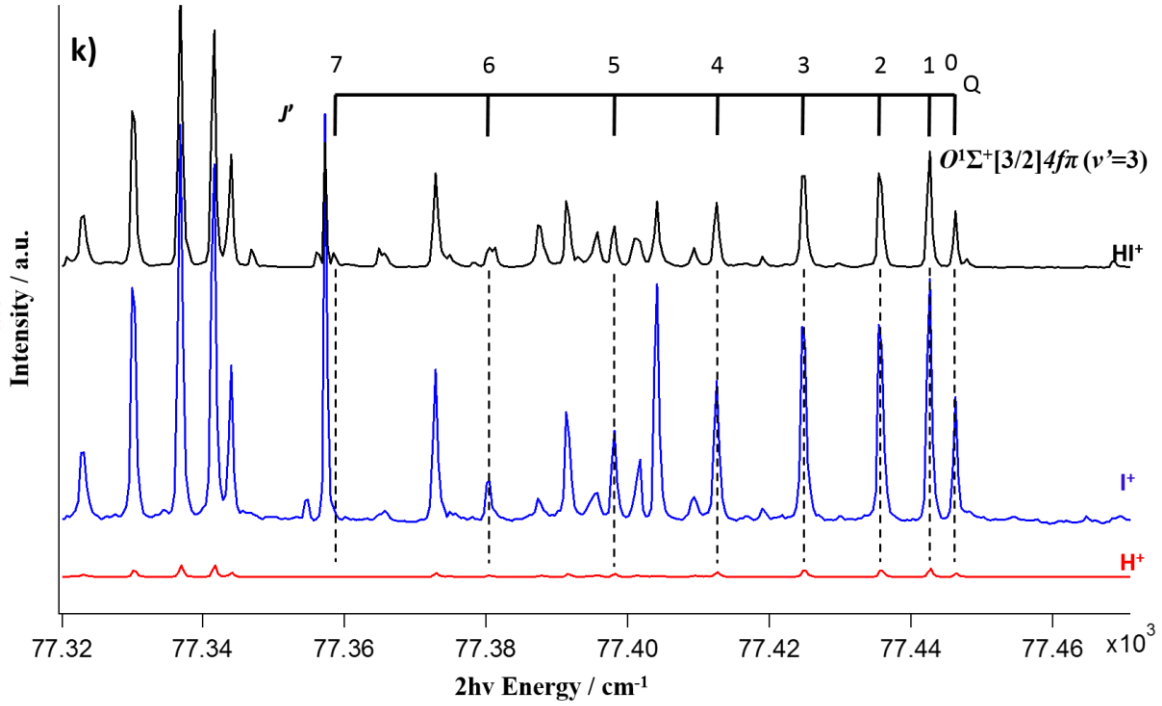
k)
J'
7
6
5
4
3
2
1
0
Q
$O^1\Sigma^+[3/2]4f\pi$ (v'=3)
HI+
I+
H+
Intensity / a.u.
77.32
77.34
77.36
77.38
77.40
77.42
77.44
77.46
x10^3
2hv Energy / cm-1

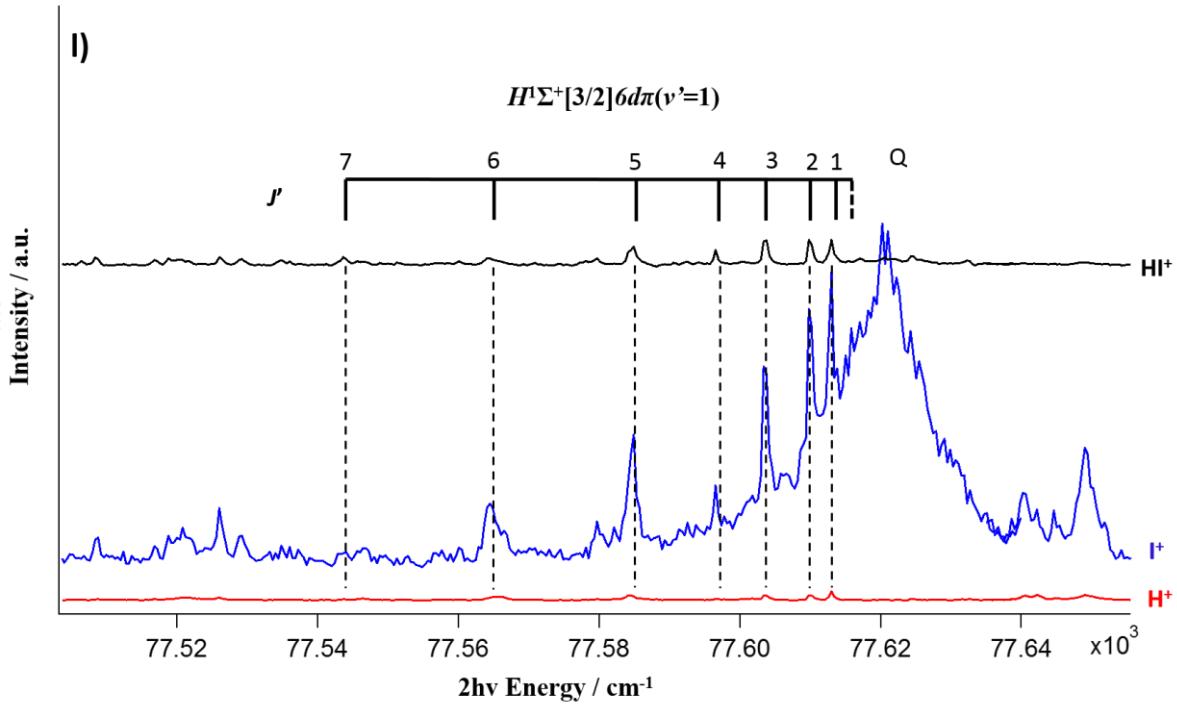
l)
$H^1\Sigma^+[3/2]6d\pi$(v'=1)
J'
7
6
5
4
3
2
1
Q
HI+
I+
H+
Intensity / a.u.
77.52
77.54
77.56
77.58
77.60
77.62
77.64
x10^3
2hv Energy / cm-1

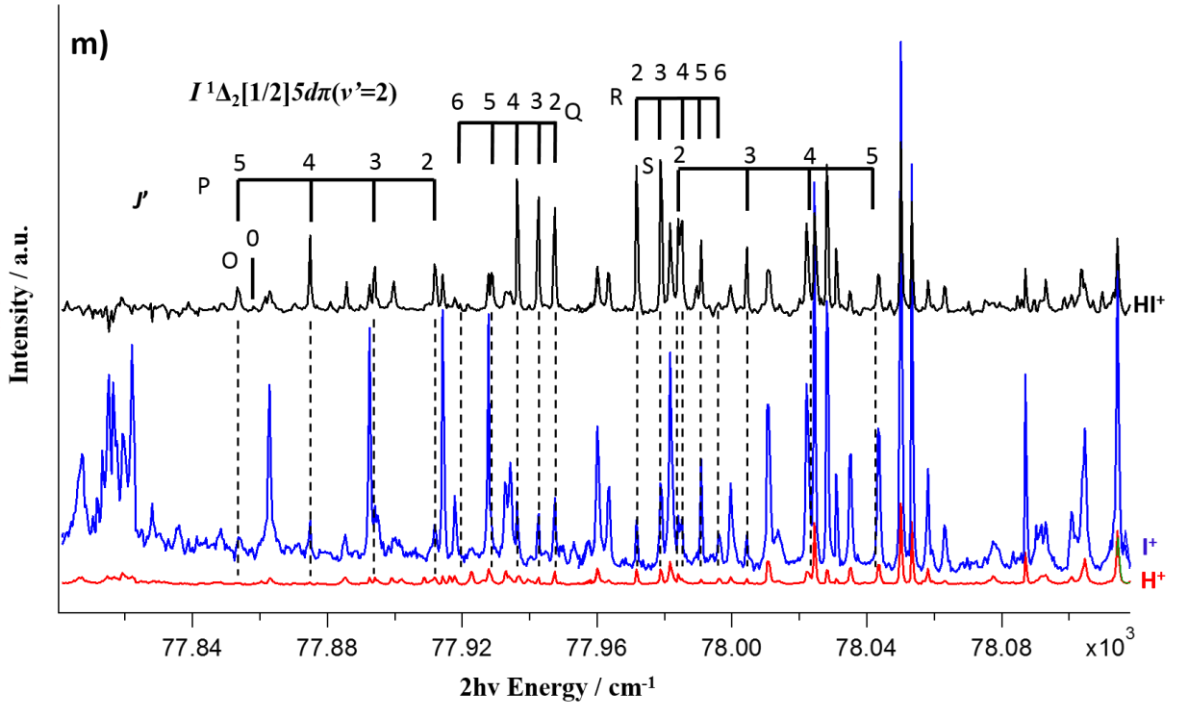
m)
$I\,^1\Delta_2[1/2]5d\pi(v'=2)$
J'
P
O
Q
R
S
HI+
I+
H+
Intensity / a.u.
2hv Energy / cm-1
x10^3

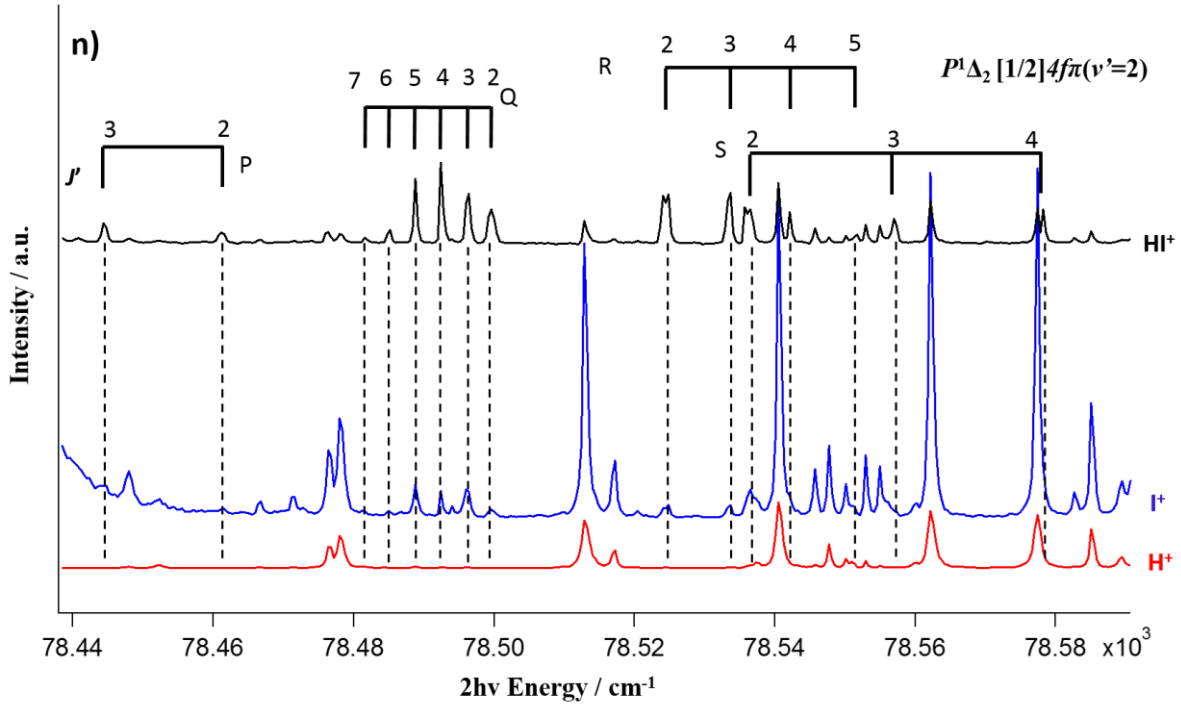
n)
$P^1\Delta_2\,[1/2]4f\pi(v'=2)$
J'
P
Q
R
S
HI+
I+
H+
Intensity / a.u.
2hv Energy / cm-1
x10^3

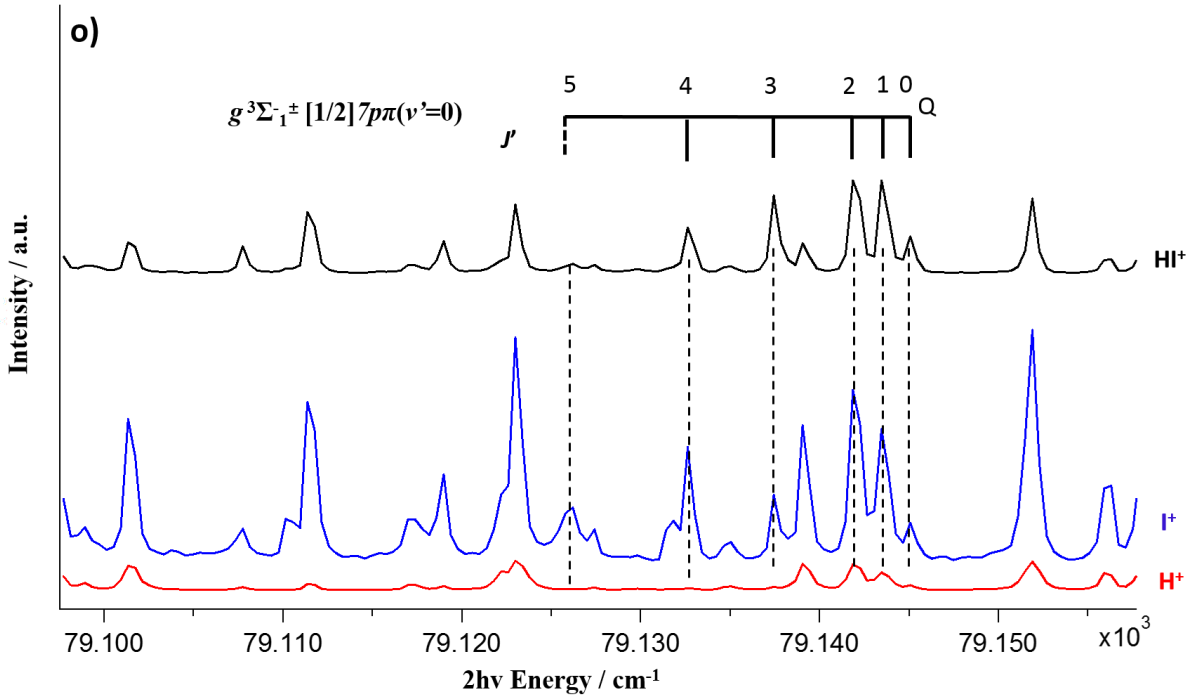
o)
$g\,^3\Sigma^-_1{}^{\pm}$ [1/2] 7pπ(v'=0)
J'
5 4 3 2 1 0 Q
HI+
I+
H+
Intensity / a.u.
79.100 79.110 79.120 79.130 79.140 79.150 x10^3
2hv Energy / cm-1

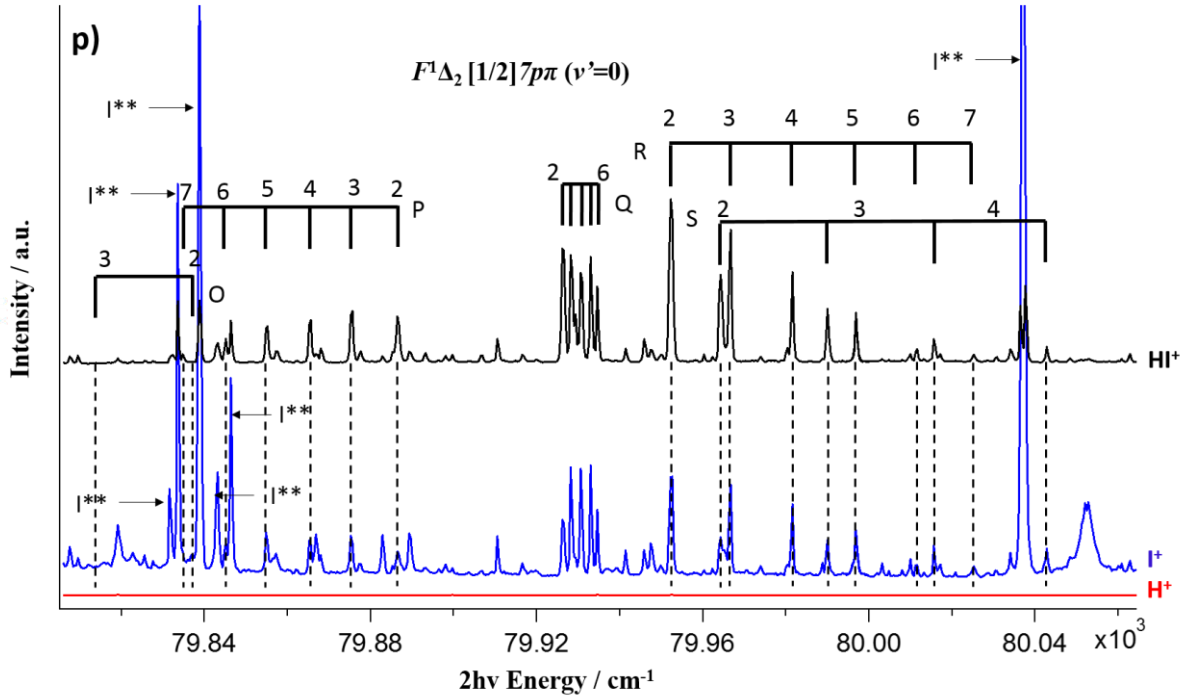
p)
$F^1\Delta_2$ [1/2] 7pπ (v'=0)
|**
7 6 5 4 3 2 P
3 2 O
2 6 Q
2 3 4 5 6 7 R
2 3 4 S
HI+
I+
H+
Intensity / a.u.
79.84 79.88 79.92 79.96 80.00 80.04 x10^3
2hv Energy / cm-1

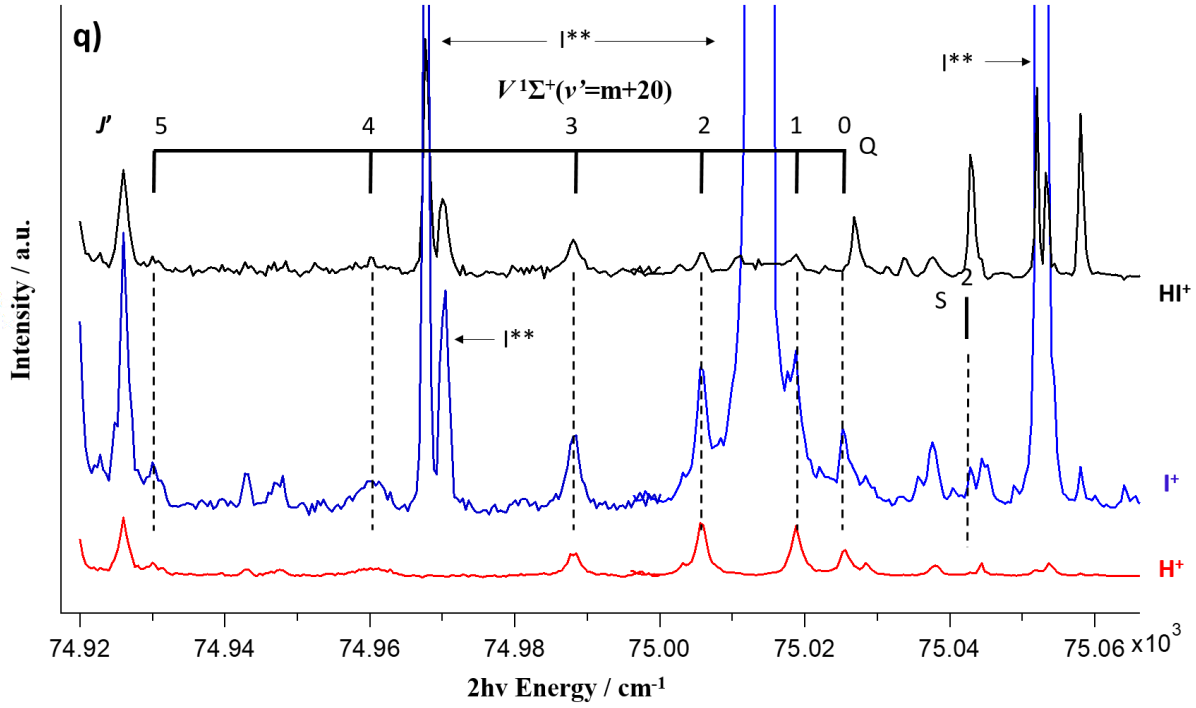
q)
I**
I**
V ¹Σ⁺(v'=m+20)
J'
5
4
3
2
1
0
Q
S
2
I**
HI⁺
I⁺
H⁺
Intensity / a.u.
74.92
74.94
74.96
74.98
75.00
75.02
75.04
75.06
x10³
2hv Energy / cm⁻¹

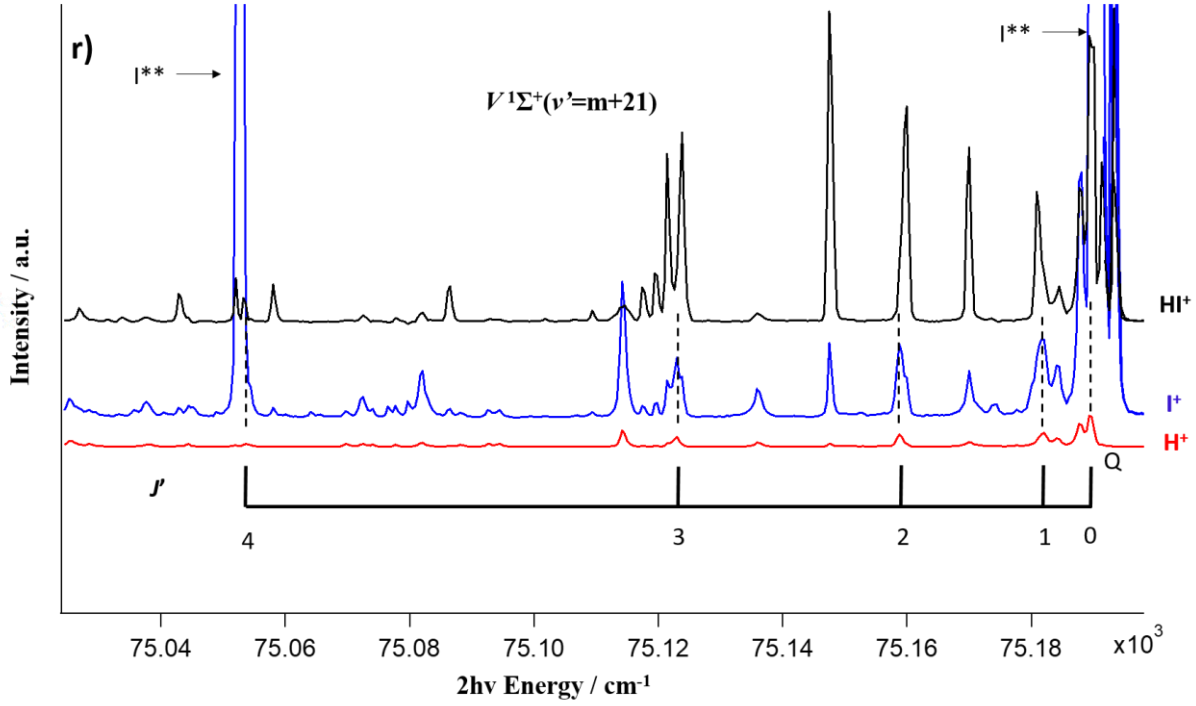
r)
I**
I**
V ¹Σ⁺(v'=m+21)
HI⁺
I⁺
H⁺
Q
J'
4
3
2
1
0
Intensity / a.u.
75.04
75.06
75.08
75.10
75.12
75.14
75.16
75.18
x10³
2hv Energy / cm⁻¹

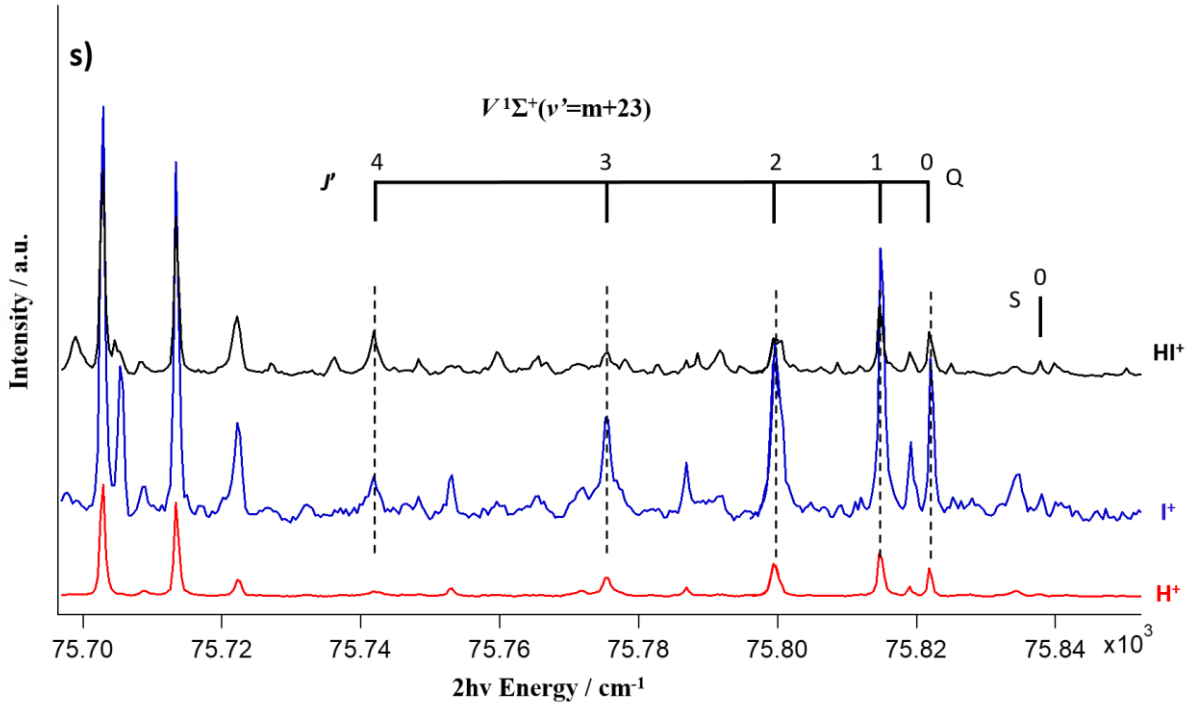
s)
$V\,^1\Sigma^+(v'=m+23)$
J'
4
3
2
1
0
Q
S
0
HI+
I+
H+
Intensity / a.u.
75.70
75.72
75.74
75.76
75.78
75.80
75.82
75.84
x10^3
2hv Energy / cm-1

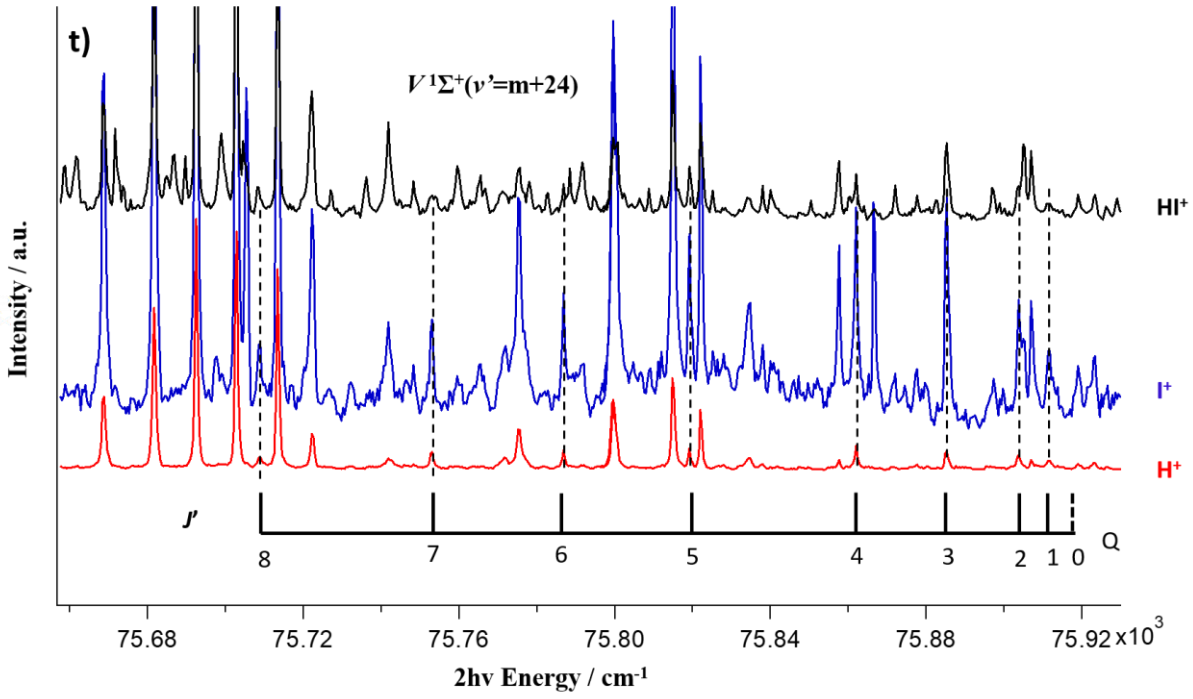
t)
$V\,^1\Sigma^+(v'=m+24)$
HI+
I+
H+
J'
8
7
6
5
4
3
2
1
0
Q
Intensity / a.u.
75.68
75.72
75.76
75.80
75.84
75.88
75.92
x10^3
2hv Energy / cm-1

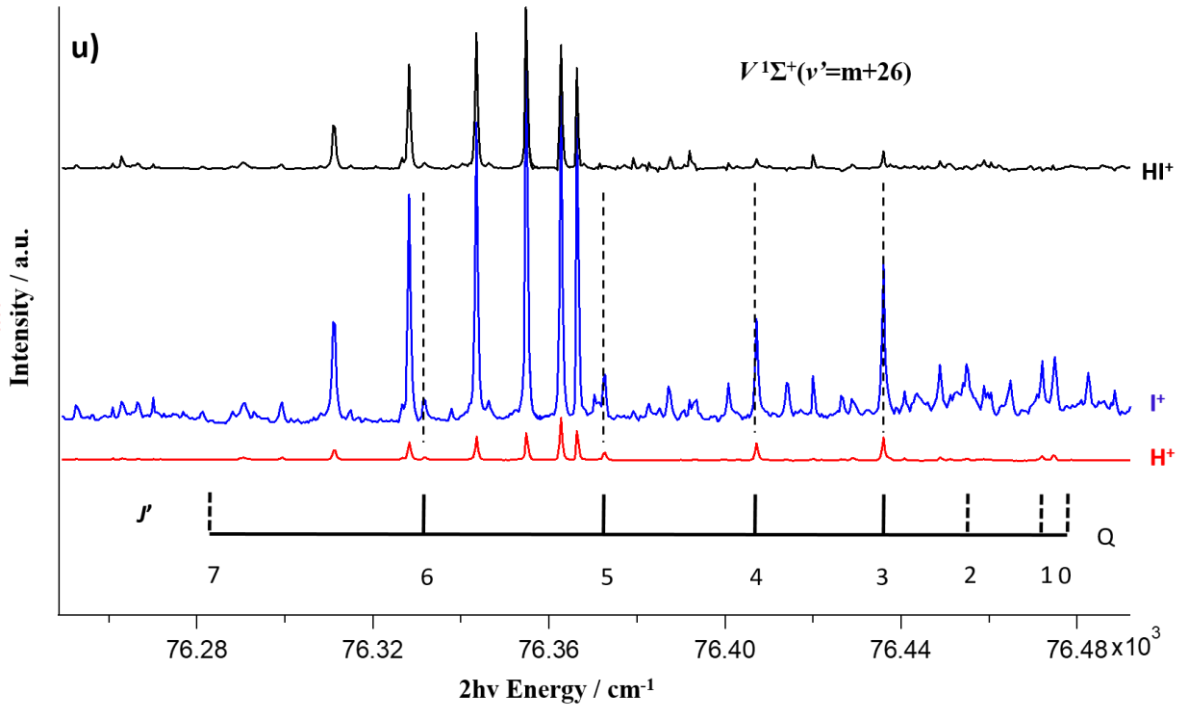
u)
$V\,^1\Sigma^+(v'=m+26)$
HI+
I+
H+
J'
Q
7
6
5
4
3
2
1 0
Intensity / a.u.
76.28
76.32
76.36
76.40
76.44
76.48 x10^3
2hv Energy / cm-1

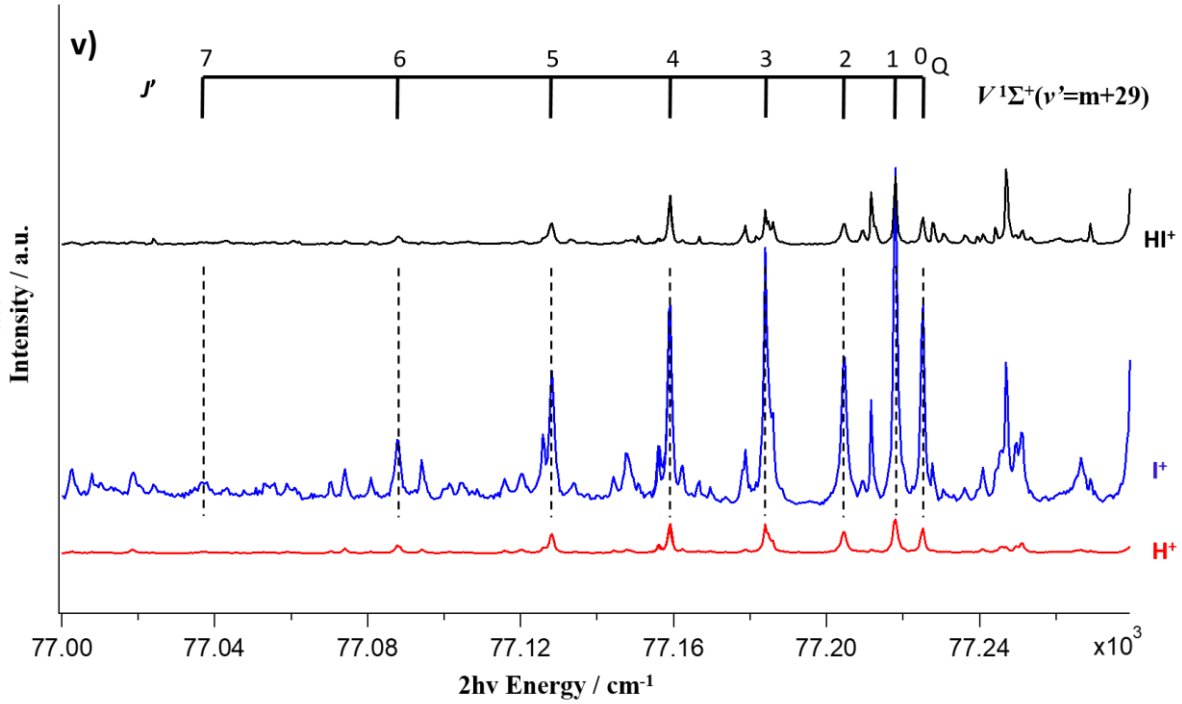
v)
J'
7
6
5
4
3
2
1
0
Q
$V\,^1\Sigma^+(v'=m+29)$
HI+
I+
H+
Intensity / a.u.
77.00
77.04
77.08
77.12
77.16
77.20
77.24
x10^3
2hv Energy / cm-1

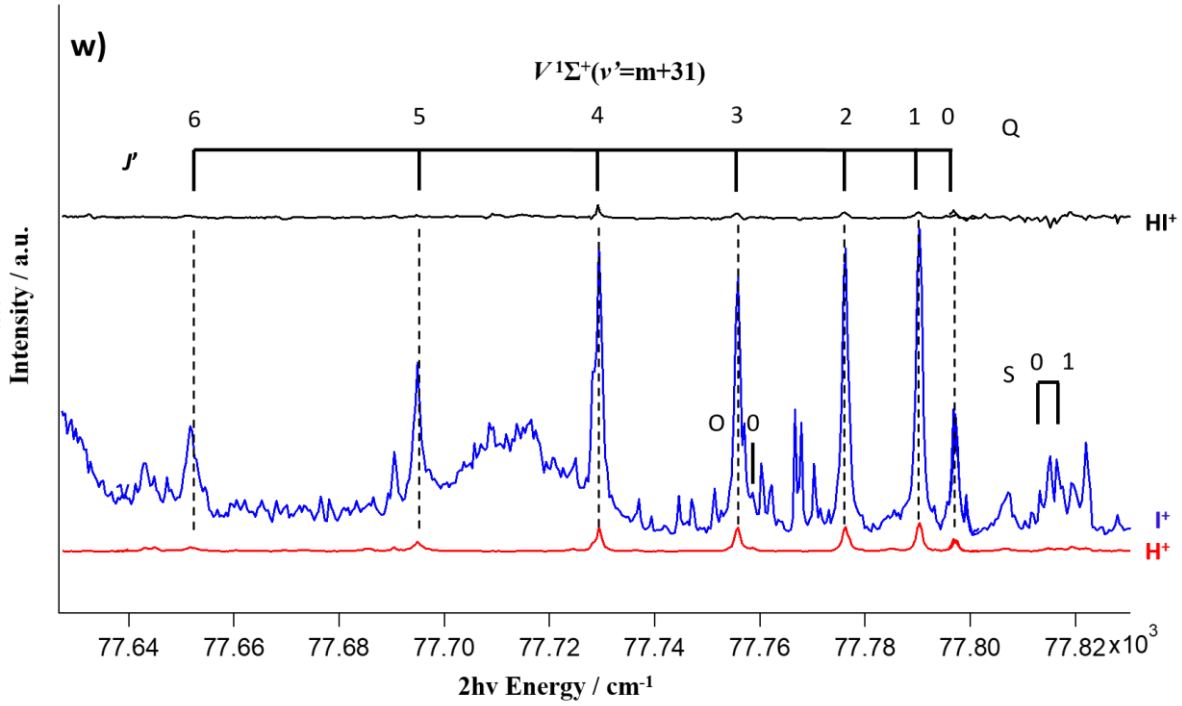
w)
V ¹Σ⁺(v'=m+31)
J'
6
5
4
3
2
1
0
Q
HI⁺
I⁺
H⁺
O 0
S 0 1
Intensity / a.u.
77.64
77.66
77.68
77.70
77.72
77.74
77.76
77.78
77.80
77.82
x10³
2hv Energy / cm⁻¹

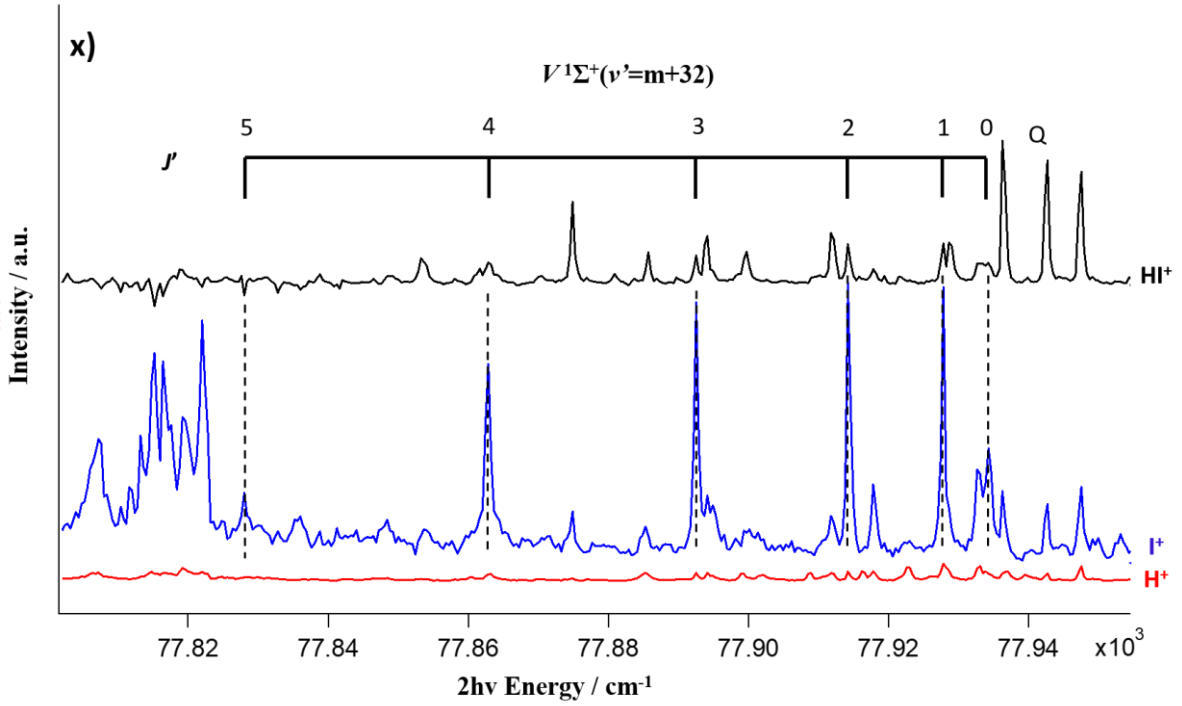
x)
V ¹Σ⁺(v'=m+32)
J'
5
4
3
2
1
0
Q
HI⁺
I⁺
H⁺
Intensity / a.u.
77.82
77.84
77.86
77.88
77.90
77.92
77.94
x10³
2hv Energy / cm⁻¹

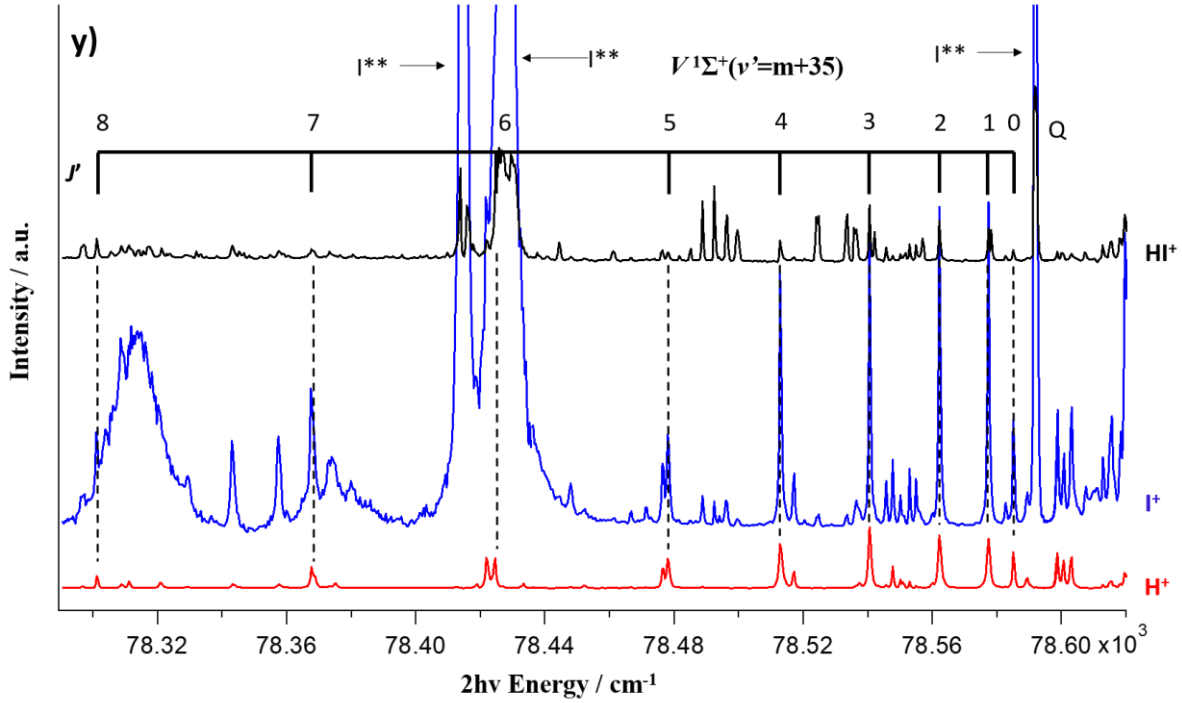
y)
I** →
←I**
V ¹Σ⁺(v'=m+35)
I** →
8
7
6
5
4
3
2
1
0
Q
J'
HI⁺
I⁺
H⁺
Intensity / a.u.
78.32
78.36
78.40
78.44
78.48
78.52
78.56
78.60 x10³
2hv Energy / cm⁻¹

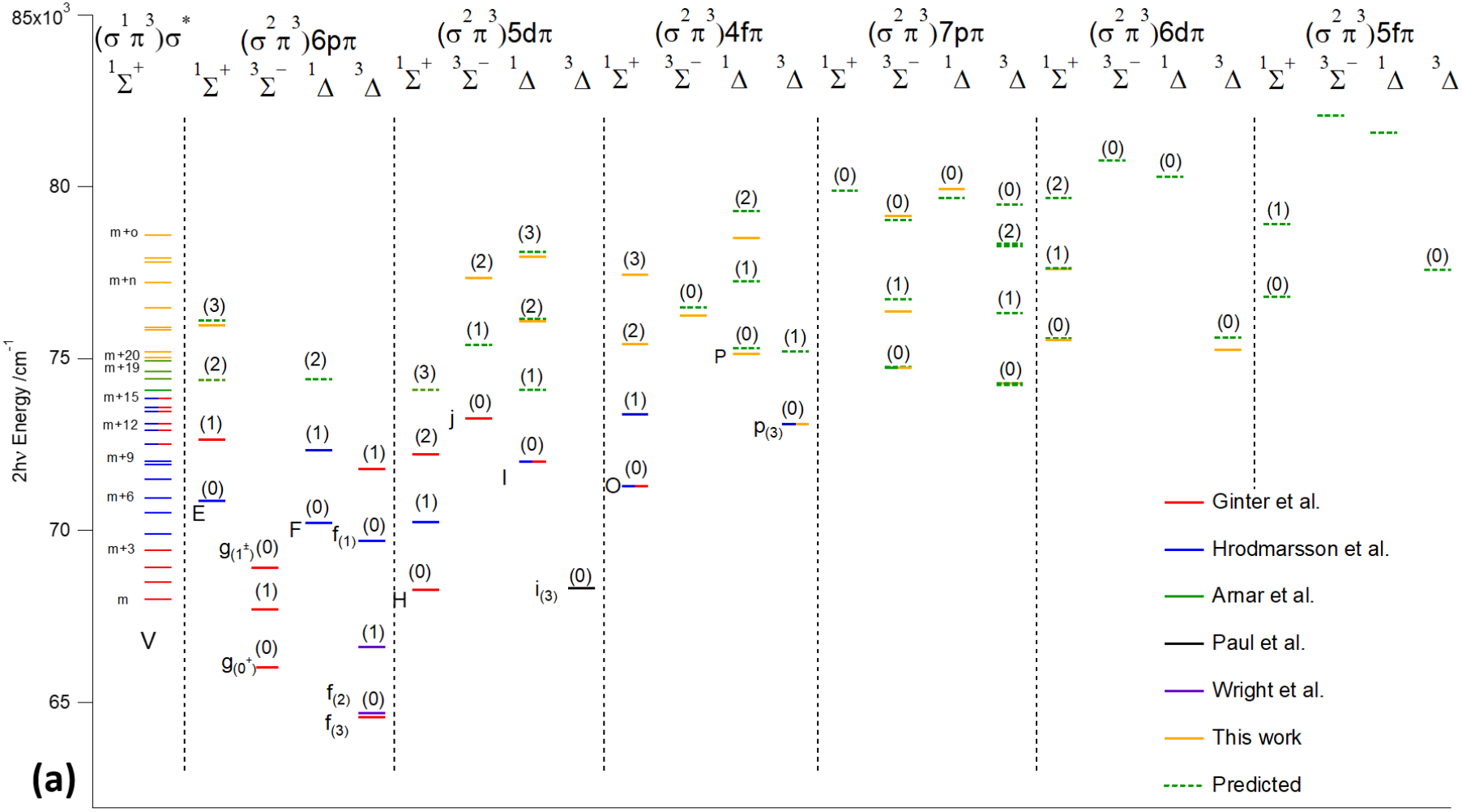
85x10^3
80
75
70
65
2hν Energy /cm^-1
(σ^1π^3)σ*
(σ^2π^3)6pπ
(σ^2π^3)5dπ
(σ^2π^3)4fπ
(σ^2π^3)7pπ
(σ^2π^3)6dπ
(σ^2π^3)5fπ
1Σ+ 1Σ+ 3Σ− 1Δ 3Δ 1Σ+ 3Σ− 1Δ 3Δ 1Σ+ 3Σ− 1Δ 3Δ 1Σ+ 3Σ− 1Δ 3Δ 1Σ+ 3Σ− 1Δ 3Δ 1Σ+ 3Σ− 1Δ 3Δ 1Σ+ 3Σ− 1Δ 3Δ
m+o
m+n
m+20
m+19
m+15
m+12
m+9
m+6
m+3
m
V
E
F
H
I
O
P
j
Ginter et al.
Hrodmarsson et al.
Arnar et al.
Paul et al.
Wright et al.
This work
Predicted
(a)

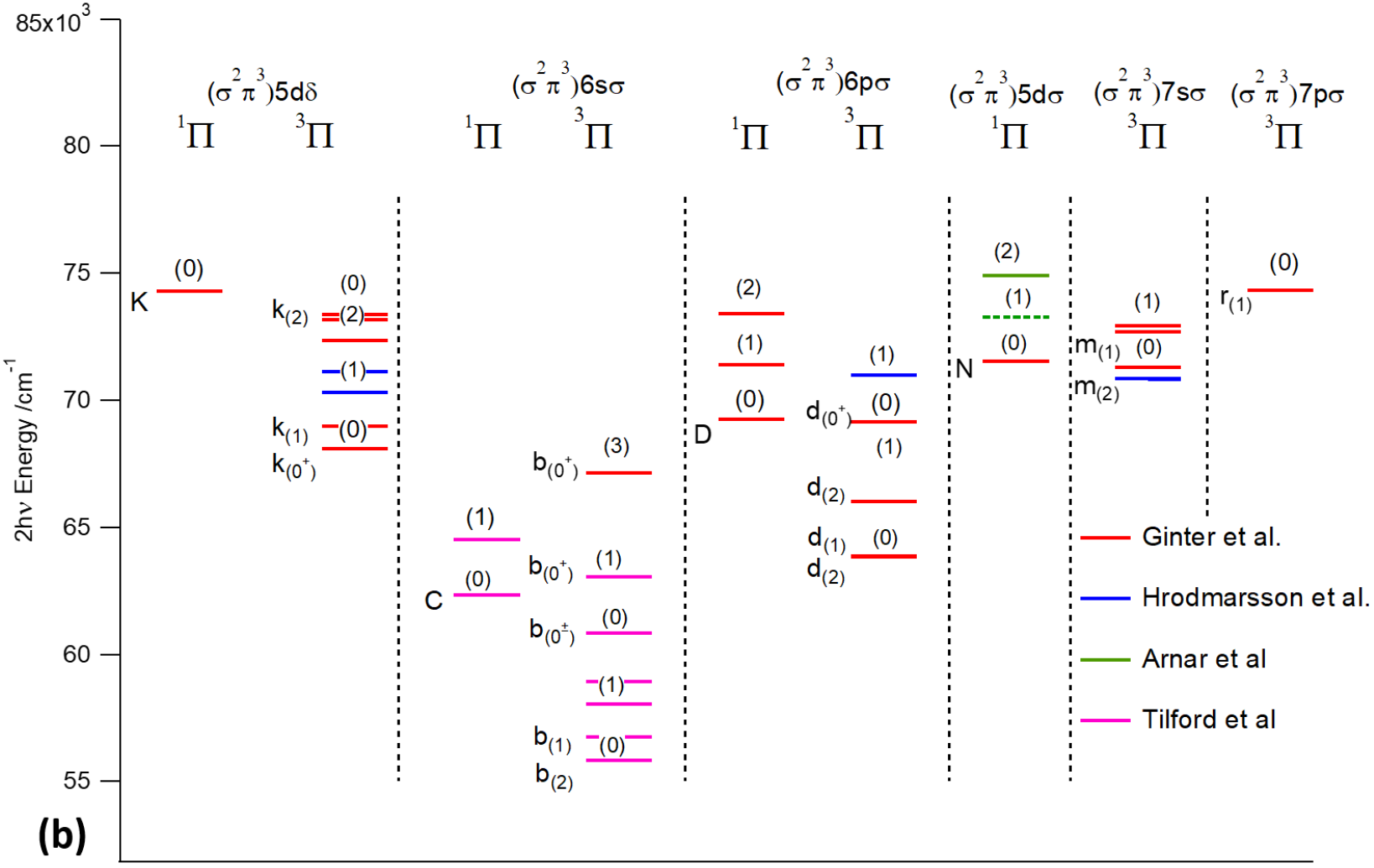
85x10^3
80
75
70
65
60
55
2hν Energy /cm^-1
(σ²π³)5dδ
(σ²π³)6sσ
(σ²π³)6pσ
(σ²π³)5dσ
(σ²π³)7sσ
(σ²π³)7pσ
¹Π
³Π
K
k(2)
k(1)
k(0⁺)
C
b(0⁺)
b(0±)
b(1)
b(2)
D
d(0⁺)
d(1)
d(2)
N
m(1)
m(2)
r(1)
Ginter et al.
Hrodmarsson et al.
Arnar et al
Tilford et al
(b)

a. ***Ref.: S. G. TILFORD, M. L. GINTER, AND A. M. BASS, J. Mol. Spectrosc. 34, 327-340 (1970)***)
b. ***Ref.: M. L. GINTER, S. G. TILFORD, AND A. M. BASS, J. Mol. Spectrosc. 57, 271-283 (1975)***)
c. ***Ref.: D. S. GINTER, M. L. GINTER, AND S. G. TILFORD, J. Mol. Spectrosc. 92, 40-54 (1982)***)
d. ***Ref.: H. R. Hróðmarsson, H. Wang, and Á. Kvaran, J. Mol. Spectrosc. 290,5 (2013)***)
e. ***Ref.: S. A. Wright and J. D. McDonald, J. Chem. Phys. 101, 238 (1994)***)
f. ***Ref.: S. T. Pratt and M. L. Ginter, J. Chem. Phys. 102, 5(1995)***)
g. ***Ref.: H. R. Hróðmarsson, H. Wang, and Á. Kvaran, J. Chem. Phys. 142, 244312(2015)***)
h. ***Ref.: P. M. Regan, D. Ascenzi, E. Wrede, P. A. Cook, M. N. R. Ashfold and A. J. Orr-Ewing, Phys. Chem. Chem. Phys., 23, 2(2000)***)
i. ***Ref.: A. Hafliðason, M.X Jiang and A, Kvaran, Phys. Chem. Chem. Phys., 21, 23154(2019)***)

4.4 Paper 4

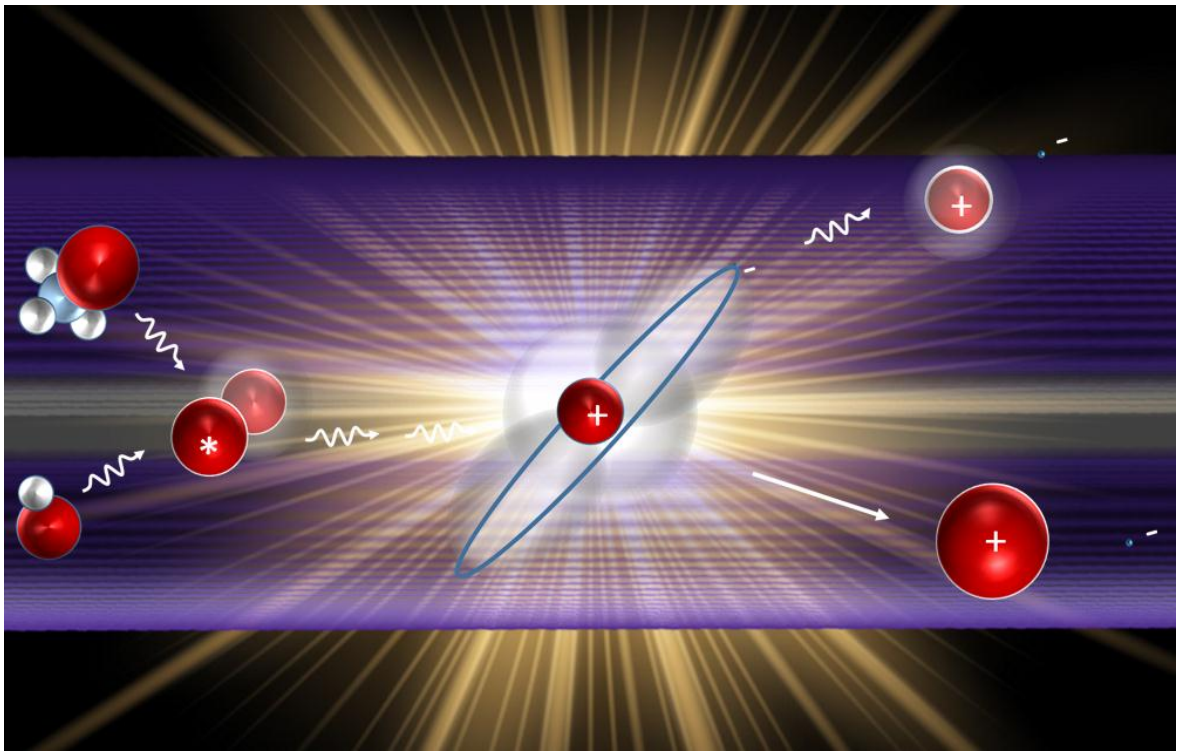

Arnar Hafliðason, Meng-Xu Jiang and Ágúst Kvaran, *Photo and autoionization processes of superexcited iodine atoms in MPI of CH_3I and HI*, *Chem.Phys*, **541**, p: 111016, **(2021)**.

DOI: 10.1016/j.chemphys.2020.111016

Chemical Physics 541 (2021) 111016

Contents lists available at ScienceDirect

Chemical Physics

journal homepage: www.elsevier.com/locate/chemphys

Photo- and autoionization processes of superexcited iodine atoms in MPI of CH_3I and HI

Arnar Hafliðason, Meng-Xu Jiang, Ágúst Kvaran *

Science Institute, University of Iceland, Dunhagi 3, 107 Reykjavík, Iceland

ARTICLE INFO

Keywords:
Autoionization
Superexcited states
Photofragmentation
Rydberg states
REMPI (Resonance enhanced multiphoton ionization)

ABSTRACT

REMPI data was recorded for CH_3I and HI for the two-photon excitation region of 76,680–82,620 cm^{-1}. I^+ signals reveal number of peaks of varying line widths and intensities. These are attributed to two-photon resonant excitation of iodine atoms $I(^2P_{3/2})$ and $I^*(^2P_{1/2})$ to Rydberg and superexcited states followed by one-photon ionization and autoionization. Laser power dependence experiments and line intensities reveal that the photoionization of I/I* follows one-photon molecular dissociation. Quantum defect analysis and correlation inspections of line widths were applied to identify and characterize number of new, not previously observed, superexcited atomic states of ion cores $^3P_{0,1}$ and $^1D_2$. Mechanisms of autoionization processes are summarized and discussed. Particularly fast autoionization processes of superexcited iodine atoms of ion core $^1D_2$ are observed. Comparison of observed line widths with expected trends in n proved to be very useful in the analysis procedure and to identify state interactions.

1. Introduction

Formation of the ground state iodine atom $I(^2P_{3/2})$ (hereby labelled as I) and its spin–orbit excited counterpart, $I^*(^2P_{1/2})$ (hereby labelled as I*), by photodissociation of molecules such as CH_3I and HI in the A-bands in the region of about 190–300 nm is well known [1–11]. This involves excitation of nonbonding $5p\pi$ electrons localized on the iodine atoms to the antibonding molecular orbitals followed by dissociation to form the CH_3/H and I/I* fragments. I/I* can be detected by resonance enhanced multiphoton ionization (REMPI) involving resonant excitation of 5*p* electrons to Rydberg atomic states (Fig. 1) [5,6,12–15]. Typically excitation to *ns* and *nd* Rydberg orbitals are observed in one-photon resonant excitations, whereas transfer to *np* and *nf* Rydberg orbitals are observed in two-photon resonant excitations. Most atomic lines, detected have been assigned to resonant transitions to Rydberg states converging to the lowest energy ground state ions $I^+(^3P_2)$ (hereby labelled as I**) [16]. Number of lines have been assigned to transitions to superexcited Rydberg states converging to the spin–orbit and/or spin excited atom ions of the ground electron configuration $(5s^25p^4)$ (for clarity reason (see below) we hereby distinguish those states by the different notation $I^{\#}$) (Fig. 1).

Since the original work by Minnhagen [17] on energy levels of atomic iodine, based on spectroscopic measurements and theoretical interpretations in 1962, number of investigations by different methods have appeared. In 1981 Berkowitz *et al.* reported an observation of series of superexcited states ($I^{\#}$) for *s* and *d* Rydberg electrons and the ion cores $^3P_0$, $^3P_1$, $^1D_2$ and $^1S_0$ in photoionization spectra [18]. Sarma *et al.* (1983) recorded absorption spectrum showing *s* and *d* Rydberg series (I** and $I^{\#}$) converging to the $^3P_2$, $^3P_0$ and $^3P_1$ ion species [19]. Using multiphoton ionization (MPI), Pratt *et.al.* (1985–1986) observed numerous I** Rydberg states of iodine, belonging to *s, p, d* and *f* series converging to the $^3P_2$ ion limit [20–22]. Zhu and Grant (1993) identified, in threshold photoionization spectra, two *p* and *f* Rydberg series converging to the $^3P_1$ ion core [23]. Electron signals detected, were supposed to be formed along with $I^+(^3P_2)$ by autoionization of $I^{\#}$. Jung *et al.* (1997) applied photoelectron spectroscopy to record electron images for photolysis of CH_3I in the A-band followed by probing of the iodine atoms by (2 + 1) REMPI [12]. This allowed determination of branching ratios for different ion core formation after autoionization of superexcited Rydberg states ($I^{\#}$) based on transitions via different intermediate states. Gu *et al.* (2003) observed autoionization in iodine atoms by MPI and photoelectron spectroscopy following excitation to *s* and *d* series of superexcited Rydberg states built on the $^3P_1$ ion core for principal quantum numbers up to $n = 47$ [24]. Hu *et al.* (2007) reported

* Corresponding author.
E-mail addresses: arnarhaf@hi.is (A. Hafliðason), mej7@hi.is (M.-X. Jiang), agust@hi.is (Á. Kvaran).
URL: https://notendur.hi.is/agust/ (Á. Kvaran).

https://doi.org/10.1016/j.chemphys.2020.111016
Received 17 August 2020; Received in revised form 6 October 2020; Accepted 7 October 2020
Available online 12 October 2020

spectral peaks due to two-photon transitions from I to I** and from I* to $I^{\#}$. The latter group of peaks (for $I^{\#}$) were found to be significantly broader [5]. Based on ion angular distributions following one-photon excitation by synchrotron radiation source Eypper *et al.* (2010) observed autoionization of $I^{\#}$ with *s* and *d* Rydberg electrons, converging to the $^1S_0$ [25], $^3P_1$ and $^1D_2$ [26] ion species. By use of a photoelectron imaging technique coupled with (2 + 1) REMPI via *p* Rydberg electron I** atoms Shen *et al.* (2009) characterized iodine atom Rydberg substates as well as state interactions between I** and $I^{\#}$ [27].

The superexcited iodine atom states ($I^{\#}$) consist of spin–orbit and/or spin excited ion cores and excited Rydberg electrons (i.e. doubly excited states). The autoionization processes involve simultaneous ejection of the Rydberg electrons and relaxation of the core configurations. There are two major autoionization processes depending on whether the relaxation within the ion core involves i) electron transfer within the *p* valence electron orbitals with no overall exchange of momenta, mainly driven by Coulomb forces (Coulomb transfer mechanism) or ii) valence electron spin-flip and an overall exchange of momenta (Spin-flip mechanism). The Spin-flip mechanism is further divided into spin–spin and spin–orbit processes depending on the interaction driving forces involved [28–30]. The strength and appearance of these processes are determined by selection rules and transition probabilities for transitions from the Rydberg states to continuum states of a free electron along with the ion cores [28]. Typically transition probabilities decrease (hence lifetimes increase) with increasing overall variation in the quantum numbers *L*, *S* and *l* for the transfer to give relatively broad peaks for the Coulomb transfer mechanism and sharper peaks for the spin-flip mechanisms (see Fig. 2). The spin–orbit and spin–spin processes further differ in the possible extent of quantum number variations as shown in Fig. 2. Generally the *L* and *S* quantum numbers are considered to be less well defined as the number of electrons increase to make the *L-S* coupling scheme less reliable with atom mass. Nevertheless the Coulomb transfer mechanism (i) has been assumed to obey the *L-S* coupling scheme for heavier atoms [28,31]. Couplings relevant to the spin-flip mechanisms (ii), on the other hand, are more complicated and depart from the *L-S* scheme. These are more appropriately described by a pair coupling (referred to as the $[J_cK]$ coupling) [28], where *K* is the resultant angular momentum quantum number for a combination of the core total angular momentum ($\boldsymbol{J_c}$) and the Rydberg electron orbital angular momentum ($\boldsymbol{l}$). The pair coupling can also be used to describe the Coulomb transfer mechanism (i). Correspondingly, a suitable labelling of Rydberg states for iodine (both I** and $I^{\#}$) (and heavy atoms in general) is as $[^{2S+1}L_{Jc}]nl[K]_J$, where $[^{2S+1}L_{Jc}]$ represents the term of the ion core and *n* is the principal quantum number of the Rydberg electron in orbital *l*. *J* is the total angular momentum after combination of $\boldsymbol{K}$ (see above) and the Rydberg electron spin ($\boldsymbol{s}$).

In this paper we present I^+ signals of mass resolved REMPI data for CH_3I and HI in the high energy two-photon excitation region of 76,680–82,620 cm^{-1} (one-photon wavelength range of 242.07–260.82 nm) and laser power dependence of signals for HI. The data reveal iodine atomic lines due to (2 + 1) REMPI of I via I** and $I^{\#}$ as well as due to two-photon resonant excitation of I* to $I^{\#}$ followed by autoionization to form $I^+(^3P_2)$ (hereby named (2 + a) REMPI where "a" refers to "autoionization"). I and I* are formed by one-photon photolysis in different ratios depending on the molecules. Quantum defect calculations and correlation analyses of the peaks line width dependence on n^* (the effective principal quantum number) allowed detailed characterization of number of new superexcited (doubly excited) Rydberg states ($I^{\#}$) involved. The line widths are found to vary dramatically depending on the autoionization processes and superexcited states involved.

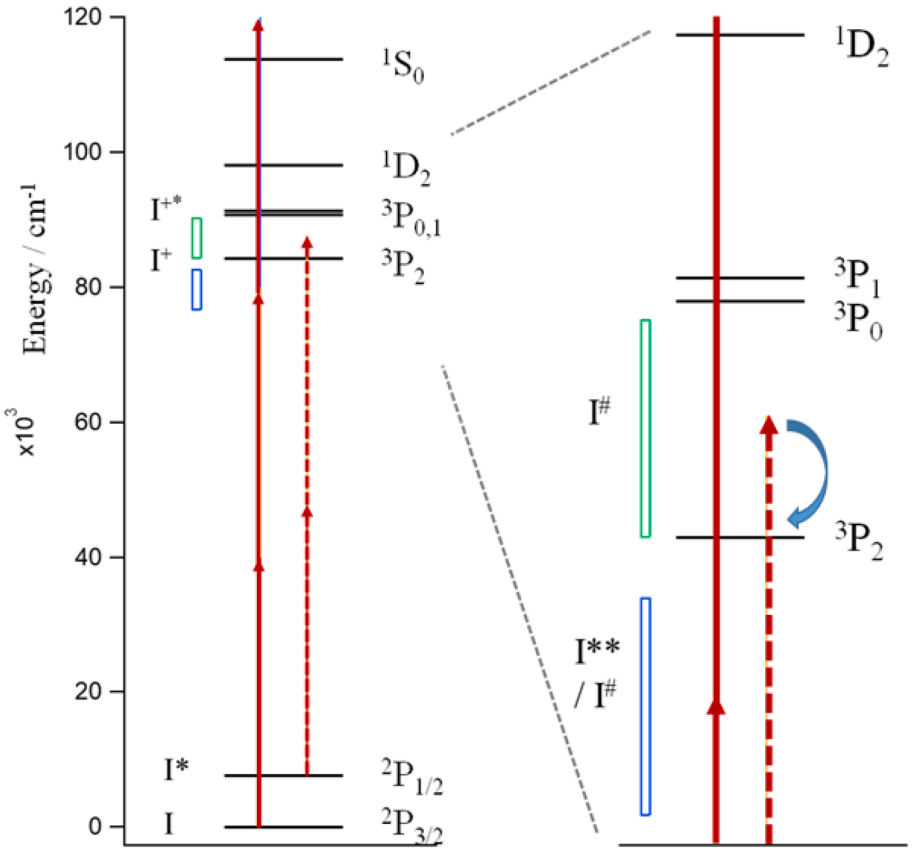

Fig. 1. Energy levels of I/I* and I^+/I^{+*} and selected excitations of I ((2 + 1)REMPI via I** and $I^{\#}$; red unbroken arrows) and I* (two-photon resonant excitation to $I^{\#}$ followed by autoionization (2 + a) REMPI; red broken arrows) (see main text). The two-photon excitation ranges relevant to the work presented in this paper are marked by blue (for I) and green (for I*) boxes.

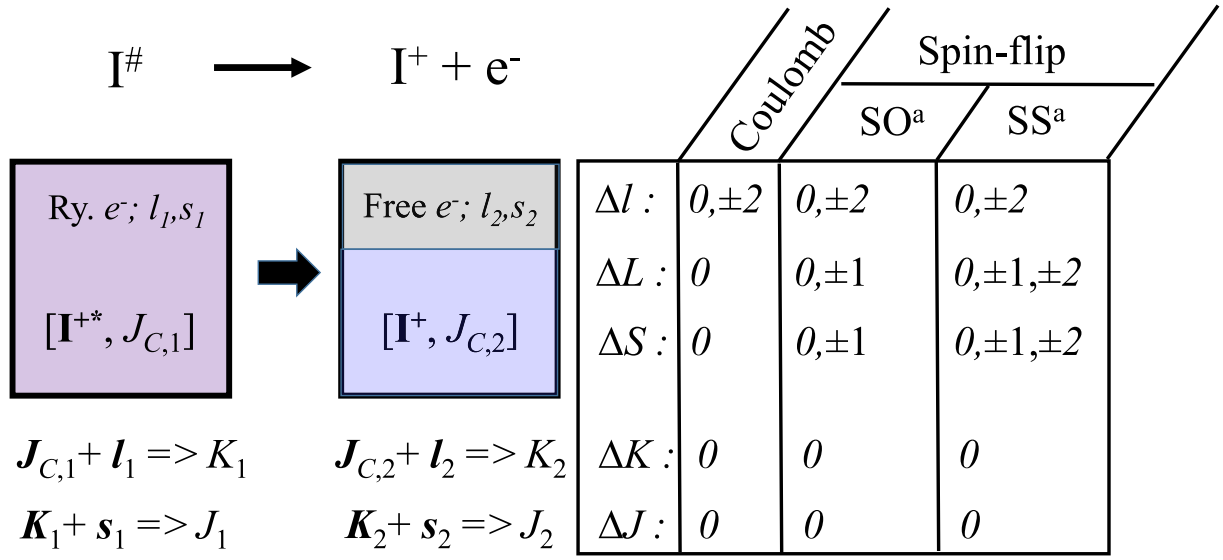

Fig. 2. Schematic representation of autoionization processes and selection rules [28] relevant to observations presented in this paper. l_i and s_i; i = 1,2 are the orbital and spin angular momentum quantum numbers for the Rydberg and free electrons, respectively. J_{ci}; i = 1,2 are the total angular momentum quantum numbers for the ion cores I^{+*} and the ion I^+, respectively. Bold letters represent corresponding angular momentum vectors. K_i and J_i are quantum numbers derived from the vector combinations as shown. See also main text. [a] SO = Spin-orbit, SS = Spin-spin.

2. Experimental

The experimental apparatus and equipment parameters resemble that described in previous publications [32–35]. Equipment and condition parameters are listed in reference [11]. Mass resolved REMPI data was collected for HI and CH_3I molecular beams. The molecular beams were created by a jet expansion of the compounds diluted in argon through a pulsed nozzle. The HI molecular beam was created by a jet expansion of a HI:Ar ~1:2 gas mixture, whereas the CH_3I beam was created by flowing argon over CH_3I liquid sample stored in a water cooled trap. Frequency doubled laser radiation was focused on the molecular beam inside an ionization chamber between a repeller and extractor plates. Ions formed by multiphoton excitations were directed into a time-of-flight tube and detected by a micro-channel plates (MCP's) detector. Signals were fed into a LeCroy WaveSurfer 44 MXs-A, 400 MHz storage oscilloscope and recorded. The laser power was kept at a minimum to avoid signal saturation and power broadening effects and the electric field between the repeller and the extractor plates was kept at a minimum to avoid field ionization. Laser calibration was acquired from known atomic lines of iodine (2 + 1) REMPI peaks. Accuracy of calibration was typically found to be about ±1.0 cm^{-1} on the two-photon wavenumber scale.

I^+ signal intensities, $I(I^+)$ for atomic lines formed by HI photolysis were measures for different laser power to estimate the number of photons required for the ionization. This was achieved by ion signal measurements with $(I(I^+))$ and without $(I_0(I^+))$ four quartz windows stacked together and inserted in the laser beam prior to focusing on the molecular beam. The transmittance of the windows was measured as a function of wavelength with a spectrophotometer (Perkin Elmer; Lambda 25 UV/VIS Spectrometer).

3. Results and analysis

Mass resolved REMPI data was collected for the two-photon excitation region of 76,680–82,620 cm^{-1} for CH_3I and HI. REMPI spectra for I^+ were derived from the data (see Fig. 3 and reference [11]). Number of spectral peaks observed were found to be common to both compounds. These were assigned to two-photon resonant transitions of iodine atoms to Rydberg states. They vary a lot in intensity and line width. In addition the HI spectrum shows fine peak structure, which is attributed to two-photon resonant transitions to molecular Rydberg or ion-pair states of HI [35]. The iodine atomic lines can be divided into two major groups (see Fig. 1) as, a) lines due to (2 + 1) REMPI of I via resonant excitation to I** and $I^{\#}$ lower in energy than the ionization limit for the ground state ion $(I^+(^3P_2))$ of 84,292 cm^{-1} [16,26], and b) lines due to two-photon resonant excitation of I* to $I^{\#}$ followed by autoionization to form $I^+(^3P_2)$. Furthermore, few weak lines, which could not be assigned, were observed [11].

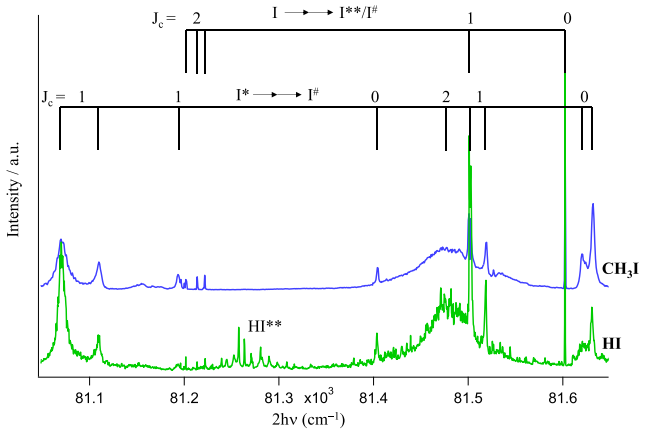

Fig. 3. I^+ REMPI of CH_3I and HI for the two-photon excitation region of 81,050–81650 cm^{-1} and assignments of main spectral features. Iodine atomic lines for I (2 + 1) REMPI (top) and I* (2 + a) REMPI (a = autoionization) (below) are marked. J_c quantum numbers for the excited atom (I**, $I^{\#}$) ion cores are indicated. Molecular structure due to two-photon resonant transitions of HI to a Rydberg state (HI**) is marked.

The assignment of peaks was based on quantum defect analysis: The iodine atomic line positions (ν) for excitation of I and I* (ν ($I,I^* \rightarrow I^{**},I^{\#}$)) can be expressed as

$$\nu(\, I, I^* \rightarrow I^{**}, I^{\#}) = E(I^{**}, I^{\#}) - E(I, I^*) \quad (1a)$$

where

$$E(I^{**}, I^{\#}) = IE[I^+/I^{+*}] - \frac{R_I}{(n - \delta(l))^2} \quad (1b)$$

*E(I**,I#)* and *E(I,I*)* are the energies of the Rydberg (I** or $I^{\#}$) and ground state (I or I*) iodine atoms, respectively. *IE*$[I^+/I^{+*}]$ is the ionization energy of I to form I^+ or I^{+}* to which the Rydberg states converge. R_I is the Rydberg constant appropriate for iodine (109,736.85 cm^{-1} [5]), n is the principal quantum number of the Rydberg electron and $\delta(l)$ is its quantum defect value, which depends on l. By matching observed atomic line positions and corresponding values calculated by Eq. (1) for known ionization energies [36] and given n, the $\delta(l)$ were derived. $\delta(l)$ values of about 4.00, 3.50, 2.40 and 0.05 have been found to be typical for the *s(l = 0)*, *p(1)*, *d(2)* and *f(3)* Rydberg electron orbitals [18–20,23–26]. This allowed assignment of the Rydberg states in terms of $[^{2S+1}L_{Jc}]nl$ (see Section 1). Determination of $[K]_J$ (substates) to derive a full Rydberg state assignment ($[^{2S+1}L_{Jc}]nl[K]_J$; see Section 1) was further attempted by correlation analysis of line series with respect to line widths and, to a lesser extent, line intensities. This involved exploration of trends in line widths and line positions for known and new lines as will be described in more detail below. Atomic line widths (FWHM) were determined from Gaussian line shape fitting (see Tables 1–3).

Halogen atom ions X^+ (X = I, Br) can be formed via multiphoton as well as one-photon excitation of the hydrogen halides [37,38] and methyl halides [13,39] parent molecules prior to dissociation. In order to clarify what is the mechanism of the I^+ formation via resonant excitation of I* we performed laser power dependence measurements to search for the total number of photons required for the ionization of HI in the following way.

The rate of I^+ formation ($d[I^+]/dt$) due to photolysis of RI (RI = CH_3I, HI),

$$RI + mh\nu \rightarrow R + I^+ + e^- \quad (2a)$$

is

$$d[I^+]/dt = I(I^+) = k[RI]\,[h\nu]^m \quad (2b)$$

where $[I^+]$, [RI] and $[h\nu]$ are the densities of I^+, RI and $h\nu$, respectively, in the molecular beam at the laser focal point. *I(I^+)* is the measured I^+ signal intensity, m is the number of photons needed for the ionization and k is a rate constant. *I(I^+)* measurements (*$I_0(I^+)$* and *I(I^+)*) for two different photon flux densities ($[h\nu]_0$ and $[h\nu]$) (see Section 2), but otherwise same experimental conditions, allowed an estimate of m from,

$$\frac{I(I^+)}{I_0(I^+)} = \left(\frac{[h\nu]}{[h\nu]_0}\right)^m = \left(\frac{I(laser)}{I_0(laser)}\right)^m \quad (2c)$$

$$m = \ln\left(\frac{I(I^+)}{I_0(I^+)}\right) \Big/ \ln\left(\frac{I(laser)}{I_0(laser)}\right) \quad (2d)$$

where *I_0(laser)* and *I(laser)* are the relative laser beam intensities before focusing on the molecular beam. I^+ signal measurements for total of fifteen iodine atomic lines due to transitions from I* to $I^{\#}$ were performed for HI photolysis. They resulted in noninteger values of m in the region of about 2.5–3.5 to give an average integer value for m of 3 for the number of photons required for the ionization (see more details below in section B) [11].

The ratio of signal intensities of lines due to ionization of I* (*I(I*)*) to intensities of lines due to ionization of I (*I(I)*) (i.e. *I(I*)/I(I)*) is generally found to be larger for CH_3I than for HI. This is what might be expected in the case of I and I* formation by one-photon dissociation of the molecules since the branching fraction (I*/(I*+I)) is found to be significantly larger for CH_3I [40] than for HI [6] in the one-photon excitation region of concern (i.e. 38,340–41,310 cm^{-1}/242.07–260.82 nm). This observation could be used to distinguish lines due to I* and I ionization.

A. I atom (2 + 1) REMPI lines

All the I-atom (2 + 1) REMPI lines detected correspond to resonant transitions to iodine Rydberg states lower in energy than the ionization energy for the ground state ion ($I^+(^3P_2)$; IE = 84,292 cm^{-1} [26]) after photodissociation of CH_3I and HI (Fig. 1) via repulsive valence states (CH_3I* and HI*) according to,

$$CH_3I + h\nu \rightarrow CH_3I^* \rightarrow CH_3 + I \quad (3a,i)$$

$$HI + h\nu \rightarrow HI^* \rightarrow H + I \quad (3a,ii)$$

$$I + 2h\nu \rightarrow I^{**}/I^{\#} \quad (3b)$$

$$I^{**}/I^{\#} + h\nu \rightarrow I^+ + e^- \quad (3c)$$

Total of thirty-nine previously reported lines due to transitions to I** $[^3P_2]nl$ (fifteen for p orbitals ($l = 1$) and twenty-four for f ($l = 3$)), seven for $I^{\#}[^3P_{0,1}]nl$ (for 7*p*) and five for $I^{\#}[^1D_2]6p$ were identified (see reference [11]). In addition three new lines, which belong to these series were observed and assigned as,

1) $I^{**}[^3P_2]10p[1]_{3/2}$ ($\nu(I \rightarrow I^{**})$ = $E(I^{**})$ = 81,761.1 cm^{-1}; δ = 3.419; FWHM = 0.990 cm^{-1}),
2) $I^{\#}[^1D_2]6p[1]_{1/2}$ ($\nu(I \rightarrow I^{\#})$ = $E(I^{\#})$ = 82,267.3 cm^{-1}; δ = 3.361; FWHM = 1.325 cm^{-1}),
3) $I^{**}[^3P_2]11p[1]_{3/2}$ ($\nu(I \rightarrow I^{**})$ = $E(I^{**})$ = 82,423.2 cm^{-1}; δ = 3.343; FWHM = 0.740 cm^{-1})

The quantum defect analysis ($\delta(l)$ evaluation) formed the basis of the n and l assignments.

The 82,267.3 cm^{-1} line ((2)) was assigned to the only yet unobserved combination of $[K]_J = [1]_{1/2}$. The 81,761.1 cm^{-1} and 82,423.2 cm^{-1}

Table 1
I* (2 + a) REMPI lines for two-photon resonant excitation to $I^{\#}$ $[^3P_0]$ nl $[K]_J$ followed by autoionization ("a" in (2 + a)) to form $I^+(^3P_2) + e^-$ for MPI of CH_3I and HI: Assignments (Core terms, nl, K, J), line positions (2hν(cm^{-1})), $I^{\#}$ energies (E_T (cm^{-1})), quantum defect parameters (δ), line widths (FWHM (cm^{-1})) and references.

Core	*nl*	K	J	2 h ν (cm^{-1})	E_T (cm^{-1})	δ	FWHM(cm^{-1})	references
$[^3P_0]$	8*p*	[1]	1/2	77,621.2	85,224.1	3.54	19.1	a
$[^3P_0]$	8*p*	[1]	3/2	77,708.2	85,311.1	3.50	17.3	a
$[^3P_0]$	9*p*	[1]	1/2	79,461.8	87,064.7	3.54	10.3	a
$[^3P_0]$	9*p*	[1]	3/2	79,516.1	87,119.0	3.50	13.8	a
$[^3P_0]$	10*p*	[1]	3/2	80,547.5	88,150.4	3.49	5.4	a
$[^3P_0]$	12*p*	[1]	1/2	81,620.8	89,223.7	3.50	4.4	a
$[^3P_0]$	12*p*	[1]	3/2	81,632.8	89,235.7	3.46	3.3	a
$[^3P_0]$	13*p*	[1]	1/2	81,920.0	89,522.9	3.51	2.2	a , b
$[^3P_0]$	13*p*	[1]	3/2	81,932.4	89,535.3	3.46	2.1	a
$[^3P_0]$	6*f*	[3]	5/2	80,069.7	87,672.6	0.02	5.3	a
$[^3P_0]$	7*f*	[3]	5/2	80,875.3	88,478.2	0.04	3.0	a
$[^3P_0]$	8*f*	[3]	5/2	81,404.8	89,007.7	0.05	2.2	a

a: This work b: Reference [41].

Table 2
I* (2 + a) REMPI lines for two-photon resonant excitation to $I^{\#}$ $[^3P_1]$ nl $[K]_J$ followed by autoionization ("a" in (2 + a)) to form $I^+(^3P_2) + e^-$ for MPI of CH_3I and HI: Assignments (Core terms, nl, K, J), line positions (2hν(cm^{-1})), $I^{\#}$ energies (E_T (cm^{-1}), quantum defect parameters (δ), line widths (FWHM (cm^{-1})) and references.

Core	*nl*	K	J	2 h ν (cm^{-1})	E_T (cm^{-1})	δ	FWHM(cm^{-1})	references
$[^3P_1]$	8*p*	[2]	5/2	78,200.4	85,803.3	3.56	16.1	a, c
$[^3P_1]$	8*p*	[1]	1/2	78,314.5	85,917.4	3.52	18.7	a, c
$[^3P_1]$	8*p*	[0]	1/2	78,377.4	85,980.3	3.49	8.0	a
$[^3P_1]$	8*p*	[1]	3/2	78,425.7	86,028.6	3.47	5.0	a, b, c
$[^3P_1]$	8*p*	[2]	3/2	78,690.8	86,293.7	3.36	4.8	a, c
$[^3P_1]$	9*p*	[2]	3/2	80,055.2	87,658.1	3.57	3.5	a, b, c
$[^3P_1]$	9*p*	[1]	1/2	80,119.4	87,722.3	3.52	3.8	a, b, c
$[^3P_1]$	9*p*	[0]	1/2	80,175.6	87,778.5	3.48	4.6	a, b, c
$[^3P_1]$	10*p*	[2]	5/2	81,110.5	88,713.4	3.59	6.8	a
$[^3P_1]$	10*p*	[1]	1/2	81,194.1	88,797.0	3.48	4.3	a
$[^3P_1]$	11*p*	[0]	1/2	81,764.0	89,366.9	3.62	2.7	a, b
$[^3P_1]$	11*p*	[1]	1/2	81,867.3	89,470.2	3.42	5.9	a, b
$[^3P_1]$	12*p*	[1]	3/2	82,274.5	89,877.4	3.46	1.5	a, b
$[^3P_1]$	12*p*	[2]	3/2	82,297.7	89,900.6	3.39	1.7	a, b
$[^3P_1]$	12*p*	[0]	1/2	82,319.2	89,922.1	3.33	2.4	a
$[^3P_1]$	4*f*	[2]	3/2,5/2	76,787.7	84,390.6	0.04	6.4	a, b, c
$[^3P_1]$	4*f*	[3]	5/2	76,875.3	84,478.2	0.01	4.1	a, b, c
$[^3P_1]$	5*f*	[2]	3/2,5/2	79,315.6	86,918.5	0.04	5.2	a, b, c
$[^3P_1]$	5*f*	[3]	5/2	79,357.2	86,960.1	0.02	2.4	a, b, c
$[^3P_1]$	6*f*	[2]	3/2,5/2	80,679.3	88,282.2	0.05	4.1	a, b, c
$[^3P_1]$	6*f*	[3]	5/2	80,703.3	88,306.2	0.03	1.7	a, b, c
$[^3P_1]$	7*f*	[2]	3/2,5/2	81,503.3	89,106.2	0.06	3.4	a, b
$[^3P_1]$	7*f*	[3]	5/2	81,520.2	89,123.1	0.03	2.1	a, b
$[^3P_1]$	8*f*	[2]	3/2,5/2	82,038.4	89,641.3	0.06	2.5	a, b
$[^3P_1]$	8*f*	[3]	5/2	82,049.7	89,652.6	0.03	1.5	a, b
$[^3P_1]$	9*f*	[2]	3/2,5/2	82,407.6	90,010.5	0.05	1.9	a, b
$[^3P_1]$	9*f*	[3]	5/2	82,412.8	90,015.7	0.04	1.6	a, b

a: This work b: Reference 23c: Reference 5

Table 3
I* (2 + a) REMPI lines for two-photon resonant excitation to $I^{\#}$ $[^1D_2]$ nl $[K]_J$ followed by autoionization ("a" in (2 + a)) to form $I^+(^3P_2) + e^-$ for MPI of CH_3I and HI: Assignments (Core terms, nl, K, J), line positions (2hν(cm^{-1})), $I^{\#}$ energies (E_T (cm^{-1}), quantum defect parameters (δ), line widths (FWHM (cm^{-1})) and references.

Core	*nl*	K	J	2 h ν (cm^{-1})	E_T (cm^{-1})	δ	FWHM(cm^{-1})	references
$[^1D_2]$	7*p*	[2]	3/2	81,071.7	88,674.6	3.57	14.4	a, b, c
$[^1D_2]$	7*p*	[2]	5/2	81,477.7	89,080.6	3.50	72.3	a

a: This work b: Reference [23] c: Reference [5]

lines ((1) and (3)) were both assigned to $[K]_J = [1]_{3/2}$ because the best constancy in δ(*l*) values was obtained for the $np[1]_{3/2}$ line series. All the lines are sharp with FWHM in the range of 0.70–1.30 cm^{-1}.

B. Two-photon excitation of I* and $I^{\#}$ autoionization

All the two-photon excitations of I*, detected correspond to resonant transitions to superexcited Rydberg states ($I^{\#}$) in the energy region between the ground ion ($I^+(^3P_2)$; 84,292 cm^{-1} [16,26]) and the first spin–orbit excited ion ($I^{+*}(^3P_0)$; 90,743 cm^{-1} [16]) The power dependence experiments mentioned before (see above) suggest that three photons are required for the molecular ionization to form I^+. The most plausible ionization mechanism for a total of three-photon molecular excitation involves autoionization to form $I^+(^3P_2)$ as the final step (see Fig. 1),

$$CH_3I + h\nu \rightarrow CH_3I^* \rightarrow CH_3 + I^* \quad (4a,i)$$

$$HI + h\nu \rightarrow HI^* \rightarrow H + I^* \quad (4a,ii)$$

$$I^* + 2h\nu \rightarrow I^{\#} \quad (4b)$$

$$I^{\#} \rightarrow I^+(P_2) + e^- \quad (4c)$$

A total of twenty five, previously observed and sixteen new atomic lines were identified and assigned, all of which either involved transfer of electrons to *np* or *nf* Rydberg orbitals for the ion cores $I^{+*}(^3P_0)$, $I^{+*}(^3P_1)$ and $I^{+*}(^1D_2)$.

It has been shown [28,30] that members of autoionizing Rydberg series do have resonance linewidths (Γ) which vary approximately linearly with $(n^*)^{-3}$, where n^* is the effective quantum number ($n^* = n - \delta(l)$). Thus, exploration of trends in line widths as a function of $(n - \delta(l))^{-3}$ (correlation analysis), could be used to estimate what autoionizing Rydberg series, with respect to $[K]_J$ values (substates; see above), the observed lines belong to. Furthermore, the relative line widths, whether broad, medium or sharp (hence short, medium or long lifetimes with respect to autoionization) is indicative of the major autoionization processes involved (see Fig. 2 and Section 1). Analysis and assignments of the three groups of lines for the ion cores $I^{+*}(^3P_0)$, $I^{+*}(^3P_1)$ and $I^{+*}(^1D_2)$ will now be dealt with in more detail.

Formation and autoionization of $I^{\#}[^3P_0]$ nl $[K]_J$

A total of twelve lines were assigned to transitions to superexcited Rydberg iodine atoms ($I^{\#}$) with ion core $I^{+*}[^3P_0]$ (i.e. $I^{\#}[^3P_0]$ *nl* $[K]_J$), corresponding to an ionization energy of $IE[J_c = 0] = 90{,}742$ cm^{-1} (see Fig. 4 and Table 1). Judging from the quantum defect analysis nine of these were found to belong to *np* series ($n = 8$–10, 12, 13; $\delta = 3.46$–3.54; see Fig. 4) and three to *nf* series ($n = 6$–8; $\delta = 0.02$–0.05; see Fig. 4). The lines for the *np* series appear in close pairs for same *n* (except for $n = 10$), whereas only one peak per *n* is seen in the *nf* series. All the lines, except for one, are new observations. A line for the two-photon excitation of 81,920 cm^{-1}, previously observed by Zhu *et al.* [23] and assigned to $I^{\#}[^3P_1]11p$ was reassigned to $I^{\#}$ $[^3P_0]13p$.

Plots of line widths as a function of $(n - \delta(l))^{-3}$ are shown in Fig. 5.

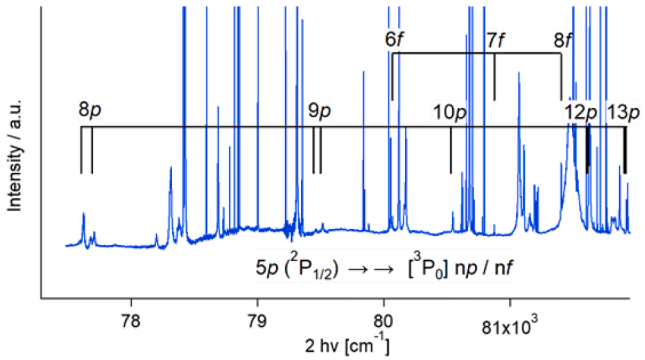

Fig. 4. I^+ REMPI of CH_3I for the two-photon excitation region of 77,500–82,000 cm^{-1} highlighting iodine atomic lines due to I* (2 + a) REMPI (a = autoionization) via $I^{\#}[^3P_0]np$ and $I^{\#}[^3P_0]nf$ superexcited Rydberg states (see Table 1 and main text).

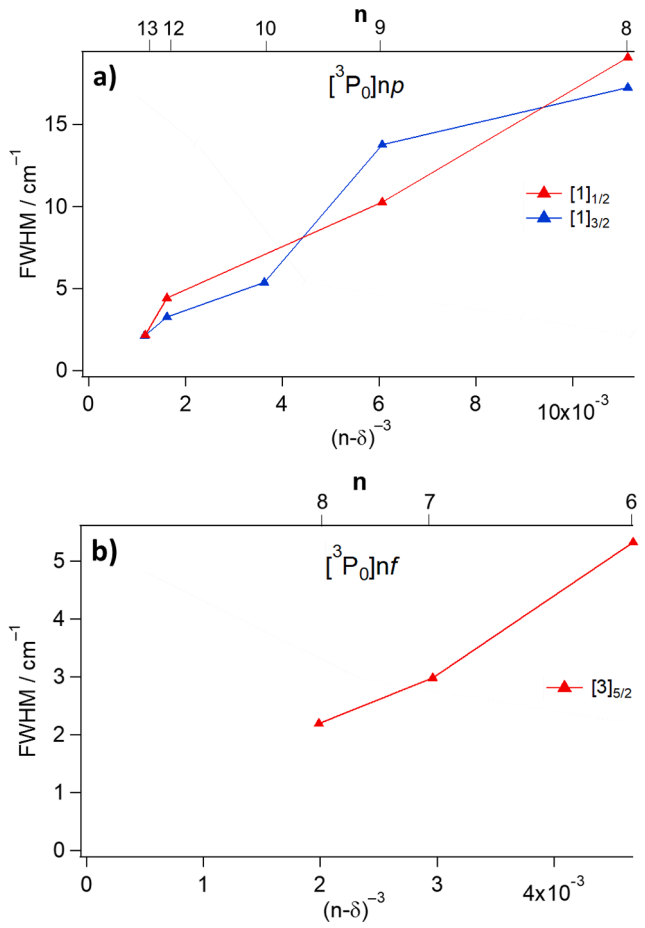

Fig. 5. Line widths (FWHM (cm^{-1})) as a function of $(n - \delta)^{-3}$ (bottom x-axis)/ n (top x-axis) (see main text) for iodine atomic lines due to I* (2 + a) REMPI (a = autoionization) via $I^{\#}[^3P_0]np[1]_{1/2}$ (a; red), $I^{\#}[^3P_0]np[1]_{3/2}$ (a; blue) and $I^{\#}[^3P_0]nf[3]_{5/2}$ (b) Rydberg states (see Table 1 and main text).

The paired *np* lines (same *n*) have been distinguished in terms of relative intensities to give two "close to linear" series (stronger and weaker lines, respectively), of similar line widths (medium broad peaks) (Fig. 5**a**), whereas only one "close to linear" series of rather sharp peaks is seen for the *nf* lines (Fig. 5**b**). The former two series (*np*; Fig. 5**a**) are assigned to the $[K]_J = [1]_{1/2}$ and $[1]_{3/2}$ states, respectively (i,e. $K = J_c + l = 0 + 1$; $J = K + s = 1 \pm 1/2$). The stronger peaks in the line-pair series are assumed to correspond to the more favourable $\Delta J = 0$ (hence to the $[K]_J = [1]_{1/2}$ state) transition. The *nf* series is assigned to the only possible $[K]_J$ combination of $[3]_{5/2}$ ($K = J_c + l = 0 + 3$; $J = K + s = 3$ - ½; $J = 3 +$ ½ excluded).

Formation and autoionization of $I^{\#}[^3P_1]$ nl $[K]_J$

A total of twenty-seven lines were assigned to transitions to super-excited Rydberg iodine atoms ($I^{\#}$) with ion core $I^{+*}[^3P_1]$ (i.e. $I^{\#}[^3P_1]$ *nl* $[K]_J$), corresponding to an ionization energy of $IE[J_c = 1] = 91{,}382$ cm^{-1} (see Fig. 6 and Table 2). Judging from quantum defect analysis fifteen of these were found to belong to *np* series (n = 8–12; δ = 3.33–3.63; see Fig. 6) and twelve to *nf* series (n = 4–9; δ = 0.01–0.06; see Fig. 6). The series appear in groups of peaks for the same *n*, five or fewer peaks for the *np* series and two for the *nf* (Table 3). The lower energy excitation peaks of the line pairs for the *nf* series are found to be noticeably stronger in intensity. Four of the *np* lines are new, whereas other peaks have been observed before and assigned by Hu *et al.* [5] and Zhu *et al.* [23] The four new lines are assigned to transitions to the 8*p* (δ = 3.49), 10*p* (two lines; δ = 3.59 and 3.48) and 12*p* (δ = 3.33) Rydberg orbitals.

Plots of line widths as a function of $(n - \delta(l))^{-3}$ are shown in Fig. 7. Previously observed data points for the various $I^{\#}[^3P_1]$ *nl* $[K]_J$ series (Table 2) are found to be close to linear except for the $[K]_J = [1]_{1/2}$ series (Fig. 7**a**). The new data points for the 78,377.4 cm^{-1} (E_T = 85,980.3 cm^{-1}; $I^{\#}[^3P_1]8p$) and 82,319.2 cm^{-1} (E_T = 89,922.1 cm^{-1}; $I^{\#}[^3P_1]12p$) lines fit in nicely as the n = 8 and 12 components of the $I^{\#}[^3P_1]np$ $[0]_{1/2}$ series, respectively, and the 81,194.1 cm^{-1} (E_T = 88,797.0 cm^{-1}; $I^{\#}[^3P_1]10p$; δ = 3.48) line could be the n = 10 component of an apparently curved plot for the $I^{\#}[^3P_1]np$ $[1]_{1/2}$ series. We, therefore assign the 78,377.4, 82,319.2 and 81,194.1 cm^{-1} lines to the $I^{\#}[^3P_1]8p$ $[0]_{1/2}$, $I^{\#}[^3P_1]12p$ $[0]_{1/2}$ and $I^{\#}[^3P_1]10p$ $[1]_{1/2}$ states, respectively. The 81,110.5 cm^{-1} (E_T = 88,713.4 cm^{-1}; $I^{\#}[^3P_1]10p$; δ = 3.59) line we assign to the $I^{\#}[^3P_1]10p$ $[2]_{5/2}$ state to replace a previous assignment of a much broader peak at 81,071.7 cm^{-1} (E_T = 88,674.6 cm^{-1}) close by [5,23], which we have reassigned (see more detail below in subsection "Formation and autoionization of $I^{\#}[^1D_2]$ *nl* $[K]_J$" and Table 2). This rearrangement gives relative line widths of the peaks for $[K]_J = [2]_{5/2}$; n = 8 and 10 closer to what might be expected as a function of $(n - \delta)^{-3}$ (Fig. 7**a**). The plot of the line widths for the *nf* series (Fig. 7**b**) show two clearly separate curves for the $[2]_{3/2,5/2}$ (larger FWHM/shorter lifetime; lines for J = 3/2 and 5/2 cannot be separated) and $[3]_{5/2}$ (smaller FWHM/longer lifetime) components.

Formation and autoionization of $I^{\#}[^1D_2]$ nl $[K]_J$

The line at 81,477.7 cm^{-1}, (E_T = 89,080.6 cm^{-1}) fits nicely n = 7 in the $I^{\#}[^1D_2]np$ series for $\delta(l = 1) = 3.50$. It has an order of magnitude

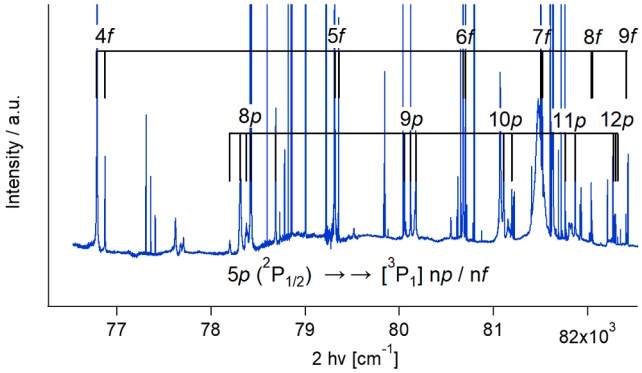

Fig. 6. I^+ REMPI of CH_3I for the two-photon excitation region of 76,500–82,500 cm^{-1} highlighting iodine atomic lines due to I* (2 + a) REMPI (a = autoionization) via $I^{\#}[^3P_1]np$ and $I^{\#}[^3P_1]nf$ superexcited Rydberg states (see Table 2 and main text).

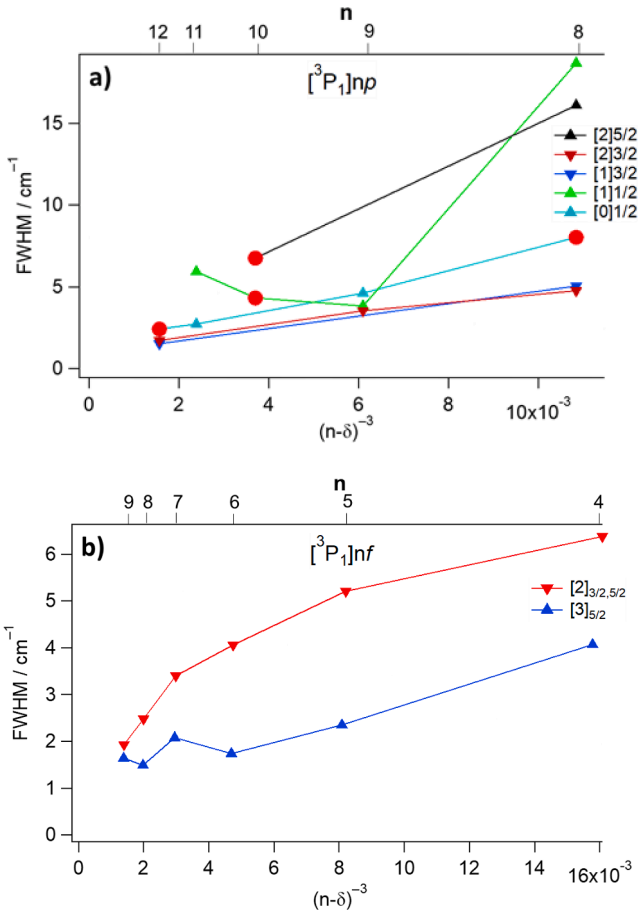

Fig. 7. Line widths (FWHM (cm^{-1})) as a function of $(n - \delta)^{-3}$ (bottom x-axis)/ n (top x-axis) (see main text) for iodine atomic lines due to I* (2 + a) REMPI (a = autoionization) via $I^{\#}[^3P_1]np[K]_J$ (a; $[K]_J$ indicated in figure), $I^{\#}[^3P_1]nf[2]_{3/2,5/2}$ (b; red) and $I^{\#}[^3P_1]nf[3]_{5/2}$ (b; blue) Rydberg states (see Table 2 and main text). Triangle dots are from others work; Circular dots are from this work.

bigger line width (FWHM = 72.3 cm^{-1}) compared to most other lines involving autoionization (See Fig. 8). This is what might be expected for a Coulomb interaction driven autoionization corresponding to unchanged L and S quantum numbers in the L-S scheme (see Fig. 2). The particularly big line width in association with a large relative intensity further favours an unchanged l quantum number ($\Delta l = 0$) in the autoionization process. It can be shown that the only $I^{\#}[^1D_2]7p$ state which satisfies the criteria of $\Delta L = \Delta S = 0$ as well as $\Delta l = 0$ corresponds to $[K]_J = [2]_{5/2}$. Consequently, we assign the 81,477.7 cm^{-1} line to the $I^{\#}[^1D_2]7p[2]_{5/2}$ state.

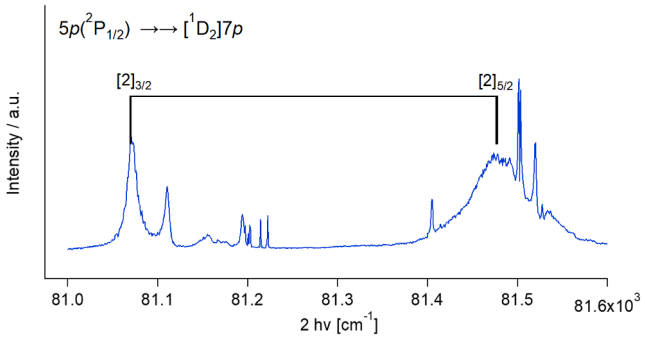

Fig. 8. I^+ REMPI of CH_3I for the two-photon excitation region of 81,000–81,600 cm^{-1} highlighting iodine atomic lines due to I* (2 + a) REMPI (a = autoionization) via $I^{\#}[^1D_2]7p$ Rydberg states (see Table 3 and main text).

The line at 81,071.7 cm^{-1} (E_T = 88,674.6 cm^{-1}) previously assigned to the $I^{\#}[^3P_1]10p$ $[2]_{5/2}$ state [5,23] (see also section "Formation and autoionization of $I^{\#}[^3P_1]$ nl $[K]_J$." above) we also assign to an $I^{\#}$ $[^1D_2]7p$ state based on similar arguments. Firstly, the line is only about 400 cm^{-1} higher than the 81,477.7 cm^{-1} ($I^{\#}[^1D_2]7p[2]_{5/2}$) line and fits $n = 7$ in the $I^{\#}[^1D_2]np$ series for $\delta(l = 1) = 3.57$. Secondly, it is a relatively intense line with big line width (FWHM = 13.1 cm^{-1}; see Fig. 8) by analogy with the 81,477.7 cm^{-1} ($I^{\#}[^1D_2]7p[2]_{5/2}$) line, which favours an $I^{\#}$ $[^1D_2]$ assignment. There are four remaining $[K]_J$ combinations possible for $I^{\#}[^1D_2]7p$, all of which correspond to spin-flip mechanisms for autoionization to $(I^+(^3P_2) + e^-)$ for $\Delta l = 0$ ($\Delta L = \Delta S = 1$ for $[K]_J = [1]_{1/2}$, $[1]_{3/2}$ and $[3]_{5/2}$) and $\Delta L = \Delta S = 2$ for $[K]_J = [2]_{3/2}$). Our data does not allow distinction between those possibilities. Angular distributions and photoelectron images given by Hu et al. [5] on the other hand reveal close resemblance in angular distributions for the line of the $[K]_J = [2]_{3/2}$ substate and this line. We, therefore assign the 81,071.7 cm^{-1} line to the $I^{\#}$ $[^1D_2]7p[2]_{3/2}$ state (see Table 3).

4. Discussion

The assignment procedure of the iodine atom autoionization lines as described in the previous section was stepwise. Firstly, the Rydberg states were characterized in terms of the principal quantum numbers (n) and orbital angular momentum quantum numbers (l) of the Rydberg electrons as well as the ion cores by a quantum defect analysis. Secondly, the substates were characterized in terms of the K and J quantum numbers (see Fig. 2) by a correlation analysis of the line width dependence on $(n - \delta(l))^{-3}$ (where $\delta(l)$ is the quantum defect parameter depending on l) and by line intensity considerations to some extent. Whereas the first step is a standard analysis procedure, the second step is somewhat unconventional. Originally an attempt was made to assign lines to substates based on patterns of relevant energy levels and previously observed spectral lines [5,23], but without success. In previous work on iodine atom lines either angular distributions and corresponding anisotropy parameters (β) , or correlation analyses based on centroid diagrams [28] were used to characterize the substates. The correlation analysis of the line widths (and intensities) used here is subject to the criteria that lines in Rydberg series of common ion core and l quantum numbers increase approximately linearly with $(n - \delta(l))^{-3}$. It can be a useful method for state assignments. It was used here to distinguish between the $[1]_{1/2}$ and $[1]_{3/2}$ substates for lines of the $I^{\#}[^3P_0]np$ series (Fig. 5**a**) and between the $[0]_{1/2}$, $[1]_{1/2}$ and $[2]_{5/2}$ substates for lines of the $I^{\#}[^3P_1]np$ series (Fig. 7**a**) as well as in a reassignment of a spectral line (81,071.7 cm^{-1}). Furthermore, trends in the line widths vs. $(n - \delta(l))^{-3}$ for both the line series of $[^3P_0]nf$ (Fig. 5**b**) and $[^3P_1]nf$ (Fig. 7**b**) strongly verify previous assignments.

Whereas correlation analyses of the line widths are primarily suitable for spectra assignments these can also be useful to identify state interactions by showing deviations from regular trends. In particular this may be expected as the density of states/n increases. Thus, the apparent curvature seen in the plot of the line widths for the $I^{\#}[^3P_1]np$ $[1]_{1/2}$ series (Fig. 7**a**) could be the result of a mixing of states of analogous symmetry close in energy. An apparently enhanced line width of the 81,867.3 cm^{-1} ($I^{\#}[^3P_1]11p$ $[1]_{1/2}$) peak is found to match a decrease in the line width of the 81,920.0 cm^{-1} ($I^{\#}[^3P_0]13p$ $[1]_{1/2}$) peak which suggests that the respective Rydberg states ($I^{\#}$ $[^3P_1]11p$ $[1]_{1/2}$ and $I^{\#}$ $[^3P_0]13p$ $[1]_{1/2}$), which are only 53 cm^{-1} apart in energy, are significantly mixed. Fluctuations observed in the line width plots for the $[^3P_0]$ np series (Fig. 5 **a**) and deviations from linearity of those for the $[^3P_1]nf$ series for high n's (Fig. 7**b**) could also be perturbation effects due to state mixing.

Relative intensities of atomic lines were used to distinguish the $I^{\#}$ $[^3P_0]np[1]_{1/2}$ and $I^{\#}$ $[^3P_0]np[1]_{3/2}$ line series. This was based on the assumption that lines of transitions $\Delta J = 0$ might be expected to be the stronger than lines of $\Delta J \neq 0$. This assumes that the relative ion-signal intensities are primarily determined by the two-photon absorption

step and not by the autoionization step, nor are possible perturbation effects assumed to be important, which may be questionable. This argument, however, gains support from intensity observations for the I (2 + 1) REMPI lines, where lines due to $\Delta J = 0$ transitions are generally found to be the strongest. Furthermore, there is an indication that the same applies to the $[^3P_1]np\ [1]_{1/2}$ lines in comparison with the other $[^3P_1]np\ [K]_J$ line series. Finally, lowering in line intensities proportional to n^{-3}, which is well known effect in absorption, is generally found to be the case for the line series reported. This effect further supports the importance of the absorption step in the overall ionization process.

The line width of the 81,477.7 cm^{-1} ($I^{\#}[^1D_2]7p\ [2]_{5/2}$) peak outranges all the others observed. Therefore, we concluded that the autoionization process involved might be driven by a Coulomb interaction of favourable selection rules (corresponding to $\Delta L = \Delta S = \Delta l \neq 0$; Fig. 2). Line widths of transitions to other $[K]_J = [2]_{5/2}$ states (see $I^{\#}[^3P_1]np\ [2]_{5/2}$ and $I^{\#}[^3P_1]nf\ [2]_{5/2}$ in Table 2) corresponding to $\Delta L = \Delta S = 0$ and $\Delta l = 0$ (*np*) and $\Delta l = 2$ (*nf*) are significantly smaller, suggesting that the autoionization of $I^{\#}[^1D_2]nl$ states (^2D and ^2P states in particular) to form $I^+(^3P_2)$ is considerably more favourable and faster. This could explain why the line width of the 88,674.6 cm^{-1} ($I^{\#}[^1D_2]7p\ [2]_{3/2}$) peak of 14.4 cm^{-1} also is quite large although it involves the relatively less favourable spin-flip mechanism.

5. Summary and conclusions

I^+ REMPI spectra were derived from mass resolved REMPI data for CH_3I and HI for the high energy two-photon excitation region of 76,680–82,620 cm^{-1}. Comparison of the spectra structures for the two compounds and laser power dependence experiments revealed large number iodine atomic resonances due to ground state iodine atom (I ($^2P_{3/2}$)) (2 + 1) REMPI and two-photon excitation of spin–orbit excited iodine atoms (I*($^2P_{1/2}$)) followed by autoionization (I* (2 + a) REMPI) after one-photon dissociation of the molecules. Number of new lines, not previously observed, were discovered. Detailed quantum defect analysis allowed assignment of the lines in terms of transitions to Rydberg states specified by Rydberg electron principal quantum numbers (*n*), its orbital angular momentum quantum numbers (*l*) (orbitals) and ion core terms. The I (2 + 1) REMPI lines are due to excitations to Rydberg states (I**) in series converging to the ground state ion ($I^+(^3P_2)$) as well as to some superexcited Rydberg states ($I^{\#}$) converging either to spin–orbit ($I^{+}*(^3P_{0,1})$) or spin ($I^{+}*(^1D_2)$) excited ions, all of which are lower in energy than the ionization limit for the ground state ion. The I* (2 + a) REMPI lines are due to excitations to superexcited Rydberg states ($I^{\#}$) in series which are either converging to the spin–orbit ($I^{+}*(^3P_{0,1})$) or the spin ($I^{+}*(^1D_2)$) excited ions of energies between the ground state ion ($I^+(^3P_2)$) and the first spin–orbit excited ion ($I^{+*}(^3P_0)$). As a consequence, the autoionization processes involve electron ejections in association with formation of the ground state ion ($I^+(^3P_2)$) (See Fig. 1). These involve either electron transfer or spin-flip within the *p* valence electrons of the ion cores.

Line widths and intensities of peaks vary dramatically depending on the ionization processes and excited states involved. The I (2 + 1) REMPI lines are generally found to be sharp (FWHM = 0.70 – 1.30 cm^{-1}) indicating of a relatively long lifetime of the intermediate states (I** and $I^{\#}$, below the ionization limit), which are mainly determined by the radiative decay rate. The I* (2 + a) REMPI lines are generally found to be wider and to vary in the range between 1.5 and 72 cm^{-1} (Tables 1–3). The increased line widths, hence shorter lifetimes of $I^{\#}$, must be caused by the additional autoionization processes, the rate of which vary significantly depending on the driving forces and selection rules. As a rule of thumb, autoionization rates decrease (hence lifetimes of $I^{\#}$ increase) with increasing overall variations in the quantum numbers *L*, *S* and *l* for the transitions of $I^{\#}$ to form $I^+(^3P_2)$ and a free electron (Fig. 2). Typically autoionization processes driven by Coulomb interaction forces (Coulomb transfer mechanism) are the fastest (shortest living $I^{\#}$), whereas those driven by spin–orbit or spin–spin forces (Spin-flip mechanisms) are slower (longer living $I^{\#}$). Particularly fast autoionization processes of $I^{\#}[^1D_2]nl$ states to form $I^+(^3P_2)$ were identified and characterized.

Line widths determined by autoionization processes of unperturbed line series are known to vary linearly with n^{*-3}, where n^* is the effective quantum number. This criteria was used to further distinguish superexcited Rydberg substates ($I^{\#}$) in terms of the *K* (quantum number for combination of the ion core total angular momentum ($\boldsymbol{J_c}$) and the Rydberg electron orbital angular momentum($\boldsymbol{l}$)) and *J* (total angular momentum) quantum numbers. This was achieved in an unconventional way, by considering trends in line widths as a function of n^{*-3} and by intensity assumptions. Deviations from the regular trend of predicted line widths due to state interactions/mixing are evident in some cases. Furthermore, for the smallest line widths deviation from the linear trend of FWHM vs. n^{*-3} (i.e. autoionization effect) could also be affected by competition with the comparable rates of radiative decay.

This paper adds to an ever growing information and knowledge on autoionization processes within atoms. The importance of autoionization in atom and molecular ionization processes is evident and its validity in comparison with direct ionization is unquestionable. The complexity of the processes increases rapidly as the system (atoms or molecules) involved increases in size. Possible coupling mechanisms/driving forces increase and state interactions/mixing become more important as the density of states increases. The heavy iodine atom, dealt with here is an ideal candidate for to explore many relevant effects. We hope that this work will prompt further theoretical as well as experimental investigations which might aid in clarifying the nature and interpretations proposed here.

CRediT authorship contribution statement

Arnar Hafliðason: Conceptualization, Methodology, Investigation, Writing - original draft. **Meng-Xu Jiang:** Data curation, Investigation. **Ágúst Kvaran:** Supervision, Investigation, Writing - review & editing.

Declaration of Competing Interest

The authors declare that they have no known competing financial interests or personal relationships that could have appeared to influence the work reported in this paper.

Acknowledgements

The financial support of the University Research Fund, University of Iceland and the Icelandic Research Fund (Grant No. 184693-052) is gratefully acknowledged. We would like to thank Huasheng Wang for useful help with the experiments.

Appendix A. Supplementary data

Supplementary data to this article can be found online at https://doi.org/10.1016/j.chemphys.2020.111016.

References

[1] D.W. Chandler Jr., J.W. Thoman, M.H.M. Janssen, D.H. Parker, Chem. Phys. Lett. 156 (1989) 151.
[2] L. Rubio-Lago, A. Garcia-Vela, A. Arregui, G.A. Amaral, L. Banares, J. Chem. Phys. 131 (2009), 174309.
[3] M.G. Gonzalez, J.D. Rodriguez, L. Rubio-Lago, A. Garcia-Vela, L. Banares, Phys. Chem. Chem. Phys. 13 (2011) 16404.
[4] S.M. Poullain, D.V. Chicharro, L. Rubio-Lago, A. Garcia-Vela, L. Banares, Philos. Trans. R. Soc. A-Math. Phys. Eng. Sci. 375 (2017) 18.
[5] C.J. Hu, S.X. Pei, Y.L. Chen, K.P. Liu, J. Phys. Chem. A 111 (2007) 6813.
[6] P.M. Regan, D. Ascenzi, C. Clementi, M.N.R. Ashfold, A.J. Orr-Ewing, Chem. Phys. Lett. 315 (1999) 187.
[7] S. Manzhos, H.P. Loock, B.L.G. Bakker, D.H. Parker, J. Chem. Phys. 117 (2002) 9347.

[8] J.P. Camden, H.A. Bechtel, D.J.A. Brown, A.E. Pomerantz, R.N. Zare, R.J. Le Roy, J. Phys. Chem. A 108 (2004) 7806.
[9] D.J. Gendron, J.W. Hepburn, J. Chem. Phys. 109 (1998) 7205.
[10] L. McDonnell, A.J.R. Heck, J. Mass Spectrom. 33 (1998) 415.
[11] see Supplementary material.
[12] Y.-J. Jung, Y.S. Kim, W.K. Kang, K.-H. Jung, J. Chem. Phys. 107 (1997) 7187.
[13] K. Matthiasson, G. Koumarianou, M.X. Jiang, P. Glodic, P.C. Samartzis, Á. Kvaran, Phys. Chem. Chem. Phys. 22 (2020) 4984.
[14] A. Haflidason, M.X. Jiang, Á. Kvaran, Phys. Chem. Chem. Phys. 21 (2019) 23154.
[15] H.R. Hrodmarsson, H.S. Wang, Á. Kvaran, J. Mol. Spectrosc. 324 (2016) 56.
[16] NIST database on Atomic Energy Levels; (National Institute of Standards and Technology) and references therein.
[17] L. Minnhagen, Arkiv för Fysik 21 (1962) 415.
[18] J. Berkowitz, C.H. Batson, G.L. Goodman, Phys. Rev. A 24 (1981) 149.
[19] V.N. Sarma, Y.N. Joshi, Can. J. Phys. 61 (1983) 1434.
[20] S.T. Pratt, Phys. Rev. A 32 (1985) 928.
[21] S.T. Pratt, Phys. Rev. A 33 (1986) 1718.
[22] S.T. Pratt, P.M. Dehmer, J.L. Dehmer, Chem. Phys. Lett. 126 (1986) 12.
[23] Y.F. Zhu, E.R. Grant, J. Phys. Chem. 97 (1993) 9582.
[24] Y.Y. Gu, A.M. Chojnacki, C.J. Zietkiewicz, A.A. Senin, J.G. Eden, J. Chem. Phys. 119 (2003) 12342.
[25] M. Eypper, F. Innocenti, A. Morris, S. Stranges, J.B. West, G.C. King, J.M. Dyke, J. Chem. Phys. 132 (2010) 11.
[26] M. Eypper, F. Innocenti, A. Morris, J.M. Dyke, S. Stranges, J.B. West, G.C. King, J. Chem. Phys. 133 (2010) 9.
[27] H. Shen, L.Q. Hua, C.J. Hu, B. Zhang, J. Mol. Spectrosc. 257 (2009) 200.
[28] J. Berkowitz, Adv. Chem. Phys. 72 (1988) 1.
[29] N. Stolterfoht, Phys. Rep.-Rev. Sec. Phys. Lett. 146 (1987) 315.
[30] J. Berkowitz, Photoabsorption, Photoionization, and Photoelectron Spectroscopy, Academic press, 1979.
[31] L.E. Howard, K.L.J. Andrew, Opt. Soc. Am. B-Opt. Phys. 2 (1985) 1032.
[32] H.R. Hrodmarsson, H.S. Wang, Á. Kvaran, J. Mol. Spectrosc. 290 (2013) 5.
[33] H.R. Hrodmarsson, H. Wang, Á. Kvaran, J. Chem. Phys. 140 (2014), 244304.
[34] H.R. Hrodmarsson, H. Wang, Á. Kvaran, J. Chem. Phys. 142 (2015), 244312.
[35] M.X. Jiang, A. Haflidason, Á. Kvaran, J. Mol. Spectrsocopy 372 (2020), 111329.
[36] N. Thire, R. Cireasa, D. Staedter, V. Blanchet, S.T. Pratt, Phys. Chem. Chem. Phys., 13, 18485.
[37] H.R. Hrodmarsson, A. Kartakoullis, D. Zaouris, P. Glodic, H. Wang, P.C. Samartzis, Á. Kvaran, Phys. Chem. Chem. Phys. 19 (2017) 11354.
[38] H.R. Hróðmarsson, Á. Kvaran, Phys. Chem. Chem. Phys. 17 (2015) 32517.
[39] A. Hafliðason, P. Glodic, G. Koumrianou, P.C. Samartzis, Á. Kvaran, Phys. Chem. Chem. Phys. 21 (2019) 10391.
[40] A.B. Alekseyev, H.P. Liebermann, R.J. Buenker, J. Chem. Phys. 126 (2007) 11.
[41] Y.F. Zhu, E.R. Grant, H. Lefebvrebrion, J. Chem. Phys. 99 (1993) 2287.

4.4.1 Supporting information

Photo- and autoionization processes of superexcited iodine atoms in MPI of CH_3I and HI

Arnar Hafliðason[#], Meng-Xu Jiang[#] and Ágúst Kvaran*

Science Institute, University of Iceland, Dunhagi 3, 107 Reykjavík, Iceland.

Supplementary material

Content: **pages:**

Figure S1 (a – o): CH_3I and HI I^+ REMPI spectra showing assignments for I, 5*p* ($^2P_{3/2}$) (2 + 1) REMPI lines

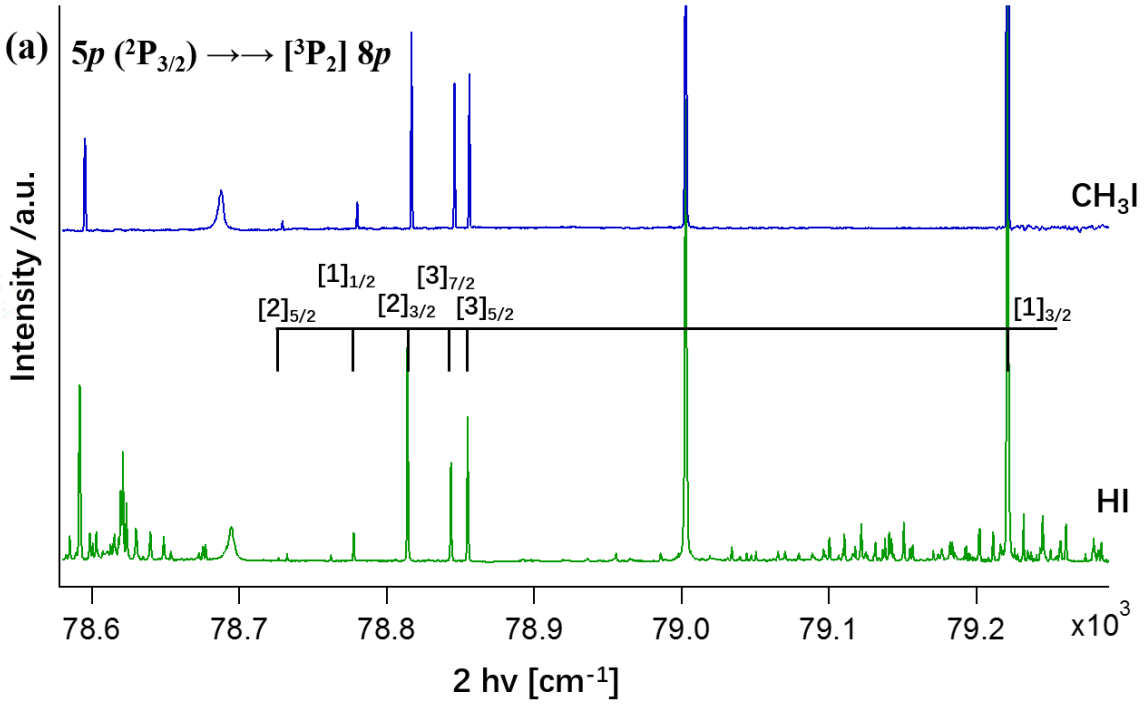

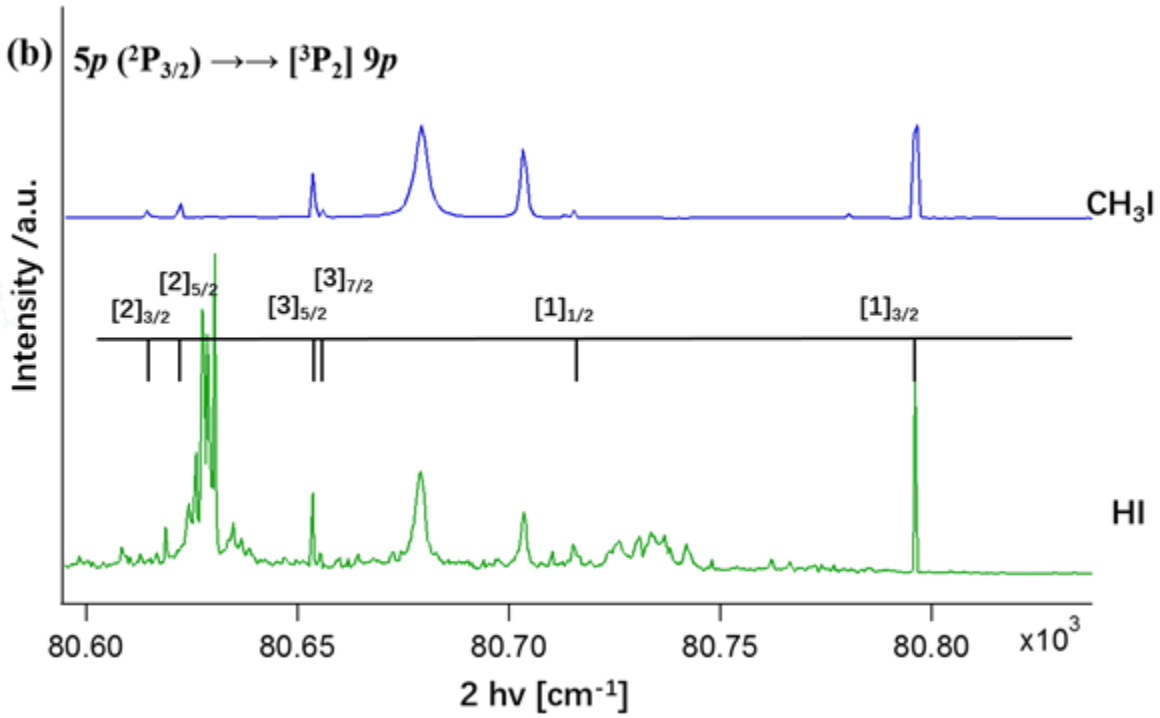

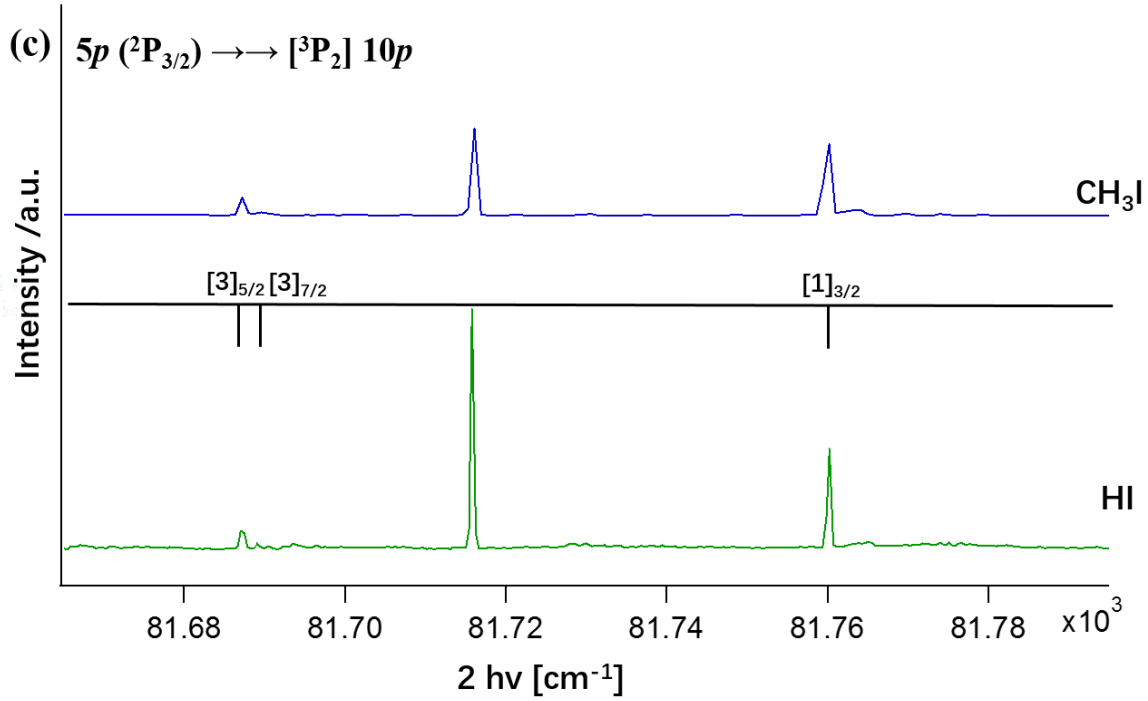
(c)
5p (²P3/2) →→ [³P2] 10p
Intensity /a.u.
CH3I
[3]5/2 [3]7/2
[1]3/2
HI
81.68
81.70
81.72
81.74
81.76
81.78
x10³
2 hv [cm⁻¹]

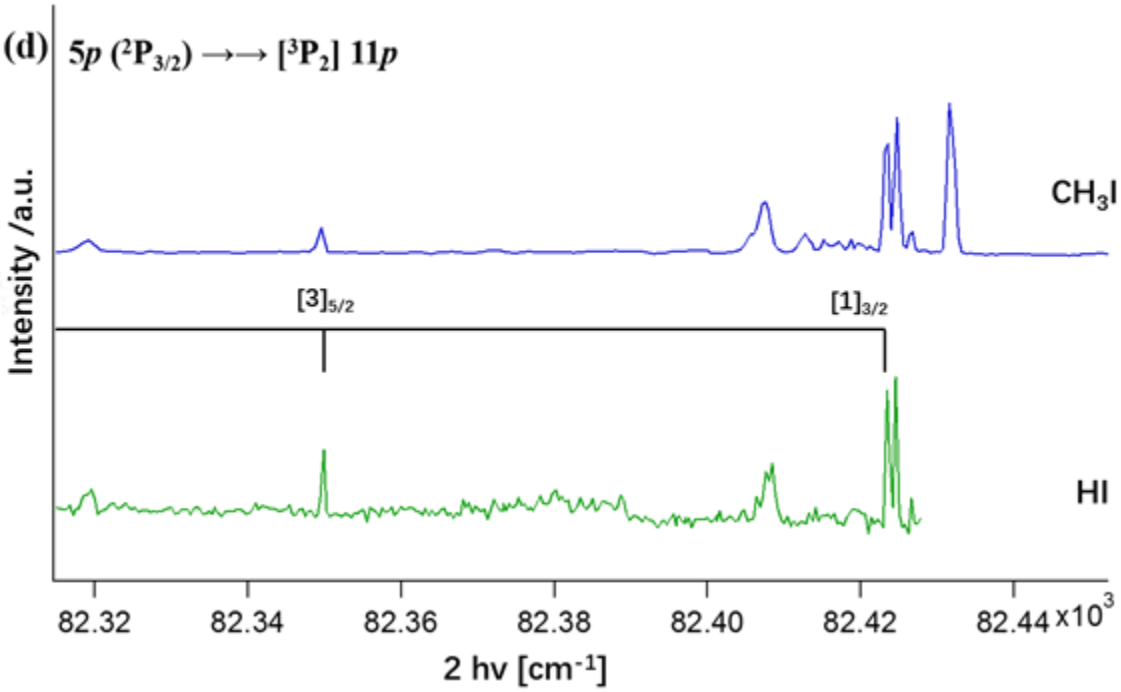
(d)
5p (²P3/2) →→ [³P2] 11p
Intensity /a.u.
CH3I
[3]5/2
[1]3/2
HI
82.32
82.34
82.36
82.38
82.40
82.42
82.44
x10³
2 hv [cm⁻¹]

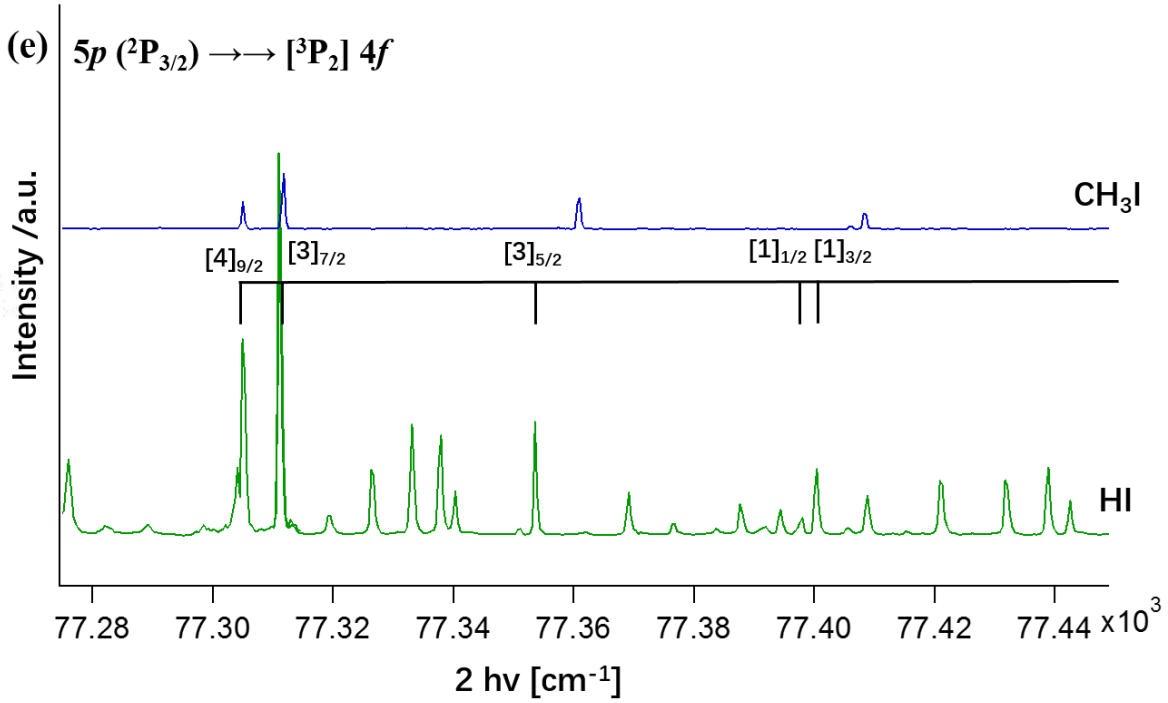
(e)
5p (2P3/2) →→ [3P2] 4f
Intensity /a.u.
CH3I
HI
[4]9/2
[3]7/2
[3]5/2
[1]1/2 [1]3/2
77.28
77.30
77.32
77.34
77.36
77.38
77.40
77.42
77.44 x10^3
2 hv [cm-1]

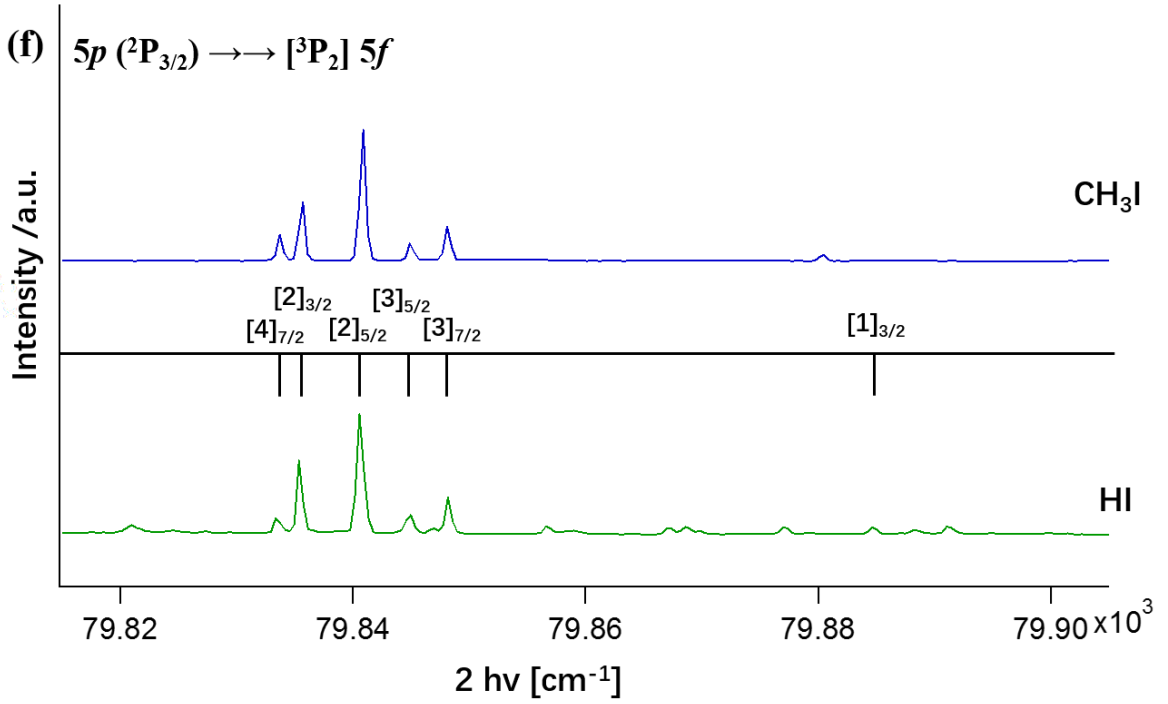
(f)
5p (2P3/2) →→ [3P2] 5f
Intensity /a.u.
CH3I
HI
[2]3/2
[3]5/2
[4]7/2
[2]5/2
[3]7/2
[1]3/2
79.82
79.84
79.86
79.88
79.90 x10^3
2 hv [cm-1]

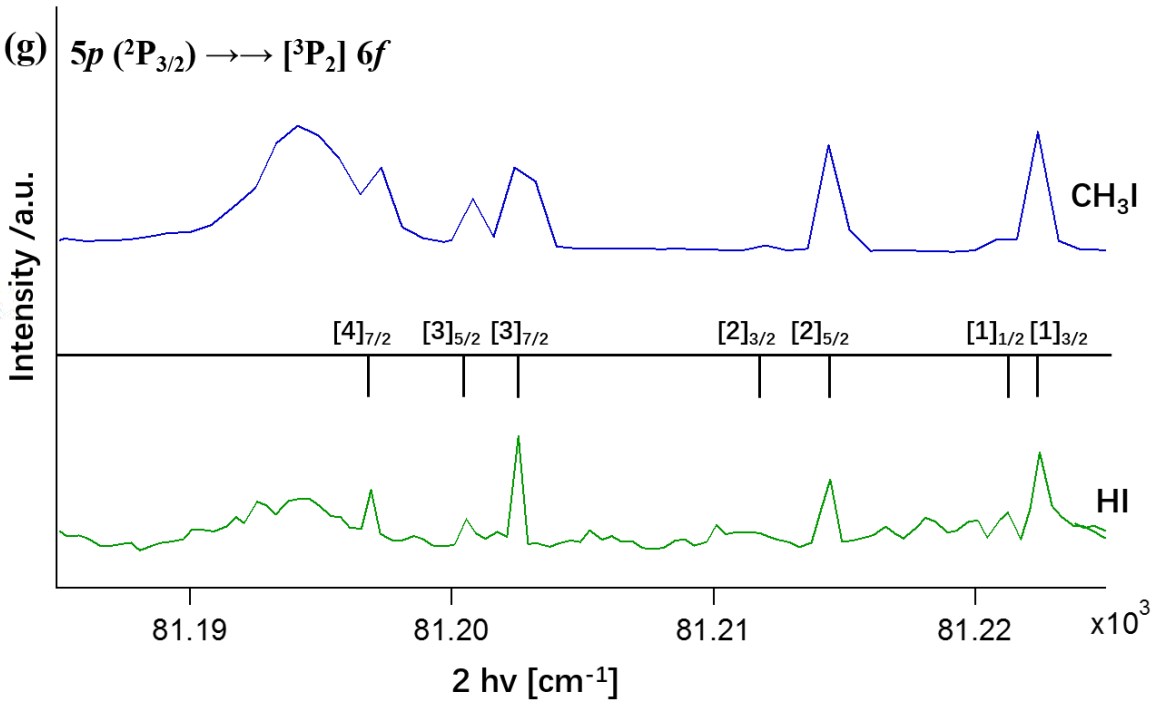
(g)
5p (2P3/2) →→ [3P2] 6f
Intensity /a.u.
CH3I
[4]7/2
[3]5/2
[3]7/2
[2]3/2
[2]5/2
[1]1/2
[1]3/2
HI
81.19
81.20
81.21
81.22
x10^3
2 hv [cm-1]

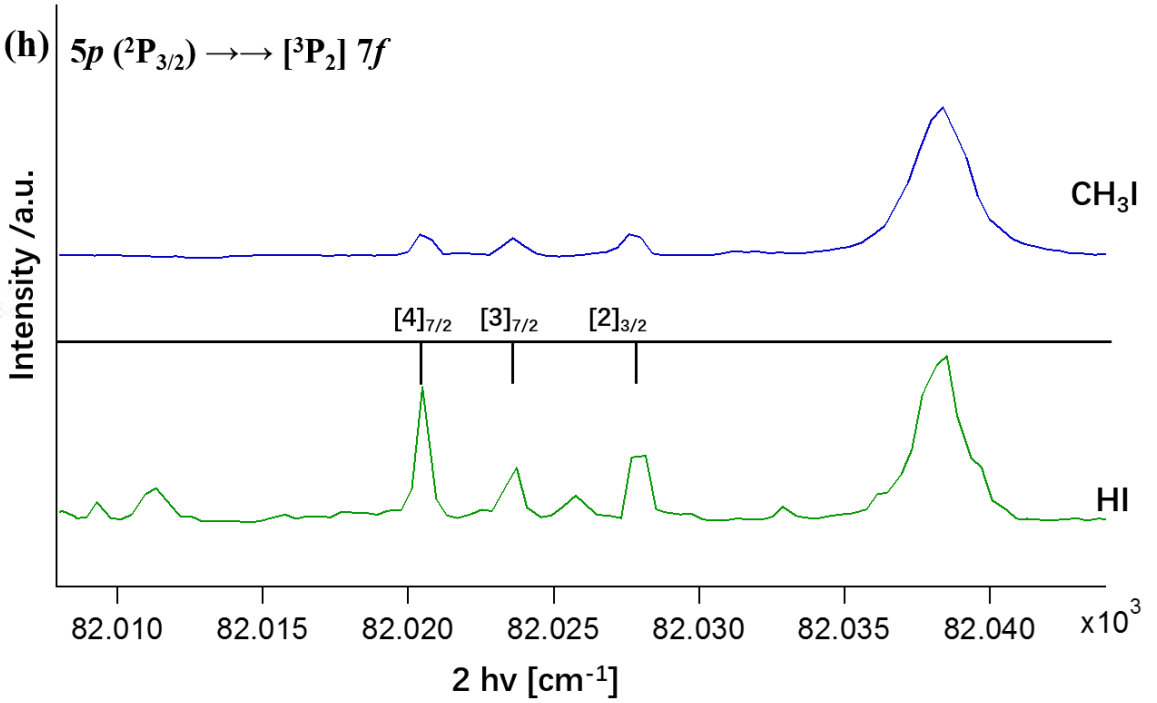
(h)
5p (2P3/2) →→ [3P2] 7f
Intensity /a.u.
CH3I
[4]7/2
[3]7/2
[2]3/2
HI
82.010
82.015
82.020
82.025
82.030
82.035
82.040
x10^3
2 hv [cm-1]

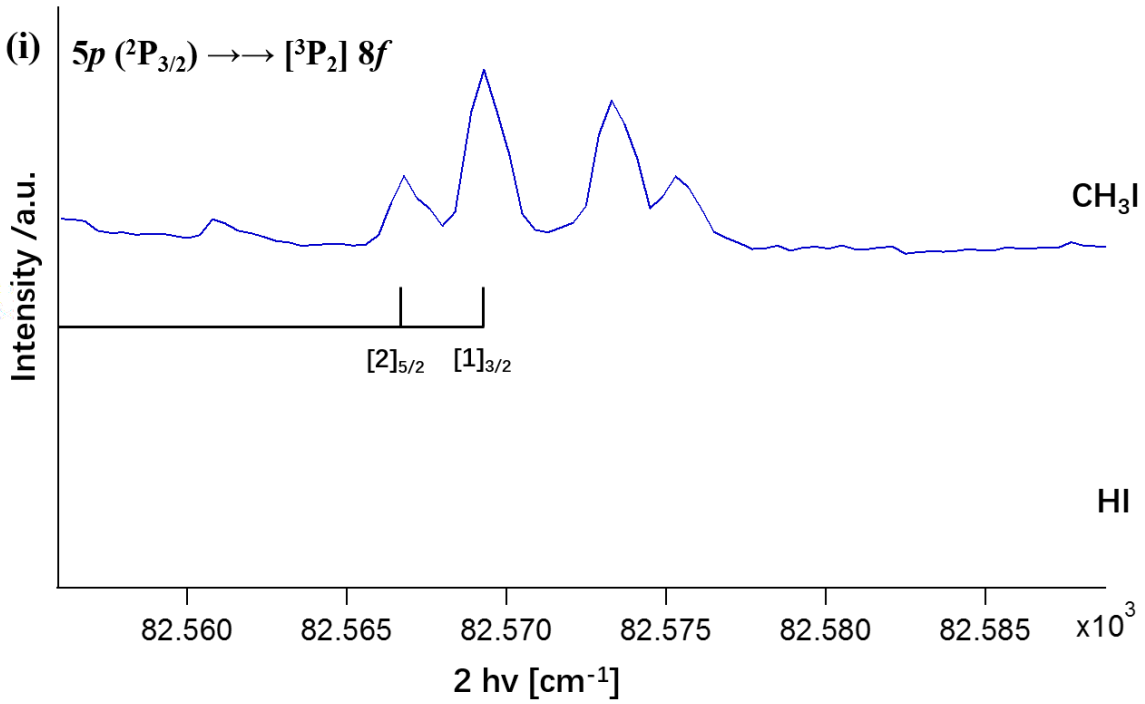
(i)
5p (²P3/2) →→ [³P2] 8f
Intensity /a.u.
CH3I
HI
[2]5/2
[1]3/2
82.560
82.565
82.570
82.575
82.580
82.585
x10³
2 hv [cm⁻¹]

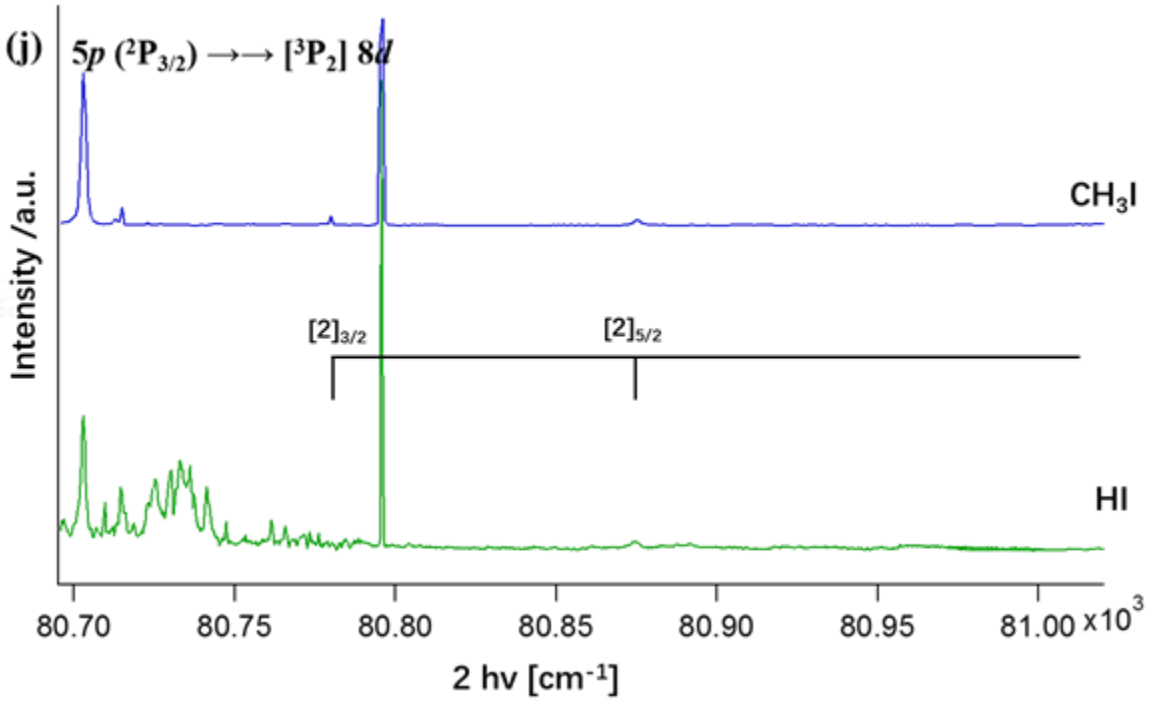
(j)
5p (²P3/2) →→ [³P2] 8d
Intensity /a.u.
CH3I
HI
[2]3/2
[2]5/2
80.70
80.75
80.80
80.85
80.90
80.95
81.00
x10³
2 hv [cm⁻¹]

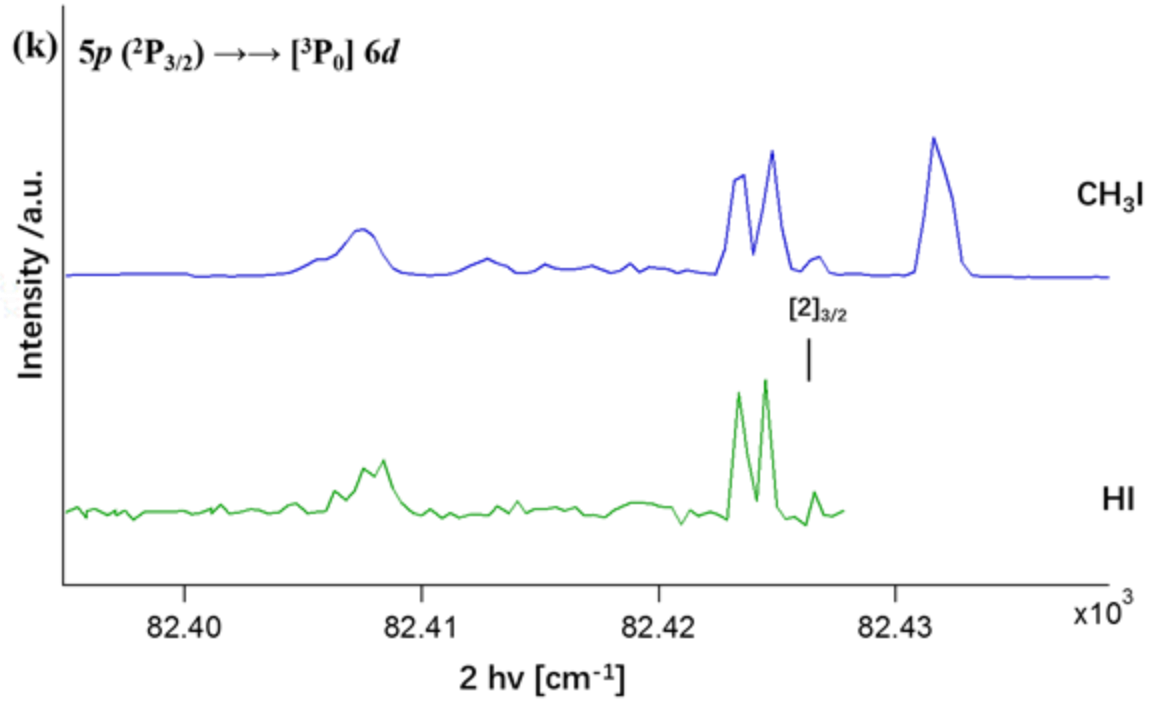
(k) 5p (²P3/2) →→ [³P0] 6d
Intensity /a.u.
CH3I
[2]3/2
HI
82.40
82.41
82.42
82.43
x10³
2 hv [cm⁻¹]

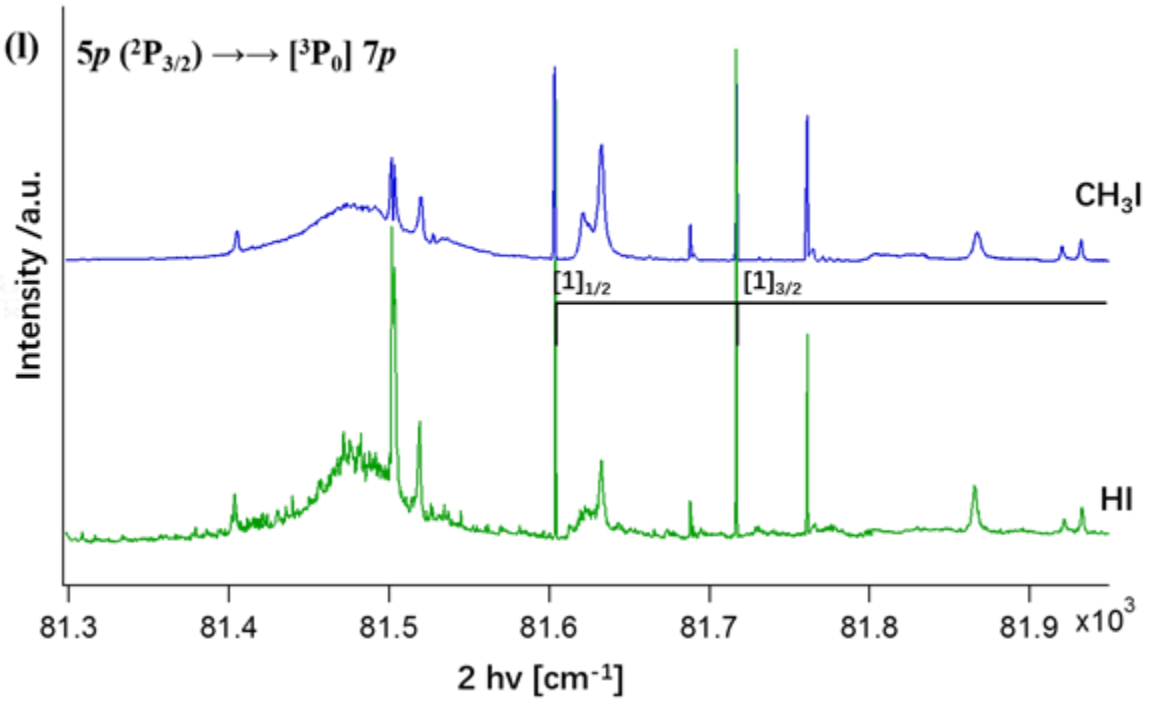
(l) 5p (²P3/2) →→ [³P0] 7p
Intensity /a.u.
CH3I
[1]1/2
[1]3/2
HI
81.3
81.4
81.5
81.6
81.7
81.8
81.9
x10³
2 hv [cm⁻¹]

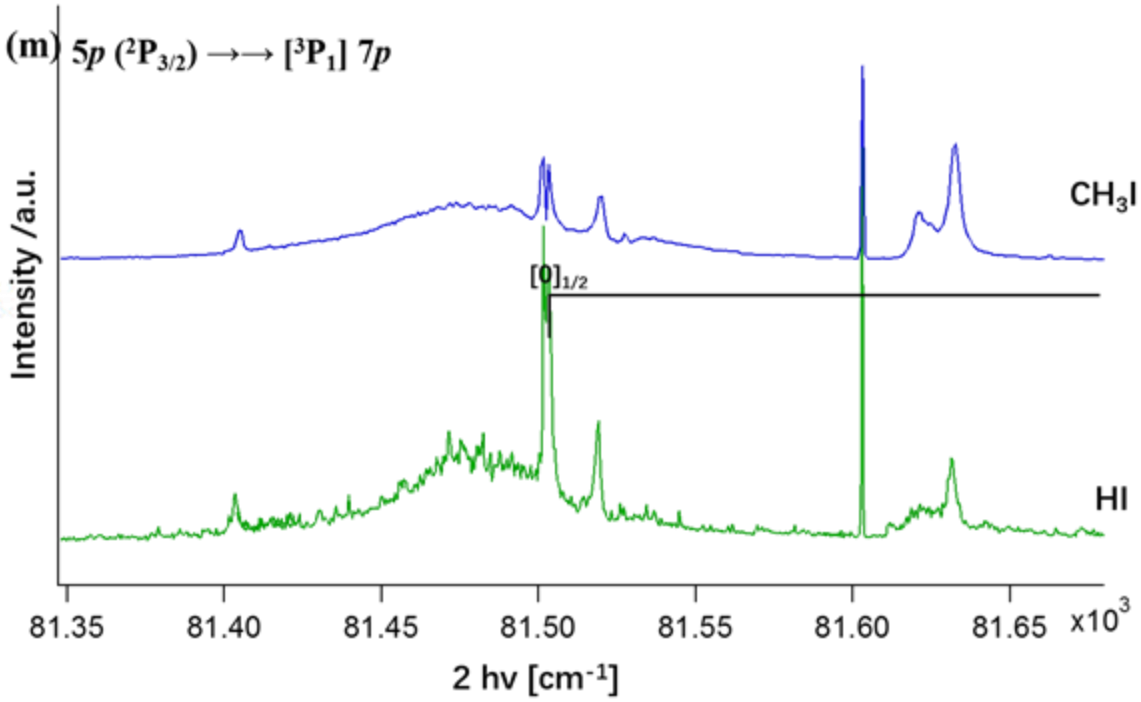
(m) 5p (²P3/2) →→ [³P1] 7p
Intensity /a.u.
CH3I
[0]1/2
HI
81.35
81.40
81.45
81.50
81.55
81.60
81.65
x10³
2 hv [cm⁻¹]

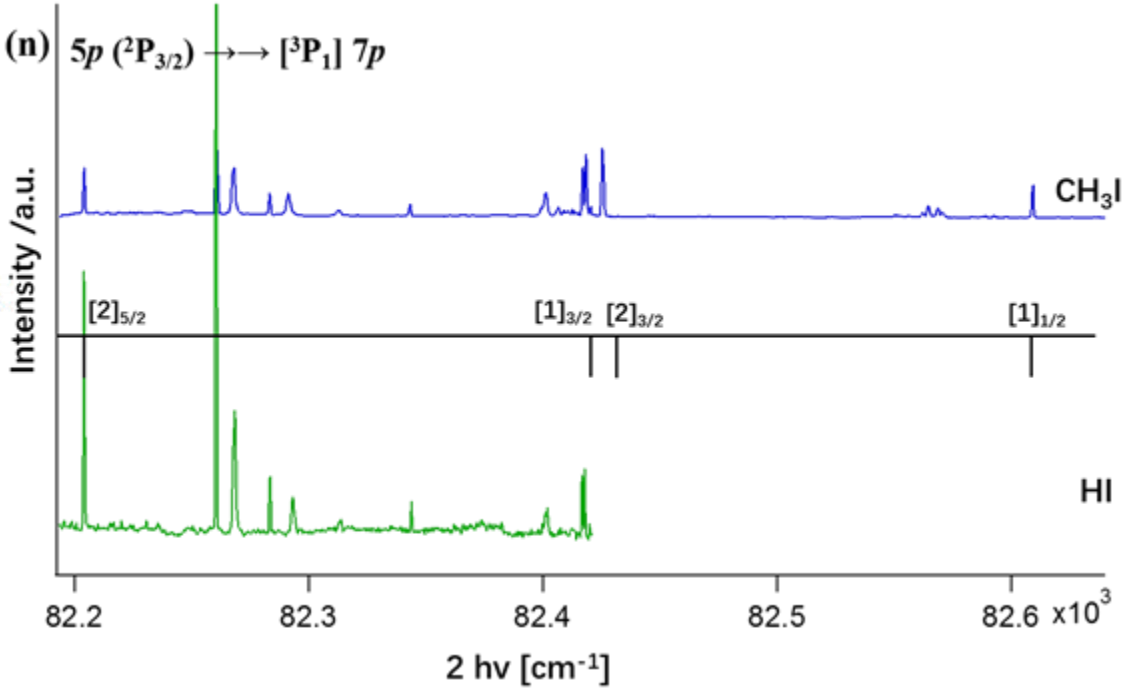
(n) 5p (²P3/2) →→ [³P1] 7p
Intensity /a.u.
CH3I
[2]5/2
[1]3/2
[2]3/2
[1]1/2
HI
82.2
82.3
82.4
82.5
82.6
x10³
2 hv [cm⁻¹]

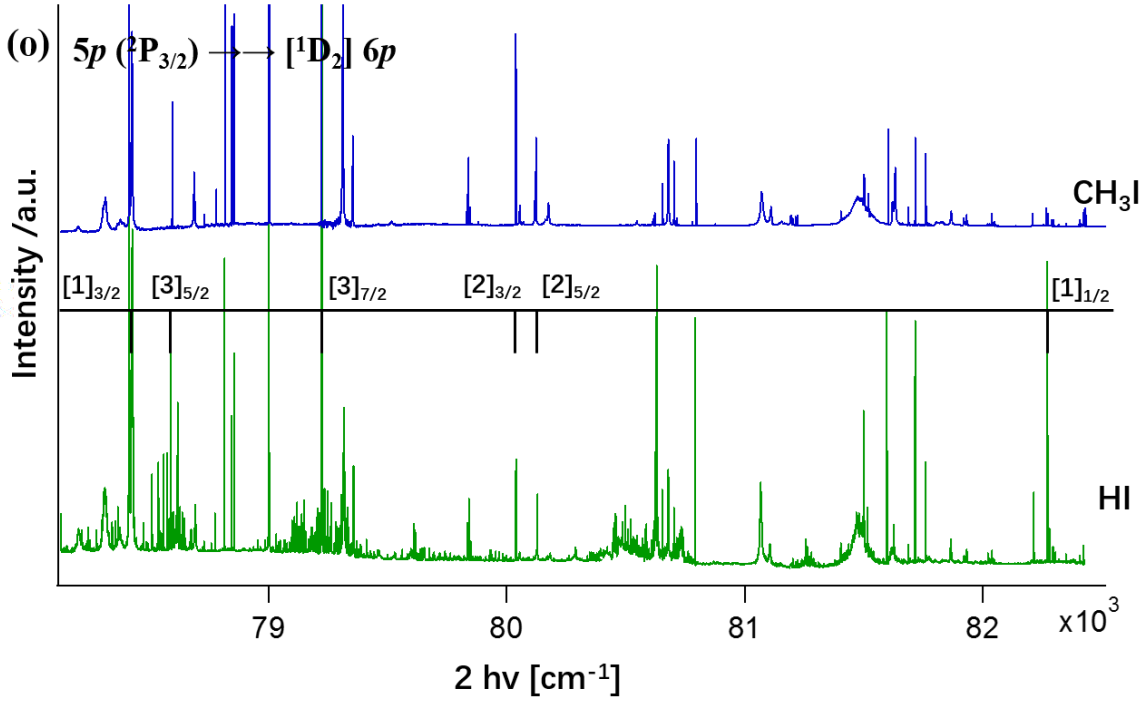
(o) 5p (2P3/2) → [1D2] 6p
Intensity /a.u.
CH3I
HI
[1]3/2
[3]5/2
[3]7/2
[2]3/2
[2]5/2
[1]1/2
79
80
81
82
x10^3
2 hv [cm-1]

Figure S2 (a - x): CH_3I and HI I^+ REMPI spectra showing assignments for I*, 5*p* ($^2P_{1/2}$) (2 + a)(a: autoionization) REMPI lines.

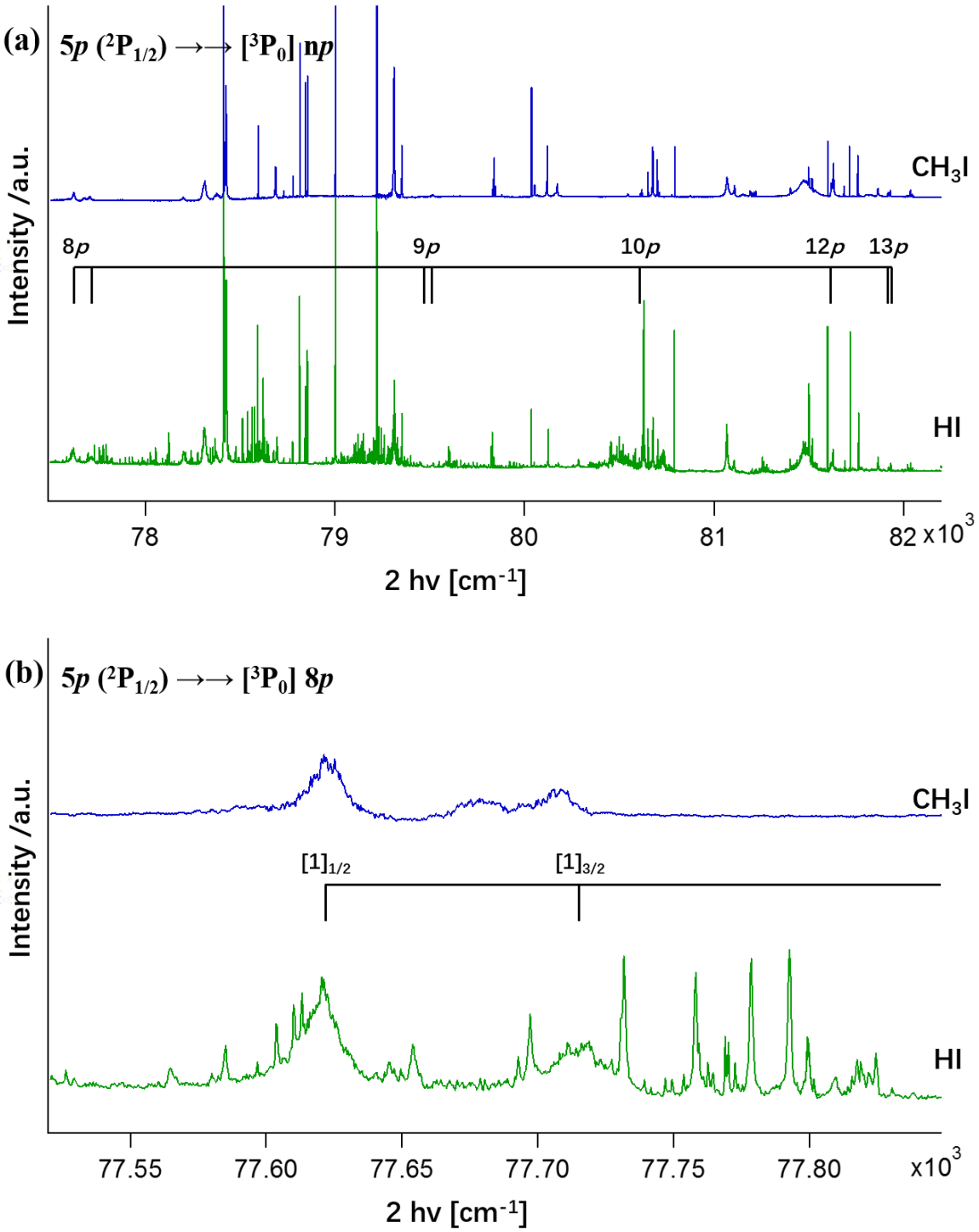

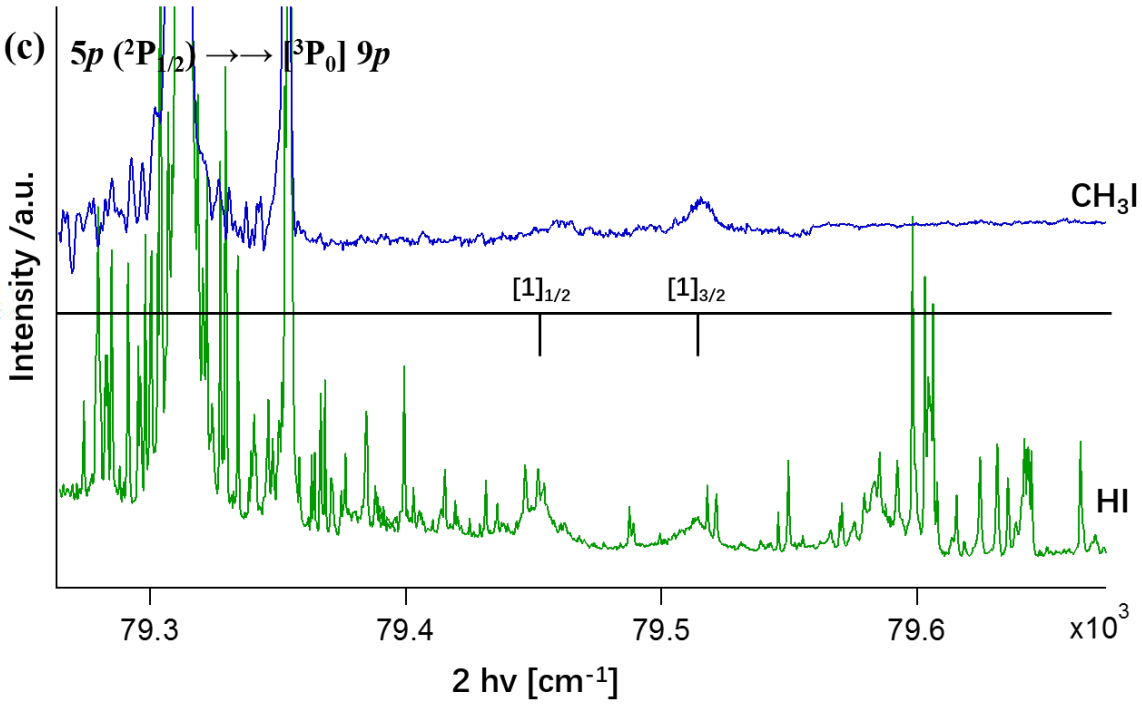
(c)
5p (2P1/2) →→ [3P0] 9p
Intensity /a.u.
CH3I
[1]1/2
[1]3/2
HI
79.3
79.4
79.5
79.6
x10^3
2 hv [cm-1]

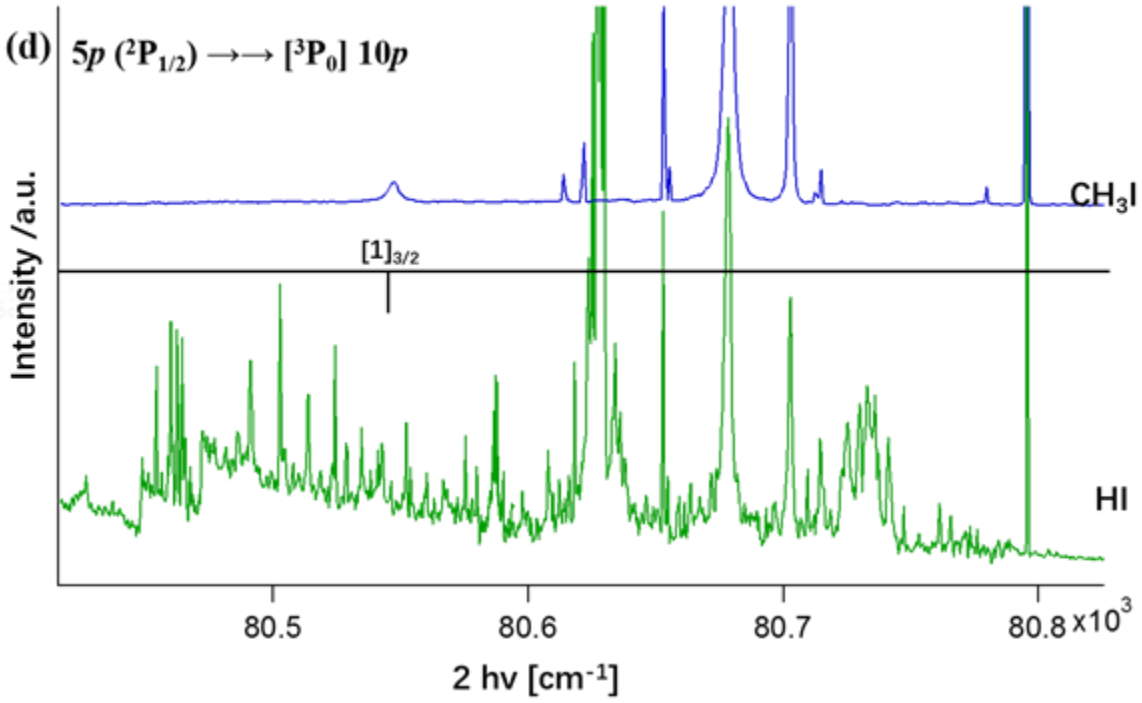
(d)
5p (2P1/2) →→ [3P0] 10p
Intensity /a.u.
CH3I
[1]3/2
HI
80.5
80.6
80.7
80.8
x10^3
2 hv [cm-1]

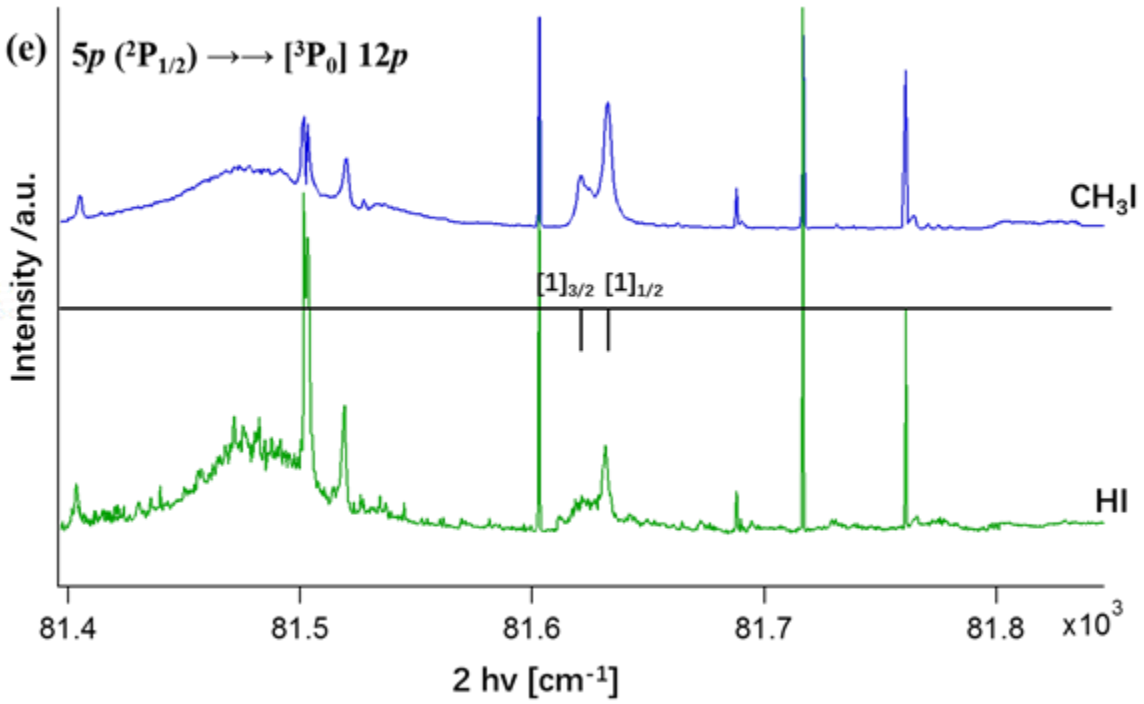
(e)
5p (²P1/2) →→ [³P0] 12p
Intensity /a.u.
CH3I
[1]3/2 [1]1/2
HI
81.4
81.5
81.6
81.7
81.8
x10³
2 hv [cm⁻¹]

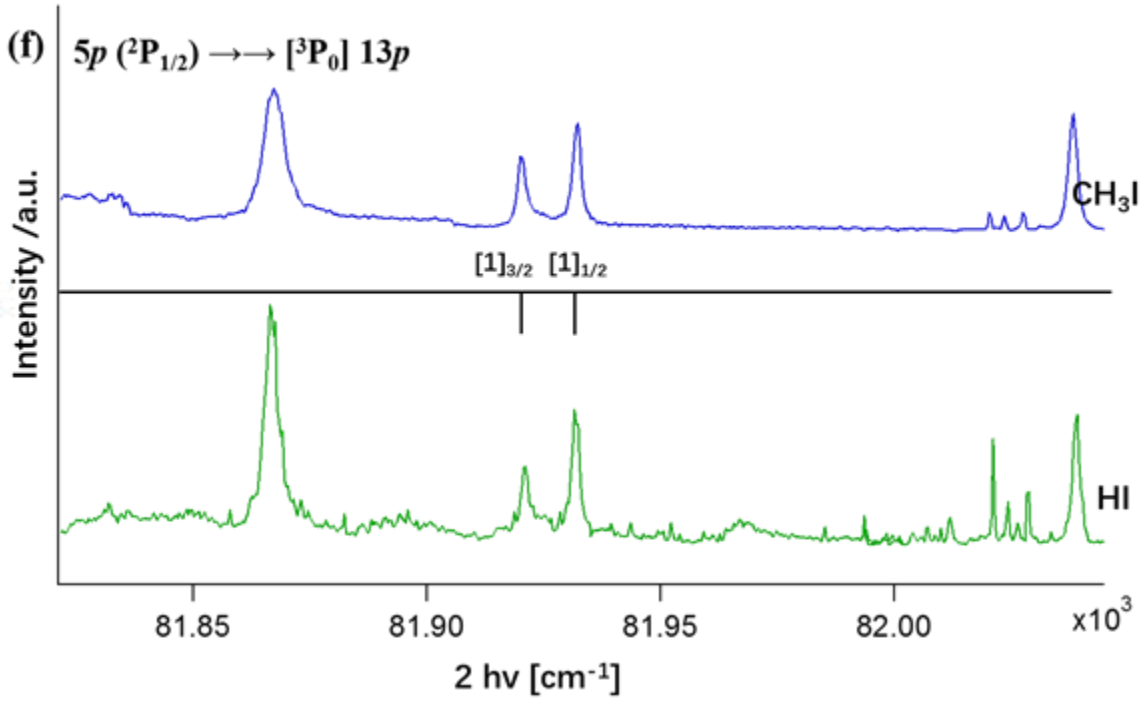
(f)
5p (²P1/2) →→ [³P0] 13p
Intensity /a.u.
CH3I
[1]3/2 [1]1/2
HI
81.85
81.90
81.95
82.00
x10³
2 hv [cm⁻¹]

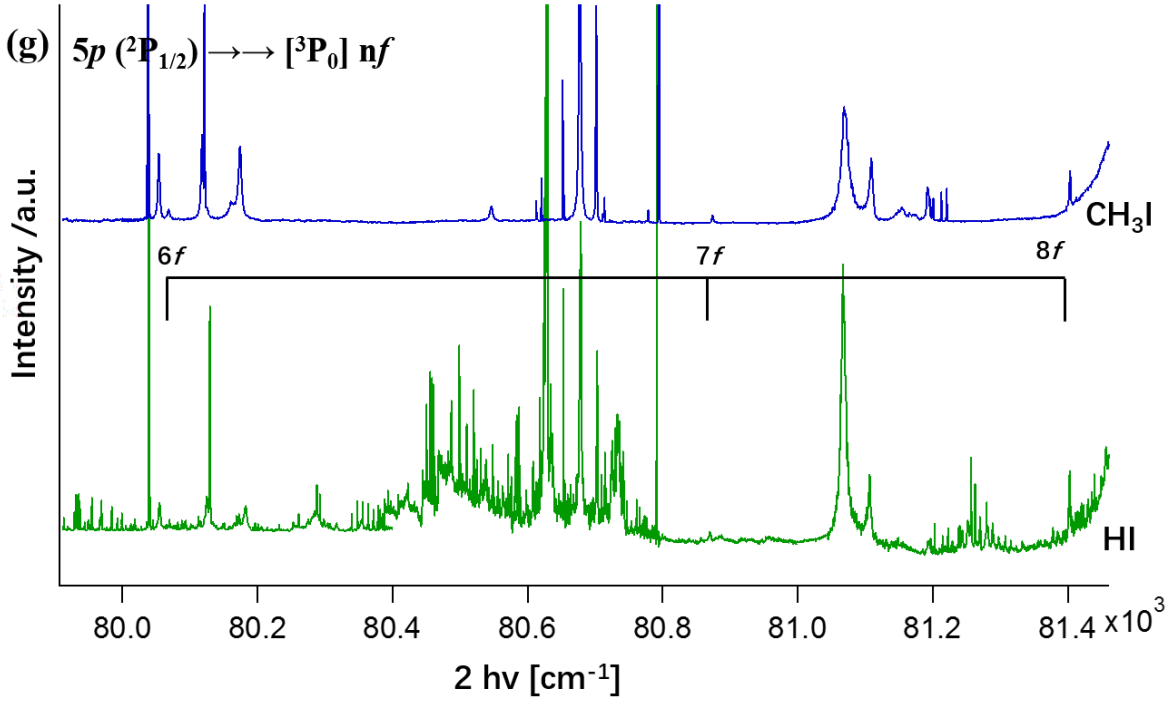
(g)
5p (²P1/2) →→ [³P0] nf
Intensity /a.u.
CH3I
6f
7f
8f
HI
80.0
80.2
80.4
80.6
80.8
81.0
81.2
81.4
x10³
2 hv [cm⁻¹]

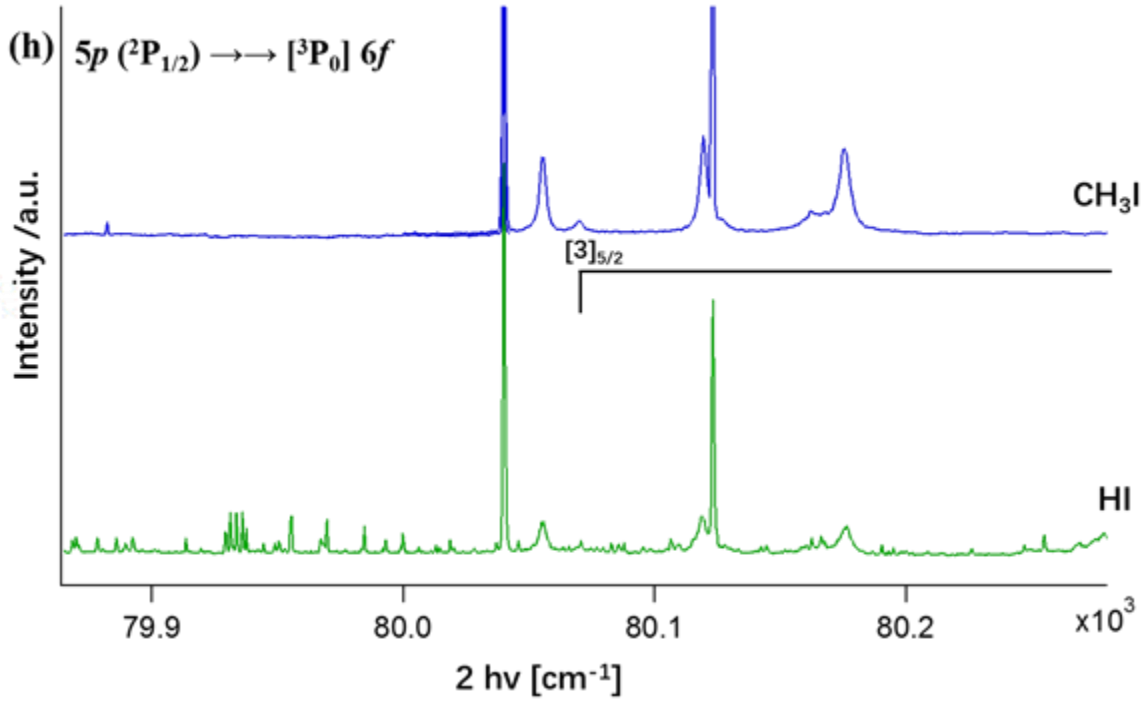
(h)
5p (²P1/2) →→ [³P0] 6f
Intensity /a.u.
CH3I
[3]5/2
HI
79.9
80.0
80.1
80.2
x10³
2 hv [cm⁻¹]

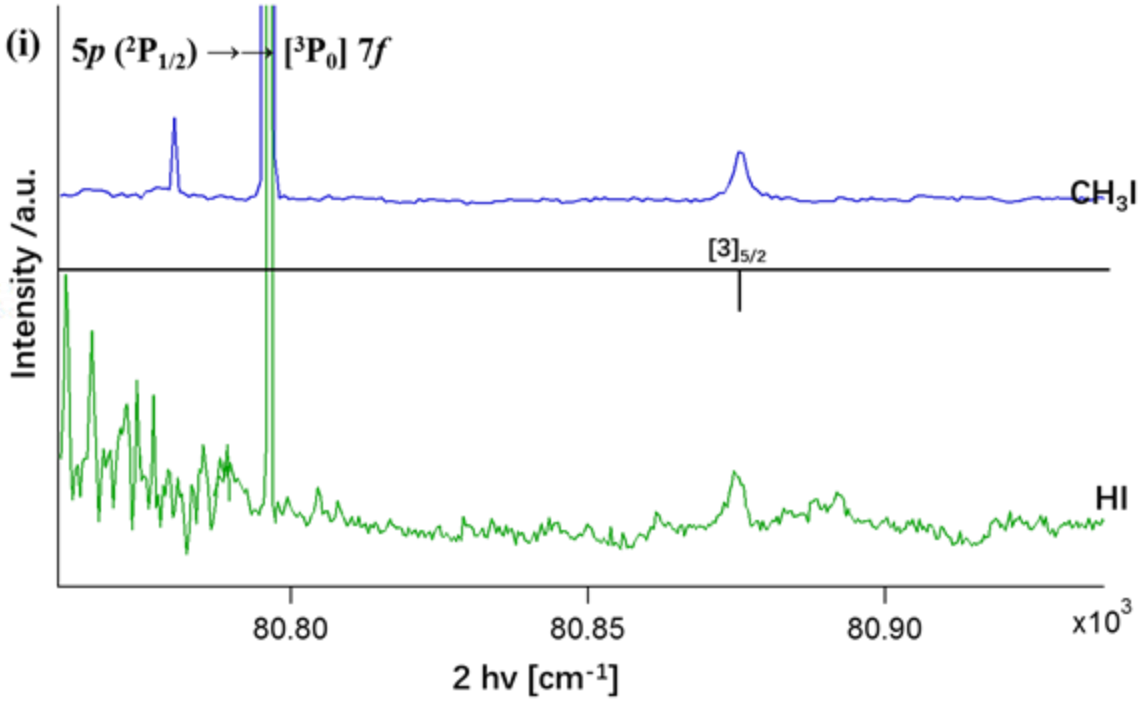
(i)
5p (²P1/2) →→ [³P0] 7f
Intensity /a.u.
CH3I
[3]5/2
HI
80.80
80.85
80.90
x10³
2 hv [cm⁻¹]

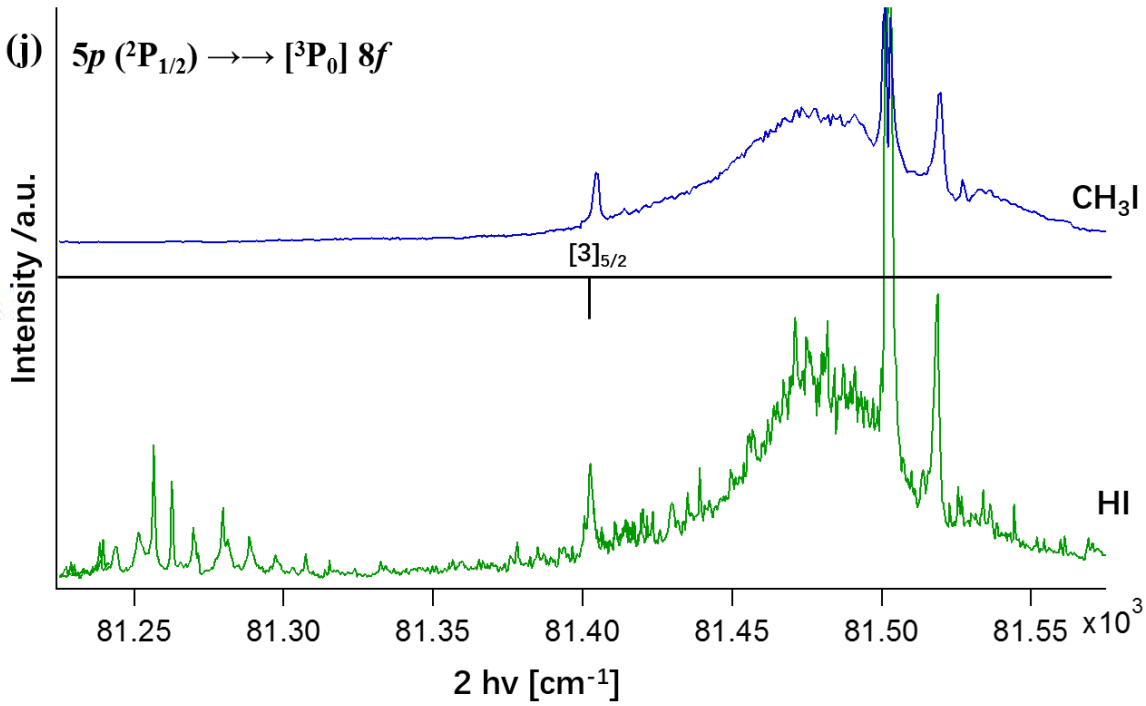
(j)
5p (²P1/2) →→ [³P0] 8f
Intensity /a.u.
CH3I
[3]5/2
HI
81.25
81.30
81.35
81.40
81.45
81.50
81.55
x10³
2 hv [cm⁻¹]

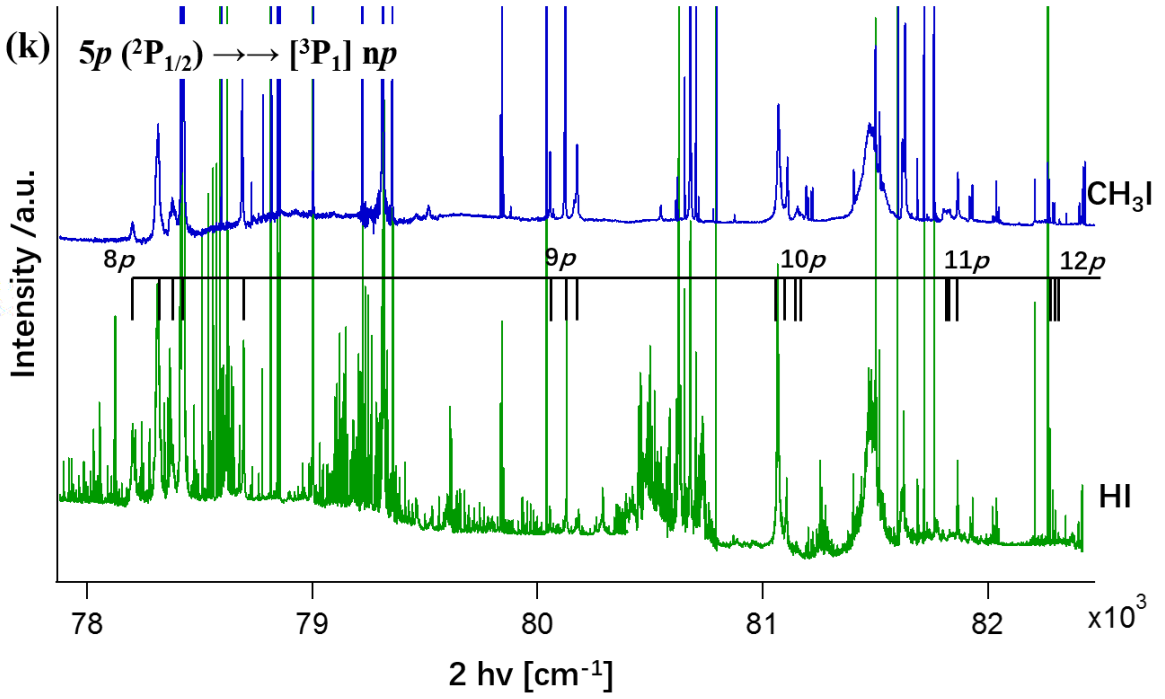
(k)
5p (²P1/2) →→ [³P1] np
Intensity /a.u.
CH3I
HI
8p
9p
10p
11p
12p
78
79
80
81
82
x10³
2 hv [cm⁻¹]

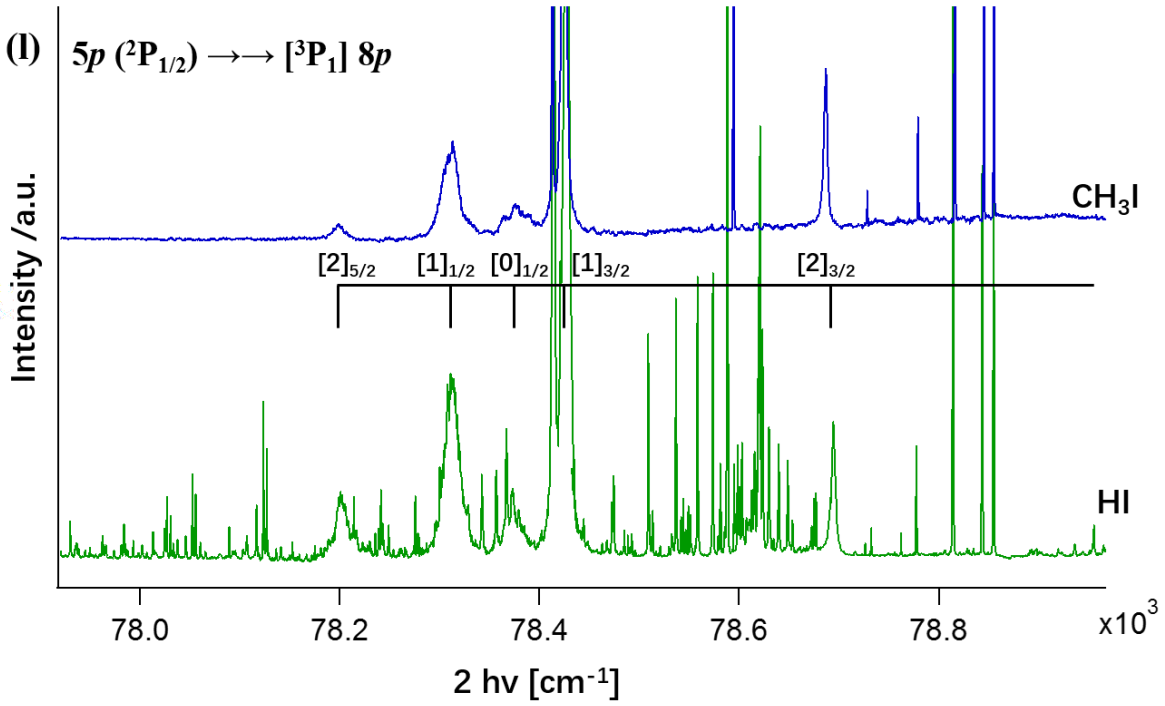
(l)
5p (²P1/2) →→ [³P1] 8p
Intensity /a.u.
CH3I
HI
[2]5/2
[1]1/2
[0]1/2
[1]3/2
[2]3/2
78.0
78.2
78.4
78.6
78.8
x10³
2 hv [cm⁻¹]

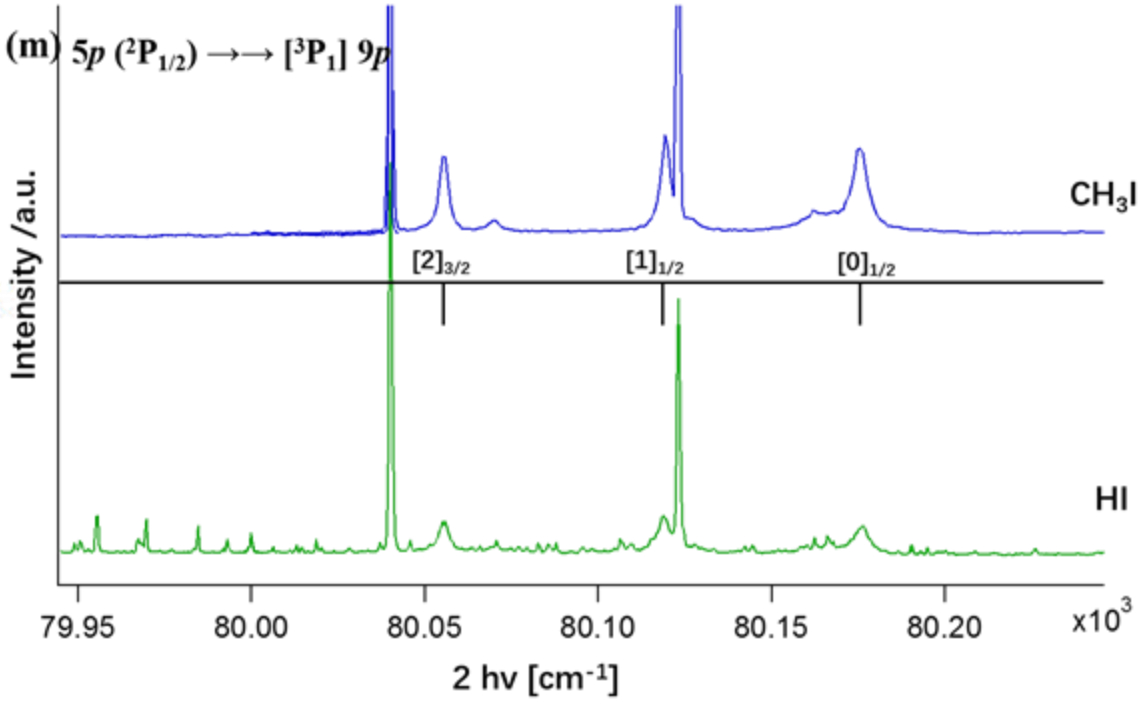
(m) 5p (²P1/2) →→ [³P1] 9p
Intensity /a.u.
CH3I
[2]3/2
[1]1/2
[0]1/2
HI
79.95
80.00
80.05
80.10
80.15
80.20
x10³
2 hv [cm⁻¹]

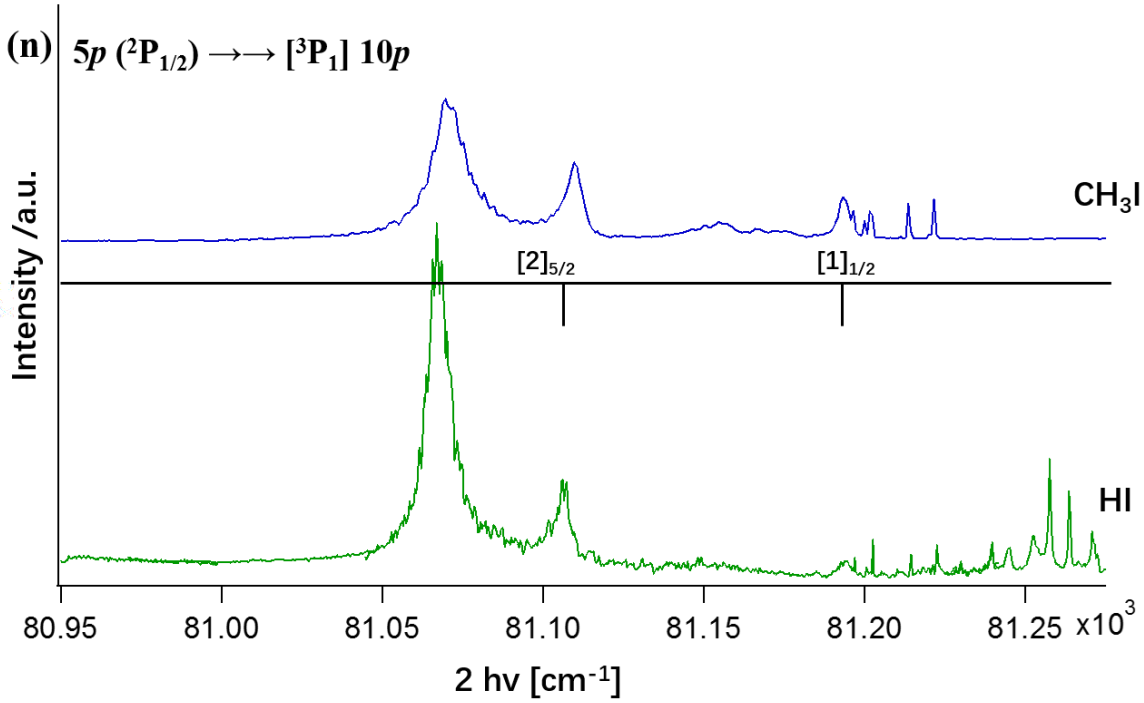
(n) 5p (²P1/2) →→ [³P1] 10p
Intensity /a.u.
CH3I
[2]5/2
[1]1/2
HI
80.95
81.00
81.05
81.10
81.15
81.20
81.25
x10³
2 hv [cm⁻¹]

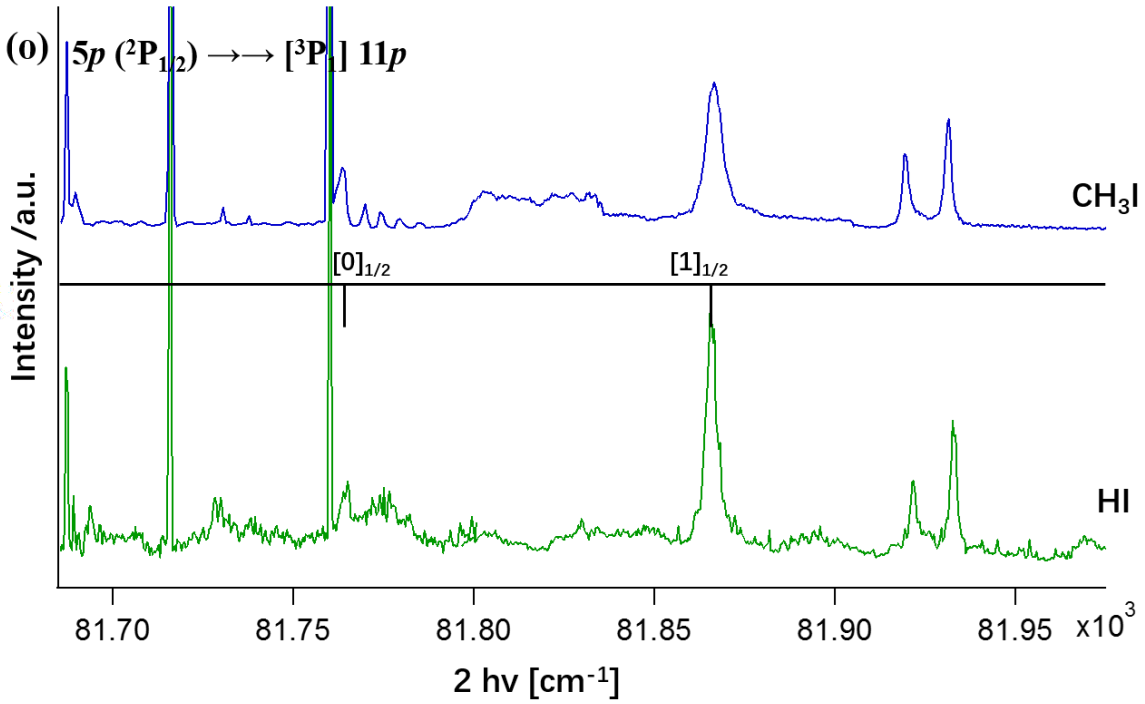
(o) 5p (²P1/2) →→ [³P1] 11p
Intensity /a.u.
CH3I
HI
[0]1/2
[1]1/2
81.70
81.75
81.80
81.85
81.90
81.95
x10³
2 hv [cm⁻¹]

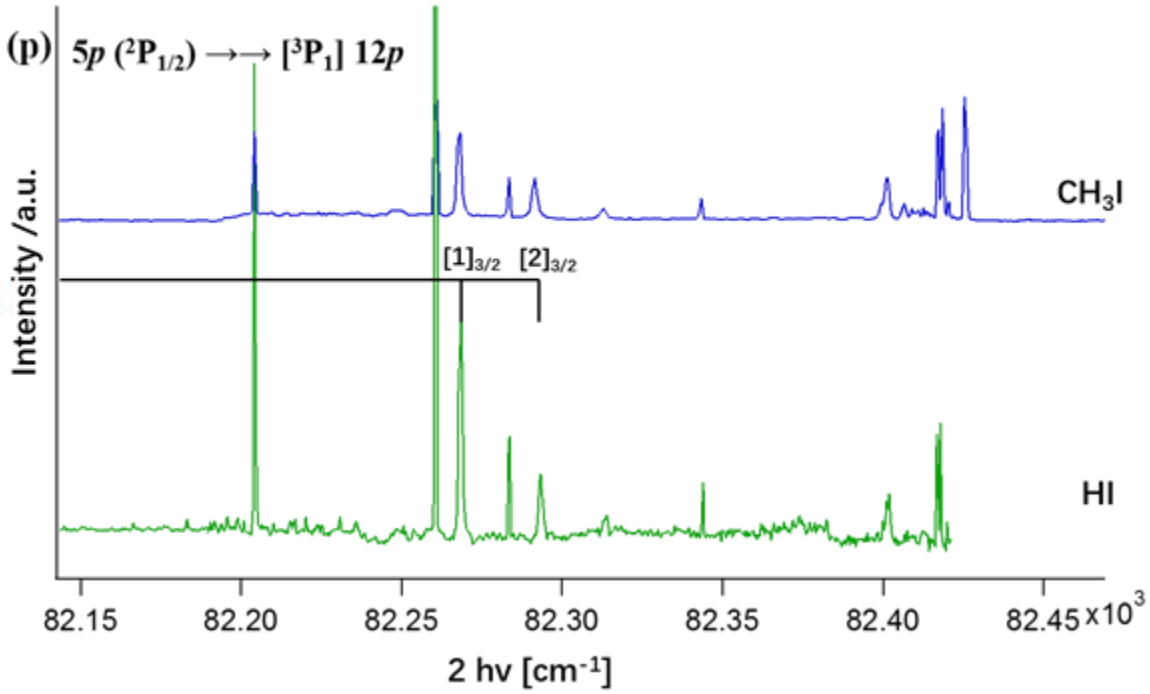
(p) 5p (²P1/2) →→ [³P1] 12p
Intensity /a.u.
CH3I
HI
[1]3/2
[2]3/2
82.15
82.20
82.25
82.30
82.35
82.40
82.45
x10³
2 hv [cm⁻¹]

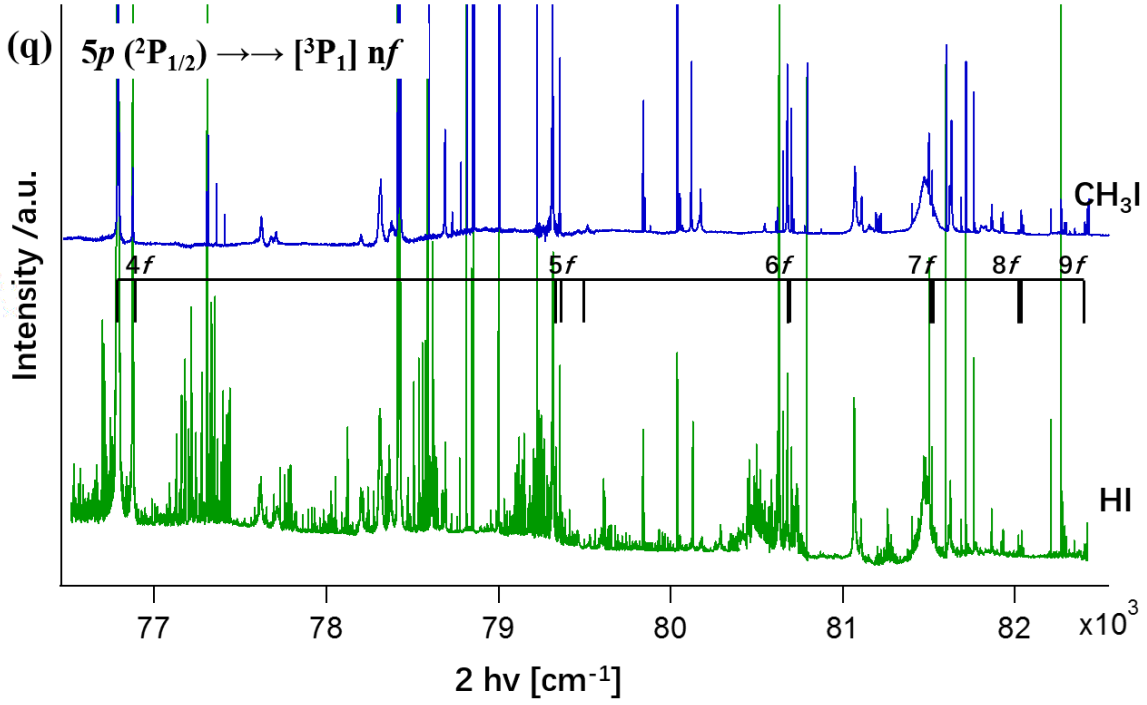
(q)
5p (²P1/2) →→ [³P1] nf
Intensity /a.u.
CH3I
HI
4f
5f
6f
7f
8f
9f
77
78
79
80
81
82
x10³
2 hv [cm⁻¹]

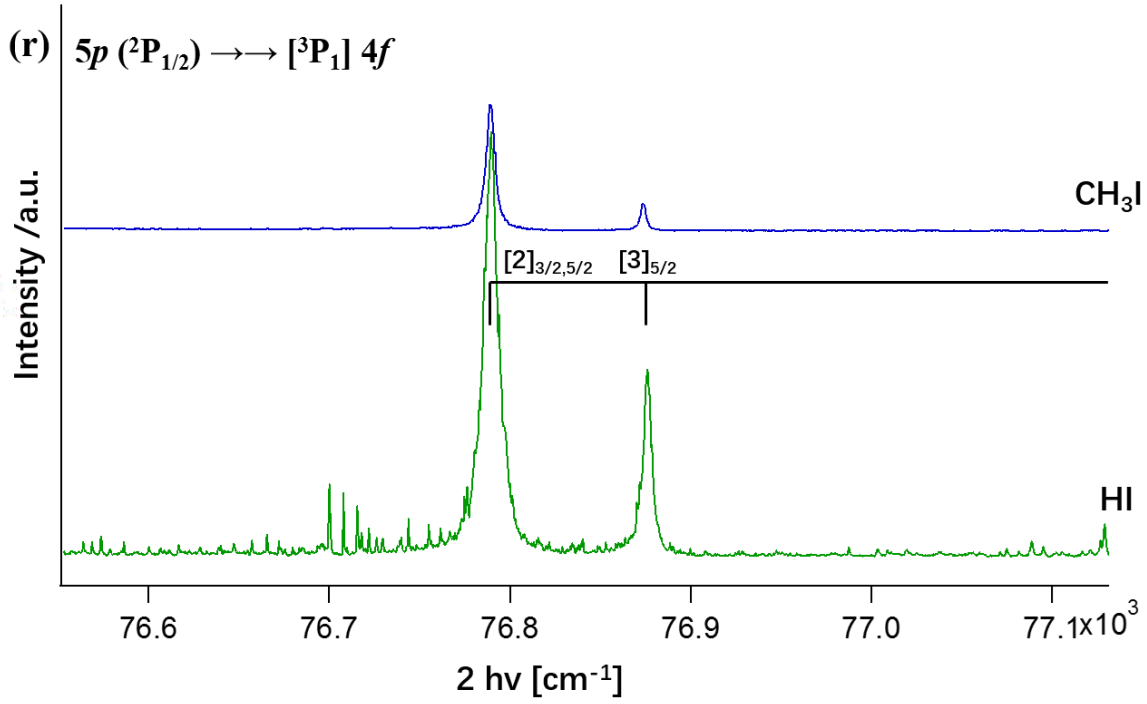
(r)
5p (²P1/2) →→ [³P1] 4f
Intensity /a.u.
CH3I
HI
[2]3/2,5/2
[3]5/2
76.6
76.7
76.8
76.9
77.0
77.1
x10³
2 hv [cm⁻¹]

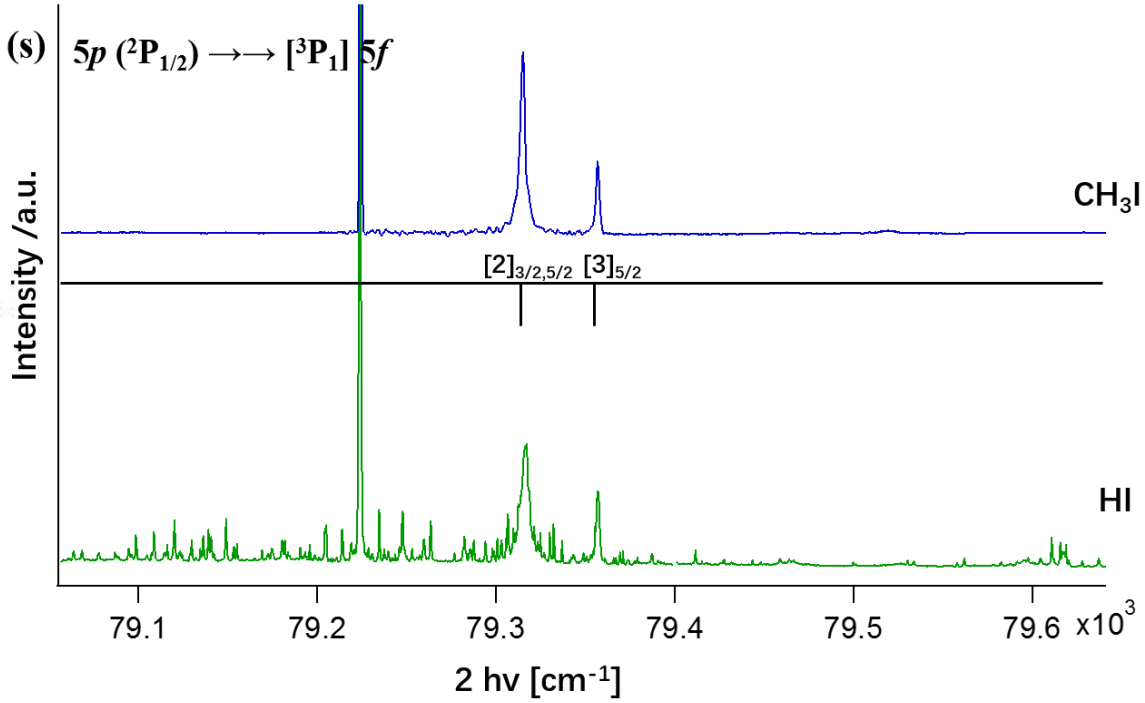
(s)
5p (²P1/2) →→ [³P1] 5f
Intensity /a.u.
CH3I
[2]3/2,5/2
[3]5/2
HI
79.1
79.2
79.3
79.4
79.5
79.6
x10³
2 hv [cm⁻¹]

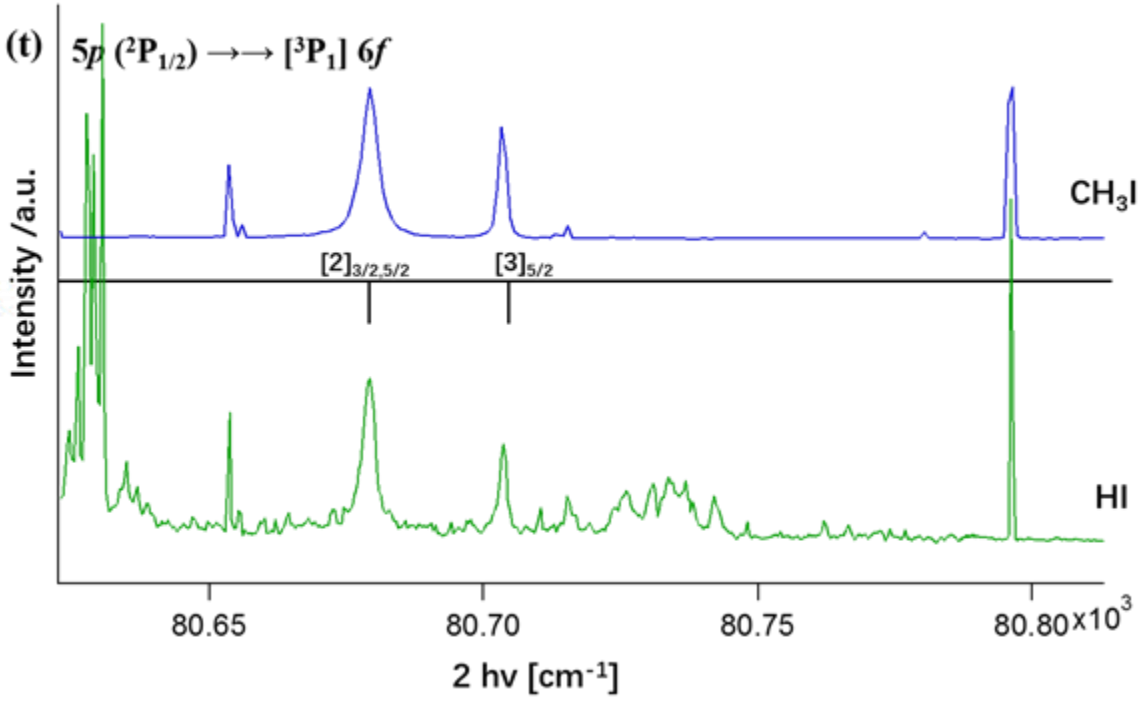
(t)
5p (²P1/2) →→ [³P1] 6f
Intensity /a.u.
CH3I
[2]3/2,5/2
[3]5/2
HI
80.65
80.70
80.75
80.80
x10³
2 hv [cm⁻¹]

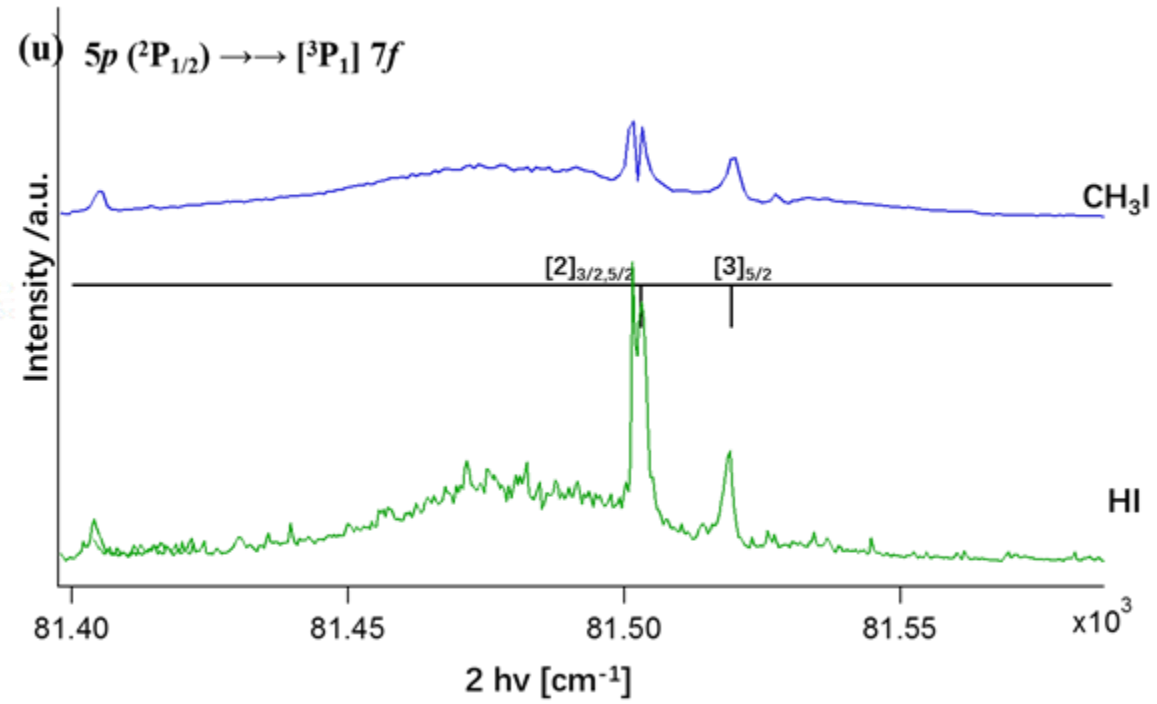
(u) 5p (²P1/2) →→ [³P1] 7f
Intensity /a.u.
CH3I
[2]3/2,5/2
[3]5/2
HI
81.40
81.45
81.50
81.55
x10³
2 hv [cm⁻¹]

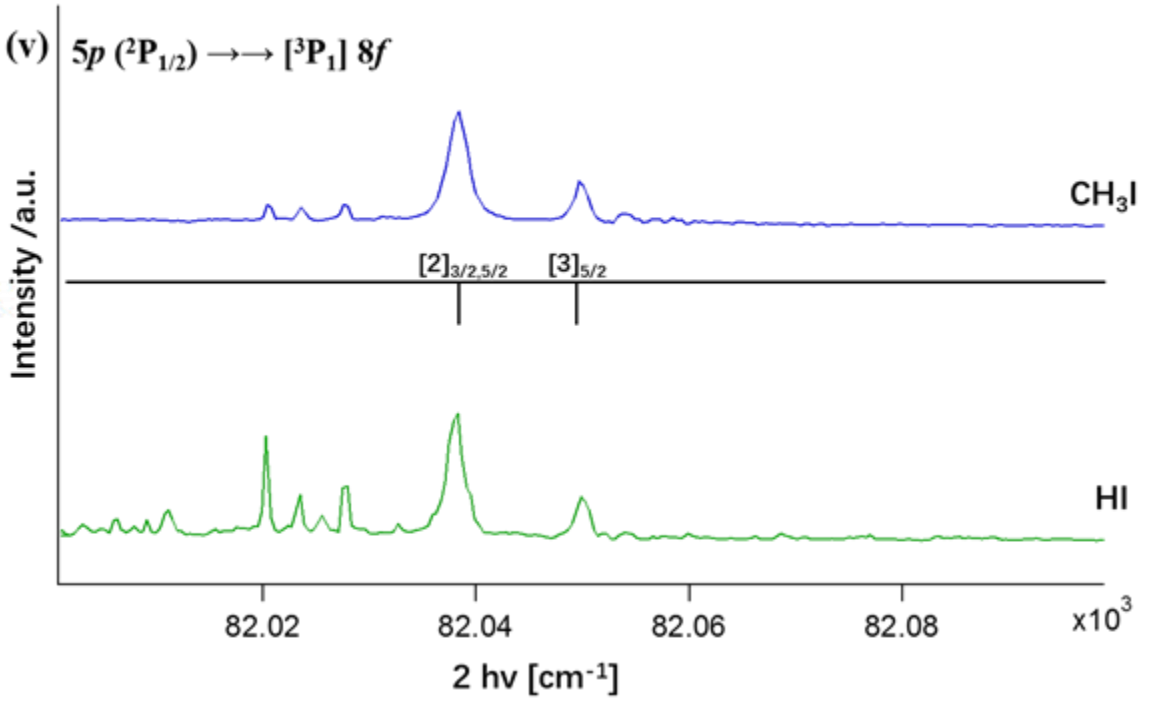
(v) 5p (²P1/2) →→ [³P1] 8f
Intensity /a.u.
CH3I
[2]3/2,5/2
[3]5/2
HI
82.02
82.04
82.06
82.08
x10³
2 hv [cm⁻¹]

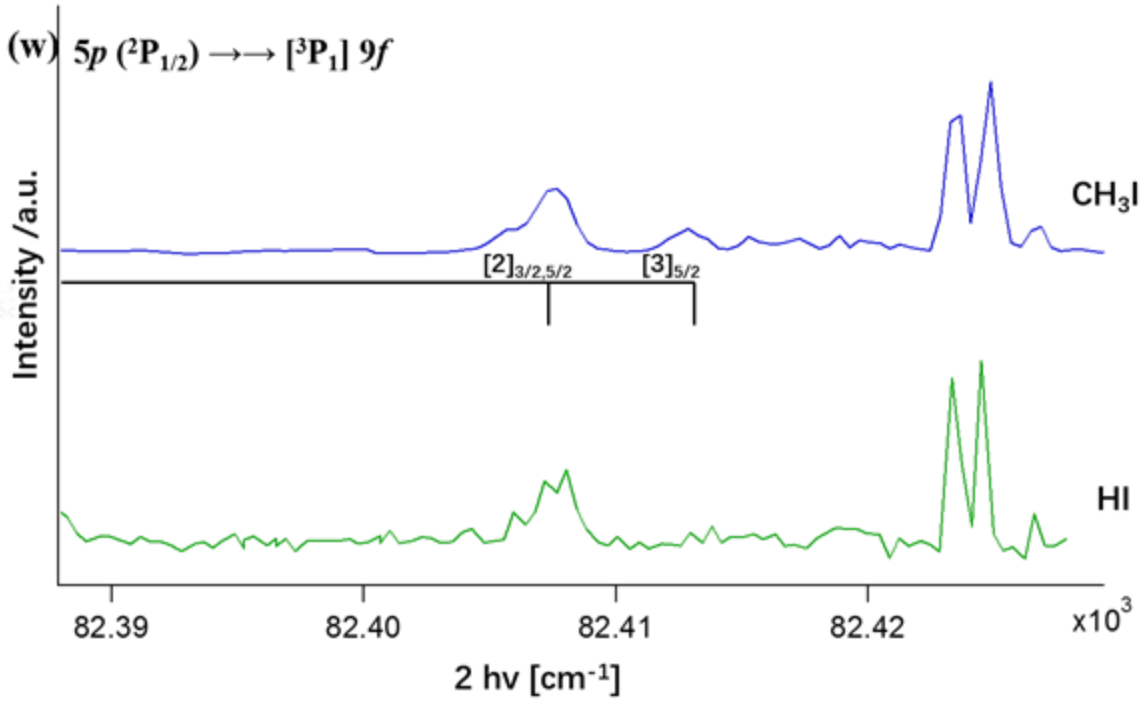
(w) 5p (²P1/2) →→ [³P1] 9f
Intensity /a.u.
CH3I
HI
[2]3/2,5/2
[3]5/2
82.39
82.40
82.41
82.42
x10³
2 hv [cm⁻¹]

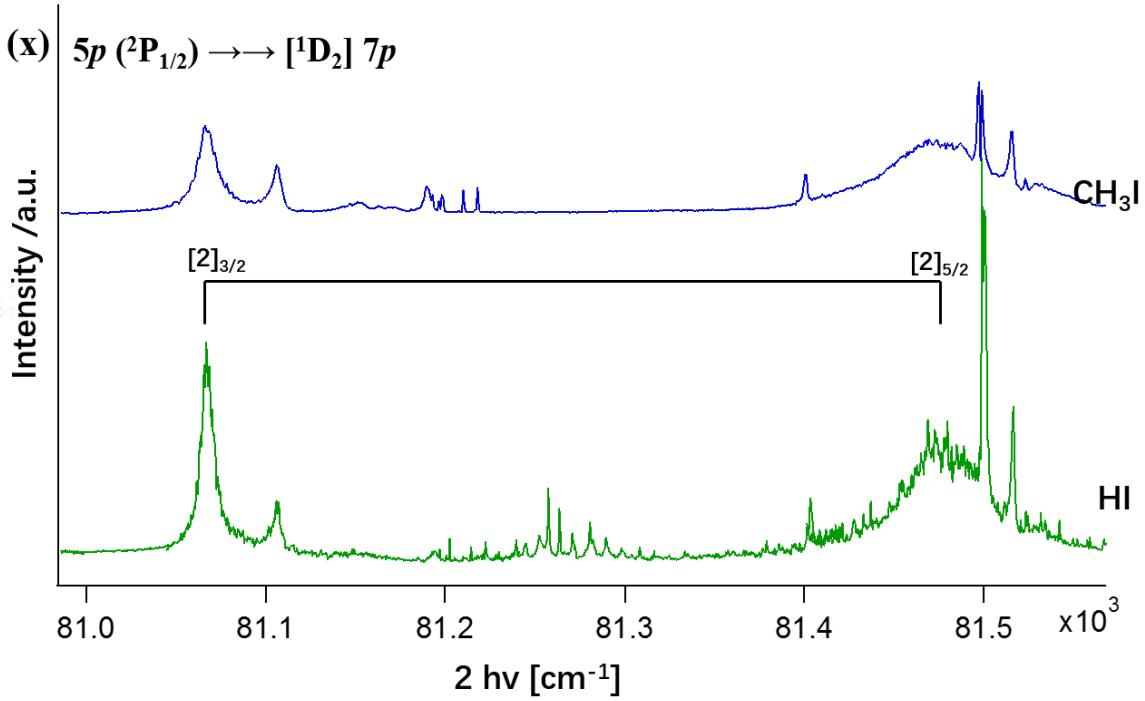
(x) 5p (²P1/2) →→ [¹D2] 7p
Intensity /a.u.
CH3I
HI
[2]3/2
[2]5/2
81.0
81.1
81.2
81.3
81.4
81.5
x10³
2 hv [cm⁻¹]

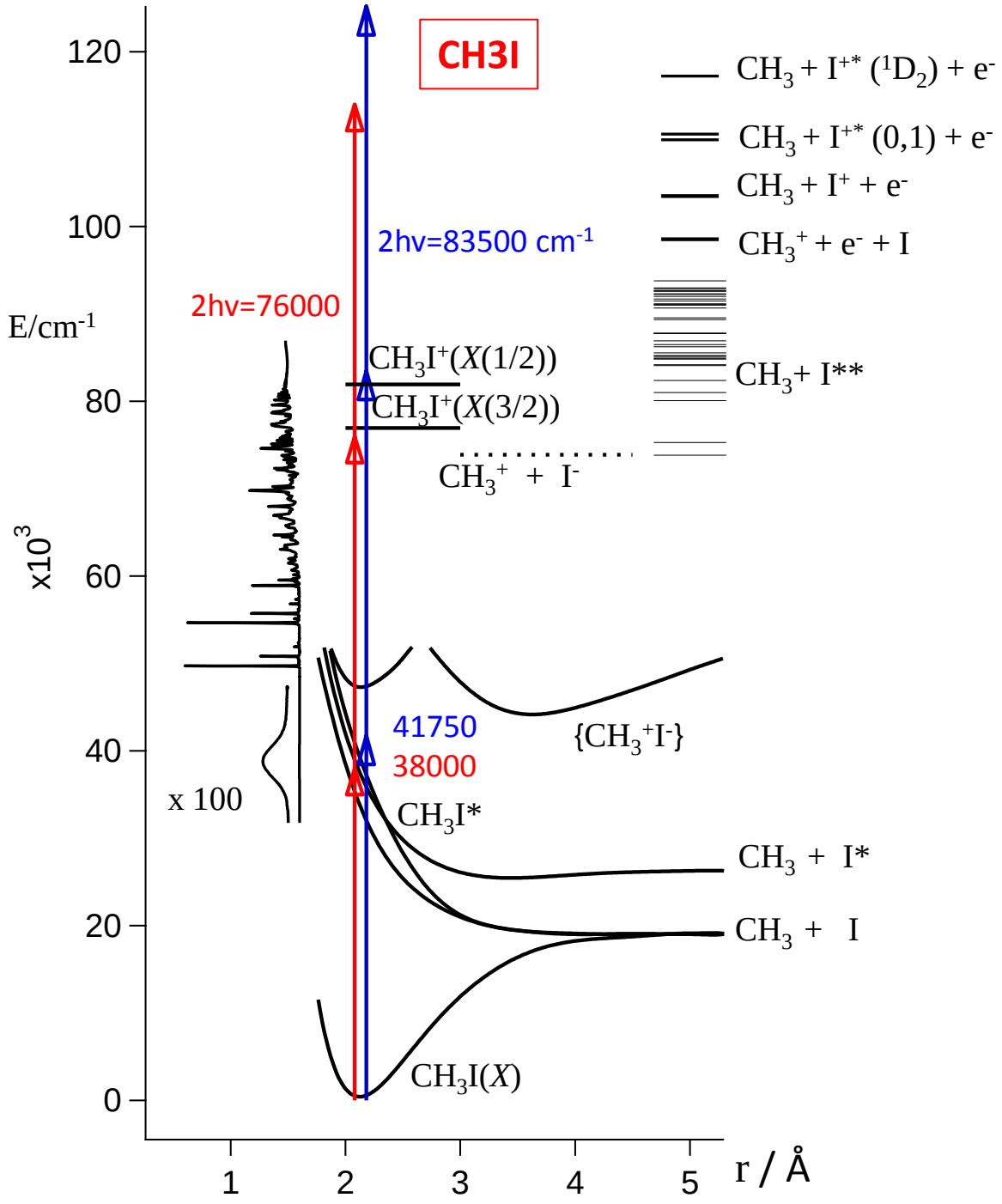

Sig. S3a: *Energetics and excitations vs. absorption spectra for CH_3I: Potential energy curves for the ground state ($CH_3I(X)$), A-band repulsive states (CH_3I^*: $^3Q_1$, $^1Q_1$, $^3Q_0$), the lowest energy Rydberg state (CH_3I^{**}) and an ion-pair state ($CH_3^+I^-$) derived from reference 1 and energy thresholds. Arrows indicate photoexcitations as marked ($1h\nu$ = 38 000 cm^{-1}, red color; $1h\nu$ = 41 750 cm^{-1}, blue color). The absorption spectrum for CH_3I from reference 2 is inserted and rotated to the left.*

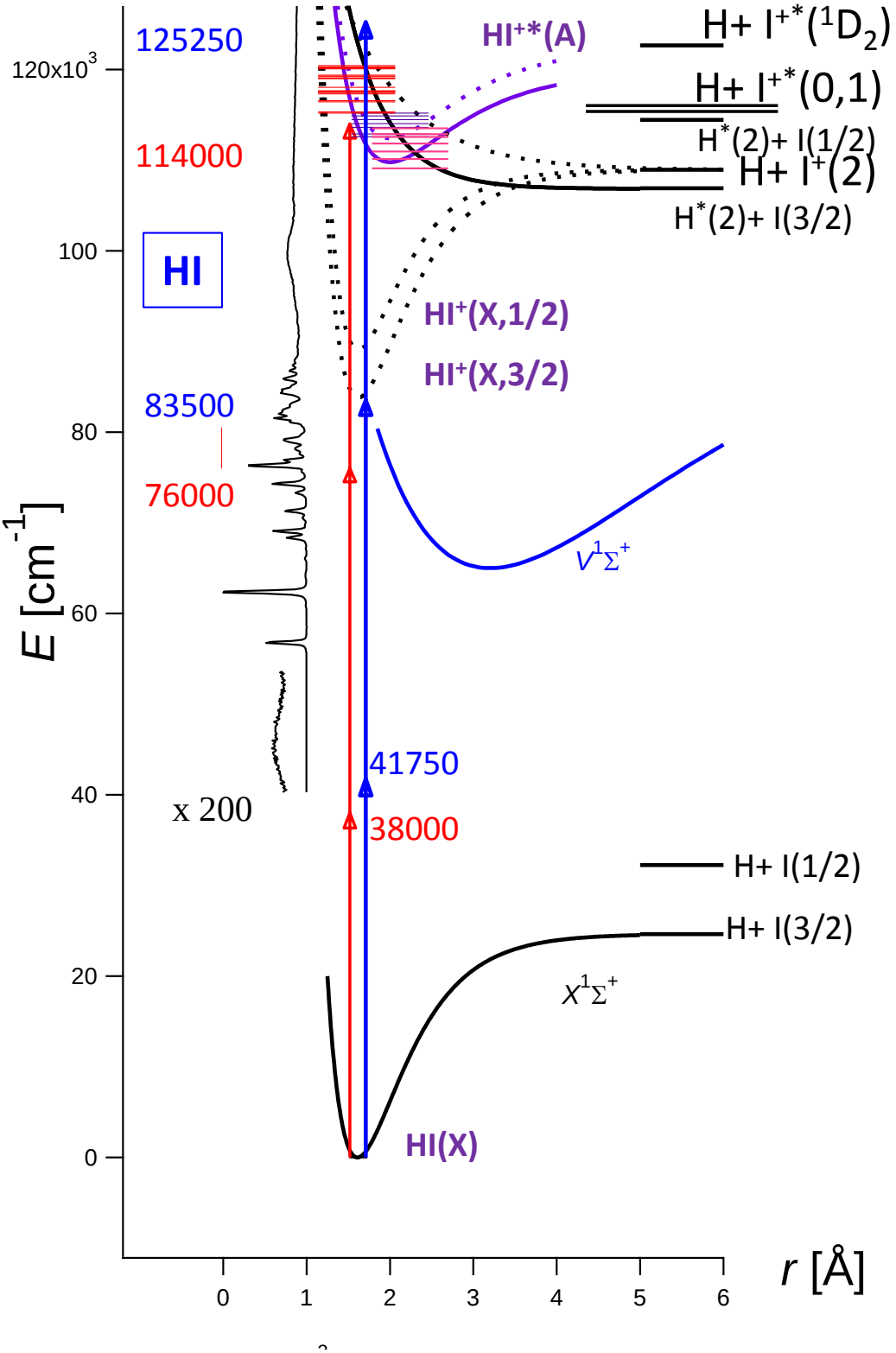

Sig. S3b: *Energetics and excitations vs. absorption spectra for HI: Potential energy curves for the ground state (HI(X)), the ion-pair state (V), the ionic states[3] and energy thresholds are shown. Arrows indicate photoexcitations as marked ($1h\nu$ = 38 000 cm^{-1} , red color; $1h\nu$ = 41 750 cm^{-1} , blue color). The absorption spectrum for HI from reference 4 is inserted and rotated to the left.*

Tables:

Table S1: Laser power dependence of I^+ formation for iodine atomic lines: Number of photons (n) required to form I^+ in in multiphoton ionization of HI: Line specifications, line positions ($2h\nu(cm^{-1})$), Excited atomic state ($I^{\#}$) energies (E_T (cm^{-1}) and n values (see main text).

#	Core & Ryd el	K	J	$2h\nu$ (cm^{-1})	E_T (cm^{-1})	n (real numbers)	n (integer numbers)
1	$5s^25p^4$ **[$^3P_1$]** 4*f*	[2]	3/2,5/2	76 787.7	84 390.6	2.51	**3**
2	$5s^25p^4$ **[$^3P_1$]** 4*f*	[3]	5/2	76 875.3	84 478.2	2.63	**3**
3	$5s^25p^4$ **[$^3P_0$]** 8*p*	[1]	1/2	77 621.2	85 224.1	2.44	**2**
4	$5s^25p^4$ **[$^3P_0$]** 8*p*	[1]	3/2	77 708.2	85 311.1	2.89	**3**
5	$5s^25p^4$ **[$^3P_1$]** 8*p*	[2]	5/2	78 200.4	85 803.3	3.22	**3**
6	$5s^25p^4$ **[$^3P_1$]** 8*p*	[0]	1/2	78 377.4	85 980.3	3.55	**4**
7	$5s^25p^4$ **[$^3P_1$]** 8*p*	[1]	3/2	78 425.7	86 028.6	3.13	**3**
8	$5s^25p^4$ **[$^3P_1$]** 8*p*	[2]	3/2	78 690.8	86 293.7	3.06	**3**
9	$5s^25p^4$ **[$^3P_1$]** 5*f*	[2]	3/2,5/2	79 315.6	86 918.5	2.87	**3**
10	$5s^25p^4$ **[$^3P_1$]** 5*f*	[3]	5/2	79 357.2	86 960.1	2.89	**3**
11	$5s^25p^4$ **[$^3P_0$]** 9*p*	[1]	1/2	79 461.8	87 064.7	3.08	**3**
12	$5s^25p^4$ **[$^3P_0$]** 9*p*	[1]	3/2	79 516.1	87 119.0	3.33	**3**
13	$5s^25p^4$ **[$^3P_1$]** 9*p*	[2]	3/2	80 055.2	87 658.1	3.08	**3**
14	$5s^25p^4$ **[$^3P_1$]** 9*p*	[1]	1/2	80 119.4	87 722.3	3.54	**4**
15	$5s^25p^4$ **[$^3P_1$]** 9*p*	[0]	1/2	80 175.6	87 778.5	3.34	**3**

Table S2. I atom (2 + 1) REMPI lines for resonant excitation to $I^{\#}$ [$^{2S+1}L_{Jc}$] *nl* [K]$_J$ and two new lines for I[$^3P_2$] np [1]$_{3/2}$; n = 10,11(see main text) for MPI of CH_3I and HI: Assignments, line positions (cm^{-1}), δ-values and line widths (FWHM (cm^{-1})) and references.**

Core	*nl*	K	J	2hn (cm-1)	δ	FWHM	Reference
(^{3P2})	4f	[4]	7/2,	77304.8	0.04	0.517	a , b
(^{3P2})	4f	[3]	7/2,	77311.6	0.04	0.554	a , b
(^{3P2})	4f	[2]	5/2,	77360.8	0.02	0.632	a , b
(^{3P2})	4f	[1]	1/2,	77406.0	0.01	0.490	a , b
(^{3P2})	4f	[1]	3/2,	77408.4	0.01	0.604	a , b
(^{3P2})	5f	[4]	7/2,	79833.2	0.04	0.547	a , b
(^{3P2})	5f	[2]	3/2,	79835.2	0.04	0.542	a , b
(^{3P2})	5f	[2]	5/2,	79840.4	0.04	0.587	a , b
(^{3P2})	5f	[3]	5/2,	79844.4	0.03	0.536	a , b
(^{3P2})	5f	[3]	7/2,	79847.6	0.03	0.591	a , b
(^{3P2})	5f	[1]	3/2,	79880.0	0.01	0.653	a , b
(^{3P2})	6f	[4]	7/2,	81197.3	0.05	0.594	a , b
(^{3P2})	6f	[3]	5/2,	81200.8	0.04	0.597	a , b
(^{3P2})	6f	[3]	7/2,	81202.4	0.04	0.755	a , b
(^{3P2})	6f	[2]	3/2,	81212.0	0.03	0.795	a , b
(^{3P2})	6f	[2]	5/2,	81214.4	0.03	0.742	a , b
(^{3P2})	6f	[1]	1/2,	81220.8	0.03	0.957	a , b
(^{3P2})	6f	[1]	3/2,	81222.4	0.02	0.520	a , b
(^{3P2})	7f	[4]	7/2,	82020.4	0.05	0.637	a , b
(^{3P2})	7f	[3]	7/2,	82023.6	0.05	0.790	a , b
(^{3P2})	7f	[2]	3/2,	82027.6	0.04	0.813	a , b
(^{3P2})	8f	[2]	5/2,	82568.3	0.03	1.186	a , b
(^{3P2})	8f	[1]	3/2,	82571.2	0.02	1.408	a , b
(^{3P2})	8d	[2]	3/2,	80780.4	2.41	0.768	a , b
(^{3P2})	8d	[2]	5/2,	80876.1	2.33	1.837	a , b
(^{3P2})	9d	[1]	3/2,	81731.4	2.46	---	a , b
(^{3P2})	9d	[1]	1/2,	81738.6	2.45	---	a , b
(^{3P2})	10d	[3]	7/2,	82289.7	2.60	---	a , b
(^{3P2})	8p	[2]	5/2,	78729.2	3.56	0.643	a , b

(^{3P2})	8p	[1]	1/2,	78780.0	3.54	0.804	a , b
(^{3P2})	8p	[2]	3/2,	78816.8	3.52	0.735	a , b
(^{3P2})	8p	[3]	7/2,	78846.0	3.51	0.662	a , b
(^{3P2})	8p	[3]	5/2,	78856.0	3.51	0.686	a , b
(^{3P2})	8p	[1]	3/2,	79221.2	3.35	0.873	a , b
(^{3P2})	9p	[2]	3/2,	80614.4	3.54	0.947	a , b
(^{3P2})	9p	[2]	5/2,	80622.4	3.53	0.601	a , b
(^{3P2})	9p	[3]	5/2,	80653.6	3.51	0.765	a , b
(^{3P2})	9p	[3]	7/2,	80656.0	3.51	0.574	a , b
(^{3P2})	9p	[1]	1/2,	80715.4	3.46	0.814	a , b
($^{3}P_{2}$)	9p	[1]	3/2	80796.5	3.40	1.351	a , b
($^{3}P_{2}$)	10*p*	[3]	5/2	81688.1	3.51	0.809	a , b
($^{3}P_{2}$)	10*p*	[3]	7/2	81690.5	3.51	2.104	a , b
($^{3}P_{2}$)	10*p*	[1]	3/2	81761.1	3.42	1.017	a
($^{3}P_{2}$)	11*p*	[3]	5/2	82348.8	3.49	1.109	a , b
($^{3}P_{2}$)	11*p*	[1]	3/2	82423.2	3.34	0.989	a

a: This work b: Reference 5 c: Reference 6

Table S3. I atom (2 + 1) REMPI lines for resonant excitation to $I^{\#}$ [$^{2S+1}L_{Jc}$] nl $[K]_J$ ($^{2S+1}L_{Jc}$ = $^3P_{0,1}$, $^1D_2$) for MPI of CH_3I and HI:
Assignments (Core terms, nl, K, J), line positions (2hν(cm^{-1})), quantum defect parameters (δ), line widths (FWHM (cm^{-1})) and references.

Core	*nl*	K	J	2hν (cm^{-1})	δ	FWHM	Reference
[$^3P_0$]	7*p*	[1]	1/2	81 603.2	3.54	0.71	a , b , c
[$^3P_0$]	7*p*	[1]	3/2	81 717.0	3.51	0.71	a , b , c
[$^3P_1$]	7*p*	[0]	1/2	81 501.7	3.55	1.31	a , b , c
[$^3P_1$]	7*p*	[2]	5/2	82 210.4	3.54	0.69	a , b , c
[$^3P_1$]	7*p*	[1]	3/2	82 424.8	3.50	0.72	a , b , c
[$^3P_1$]	7*p*	[2]	3/2	82 431.6	3.50	1.08	a , b , c
[$^3P_1$]	7*p*	[1]	1/2	82 615.6	3.46	0.68	a , b , c
[$^1D_2$]	6*p*	[1]	3/2	78 413.6	3.63	0.86	a , b , c
[$^1D_2$]	6*p*	[3]	5/2	78 595.2	3.62	1.05	a , b , c
[$^1D_2$]	6*p*	[3]	7/2	79 002.8	3.60	1.27	a , b , c
[$^1D_2$]	6*p*	[2]	3/2	80 040.0	3.53	1.02	a , b , c
[$^1D_2$]	6*p*	[2]	5/2	80 123.4	3.52	1.09	a , b , c
[$^1D_2$]	6*p*	[1]	1/2	82 267.3	3.36	1.33	a

a: This work b: Reference 5 c: Reference 6

Table S4. Iodine atomic lines of unknown origin / unassigned.

2hν (cm^{-1})	FWHM
80 780.4	0.768
80 876.1	1.837
81 731.4	---
81 738.6	---
82 289.7	---
82 426.8	0.73

Table S5. Typical equipment and condition parameters for REMPI experiments.

Sample	HI gas (Matheson gas products inc.)	CH_3I liquid Fluka, ≥99.0% Sigma-Aldrich chemie Gmbh
Pump lasers	Lambda Physik COMPex 205 excimer laser,308nm	Nd:YAG laser (EKSPLA NL300 Series, 355nm
Dye laser	Coherent ScanMatePro dye laser	
Laser dyes	C540A, C503	
Frequency doubling crystal	Sirah BBO-2	
Laser repetition rate	10 Hz	
Dye laser line width	0.095 cm^{-1}	
Pulse energies	0.1-0.3 mJ/pulse	
Nozzle size	500 μm	
Sample backing pressure	2.0-2.5 bar (HI); 1 bar (CH_3I)	
Pressure inside ionization chamber	10^{-6} mbar	
Nozzle opening time	150-200 μs	
Delay time for laser excitation	450-550 μs	
Excitation wavenumber step size	0.10 cm^{-1}	
Electric field in the ionization region	500 – 1000 Vcm^{-1}	
Time of flight step size	10 ns	
Time of flight tube length	70 cm	
Focal lens distance	200 mm	

References

(1) Alekseyev, A. B.; Liebermann, H. P.; Buenker, R. J. *J. Chem. Phys.* **2007**, *126*, 11.

(2) Eden, S.; Limao-Vieira, P.; Hoffmann, S. V.; Mason, N. J. *Chemical Physics* **2007**, *331*, 232.

(3) Hróðmarsson, H. R.; Kvaran, Á. *Physical Chemistry Chemical Physics* **2015**, *17*, 32517.

(4) Brion, C. E.; Dyck, A.; Cooper, G. *Journal of Electron Spectroscopy and Related Phenomena* **2005**, *144*, 127.

(5) *NIST Chemistry WebBook*; NIST (National Institute of Standards and Technology) Chemistry WebBook.

(6) Minnhagen, L. *Arkiv för Fysik* **1962**, *21*, 415.

4.5 Paper 5

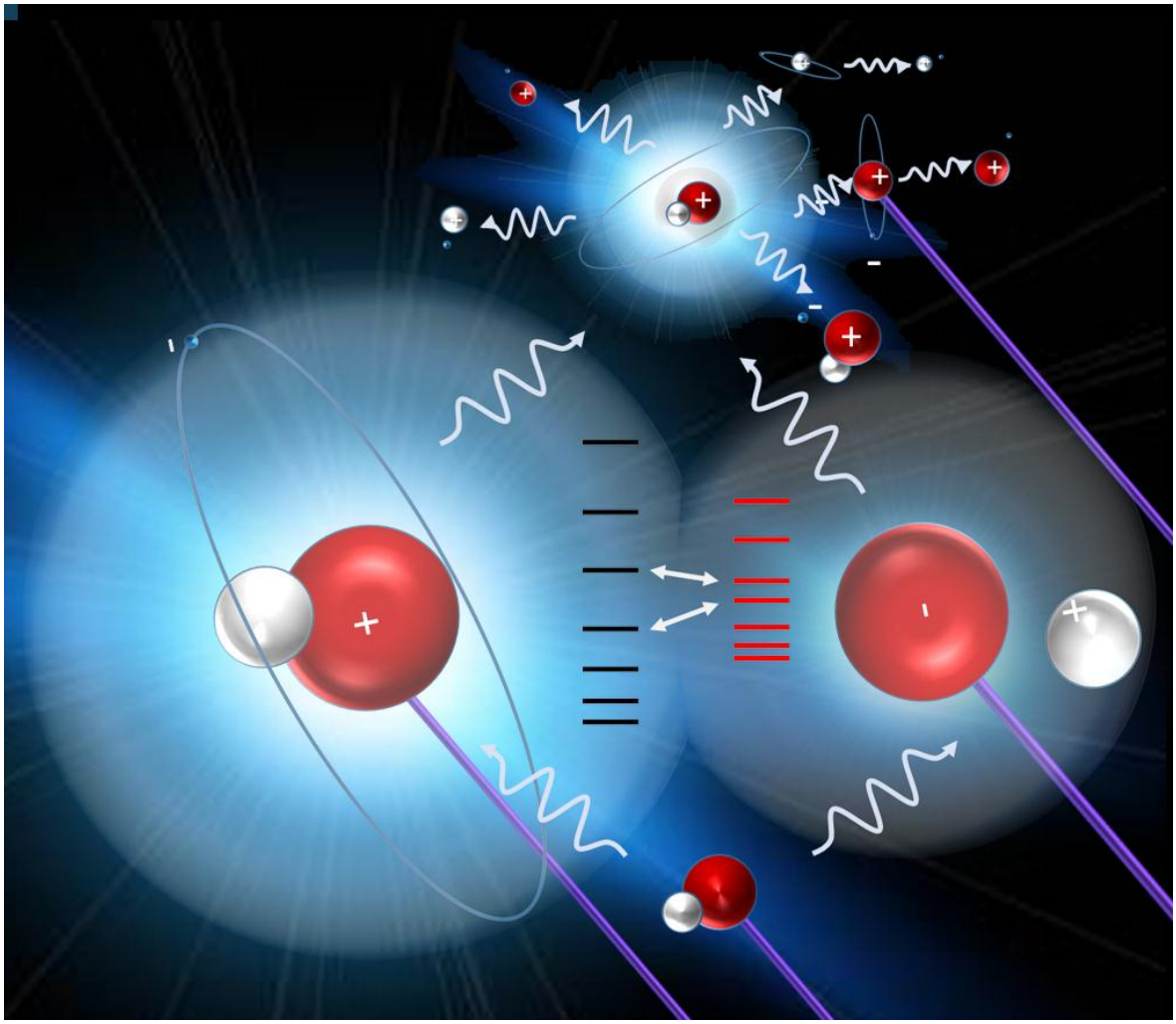

Meng-Xu Jiang and Ágúst Kvaran, *High energy state interactions, energetics and multiphoto-fragmentation processes of HI*, Physical Chemistry *Chem.Phys* (PCCP)**,** **24**, 6676 - 6689, (**2022**).

DOI: 10.1039/D1CP05714F

PCCP

ROYAL SOCIETY OF CHEMISTRY

PAPER

Cite this: *Phys. Chem. Chem. Phys.*, 2022, **24**, 6676

High energy state interactions, energetics and multiphoto-fragmentation processes of HI†

Meng-Xu Jiang and Ágúst Kvaran *

Received 14th December 2021,
Accepted 14th February 2022

DOI: 10.1039/d1cp05714f

rsc.li/pccp

Mass resolved multiphoton ionization data for two-photon resonant excitations (REMPI) in the 69 000–79 000 cm^{-1} region were recorded for HI. REMPI spectra of fragment and molecular ions were derived from the data and analysed to obtain information relevant to the state interactions, energetics and photofragmentation processes of intermediate Rydberg and ion-pair states (HI**). Spectral perturbations observed as line shifts and intensity anomalies acted complementarily to demonstrate the effects of the state interactions. The interaction strength and character mixing of Rydberg states and Rydberg and ion-pair states of different interaction types and the states energetics were quantified by deperturbation analysis for the high energy region of 75 000–79 000 cm^{-1}, which is dense in states. Energetics of new, not previously observed, Rydberg states, detected in the lower energy excitation region of 69 000–75 000 cm^{-1} was characterized by simulation calculations. Ion intensity borrowing effects, found in the spectra of interacting states, are evidence of alterations in two-photon transition probabilities due to state mixing. Based on variations in relative spectral line intensities the major photofragmentation processes involved are proposed. These involve one-photon excitation of the intermediate states (HI**) to form repulsive superexcited states ($HI^{\#}$) followed by autoionization, dissociation, photodissociation and photoionization processes to form ions. The importance of state interactions in multiphoton-fragmentation processes is evident from the work.

I. Introduction

Hydrogen halides are ideal candidates for high energy photofragmentation, state interaction and energetics studies of molecules by spectroscopic means. This is due to their heavy (halogen atoms) *vs.* light (hydrogen) fragment particle combination which generally results in highly resolvable rotational spectral structures and a relatively clear distinction between different perturbation effects of Rydberg and valence states.[1–21] In this respect hydrogen iodide (HI), with its large iodine atom mass, is particularly interesting. A large number of Rydberg and ion-pair vibrational states (HI**) have been assigned and characterized both in absorption[21–23] and resonance enhanced multiphoton ionization (REMPI)[24–30] for the excitation energy region of about 66 000–75 000 cm^{-1}. Photofragmentation processes have been explored by mass resolved REMPI,[24–30] photoelectron spectra[31–35] and velocity map imaging (VMI)[36,37] studies.

In our previous work on mass resolved REMPI of the hydrogen halides (HCl,[38–40] HBr[38,41,42] and HI[28–31,43]) we have observed and analysed a number of spectral perturbations which appear as spectra line shifts (LS-effect), line intensity irregularities (LI-effect) or line width variations (LW-effect). These effects have been interpreted to be due to state interactions between Rydberg and ion-pair states or between different Rydberg states. The interactions involve energy level-to-level repulsion effects which forms the basis of the LS-effects and state mixing which can affect transition probabilities or changes in predissociation mechanisms, hence the lifetime, which can appear as the LI and LW-effects. Interactions between states of the same symmetry or for unaltered total electronic angular momentum quantum numbers, *i.e.* homogeneous interactions ($\Delta\Omega = 0$), are the strongest. These can appear as line shifts (LS-effects) and smooth variations in line intensities (LI-effects) and/or line widths (LW-effects) for transitions to a wide range of energy levels (off-degenerate interactions).[29,38,39,41,42] In contrast interactions between states of different symmetry/different total electronic angular momentum quantum numbers, *i.e.* heterogeneous interactions ($\Delta\Omega \neq 0$), are weaker. These characteristically appear as localized LS-, LI- and/or LW-effects corresponding to transitions to few (typically two) energy levels close in energy (near-degenerate interactions).[9,10,29–31,39,42,43] Interactions between states of different spins, such as singlet-to-triplet interactions as well as for different total electronic angular momentum quantum numbers, are particularly weak near-degenerate interactions. These characteristically only appear as weak localized LI- and/or LW-effects without any significant LS-effects.[40] Deperturbation

Science Institute, University of Iceland, Dunhagi 3, 107 Reykjavík, Iceland.
E-mail: agust@hi.is, mej7@hi.is; Web: https://notendur.hi.is/~agust/;
Tel: +354-525-4800

† Electronic supplementary information (ESI) available. See DOI: 10.1039/d1cp05714f

analyses of LS-effects have allowed the evaluation of state interaction strengths as well as zero order rotational energy parameters (B_0' and D_0'), corresponding to unperturbed states.[31,38] While analyses of LI-effects have allowed estimates of interaction strengths[9,39,40] intensity anomalies (both LI- and LW-effects) have been mainly proved to be useful for qualitative identification of state interactions.[28–31,42,43] The nature and strength of excited state interactions and mixing determine intersystem crossing, which can further affect photofragmentation processes such as photodissociation and photoionization in multiphoton excitations. Therefore, mass resolved REMPI spectral analyses in association with state interaction analyses have been proved to be useful tools for interpreting photofragmentation processes.

In this paper we present and characterize state interactions and relevant dynamics observed in mass resolved REMPI involving two-photon resonant excitations to the Rydberg and ion-pair (valence) states of HI in the high energy region of 75 000–79 000 cm^{-1}, which is dense in states and has not been explored before. This energy region is rich in the number and variety of Rydberg and ion-pair vibrational states and involves both state interactions between Rydberg and ion-pair states and between Rydberg states of different strengths, both homogeneous and heterogeneous in nature. H^+, I^+ and HI^+ REMPI spectra derived for this excitation energy region allow identification and characterization of the following four (a–d) state interactions by simultaneous analysis of line shift (LS), line intensity (LI) and line width (LW) spectral perturbation effects:

(a) $P^1\Delta_2$ [1/2]4fπ ($v' = 0$) Rydberg state ↔ $k^3\Pi_2$ [1/2]5dδ ($v' = 1$) Rydberg state, ($\Delta\Omega = 0$)

(b) $j^3\Sigma^-_{0+}$ [1/2]5dπ ($v' = 1$) Rydberg state ↔ $V^1\Sigma^+$ ($v' = m + 22$) ion-pair state, ($\Delta\Omega = 0$)

(c) $M^1\Pi_1$ [1/2]7sσ ($v' = 0$) Rydberg state ↔ $V^1\Sigma^+$ ($v' = m + 29$) ion-pair state, ($\Delta\Omega \neq 0$)

(d) $r^3\Pi_0$ [1/2]7pσ ($v' = 0$) Rydberg state ↔ $V^1\Sigma^+$ ($v' = m + 36$) ion-pair state. ($\Delta\Omega = 0$)

Furthermore, detailed exploration of the lower energy spectral region of 69 500–75 000 cm^{-1} allowed the observation and characterization of four new states to fill a gap of unidentified states in a series of HI Rydberg states.[44] All the analyses presented in this paper allowed the characterization of state energetics as well as predictions of multiphoton-fragmentation processes involved upon its excitations. Furthermore, the work demonstrates the importance of the nature of intermediate states in stepwise photoexcitations on selective fragment formation. Figures and tables that are necessary to explain the data and interpretations are included in the main text, whereas further useful supporting material can be found in the ESI (ref. 45).

II. Experimental

The experimental apparatus and equipment parameters resembled that described in previous publications.[28–31] Mass resolved REMPI data for HI molecular beam were collected for the two-photon excitation region of 69 000–79 000 cm^{-1}. A molecular beam was created by jet expansion of a diluted gas mixture of HI in argon (HI : Ar ~ 1 : 2) through a 500 μm pulsed nozzle with a backing pressure of about 2.0–2.5 bar. Pressure inside the ionization chamber was about 10^{-6} mbar during experiments. The pulsed nozzle was typically kept open for about 140 μs. The excitation radiation was generated by a Nd:YAG laser (EKSPLA NL300 Series, 355 nm) pumped Coherent ScanMatePro dye laser (C-540A and C-503 dyes) followed by frequency doubling with a BBO crystal. The laser beam was focused on the molecular beam using a 200 mm quartz focal lens between a repeller and extractor plates. Ions were directed into a 70 cm long time-of-flight (TOF) tube and detected using a microchannel plate (MCP) detector to record the ion yield as a function of mass and laser radiation wavenumber. Signals were fed into a LeCroy WaveSurfer 44 MXs-A, 400 MHz storage oscilloscope. To prevent saturation effects and power broadening the laser power was minimized. Laser wavenumber calibration was based on observed iodine atom (2 + 1) REMPI lines. The accuracy of calibration was typically found to be about ±2.0 cm^{-1} on the two-photon wavenumber scale.

III. Results and analysis

Mass resolved REMPI data for HI were collected in the form of ion intensities as a function of excitation wavenumber for the two-photon excitation region of 69 000–79 000 cm^{-1}. REMPI spectra of ions formed (H^+, I^+ and HI^+) were derived from the data as intensities *vs.* two-photon excitation wavenumber (see Fig. 1 and Fig. S1, S2 in ref. 45). The spectra show structure due to two-photon resonant transitions from rotational energy levels in the ground electronic state to large number of Rydberg and ion-pair vibrational states, prior to n photon ionization, *i.e.* (2 + n) REMPI spectra. In addition, atomic iodine lines due to (2 + 1) REMPI of ground state iodine atoms *via* Rydberg states (I**) were detected. An emphasis was laid on the search for perturbation effects as deviations from a regular spectral structure. This appears in the form of spectral line shifts (LS-effect) and line intensity anomalies (LI- and LW-effects) and is indicative of state interactions. Furthermore, detection of predicted spectra, yet unobserved, was searched for.[44] Detailed exploration of the data revealed four systems (a–d) of perturbations/state interactions in the high energy/larger density of states region of 75 000–79 000 cm^{-1} (*i.e.* a: 75 000–75 200 cm^{-1}, b: 75 300–75 700 cm^{-1}, c: 77 000–77 300 cm^{-1} and d: 78 500–78 700 cm^{-1}), including observations of two new ion-pair vibrational states and three new Rydberg states (see Section A below). In addition, exploration of the lower energy region of 69 000–75 000 cm^{-1} revealed four new Rydberg states (see section B below). Analyses (see below) further revealed reassignments of some previously observed spectra.

The molecular spectra, which were analysed, were simulated using the PGOPHER software[46] (see Fig. S3 in ref. 45) by assuming an unperturbed spectral structure where the rotational energy ($E_{J'}(i)$; cm^{-1}) for a state i is described by the expression

$$E_{J'}(i) = \nu^0 + B'J'(J' + 1) - D'J'^2(J' + 1)^2, \quad (1)$$

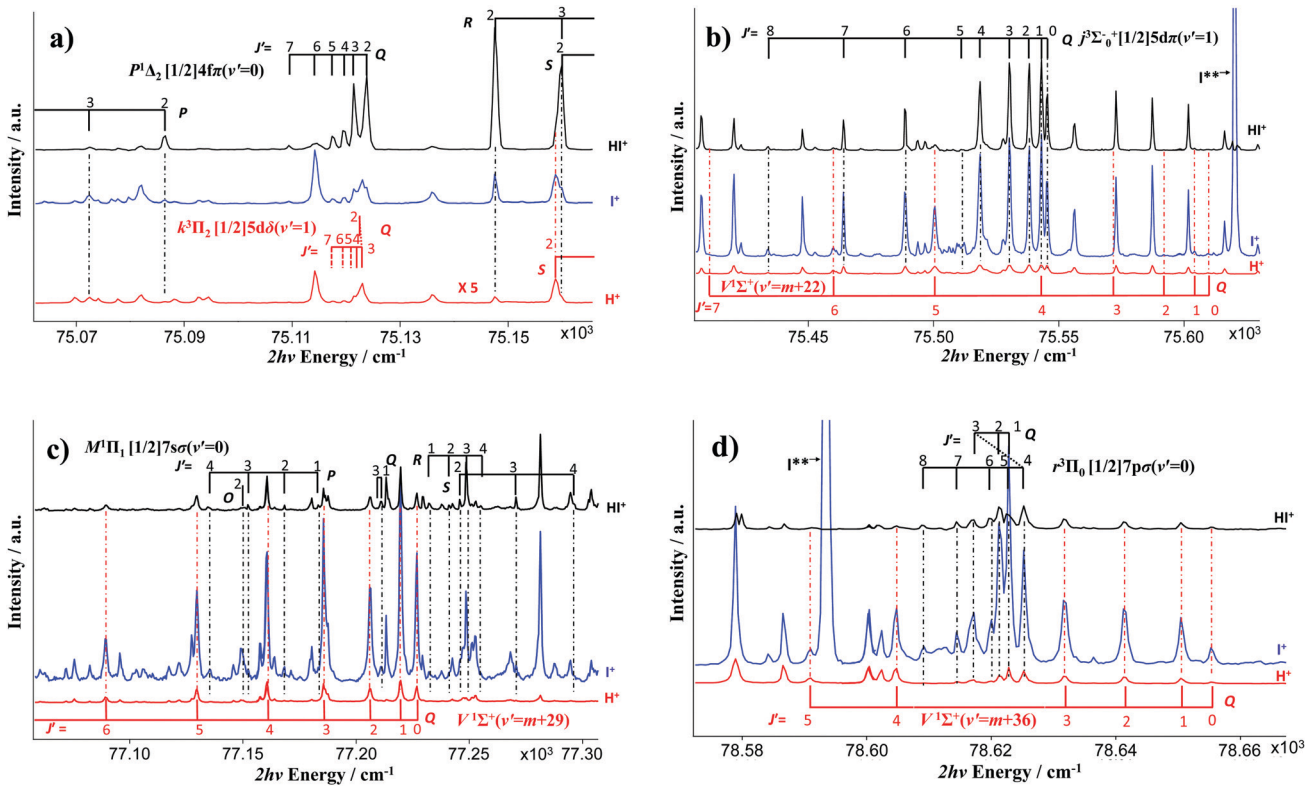

Fig. 1 Mass resolved (H^+(red), I^+(blue) and HI^+(black) ions) (2 + *n*) REMPI spectra as a function of two-photon excitation wavenumber for HI. Rotational line assignments for two-photon resonant transitions from the ground state $X^1\Sigma^+$ ($v'' = 0$) to, (a) $P^1\Delta_2$ [1/2]4fπ($v' = 0$) and $k^3\Pi_2$ [1/2]5dδ($v' = 1$), (b) $j^3\Sigma^-_{0+}$[1/2]5dπ($v' = 1$) and $V^1\Sigma^+$ ($v' = m + 22$), (c) $M^1\Pi_1$[1/2]7sσ($v' = 0$) and $V^1\Sigma^+$ ($v' = m + 29$), and (d) $r^3\Pi_0$ [1/2]7pσ($v' = 0$) and $V^1\Sigma^+$ ($v' = m + 36$) are indicated (m is an unknown integer). Iodine atomic lines due to two-photon resonant transitions from ground state iodine atoms to atomic Rydberg states (I**) are also indicated. The H^+ spectrum in (a) is magnified (×5).

and the line intensities are determined by transition probabilities for two-photon absorption[47–49] between two states for a Boltzmann distribution. Best fit of experimental and calculated spectra allowed the determination of the band origin (ν^0) and the rotational constants, B' and D', assuming known spectroscopic constants (B'' = 6.43 cm^{-1} and D'' = 2.05 × 10^{-4} cm^{-1}) for the ground state $X^1\Sigma^+$ ($v'' = 0$) (see Table 1). Significant discrepancy in line positions and intensities between the calculated and experimental spectra was an indication of perturbation effects due to state interactions.

Deperturbation analysis with respect to discrepancies in line positions (LS-effects) (hence discrepancies in level energies) allows the determination of zero order parameters for the band origin (ν_0^0) and the rotational constants ($B_0^{'}$ and $D_0^{'}$) corresponding to the energies of unperturbed states ($E^0_{J'}(i)$),

$$E^0_{J'}(i) = \nu_0^0 + B_0^{'}J'(J'+1) - D_0^{'}J'^2(J'+1)^2, \quad i = 1, 2 \qquad (2)$$

The Hamiltonian matrix for interactions of two states (i = 1, 2) between energy levels with the same J' quantum numbers is,[50]

$$\begin{bmatrix} E^0_{J'}(1) & W_{12} \\ W_{12} & E^0_{J'}(2) \end{bmatrix} \qquad (3)$$

where W_{12} is the interaction strength. This gives

$$E_{J'}(i) = \frac{1}{2}\left(E^0_{J'}(1) + E^0_{J'}(2)\right) \pm \frac{1}{2}\sqrt{4|W_{12}|^2 + \left(E^0_{J'}(1) - E^0_{J'}(2)\right)^2}, \quad i = 1, 2 \qquad (4)$$

For homogeneous interactions, W_{12} is a constant, whereas for heterogeneous interactions

$$W_{12} = W_{12}^{'}\sqrt{(J'(J'+1))} \qquad (5)$$

where $W_{12}^{'}$ is a constant. The fractional state mixing (c_1^2 and c_2^2) were evaluated from the energy difference of the J' levels for the interacting states ($\Delta E_{J'} = E_{J'}(1) - E_{J'}(2)$) and W_{12} as,[9,40]

$$c_2^2 = \frac{1}{2} \pm \frac{\sqrt{|\Delta E_{J'}|^2 - 4|W_{12}|^2}}{2|\Delta E_{J'}|} \qquad (6)$$

$$c_1^2 = 1 - c_2^2$$

Intensity anomalies in the form of LI-effects and/or LW-effects are indicative of J' dependent state mixing. A change in states mixing corresponds to a change in the states character. Thus, an increasing mixing of a Rydberg state with the ion-pair state for a hydrogen halide molecule (HX) corresponds

Table 1 (a) State interactions; characterization of spectra and states involved in state interactions a–d (see the main text). Rydberg and ion-pair states specifications ($Ry^{2S+1}\Lambda_{\Omega}[\Omega_c]nl\lambda$) (see the main text), vibrational quantum numbers (v'), parity, band origin (ν^0), rotational parameters (B', D'), relative intensities, quantum defect values (δ) and line series derived from Rydberg state spectra. (b) New Rydberg states; characterization of spectra and states (see the main text). Rydberg state specifications ($Ry^{2S+1}\Lambda_{\Omega}[\Omega_c]nl\lambda$) (see the main text), vibrational quantum numbers (v'), parity, band origin (ν^0), rotational parameters (B', D'), relative intensities, quantum defect values (δ) and line series derived from Rydberg state spectra

State specifications	v'	Parity	ν^0/cm^{-1}	B'/cm^{-1}	$D' \times 10^4/cm^{-1}$	Int.[c]	Quantum defect δ	Line series observed	Relative ion intensities	Ref.
(a)										
$P^1\Delta_2$ [1/2]4fπ	0	e	75124.9[a]	6.11[a]	9.8[a]	ms	1.20	O, Q, S	$I(HI^+) > I(I^+) > I(H^+)$	d,e
		f	75123.0[b]	6.27[b]	30.9[b]			P, R		
			75124.6[a]	6.15 [a]	7.8[a]					
$k^3\Pi_2$ [1/2]5dδ	1	e	75123.0[a]	6.26[a]	7.9[a]	ms	2.39	Q,S	$I(I^+) > I(HI^+) > I(H^+)$	e
			75124.0[b]	6.26[b]	7.0[b]					
$j^3\Sigma^-{}_0{}^+$[1/2]5dπ	1	e	75546.1[a]	5.14[a]	54.0[a]	vs	2.36	Q	$I(I^+) > I(HI^+) \gg I(H^+)$	d,e
			75546.0[b]	5.16[b]	54.8[b]					
$V^1\Sigma^+$	m + 22	e	75612.6[a]	2.80[a]	12.0[a]	m		Q	$I(I^+) > I(H^+) > I(HI^+)$	e
			75610.0[b]	2.98[b]	38.8[b]					
$M^1\Pi_1$ [1/2]7sσ	0	e	77212.1[a]	5.97[a]	−81.0[a]	vw	3.96	O, Q, S	$I(HI^+) \gg I(I^+) > I(H^+) \approx 0$	e
		f	77214.0[b]	5.72[b]	−50.6[b]			P, R		
			77211.9[a]	5.87[a]	−20.0[a]					
$V\ ^1\Sigma^+$	m + 29	e	77226.8[a]	2.98[a]	−26.0[a]	m		Q	$I(I^+) > I(H^+) \approx I(HI^+)$	d,e
			77224.0[b]	3.46[b]	38.4[b]					
$r^3\Pi_0$ [1/2]7pσ	0	e	78623.0[a]	6.30[a]	28.0[a]	s	3.76	Q	$I(I^+) > I(HI^+) \gg I(H^+)$	e
			78625.0[b]	6.33[b]	35.8[b]					
$V^1\Sigma^+$	m + 36	e	78655.0[a]	3.90[a]	−65.0[a]	ms		Q	$I(I^+) > I(H^+) > I(HI^+)$	e
			78654.0[b]	3.48[b]	−27.1[b]					
(b)										
$d^3\Pi_1$[3/2] 6pσ	3	e	69691.6	6.08	3.7	vw	3.67	O, Q, S	$I(HI^+) > I(I^+) > I(H^+)$	e
		f	69691.6	5.93	18.0			P, R		
$f^3\Delta_2$ [3/2]7pπ	0	e	74500.9	5.58	−8.4	w	3.56	O, Q, S	$I(HI^+) > I(I^+) > I(H^+)$	d,e
		f	74509.4	5.69	35.8			P, R		
$m^3\Pi_2$[1/2]7sσ	2	f	74484.1	5.10	−57.8	w	4.14	P, R	$I(HI^+) > I(I^+) > I(H^+)$	e
$m^3\Pi_1$[1/2]7sσ	2	e	74571.3	5.90	—	w	4.13	O, Q, S	$I(HI^+) > I(I^+) > I(H^+)$	e
		f	74581.8	5.81	—			P, R		

[a] Undeperturbed (perturbed) values; this work. [b] Deperturbed values; this work. [c] Definitions of abbreviations: vw: very weak; w: weak; m: medium intense; ms: medium-to-strong; (s: strong), vs: very strong. [d] Ref. 44. [e] This work.

to an enhanced ion-pair character of the Rydberg state and *vice versa*. This can alter transition probabilities as well as fragmentation (both photodissociation and photoionization) processes, hence relative ion signal intensities and line widths. Variations in ratios of fragment ion intensities ($I(H^+)$, $I(X^+)$) over the parent molecular ion intensities ($I(HX^+)$) or the total ion intensities as a function of J' have proven to be a useful tool as an indication for state mixing (hence state interaction), both quantitatively[29,38–40] and qualitatively.[29–31,43] Thus, in the case of Rydberg to ion-pair state interactions such intensity ratios typically increase by an enhanced ion-pair state character (decrease by an enhanced Rydberg state character) in the state mixing. Due to large density of states, hence severe overlap of spectral peaks, evaluations or estimates of line intensity ratios and line widths as a function of J' could merely be used here as qualitative indications of the state mixing and/or in support of the line shift/deperturbation analysis described above.

Assignment or reassignment of Rydberg and ion-pair state spectra was based on a number of factors. First, rotational line assignments and state symmetries were determined from the spectral structure. Second, a distinction between $^1\Sigma(\Omega = 0)$ Rydberg and ion-pair states could be made based on the rotational constants B' derived from the simulations as well as relative ion-intensities. Thus, the B' values for the ion-pair vibrational states are generally found to be lower than those for the Rydberg states and the relative ion intensities typically vary as $I(I^+) \geq I(H^+) \sim I(HI^+)$ for the ion-pair states and as $I(HI^+) > I(I^+) > I(H^+)$ for the Rydberg states. Third, detailed quantum defect analyses of the Rydberg states were particularly useful in this context. This was performed by using the following expression for the band origin (ν^0):

$$\nu^0(HI^{**}[\Omega_c, v]nl\lambda) = IE([\Omega_c, v]) - \frac{R_\infty}{(n - \delta(l))^2}; \qquad (7)$$

where $HI^{**}[\Omega_c, v]nl\lambda$ refers to a Rydberg state which converges to either of the two spin–orbit components (Ω_c = 3/2, 1/2) of the ground ionic state $HI^+(X^2\Pi)$ at the vibrational level v, for a Rydberg electron with a principal quantum number n, in a molecular orbital λ, corresponding to an iodine atom orbital l. $IE([\Omega_c, v])$ is the ionization energy of $HI(X^1\Sigma^+ (v'' = 0, J'' = 0))$ to form $HI^+([\Omega_c, v])$.[51] R_∞ is the Rydberg constant and $\delta(l)$ is the quantum defect value, which depends on l. By matching experimental and calculated band origins (ν^0) for known values of IE and n, $\delta(l)$ could be derived. The $\delta(l)$ values are characteristic for Rydberg state series and have been found to be close to those of the iodine atom (*i.e.* about 4.00, 3.50, 2.40 and 0.05 for the s(l = 0), p(1), d(2) and f(3) Rydberg electrons, respectively[52]) within the ranges of about 3.5–3.7, 2.3–2.5 and 1.0–1.3 for the p(1), d(2) and f(3) HI molecule Rydberg electrons, which are relatively large values due to the heavy iodine atom.[44] Fourth, vibrational quantum numbers, v', for ion-pair vibrational states are labelled

as $v' = m + i$, where m and i are positive integers; m is unknown whereas i ranges from zero upwards.[23,43,44] The choice of i values, which are uncertain,[44] is based on a realistic pattern of the vibrational ladder.

A. State interactions

In what follows perturbation analysis relevant to four state interactions (a–d) of different strength and nature observed in the high energy, two-photon excitation region of 75 000–79 000 cm^{-1} will be described:

(a) Rydberg to Rydberg state interaction; 75 000–75 200 cm^{-1}, $P^1\Delta_2$ [1/2]4f$\pi(v' = 0) \leftrightarrow k^3\Pi_2$ [1/2]5d$\delta(v' = 1)$; $\Delta\Omega = 0$

HI^+, I^+ and H^+ REMPI spectra for the two-photon excitation region of 75 000–75 200 cm^{-1} are shown in Fig. 1a. Perturbations in a medium-to-strong (ms) spectrum with a band origin of ν^0 = 75 124.6 cm^{-1} for $I(HI^+) > I(I^+) > I(H^+)$, O, P, Q, R and S lines due to transition to the $P^1\Delta_2$ [1/2]4f$\pi(v' = 0)$ Rydberg state were identified.[44] These appear as LS-effects and intensity anomalies (LI/LW-effects) for low J' values ($J' \approx 2$–3) in the Q line series of the HI^+ spectrum in particular (see Fig. 1a). A closer look at the spectral structure in this region reveals a new state spectrum close in energy with medium-to-strong (ms) O, Q and S lines of $I(I^+) > I(HI^+) > I(H^+)$ for a band origin of 75 123 cm^{-1}. Fitting of the Q-lines structure by Gaussian line shapes allowed evaluation of peak positions for both state spectra and an estimate of peak intensities for the $P^1\Delta_2$ [1/2]4f$\pi(v' = 0)$ spectrum. The rotational energy levels ($E_{J'}$) of the excited states were derived from the line positions for given (known) energy levels of the ground state (Fig. 2a).[43] These show that the largest repulsion effect, hence largest mixing, is to be expected for the near-degenerate $J' = 2$–3 energy levels. Judging from a coupling scheme for bound states within the hydrogen halides[53] a perturbing state for the $^1\Delta_2$ state could either be a $^1\Pi_1$ or a $^3\Pi_2$ state in which case the interaction would be due to a heterogeneous ($\Delta\Omega \neq 0$) L-uncoupling (JL) or a homogeneous ($\Delta\Omega = 0$) spin–orbit (SO) coupling, respectively. A quantum defect value of $\delta = 2.38$ is obtained by assuming that the Rydberg state is the $v' = 1$ level of the $k^3\Pi_2$ [1/2]5dδ state, in close agreement with $\delta = 2.36$ derived for the $k^3\Pi_2$ [1/2]5d$\delta(v' = 0)$ state.[23] We, therefore, assign the perturbing state spectrum to the $k^3\Pi_2$ [1/2]5dδ ($v' = 1$) state.

Fig. 2b shows the energy mismatch of the perturbed and unperturbed levels $\left(E_{J'} - E^0_{J'}\right)$ as a function of J' (reduced term plots) for the two states. It shows the largest change in energy for the near-degenerate levels $J' = 2$. Line intensities and line shapes could not be derived from the data to deduct precise intensity ratios and line widths (see above) as a function of J' for both spectra because of severe overlap of peaks. Total ion intensities *vs.* J' derived from the P state spectrum, however, show a clear maximum for $J' = 2$ and a gradual decrease with $J' \geq 2$ (Fig. 2c). Furthermore, there is an indication that the ion intensity ratio, $I(I^+)/I(HI^+)$, for the Q line of $J' = 2$ level for the P state spectrum is low compared to other lines in the series and its line width is significantly larger. All these observations suggest that state interaction between the two Rydberg states (P and k) is involved. By assuming a homogeneous interaction,

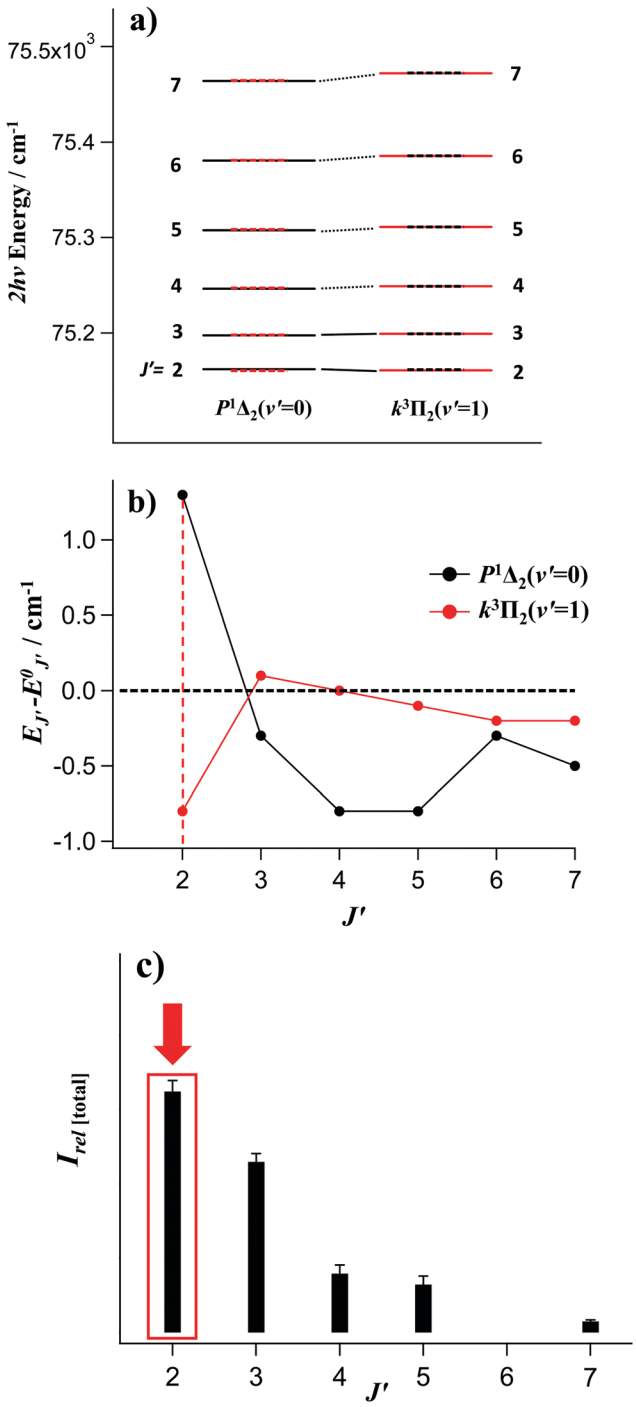

Fig. 2 Effects of state interaction $P^1\Delta_2$ [1/2]4f$\pi(v' = 0) \leftrightarrow k^3\Pi_2$ [1/2]5d$\delta(v' = 1)$. (a) Rotational energy levels of the $P^1\Delta_2$ [1/2]4f$\pi(v' = 0)$ and $k^3\Pi_2$ [1/2]5d$\delta(v' = 1)$ states, derived from the REMPI spectra (solid lines) and derived using deperturbation calculations (zero order energy levels; broken horizontal lines). Level-to-level state interactions are indicated by solid (near-degenerate interactions) and dotted (off-degenerate interactions) black lines. (b) Difference between perturbed (experimental; $E_{J'}$) and unperturbed (zero order; $E^0_{J'}$) energy levels $\left(E_{J'} - E^0_{J'}\right)$ as a function of J′ (reduced term plots) for the P and k states. (c) Total ion intensities (*I*(total)) *vs.* J′ derived from the Q lines of the P spectrum.

hence W_{12} = constant (see above), deperturbation analysis gives the zero order band origins and rotational constants listed in

Table 2 State interactions; J' level proximity ($\Delta E_{J'} = E_{J'}(1) - E_{J'}(2)/\mathrm{cm}^{-1}$), interaction strength (W_{12}/cm^{-1}) and fractional state mixing (c_1^2, c_2^2)

$P^1\Delta_2$ [1/2]4fπ(v' = 0) ↔ $k^3\Pi_2$ [1/2]5dδ(v' = 1)					$j^3\Sigma^-_{0+}$[1/2]5dπ(v' = 1) ↔ $V^1\Sigma^+$ (v' = m + 22)				
J'	$\Delta E_{J'}$	W_{12}	c_1^2	c_2^2	J'	$\Delta E_{J'}$	W_{12}	c_1^2	c_2^2
2	−1.4	0.7	0.647	0.353	0	64.5	6.4	0.990	0.010
3	1.6	0.7	0.753	0.247	1	61.7	6.4	0.989	0.011
4	2.5	0.7	0.917	0.083	2	53.4	6.4	0.986	0.014
5	3.5	0.7	0.960	0.040	3	40.3	6.4	0.974	0.026
6	4.8	0.7	0.979	0.021	4	23.9	6.4	0.923	0.077
7	8.1	0.7	0.993	0.007	5	−12.8	6.4	0.438	0.562
					6	−28.4	6.4	0.947	0.053
					7	−54.0	6.4	0.986	0.014

$M^1\Pi_1$ [1/2]7sσ(v' = 0) ↔ $V^1\Sigma^+$ (v' = m + 29)					$r^3\Pi_0$ [1/2]7pσ(v' = 0) ↔ $V^1\Sigma^+$ (v' = m + 36)				
J'	$\Delta E_{J'}$	W_{12}	c_1^2	c_2^2	J'	$\Delta E_{J'}$	W_{12}	c_1^2	c_2^2
1	9.1	0.6	0.996	0.004	1	27.6	7.2	0.927	0.073
2	−4.9	1.0	0.959	0.041	2	20.0	7.2	0.848	0.152
3	−21.8	1.4	0.996	0.004	3	14.4	7.2	0.531	0.469
4	−43.5	1.8	0.998	0.002	4	−20.5	7.2	0.857	0.143
5	−70.5	2.2	0.999	0.001	5	−40.1	7.2	0.967	0.033
					6	−59.9	7.2	0.985	0.015

Table 1a for both interacting states. The rotational constant of $B' = 6.26\ \mathrm{cm}^{-1}$ for the $k^3\Pi_2$ [1/2]5dδ(v' = 1) state is lower than the value of $B' = 6.40\ \mathrm{cm}^{-1}$ for $k^3\Pi_2$ [1/2]5dδ(v' = 0)[23] as might be expected and supports the new state assignment. A value of $W_{12} = 0.7\ \mathrm{cm}^{-1}$ was obtained for the interaction strength, which allowed determination of the fractional state mixing (c_1^2 and c_2^2) as a function of J' (Table 2). Thus, a maximum percentage mixing of about 65% : 35% is obtained for the J' = 2 levels.

(b) Rydberg to ion-pair state interaction; 75 300–75 700 cm^{-1}, $j^3\Sigma^-_{0^+}$[1/2]5dπ(v' = 1) ↔ $V^1\Sigma^+$ (v' = m + 22); ΔΩ = 0

HI^+, I^+ and H^+ REMPI spectra for the two-photon excitation region of 75 300–75 700 cm^{-1} are shown in Fig. 1b. A very strong (vs) spectrum with a band origin of $\nu^0 = 75546.6\ \mathrm{cm}^{-1}$ for $I(I^+) > I(HI^+) \gg I(H^+)$, Q lines only, showing some perturbations has been assigned to the $H^1\Sigma^+$[3/2]6dπ (v' = 0) Rydberg state.[44] The perturbations appear as LS-effects as well as LI/LW-effects in the Q line series for J' = 4–6 in particular. A closer look at the spectral structure in this region reveals a new state spectrum close in energy with medium intense (m) Q lines only, of $I(I^+) > I(H^+) > I(HI^+)$ for a band origin of 75612.6 cm^{-1} and typical structure of an ion-pair state spectrum. This was considered to be the perturbing state spectrum. Energetic reconsiderations as well as the perturbation analysis described below revealed a reassignment of the $\nu^0 = 75546.6\ \mathrm{cm}^{-1}$ band in terms of the spectral lines (see Table 1a) as well as the electronic state specifications (see more details below). The rotational energy levels (E_J) of the excited states were derived from the line positions (Fig. 3a). These show that the largest repulsion effect, hence largest mixing, is to be expected for the near-degenerate J' = 4–5 levels. A quantum defect value of δ = 2.36 is obtained by assuming that the Rydberg state is the v' = 1 level of the $j^3\Sigma^-_{0+}$[1/2]5dπ state in perfect agreement with the values of δ = 2.37 and 2.37 for the $j^3\Sigma^-_{0+}$[1/2]5dπ (v' = 0, 2) states, respectively. We, therefore, reassign the $\nu^0 = 75546.6\ \mathrm{cm}^{-1}$ band spectrum to the $j^3\Sigma^-_{0+}$[1/2]5dπ (v' = 1) state. The new ion-pair state spectrum at $\nu^0 = 75612.6\ \mathrm{cm}^{-1}$ is assigned to the $V^1\Sigma^+$ (v' = m + 22) state, which is missing in the ion-pair vibrational ladder.[44]

Fig. 3b shows the reduced term plots ($(E_{J'} - E^0_{J'})$ *vs.* J') for the two states. The plots show a characteristic ''near-mirror image'' effect, such that an increase in $E_{J'} - E^0_{J'}$, for one of the states, results in a decrease in the corresponding value for the other state and *vice versa* and the largest change in energy for J' = 5. This is a characteristic effect of a level-to-level repulsion interaction of medium strength for the near-degenerate levels of J' = 5. Striking intensity anomalies are also observed in the region of the J' = 4–6 lines for both state spectra. These appear as a large drop in total ion intensities of the J' = 5 peaks in the $j^3\Sigma^-_{0+}$[1/2]5dπ (v' = 1) REMPI spectra accommodated by an increase in the total ion intensities of the corresponding peaks (J' = 5) in the $V^1\Sigma^+$ (v' = m + 22) spectra (Fig. 1b and 3c). Although relative fragment ion signals to the parent ion signal could not be determined precisely for the $j^3\Sigma^-_{0+}$[1/2]5dπ (v' = 1) spectrum there is an indication of a rise in a plot of the ratio of $I(I^+)/I(HI^+)$ *vs.* J' for the near-degenerate levels J' = 4, 5 (see above). Similarly, while line widths could not be determined for the J' = 5 lines there is a clear indication of a rise in plots of line widths *vs.* J' towards the near-degenerate J' region (see Fig. 3c). By assuming a homogeneous interaction, hence W_{12} = constant (see above) deperturbation analysis gives the zero order band origins and rotational constants listed in Table 1a for both interacting states. Thus, the rotational constant of $B_0^{'} = 5.14\ \mathrm{cm}^{-1}$ for the $j^3\Sigma^-_{0+}$[1/2]5dπ(v' = 1) state is in between those of the v' = 0 (5.37 cm^{-1}) and v' = 2 (5.09 cm^{-1}) states as expected, which further supports the new assignment. A value of $W_{12} = 6.4\ \mathrm{cm}^{-1}$ was obtained for the interaction strength, which allowed the determination of the fractional state mixing (c_1^2 and c_2^2) as a function of J' (Table 2). A maximum percentage mixing of about 50% is obtained for the J' = 5 levels.

(c) Rydberg to ion-pair state interaction; 77 000–77 300 cm^{-1}, $M^1\Pi_1$ [1/2]7sσ(v' = 0) ↔ $V^1\Sigma^+$ (v' = m + 29); ΔΩ ≠ 0

HI^+, I^+ and H^+ REMPI spectra for the two-photon excitation region of 77 000–77 300 cm^{-1} are shown in Fig. 1c. A medium intense (m) spectrum with a band origin of $\nu^0 = 77226.8\ \mathrm{cm}^{-1}$ for $I(I^+) > I(H^+) \sim I(HI^+)$, Q lines only, showing some perturbations, has been assigned to the $V^1\Sigma^+$ (v' = m + 29) ion-pair vibrational state.[44] The perturbations appear as irregularities in line intensities (LI/LW-effects) near J' = 2. An exploration revealed a new state spectrum close in energy with very weak (vw) O, P, Q, R and S lines, of $I(HI^+) \gg I(I^+) > I(H^+) \sim 0$ for a band origin of 77212.1 cm^{-1}, which was considered to be a perturbing Rydberg state spectrum. The structure of the spectrum indicated that it is due to a transition to a $^1\Pi_1$ state. An interaction between a $^1\Sigma^+(0)$ ($V^1\Sigma^+$ (v' = m + 29)) and a $^1\Pi_1$ state is due to a heterogeneous ($\Delta\Omega \neq 0$) L-uncoupling (JL).[53] Simulation calculations allowed evaluation of first order (without taking account of perturbation) spectroscopic parameters (ν^0, B' and D'; eqn (1)) corresponding to the two different parity doublet components e and f[8] (Table 1a). The rotational energy levels (E_J) of the excited states were derived from the line positions (Fig. 4a). These show that the largest repulsion effect, hence largest mixing, is to be expected for the near-degenerate J' = 1–2 levels.

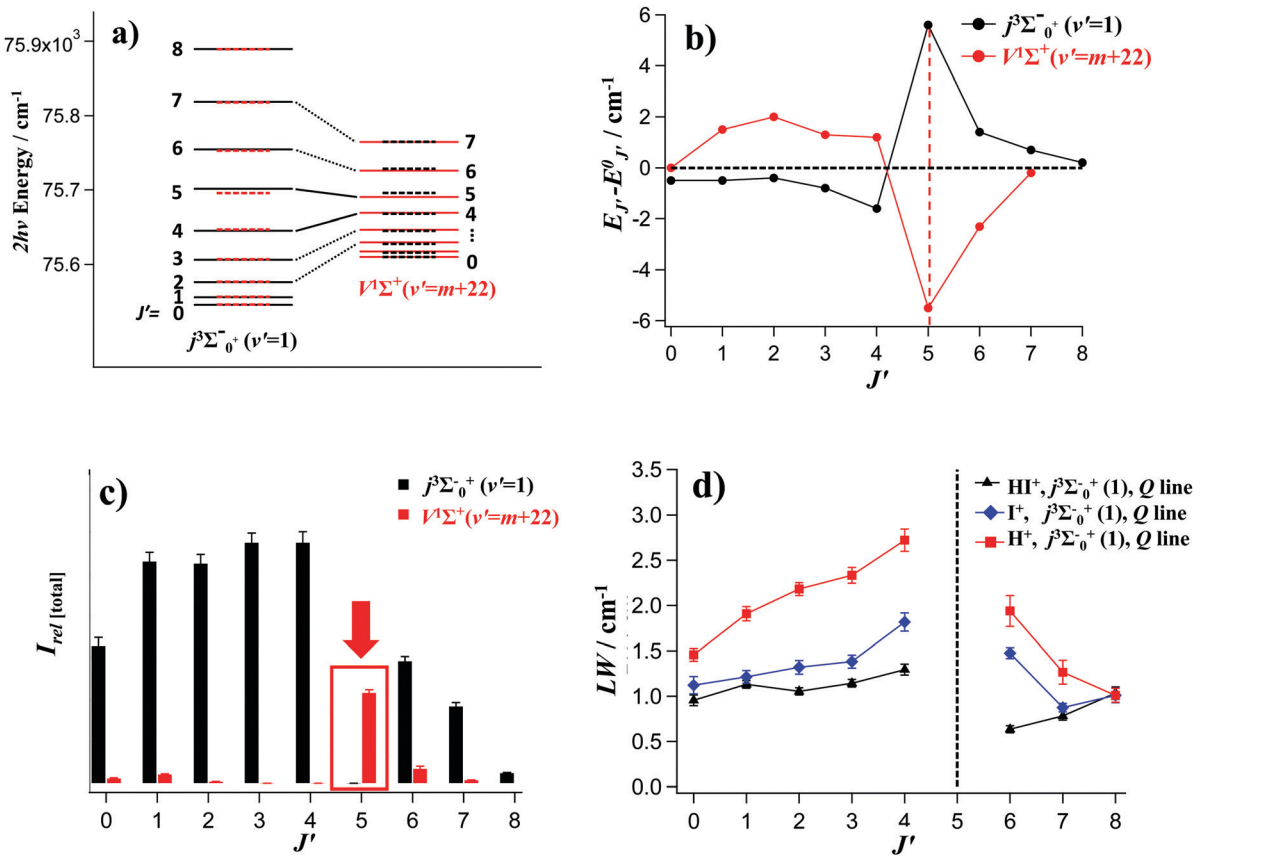

Fig. 3 Effects of state interaction $j^3\Sigma^-_0{}^+[1/2]5d\pi(v' = 1) \leftrightarrow V^1\Sigma^+$ ($v' = m + 22$). (a) Rotational energy levels of the $j^3\Sigma^-_0{}^+[1/2]5d\pi(v' = 1)$ and $V^1\Sigma^+$ ($v' = m + 22$) states, derived from the REMPI spectra (solid lines) and derived by deperturbation calculations (zero order energy levels; broken horizontal lines). Level-to-level state interactions are indicated by solid (near-degenerate interactions) and dotted (off-degenerate interactions) black lines. (b) Difference between perturbed (experimental; $E_{J'}$) and unperturbed (zero order; $E^0_{J'}$) energy levels $\left(E_{J'} - E^0_{J'}\right)$ as a function of J' (reduced term plots) for the j and V states. (c) Total ion intensities (I(total)) *vs.* J' derived from the Q lines of both spectra. (d) Rotational line widths *vs.* J' derived from the Q lines of the I^+, H^+, HI^+ ion signals for the j state.

A quantum defect value of $\delta = 3.96$ is obtained by assuming that the Rydberg state is the $v' = 0$ level of the $M^1\Pi_1$ [1/2]7sσ state, which is close to that derived for the analogous $C^1\Pi_1$ [1/2]6sσ($v' = 0$) state of $\delta = 3.97$.[22] We, therefore, assign the perturbing Rydberg state spectrum to the $M^1\Pi_1$ [1/2]7sσ ($v' = 0$) state.

A small but significant shift in energy levels (for $J' = 1$ in particular) due to the interaction is detected (see Fig. 4a). The perturbation mainly appears as line intensity drops for the $J' = 2$ peaks in the REMPI spectra for the $V^1\Sigma^+$ ($v' = m + 29$) state (Fig. 1c and 4b). Furthermore, a significant increase in the ratios of the fragment ion intensities ($I(H^+)$, $I(I^+)$) over the molecular ion intensities ($I(HI^+)$) as well as in the line widths as a function of J' is also seen in the $V^1\Sigma^+$ ($v' = m + 29$) state spectra for $J' = 2$ (see Fig. 4c). By assuming a heterogeneous interaction with J' dependent W_{12} (for W'_{12} = constant; eqn (5)) deperturbation analysis gives the zero order band origins and rotational constants listed in Table 1a for both interacting states. A value of $W'_{12} = 0.4$ cm^{-1} was obtained, which allowed determination of the fractional state mixing ($c_1{}^2$ and $c_2{}^2$) as a function of J' (Table 2). A maximum percentage mixing of about 96% : 4%, only, is obtained for the $J' = 2$ levels.

(d) Rydberg to ion-pair state interaction; 78 500–78 700 cm^{-1}, $r^3\Pi_0$ [1/2]7pσ($v' = 0$) ↔ $V^1\Sigma^+$ ($v' = m + 36$); $\Delta\Omega = 0$

HI^+, I^+ and H^+ REMPI spectra for the two-photon excitation region of 78 500–78 700 cm^{-1} are shown in Fig. 1d. Spectra in this region have not been assigned before. Two new spectra of Q lines only were identified in this spectral region, one, strong (s), with a band origin of $\nu^0 = 78623.0$ cm^{-1} for $I(I^+) > I(HI^+) \gg I(H^+)$ and another one, medium-to-strong (ms), with a band origin of $\nu^0 = 78655.0$ cm^{-1} for $I(I^+) > I(H^+) > I(HI^+)$. Both spectra show relatively large perturbation effects near the region of the $J' = 3$–4 lines, suggesting that the state interaction involved is homogeneous ($\Delta\Omega = 0$). The perturbations appear primarily in the form of LS-effects but also as LI/LW-effects. Judging from the spectral structures and simulation calculations the former spectrum is identified as a Rydberg state spectrum with a relatively high rotational constant ($B' = 6.30$ cm^{-1}) for the excited state, whereas the latter is found to be an ion-pair state spectrum with a lower rotational constant ($B' = 3.90$ cm^{-1}) for the excited state (Table 1a). Fitting of the rotational line peak structures allowed evaluation of peak positions for both state spectra. The rotational energy levels ($E_{J'}$) of the excited states were derived from the line positions (Fig. 5a). These show that the largest repulsion effect, hence largest mixing,

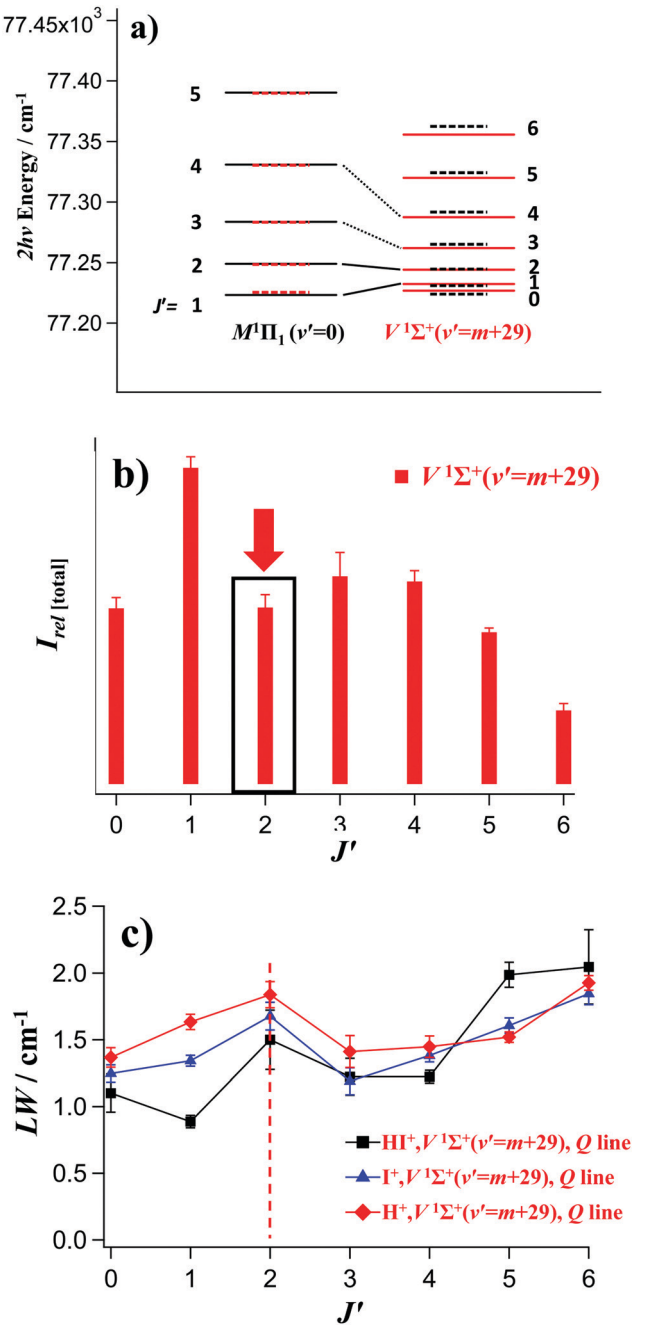

Fig. 4 Effects of state interaction $M^1\Pi_1$ [1/2]7sσ(v' = 0) ↔ $V^1\Sigma^+$ (v' = m + 29). (a) Rotational energy levels of the $M^1\Pi_1$[1/2]7sσ(v' = 0) and $V^1\Sigma^+$ (v' = m + 29) states, derived from the REMPI spectra (solid lines) and derived using deperturbation calculations (zero order energy levels; broken horizontal lines). Level-to-level state interactions are indicated by solid (near-degenerate interactions) and dotted (off-degenerate interactions) black lines. (b) Total ion intensities (*I*(total)) *vs.* J' derived from the Q lines of the V spectrum. (c) Rotational line widths *vs.* J' derived from the Q lines of the I^+, H^+, HI^+ ion signals for the V state.

is to be expected for the near-degenerate J' = 3–4 levels. A quantum defect value of δ = 3.76 is obtained by assuming that the Rydberg state is the v' = 0 level of the $r^3\Pi_0$ [1/2]7pσ state, in reasonable agreement with that derived for the $d^3\Pi_0$ [1/2]6pσ (v' = 0) (δ = 3.65) state. We, therefore, assign the new perturbing Rydberg state spectrum to the $r^3\Pi_0$ [1/2]7pσ (v' = 0) state. The new ion-pair state spectrum is assigned to the highest, yet unobserved ion-pair vibrational state $V^1\Sigma^+$ (v' = m + 36).[44]

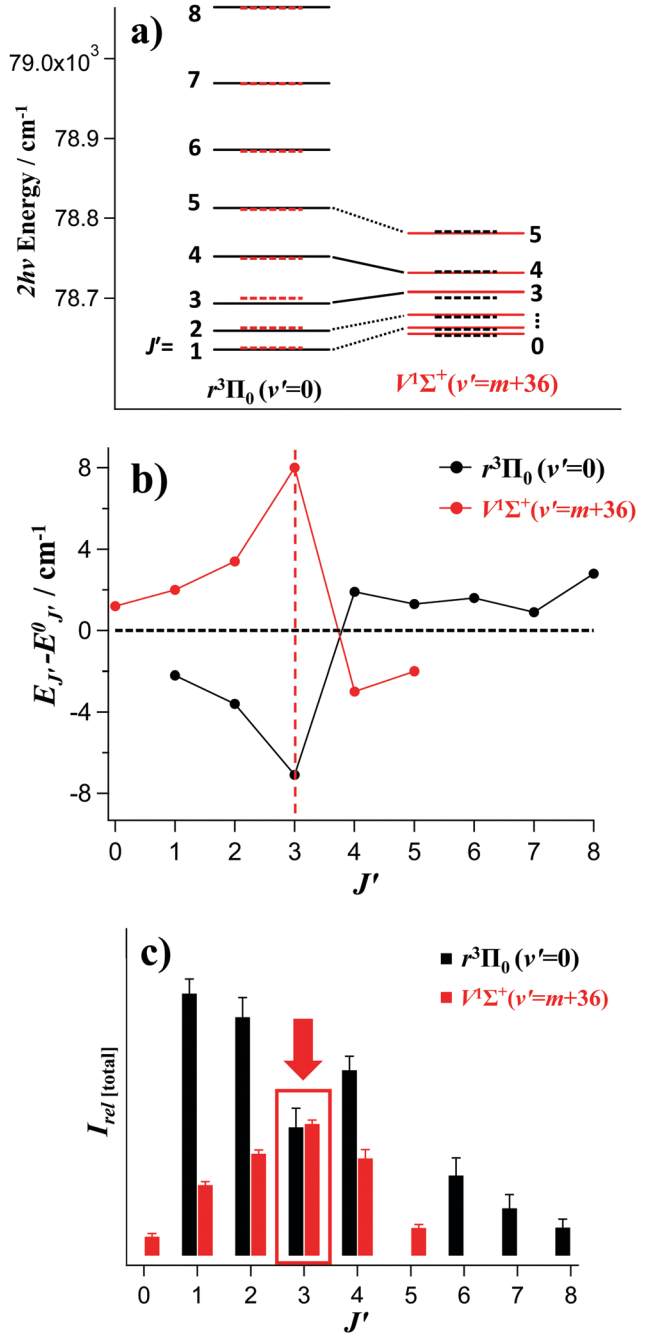

Fig. 5 Effects of state interaction $r^3\Pi_0$ [1/2]7pσ(v' = 0) ↔ $V^1\Sigma^+$ (v' = m + 36). (a) Rotational energy levels of $r^3\Pi_0$ [1/2]7pσ (v' = 0) and $V^1\Sigma^+$ (v' = m + 36) states, derived from the REMPI spectra (solid lines) and derived using deperturbation calculations (zero order energy levels; broken horizontal lines). Level-to-level state interactions are indicated by solid (near-degenerate interactions) and dotted (off-degenerate interactions) black lines. (b) Difference between perturbed (experimental; $E_{J'}$) and unperturbed (zero order; $E^0_{J'}$) energy levels $\left(E_{J'} - E^0_{J'}\right)$ as a function of J' (reduced term plots) for the r and V the states. (c) Total ion intensities (*I*(total)) *vs.* J' derived from the Q lines of both spectra.

Fig. 5b shows the reduced term plot ($(E_{J'} - E^0_{J'})$ *vs.* J'). It shows the characteristic ''near-mirror image'' effect (see above and ref. 31 and 43), and the largest change in the energy for $J' = 3$, a characteristic effect of a level-to-level repulsion interaction of medium strength for near-degenerate levels close to $J' = 3$. Line intensities and line shapes could not be derived easily from the data to deduct precise intensity ratios and line widths as a function of J'. Total ion intensities *vs.* J' derived from both spectra, however, show minima and maxima for $J' = 3$ for the r and V spectra, respectively (Fig. 1d and 5c). By assuming a homogeneous interaction, hence W_{12} = constant, deperturbation analysis gives the zero order band origins and rotational constants listed in Table 1a for both interacting states. A value of W_{12} = 7.2 cm^{-1} was obtained for the interaction strength, which allowed determination of the fractional state mixing (c_1^2 and c_2^2) as a function of J' (Table 2). A maximum percentage mixing of about 53% : 47% is obtained for the $J' = 3$ levels.

B. New Rydberg states

In what follows identification and characterization of four new Rydberg states (a–d) observed in the two-photon excitation region of 69 000–75 000 cm^{-1} will be described:

(a) $d^3\Pi_1$ [3/2]6pσ ($v' = 3$), ν^0 = 69691.6 cm^{-1}. Very weak (vw) but clear O, P, Q, R and S lines of relative signal intensities as $I(HI^+) > I(I^+) > I(H^+)$ were observed for ν^0 = 69691.6 cm^{-1}. The overall spectral structure is indicative of a Π-Rydberg state spectrum with B' values of 6.08 cm^{-1} and 5.93 cm^{-1} for the e and f parity doublet components, respectively, derived from the simulation (Table 1b). Quantum defect analysis suggest that this could be $v' = 3$ of the $d^3\Pi_1$[3/2]6pσ state with $\delta = 3.67$, in close agreement with the value of $\delta = 3.65$ for the $d^3\Pi_1$[3/2]6pσ ($v' = 0$) and ($v' = 1$) states.[54] Furthermore, the B' values derived are close to those obtained for the $d^3\Pi_1$[3/2]6pσ ($v' = 0$) and ($v' = 1$) states of 6.065 cm^{-1} and 5.926 cm^{-1}, respectively.[54]

(b) $f^3\Delta_2$ [3/2]7pπ ($v' = 0$), ν^0 = 74500.9 cm^{-1}. Weak (w) O, P, Q, R and S lines of relative signal intensities as $I(HI^+) > I(I^+) > I(H^+)$ were observed for ν^0 = 74500.9 cm^{-1}. The overall spectral structure is indicative of a Δ Rydberg state spectrum. Simulation calculations revealed B' values of 5.58 cm^{-1} and 5.69 cm^{-1} for the e and f parity doublet components, respectively, split by about 8.5 cm^{-1} (Table 1b). Quantum defect analysis suggest that this could be $v' = 0$ of the $f^3\Delta_2$ [3/2]7pπ state with $\delta = 3.56$ in close agreement with the values of $\delta = 3.52$ and $\delta = 3.54$ for the 7pπ states $g^3\Sigma^-_{0+}$ [3/2]7pπ ($v' = 0$) and $F^1\Delta_2$ [1/2]7pπ($v' = 0$), respectively.[44] Instead we reassign a spectrum with a band origin of ν^0 = 74 271 cm^{-1}, which has been assigned to the $f^3\Delta_2$ [3/2]7pπ($v' = 0$) state before,[44] to the $F^1\Delta_2$ [1/2]6pπ ($v' = 2$) state with $\delta = 3.59$ in perfect agreement with the same value ($\delta = 3.59$) for both $F^1\Delta_2$ [1/2]6pπ ($v' = 0$) and ($v' = 1$) states.[28,30,44] A gradual decrease in the B' values with v' for the vibrational states of $F^1\Delta_2$ [1/2]6pπ from 6.32 cm^{-1} ($v' = 0$)[28,44] to 6.13 cm^{-1} ($v' = 1$)[30,44] to 5.93 cm^{-1} ($v' = 2$),[44] as expected, further supports this reassignment.

(c–d) $m^3\Pi_2$[3/2]7sσ ($v' = 2$); ν^0 = 74484.1 cm^{-1} and $m^3\Pi_1$[3/2]7sσ($v' = 2$); ν^0 = 74571.3 cm^{-1}. Two weak (w) spectral systems of P, R and O, P, Q, R, S lines, of relative signal intensities as $I(HI^+) > I(I^+) > I(H^+)$ were identified for ν^0 = 74484.1 cm^{-1} and ν^0 = 74571.3 cm^{-1}, respectively. Only limited number of spectral lines could be observed for these systems in a region (74 440–74 620 cm^{-1}) of largely overlapping spectral lines. Both spectral structures are indicative of Π Rydberg states. A B' value of 5.10 cm^{-1} was obtained for the ν^0 = 74484.1 cm^{-1} system (P and R lines/f parity doublet component only) and B' values of 5.90 cm^{-1} and 5.81 cm^{-1} were obtained for the e (ν^0 = 74571.3 cm^{-1}; O, Q, and S lines) and f (ν^0 = 74581.8 cm^{-1}; P and R lines) parity doublet components, respectively (Table 1b). Quantum defect analyses suggest that these could be $v' = 2$ of the $m^3\Pi_2$[3/2]7sσ and $m^3\Pi_1$[3/2]7sσ states with $\delta = 4.14$ and 4.13, respectively, in close agreement with the corresponding values of $\delta = 4.09$ and 4.04 for the $v' = 0$ state[23,44] and $\delta = 4.12$ and 4.09 for the $v' = 1$ state.[23,44] The decrease in the B' value for $v' = 2$ compared to those for the $v' = 0$ and 1 states,[23,44] as expected, further supports these assignments.

IV. Discussion

A. State interactions and energetics

Fig. 6 shows the fractional state mixing as a function of J' for the four state interactions describe above (a–d; see Section III, A) as derived from the deperturbation analysis. The major characteristics are as follows:

(i) In all cases the largest mixing (minimum difference in c_1^2 and c_2^2) is obtained for the nearest-to-degenerate J' levels ($J' = 2$ for (a), $J' = 5$ for (b), $J' = 2$ for (c) and $J' = 3$ for (d); see broken vertical lines in Fig. 6), *i.e.* for the smallest energy difference between interacting levels ($\Delta E_{J'}$) in each case (see Table 2).

(ii) ''Sharper mixings'' (narrower peaks in plots shown in Fig. 6) are obtained for the Rydberg to ion-pair state interactions (b–d) than for the Rydberg to Rydberg state interaction (a), *i.e.*, the mixing is dominant for the nearest-to-degenerate levels in the case of the Rydberg to ion-pair interactions (b–d), whereas it changes more gradually for a larger range of J' levels in the case of the Rydberg to Rydberg state interaction (a). This is a result of a larger difference in rotational level spacing/rotational constants B' for Rydberg and ion-pair states (see Fig. 3a, 4a and 5a) than for two Rydberg states (see Fig. 2a).

(iii) The mixings are by far bigger for the homogeneous ($\Delta\Omega = 0$) state interactions (a, b, d) than for the heterogeneous ($\Delta\Omega \neq 0$) interaction (c).

There is a close correlation between the mixing, as determined by the line shifts (Fig. 6), and the total ion intensity alterations observed (Fig. 2c (case (a)), Fig. 3c (case (b)), Fig. 4b (case (c)) and Fig. 5c (case (d))).

(a) P($v' = 0$) *vs.* $k(v' = 1)$: a gradual decrease in the total ion intensity of the Q lines for the P($v' = 0$) state spectrum with J' for $J' = 2$–7 (Fig. 2c) matches the corresponding decrease in mixing between the P($v' = 0$) and k($v' = 1$) Rydberg states (Fig. 6a).

(b) j($v' = 1$) *vs.* V($v' = m + 22$): ''sharp'' minima and maxima observed in the plots of the total ion intensities *vs.* J' for $J' = 5$ of the Q line series for the j($v' = 1$) and V($v' = m + 22$) spectra, respectively (Fig. 3c), match the corresponding maximum in the mixing (Fig. 6b).

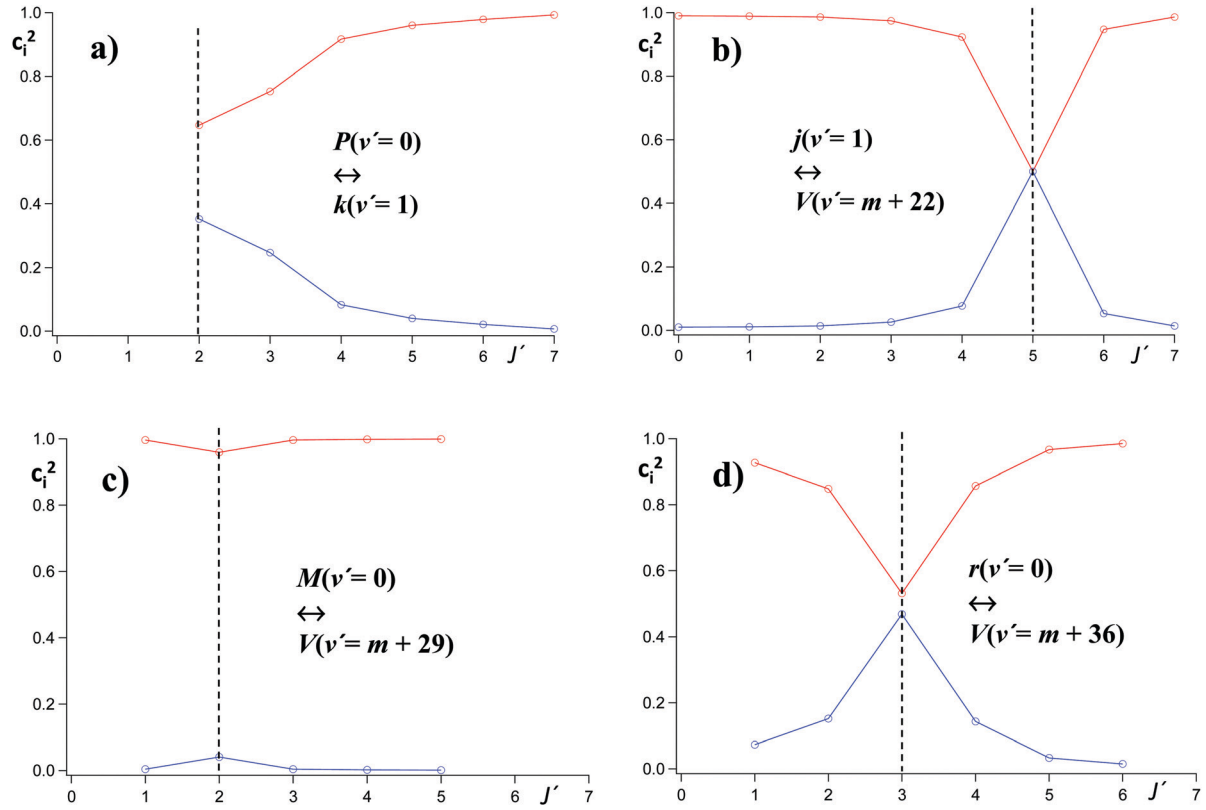

Fig. 6 Fractional state mixing (c_1^2 and c_2^2; see eqn (6)) as a function of J' for the state interactions $P^1\Delta_2$ [1/2]4fπ (v' = 0) *vs.* $k^3\Pi_2$ [1/2]5dδ (v' = 1) (a), $j^3\Sigma^-_{0+}$[1/2]5dπ (v' = 1) *vs.* $V^1\Sigma^+$ (v' = m + 22) (b), $M^1\Pi_1$ [1/2]7sσ (v' = 0) *vs.* $V^1\Sigma^+$ (v' = m + 29) (c) and $r^3\Pi_0$ [1/2]7pσ (v' = 0) *vs.* $V^1\Sigma^+$ (v' = m + 36) (d).

(c) M(v' = 0) *vs.* V(v' = m + 29): a drop in the plots of total ion intensity *vs.* J' for J' = 2 of the Q lines for the V(v' = m + 29) state spectrum (Fig. 4b) matches the corresponding maximum in the mixing (Fig. 6c).

(d) r(v' = 0) *vs.* V(v' = m + 36): minima and maxima observed in the plots of the total ion intensities *vs.* J' for J' = 3 of the Q line series for the r(v' = 0) and V(v' = m + 36) spectra, respectively (Fig. 5d), match the corresponding maximum in the mixing (Fig. 6d).

All these ion intensity observations (cases a–d) can be associated with ''intensity borrowing'' of one of the spectra from the other of the two interacting states due to corresponding changes in transition probabilities (*i.e.* ''transition probability borrowing'') due to mixing. Thus, in the (b) and (d) cases, where simultaneous total intensity maxima and minima of rotational lines for the nearest-to-degenerate J' levels are observed, these must be due to an ''intensity borrowing'' by V(v' = m + 22) from j(v' = 1) (case (b)) and by V(v' = m + 36) from r(v' = 0) (case (d)). Only total ion intensity plots could be derived for one of the two interacting states for the cases (a) and (c). The clear drop in the Q line intensity of the V(v' = m + 29) spectrum for J' = 3, however, is a strong indication of an intensity borrowing by M(v' = 0) from V(v' = m + 29) (case (c)). Although the observed decrease in the ion intensity of the Q lines for the P(v' = 0) state spectrum with J' could be an effect of changing transition probabilities, it is likely also to be associated with an ''intensity borrowing'' of P(v' = 0) from k(v' = 1) (case (a)). In summary the ''intensity borrowing'' effects are as follows:

(a) $P^1\Delta_2$ [1/2]4fπ (v' = 0), [ms] ⇐ $k^3\Pi_2$ [1/2]5dδ (v' = 1), [ms]
(b) $j^3\Sigma^-_{0+}$[1/2]5dπ (v' = 1), [vs] ⇒ $V^1\Sigma^+$ (v' = m + 22), [m]
(c) $M^1\Pi_1$ [1/2]7sσ (v' = 0), [vw] ⇐ $V^1\Sigma^+$ (v' = m + 29), [m]
(d) $r^3\Pi_0$ [1/2]7pσ (v' = 0), [s] ⇒ $V^1\Sigma^+$ (v' = m + 36), [ms]

where the relative total intensities are marked inside square brackets and the arrows indicate the ''intensity flow''. Furthermore, the effect of ''intensity borrowing'', for the b, c and d cases, matches the relative total intensities of the interacting state spectra (see inside square brackets above) such that the lower intensity spectrum in each case gains intensity from the higher intensity spectrum.

The results presented here involve observations of (2 + n) REMPI spectra due to resonant transitions to three nsσ, ($\Omega \neq 0$) Rydberg states, $M^1\Pi_1$ [1/2]7sσ (ν^0 = 77214.0 cm^{-1}), $m^3\Pi_2$[1/2]7sσ (ν^0 = 74484.1 cm^{-1}) and $m^3\Pi_1$[1/2]7sσ (ν^0 = 74571.3 cm^{-1} (e)) and its characterization (see Table 1). While several nsσ Rydberg state spectra of HI have been observed in absorption[23] corresponding (2 + n) REMPI spectra have been found to be virtually unobservable.[26] Thus, only one weak spectrum (for the $m^3\Pi_2$[1/2]7sσ (v' = 0) Rydberg state; ν^0 = 70841.5 cm^{-1}) has been reported.[28] Weak or negligible intensities in (2 + n) REMPI are due to low transition probabilities for the two-photon resonant excitation step as governed by the unfavourable selection rule for electron transition from npπ to σ orbitals. This is in contrast with the more favourable selection rule for transition from npπ to π orbitals of $^1\Sigma$ and $^1\Delta$ states, which are easily detected in (2 + n) REMPI.[26,28–31] The detections

of the nsσ, ($\Omega \neq 0$) state spectra observed, all of which are in a high energy (hence high density of states) excitation region ($2h\nu > 74\ 400\ cm^{-1}$; see above), could be a reason of a state mixing which causes "intensity borrowing". Thus, the $M^1\Pi_1$ [1/2]7sσ state is known to mix with the $V^1\Sigma^+$ state (see above) and the $m^3\Pi_2$[1/2]7sσ and $m^3\Pi_1$[1/2]7sσ states are observed in a spectral region of largely overlapping spectra, which indicates a high density of states close in energy.

The new and reassigned Rydberg state spectra described above (Section III, A and B) add to and clarify further an ever growing scheme of Rydberg state series which are converging to either of the two spin–orbit components (Ω_c = 3/2, 1/2) of the ground ionic state $HI^+(X^2\Pi)$ (see ref. 28–31). Furthermore, the two new ion-pair vibrational states (V(v')), of ν^0 = 75610.0 and 78654.0 cm^{-1}, identified (see Section IIIA) were assigned to the vibrational quantum numbers $v' = m + i$ where m is an unknown integer and i = 22 and 36, respectively. These assignments were based on an assumption of a realistic continuation of an irregular vibrational energy ladder affected by severe interactions with Rydberg states (see ref. 28–31).

B. Photofragmentation processes

Variations in relative spectral line intensities with ion masses and/or J' quantum numbers are informative regarding photofragmentation processes, which are involved.

The relative ion signal intensities observed for the Rydberg state spectra in the lower energy region of 69 000–75 000 cm^{-1}, which vary as $I(HI^+) > I(I^+) > I(H^+)$ (see Table 1b), are typical for HI spectra of Rydberg states which experience limited mixing with the ion-pair state.[28,29,43,44] Typical relative ion intensities for ion-pair vibrational states in the same excitation region, on the other hand, vary as $I(I^+) > I(H^+) \geq I(HI^+)$.[28–30,43,44] Spectra of Rydberg states which are strongly mixed (*e.g.* homogeneously coupling ($\Delta\Omega$ = 0)) with the ion-pair state show relative ion intensities intermediate between those for "pure" Rydberg states and ion-pair states, depending on the interaction strength. Commonly/typically $I(I^+) > I(HI^+) > I(H^+)$ is observed (see Table 1b and ref. 29, 30 and 44). As shown in Table 1a the relative ion intensities for Rydberg as well as ion-pair state spectra in the higher energy excitation region of 75 000–79 000 cm^{-1} are along the same lines as observed for the lower energy region. This suggests that the same major fragmentation (both dissociation and ionization) processes apply for both regions. It has been proposed that ion formation in multiphoton ionization *via* two-photon resonant excitations less than about 75 000 cm^{-1} to intermediate Rydberg and ion-pair states ($HI^{**}(v')$) involves further third photon excitation of the intermediate states or its coupled conjugates to superexcited state(s) ($HI^{\#}$) followed by a number of fragmentation (autoionization, dissociation, photodissociation and ionization) processes (see Table 3).[31,43] The proportion of the various $HI^{**}(v')$ photofragmentation steps depends on the fractional contributions of the Rydberg and ion-pair character in state mixing (fractional state mixing), hence the internuclear distance range during the excitation (see Table 3). The process of $HI^{\#}$ dissociation to form I^+ directly ((iii) in Table 3) is limited to energies above the threshold for $I^+ + H + e$ formation of about 108 939 cm^{-1} (three-photon excitation; corresponding to a two-photon excitation of about 72 626 cm^{-1}). However, the spectrum for the d($v' = 3$) state (ν^0 = 69691.6 cm^{-1} (Table 1b)), for which a three-photon excitation to form $HI^{\#}$ is less than the threshold, shows relative ion intensities comparable to that for higher energy states (*i.e.* $I(HI^+) > I(I^+) > I(H^+)$). Similar observations have been found for more low energy Rydberg state spectra reported earlier.[28,29] Furthermore, there are no obvious transitions in terms of relative ion intensities for the ion-pair vibrational state spectra to be seen for excitations on either side of the $I^+ + H + e$ energy threshold.[28–31] We, therefore, conclude that the channel of I^+ formation by direct dissociation of $HI^{\#}$ ((iii) in Table 3) is not a major channel for I^+ formation in the total excitation region of concern and that photoionization of I^{**} after dissociation of $HI^{\#}$ to form $H + I^{**}$ is the main source for I^+ formation (channel (iv) in Table 3). It should be emphasized, however, that a minor contribution from channel (iii) cannot be ruled out. In conclusion Fig. 7 summarizes the major photofragmentation processes, which we propose, that applies for the two-photon excitation region of about 69 000–79 000 cm^{-1} and can explain the major relative ion intensity observations as shown in the figure.

The higher excitation energy region ($2h\nu$ = 75 000–79 000 cm^{-1}/$3h\nu$ = 112 500–118 500 cm^{-1}), including the state interactions presented in this paper, corresponds to three-photon excitations to energies within the bound region of the excited molecular ion state $HI^+{}^*(A^2\Sigma^+)$ (112 580–122 667 cm^{-1}) which correlates with $H + I^+{}^*(^1D_2)$ (see Fig. 8). It has been argued that a superexcited state ($HI^{\#}$) in a Rydberg series which converges

Table 3 Proposed main photofragmentation processes after (2 + 1) resonance enhanced multiphoton excitation *via* Rydberg and ion-pair states or its coupled conjugates to form superexcited state(s), $HI^{\#}$.[31,43]

No.	Number of photons required/n in $nh\nu$	Processes after $HI^{\#}$ formation	Processes[a]	Ions formed	Internuclear distance range	Relative state character[a]
i	3	$HI^{\#} \rightarrow HI^+(v^+_{low}) + e$	A	HI^+	Short	Ry ≫ I-p
ii	3	$HI^{\#} \rightarrow HI^+(v^+_{high}) + e$	A	HI^+	Medium	Ry ≈ I-p
	4	$HI^+(v^+_{high}) + h\nu \rightarrow H^+ + I$	PD	H^+		
iii	3	$HI^{\#} \rightarrow H + I^+ + e$	D	I^+	Medium to long	Ry < I-p
iv	3	$HI^{\#} \rightarrow H + I^{**}$	D			
	4	$I^{**} + h\nu \rightarrow I^+ + e$	PI	I^+	Medium to long	Ry < I-p
v	3	$HI^{\#} \rightarrow H^* + I$	D			
	4	$H^* + h\nu \rightarrow H^+ + e$	PI	H^+	Medium to long	Ry < I-p

[a] Definitions of abbreviations: A: autoionization; PD: photodissociation; D: dissociation; PI: photoionization; Ry: Rydberg states; I-p: ion-pair state.

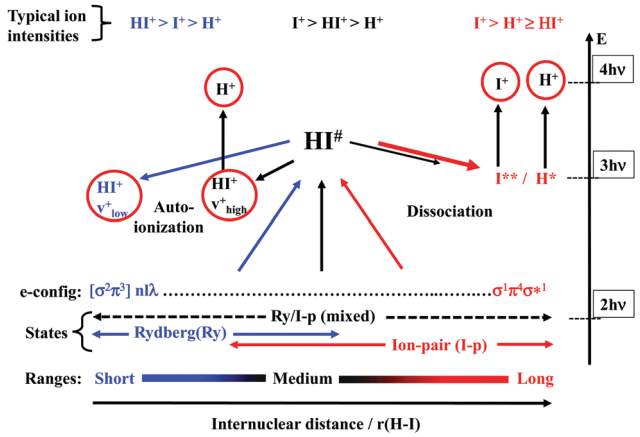

Fig. 7 Schematic diagram for the main photofragmentation process involved in (2 + *n*) REMPI *via* resonant excitation to Rydberg and ion-pair states and mixed states *vs.* internuclear distance/distance ranges for two-photon excitation of 69 000–79 000 cm^{-1} (see the main text for further clarification). Dominant Rydberg state, ion-pair state and mixed state characters are indicated in blue, red and black, respectively. $HI^{\#}$ denotes repulsive superexcited state(s) formed. Ions formed are highlighted by red circles. A number of photons required for species formed are indicated in the right. The relative weight of processes and ion formations are indicated by arrows and circles with different boldness. Typical relative ion intensities observed are indicated at the top.

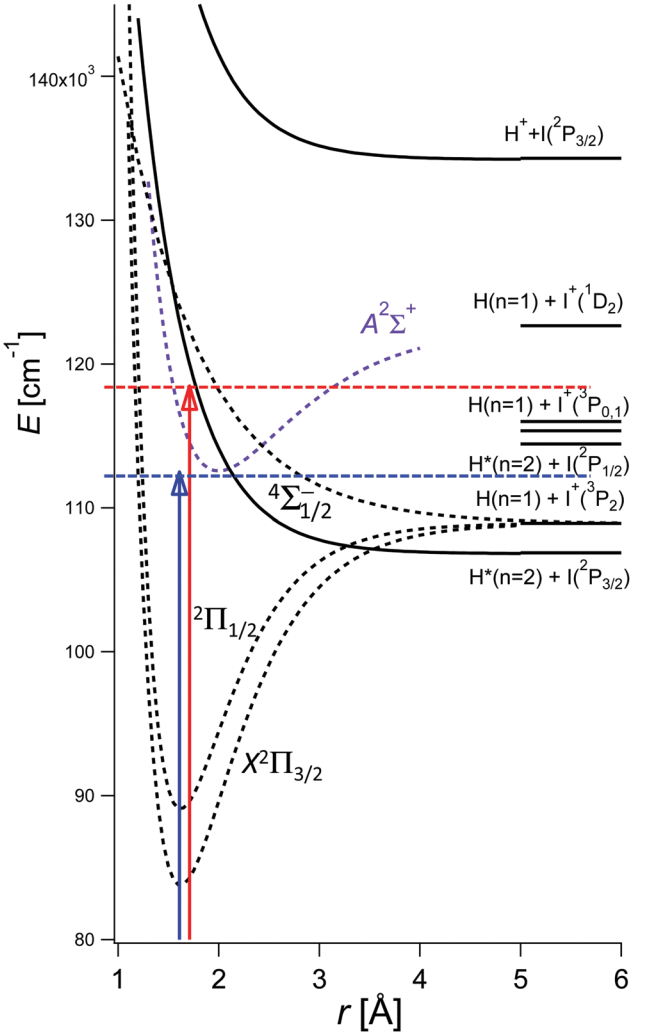

Fig. 8 Potential energy curves, asymptotic energies and photon excitations relevant to the two-photon excitations to the high energy region of 75 000–79 000 cm^{-1} (three-photon excitations of 112 500 (blue)–118 500 cm^{-1} (red)), which is dense in states (see the main text for further clarification). The potential curves for the $X^2\Pi$, $A^2\Sigma^+$, $[A^2\Sigma^+]5d\pi$ and the repulsive states are derived from ref. 35, 36, 59 and 60 respectively.

to the $HI^+*(A^2\Sigma^+)$ ionic state (*i.e.* a bound $[A^2\Sigma^+]5d\pi$ state) plays an important role in multiphoton ionization processes.[36,55,56] We disfavor, however, major importance of states within Rydberg series which converge to the $HI^+*(A^2\Sigma^+)$ ionic state for $HI^{\#}$ in the (2 + 1) resonance enhanced multiphoton (REMP) excitation scheme presented here for the following reasons. First, excitations from a bound HI** Rydberg or ion-pair state to a bound superexcited $HI^{\#}$ state, with discrete energy levels, will involve resonant transitions from HI** to $HI^{\#}$ built on top of the initial resonant transitions from HI(X) to HI**, which would affect relative intensities of individual spectral lines within the rotational line series. That contradicts our observations for relative rotational line intensities, which, in the cases of negligible state interactions for HI**, match smoothly varying intensities with J' quantum numbers built on top of a single resonant transition step between discrete rotational energy levels of two states only. Second, there is no obvious alteration in the relative ion intensities seen for excitations corresponding to three-photon excitations on either energy-side of the convergence limit (*i.e.* the $HI^+*(A^2\Sigma^+)$ low energy limit) for $[A^2\Sigma^+]nl\lambda$ Rydberg states. We, therefore, conclude that the superexcited state $HI^{\#}$, formed prior to the major ionization channels (Fig. 8) is a continuum state of non-discrete energies. These could be repulsive states which correlate diabatically with $H^*(n = 2) + I/I^*$ and $H(n = 1) + I^{**}$ and belong to Rydberg series which converge to the corresponding repulsive ionic states which correlate with $H^+ + I/I^*$ and $H(n = 1) + I^+(^3P_{2,1,0})$, respectively (see Fig. 8) to give the H* and I** fragments by direct dissociation prior to photoionization. This is along the same lines as our findings for the corresponding $HBr^{\#}$ superexcited states involved in (2 + *n*) REMPI of HBr in the case of H^+ formation.[18,57,58]

Changes in rotational line widths of ion signals due to interactions between Rydberg and ion-pair states have been interpreted in terms of changes in lifetime as a result of alterations in the states character due to its mixing.[28–31] Alternatively, changes in line widths due to the interactions/state mixing (see Fig. 3d and 4c) can be associated with changes in velocities (hence kinetic energies) of the ions, formed due to opening of, or changes in the contributions of, new fragmentation channels. Such effects could alter the time of flight of the ions (in the TOF tube), hence the arrival time at the MCP detector, to change the line widths, which, as a result, will depend on the fractional mixing of the states and the proposed fragmentation scheme in Fig. 7.

V. Summary and conclusions

Mass resolved REMPI data for HI were collected for the two-photon excitation region of 69 000–79 000 cm^{-1}. HI^+, I^+ and H^+ REMPI spectra, derived from the data, reveal the rotational

structure due to two-photon resonant transitions from the ground molecular state ($X^1\Sigma^+$ ($v'' = 0$)) to a large number of Rydberg and ion-pair vibrational states. Different ion REMPI spectra for individual vibrational transitions are identical in terms of rotational line positions but differ in relative ion intensities. Individual ion spectral structures (with respect to line positions and relative intensities), in many instances, could be simulated by calculated spectra due to two-photon transitions to rotational energy levels of excited vibrational states by assuming statistical (Boltzmann) population distributions to derive spectroscopic parameters involved. Spectral perturbations in the form of deviations from regular patterns (with respect to line positions, relative intensities as well as line widths) as predicted by the simulation calculations, however, were observed in some instances, indicating state interactions. Four sets of vibrational spectra, each for two spectra close in energy, in the higher energy region of 75 000–79 000 cm^{-1} were found to display clear spectral perturbations in a consistent manner with respect to both line shifts and line intensity anomalies. These observations were found to be due to state interactions between the corresponding two excited states in each set. Deperturbation analysis, based on deviations of line positions, hence rotational energy levels, from regular patterns allowed evaluation of interaction strengths and fractional state mixing as well as zero order (unperturbed) spectroscopic parameters. Anomalies in total ion intensities as a function of rotational quantum numbers J' were indicative of intensity borrowing *vs.* intensity giving effects due to character mixing of the interacting states. Rydberg to Rydberg and Rydberg to ion-pair state interactions for both homogeneous ($\Delta\Omega = 0$) and heterogeneous ($\Delta\Omega \neq 0$) couplings between states were identified and characterized. These analyses as well as simulation calculations for spectra in the lower energy region of 69 000–75 000 cm^{-1} further allowed identification and characterization of seven new, not previously observed, Rydberg state spectra and two new ion-pair vibrational state spectra. Furthermore, the analysis revealed reassignment of one Rydberg state spectrum previously observed. Among the new Rydberg state spectra, observed, there were three weak ones due to transitions to nsσ Rydberg states ($\Omega \neq 0$), rarely seen in ($2 + n$) REMPI due to un-favourable selection rules. Most likely these are observable due to intensity borrowing from interacting state(s) with higher transition probabilities for two-photon absorption. The assignment of the Rydberg state spectra relied on quantum defect analysis, which are subject to deficiencies. We believe that experiments on the isotopologue DI and relevant isotope shift analyses might be useful to complete the present picture of the HI Rydberg state structure.

It has been proposed that ion formation in multiphoton ionization *via* two-photon resonant excitation to intermediate states ($HI^{**}(v')$) involves further third photon excitation to superexcited state(s) ($HI^{\#}$) followed by a number of fragmentation processes (see Table 3). Variations in relative spectral line intensities with ion masses and J' quantum numbers are found to be informative regarding the photofragmentation processes involved. Relative ion signal intensities ($I(HI^+)$ *vs.* $I(I^+)$ *vs.* $I(H^+)$) are found to be comparable for all spectra of pure Rydberg states, which experience limited mixing with the ion-pair vibrational state ($I(HI^+) > I(I^+) > I(H^+)$) on one hand and for ion-pair state spectra ($I(I^+) > I(H^+) \geq I(HI^+)$) on the other hand in the overall excitation region (69 000–79 000 cm^{-1}). The relative ion intensities of spectra for Rydberg states mixed with the ion-pair state are intermediate between these cases, depending on the interaction strength. Typically, $I(I^+) > I(HI^+) > I(H^+)$ for large mixing/strong (homogeneous) coupling (see Fig. 7). Analysis of the rotational structure of Rydberg state spectra reveals that these are formed by two-photon resonant rotational transitions from the ground state to the Rydberg states followed by ion formation processes without any further resonant excitation steps. These observations indicate that superexcited states ($HI^{\#}$) involved are repulsive states correlating diabatically with I** + H and/or H* + I/I*, where I** is iodine atom Rydberg states and H* is H*($n = 2$). The major ionization channels are proposed to consist of autoionization to form HI^+ prior to photodissociation to form H^+ and one-photon ionization of the I** and H* fragments to a degree which depends on the Rydberg and ion-pair state character of the resonant intermediate state HI** and corresponding dominant internuclear distance as indicated in Fig. 7.

In addition to presenting specific information relevant to state interactions (interaction strength and state mixing parameters) and energetics (spectroscopic information) of high energy HI states this paper includes information relevant to the relationship between high energy molecular state properties and photofragmentation (photodissociation and photoionization) processes. The importance of state interaction strength, nature and mixing of resonance states in multiphoton-fragmentation processes is evident by the examples presented here. Furthermore, the effect of state mixing, hence state character, on transition probabilities is evident by ion intensity borrowing *vs.* intensity giving effects clearly seen in REMPI spectra of the interacting states. More generally this work demonstrates how a stepwise photoexcitation to metastable (superexcited) states *via* neutral molecular states can allow selective fragmentation, depending on the nature and/or degree of state mixing of the intermediate states. We, therefore, feel that this paper is of importance to shed light on the effect of excited state properties on competing channels in photoexcitation dynamics of molecules in general.

Conflicts of interest

There is no conflict to declare.

Acknowledgements

The financial support from the University Research Fund, University of Iceland and the Icelandic Research Fund (Grant No. 184693-053) is gratefully acknowledged. We would like to thank Huasheng Wang and Jingming Long for useful help with the experiments.

References

1 S. G. Tilford, M. L. Ginter and J. T. Vanderslice, *J. Mol. Spectrosc.*, 1970, **33**, 505.

2 J. B. Nee, M. Suto and L. C. Lee, *J. Chem. Phys.*, 1986, **85**, 4919.
3 D. S. Ginter, M. L. Ginter and S. G. Tilford, *J. Mol. Spectrosc.*, 1981, **90**, 152.
4 R. F. Barrow and J. G. Stamper, *Proc. R. Soc. A*, 1961, **263**, 277.
5 R. F. Barrow and J. G. Stamper, *Proc. R. Soc. A*, 1961, **263**, 259.
6 K. Wang and V. McKoy, *J. Chem. Phys.*, 1991, **95**, 8718.
7 Y. Xie, P. T. A. Reilly, S. Chilukuri and R. J. Gordon, *J. Chem. Phys.*, 1991, **95**, 854.
8 D. S. Green, G. A. Bickel and S. C. Wallace, *J. Mol. Spectrosc.*, 1991, **150**, 303.
9 Á. Kvaran, H. S. Wang, K. Matthiasson, A. Bodi and E. Jonsson, *J. Chem. Phys.*, 2008, **129**, 164313.
10 K. Matthiasson, H. S. Wang and Á. Kvaran, *J. Mol. Spectrosc.*, 2009, **255**, 1.
11 R. Callaghan and R. J. Gordon, *J. Chem. Phys.*, 1990, **93**, 4624.
12 K. Wang and V. McKoy, *J. Chem. Phys.*, 1991, **95**, 7872.
13 A. E. Belikov, M. M. Ahern and M. A. Smith, *Chem. Phys.*, 1998, **234**, 195.
14 Á. Kvaran, B. G. Waage and H. Wang, *J. Chem. Phys.*, 2000, **113**, 1755.
15 D. Ascenzi, S. Langford, M. Ashfold and A. Orr-Ewing, *Phys. Chem. Chem. Phys.*, 2001, **3**, 29.
16 Á. Kvaran, Á. Logadóttir and H. Wang, *J. Chem. Phys.*, 1998, **109**, 5856.
17 P. M. Regan, D. Ascenzi, E. Wrede, P. A. Cook, M. N. R. Ashfold and A. J. Orr-Ewing, *Phys. Chem. Chem. Phys.*, 2000, **2**, 5364.
18 D. Zaouris, A. Kartakoullis, P. Glodic, P. C. Samartzis, H. R. Hróðmarsson and Á. Kvaran, *Phys. Chem. Chem. Phys.*, 2015, **17**, 10468.
19 S. Kauczok, C. Maul, A. I. Chichinin and K. H. Gericke, *J. Chem. Phys.*, 2010, **133**, 024301.
20 C. Romanescu and H. P. Loock, *J. Chem. Phys.*, 2007, **127**, 124304.
21 C. Romanescu and H. P. Loock, *Phys. Chem. Chem. Phys.*, 2006, **8**, 2940.
22 S. G. Tilford, M. L. Ginter and A. M. Bass, *J. Mol. Spectrosc.*, 1970, **34**, 327–340.
23 D. S. Ginter, M. L. Ginter and S. G. Tilford, *J. Mol. Spectrosc.*, 1982, **92**, 40–54.
24 D. S. Ginter, M. L. Ginter, S. G. Tilford and A. M. Bass, *J. Mol. Spectrosc.*, 1982, **92**, 55–66.
25 S. A. Wright and J. D. McDonald, *J. Chem. Phys.*, 1994, **101**, 238–245.
26 S. T. Pratt and M. L. Ginter, *J. Chem. Phys.*, 1995, **102**, 1882–1888.
27 Á. Kvaran, Á. Logadóttir and H. Wang, *J. Chem. Phys.*, 1998, **109**, 5856–5867.
28 H. R. Hróðmarsson, H. S. Wang and Á. Kvaran, *J. Mol. Spectrosc.*, 2013, **290**, 5–12.
29 H. R. Hróðmarsson, H. S. Wang and Á. Kvaran, *J. Chem. Phys.*, 2014, **140**, 244304.
30 H. R. Hróðmarsson, H. S. Wang and Á. Kvaran, *J. Chem. Phys.*, 2015, **142**, 244312.
31 H. R. Hróðmarsson and Á. Kvaran, *Phys. Chem. Chem. Phys.*, 2015, **17**, 32517.
32 T. A. Carlson, P. Gerard, M. O. Krause, G. V. Wald, J. W. Taylor and F. A. Grimm, *J. Chem. Phys.*, 1986, **84**, 4755–4759.
33 D. J. Hart and J. W. Hepburn, *Chem. Phys.*, 1989, **129**, 51–64.
34 S. T. Pratt, *J. Chem. Phys.*, 1994, **101**, 8302–8309.
35 A. J. Yencha, P. Baltzer, A. J. Cormack, Y. Li, H.-P. Liebermann, A. B. Alekseyev and R. J. Buenker, *J. Chem. Phys.*, 2003, **119**, 5943–5948.
36 Y. Hikosaka and K. Mitsuke, *J. Chem. Phys.*, 2004, **121**, 792–799.
37 P. M. Regan, D. Ascenzi, E. Wrede, P. A. Cook, M. N. R. Ashfold and A. J. Orr-Ewing, *Phys. Chem. Chem. Phys.*, 2000, **2**, 5364–5374.
38 J. Long, H. Wang and Á. Kvaran, *J. Chem. Phys.*, 2013, **138**, 044308.
39 K. Matthiasson, J. M. Long, H. S. Wang and Á. Kvaran, *J. Chem. Phys.*, 2011, **134**, 164302.
40 Á. Kvaran, K. Matthiasson and H. S. Wang, *J. Chem. Phys.*, 2009, **131**, 044324.
41 J. Long, H. Wang and Á. Kvaran, *J. Mol. Spectrosc.*, 2012, **282**, 20.
42 J. Long, H. R. Hróðmarsson, H. Wang and Á. Kvaran, *J. Chem. Phys.*, 2012, **136**, 214315.
43 A. Hafliðason, M. X. Jiang and Á. Kvaran, *Phys. Chem. Chem. Phys.*, 2019, **21**, 23154.
44 M. X. Jiang, A. Hafliðason and Á. Kvaran, *J. Mol. Spectrosc.*, 2020, **372**, 111329.
45 See ESI.
46 PGOPHER, *a program for rotational, vibrational and electronic spectra*, C. M. Western, University of Bristol, 10.1.180, University of Bristol, 2003–2018, http://pgopher.chm.bris.ac.uk/.
47 Á. Kvaran, H. Wang and B. G. Waage, *Can. J. Phys.*, 2001, **79**, 197–210.
48 R. G. Bray and R. M. Hochstrasser, *Mol. Phys.*, 1976, **31**, 1199–1211.
49 J. B. Halpern, *J. Mol. Spectrosc.*, 1980, **79**, 1–30.
50 H. Lefebvre-Brion and R. W. Field, *The Spectra and Dynamics of Diatomic Molecules*, Elsevier, Amsterdam, 2004.
51 NIST Chemistry WebBook – (National Institute of Standards and Technology) https://webbook.nist.gov/chemistry/nameser/.
52 A. Hafliðason, M. X. Jiang and Á. Kvaran, *Chem. Phys.*, 2021, **541**, 111016.
53 M. H. Alexander, X. Li, R. Liyanage and R. J. Gordon, *Chem. Phys.*, 1998, **231**, 331–343.
54 M. L. Ginter, S. G. Tilford and A. M. Bass, *J. Mol. Spectrosc.*, 1975, **57**, 271–283.
55 J. H. D. Eland and J. Berkowitz, *J. Chem. Phys.*, 1977, **67**, 5034.
56 N. Bowering, M. Miillert, M. Salzmann and U. Heinzmann, *J. Phys. B: At., Mol. Opt. Phys.*, 1991, **24**, 4793–4801.
57 P. Glodic, D. Zaouris, P. C. Samartzis, A. Hafliðason and Á. Kvaran, *Phys. Chem. Chem. Phys.*, 2016, **18**, 26291.
58 H. Hróðmarsson, A. Kartakoullis, D. Zaouris, P. Glodic, H. Wang, P. C. Samartzis and Á. Kvaran, *Phys. Chem. Chem. Phys.*, 2017, **19**, 11354.
59 C. J. Zietkiewicz, Y.-Y. GU, A. M. Farkas and J. G. Eden, *J. Chem. Phys.*, 1994, **101**, 86.
60 S. Manzhos, H.-P. Loock, B. L. G. Bakker and D. H. Parker, *J. Chem. Phys.*, 2002, **117**, 9347.

4.5.1 Supporting information

High energy state interactions, energetics and multiphoto-fragmentation processes of HI

Meng-Xu Jiang and Ágúst Kvaran*

Science Institute, University of Iceland, Dunhagi 3, 107 Reykjavík, Iceland.

Supplementary material: Supporting material (figures and tables) to go with the main text of the paper ” High energy state interactions, energetics and multiphoto-fragmentation processes of HI”

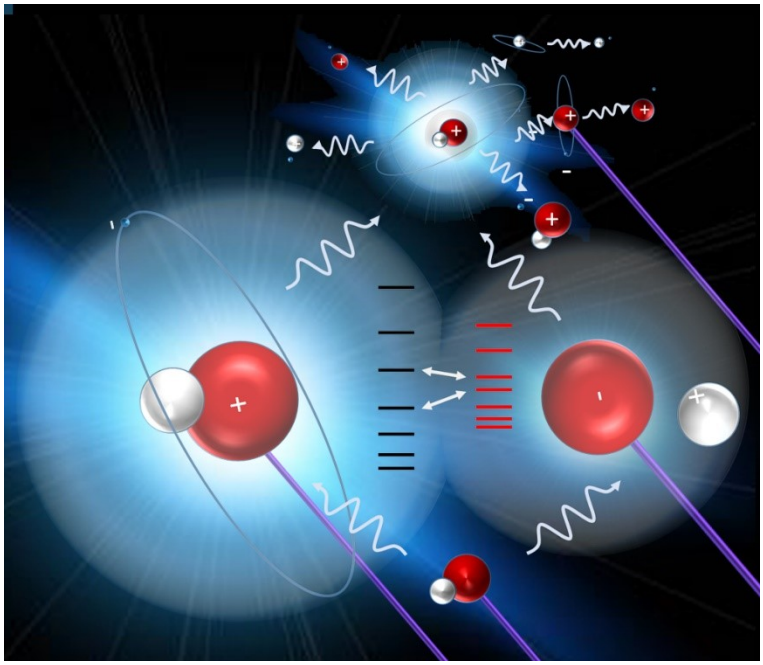

Content: pages:

Figures:

Tables:

Tables S2:

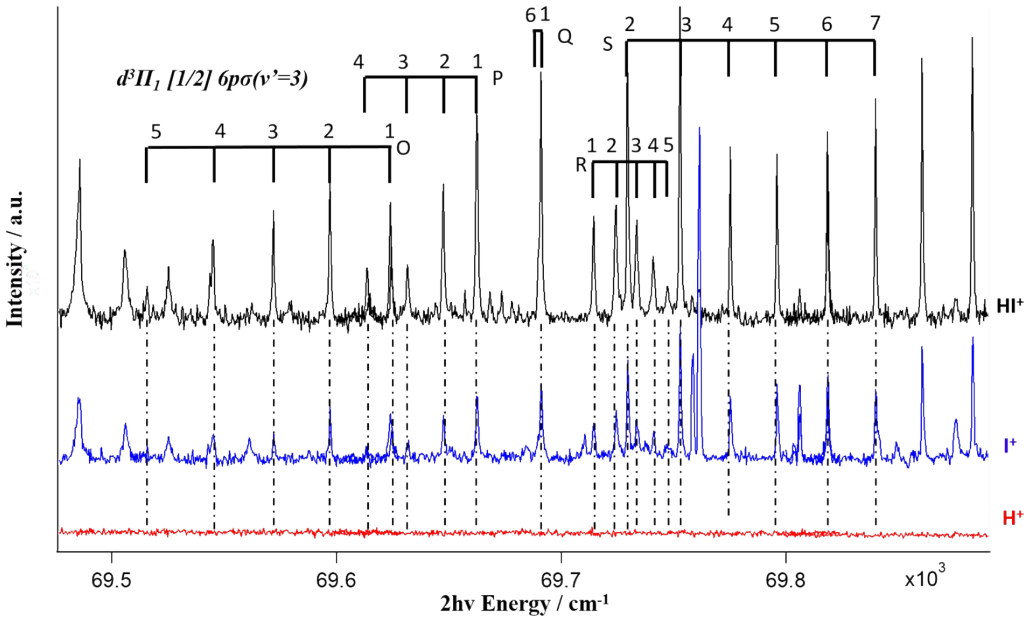

Fig. S1 a) REMPI spectra for HI for 2hν resonant transition in the excitation region of 69480 – 69900 cm^{-1}. Top (black) is the HI^+ ion, middle (blue) is I^+ ion, bottom (red) is H^+ ion. The new $d^3\Pi_1$ [3/2] 6pσ(v'=3) Rydberg states was located and assigned in the HI^+ and I^+ spectra.

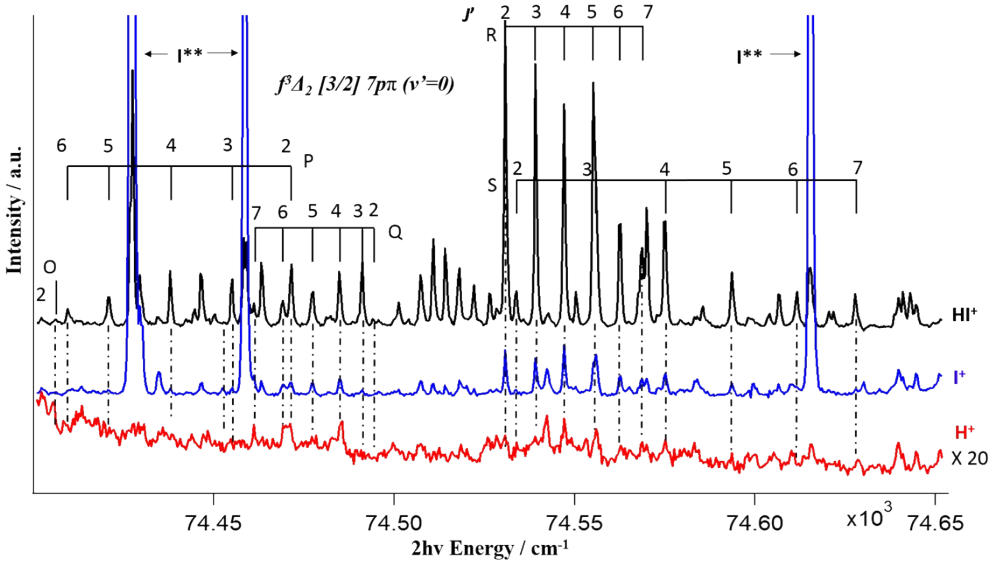

Fig. S1 b) REMPI spectra for HI due to 2hν resonance transition in the energy region of 74 440 – 74 620 cm^{-1}. Ions are indicated. Assignment of rotational line of the $F^1\Delta_2$ [1/2] 6pπ (v'=2) Rydberg state spectrum in the HI^+ ion spectrum is shown.

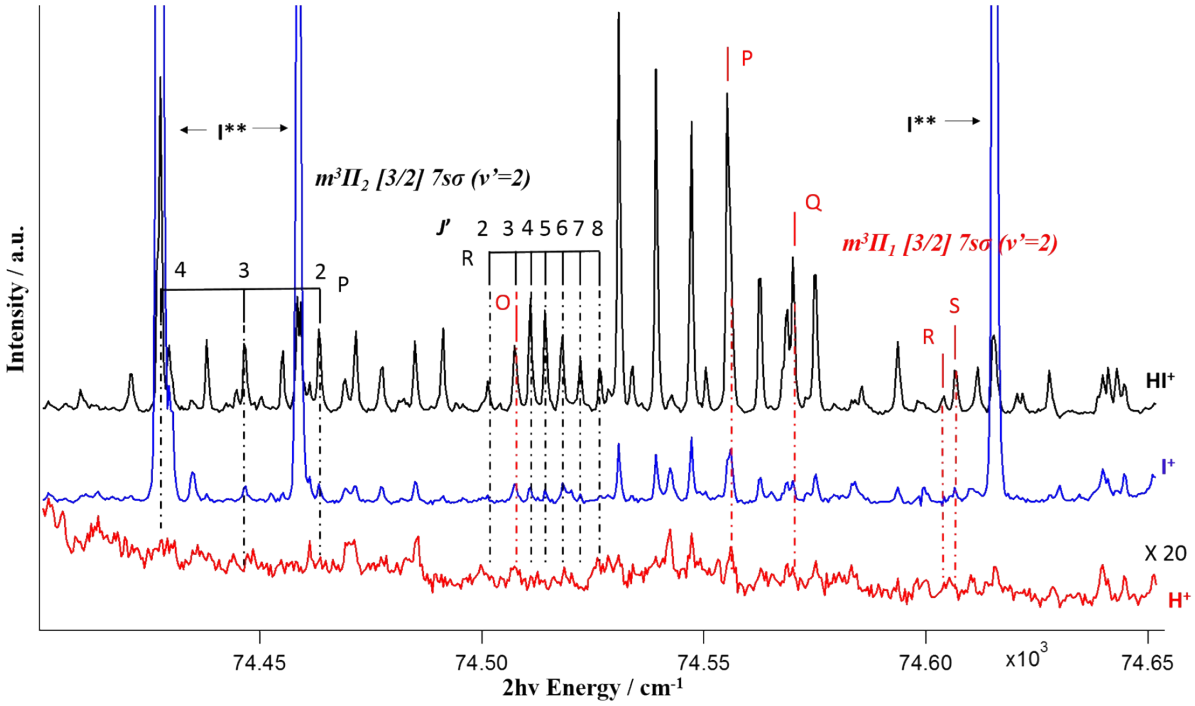

Fig. S1 c) REMPI spectra of HI due to 2hν resonance transition in the excitation region of 74 440 – 74 620 cm^{-1}. Assignment of rotational line of the $m^3\Pi_{2,1}[1/2]7s\sigma$ (v'=2) Rydberg state spectrum in the HI^+ ion spectrum is indicated.

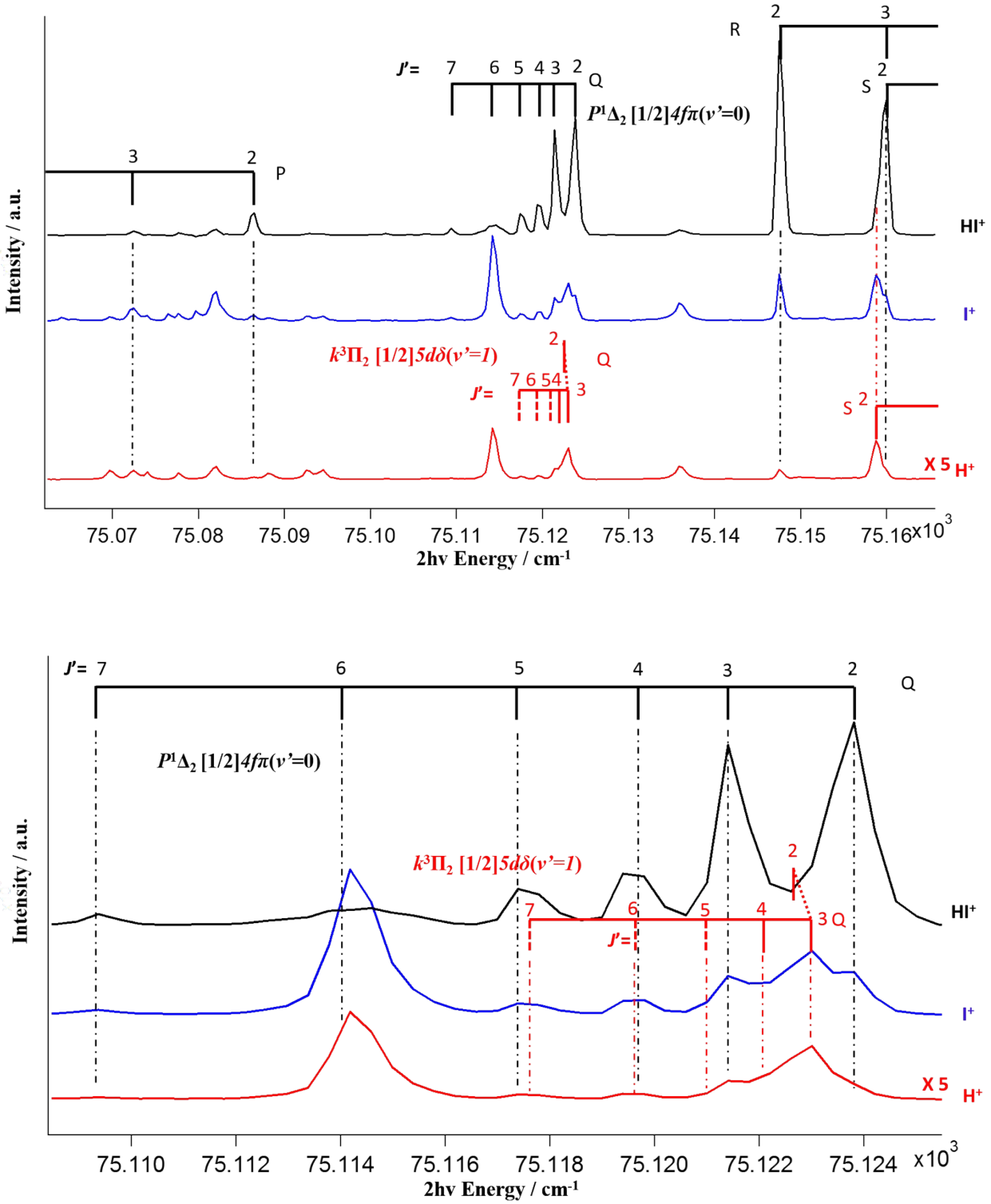

Fig S2 a) REMPI spectra for HI due to 2hν resonance transition in the excitation region of 75000 – 75200 cm^{-1}. Top (black): HI$^+$ ion, middle (blue): I$^+$ ion, bottom (red): H$^+$ ion. The new $k^3\Pi_2$ [1/2]5dδ(v'=1) Rydberg state spectrum was located and assigned.

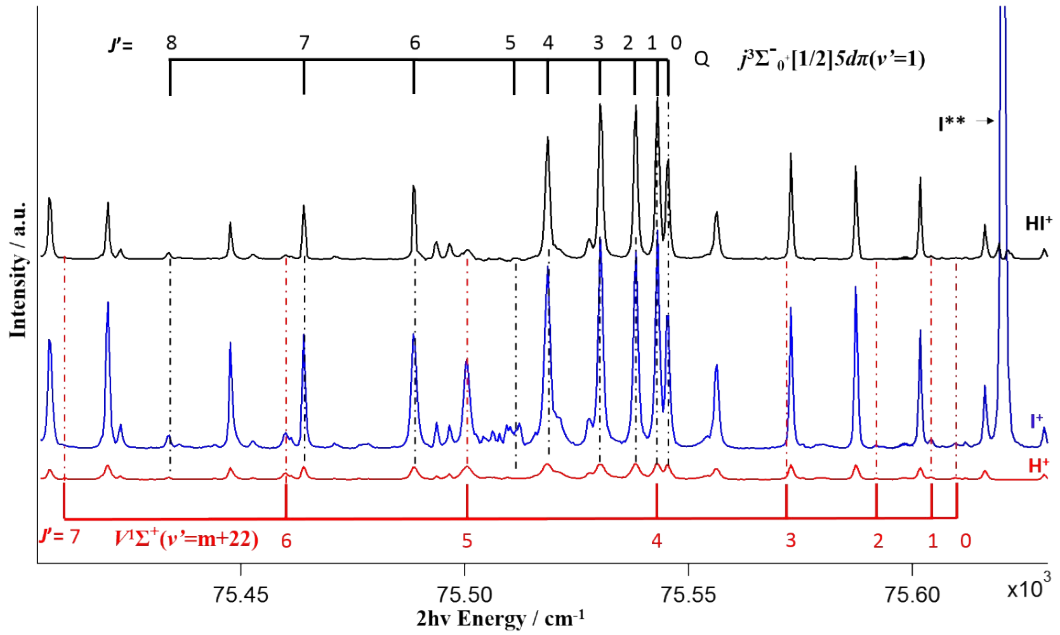

Fig. S2 b) REMPI spectra for HI due to 2hν resonance transition in the excitation region of 75300 – 75700 cm^{-1}. Assignment of rotational *Q*-lines, $J' = 0$ -7 for the $V^1\Sigma^+(v' = m + 22)$ ion-pair vibrational state in the I^+ and H^+ ion spectrum is shown.

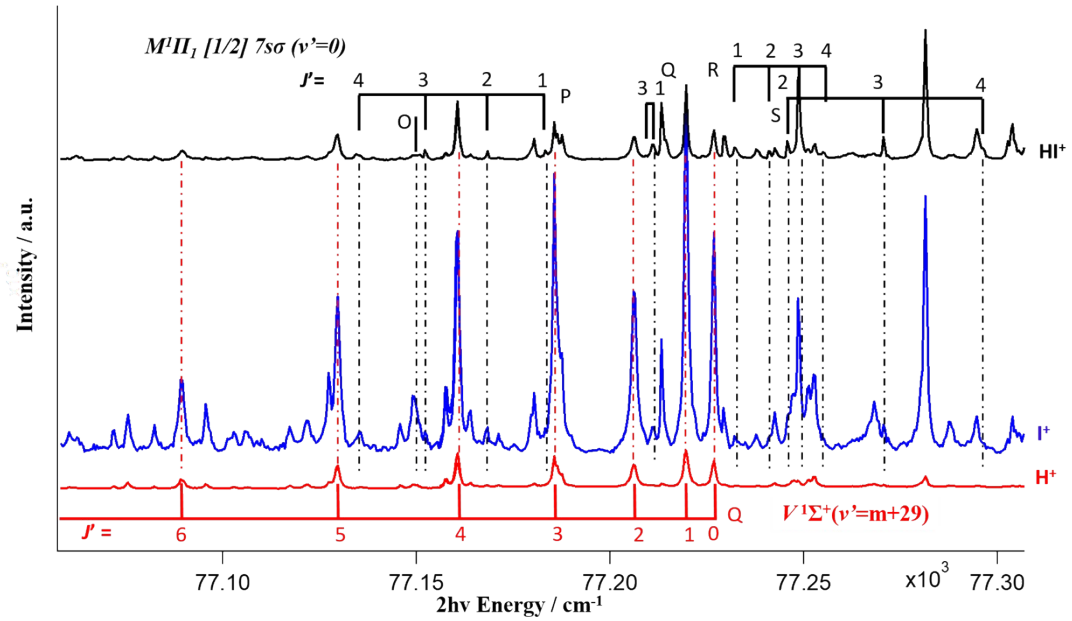

Fig. S2 c) REMPI spectra for HI due to 2hν resonance transition in the excitation region of 77000 – 77300cm^{-1}. Ions are indicated. The new $M^1\Pi_1$ [1/2]7sσ(v'=0) Rydberg state spectrum was located and assigned.

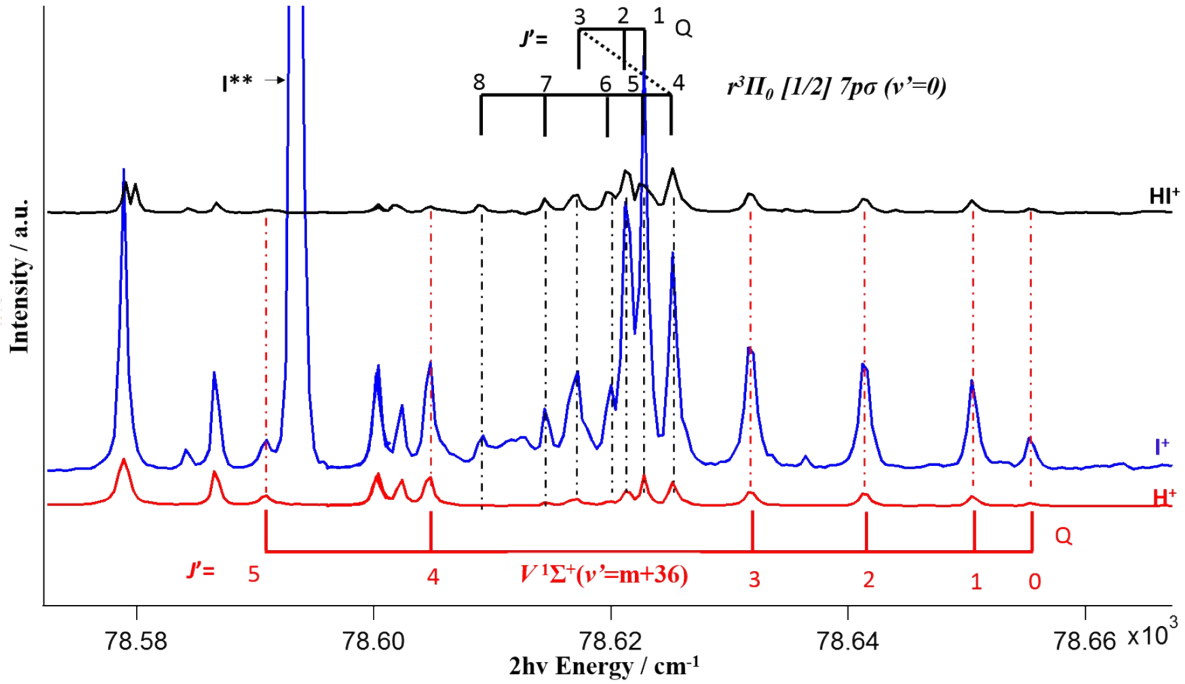

Fig. S2 d) REMPI spectra for HI due to 2hν resonance transition in the excitation region of 78500 – 78700 cm^{-1}. Top (black): HI^+ ion, middle (blue): I^+ ion, bottom (red): H^+ ion. The new $R^1\Pi_1$ [1/2]7pσ(v'=0) Rydberg state spectrum and $V^1\Sigma^+$(v'=m+36)) ion-paired state spectrum were located and assigned.

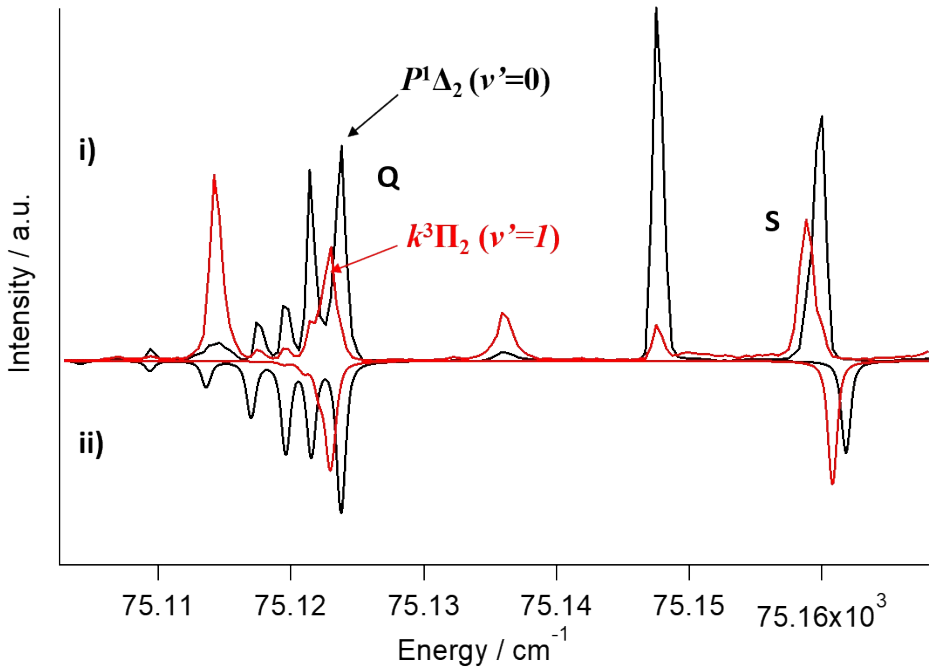

Fig. S3 a) Simulation of $P^1\Delta_2$ [1/2]4fπ(v'=0) and $k^3\Pi_2$ [1/2]5dδ(v'=1) system, i) Experimental data; ii) calculated.

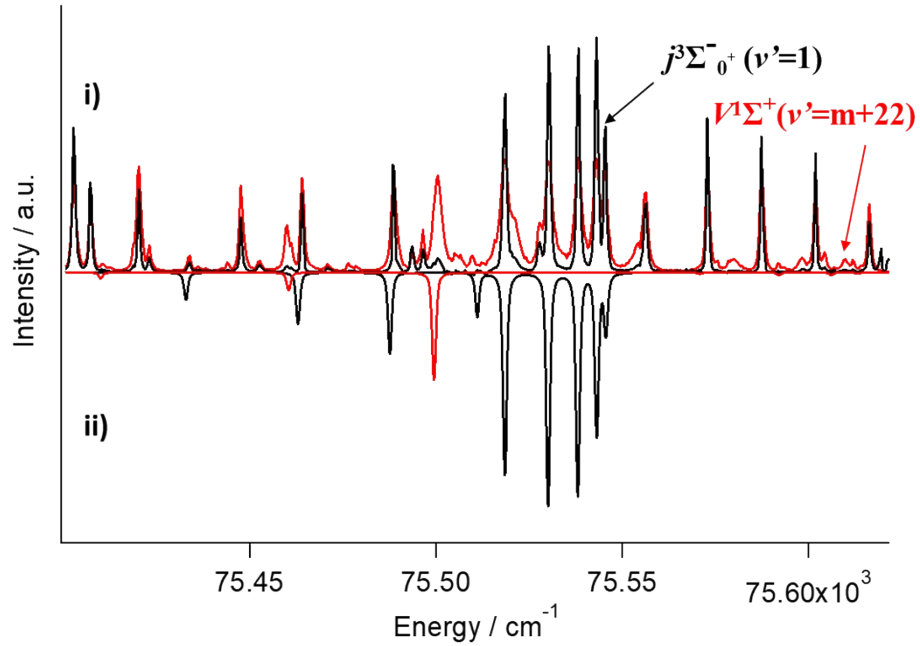

Fig. S3 b) Simulation of $j^3\Sigma^-_{0^+}$[1/2]5dπ(v'=1) and $V^1\Sigma^+$(v'=m+22) system, i) Experimental data; ii) calculated.

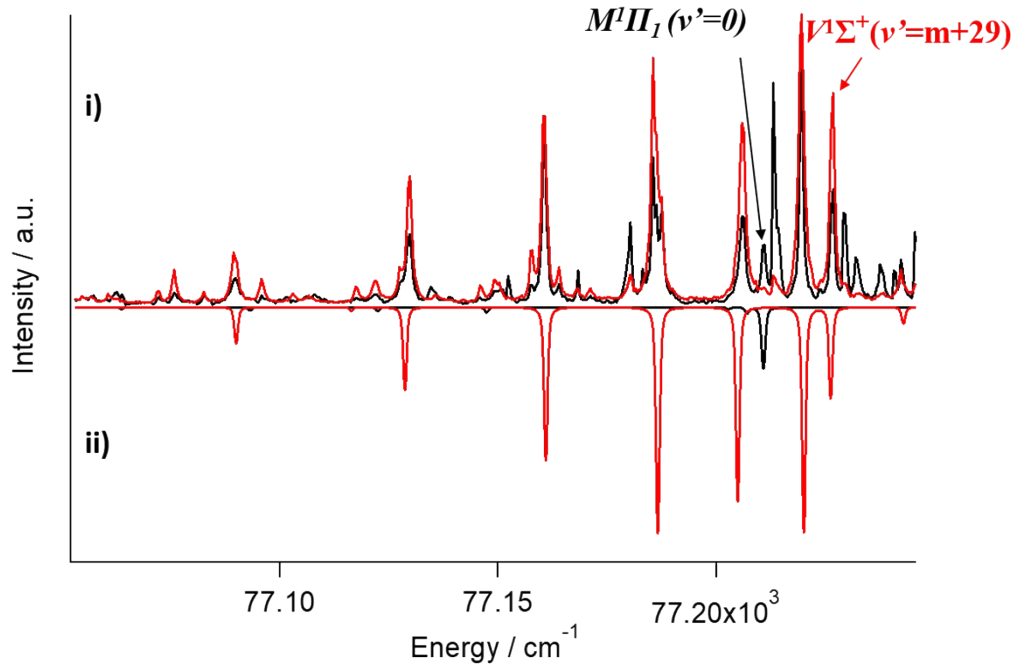

Fig. S3 c) Simulation of $M^1\Pi_1$ [1/2]7sσ(v'=0) and $V^1\Sigma^+$(v'=m+29) system, i) Experimental data; ii) calculated.

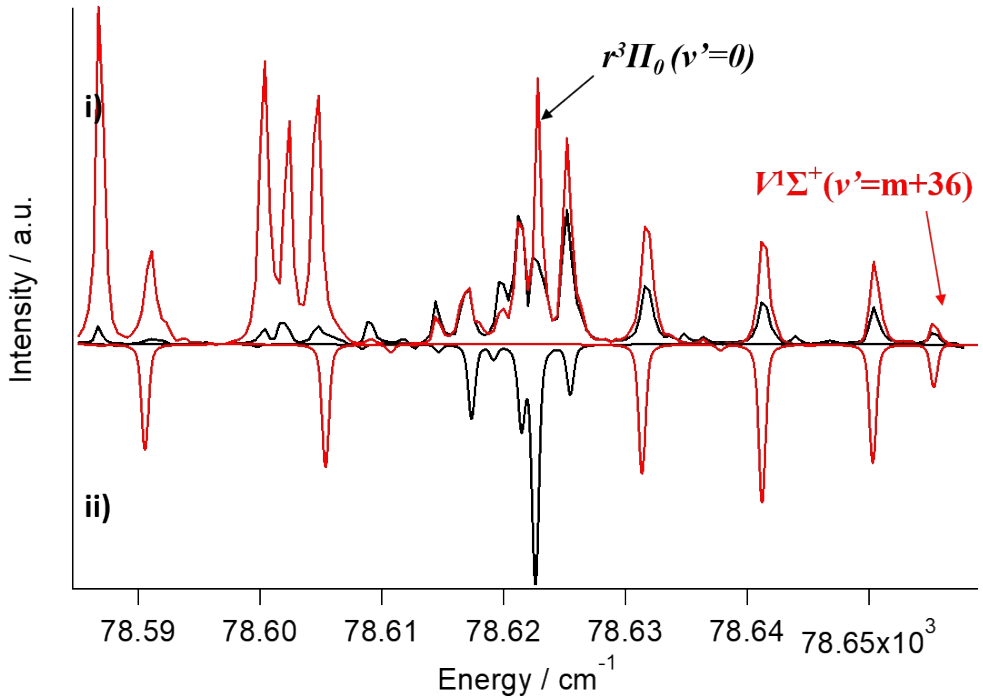

Fig. S3 d) Simulation of $r^3\Pi_0$ [1/2]7pσ(v'=0) and $V^1\Sigma^+$(v'=m+36) system, i) Experimental data; ii) calculated.

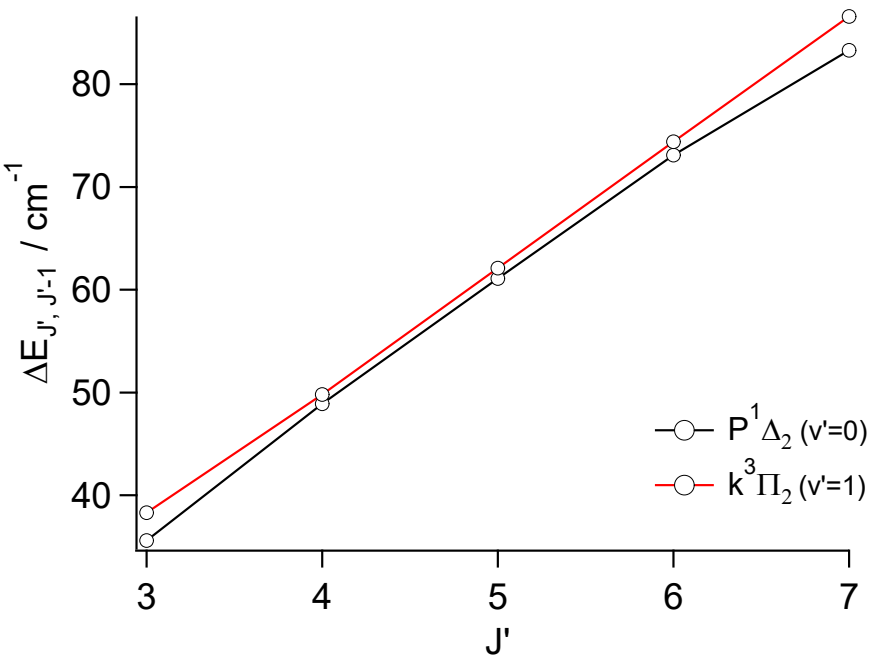

Fig. S4 a) Perturbation effects due to the $P^1\Delta_2$ [1/2]4fπ(v'=0) and $k^3\Pi_2$ [1/2]5dδ(v'=1) state interaction. Spacing between rotational levels ($\Delta E_{J, J-1}$) as a function of J'; experimental values

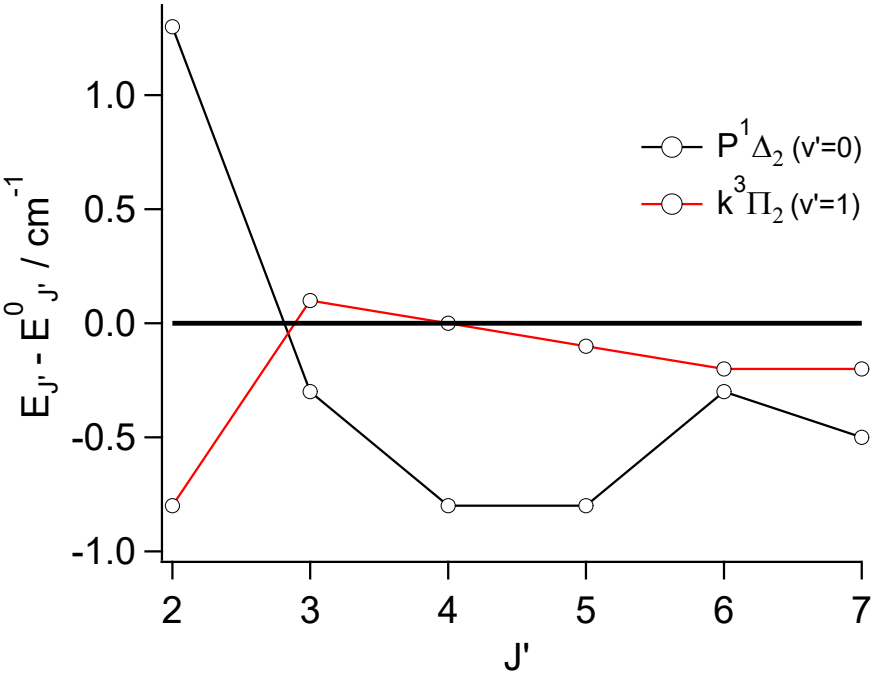

Fig.S4 b) Perturbation effects due to the $P^1\Delta_2$ [1/2]4fπ(v'=0) and $k^3\Pi_2$ [1/2]5dδ(v'=1) state interaction. Reduced term value plots: Deperturbed energy level values subtracted from experimental energy level values

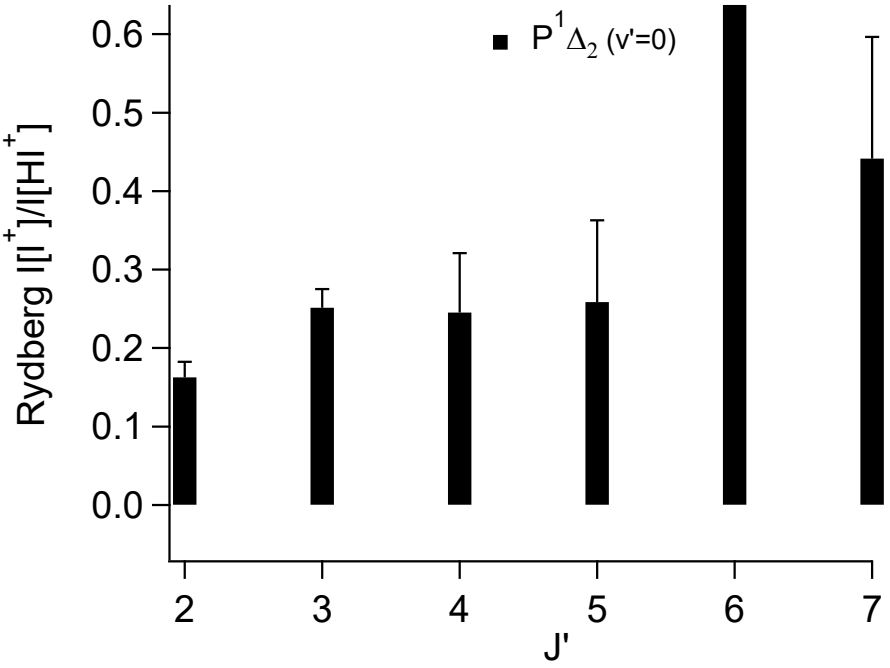

Fig. S4 c) Perturbation effects due to the $P^1\Delta_2$ [1/2]4fπ(v'=0) and $k^3\Pi_2$ [1/2]5dδ(v'=1) state interaction. Relative ion-signal intensities ($I(I^+)/I(HI^+)$) vs. J' derived from the Q-rotational lines for the $P^1\Delta_2$ [1/2]4fπ(v'=0) spectrum.

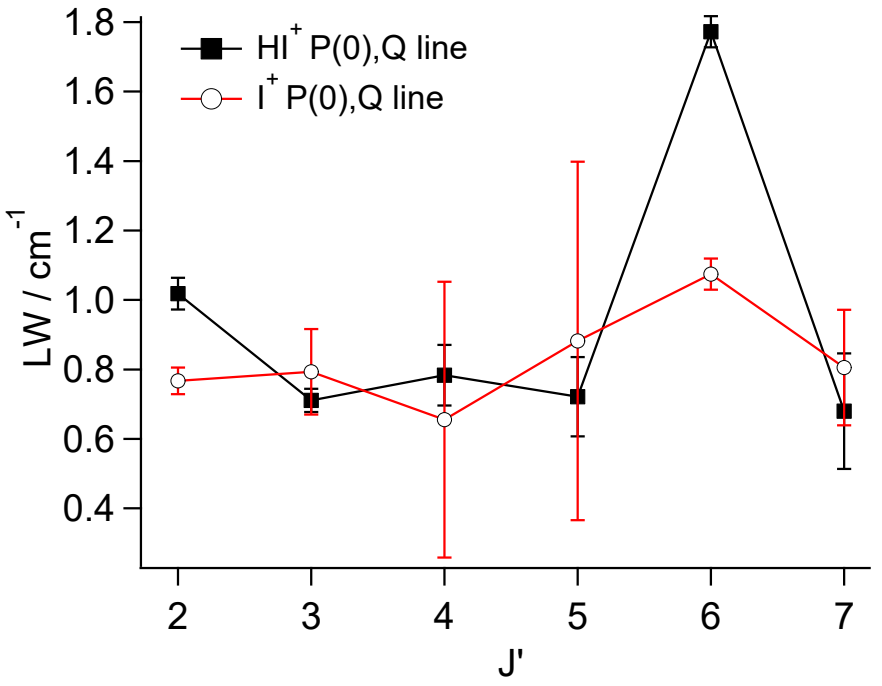

Fig. S4 d) Perturbation effects due to the $P^1\Delta_2$ [1/2]4fπ(v'=0) and $k^3\Pi_2$ [1/2]5dδ(v'=1) state interaction. Rotational line-widths vs J' derived from the Q lines of the I^+ signals for the $P^1\Delta_2$ [1/2]4fπ(v'=0) state spectrum.

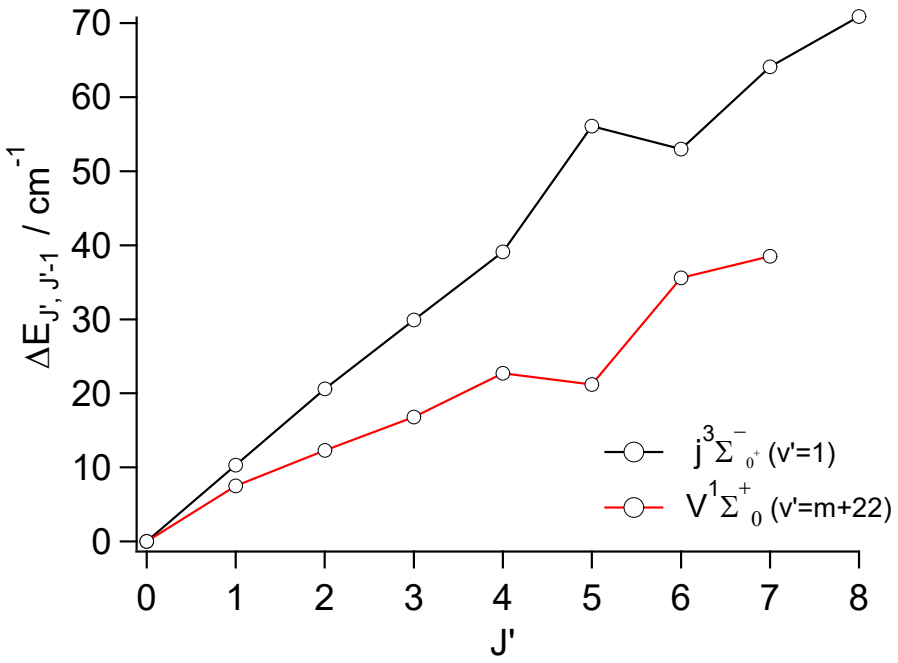

Fig. S5 a) Perturbation effects due to the $j^3\Sigma^-_{0^+}[1/2]5d\pi(v'=1)$ and $V^1\Sigma^+(v'=m+22)$ state interaction. Spacing between rotational levels ($\Delta E_{J,\,J-1}$) as a function of J'.

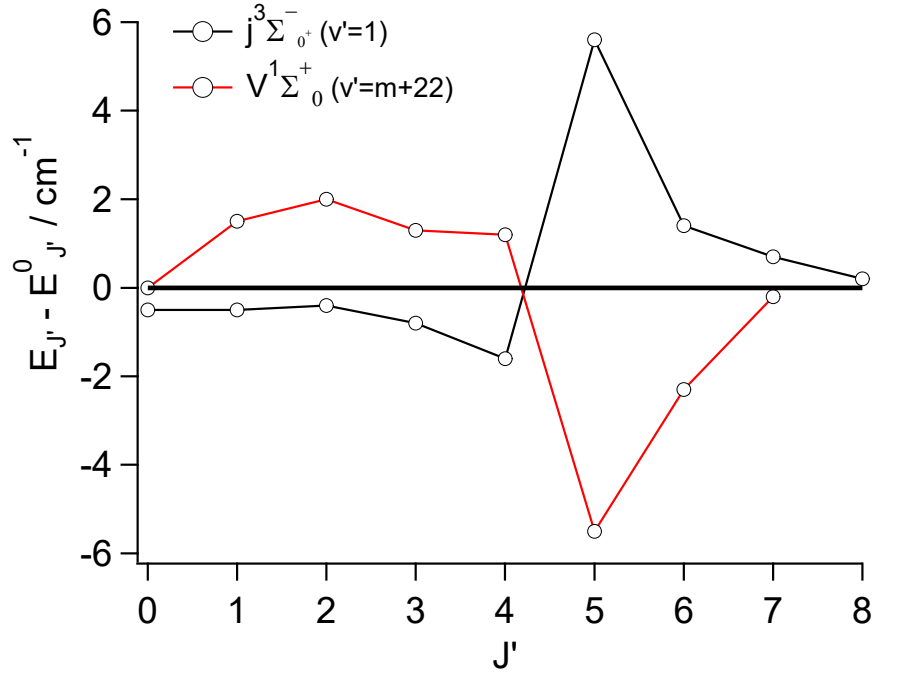

Fig. S5 b) Perturbation effects due to the $j^3\Sigma^-_{0^+}[1/2]5d\pi(v'=1)$ and $V^1\Sigma^+(v'=m+22)$ state interaction. Reduced term value plots: Deperturbed energy level values subtracted from experimental energy level values.

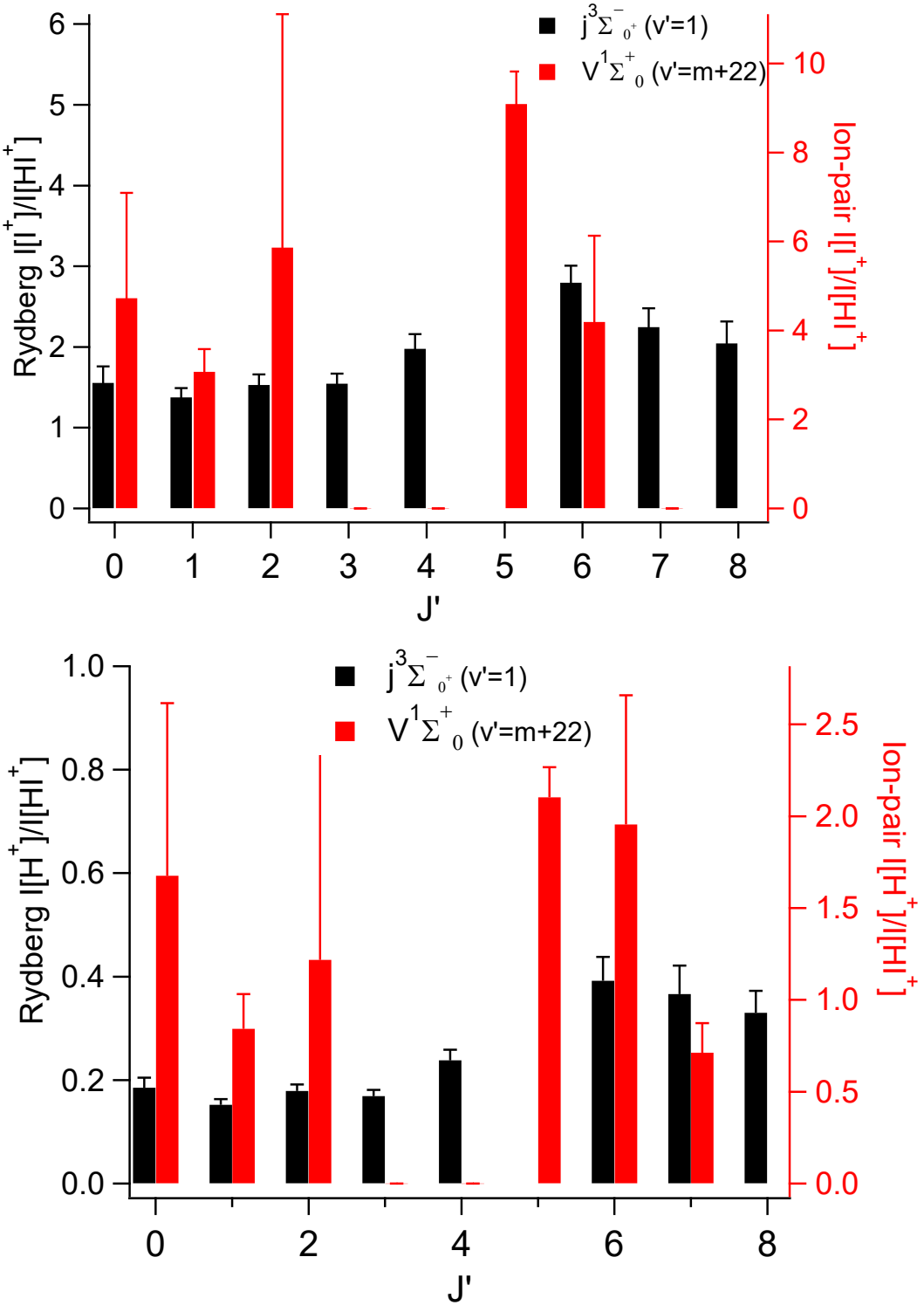

Fig. S5 c) Perturbation effects due to the $j^3\Sigma^-_{0^+}[1/2]5d\pi(v'=1)$ and $V^1\Sigma^+(v'=m+22)$ state interaction. Relative ion-signal intensities ($I(I^+)/I(HI^+)$ and $I(H^+)/I(HI^+)$) vs. J' derived from the Q-rotational lines for the $j^3\Sigma^-_{0^+}[1/2]5d\pi(v'=1)$ and $V^1\Sigma^+(v'=m+22)$ spectra.

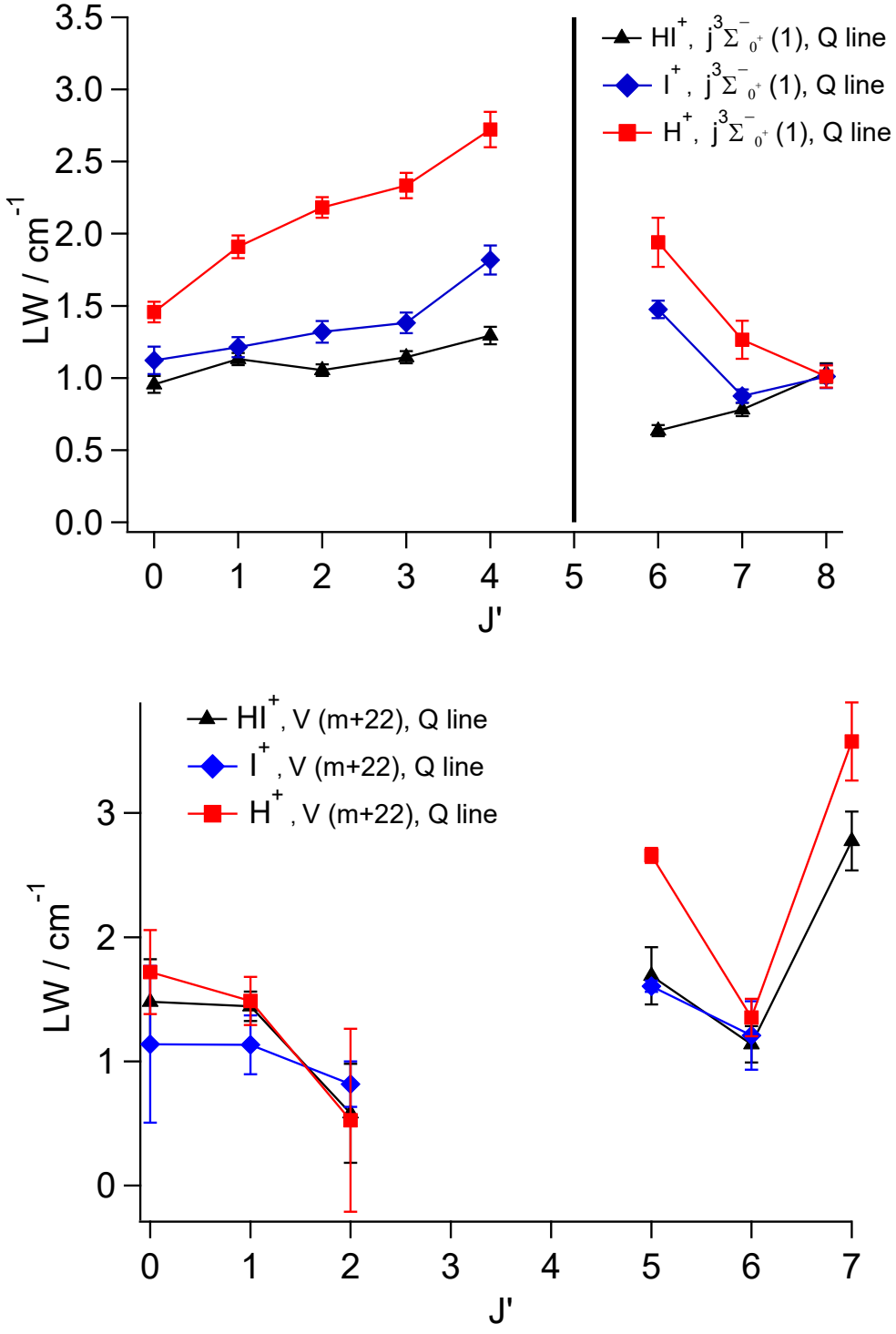

Fig. S5 d) Perturbation effects due to the $j^3\Sigma^-_{0^+}[1/2]5d\pi(v'=1)$ and $V^1\Sigma^+(v'=m+22)$ state interaction. Rotational line widths vs J' derived from the Q lines of ion-spectra for the $j^3\Sigma^-_{0^+}[1/2]5d\pi(v'=1)$ and $V^1\Sigma^+(v'=m+22)$ state spectra.

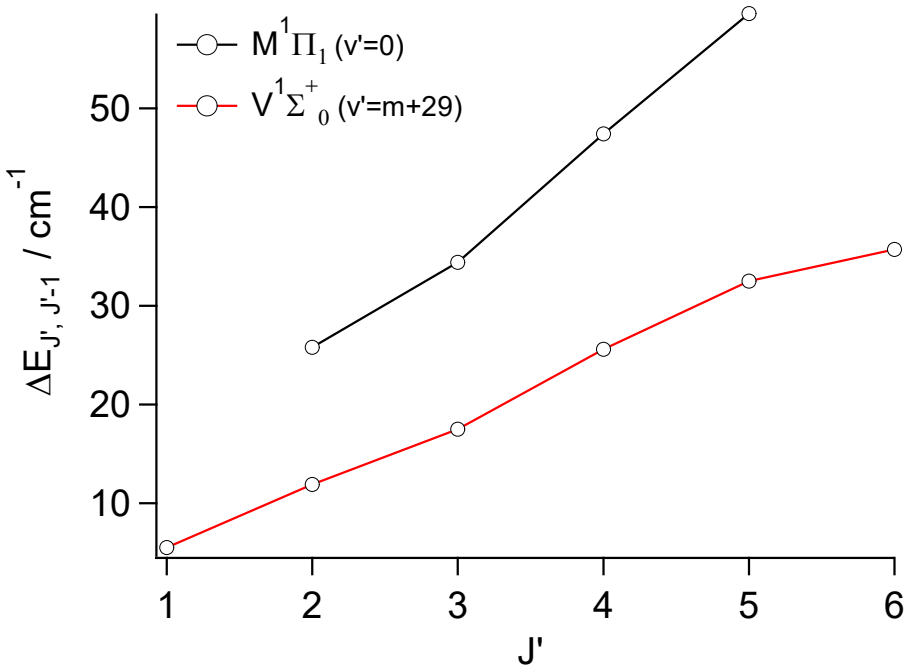

Fig. S6 a) Perturbation effects due to the $M^1\Pi_1$ [1/2]7sσ(v'=0) and $V^1\Sigma^+$(v'=m+29) states interaction. Spacing between rotational levels ($\Delta E_{J, J-1}$) as a function of J'.

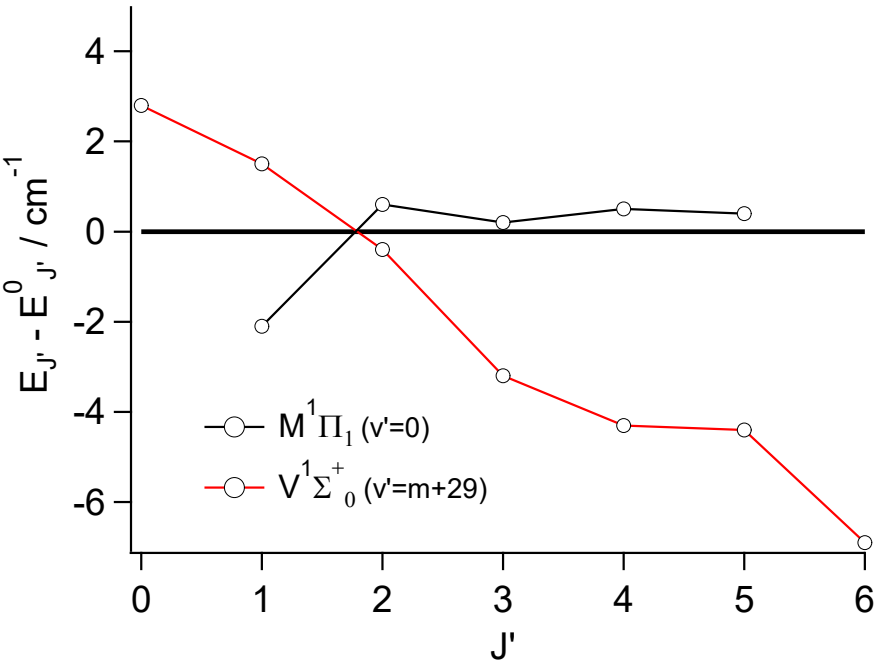

Fig. S6 b) Perturbation effects due to the $M^1\Pi_1$ [1/2]7sσ(v'=0) and $V^1\Sigma^+$(v'=m+29) states interaction. Reduced term value plots: Deperturbed energy level values subtracted from experimental energy level values.

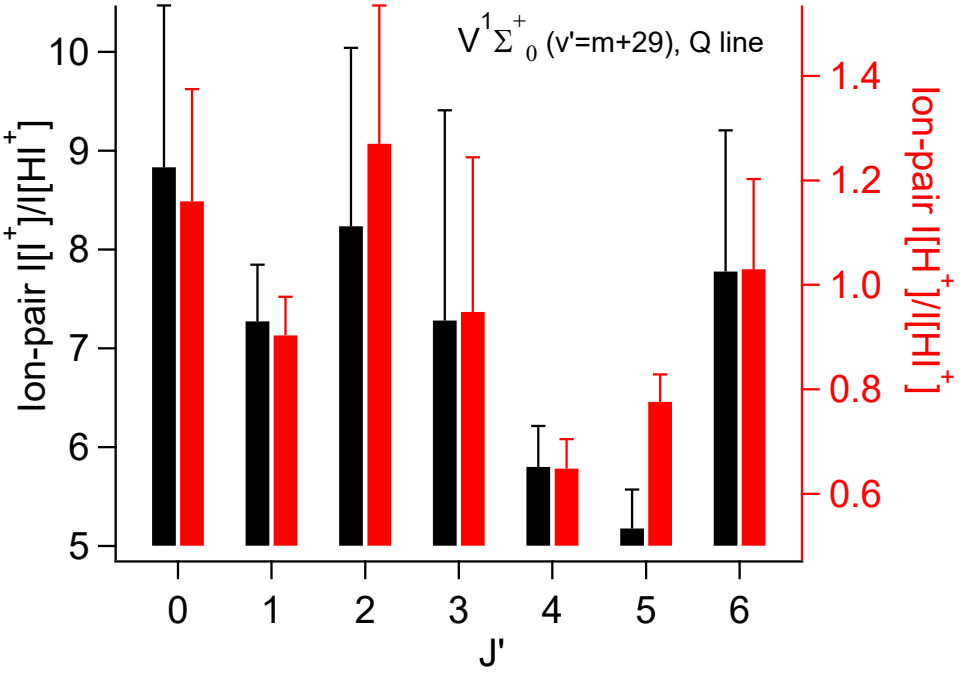

Fig. S6 c) Perturbation effects due to the $M^1\Pi_1$ [1/2]7sσ(v'=0) and $V^1\Sigma^+$(v'=m+29) states interaction. Relative ion-signal intensities ($I(I^+)/I(HI^+)$ and $I(H^+)/I(HI^+)$ vs. J' derived from the Q-rotational lines for the $V^1\Sigma^+$(v'=m+29) spectrum.

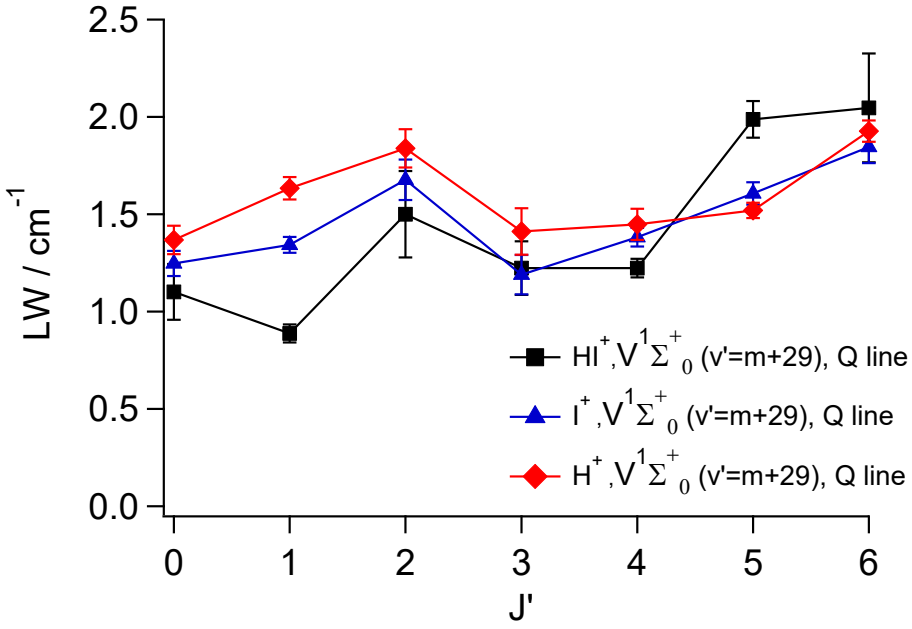

Fig. S6 d) Perturbation effects due to the $M^1\Pi_1$ [1/2]7sσ(v'=0) and $V^1\Sigma^+$(v'=m+29) states interaction. Rotational line-widths vs J' derived from the Q lines of the ion-spectra for the $V^1\Sigma^+$(v'=m+29) state.

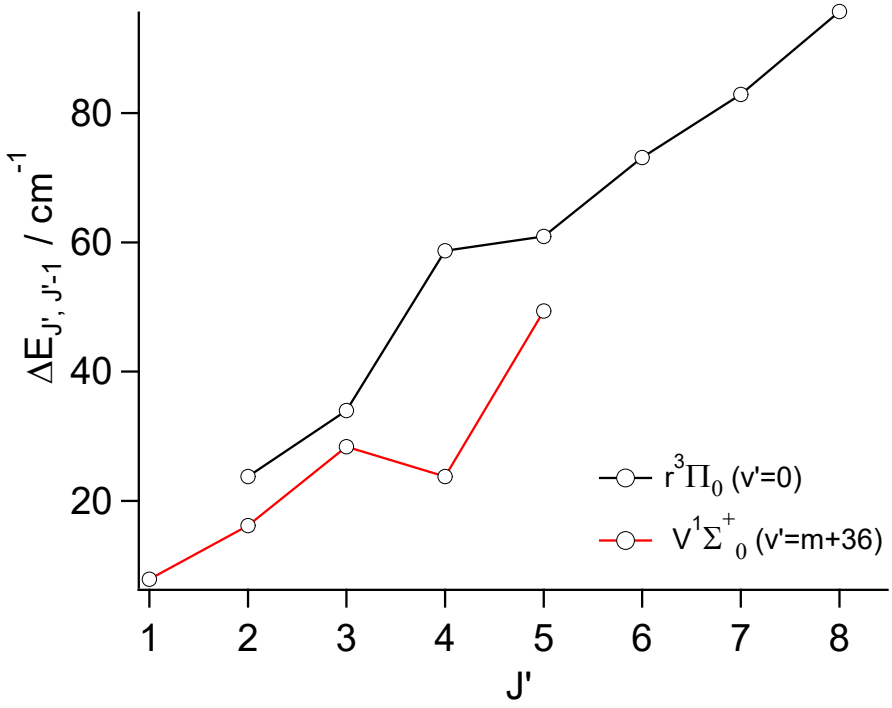

Fig. S7 a) Perturbation effects due to the $r^3\Pi_0$ [1/2]7pσ(v'=0) and $V^1\Sigma^+$(v'=m+36) state interaction. Spacing between rotational levels ($\Delta E_{J, J-1}$) as a function of J'.

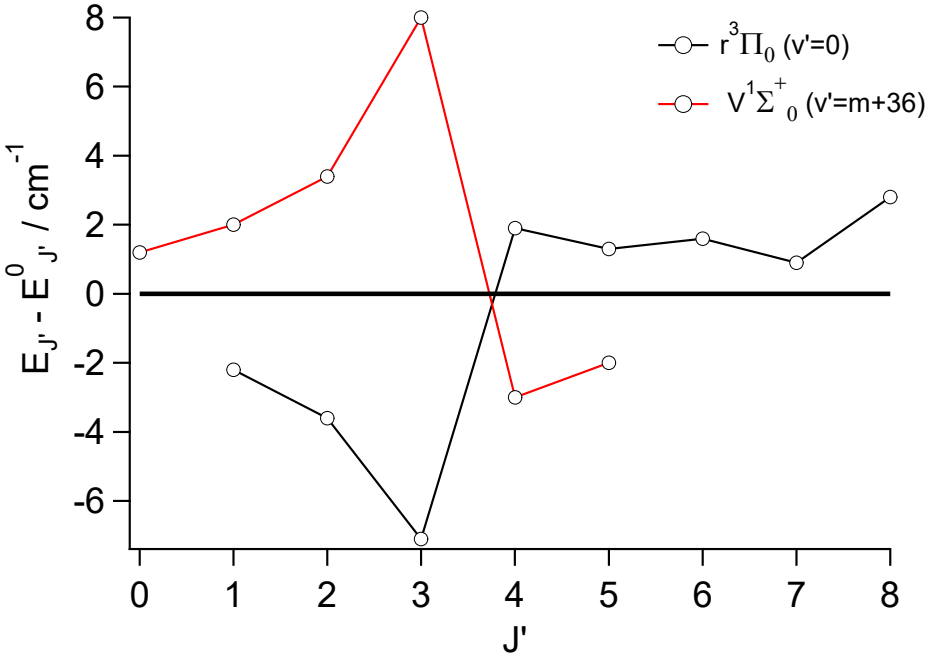

Fig. S7 b) Perturbation effects due to the $r^3\Pi_0$ [1/2]7pσ(v'=0) and $V^1\Sigma^+$(v'=m+36) state interaction. Reduced term value plots: Deperturbed energy level values subtracted from experimental energy level values.

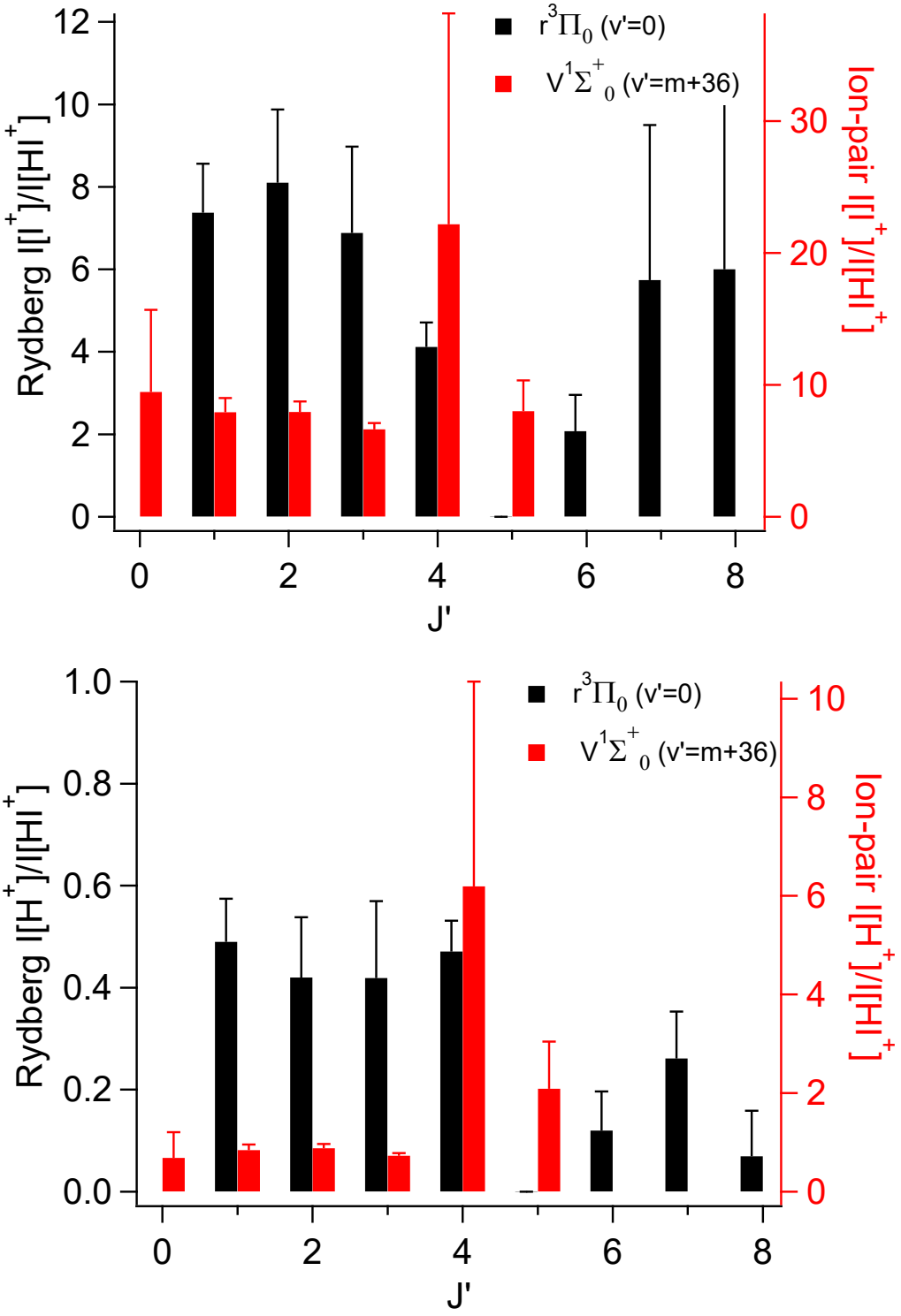

Fig. S7 c) Perturbation effects due to the $r^3\Pi_0$ [1/2]7pσ(v'=0) and $V^1\Sigma^+$(v'=m+36) state interaction. Relative ion-signal intensities ($I(I^+)/I(HI^+)$ and $I(H^+)/I(HI^+)$ vs. J' derived from the Q-rotational lines for the $r^3\Pi_0$ [1/2]7pσ(v'=0) and $V^1\Sigma^+$(v'=m+36) spectra.

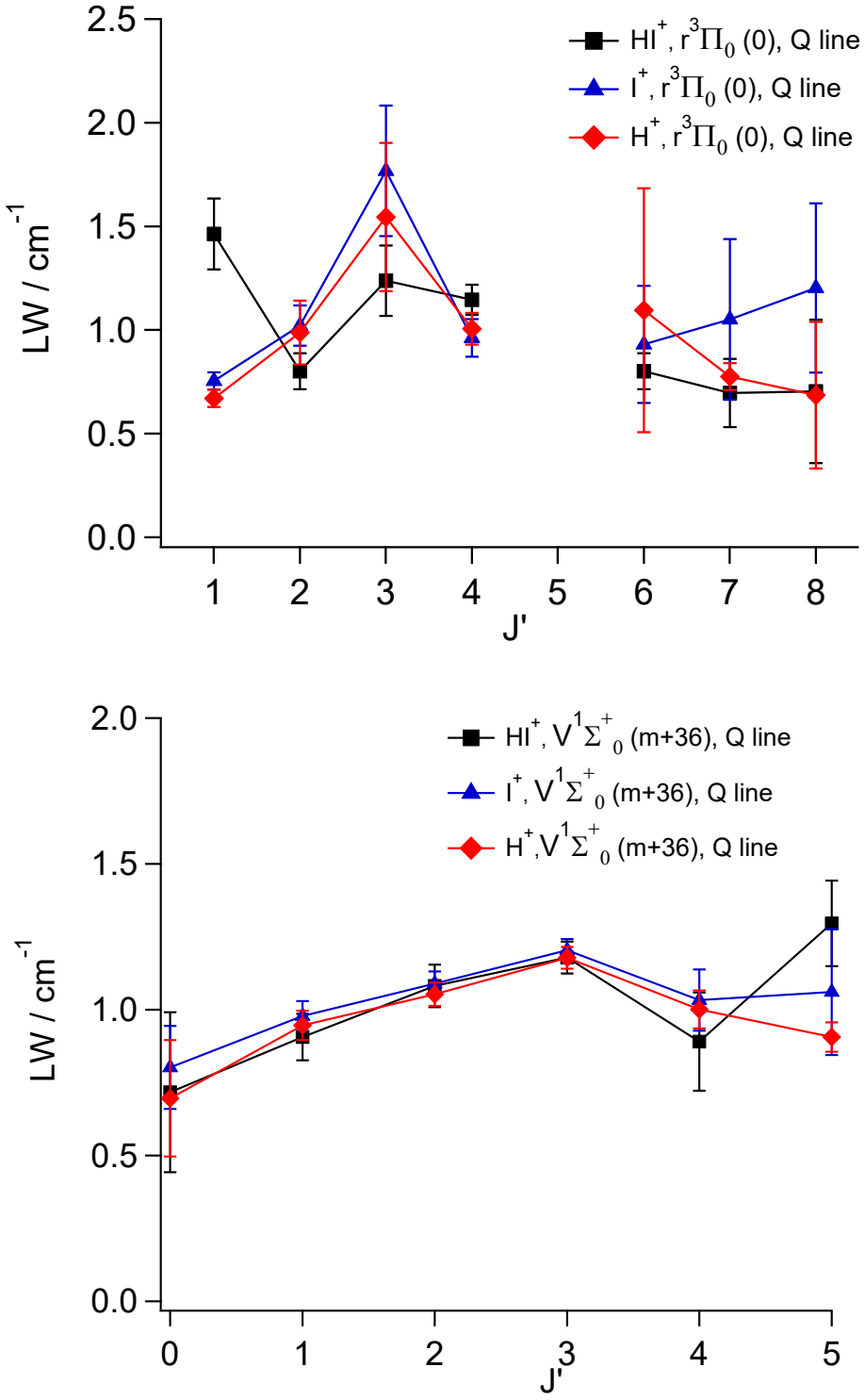

Fig. S7 d) Perturbation effects due to the $r^3\Pi_0$ [1/2]7pσ(v'=0) and $V^1\Sigma^+$(v'=m+36) state interaction. Rotational line widths vs. J' derived from the Q lines of the ion-spectra for the $r^3\Pi_0$ [1/2]7pσ(v'=0) and $V^1\Sigma^+$(v'=m+36) states.

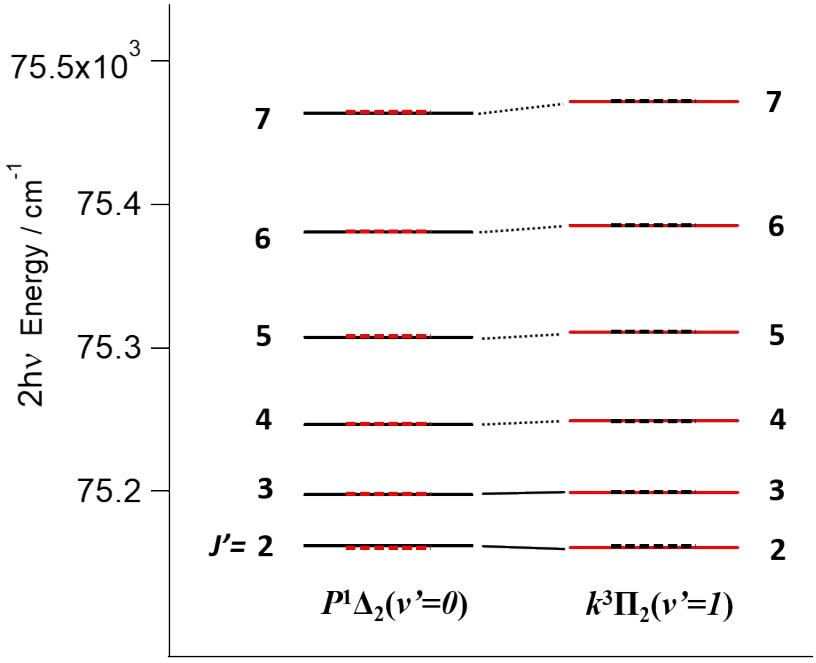

Fig. S8 a) Energy level diagram showing deperturbed (broken lines) and perturbed (solid lines) rotational energy levels for $P^1\Delta_2$ [1/2]4fπ(v'=0) and $k^3\Pi_2$ [1/2]5dδ(v'=1).

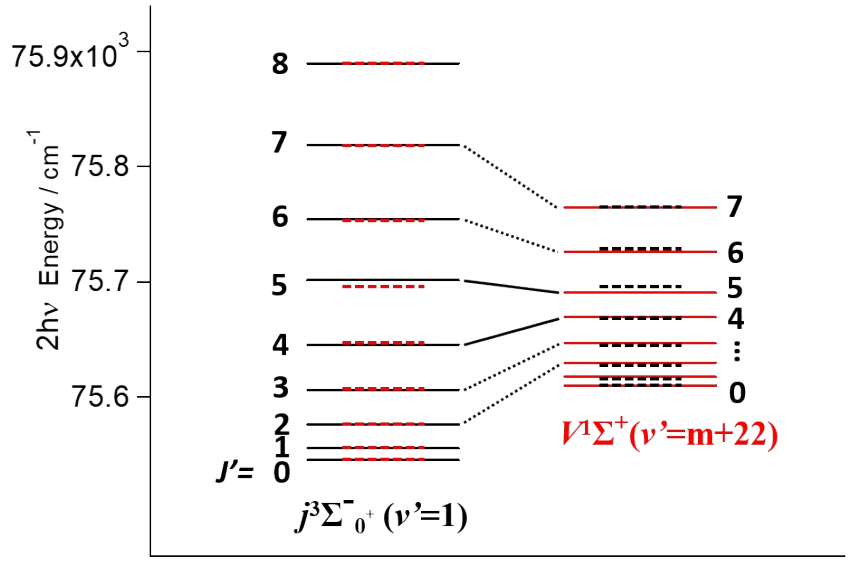

Fig. S8 b) Energy level diagram showing deperturbed (broken lines) and perturbed (solid lines) rotational energy levels for $j^3\Sigma^-_{0^+}$[1/2]5dπ(v'=1) and $V^1\Sigma^+$(v'=m+22).

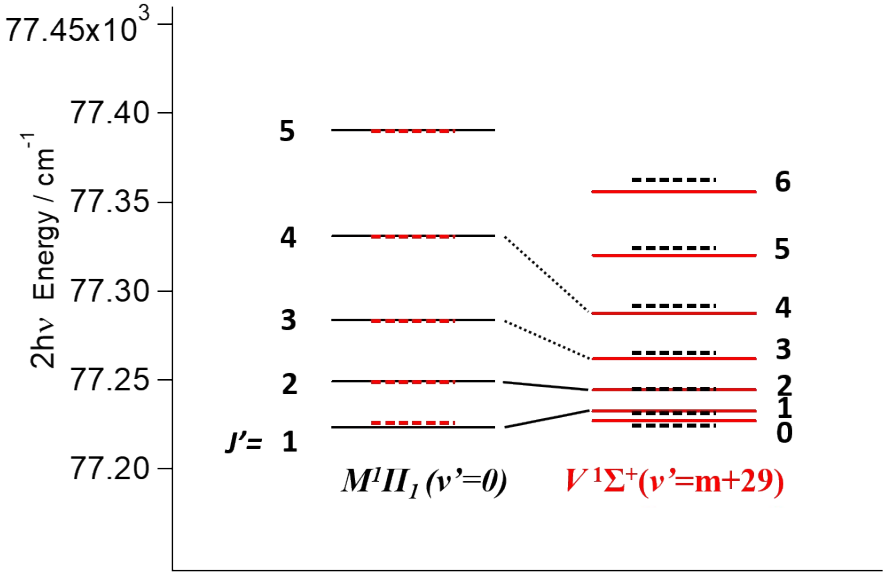

Fig. S8 c) Energy level diagram showing deperturbed (broken lines) and perturbed (solid lines) rotational energy levels for $M^1\Pi_1$ [1/2]7sσ(v'=0) and $V^1\Sigma^+$(v'=m+29).

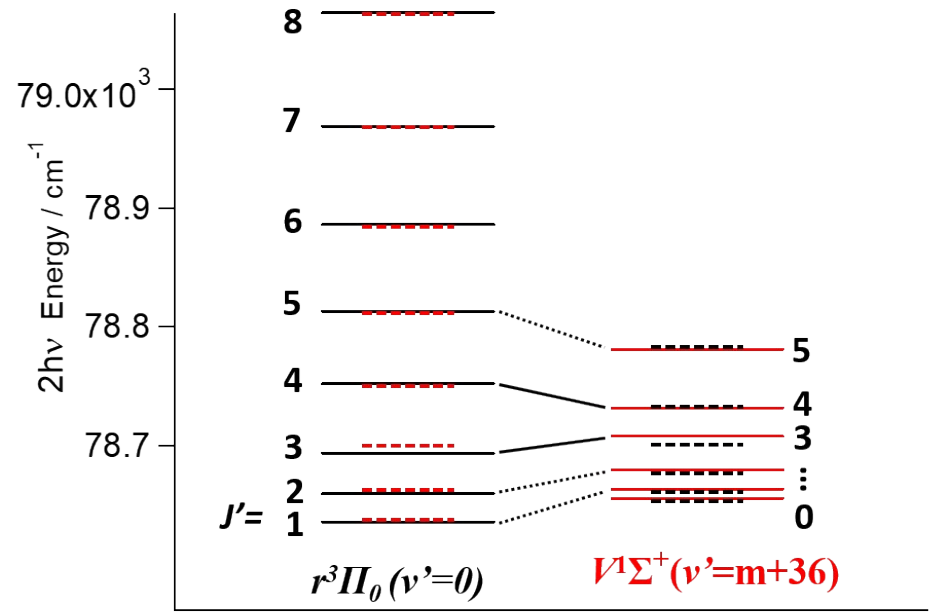

Fig. S8 d) Energy level diagram showing deperturbed (broken lines) and perturbed (solid lines) rotational energy levels for $r^1\Pi_0$ [1/2]7pσ(v'=0) and $V^1\Sigma^+$(v'=m+36).

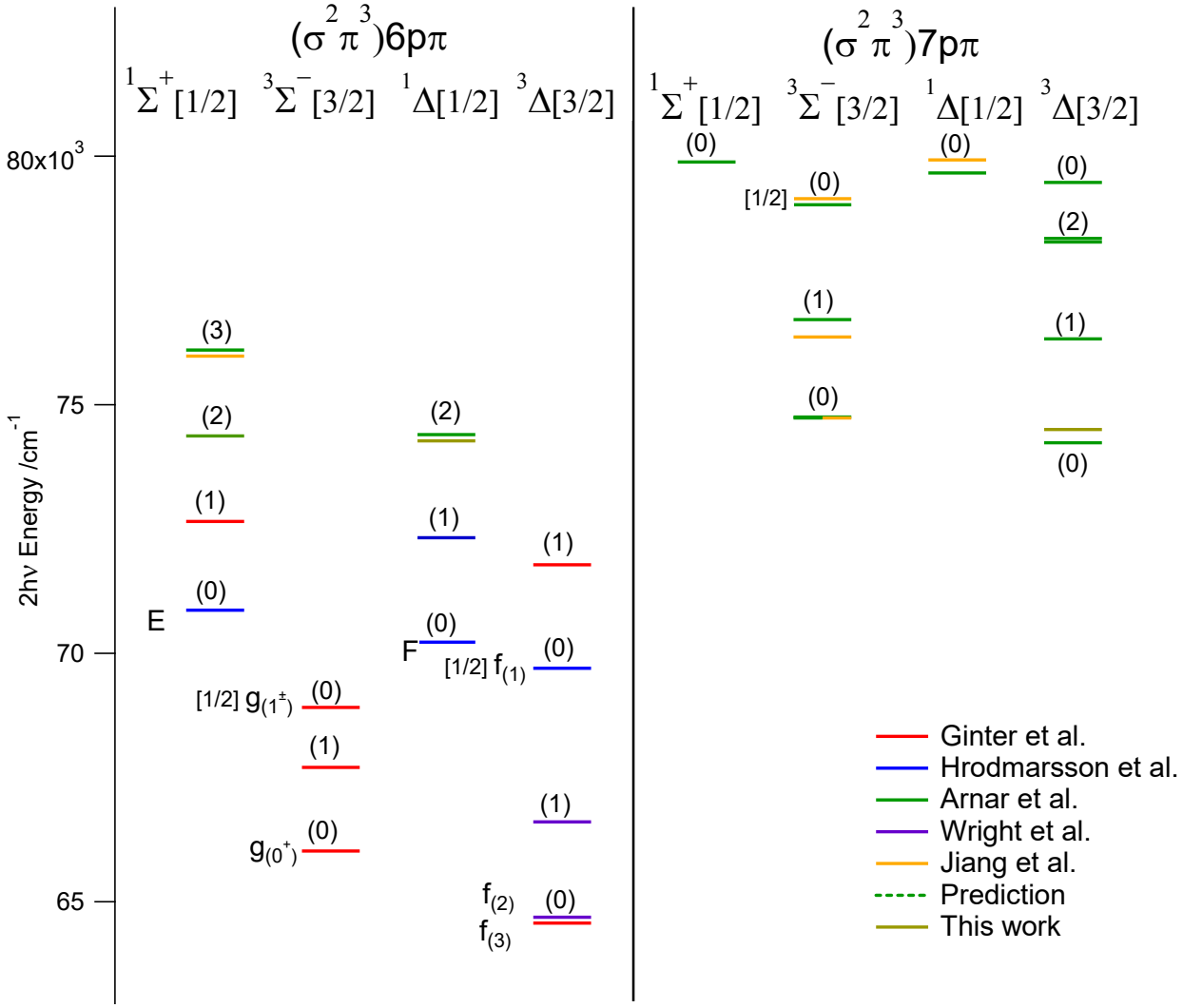

Fig. S9 a) $^{1,3}\Sigma$ and $^{1,3}\Delta$, $[\Omega_c]$npπ (n = 6, 7) Rydberg states of HI.

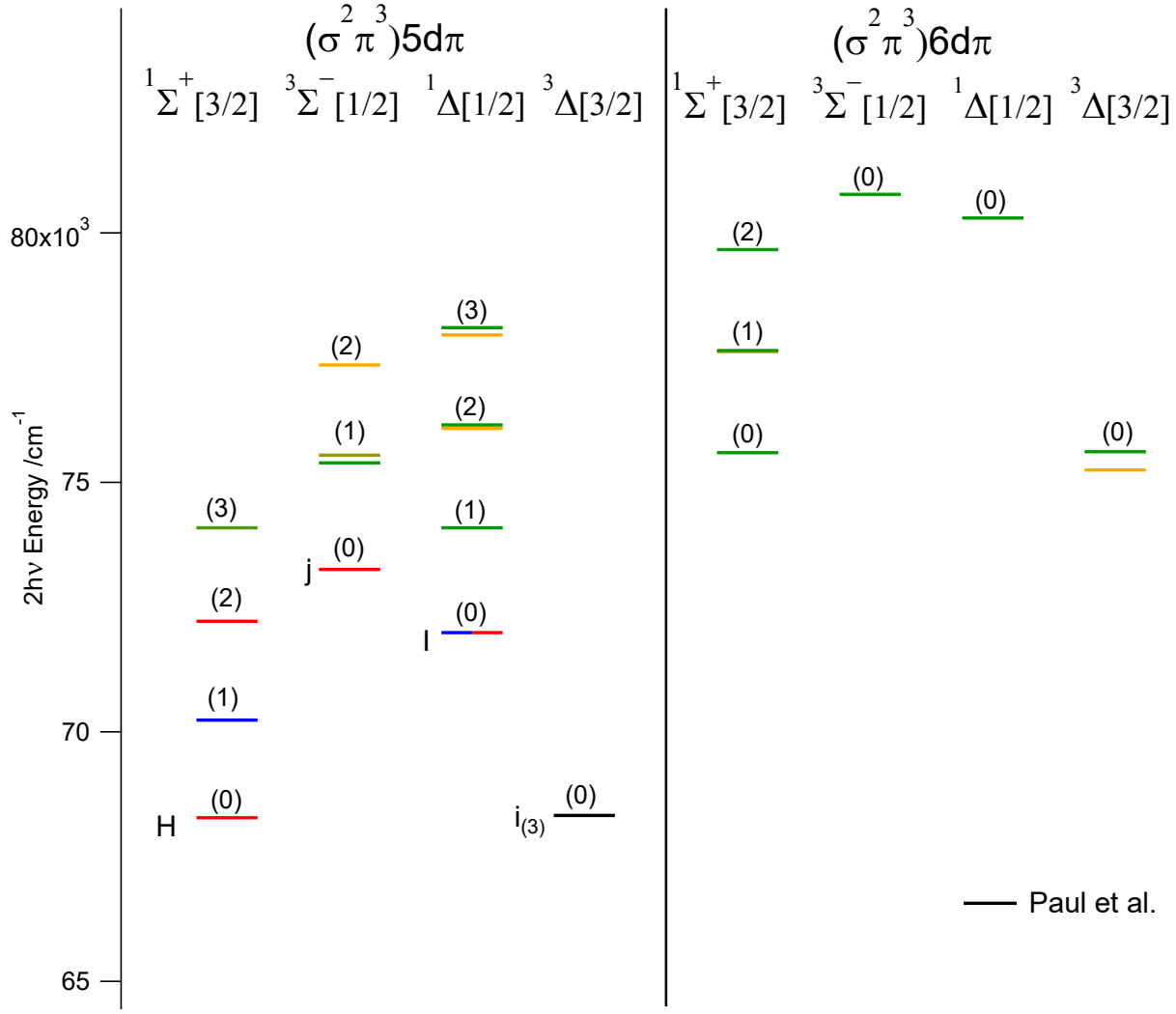

Fig. S9 b) $^{1,3}\Sigma$ and $^{1,3}\Delta$, $[\Omega_c]$ndπ (n = 5, 6) Rydberg states of HI.

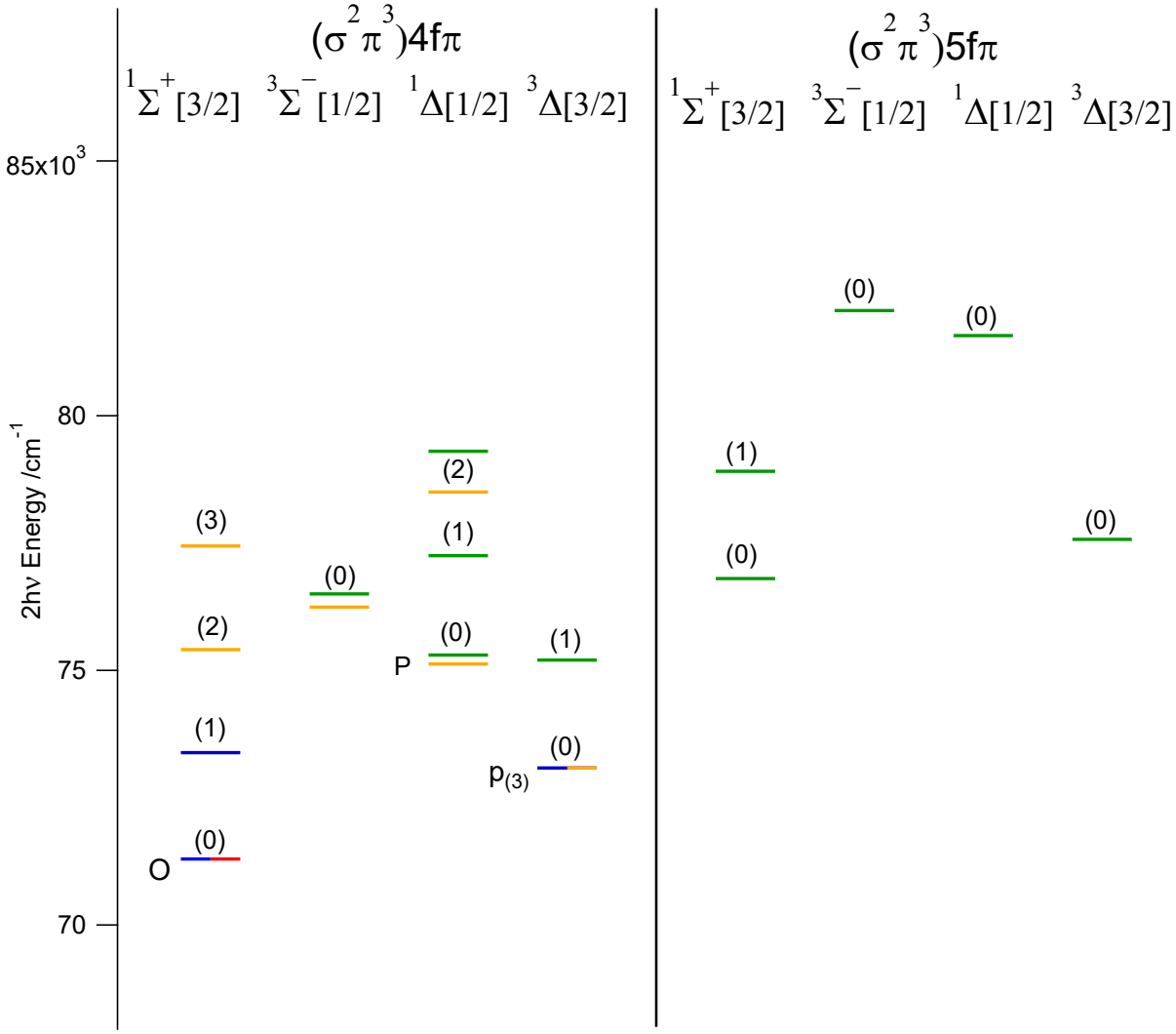

Fig. S9 c) $^{1,3}\Sigma$ and $^{1,3}\Delta$, $[\Omega_c]\mathrm{nf}\pi$ ($n = 4, 5$) Rydberg states of HI.

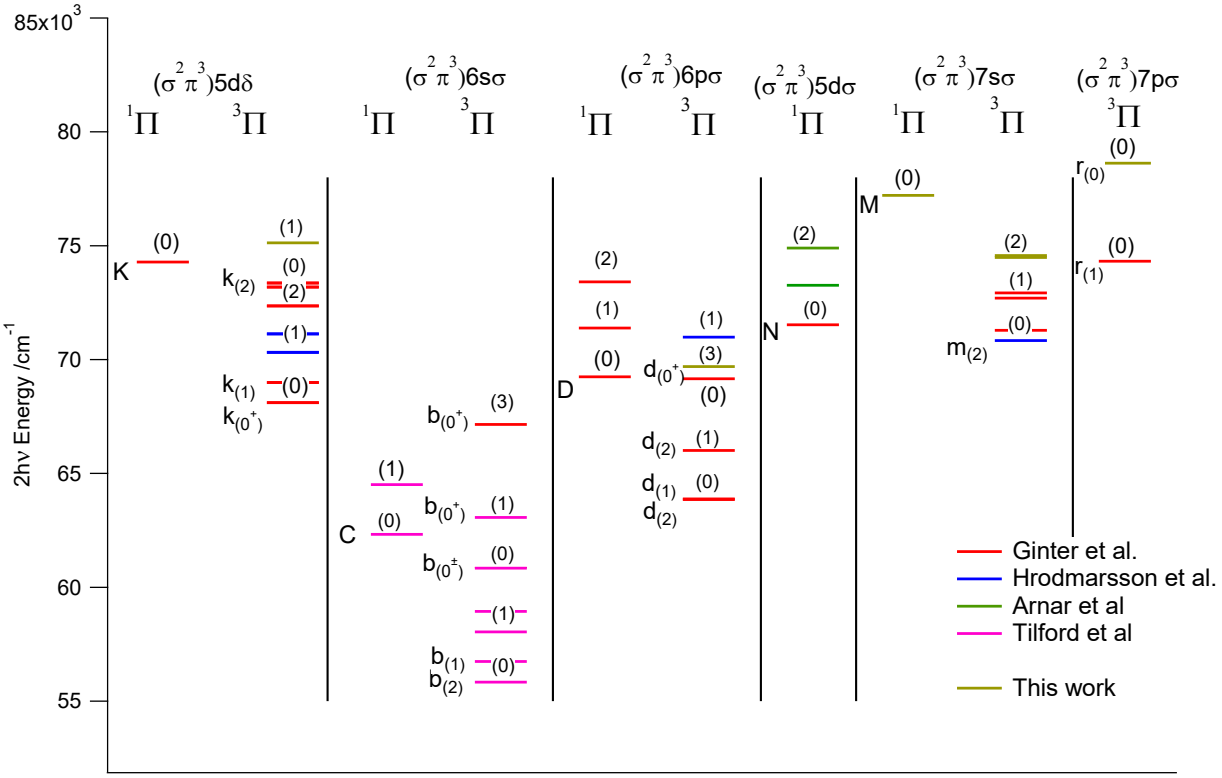

Fig. S9 d) $^{1,3}\Pi$ Rydberg states of HI with σ and δ Rydberg electrons.

Fig. S9: Energy level diagram of known Rydberg states for HI converging to the ground ionic states $X^2\Pi$ [3/2,1/2] as well as some predicted states.

a) $^{1,3}\Sigma$ and $^{1,3}\Delta$, $[\Omega_c]np\pi$ (n = 6, 7) Rydberg states.

b) $^{1,3}\Sigma$ and $^{1,3}\Delta$, $[\Omega_c]nd\pi$ (n = 5, 6) Rydberg states.

c) $^{1,3}\Sigma$ and $^{1,3}\Delta$, $[\Omega_c]nf\pi$ (n = 4, 5) Rydberg states.

d) $^{1,3}\Pi$ Rydberg states with σ and δ Rydberg electrons.

Solid lines (different colors) correspond to previously detected bands [1-11] and present work (orange lines), as specified in the figures. Green dotted lines correspond to predicted states according to quantum defect analyses.

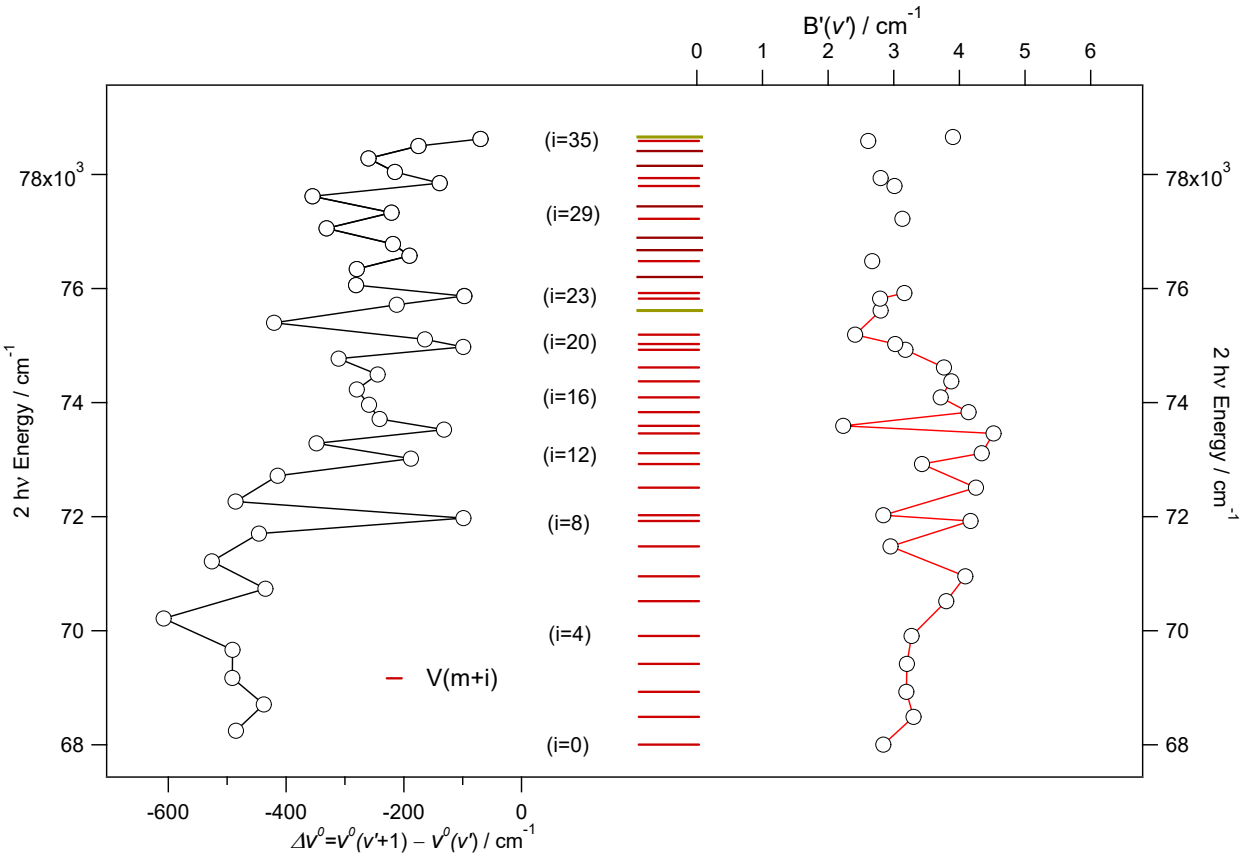

Fig. S10 Vibrational energy levels the $V\,^1\Sigma^+_{0+}(\sigma\pi^4)\sigma^*$ (red) ion-pair state as well as vibrational energy level spacing ($\Delta\nu^0(v'+1, v') = \nu^0(v'+1, v') - \nu^0(v')$) for the $V^1\Sigma^+$ ion-pair state (black curve rotated to the left) and rotational constants ($B'(v')$) (rotated to the right) (● – observed, ○–predicted or guessed.

Tables:

Table S1. Rotational lines of Rydberg and ion-pair state spectra:

(a – c): Rotational lines for new Rydberg state spectra, (a) $d^3\Pi_1[3/2]$ 6p$\sigma(v'=3)$, (b) $f^3\Delta_2$ [3/2]7pπ ($v'=2$) *and* (c) $m^3\Pi_{2,1}[3/2]7s\sigma(v'=2)$.

(d – g): Rotational lines of Rydberg and ion-pair state spectra which exhibit state interactions, (d) $P^1\Delta_2$ [1/2]4f$\pi(v'=0)$ and $k^3\Pi_2$ [1/2]5d$\delta(v'=1)$, (e) $j^3\Sigma^-_0{}^+$[1/2]5d$\pi(v'=1)$ and $V^1\Sigma^+(v'=m+22)$, (f) $M^1\Pi_1$ [1/2]7s$\sigma(v'=0)$ and $V^1\Sigma^+(v'=m+29)$ (g) $r^1\Pi_1$ [1/2]7p$\sigma(v'=0)$ and $V^1\Sigma^+(v'=m+36)$

.

Table S1a. Rotational line wavenumbers for the HI $d^3\Pi_1$ [3/2]6pσ←← $X\,^1\Sigma^+$ (3,0) spectrum.

J'	O (J)	P (J)	Q (J)	R (J)	S (J)
0					
1	69624.5	69662.5	69691.1	69714.5	
2	69597.9	69647.5	69689.9	69724.3	69729.5
3	69572.7	69631.6		69733.6	69752.9
4	69546.2	69614.7		69741.0	69775.2
5	69516.6			69747.4	69796.1
6					69818.1
7					69839.6
8					

Table S1b. Rotational line wavenumbers for the HI $f^3\Delta_2$ [3/2]7pπ←← $X\,^1\Sigma^+$ (0,0) spectrum.

J'	O (J)	P (J)	Q (J)	R (J)	S (J)
0					
1					
2	74406	74471.7	74494.1	74530.8	74534.0
3		74455.2	74491.3	74539.2	74555.2
4		74438.0	74484.9	74547.2	74575.2
5		74420.8	74477.7	74555.2	74593.7
6		74409.6	74469.3	74562.4	74627.8
7			74452.8	74568.8	75282.1
8					

Table S1c. Rotational line wavenumbers for the HI $m^3\Pi_{2,1}$[3/2]7sσ ←← $X\,^1\Sigma^+$ (2,0) spectrum.

J′	***O (J)***	***P (J)***	***Q (J)***	***R (J)***	***S (J)***
			$m^3\Pi_2$		
0					
1					
2		74463.3		74501.3	
3		74446.4		74507.4	
4		74428.4		74510.9	
5				74514.2	
6				74518.2	
7				74522.2	
8				74526.4	
			$m^3\Pi_1$		
0					
1	74507.4	74555.2	74570.0	74604.1	
2					74606.5

Table S1d. Rotational line wavenumbers for the HI $P^1\Delta_2$ [1/2]4fπ(v'=0) and $k^3\Pi_2$ [1/2]5dδ($v'=1$)←← $X\,^1\Sigma^+$ ($v''=0$) spectra.

J′	***O (J)***	***P (J)***	***Q (J)***	***R (J)***	***S (J)***
			$P^1\Delta_2$		
0					
1					
2	75033.8	75086.3	75123.8	75147.6	75159.9
3	75005.8	75072.5	75121.4	75159.8	75180.8
4		75058.1	75119.6	75169.9	75208.4
5		75042.9	75117.4	75181.0	75232.6
6		75026.8	75114.6	75191.3	75257.6
7		75011	75109.4		75282.1
			$k^3\Pi_2$		
0					
1					
2	75059.9		75122.4		75158.7
3			75123.0		75184.1
4			75122.1		
5			75120.9		
6			75119.4		
7			75117.5		

Table S1e. Rotational line wavenumbers for the HI $j^3\Sigma^-_{0^+}[1/2]5d\pi(v'=1)$ and $V^1\Sigma^+(v'=m+22)\leftarrow\leftarrow$ X $^1\Sigma^+$ ($v''=0$) spectra.

J'	***Q (J)***	***Q (J)***
	$j^3\Sigma^-_{0^+}$	$V^1\Sigma^+$
0	75545.5	75610.0
1	75543.1	75604.8
2	75538.3	75591.7
3	75530.2	75570.5
4	75518.6	75542.5
5	75511.4	75500.4
6	75488.5	75460.1
7	75464.1	75410.1
8	75434.0	

Table S1f. Rotational line wavenumbers for the HI $M^1\Pi_1$ [1/2]7s$\sigma(v'=0)$ and $V^1\Sigma^+(v'=m+29)\leftarrow\leftarrow$ X $^1\Sigma^+$ ($v''=0$) spectra.

J'	***O (J)***	***P (J)***	***Q (J)***	***R (J)***	***S (J)***	***Q (J)***
			$M^1\Pi_1$			$V^1\Sigma^+$
0						77226.9
1	77149.2	77183.3	77210.64	77232.3		77219.7
2		77168.4	77211.09	77241.1	77245.8	77206.2
3		77152.2	77207.46	77249.3	77270.6	77185.7
4		77134.6	77204.14	77255.1	77296.2	77160.6
5			77200.43			77129.8
6						77089.6
7						
8						

Table S1g. Rotational line wavenumbers for the HI $r^3\Pi_0$ [1/2]7pσ(v'=0) and $V^1\Sigma^+$(v'=m+36) ←← $X\,^1\Sigma^+$ (v''=0) spectra.

J'	***Q* (*J*)**	***Q* (*J*)**
	$r^3\Pi_0$	$V^1\Sigma^+$
0		78655.2
1	78622.8	78650.4
2	78621.2	78641.2
3	78617.2	78631.6
4	78625.2	78604.7
5	78622.8	78590.8
6	78620.0	
7	78614.4	
8	78609.1	

Table S2.

a) New HI Rydberg states: Rydberg state specifications ($Ry\ ^{2S+1}\Lambda_\Omega[\Omega_c]nl\lambda$) (see main text), vibrational quantum numbers (***v'***), symmetry, band origin ($\mathbf{\nu^0}$), rotational parameters (***B'***,***D'***), relative intensities, quantum defect values (δ) and line series observed in Rydberg state spectra.

State specifications	***v'***	**Symmetry**	$\mathbf{\nu^0}$ **/cm^{-1}**	***B'*/ cm^{-1}**	***D'**10^4 / cm^{-1}**	**Int.**	**Quantum defect δ**	**Line series observed**
$d^3\Pi_1$[3/2] 6pσ	3	e	69691.6	6.08	3.7	vw	3.67	*O,Q,S*
		f	69691.6	5.93	18.0			*P,R*
$f^3\Delta_2$ [3/2]7pπ	0	e	74500.9	5.58	-8.4	w	3.56	*O,Q,S*
		f	74509.4	5.69	35.8			*P,R*
$m^3\Pi_2$[1/2]7sσ	2	f	74484.1	5.10	-57.8	w	4.14	*P,R*
$m^3\Pi_1$[1/2]7sσ	2	e	74571.3	5.90	---	w	4.13	*O,Q,S*
		f	74581.8	5.81				*P,R*

b) Interacting Rydberg and ion-pair states: Rydberg and ion-pair states specifications (*Ry* $^{2S+1}\Lambda_{\Omega}[\Omega_c]nl\lambda$) (see main text), vibrational quantum numbers (***v′***), symmetry, band origin (**v^0**), rotational parameters (***B′***,***D′***), relative intensities, quantum defect values (***δ***) and line series observed in Rydberg state spectra.

State specifications	*v'*	Symm.	v^0 /cm^{-1}	*B′*/ cm^{-1}	*D′**10^4 / cm^{-1}	Int.	Quantum defect *δ*	Line series observed
$P^1\Delta_2$ [1/2]4fπ	0	e	75124.9 [a]	6.11 [a]	9.8 [a]	ms	1.20	*O,Q,S*
			75123.0 [b]	6.27 [b]	30.9 [b]			
		f	75124.6 [a]	6.15 [a]	7.8 [a]			*P,R*
$k^3\Pi_2$ [1/2]5dδ	1	e	75123.0 [a]	6.26 [a]	7.9 [a] 7.0[b]	ms	2.39	*Q,S*
			75124.0[b]	6.26[b]				
$j^3\Sigma^-_0{}^+$[1/2]5dπ	1	e	75546.1 [a]	5.14 [a]	54.0 [a]	vs	2.36	*Q*
			75546.0 [b]	5.16 [b]	54.8 [b]			
$V^1\Sigma^+$	*m*+22	e	75612.6 [a]	2.80 [a]	12.0 [a]	m		
			75610.0 [b]	2.98 [b]	38.8 [b]			
$M^1\Pi_1$ [1/2]7sσ	0	e	77212.1 [a]	5.97 [a]	-81.0 [a]	vw	3.96	*O,Q,S*
			77214.0 [b]	5.72 [b]	-50.6 [b]			
		f	77211.9 [a]	5.87 [a]	-20.0 [a]			*P,R*
$V^1\Sigma^+$	*m*+29	e	77226.8 [a]	2.98 [a]	-26.0 [a]	m		*Q*
			77224.0 [b]	3.46 [b]	38.4 [b]			
$r^3\Pi_0$ [1/2]7pσ	0	e	78623.0 [a]	6.30 [a]	28.0 [a]	s	3.76	*Q*
			78625.0 [b]	6.33 [b]	35.8 [b]			
$V^1\Sigma^+$	*m*+36	e	78655.0 [a]	3.90 [a]	-65.0 [a]	ms		*Q*
			78654.0 [b]	3.48 [b]	-27.1 [b]			

[a]Underperturbed(perturbed) values; this work
[b] Derperturbed values; this work

Table S3. State interactions; J' level proximity ($\Delta E_{J'} = E_{J'}(1) - E_{J'}(2)$ / cm^{-1}), interaction strength (W_{12} / cm^{-1}) and fractional state mixing (c_1^2, c_2^2).

$P^1\Delta_2$ [1/2]4fπ(v' = 0) ↔ $k^3\Pi_2$ [1/2]5dδ(v' = 1)					$j^3\Sigma^-_0{}^+$[1/2]5dπ(v'=1) ↔ $V^1\Sigma^+$(v' = m + 22)				
J'	$\Delta E_{J'}$	W_{12}	c_1^2	c_2^2	J'	$\Delta E_{J'}$	W_{12}	c_1^2	c_2^2
2	-1.4	0.7	0.647	0.353	0	64.5	6.4	0.990	0.010
3	1.6	0.7	0.753	0.247	1	61.7	6.4	0.989	0.011
4	2.5	0.7	0.917	0.083	2	53.4	6.4	0.986	0.014
5	3.5	0.7	0.960	0.040	3	40.3	6.4	0.974	0.026
6	4.8	0.7	0.979	0.021	4	23.9	6.4	0.923	0.077
7	8.1	0.7	0.993	0.007	5	¦12.8	6.4	0.438	0.562
					6	¦28.4	6.4	0.947	0.053
					7	¦54.0	6.4	0.986	0.014

$M^1\Pi_1$ [1/2]7sσ(v'=0) ↔ $V^1\Sigma^+$(v' = m + 29)					$r^3\Pi_0$ [1/2]7pσ(v'= 0) ↔ $V^1\Sigma^+$(v'= m + 36)				
J'	$\Delta E_{J'}$	W_{12}	c_1^2	c_2^2	J'	$\Delta E_{J'}$	W_{12}	c_1^2	c_2^2
1	9.1	0.6	0.996	0.004	1	27.6	7.2	0.927	0.073
2	-4.9	1.0	0.959	0.041	2	20.0	7.2	0.848	0.152
3	¦21.8	1.4	0.996	0.004	3	14.4	7.2	0.531	0.469
4	¦43.5	1.8	0.998	0.002	4	¦20.5	7.2	0.857	0.143
5	¦70.5	2.2	0.999	0.001	5	¦40.1	7.2	0.967	0.033
					6	¦59.9	7.2	0.985	0.015

Table S4. Summary of Rydberg states and spectra, previously observed and reassigned[a]. Rydberg state specifications ($Ry\ ^{2S+1}\Lambda_{\Omega}[\Omega_c]nl\lambda$), vibrational quantum numbers ($\boldsymbol{v'}$), band origin ($\boldsymbol{\nu^0}$), rotational parameters ($\boldsymbol{B'}$, $\boldsymbol{D'}$), quantum defect values ($\boldsymbol{\delta}$) and references of previous observations.

State specifications	v'	ν^0 /cm^{-1}	B' / cm^{-1}	$D'*10^4$ /cm^{-1}	Quantum defect δ	Refs.
$[\Omega_c]ns\sigma$ (n = 6,7)						
$b\ ^3\Pi_2[3/2]6s\sigma$	0	55 833.1	6.348	--	4.02	[1]
	1	58 040.5	6.173	--	4.02	[1]
$b\ ^3\Pi_1[3/2]6s\sigma$	0	56 738.3	6.427	--	3.99	[1]
	1	58 937±20	--	--	3.98	[1]
$b\ ^3\Pi_0^{\pm}[1/2]6s\sigma$	0	60 857.9	6.426	--	4.03	[1]
	1	63 064.0	6.245	--	4.03	[1]
	3	67 150.3	5.693	2.3	4.02	[2]
$C\ ^1\Pi_1[1/2]6s\sigma$	0	62 325±10	--	--	3.97	[1]
	1	64 508±10	--	--	3.89	[1]
$m\ ^3\Pi_2[3/2]7s\sigma$	0	70 837.6/70 841.5	6.11/ 6.21 ± 0.04	1.94/ 12± 5	4.09	[3]/[4]
	1	72 697.2	6.014	2.30	4.12	[3]
	2	74484.1	5.10	-57.8	4.14	[11]
$m\ ^3\Pi_1[3/2]7s\sigma$	0	71 287.3	6.254	3.18	4.04	[3]
	1	72 924.8/72 945.0	6.205/6.16	4.6/−16	4.09	[3]/[6]
	2	74571.3	5.90	---	4.13	[11]
$M^1\Pi_1$ [1/2]7sσ	0	77212.1	5.97	-81.0	3.96	[11]
$[\Omega_c]np\sigma$ (n = 6,7)						
$d\ ^3\Pi_2[3/2]6p\sigma$	0	63 854.9	6.065	1.7	3.65	[2]
	1	66 009.4	5.926	1.5	3.65	[2]
$d\ ^3\Pi_1[3/2]6p\sigma$	0	63 883	--	--		[2]
	3	69691.6	6.08	3.7	3.67	[11]
$d\ ^3\Pi_0^+[1/2]6p\sigma$	0	69 157	6.117	2.1	3.65	[2]
	1	70 988.2	5.79 ± 0.12	−290 ± 40	3.67	[4]
$D^1\Pi_1[1/2]6p\sigma$	0	69 244.5	6.198	2.1	3.65	[2]/[3]
	1	71 382.4	6.052	1.92	3.65	[3]
	2	73 412.3	5.937	12.6	3.65	[3]

$r\,^3\Pi_1[3/2]7p\sigma$	0	74 320	6.040	-4.48	3.59	[3]
$r^3\Pi_0\,[1/2]7p\sigma$	0	78623.0	6.30	28.0	3.76	[11]
$\boldsymbol{[\Omega_c]n}p\pi$ ***(n = 6,7)***						
$E\,^1\Sigma^+[1/2]6p\pi$	0	70 850.5/70 866.3	6.00/ 5.94 ± 0.17	128/ −11± 21	3.55	[3]/[4]/[10]
	1	72 650.8/ 72 654.3	5.29/5.19	4.63/−16	3.57	[3]/[4]/[10]
	3	75 982.3	4.10	-30	3.61	[10]
$f\,^3\Delta_3[3/2]6p\pi$	0	64 572.6	5.715	−7.6	3.61	[2]
$f\,^3\Delta_2[3/2]6p\pi$	0	64 693.9/64 691	6.737/6.80 ± 0.03	10.6/2.9 ± 1.2	3.60	[3]/[5]
	1	66 610	6.17± 0.01	15± 3	3.62	[5]/[7]
$f\,^3\Delta_1[1/2]6p\pi$	0	69 687.0/69 699.9	6.135/6.31 ± 0.02	1.92/4.6 ± 1.0	3.62	[2]/[3]/[4]
	1	71 780.5	5.957	9.73	3.62	[3]
$F\,^1\Delta_2[1/2]6p\pi$	0	70 228.3/70 223.6	6.30/ 6.32 ± 0.01	1.2/ 2.6 ± 0.6	3.59	[2]/[3]/[4]
	1	72 324.0	6.13	0.0003	3.59	[6]
	2	74 272.8	5.93	77	3.59	[11]
$g\,^3\Sigma^-_{0+}[3/2]6p\pi$	0	66 022.6	6.110	2.5	3.51	[3]
	1	67 704.4	5.62	28	3.54	[3]
$g\,^3\Sigma^-_1{}^{\pm}[1/2]6p\pi$	0	68 908.8	6.06	1.7	3.67	[3]
$f^3\Delta_2[3/2]7p\pi$	0	74500.9	5.58	-8.4	3.56	[11]
$g\,^3\Sigma^-_{0+}\,[3/2]7p\pi$	0	74 735.2	6.10	14.8	3.52	[8]/[10]
	1	76 364.4	4.36	-38	3.61	[10]
$g\,^3\Sigma^-_1{}^{\pm}[1/2]7p\pi$	0	79 145.1	5.77	25.9	3.68	[10]
$F^1\Delta_2[1/2]7p\pi$	0	79 923.5	6.74	10	3.54	[10]
$\boldsymbol{[\Omega_c]n}d\sigma$ ***(n = 5)***						
$N\,^1\Pi_1[1/2]5d\sigma$	0	71 526.2	6.163	1.74	2.50	[3]
	2	74 899.2	6.17	6.2	2.56	[8]
$\boldsymbol{[\Omega_c]n}d\pi$ ***(n = 5)***						
$H\,^1\Sigma^+[3/2]5d\pi$	0	68 277.3	5.78	5.0	2.34	[3]/[10]
	1	70 242.1/70 236.1	5.95/6.34 ± 0.01	125/1100 ± 20	2.36	[3]/[4]/[10]
	2	72 217.6	4.35	24.2	2.36	[3]/[10]
$i\,^3\Delta_3[3/2]5d\pi$	0	68 326.2	6.21	−25	2.34	[9]

$I\,^1\Delta_2[1/2]5d\pi$	0	71 990/71 989.4	6.312/ 6.31 ± 0.01	2.7/ 2.4 ± 0.1	2.47	[7]/[4]
	2	76 080.8	5.82	9	2.47	[10]
	3	77 954.1	5.55	-2.6	2.48	[10]
$j\,^3\Sigma^-_{0+}[1/2]5d\pi$	0	73 254.9/73 252.0	5.71/5.63	47.5/46	2.37	[6]
	1	75546.1	5.14	54.0	2.36	[11]
	2	77 346.0	5.09	-79	2.37	[10]
$H^1\Sigma^+[3/2]6d\pi$	1	77 615.4	5.56	90	2.36	[10]
$i^3\Delta_2[3/2]6d\pi$	0	75 246.1	6.14	5	2.42	[10]
$\boldsymbol{[\Omega_c]nd\delta}$ ***(n = 5)***						
$k\,^3\Pi_{0^\pm}[3/2]5d\delta$	0	68 110.7	6.24	3	2.35	[3]
	1	70 320.4/70 310.8	5.058/5.13 ± 0.03	−21/ −4 ± 9	2.35	[3]/[4]
	2	72 353.1/72 355.6	5.650/5.86	−5.49/42	2.35	[3]
$k\,^3\Pi_1[3/2]5d\delta$	0	68 991.8	6.459	3.3	2.28	[3]
	1	71 125.0/71 126.4	6.30/6.22 ± 0.02	4.82/−2.6 ±1.6	2.27	[3]/[4]
	2	73 180.7/73 176.7	6.034/6.13	8.72/23	2.27	[3]
$k\,^3\Pi_2[1/2]5d\delta$	0	73 360.9	6.403	6.123	2.36	[3]
	1	75123.0	6.26	7.9	2.39	[11]
$K\,^1\Pi_1[1/2]5d\delta$	0	74 282.1	6.255	6.09	2.28	[3]
$\boldsymbol{[\Omega_c]nf\pi}$ ***(n = 4,5)***						
$O\,^1\Sigma^+[3/2]4f\pi$	0	71 301.9/71 294.7	5.82/ 6.25 ± 0.22	--/ 33± 26	1.04	[7]/[4]
	1	73 383.6/73 384.2	5.819/5.70	4.46/0	1.04	[3]/[7]/[6]
	2	75 410.1	5.19	38	1.04	[10]
	3	77 448.2	4.56	-51	1.03	[10]
$p\,^3\Delta_2[3/2]4f\pi$	0	73 081.7	6.35	2.0	0.8	[6]/ [11]
$P^1\Delta_2[1/2]4f\pi$	0	75 124.6	6.15	8	1.20	[10]
	2	78 502.6	5.67	-52	1.27	[10]
$q^3\Sigma^-_{0+}[1/2]4f\pi$	0	76 234.4	5.50	160	1.08	[10]

New states.

Table S5. Summary of ion-pair states and spectra, previously observed. State specifications, vibrational quantum numbers (***v'*** = *m* + *i*; *m* unknown integer), band origin ($\mathbf{v^0}$), rotational parameters (***B'***, ***D'***) and references.

State specification	***v'*** [a]	$\mathbf{v^0}$ **/cm^{-1}**	***B´*** **/ cm^{-1}**	***D´**10^4 /cm^{-1}**	**Refs.**
$V\,^1\Sigma^+_{0+}$ $(\sigma\pi^4)\sigma^*$	*m*	68 004.4	2.84	2.0	[2]/[3]
	m+1	68 489.4	3.3	--	[2]/[3]
	m+2	68 927.3	3.19	−1.1	[2]/[3]
	m+3	69 418.5	3.25	--	[2]/[3]
	m+4	69 909.9/69 903.3	3.273/ 2.94 ± 0.18	6.54/ 10± 40	[2]/[3]/[4]
	m+5	70 512.1/70 511.0	3.800/ 3.66 ± 0.02	−70.2/ 83± 4	[3]/[4]
	m+6	70 948.6/70 952.3	4.09/3.56 ± 0.10	44/ 24± 10	[3]/[4]
	m+7	71 478.4	2.95 ± 0.10	−4 ± 5	[4]
	m+8	71 920.3/71 924.4	3.97/4.17 ± 0.17	158/ 270 ± 70	[3]/[4]
	m+9	72 022.4/72 023.2	2.792/2.84 ± 0.03	−4.61/ 1 ± 4	[3]/[4]
	m+10	72 506.0/72 508.8	4.106/4.25	14.7/80	[3]/[6]
	m+11	72 923.0	3.43	19	[6]
	m+12	73 110.8	4.34	10	[6]
	m+13	73 457.8/73 459.1	3.177/4.52	−23.7/89	[3]/[6]
	m+14	73 589.5/73 590.8	2.294/2.23	−11.5/0.0	[3]/[6]
	m+15	73 822.7/73 831.8	3.679/4.14	−2.25/90	[3]/[6]
	m+16	74 090.0/74 091.0	3.724/3.71	5.8/22.6	[3]/[8]
	m+17	74 372.0	3.9	4.2	[8]
	m+18	74 615.4	3.76	3.67	[8]
	m+19	74 924.0	3.05	3.83	[8]
	m + 20	75 025.4	3.02	-33	[10]
	m + 21	75 189.5	2.41	1423	[10]
	m + 22	75612.6	2.80	12.0	[11]
	m + 23	75 822.0	2.79	63	[10]
	m + 24	75 919.1	3.16	-27	[10]
	m + 26	76 479.9	2.67	-31	[10]
	m + 29	77 226.8	3.13	14	[10]
	m + 31	77 795.6	3.01	28	[10]

	m + 32	77 934.8	2.80	11	[10]
	m + 35	78 585.1	2.61	-54	[10]
	m + 36	78655.0	3.90	-65.0	[11]

a. Vibrational quantum numbers are marked as $v' = m + i$ for positive integer numbers of i ranging from zero for the lowest vibrational level observed and m as an unknown positive integer.

New states.

References:

[1] S.G. Tilford, M.L. Ginter, A.M. Bass, *J. Mol. Spectrosc.* 34 (1970) 327.

[2] M.L. Ginter, S.G. Tilford, A.M. Bass, *J. Mol. Spectrosc.* 57 (1975) 271.

[3] D.S. Ginter, M.L. Ginter, S.G. Tilford, *J. Mol. Spectrosc.* 92 (1982) 40.

[4] H. R. Hróðmarsson, H. Wang, and Á. Kvaran, *J. Mol. Spectrosc.* 5 (2013) 290.

[5] S.A. Wright, J.D. McDonald, *J.Chem.Phys.* 101 (1994) 238-245.

[6] H. R. Hróðmarsson, H. Wang, and Á. Kvaran, *J. Chem. Phys.* 142 (2015) 244312.

[7] S.T. Pratt, M.L. Ginter, *J. Chem. Phys.* 102 (1995) 1882-1888.

[8] A. Hafliðason, M-X Jiang and Á, Kvaran, *Phys. Chem. Chem. Phys.* 21 (2019) 23154.

[9] P. M. Regan, D. Ascenzi, E. Wrede, P. A. Cook, M. N. R. Ashfold and A. J. Orr-Ewing, *Phys. Chem. Chem. Phys.* 2 (2000) 23.

[10] M-X. Jiang, A. Hafliðason and Á, Kvaran, *J. Mol. Spectrosc.* 372 (2020) 111329.

[11] This work

4.6 Paper 6

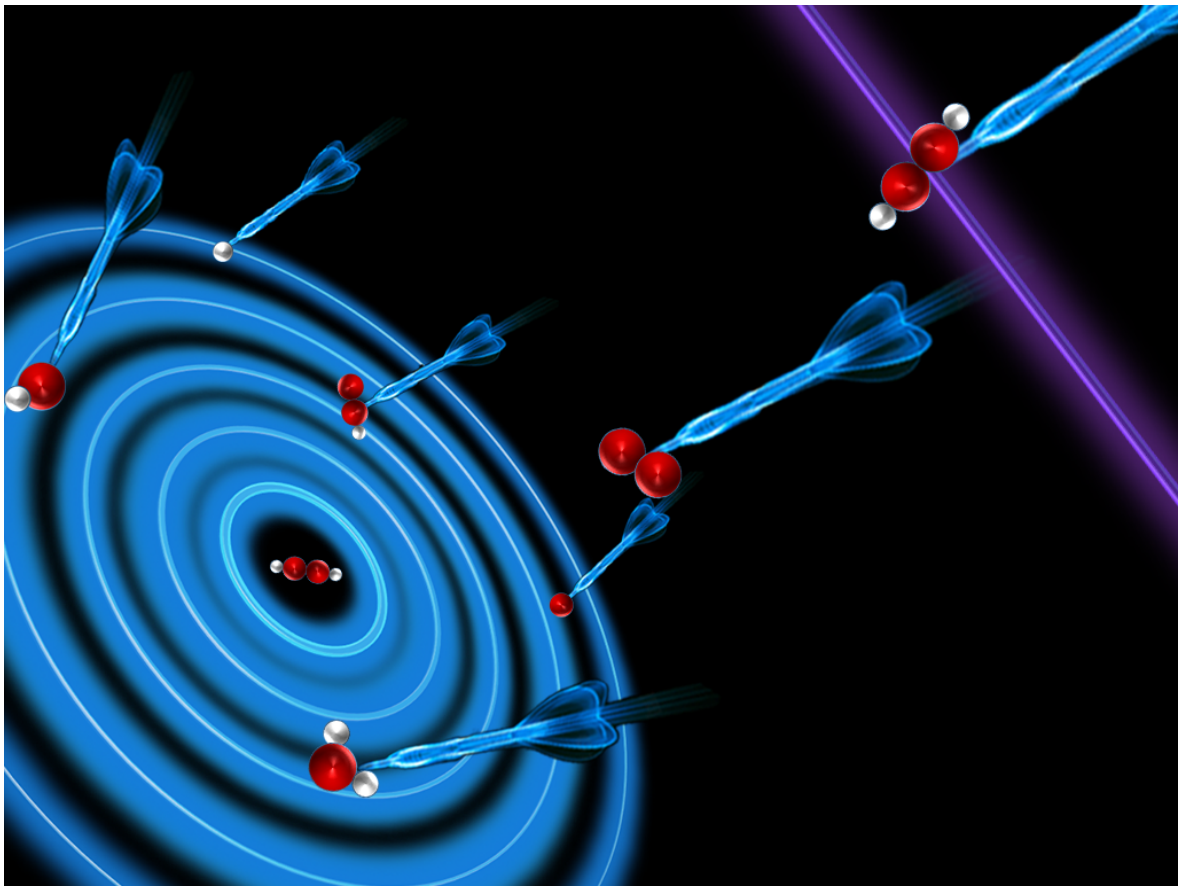

Meng-Xu Jiang, Ioannis C. Giannakidis, Peter C. Samartzis and Ágúst Kvaran, Multiphoton breakdown of acetylene; Formation of organic building block fragments, (***Accepted for publication in PCCP***)

Multiphoton breakdown of acetylene; Formation of organic building block fragments

Meng-Xu Jiang[1], Ioannis C. Giannakidis[2,3], Peter C. Samartzis[2]* and Ágúst Kvaran[1]*

1. *Science Institute, University of Iceland, Dunhagi 3, 107 Reykjavík, Iceland.*
2. *Institute of Electronic Structure and Laser, Foundation for Research and Technology-Hellas, Vassilika Vouton, 71110 Heraklion, Greece.*
3. *Department of Materials Science and Technology, University of Crete, 71003 Heraklion, Greece.*

Total number of pages in manuscript: 43
Tables: 2
Figures: 7 + Graphical abstract
Supplementary information
File: C2H2-BD-220919

*Correspondence should be addressed to:

Petros Samartzis
Institute of Electronic Structure and Laser,
Foundation for Research and Technology-Hellas,
Vassilika Vouton, 71110 Heraklion, Greece
Phone: +30-2810-391467 (office)
e-mail: sama@iesl.forth.gr

Ágúst Kvaran
Science Institute,
University of Iceland,
Dunhagi 3, 107 Reykjavík, Iceland
Phone: +354-525-4800 (office)
e-mail: agust@hi.is
www: https://notendur.hi.is/agust/

#Co-authors: e-mails:
Meng-Xu Jiang: mej7@hi.is
Ioannis C. Giannakidis : giannakidis@iesl.forth.gr

Graphical abstract

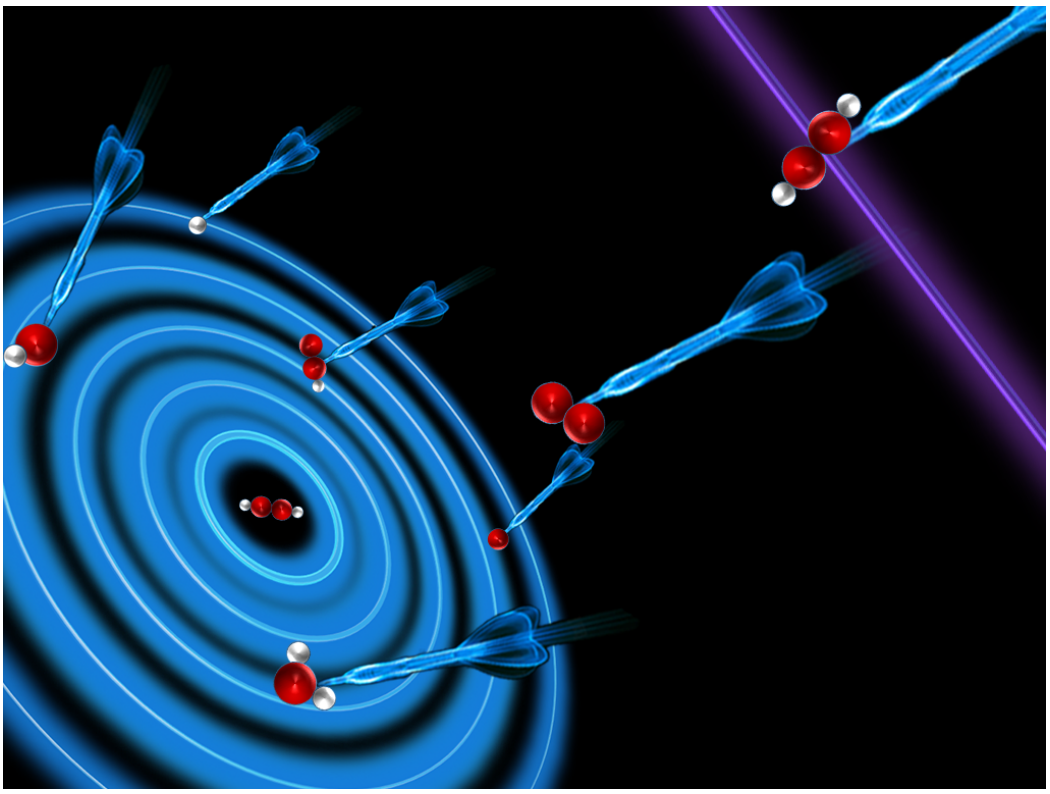

Abstract

Mass resolved REMPI spectra and electron and ion velocity map images were recorded for REMPI of acetylene in the case of two-photon resonant excitations to low lying 3p and 4p Rydberg states. Combined data analysis of ion signal intensities and electron and ion kinetic energy release distribution revealed multiphoto-fragmentation processes in terms of photodissociation and photoionization channels to form the molecular ion, $C_2H_2^+$ and the fragment ions H^+, C^+, CH^+, CH_2^+, C_2^+ and C_2H^+. The ratio of fragment ion formation over the parent ion formation increases with excitation energy. To a large extent the multiphoto-fragmentation involves initial breakdown of the molecule into ground and excited state neutral fragments by two-, three- and four- photon dissociation processes prior to multiphoton ionization. The three-photon dissociation processes via superexcited molecular state(s) are found to be most important and electronically excited fragment species play a significant role in the overall multiphoton-fragmentation. Furthermore, the data was indicative of an involvement of secondary photodissociation processes and provided information on fragment energetics as well as state interactions. The question, whether acetylene could be an important source of building block fragments for formation of organic molecules in interstellar space is addressed.

I. Introduction

Acetylene (C_2H_2), being the smallest unsaturated organic molecule with a triple bond between the two carbon atoms, is of fundamental importance in the fields of organic photochemistry,[1, 2] astrochemistry[2-4] and in organic synthesis.[5] Synthesis involving acetylene include preparation of heterocycles and construction of a number of functionalized molecules with different levels of molecular complexity.[5] Photochemical processes following absorption of VUV light have been found to form $C_2 + H_2$, C_2H +H and metastable acetylene.[1] Multiphoton excitation studies have revealed an important involvement of high energy molecular Rydberg states, in photochemical processes,[2, 6-9] different in nature depending on the states symmetry (u or g) and/or energy. Acetylene has long been known to exist in molecular clouds in interstellar space,[3, 10] where it could, upon radiation, be the source of fundamental reactive fragment species (radicals and/or ions) as building blocks for bigger organic molecules either via gas-phase photofragmentation and/or surface reactions(?). Catalytic conversion reactions of acetylene on a solid SiC grain surface have been found to lead to the formation of polycyclic aromatic hydrocarbons (PAHs) and are expected to mimic chemical processes in certain astrophysical environments.[1, 2, 11]

Resonance enhanced multiphoton excitation and ionization studies of acetylene reveal broad spectral lines due to transitions via Rydberg states, growing number of fragment ion formations and weakening of ion signals as the excitation energy is increased.[2, 6, 8, 9] These observations can be taken as evidence for opening of increased number of predissociation and fragmentation formation channels with excitation energy. Virtually all possible fragment formations (H, [2, 7, 9] H_2, [2, 7] C, [9] CH, [2] CH_2, [9] C_2, [2, 6, 7, 9] C_2H[2, 7]) have been proposed, based on direct or indirect observations. Furthermore, number of excited C_2 fragments (C_2*) have been detected.[6, 7] It has been proposed that fragmentation processes could be competing with an

isomerization into the vinylidene radical ($H_2C=C$), which is supposed to be a primary precursor for large polycyclic aromatic hydrocarbon (PAHs).[2] Our previous work on mass resolved (2 + n) REMPI of acetylene suggests that the parent molecular ion is the primary ion product for resonant excitations to the lowest gerade Rydberg states in the two-photon excitation region of about 72 700 – 75 000 cm^{-1}, whereas a significant amount of both fragments (H, C, CH, C_2, C_2H) and parent molecules are ionized via excitations to Rydberg states in the intermediate region of about 75 700 – 76 100 cm^{-1} and mainly fragment species are ionized for transitions to Rydberg states in the 82 500 – 83 050 cm^{-1} region.[9]

Recently we have been emphasizing multiphoto-fragmentation (both photodissociation and photoionization) studies of halogen-containing reagents (hydrogen halides (HX) and methyl halides (CH_3X)) by mass-resolved and velocity-map-imaging techniques in association with REMPI for two-photon resonant excitations to molecular Rydberg states.[12-17] The studies reveal various photodissociation processes for one-electron excitations of the nonbonding (nb) valence electrons localized on the halogen atoms, depending on the number of photons absorbed. The one-photon excitations, which cause transfer to repulsive valence states, are found to form the halogen atoms (X) in its ground electronic state along with H (from HX) and CH_3 (from CH_3X) prior to multiphoton ionization of the fragments. Two-photon excitations, which cause transfer to Rydberg states, have also been found to form X along with H (from HX)[18, 19] and CH_3 (from CH_3X)[16, 20] by predissociation. An additional absorption of the third photon excites the Rydberg states to metastable superexcited states above the molecular ionization limit followed by molecular autoionization and/or dissociation to form ground or excited state fragments prior to further photoionization. Furthermore, interactions between the intermediate Rydberg states and bound ion-pair /valence states have been found to affect further photon excitations for the

hydrogen halides.[12-14, 18] Indications of ion pair formation for CH_3I (*i.e.* CH_3^+/I^-)[17] suggests that this might also be the case for the methyl halides.

In the work presented here we move a step further in light of our experience from the work as described in the previous paragraph. Here we present multiphoto-fragmentation studies of acetylene by mass-resolved REMPI (MR-REMPI) and corresponding velocity-map-imaging of electrons and number of fragment ions for two-photon resonant excitations to molecular Rydberg states (VMI-REMPI). The two-photon excitation of the π -electrons in the C-C triple bond excites the molecules directly to the Rydberg states. An additional absorption of the third photon excites the Rydberg states to superexcited states above the molecular ionization limit followed by molecular autoionization and/or various dissociation processes to form the ground or excited state of number of fragments prior to further photoionization. Analyses of ion mass-resolved spectra, kinetic energy release data for electrons and ions, angular distributions of images and cross correlation analysis of the data allow us to derive a picture of the multiphoton breakdown of the molecule into reactive fragments / radicals and ions.

II. Experimental

The Velocity Map Imaging (VMI) setup used in this work has been described previously and only a brief description will be given here.[21, 22] A supersonic molecular beam of C_2H_2 (99.6 % purity) was formed by expansion through a homemade piezoeletrically-actuated nozzle valve (1 mm orifice) and skimmed (1.5 mm, Beam Dynamics) before entering the interaction region. Typically stagnation pressure of $P_0 \sim 1$ bar was used. The photolysis/photofragment ionization laser beam (2.0 – 2.5 mJ per pulse) was generated by frequency doubling of the output of an excimer laser (Lambda-Physik LPX300, operating with XeCl) pumped Dye laser

(LPD3000) using the appropriate dyes (C480, C521, C540A,) and focused (f = 30 cm) on the geometric focal point between single-electrode repeller-extractor plate arrangement where it intersects the collimated molecular beam at right angles. The apparatus was operated in "VMI mode" and the repeller was always on. Ions traversed a field-free time-of-flight region (45 cm) and a gated, position-sensitive detector (dual, imaging quality Micro-Channel Plates (MCP) array coupled to a phosphor screen) imaged the photofragment sphere. The image frame was recorded asynchronously each second (~10 laser shots) by a CCD camera and several thousand frames were averaged to form the images. The 2D slice of 3D ion distribution from each final image is extracted by an inverse Abel transformation and integrated from its center over angle to extract the speeds and over radius to extract the angular distributions of the photofragments. For photoelectrons, the repeller was negatively charged (-3kV) and the detector was not gated. To detect high-speed photoelectrons negative charge of -5kV was used for recording images No.6 and No.7 (see **Table 1**).

Mass-resolved REMPI (MR-REMPI) spectra were derived from data which was recorded in a system which has been described before.[9] In short, 20 cm quartz lens was used to focus about 10 ns laser pulses in the energy range of 0.05 – 0.30 mJ on a molecular beam.

III. Results and analysis

A. MR-REMPI

Fig. 1a shows mass spectra derived for two-photon resonant excitations to a total of seven 3p and 4p molecular Rydberg states in REMPI of acetylene (C_2H_2) (see also **Table 1**) along with

derived REMPI spectra. Relative ion signal intensities observed as a function of the excitations are shown in **Fig. 1b.** Generally, the relative ion signal of the parent molecular ion ($C_2H_2^+$) is found to decrease with excitation energy, while the relative fragment ion signals (H^+, C^+, CH^+, CH_2^+, C_2^+ and C_2H^+) generally increase with energy. More precisely, the parent molecular ion ($C_2H_2^+$) signal dominates for the lowest energy excitations (73 939 and 74 279 cm^{-1} in particular) and gradually decreases with energy to become virtually negligible for 83 006 cm^{-1}. On the contrary the C_2^+ signal gradually increases with energy, larger in intensity than all the other fragment ion signals and dominates for the highest energy resonance (83 006 cm^{-1}). The H^+, C^+ and CH^+ ion intensities reach maxima for the 82 561 cm^{-1} excitation, while the C_2H^+ relative ion signal is at a maximum for the 75 760 cm^{-1} excitation. Weak signals for CH_2^+ were detected for the highest energy excitations only.

Tables 1: Photoelectron (PE) images and the corresponding velocity map images for fragmental ions recorded for C_2H_2 via resonant transitions to specified Rydberg states.

Image no.	C_2H_2 Rydberg states; *nl*; $^1\Lambda_g$, $(v_1v_2v_3v_4v_5)$[a]	One-photon excitation/ nm	Two-photon excitation/ cm^{-1}
1	*3p*; $^1\Delta_g$, (00020)	270.364	73969
2	*3p*; $^1\Sigma_g$, (00000)	269.255	74279
3	*3p*; $^1\Sigma_g$, (01000)	268.262	74554
4	*3p*; $^1\Delta_g$, (01020)	263.992	75760
5	*3p*; $^1\Sigma_g$, (01000)	262.864	76085
6	*4p*; $^1\Delta_g$, (00000)	242.245	82561
7	*4p*; $^1\Sigma_g$, (00000)	240.947	83006

[a] n: principal quantum number for Rydberg electron. l: Rydberg electron orbital. (v_1, v_2, v_3, v_4, v_5): vibrational quantum numbers referring to vibrational modes. v_1 (C-H symmetric stretch), v_2 (C-C stretch) v_3 (C-H asymmetric stretch), v_4 and v_5 (bend).

These observations are clear indications of multiphoton excitation and ionization processes. **Fig. 2** shows the relevant energetics for the C_2H_2 molecule and various fragment thresholds as well as minimum and maximum one- to four-photon excitations of the molecule (see **Table 1**). The

figure gives an indication of what number of photons may be needed to form the various neutral species directly (molecular species) or by photodissociation (fragments) in ground and excited states prior to further (photo)ionization. First one-photon excitation is not sufficient to break any chemical bonds to form fragments and, therefore does not need to be considered here in that respect. The one-photon intermediate excitation step can be assumed to involve a transition to a virtual state (C_2H_2*) with a character determined by bound valence states close in energy,[23]

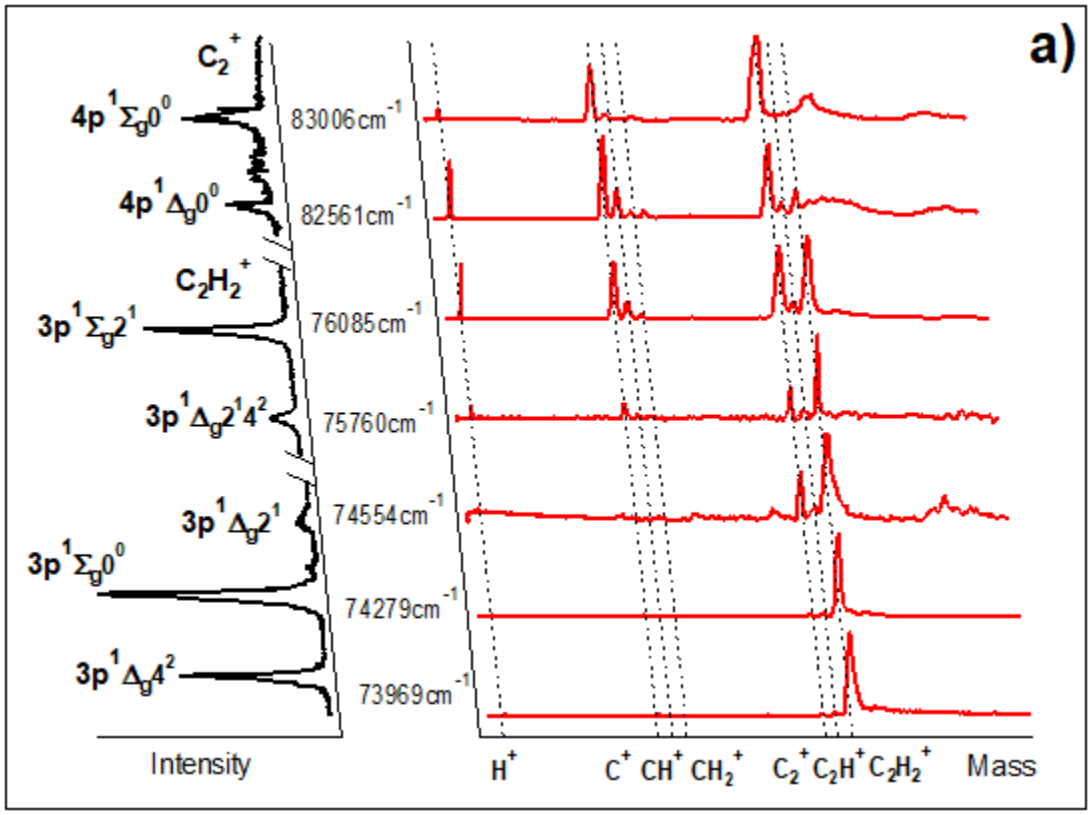

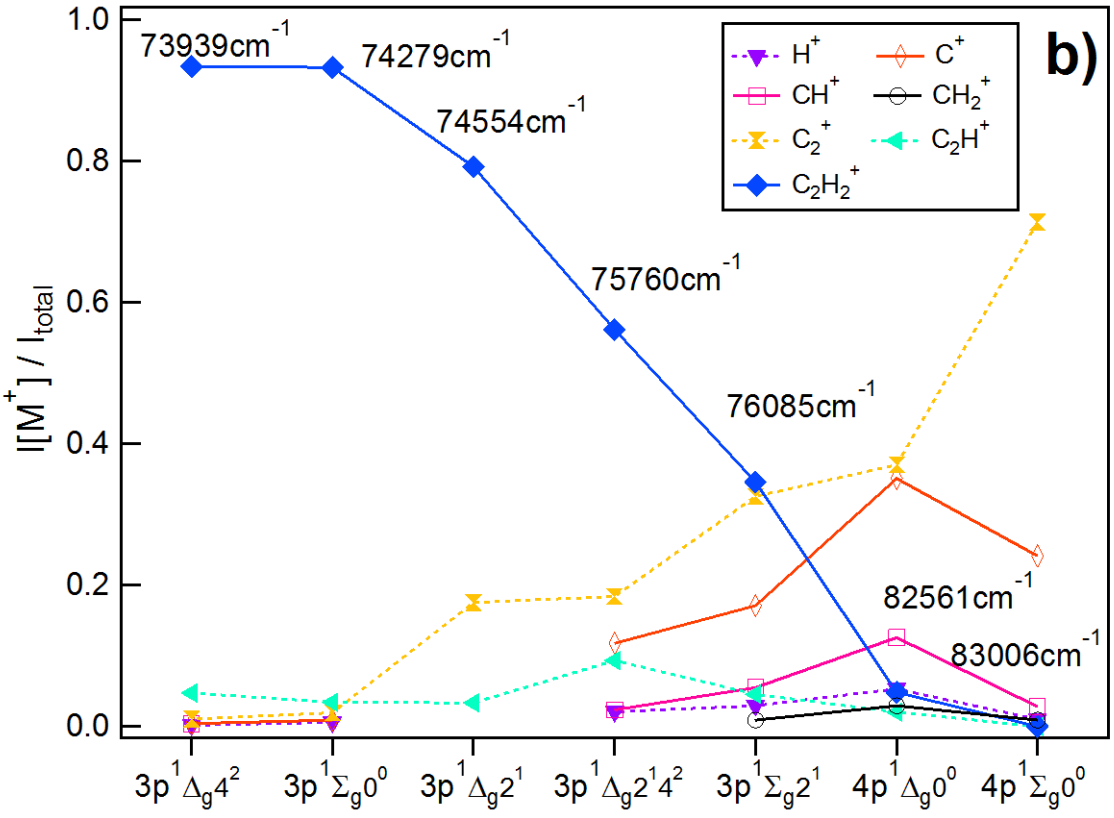

Fig. 1 ***Mass-resolved REMPI of C_2H_2:*** *(a) Mass spectra (red) and corresponding REMPI spectra (black, rotated to the left) of C_2H_2 for two-photon excitations to 3p and 4p molecular Rydberg states ($C_2H_2^+$ REMPI spectra for the 3p states / C_2^+ REMPI spectra for the 4p states) The data is partly from reference 9. b) Relative ions signal intensities, $I[M^+]/I_{total}$ vs. excitations for the ions indicated.*

C_2H_2 + **1hν** → C_2H_2*; **one-photon** "transition" to a virtual state (1)

Second, the two-photon absorption creates the molecular Rydberg states (C_2H_2**; see **Fig. 1a** and **Table 1**) by resonant excitations and could, energetically, create a number of low energy fragment pairs (F1 + F2/F2*; F1,F2: ground state/ F2*: excited state; see also reference 24) as,

C_2H_2 + **2hν** → C_2H_2**; **two-photon** resonant excitation (2)

C_2H_2** → H + C2H/C2H*; dissociation to form fragment pairs (2a)

C_2H_2** → H_2 + C_2/C_2*; dissociation to form fragment pairs (2b)

$C_2H_2^{**} \rightarrow C + CH_2/CH_2^*$; dissociation to form fragment pairs (2c)

$C_2H_2^{**} \rightarrow CH + CH$; dissociation to form fragment pairs (2d)

Third, three-photon absorption could excite the molecule beyond its ionization limit to form metastable / superexcited state(s) ($C_2H_2^{\#}$). There will be a competition between autoionization of short lived $C_2H_2^{\#}$ to form $C_2H_2^+$ and dissociation to form fragments. The fragment pairs, mentioned above (F1 + F2/F2*; see (2a – 2d)), of same or higher energy, could be formed as well as species from dissociation leading to three fragments (F1 + F2 + F3/F3*) (see also reference 24),

$C_2H_2 + \mathbf{3h\nu} \rightarrow C_2H_2^{\#}$; **three-photon** (2+1)REMP-excitation via $C_2H_2^{**}$ (3)

$C_2H_2^{\#} \rightarrow C_2H_2^+ + e^-$; autoionization (3i)

$C_2H_2^{\#} \rightarrow H + C_2H/C_2H^*$; dissociation to form fragment pairs (3a)

$C_2H_2^{\#} \rightarrow H_2 + C_2/C_2^*$; dissociation to form fragment pairs (3b)

$C_2H_2^{\#} \rightarrow C/C^* + CH_2/CH_2^*$; dissociation to form fragment pairs (3c)

$C_2H_2^{\#} \rightarrow CH + CH^*$; dissociation to form fragment pairs (3d)

$C_2H_2^{\#} \rightarrow H + H + C_2/C_2^*$; dissociation to form three fragments (3e)

$C_2H_2^{\#} \rightarrow H_2 + C/C^* + C/C^*$; dissociation to form three fragments (3f)

$C_2H_2^{\#} \rightarrow H + CH + C/C^*$; dissociation to form three fragments (3g)

The overall, inverse relationship between the ion signals for the parent molecular ion ($C_2H_2^+$) and the fragment ions (Fi^+) (*i.e.* decreasing $C_2H_2^+$ signal vs. increasing Fi^+ signals) with excitation energy (**Fig. 1b**), fits a decreasing branching into autoionizations vs. increasing

branching into dissociation with excitation energy. This strongly suggests that the processes (3) could be of major importance in the multiphoton-ionization of C_2H_2. Observed maxima and fall of in relative ion intensities as a function of the excitation energy (see above) could be an indication of a varying competition between the different dissociation processes (3a – 3g) with energy and/or due to a variation in the dissociative branching with energy at the two-photon excitation step.

Due to the metastable / short lifetime nature of the superexcited molecular state(s), $C_2H_2^{\#}$, formed by three-photon excitation (3) and the wealth of possible exit channels (3i, 3a- 3g) there is a reason to believe that further molecular photoexcitation is not important under our experimental conditions used to record the MR-REMPI (see Section II). However, ion formations due to one- (or few-) photon ionizations of highly excited fragment species formed upon photodissociation by four photons (hence an overall five-(or more) photon ionization) cannot be ruled out. Thus, for example, the H^+ signal could be formed by one-photon excitation of H*(n = 2), after four-photon excitation of the molecule (to form $C_2H_2^{\#\#}$) rather than by three-photon ionization of H(n = 1) following two- or three-photon dissociation (see also reference 24), etc.,

$C_2H_2 + \mathbf{4h\nu} \rightarrow C_2H_2^{\#\#}$;	**four-photon** (2+2) REMP-excitation via C_2H_2**	(4)
$C_2H_2^{\#\#} \rightarrow C_2H + H*(n = 2)$;	dissociation to form fragment pairs	(4a)
$C_2H_2^{\#\#} \rightarrow H_2 + C_2/C_2*$;	dissociation to form fragment pairs	(4b)
$C_2H_2^{\#\#} \rightarrow C/C* + CH_2/CH_2*$;	dissociation to form fragment pairs	(4c)
$C_2H_2^{\#\#} \rightarrow CH + CH*$;	dissociation to form fragment pairs	(4d)

$C_2H_2^{\#\#} \rightarrow H + H + C_2/C_2^*$; dissociation to form three fragments (4e)

$C_2H_2^{\#\#} \rightarrow H_2 + C/C^* + C/C^*$; dissociation to form three fragments (4f)

$C_2H_2^{\#\#} \rightarrow H + CH/CH^* + C/C^*$; dissociation to form three fragments (4g)

Notice that equations (1) – (4), above, are marked by (nx) where n is the number of photons required for each step and x are suitable letters.

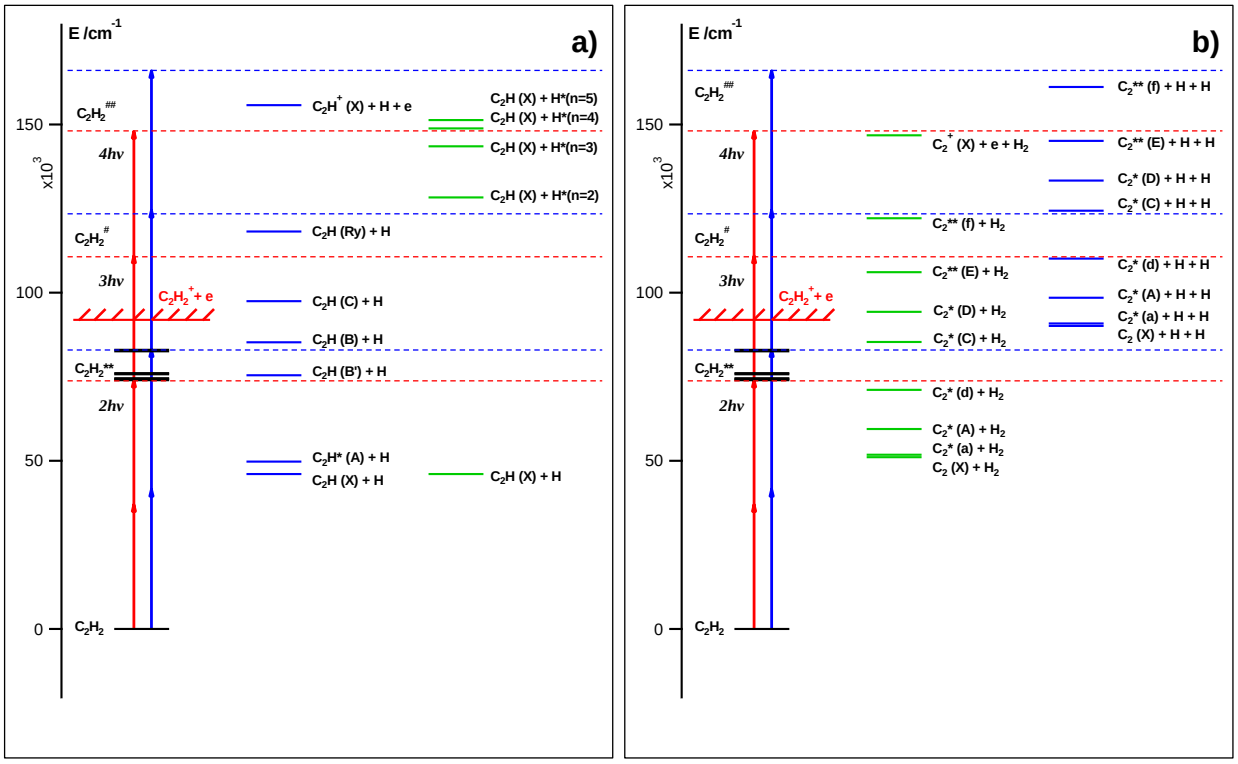

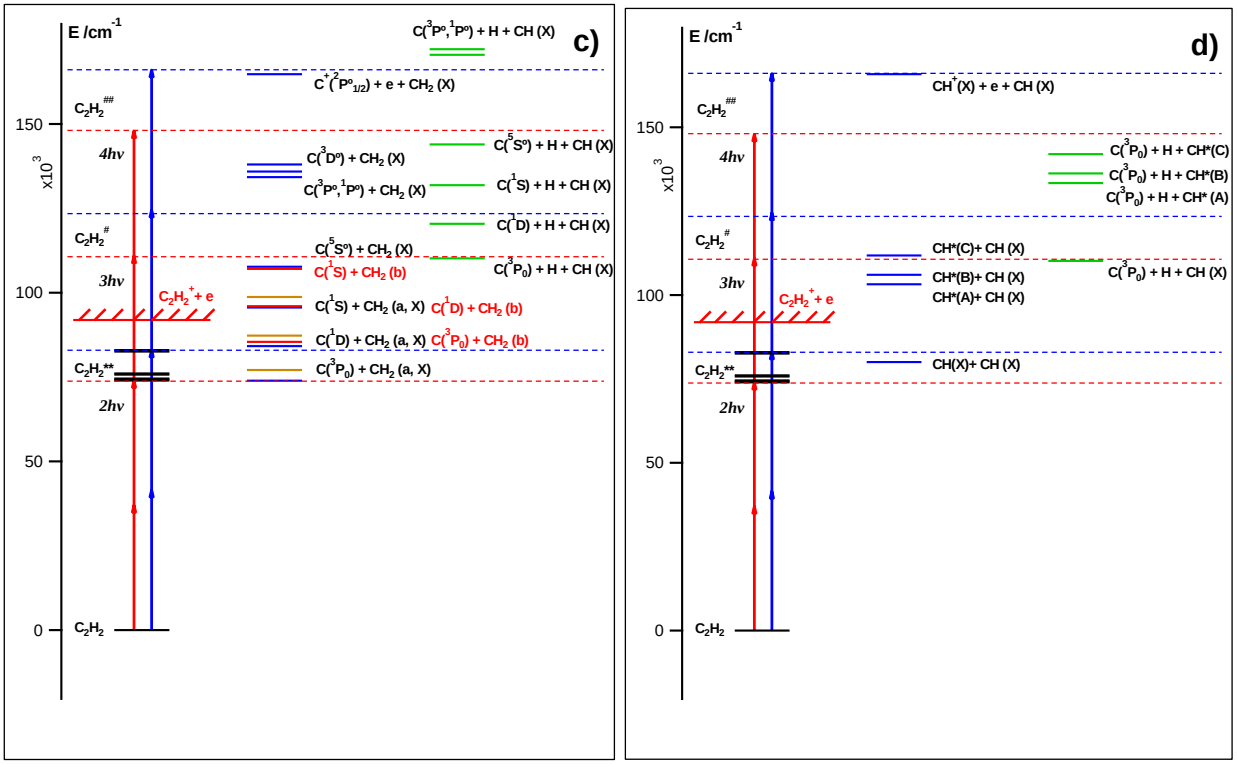

Fig. 2 ***C_2H_2 energetics and excitations:*** *Schematic energy diagrams and two-, three- and four-photon molecular excitations to the Rydberg states (C_2H_2**), first superexcited states ($C_2H_2^{\#}$) and second superexcited states ($C_2H_2^{\#\#}$), respectively (see main text). Energy levels for the C_2H_2** states (see no. 1 – 7 in* ***Table 1****) and various fragment formation thresholds are shown. The red and blue vertical arrows correspond to the two-photon resonant transitions of 73969 cm^{-1} (no. 1;* ***Table 1****) and 83006 cm^{-1}(no. 7), respectively.*

The minimum number of photons required to ionize the fragment species (m_{min}) formed according to the dissociation channels in (2) to (4) (see **Fig. 2**) range between 1 to 3,[24]

$H/H^* + mh\nu \rightarrow H^+ + e^-$; $m_{min} = 3/1$ for H/H^* (5a)

$C/C^* + mh\nu \rightarrow C^+ + e^-$; $m_{min} = 3/1,2,3$ for C/C^* (5b)

$CH/CH^* + mh\nu \rightarrow CH^+ + e^-$; $m_{min} = 3/2$ for for CH/CH^* (5c)

$CH_2/CH_2^* + mh\nu \rightarrow CH_2^+ + e^-$; $m_{min} = 3/1,2,3$ for CH_2/CH_2^* (5d)

$C_2/C_2^* + mh\nu \rightarrow C_2^+ + e^-$; $m_{min} = 3/1,2,3$ for C_2/C_2^* (5e)

$C_2H/C_2H^* + mh\nu \rightarrow C_2^+ + e^-$; m_{min} = 3/1,2,3 for C_2H/C_2H^* (5f)

$H/H^*(n = 2) + mh\nu \rightarrow H^+ + e^-$; m_{min} = 3/1,2,3 for H/H^* (5g)

In addition to these photoionization channels (5a – 5g) photodissociation of the parent molecular ion ($C_2H_2^+(X)$) to for H^+ and/or C_2H^+ also needs to be considered,

$C_2H_2^+(X) + 2h\nu \rightarrow C_2H + H^+$; ion photodissociation (5h)

$C_2H_2^+(X) + 2h\nu \rightarrow C_2H^+ + H$; ion photodissociation (5i)

Furthermore, autoionization and photodissociation of fragment species (Fi = H, C, CH,….) according to,

$Fi/Fi^* + nh\nu \rightarrow Fi^{\#} / Fi^{\#} \rightarrow Fi^+ + e^-$; photoexcitation / autoionization (5j)

$Fi/Fi^* + nh\nu \rightarrow Fi^{**} / Fi^{**} \rightarrow Fi1 + Fi2$; photodissociation (5k)

also needs to be considered.

In the subsections below (B – E) we present and describe data and relevant analysis based on velocity map images of electrons and ions (H^+, C^+, CH^+, C_2^+, C_2H^+) formed by the multiphoton excitations of concern (**Table 1**, **Fig. 1**). These are suitable to characterize what photofragmentation processes (within eqn. (2), (3), (4) and (5)) are involved.

B. Photoelectrons; e-KERs

Photoelectron images were recorded for two-photon resonant excitation of C_2H_2 to all the molecular Rydberg states listed in **Table 1** and marked in **Fig. 1a**. Electron kinetic energy release spectra (e-KERs) / photoelectron spectra (PES) were derived from the images. Selected

images, as three dimensional (3D) contour diagrams, and the corresponding e-KERs are shown in **Fig. 3** (**a,b,c**) (see also reference 24). **Fig.4** shows all the e-KERs / PES. All the spectra (images) show clear peaks (rings) varying in number and positions (KER) depending on the excitation energy. The spectra in **Fig.4** have been shifted by one- (**a**), two- (**b**) and three-(**c**) photon energy differences, ($\Delta(1h\nu) = \left| 1h\nu_i - 1h\nu_0 \right|$, (**a**); $\Delta(2h\nu) = \left| 2h\nu_i - 2h\nu_0 \right|$, (**b**); $\Delta(3h\nu) = \left| 3h\nu_i - 3h\nu_0 \right|$, (**c**)) with respect to the spectrum derived for the highest energy excitation (*i.e.* the "reference spectrum" for the one-, two- and three-photon excitations of $1h\nu_0$ = 41 503 cm^{-1}, $2h\nu_0$ = 83 006 cm^{-1} and $3h\nu_0$ = 124 509 cm^{-1}, respectively (image no. 7 in **Table 1**).

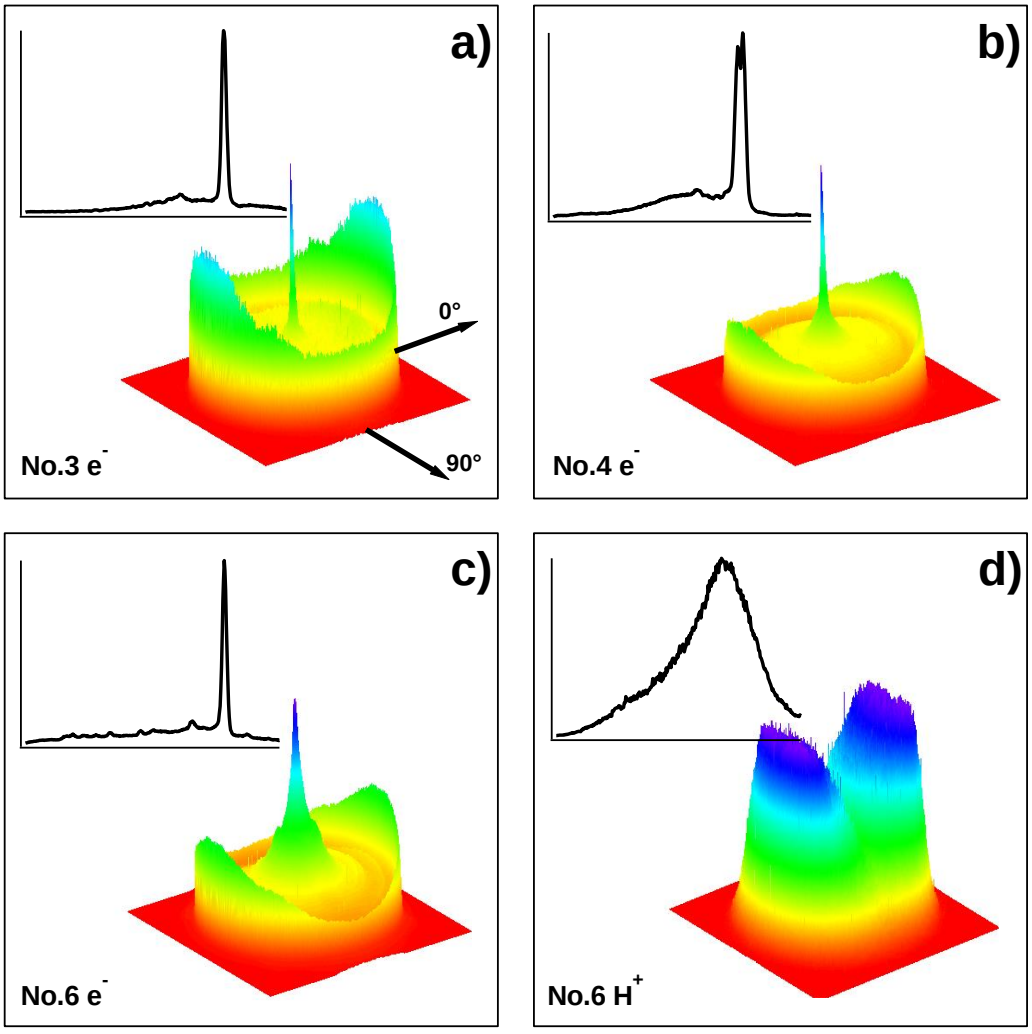

Fig. 3 ***Images and KERs:*** *Three-dimensional (3D) contour diagrams of electron (a – c) and ion (H^+, (d)) images (right, bottom) and corresponding kinetic release spectra (e-KERs (a – c) and Ion-KER (d); left top) derived from the images, for the two-photon resonant excitations of 74554 cm^{-1} (no.3 in* ***Table 1****) (a). 75760 cm^{-1} (no.4) (b), 82561 cm^{-1} (no.6) (c) and 74554 cm^{-1} (no.3) (d). The KERs are normalized to the strongest peak in each spectrum. The laser polarization direction is indicated by the axis labelled 0º.*

Thus, spectral features due to one- (**a**), two- (**b**) and three-(**c**) photon ionization of the same species will align. Calculated threshold energies (*i.e.*, maxima of kinetic energy release) for various ionization processes of relevance to our interpretation in the following paragraphs are also marked in the figures.

C_2H_2 three-photon autoionization: In the e-KERs for images no. 1 – 7 relatively sharp peaks due to autoionization of $C_2H_2^{\#}$, following three-photon excitation of $C_2H_2(X)$ via resonant excitation to all the Rydberg states (3p and 4p), are identified (**Fig. 4c**). These signals dominate for the images no. 1 – 5. These correspond to formation of $C_2H_2^+(X)$ by eqn. (3) and (3i) above for different vibrational states (v_1^+, v_2^+, v_3^+, v_4^+) as indicated in **Fig. 4c**. The threshold energies ($E_{thr}(v_1^+,v_2^+,v_3^+,v_4^+)$) shown in **Fig. 4c** are the energy differences between the three-photon excitations ($3h\nu$) and the ionization energies of C_2H_2 in the ground electronic state and the lowest vibrational energy, $C_2H_2(X; 0,0,0,0)$ to form $C_2H_2^+(X; v_1^+,v_2^+,v_3^+,v_4^+)$ (*i.e.* $IE(v_1^+,v_2^+,v_3^+,v_4^+)$),[25]

$$E_{thr}(v_1^+, v_2^+,v_3^+,v_4^+) = 3h\nu - IE(v_1^+,v_2^+,v_3^+,v_4^+) \quad (6)$$

The peaks closely resemble those observed in photoelectron spectra by Ashfold *et al.*[8], whereas our vibrational assignments differ somewhat for the excitations / spectra no. 3 – 7.

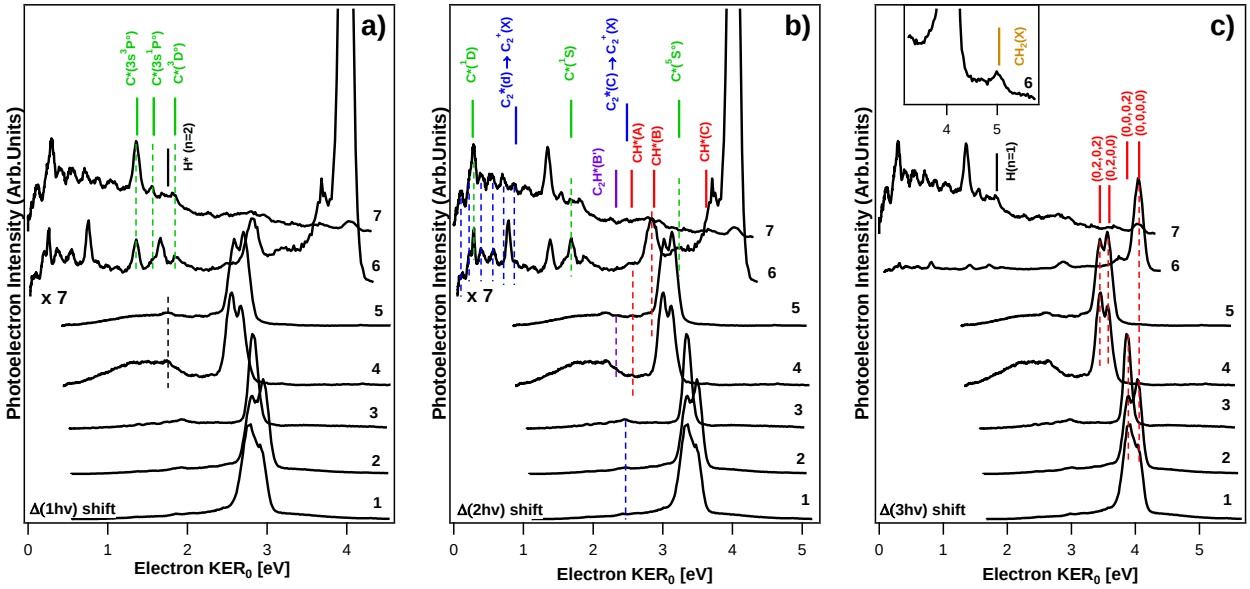

Fig. 4 ***e-KERs:*** *Electron kinetic energy release spectra (e-KERs) derived from images no. 1 – 7 (**Table 1**) plotted as a function of the kinetic energy release (KER) for the no. 7 (KER$_0$), shifted by one- (**a**), two- (**b**) and three-(**c**) photon energy differences, (Δ(1hv) (**a**); Δ(2hv) (**b**); Δ(3hv) (**c**)) with respect to the "reference spectrum", no. 7 (see main text). KER thresholds for ionization of fragments, as specified, are indicated by sticks above the spectra (a – c). KER thresholds for ionization of C_2H_2 to form the ground state ion $C_2H_2^+$ in different vibrational states ($C_2H_2^+(X, v_1^+,v_2^+,v_3^+,v_4^+)$) are indicated in (c). The inset in Fig. (c) shows an expanded part of the spectrum no.6 at high KER. The spectra are normalized to the strongest peak in each spectrum, whereas the spectrum for no. 6 has been expanded by a factor of 7 in (a) and (b).*

Fragment (Fi) ionizations: The major signals in the images /e-KERs no. 1 – 5 for the 3p Rydberg states are due to the three-photon autoionization of the parent molecule via resonant excitations to the Rydberg states. The importance of signals due to ionization of fragment species on the other hand increases for the resonant excitations to the 4p Rydberg states and dominates in the image/e-KER no. 7. Furthermore, some broad features and weak spectral peaks in the e-KERs no. 4 – 5 are also attributed to fragment ionizations. Some relevant threshold energies for ionization of various fragment species (E_{thr}(Fi/Fi*)) are marked in **Fig. 4a – 4c.** These correspond to the energy difference between photon excitations (mhν) and the ionization energy of the fragments (IE(Fi/Fi*)),[25]

$$E_{thr}(Fi/Fi^*) = mh\nu - IE(Fi/Fi^*);\ m = 1,2,3 \quad (7)$$

The thresholds are arranged in **Fig. 4a,4b** and **4c** by the number of photons (m) needed for the ionization as m = 1 in **Fig. 4a** ($\Delta(1h\nu)$ shift), m = 2 in **Fig. 4b** ($\Delta(2h\nu)$ shift) and m = 3 in **Fig. 4c** ($\Delta(3h\nu)$ shift). Judging from the comparison of thresholds and spectral peaks or features the major observations are as follows.

H*: Weak, but significant peaks are seen in the e-KERs no. 4, 5 and 6 at KER_0 = 1.75 eV in **Fig. 4a** ($\Delta(1h\nu)$ shift) which fits a one-photon ionization (m = 1) of H*(*n* = 2),

(5a): $H^*(n = 2) + 1h\nu \rightarrow H^+ + e^-$; e-KERs no. 4, 5

H*(*n* = 2) could be formed by a minimum of four- (n = 4; via $C_2H_2^{\#\#}$) photon dissociation of C_2H_2 (eqn. (4-4a)).

C*: Number of peaks associated with two- (m = 2) and one- (m = 1) photon ionization of excited carbon atoms (C*) (C*($2p^2$;^{1}D), C*($2p^2$;^{1}S) and C*($2s2p^3$;^{5}S) for m = 2 and C*(3s;^{3}P), C*(3s;^{1}P) and C*($2s2p^3$;^{3}D) for m = 1) were identified in the e-KERs no. 6 and 7 (**Fig. 4a** and **4b**),

(5b): $C^*(^1D, ^1S, ^5S) + 2h\nu \rightarrow C^+ + e^-$; e-KERs no. 6, 7

(5b): $C^*(^3P, ^1P, ^3D) + 1h\nu \rightarrow C^+ + e^-$; e-KERs no. 6, 7

These could be formed by a minimum of three- (n = 3; via $C_2H_2^{\#}$) and four- (n = 4; via $C_2H_2^{\#\#}$) photon dissociation of C_2H_2, to form the fragment pairs C* and $CH_2(X)$ according to eqn. (3c) and (4c), respectively.

CH*: Number of peaks associated with two- (m = 2) photon ionization of the excited methylidyne radical (CH*(A, B, C)) were identified in the e-KERs no. 4 – 7 as, weak peaks at

KER_0 = 2.51 eV in spectra no. 4 – 7 (CH*(A)), strong to moderate peaks at KER_0 = 2.84 eV in the spectra no. 6 and 7, respectively (CH*(B)) and weak peak at KER_0 = 3.60 eV in the spectrum no. 7 (CH*(C); see **Fig. 4b**),

(5c): $CH^*(A) + 2h\nu \rightarrow CH^+ + e^-$; e-KERs no. 4,5,6,7

(5c): $CH^*(B) + 2h\nu \rightarrow CH^+ + e^-$; e-KERs no. 6,7

(5c): $CH^*(C) + 2h\nu \rightarrow CH^+ + e^-$; e-KERs no. 7

These could be formed by a minimum of three-(n = 3) photon dissociation of C_2H_2, (via $C_2H_2^{\#}$) to form the fragment pairs CH* and CH(X) according to eqn. (3d).

CH_2: A weak but significant peak corresponding to three- (m = 3) photon ionization of the methylene ground state radical ($CH_2(X)$) was identified in the e-KER of no. 6 at KER_0 = 5.03 eV (See **Fig. 4c** and reference 24),

(5d): $CH_2 + 3h\nu \rightarrow CH_2^+ + e^-$; e-KERs no. 6

These could be formed by a minimum of two-(n = 2) photon dissociation of C_2H_2, (via $C_2H_2^{**}$) to form the fragment pairs C and $CH_2(X)$ according to eqn. (2c).

C_2*: A clear vibrational structure due to autoionization of superexcited $C_2^{\#}$ formed by two-photon excitation of C_2*(d) is seen in the low KER part of the e-KERs for no. 6 and 7 at KER_0 < 0.88 eV (**Fig. 4b**). Analyses reveal that the structure corresponds to two-photon transitions from C_2*(d, v´= 0,1) to $C_2^{\#}$ followed by autoionization to form C_2^+(X; v^+ = 0 – 6) in according to eqn. (5j) for n = 2 and Fi* = C_2*(d) (see also reference 24). Furthermore, weak peaks in no. 1 – 3 (KER_0 = 2.45 eV) are also indicative of autoionization of $C_2^{\#}$ following two-photon excitation of C_2*(C),

(5j): C_2*(d, v'= 0,1) + 2hν → $C_2^{\#}$ / $C_2^{\#}$ → C_2^+(X, v^+ = 0 - 6) + e^-; e-KERs no. 6,7

(5j): C_2*(C, v'= 0) + 2hν → $C_2^{\#}$ / $C_2^{\#}$ → C_2^+(X,v^+ = 0 - 6) + e^-; e-KERs no. 1,2,3

A minimum of two- (n = 2) and three-(n = 3) photon dissociation processes to form the C_2*(d) and C_2*(C) species along with H_2, respectively, could explain these observations.

C_2H*: Broad spectral features are seen in the low KER part of the e-KERs no. 4 and 5. These match on the "Δ(2hν) shift scale" in the region below KER_0 of about 2.3 eV (**Fig. 4b**), which corresponds to the threshold for two-photon ionization of C_2H*(B´).[28] This suggests that the broad feature is due to autoionization of $C_2H^{\#}$ to form C_2H^+(X) after two-photon excitation of C_2H*(B´), by analogy to the observation mentioned in the previous paragraph concerning C_2*(d)/$C_2^{\#}$/C_2^+(X),

(5j): C_2H*(B´) + 2hν → $C_2H^{\#}$ / $C_2H^{\#}$ → C_2H^+(X) + e^-; e-KERs no. 4,5

Closer look at the broad feature of the e-KER for no. 4[24] reveals an overlapping vibrational structure of a frequency close to that of the e CC- vibrational stretching mode (ν_3) for C_2H^+(X; ν_3).[23] A minimum of two- (n = 2) photon dissociation processes to form the C_2H*(B´) along with H could explain these observations.

C. Ions; Ion-KERs

H^+, C^+, CH^+, C_2^+ and C_2H^+ ion images were recorded for the two-photon resonant excitation of C_2H_2 to the molecular Rydberg states no. 1 - 2 and 4 – 7 as listed in **Table 1** and marked in **Fig. 1a**. Ion kinetic energy release spectra (ion-KERs) were derived from the images. A selected image, as a three dimensional (3D) contour diagram, and the corresponding ion-KER is shown in

Fig. 3d (see more data in reference 24). None of the images showed sharp rings, and all the ion-KERs typically consisted of one or two broad peaks, peaking at low kinetic energy release (KER) and tailing towards high kinetic energy release. In cases when the ions are formed by photoionization of fragments this structure is indicative of an energy redistribution among the molecule's internal degrees of freedom prior to the dissociations.[16, 17] The ion-KERs were displayed as shifted by two-, three- and four-photon energy differences ($\Delta(2h\nu) = \left| 2h\nu_i - 2h\nu_0 \right|$; $\Delta(3h\nu) = \left| 3h\nu_i - 3h\nu_0 \right|$; $\Delta(4h\nu) = \left| 4h\nu_i - 4h\nu_0 \right|$; subscript *i* refers to different spectra) with respect to the spectrum derived for the highest energy excitation (*i.e.* the "reference spectrum", no. 7; subscript 0) on the energy scale for the "reference spectrum" (KER_0; eV) to allow comparison of common spectral features due to two- , three- and four- photon dissociation processes, respectively.[12-17] Threshold kinetic energies (E_{thr}) (*i.e.* maxima of kinetic energy release), corresponding to the energy difference between the photoexcitations (nhν) and the energies of the various fragments (Fi) formed (E(Fi)) according to eqn. (2) – (4) above were evaluated,

$$E_{thr} = nh\nu - E(Fi); \qquad n = 2,3,4 \tag{8}$$

and compared with the spectra to explore the signal origins. The broad spectral features with tails towards the high kinetic energy release, lower than the threshold, could, in principle, all correspond to processes marked by the thresholds. In the following subsections we collect possible fragmentation channels, within eqn. (2) – (4), which could be responsible for the ion-KER signals, based on these criteria. Large number of relevant figures are to be found in the supporting material,[24] whereas only a limited number (see **Fig. 5**) are presented here, mainly for demonstration purposes.

H^+ KERs. The H^+ signals show broad peaks, possibly with two (low and high KER) overlapping contributions in some instances, ranging typically over about 3 eV on the total KER scale (see **Fig. 5a** and reference 22). The analyses revealed that the following fragmentation channels (nx; see above) could, in principle, be responsible for H/H* formations, prior to ionization:

(2a): $C_2H_2^{**} \rightarrow H + C_2H^*(B')$; Ion-KERs no. 6,7, low KER

(2a): $C_2H_2^{**} \rightarrow H + C_2H(X)/C_2H^*(A)$; All ion-KERs

(3a): $C_2H_2^{\#} \rightarrow H + C_2H^*(Ry)$; Ion-KERs no. 6,7, low KER

(3a): $C_2H_2^{\#} \rightarrow H + C_2H^*(C,B)$; All ion-KERs

(3e): $C_2H_2^{\#} \rightarrow H + H + C_2^*(d)$; Ion-KERs no. 4,5,6,7, low KER

(3e): $C_2H_2^{\#} \rightarrow H + H + C_2/C_2^*(A,a)$; All ion-KERs

(3g): $C_2H_2^{\#} \rightarrow CH + H + C^*(^1D)$; Ion-KERs no. 6,7, low KER

(3g): $C_2H_2^{\#} \rightarrow CH + H + C^*(^3P)$; Ion-KERs no. 4,5,6,7, low KER

(4a): $C_2H_2^{\#\#} \rightarrow C_2H + H*(n>2)$; All ion-KERs

Furthermore, a molecular ion photodissociation could also be responsible for the H^+ formation:

(3i): $C_2H_2^{\#} \rightarrow C_2H_2^+ + e^-$; followed by,

(5h): $C_2H_2^+(X) + 2h\nu \rightarrow C_2H + H^+$; All ion-KERs

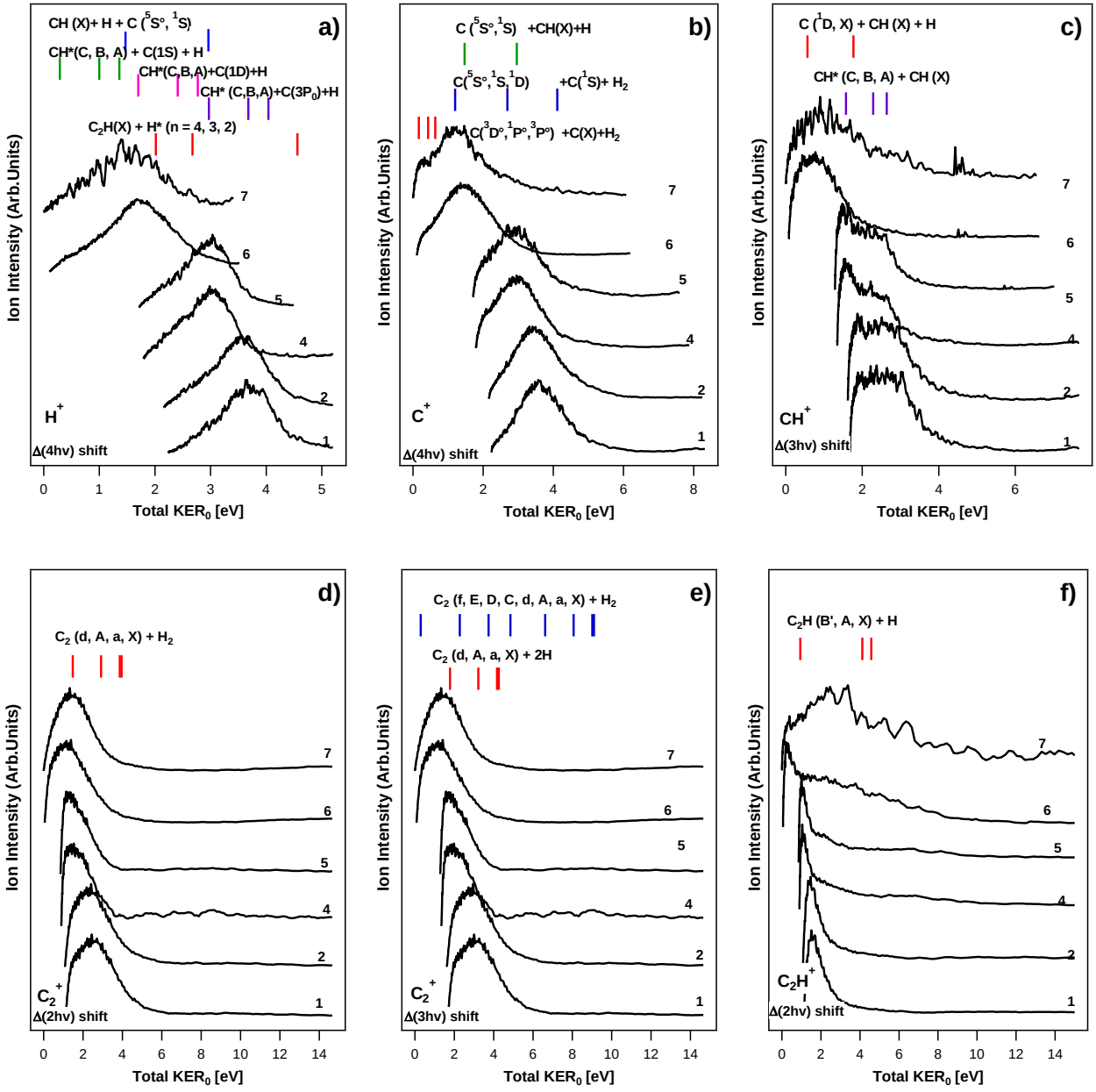

Fig. 5 Ion-KERs: Ion kinetic energy release spectra (Ion-KERs) derived from the images no.1,2,4 -7 (see **Table 1**). The spectra are plotted as a function of the total kinetic energy release for the no. 7 (Total KER_0) and shifted by n-photon energy differences ($\Delta(nh\nu)$) with respect to the "reference spectrum", no. 7 (see main text) as, $\Delta(4h\nu)$ for H^+ (a), $\Delta(4h\nu)$ for C^+ (b), $\Delta(4h\nu)$ for CH^+ (c), $\Delta(2h\nu)$ for C_2^+ (d), $\Delta(3h\nu)$ for C_2^+ (e) and $\Delta(2h\nu)$ for C_2H^+ (f). KER thresholds for fragment formations by n-photo-dissociation (n = 2, 3 and 4 for photodissociation via the C_2H_2**, $C_2H_2^{\#}$ and $C_2H_2^{\#\#}$ intermediate species), as specified, are indicated by sticks above the spectra. The spectra are normalized to the strongest peak in each spectrum.

C^+ KERs. The C^+ signals show broad peaks with overlapping contributions in all spectra, ranging typically over about 4 - 5 eV on the total KER scale (see **Fig. 5b** and reference 24). The analyses revealed that the following fragmentation channels could, in principle, be responsible for C/C* formations, prior to ionization:

(2c): $C_2H_2^{**} \rightarrow C + CH_2/CH_2^*(a)$; Ion-KERs no. 1-7, low KER

(3c): $C_2H_2^{\#} \rightarrow C/C^*(^5S,^1S,^1D) + CH_2/CH_2^*(b,a)$; All ion-KERs

(3f): $C_2H_2^{\#} \rightarrow H_2 + C/C^*(^1D) + C/C^*(^1S,^1D)$; All ion-KERs

(3g): $C_2H_2^{\#} \rightarrow H + CH + C/C^*(1D)$; Ion-KERs no. 6-7

(4c): $C_2H_2^{\#\#} \rightarrow C^*(^3D,^1P,^3P) + CH_2/CH_2^*(b,a)$; Ion-KERs no. 1-5

(4f): $C_2H_2^{\#\#} \rightarrow H_2 + C/C^*(^1S) + C/C^*(many)$; Ion-KERs no. 6-7, low KER

(4g): $C_2H_2^{\#\#} \rightarrow H + CH + C^*(^5S,^1S)$; All ion-KERs

CH^+ KERs. The CH^+ signals show broad peaks with clear overlapping contributions in no. 1 - 5, ranging typically over about 3 - 4 eV on the total KER scale (see **Fig.5c** and reference 24). The analyses revealed that the following fragmentation channels could, in principle, be responsible for CH/CH* formations prior to ionization:

(2d): $C_2H_2^{**} \rightarrow CH(X) + CH(X)$; Ion-KERs no. 6,7, low KER

(3d): $C_2H_2^{\#} \rightarrow CH + CH^*(C,B,A)$; Ion-KERs no. 1- 5

(3g): $C_2H_2^{\#} \rightarrow CH + H + C^*(^1D)$; Ion-KERs no. 6,7, low KER

(3g): $C_2H_2^{\#} \rightarrow CH + H + C$; All ion-KERs, low KER

(4g): $C_2H_2^{\#\#} \rightarrow H + CH/CH^*(C,B,A) + C/C^*(^1D,^1S)$; Ion-KERs no. 1-7

C_2^+ KERs. The C_2^+ signals show broad peaks with some overlapping contributions, ranging typically over about 4 - 5 eV on the total KER scale (see **Fig.5d** and reference 24). The

analyses revealed that the following fragmentation channels could, in principle, be responsible for C_2/C_2* formations prior to ionization (see above):

(2b): $C_2H_2^{**} \rightarrow H_2 + C_2/C_2^*$(d,A,a); All ion-KERs

(3b): $C_2H_2^{\#} \rightarrow H_2 + C_2/C_2^*$(f,E,D,C); All ion-KERs

(3e): $C_2H_2^{\#} \rightarrow H + H + C_2/C_2^*$(d,A,a); All ion-KERs

C_2H^+ KERs. The C_2H^+ signals show relatively narrow peaks at low KER for no. 1,2,4-6, ranging typically over about 1 – 2 eV on the total KER scale and a broad high KER contribution for all the images / spectra. The analyses revealed that the following fragmentation channels could, in principle, be responsible for the low KER contributions to the C_2H/C_2H^* formations prior to ionization:

(2a): $C_2H_2^{**} \rightarrow H + C_2H/C_2H^*$(B´,A); All ion-KERs, low KER

(3a): $C_2H_2^{\#} \rightarrow H + C_2H^*$(Ry); Ion-KERs no. 6,7, low KER

(3a): $C_2H_2^{\#} \rightarrow H + C_2H/C_2H^*$(C,B, B´,A); All ion-KERs

Furthermore, a molecular ion photodissociation could also be responsible for the C_2H^+ formation:

(3i): $C_2H_2^{\#} \rightarrow C_2H_2^+ + e^-$; followed by

(5i): $C_2H_2^+(X) + 2h\nu \rightarrow C_2H^+(X) + H$; All ion-KERs, low KER

D. orrelation analyses (A, B, C combined)

Based on the analyses described in sections **A** (MR-REMPI), **B** (e-KERs) and **C** (ion-KERs) above concerning possible origins of the ion (**A, C**) and corresponding electron (**B**) signals the

following results, relevant to the ion formations, are derived (correlation analyses) (see also **Fig. 1b, 4, 5** and **Table 1**):

H$^+$: H^+ signals were detected for the excitations no. 4 – 7 in MR-REMPI with a maximum relative ion signal for no. 6 (**A**) (**Fig. 1b**). e-KERs of images no. 4 - 5 suggest that one- (m = 1) photon ionization of H*(*n* = 2) is occurring (**B**) (**Fig. 4a**). Judging from the ion KERs H^+ ions could, in principle, be formed after four- (n = 4) photon dissociation of C_2H_2, via $C_2H_2^{\#\#}$, to form H*(*n* = 2) along with C_2H(X), (**C**) (see **Fig. 5a** and reference 24). In combination we conclude that the following multiphoto-fragmentation processes are important:

(4a): $C_2H_2^{\#\#} \rightarrow C_2H$ + **H***(n = 2); All excitations

(5a): H*(*n* = 2) + **1**hν $\rightarrow H^+ + e^-$; e-KERs no. 4, 5

C$^+$: C^+ signals were detected for the excitations no. 4 – 7 in MR-REMPI with a maximum relative ion signal for excitations no. 6 (**A**) (**Fig. 1b**). e-KERs of images no. 6 - 7 suggest that two- (m = 2) photon ionization of C*(^{1}D, ^{1}S, ^{5}S) and one- (m = 1) photon ionization of C*(^{3}P, ^{1}P, ^{3}D) is occurring (**B**) (**Fig. 4a and 4b**). Judging from the ion-KERs C^+ ions could, in principle, be formed after three- (n = 3) photon dissociation of C_2H_2, via $C_2H_2^{\#}$, to form C*(^{5}S,^{1}S,^{1}D) along with CH_2/CH_2*, H_2 and H + CH and after four- (n = 4) photon dissociation of C_2H_2, via $C_2H_2^{\#\#}$, to form C*(^{3}D,^{1}P,^{3}P) along with CH_2/CH_2* and H_2 as well as C*(^{5}S,^{1}S) along with H and CH (**C**) see **Fig. 5b** and reference 24). In combination we conclude that the following multiphoto-fragmentation processes could be important:

(3c): $C_2H_2^{\#} \rightarrow$ C*(^{5}S,^{1}S,^{1}D) + CH_2/CH_2*(b,a); All ion-KERs

(3f): $C_2H_2^{\#} \rightarrow H_2$ + C*(^{1}D) + C*(^{1}S,^{1}D); All ion-KERs

(3g): $C_2H_2^{\#} \rightarrow$ H + CH + C*(^{1}D); Ion-KERs no. 6-7

(4c): $C_2H_2^{\#\#} \rightarrow C^*(^3D,^1P,^3P) + CH_2/CH_2^*(b,a)$; Ion-KERs no. 1-5

(4f): $C_2H_2^{\#\#} \rightarrow H_2 + C^*(^1S) + C^*(many)$; Ion-KERs no. 6-7, low KER

(4g): $C_2H_2^{\#\#} \rightarrow H + CH + C^*(^5S,^1S)$; Ion-KERs no. 6-7, low KER

(5b): $C^*(^1D, ^1S, ^5S) + 2h\nu \rightarrow C^+ + e^-$; e-KERs no. 6, 7

(5b): $C^*(^3P, ^1P, ^3D) + 1h\nu \rightarrow C^+ + e^-$; e-KERs no. 6, 7

CH^+: Maximum relative ion signals of C_2H^+ are observed in MR-REMPI for excitation no. 6 (**A**) (**Fig. 1b**). e-KERs of images no. 4 - 7 suggest that two- (m = 2) photon ionization of number of CH* species (CH*(A,B,C)) is occurring (**B**) (**Fig. 4b**). Judging from the ion-KERs CH^+ ions could, in principle, be formed after three- (n = 3) photon dissociation of C_2H_2, via $C_2H_2^{\#}$, to form CH*(C,B,A) along with CH and after four- (n = 4) photon dissociation of C_2H_2, via $C_2H_2^{\#\#}$, to form CH*(C,B,A) along with C/C* (**C**) (see **Fig. 5c** and reference 24). In combination we conclude that the following multiphoton-fragmentation processes are important:

(3d): $C_2H_2^{\#} \rightarrow CH + CH^*(C)$; Excitations no. 4 – 7, low ion-KER

(3d): $C_2H_2^{\#} \rightarrow CH + CH^*(B,A)$; All excitations, low ion-KER

(4g): $C_2H_2^{\#\#} \rightarrow H + CH^*(C,B,A) + C^*(^1S)$; Excitations no. 6 – 7

(4g): $C_2H_2^{\#\#} \rightarrow H + CH^*(C,B,A) + C/C^*(^1D)$; All excitations

(5c): $CH^*(C,B,A) + 2h\nu \rightarrow CH^+ + e^-$; e-KERs no. 4,5,6,7

CH_2^+: The relative ion signals of low CH_2^+ intensities observed in MR-REMPI reaches maximum for no. 6 (**A**) (**Fig. 1b**). The e-KER of image no. 6 suggests that three-(m = 3) photon ionization of the ground state $CH_2(X)$ is occurring (**B**) (**Fig. 4c**). Energetically $CH_2(X)$ could be formed along with C by two-(n = 2) photon dissociation, via C_2H_2** and along with number of

C* atoms as well as C by thee- (n = 3) photon dissociation, via $C_2H_2^{\#}$ (**Fig. 2c**). In combination we conclude that the following multiphoto-fragmentation processes could be important:

(2c): $C_2H_2^{**} \rightarrow C + CH_2$; All excitations

(3c): $C_2H_2^{\#} \rightarrow C/C^* + CH_2$; All excitations

(5d): $CH_2 + 3h\nu \rightarrow CH_2^+ + e^-$; e-KER no. 6

C_2^+: The relative ion signals of C_2^+ observed in MR-REMPI are found to increase gradually with excitation (**A**) (**Fig. 1b**). e-KERs of images no. 6 and 7 suggest that two-photon ionization of C_2*(d; v´= 0,1) is occurring (**B**) (**Fig. 4b**). e-KERs of no. 1 - 3 suggest that two-photon ionization of C_2*(C) is occurring (**B**) (**Fig. 4b**). Judging from the ion-KERs C_2^+ ions could, in principle, be formed after two-(n = 2) and three- (n = 3) photon dissociation of C_2H_2, via $C_2H_2^{**}$ and $C_2H_2^{\#}$, respectively to form C_2*(d) along with H_2 (n = 2,3) and 2H (n = 3) for all excitations(**C**) (see **Fig. 5d, 5e** and reference 22). C_2^+ ions could also be formed after three- (n = 3) photon dissociation of C_2H_2 to form C_2*(C) along with H_2 for all excitations(**C**) (**Fig. 5d**). In combination we conclude that the following multiphoto-fragmentation processes are important:

(2b): $C_2H_2^{**} \rightarrow H_2 + C_2$*(d); All excitations, low ion-KER

(3b): $C_2H_2^{\#} \rightarrow H_2 + C_2$*(C); All excitations

(3e): $C_2H_2^{\#} \rightarrow H + H + C_2$*(d); All excitations, low ion-KER

(5j): C_2*(d, v'= 0,1) + $2h\nu \rightarrow C_2^{\#} / C_2^{\#} \rightarrow C_2^+$(X, v^+ = 0 - 6) + e^-; e-KERs no. 6,7

(5j): C_2*(C, v'= 0) + $2h\nu \rightarrow C_2^{\#} / C_2^{\#} \rightarrow C_2^+$(X, v^+ = 0) + e^-; e-KERs no. 1,2,3

C_2H^+: Maximum relative ion signals of C_2H^+ are observed in MR-REMPI for excitations no. 4 and 5 (**A**) (**Fig. 1b**). e-KERs of images no. 4 and 5 suggest that two- (m = 2) photon ionization of

$C_2H^*(B')$ is occurring (**B**) (**Fig. 4b**). Judging from the ion-KERs C_2H^+ ions could, in principle, be formed after two-(n = 2) and three- (n = 3) photon dissociation of C_2H_2, via $C_2H_2^{**}$ and $C_2H_2^{\#}$, respectively to form $C_2H^*(B')$ along with H for all the excitations (**C**) (see **Fig. 5f** and reference 22). In combination we conclude that the following multiphoton-fragmentation processes are important:

(2a): $C_2H_2^{**} \rightarrow H + C_2H^*(B')$; All excitations, low ion-KER

(3a): $C_2H_2^{\#} \rightarrow H + C_2H^*(B')$; All excitations, high ion-KER

(5j): $C_2H^*(B') + 2h\nu \rightarrow C_2H^{\#} / C_2H^{\#} \rightarrow C_2H^+(X) + e^-$; e-KERs no. 4,5

E. Angular distributions

All the ion images recorded display shapes corresponding to either parallel or isotropic distributions depending on the ions and the kinetic energy released (see **Fig. 3d** and reference 24). Given the number of photons and the multiple channels/pathways involved in the production of each ion and electron angular distribution recorded, a detailed fitting and analysis will not provide easily interpretable results as the extracted anisotropy parameters would be the average of multiple processes. However, to get an insight on the general trend, we fitted selected KER ranges with the one-step (non-resonant) expression for angular distribution,[15]

$$P(\theta) = A[1 + \sum_n \beta_{2n} P_{2n}(cos(\theta))] \quad (9)$$

to derive anisotropy parameters β_{2n} (n = 1 – 3), where n is the number of photons involved in the photolysis, P_{2n} is the 2n-th order Legendre polynomial and A is a scaling factor. β_{2n} parameters derived from the data are to be found in reference 22. β_2, which is a convenient parameter to indicate the degree of anisotropy of the transitions involved, ranges from +2 (purely parallel

transition) to -1 (purely perpendicular transition), *via* 0 (isotropic). These were found to be in the range of +1.3 (H^+) to -0.2(C_2H^+). There is an overall tendency toward a decreasing β_2 value with ion mass. Furthermore, a tendency of a gradual decrease in β_2 with the excitation energy is observed for all the fragment ions except C_2H^+, which shows a drop in the value from about $+0.75 \pm 0.25$ (for excitations no. 1,2,4) to about 0 ± 0.15 (for no. 5,6,7). An attempt was made to derive β_2 parameters for separate channels from images which appear to display bi- (or multi-) modal contributions by evaluations β_2 for different KER ranges (low and high ion-KER). Significantly different β_2 values were obtained for high and low ion-KER contributions of the C^+ and CH^+ images (see reference 24). No further interpretations of the angular distribution data[24] in connection with the fragmentation processes are attempted here.

IV. Discussions

$C_2H^*(B')/C_2H^+$: Judging from our data (see Section III, D) low KER peaks seen in the C_2H^+ ion-KERs no. 4 and 5 (**Fig. 5f**) are likely to be due to two-photon ionization of $C_2H^*(B')$ after a "near-resonant" energy transfer from the corresponding Rydberg states ($C_2H_2^{**}$) (**Table 1**) to form $C_2H^*(B')$ and H after two-photon excitation of C_2H_2 (eqn. (2a)). This could be used to estimate the energy of the $C_2H^*(B')$ species, which is a subject of an uncertainty: The value of the energy for the $C_2H^*(B')$ state ($E(C_2H^*(B'))$) reported in NIST[25] of 3.640 eV (29 360 cm^{-1}) is determined from an absorption spectrum recorded after photolysis of C_2H_2 trapped in a solid argon matrix.[26] In addition, calculated values of 3.81 eV (thermodynamic calculation)[27] and 3.716 eV (*ab initio* calculation)[28] have been reported for $E(C_2H^*(B'))$. An alternative estimate of $E(C_2H^*(B'))$, based on our data (gas phase condition), is as follows.

Conservation of the energy in the two-photon excitation step gives,

$$2h\nu = D_0(C_2H\text{-}H) + E(C_2H^*(B')) + E_{thr} \quad (10a)$$

where $D_0(C_2H\text{-}H)$ is the bond energy of $C_2H_2(X)$ to form $C_2H(X)$ and H and E_{thr} is the threshold energy for $C_2H^*(B')$ + H (eqn. (8)). This gives,

$$E(C_2H^*(B')) = 2h\nu - D_0(C_2H\text{-}H) - E_{thr} \quad (10b)$$

The threshold energies (E_{thr}) refer to the upper limits of the low ion kinetic energy release peaks for no. 4 and 5, which cannot be determined due to overlap of spectral contributions (see **Fig. 5f**) Using the low ion-KER peak positions (E_{peak}) as an approximation for E_{thr}, however, allows estimates of the upper limit for $E(C_2H^*(B'))$,

$$E(C_2H^*(B')) \leq 2h\nu - D_0(C_2H\text{-}H) - E_{peak} \quad (10c)$$

of about 3.54 ± 0.01 eV (see also reference 24).

C_2*/C_2^+: In what follows we will discuss the probable fragmentation channels prior to C_2^+ formation according to our observations (see section III, D) in the context of other observations.

C_2*(d) **/C_2^+**: According to our data, C_2^+ could be formed by autoionization of a superexcited state $C_2^{\#}$ formed by two-photon ionization of C_2*(d,v´= 0,1) (eqn. (5j)) for the excitations no. 6 and 7 (**Table 1**). It also shows that C_2*(d,v´= 0,1) could be formed by two-(n = 2) oton excitation of C_2H_2 (via C_2H_2**) along with H_2 (eqn. (2b)) and/or by three-(n = 3) photon excitation of C_2H_2 (via $C_2H_2^{\#}$) along with 2H (eqn. (3e)) for all the excitations(see section III, D). The following observations / arguments favor formation of C_2*(d) along with 2H by three-photon dissociation over formation of C_2*(d) along with H_2 by two-photon dissociation:

(i) Fluorescence studies based on the C_2*(d) → C_2*(a) transition (the Swan band[6]) reveal no C_2*(d) formation for C_2H_2 for one-photon excitations corresponding to the two-photon excitation region of concern here (*i.e.* 73 900 – 83 100 cm^{-1}),[30] whereas a significant C_2*(d) fluorescence is detected for excitation to the region of 110 850 – 124 650 cm^{-1}, which corresponds to the three-photon excitation here.[6, 31] This suggests that three-photons are required for the C_2*(d) formation here.

(ii) A close correlation is found between signals of REMPI spectra derived for the molecular parent ion ($C_2H_2^+$)[8, 9]and a fluorescence excitation spectrum due to C_2*(d) → C_2*(a)[6] derived for multiphoton excitations via the Rydberg states no. 1 - 6 (see **Fig. 6**). This strongly suggests that the formations of $C_2H_2^+$ and C_2*(d) are of the same origin, *i.e.* from the superexcited state(s) $C_2H_2^{\#}$, formed by three-photon excitation.

(iii) Dissociation of C_2H_2** to form C_2*(d) and H_2 (eqn. (2b)) will involve a transition via a cis-conformation geometry.[9] Calculations reveal an energy maximum for the lowest energy singlet state cis-conformer of about 76 000 ± 1 000 cm^{-1}, which excludes a corresponding dissociation of C_2H_2** for no. 1 – 3 and limits the corresponding transition / dissociation probabilities for no. 4 – 5 (energies 75 760 cm^{-1} and 76 085 cm^{-1}, respectively). Furthermore, all the Rydberg states of concern (C_2H_2**) are, to a first approximation, considered to be linear in structure,[8] which limits the possibility of transformation to a cis-geometry without additional state transfer processes.

We, therefore, conclude that C_2*(d) is formed by the three-photon dissociation mechanism (3e), rather than the by the two-photon dissociation mechanism (2b), for all the excitations. While

C_2*(d) is formed for all the excitations according to the fluorescence data,[6] C_2^+ signals from ionization of C_2*(d) (**Fig. 4**) are only observed for the excitations no. 6 and 7, for energetic reason, since only two-photons are required to ionize C_2*(d) in no. 6 and 7 compared to three-photons for no. 1 – 5. A striking difference, however, is seen in the C_2^+ signal intensities for ionization of C_2*(d) for no. 6 and 7 as no.7 >> no.6 (see **Fig. 4**). Most likely this is due to a significant difference in the branching fractions for the C_2*(d) formations ($\Gamma(C_2$*(d))) via channel (3e) for no. 6 and 7, as $\Gamma(C_2$*(d)) for no. 7 >> $\Gamma(C_2$*(d)) for no. 6. This is further evident from the striking difference in the relative intensities of the $C_2H_2^+$ REMPI signal and the C_2*(d) fluorescence signal as seen in **Fig. 6** for no. 7 as well as the relatively small $C_2H_2^+$ signal in the e-KER for no. 7 (**Fig. 4(c)**).

While (3e) is likely to be the dominant channel for the C_2*(d) formation, a contribution to the formation of C_2*(d) from photodissociation of C_2H*(B´) (see above) is worth an attention. As mentioned above (subsection "**C_2H*(B´)/C_2H^+**") our data suggests that C_2H*(B´) is formed after a two-photon excitation (via C_2H_2**) (channel (2a)). C_2H*(B´) has been found to be a long lived species[31] formed to an increasing extent with excitation energy in one-photon excitation[27] in the region of concern, reaching quantum yield of about 6.7% for the excitation to no. 7 (see **Fig. 6**). Further photoexcitation of C_2H*(B´) (in no. 6 and 7) could, energetically, form excited states (Rydberg[32] and/or valence states[33]), which are known to exist in that energy region, which could predissociate to form C_2*(d) and H (channel (5k)).[33]This could be an important additional contribution to the C_2*(d) formation, for no. 6 and 7 in particular.

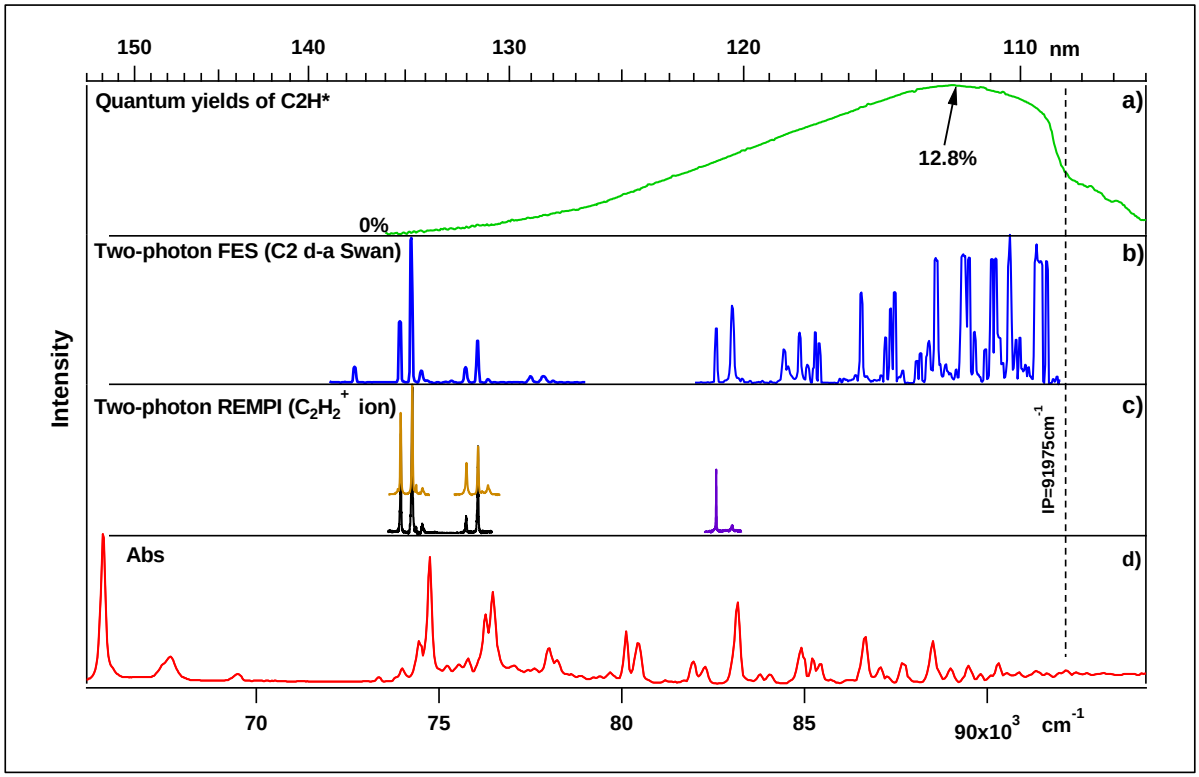

Fig. 6 ***Fragment fluorescence and acetylene spectra:*** *(a): Fluorescence quantum yield for $C_2H^*(B')$, due to the $C_2H^*(B') \rightarrow C_2H(X) + h\nu$ emission transition in one-photo-dissociation of C_2H_2.[25] (b): Fluorescence excitation spectrum of C_2H_2 for the $C_2^*(d) \rightarrow C_2^*(a) + h\nu$ (Swan band) emission transition following two-photon excitation to C_2H_2** Rydberg states.[6] (c): $C_2H_2^+$ REMPI spectra for two-photon resonant excitations to C_2H_2** Rydberg states, from references 9 (black), 8 (brown) and 6(purple). (d): Absorption spectrum of C_2H_2.[25]*

$C_2^*(C)$ /C_2^+: According to our data, C_2^+ could also be formed by autoionization of a superexcited state $C_2^{\#}$ formed by two-photon ionization of $C_2^*(C)$ (eqn. (5j)) for no. 1,2 and 3 (**Table 1**). It also shows that $C_2^*(C)$ could be formed by three-(n = 3) photon excitation of C_2H_2 (via $C_2H_2^{\#}$) along with H_2 (eqn. (3b)) for all the excitations(see section III, D). This matches the result of fluorescence studies by Han *et al.* who observed a $C_2^*(C)$ fluorescence due to the $C_2^*(C) \rightarrow C_2^*(A)$ transition for one-photon excitation of C_2H_2, which corresponds to an excitation within our three-photon excitation region, above the threshold for $C_2^*(C) + H_2$ and below the threshold for $C_2^*(C) + 2H$ (see **Fig. 2b**).[30]

C_2*(B´, v´= 3) /C_2^+: A sharp peak sticks out in the e-KER spectrum for no. 6 on the low KER side of the threshold for the C_2*(d,v´= 0) ionization (see **Fig. 4b**). Corresponding weak peak, which matches on the "Δ(2hν) shift scale" was also found for no.7, depending on the image recording conditions.[24] This suggests that these peaks are of the same origin for two-photon ionization. These could not be assigned to any ionizations of relevant atom fragments or molecular fragments (Fi/Fi*) for zero vibrational states. Instead we assign these peaks to ionizations of C_2*(B´, v´= 3). This is based on calculated potential energy curves for C_2*[34, 35] and spectroscopic parameters for C_2*(B´)[32] and C_2*(d),[23] which suggest that the peak positions match an ionization of C_2*(B´, v´= 3), which is close in energy to C_2*(d, v´= 0) (ΔE ≈ 0.1 eV) (see also reference 24). The appearance of peaks due to ionization of the v´= 3 level only and an absence of peaks due to ionization of other v´ levels of C_2*(B´) could be associated with mixing between the two states, which will depend on the Franck-Condon overlap of the vibrational wave functions and be inversely proportional to the energy gap between the v´ levels for the two states,[12-14, 18] to exaggerate the ionization process for C_2*(B´,v´= 3) due to near-resonance mixing with C_2*(d,v´= 0), *i.e.* an "intensity borrowing" effect.

CH*(C,B,A)/CH^+: Judging from our data (see Section III, D) CH^+(X) could be formed by two-(m = 2) photon ionization of CH*(C,B,A) (eqn. (5c)) (possibly via autoionization of superexcited $CH^{\#}$(eqn. (5j)) for no. 4 – 7 and that CH*(C,B,A) could be formed by three- (n = 3) and/or four-(n = 4) photon dissociation processes along with CH (channel (3d)) and C* (4g), respectively. Our prediction of the former photodissociation channels (3d) matches observations in fluorescence studies by Han *et al.*, who detected CH*(C,B,A) fluorescence due to transition from CH*(C,B,A) to CH(X) in the case of one-photon excitation of C_2H_2 in the excitation region corresponding to our three-photon excitations (see **Fig. 2b**).[30] The latter channel (4g), however

can not be ruled out. Thus, the broad range of the ion-KER spectrum for CH^+ for no. 7, in particular (see **Fig. 5c**) and observation of strong C*(^{1}S) and CH*(B) two-(m = 2) photon ionization signals in the e-KER for no. 6 (**Fig. 4b**) suggest its involvement.

C*/C$^+$: Based on our data (see Section III, D) C^+ could be formed by two-(m = 2) and one-(m = 1) photon ionization of lower (C*(^{1}D, ^{1}S, ^{5}S)) and higher (C*(^{3}P, ^{1}P, ^{3}D)) energy C* atoms, respectively for no. 6 and 7. The lower energy carbon atoms (C*(^{1}D, ^{1}S, ^{5}S)) could be formed by three-photon dissociation channels ((3c), (3f) and (3g)), whereas the higher energy atoms (C*(^{3}P, ^{1}P, ^{3}D)) would be formed by four-photon dissociation channels ((4c), (4f) and (4g)). In both cases the total number of photons (n + m) would be 5. The byproducts are either CH_2/CH_2* (channels (3c) and (4c)), H_2 (channels (3f) and (4f)) or H and CH (channels (3g) and (4g)). The observation of a CH_2(X) ionization according to the e-KER for no. 6 supports the existence of channels (3c) and/or (4c), as the source for the lower energy (C*) species. An additional contribution to the source of C*(^{1}D) could be a one-photon dissociation of CH*(A) (channel (5k)), which is found to be formed for no. 6 and 7 (see above). It has been shown by calculations[36] and experimentally[37, 38] that high lying Rydberg states of CH (CH**), which could be accessed by one-photon excitation of CH*(A) in the excitation energy region of concern, could be predissociated by a repulsive $^2\Pi$ state to form C*(^{1}D) + H. Thus, for example, CH*(A) could be formed by three-photon dissociation of C_2H_2 (along with CH(X)) followed by one-photon excitation of CH*(A) and predissociation to form C*(^{1}D) (*i.e.* total number of photons in excitation of n = 3) prior to two-(m = 2) photon ionization of C*(^{1}D) (*i.e.* n + m = 5).

V. Summary, conclusions and closing remarks

Data of Mass-Resolved (MR) REMPI (section III, A) and Velocity Map Images (VMI) of photoelectron and ion products following 2-photon resonance excitations of C_2H_2 to seven Rydberg states (VMI-REMPI) (sections III, B and C) (**Table 1**) were recorded and analyzed. The analyses involved determination of relative ion intensities, derivation of electron- and ion KER spectra as well as angular distributions for number of ions formed as a function of the excitation. Threshold energies corresponding to maxima of kinetic energy release for electrons formed in multiphoton ionization as well as fragments formed in multiphoton dissociation processes for various species (both in ground and excited states) and dissociation channels were determined. These were compared systematically with electron- and ion-KER signals / spectral features in our attempt to explore the signals origin. In combination, the analyses revealed multiphoto-fragmentation (photodissociation and/or photoionization) processes relevant to formation of the parent molecular ion ($C_2H_2^+$) (section III, A) and the fragment ions H^+, C^+, CH^+, CH_2^+, C_2^+ and C_2H^+ (section III, D). Whereas, the parent molecular ion formation dominated for the lower energy excitations, the fragment ion formation gradually increases with energy and was found to dominate for the excitation no. 7. The major photodissociation channels observed are summarized schematically in **Fig. 7** and collected in **Table 2**. First, $C_2H_2^+$ is formed by autoionization of superexcited molecules ($C_2H_2^{\#}$) formed by three-photon excitation for all the cases (no. 1 – 7; **Table 1**). This appears to be the major channel for no. 1 – 5. Second, the

Table 2 Fragment ion (Fi^+) formation processes detected.

Fi^+	photofragmentations		photoionizations		
	(nx)[a]	No. excitations[b]	m[c]	Species ionized	No. excitations[b]
H^+	4a	1 - 7	1	H*(n=2)	4,5
C^+	3c,3f	1 - 7	2	C*(low energy) [d]	6,7
C^+	3g	6,7	2	C*(low energy) [d]	6,7
C^+	4c	1 - 5	1	C*(high energy) [d]	6,7
C^+	4f,4g	6,7	1	C*(high energy) [d]	6,7
CH^+	3d,4g	1 - 7	2	CH*(A, B, C)[f]	4 - 7
CH_2^+	2c,3c	1 - 7	3	CH_2(X) [f]	6
C_2^+	3e [e]	1 - 7	2	C_2*(d) [f]	6,7
C_2^+	3b	1 - 7	2	C_2*(C) [f]	1 - 3
C_2H^+	2a,3a	1 - 7	2	C_2H*(B´)[f]	4,5

a. (nx) refers to eqn. in section III, A; n = number of photons in photo-fragmentation; x = letter, a,b,….
b. See **Table 1**
c. m = number of photons in photoionization
d. C*(low energy): C*(^{5}S,^{1}S,^{1}D); C*(high energy): C*(^{3}D,^{1}P,^{3}P)
e. Channel (3e) is favoured over (2b): see section IV, "C_2*/C_2^+"
f. CH*(A, B, C): CH valance states $A^2\Delta$, $B^2\Sigma^-$, $C^2\Sigma^+$; CH_2(X): CH_2 ground state X^2B_1; C_2*(d, C): C_2 Rydberg states $d^2\Pi_g$, $C^2\Pi_g$; C_2H*(B´): C_2H $B\,'^2A_1$

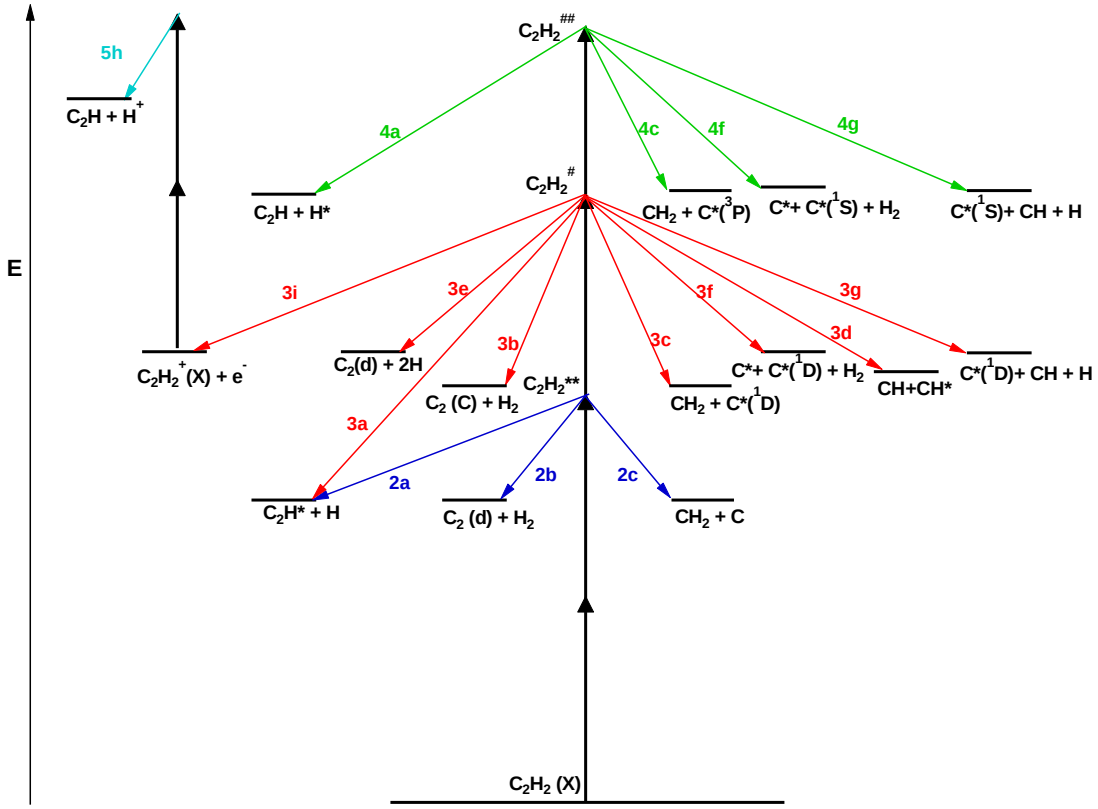

Fig. 7 ***Multiphoto-fragmentation processes:*** *Schematic energy diagram for multiphoton-excitation processes of C_2H_2 according to this work. Vertical black arrows denote photon absorption. Blue, red and green arrows denote fragmentation processes after the two-, three- and four-photon excitations, respectively. The fragmentation processes are marked by number of photons (n) required for the excitation and letters (nx) (see section III, A). C_2H_2(X) C_2H_2**, $C_2H_2^{\#}$ and $C_2H_2^{\#\#}$ are the ground-, Rydberg- and first and second superexcited states, respectively.*

various neutral fragments are formed either in ground or excited states by two-, three- or four-photon dissociation processes via the Rydberg states (C_2H_2**) or superexcited states ($C_2H_2^{\#}$ and $C_2H_2^{\#\#}$), respectively (marked as nx, where n = 2,3,4 / number of photons in the excitations and x = a – g in **Fig. 7** and **Table 2**), prior to photoionization. All in all, the three-photon dissociation processes, via the first superexcited state(s) ($C_2H_2^{\#}$) are found to play the biggest role in the overall multiphoto-fragmentation process. Whereas all the photoexcited molecular states (C_2H_2**, $C_2H_2^{\#}$ and $C_2H_2^{\#\#}$) are found to be involved in the multiphoto-fragmentation its

involvement and importance will vary, depending on the photon density. The first superexcited state(s) ($C_2H_2^{\#}$), being metastable, hence short lived, with respect to both autoionization and dissociation is an important gateway for fragment formations in competition with the molecular autoionization. Further excitation to the second superexcited state(s) ($C_2H_2^{\#\#}$), will compete with these fast fragmentation and autoionization channels and, therefore, largely diminish with decreasing photon density. The resonant excitation to the Rydberg states, to a large extent, acts as an enhancement step for further transitions to the $C_2H_2^{\#}$ state(s). Thus, in combination, it makes sense that the "intermediate" excited state / first superexcited state ($C_2H_2^{\#}$) plays the most important rule as a gateway towards the fragment formations, prior to ionization under our experimental conditions. Thus, for example, a formation of C_2*(d) along with two hydrogen atoms (2H) by three-photon dissociation is found to be favored over two-photon dissociation to form C_2*(d) along with H_2. Overall, the involvement of ionization of electronically excited state fragment species (Fi*) in the multiphoto-fragmentation processes is found to be important (**Table 2**) and the e-KER spectra reveal characteristic vibrational structure for the C_2*(d) ionization indicative of autoionization processes of superexcited $C_2^{\#}$. In addition to the major processes detected and shown in **Fig. 7** and **Table 2** further photofragmentation processes involving secondary photodissociation channels (*i.e.* photodissociation of fragment species (C_2H*(B´) and CH*(A); eqn. (5k)) followed by photoionization processes (eqn. (5x)) are also proposed (see Section IV). Furthermore, the data allowed evaluation relevant to the energetics of the C_2H*(B´) state, which is a subject of an uncertainty in the literature[24-26] (see section IV, "C_2H*(B´)/C_2H^+") and revealed a state interaction in C_2* between C_2*(d,v´= 0) and C_2*(B´,v´= 3)[34, 35] (see section IV, "C_2*(B´,v´= 3)/C_2^+").

The acetylene molecule (C_2H_2), which is the smallest organic molecule in terms of number of atoms, has been observed in interstellar space.[3, 10] The question arises whether it could be an important source of reactive organic intermediate species (radicals and ions) such as those observed in this work, upon UV radiation in space. Thus, it could act as a source of important building blocks for further creation of bigger organic molecules formed by radical and/or ion reactions either on surfaces or in space. The triple bond of the molecule is an underlying reason for large number of possible transitions by photoexcitation of the π valence electrons to Rydberg orbitals, hence formation of Rydberg states. These belong to Rydberg series which either converge to the ground ionic state (*i.e.* C_2H_2**) or excited ionic states (*i.e.* superexcited states $C_2H_2^{\#}$), latter of which are found to be important gateways for radical and excited state fragment formations. Thus, it can be argued that the "unsaturated nature" of acetylene makes it particularly suitable for formation of small organic radicals and ion species upon UV radiation corresponding to excitation to superexcited Rydberg states beyond its ionization limit (11.4 eV), corresponding to $\lambda < 109$ nm, one-photon excitation. Whereas our excitation scheme involves three-photon excitation of C_2H_2 to $C_2H_2^{\#}$ via C_2H_2** rather than one-photon excitation directly to $C_2H_2^{\#}$ the dominant selection rule of $g \leftrightarrow u$ per photon excitation (hence $g \leftrightarrow u$ for three- and odd number-photon excitations) for C_2H_2, ensures similarity for both one- and three-photon excitations to the superexcited state(s) ($C_2H_2^{\#}$) region. We, therefore, feel that our observations are of important relevance to understanding one-photon UV excitation of acetylene as well as for (multi)photo-fragmentation processes in molecules in general.

Conflict of interest. There are no conflicts to declare.

Acknowledgements

The financial support of the University Research Fund, University of Iceland and the Icelandic Research Fund (Grant No. 184693-053) is gratefully acknowledged. Aðalsteinn Kristjánsson's memorial fund for the promotion of natural sciences and chemistry is also acknowledged. The imaging part of the reported results was carried out at the Ultraviolet Laser Facility at IESL-FORTH, supported in part by the European Union's Horizon 2020 Research and Innovation Programme LASERLAB-EUROPE (Grant Agreement No. 871124)

References:

1. H. Okabe, *Can. J. Chem.*, 1983, **61**, 850-855.
2. M. S. Child, R. W. Field, D. Gauyacq, J. K. G. Watson, N. Shafizadeh, J.-H. Fillion, D. Gauyacq and S. Couris, *Philos. Trans. R. Soc. A*, 1997, **355**, 1637-1658.
3. J. H. Lacy, N. J. Evans, II, J. M. Achtermann, D. E. Bruce, J. F. Arens and J. S. Carr, *Astrophys. J*, 1989, **342**, L43.
4. T. Q. Zhao, Q. Li, B. S. Liu, R. K. E. Gover, P. J. Sarre and A. S. C. Cheung, *Phys. Chem. Chem. Phys.*, 2016, **18**, 3489-3496.
5. V. V. Voronin, M. S. Ledovskaya, A. S. Bogachenkov, K. S. Rodygin and V. P. Ananikov, *Molecules (Basel, Switzerland)*, 2018, **23**.
6. K. Tsuji, N. Arakawa, A. Kawai and K. Shibuya, *J. Phys. Chem. A*, 2002, **106**, 747-753.
7. Y. C. Hsu, M. S. Lin and C. P. Hsu, *J. Chem. Phys.*, 1991, **94**, 7832-7841.
8. M. N. R. Ashfold, B. Tutcher, B. Yang, Z. K. Jin and S. L. Anderson, *J. Chem. Phys.*, 1987, **87**, 5105-5115.
9. K. Matthíasson, H. Wang and Á. Kvaran, *Chem.Phys. L*, 2008, **458**, 58-63.
10. S. T. Ridgway, D. N. B. Hall, S. G. Kleinmann, D. A. Weinberger and R. S. Wojslaw, *Nature*, 1976, **264**, 345-346.
11. M. Frenklach and E. D. Feigelson, *Astrophys. J*, 1989, **341**, 372.
12. D. Zaouris, A. Kartakoullis, P. Glodic, P. C. Samartzis, H. Rafn Hróðmarsson and Á. Kvaran, *Phys. Chem. Chem. Phys.*, 2015, **17**, 10468-10477.
13. P. Glodic, D. Zaouris, P. C. Samartzis, A. Hafliðason and Á. Kvaran, *Phys. Chem. Chem. Phys.*, 2016, **18**, 26291-26299.

14. H. R. Hróðmarsson, A. Kartakoullis, D. Zaouris, P. Glodic, H. Wang, P. C. Samartzis and Á. Kvaran, *Phys. Chem. Chem. Phys.*, 2017, **19**, 11354-11365.
15. A. Hafliðason, P. Glodic, G. Koumarianou, P. C. Samartzis and Á. Kvaran, *Phys. Chem. Chem. Phys.*, 2018, **20**, 17423-17433.
16. A. Hafliðason, P. Glodic, G. Koumarianou, P. C. Samartzis and Á. Kvaran, *Phys. Chem. Chem. Phys.*, 2019, **21**, 10391-10401.
17. K. Matthíasson, G. Koumarianou, M.-X. Jiang, P. Glodic, P. C. Samartzis and Á. Kvaran, *Phys. Chem. Chem. Phys.*, 2020, **22**, 4984-4992.
18. J. Long, H. Wang and Á. Kvaran, *J. Chem. Phys.*, 2013, **138**, 044308.
19. J. Long, H. R. Hróðmarsson, H. Wang and Á. Kvaran, *J. Chem. Phys.*, 2013, **138**, 044308.
20. . Wang, M.L. Lipciuc, X. Yang, T. N. Kitsopoulos, *Phys. Chem. Chem. Phys.*, 2009, **11**, 2234-2240.
21. C. R. Gebhardt, T. P. Rakitzis, P. C. Samartzis, V. Ladopoulos and T. N. Kitsopoulos, *Rev. Sci. Instrum.*, 2001, **72**, 3848-3853.
22. V. Papadakis and T. N. Kitsopoulos, *Rev. Sci. Instrum.*, 2006, **77**, 083101.
23. K. Malsch, R. Rebentisch, P. Swiderek and G. Hohlneicher, *Theor. Chem. Acc.*, 1998, **100**, 171-182.
24. *See ESI*.
25. NIST Chemistry WebBook - (National Institute of Standards and Technology) https://webbook.nist.gov/chemistry/name-ser/,
26. K. W. Chang and W. R. M. Graham, *J. Chem. Phys.*, 1982, **76**, 5238-5244.
27. M. Suto and L. C. Lee, *J. Chem. Phys.*, 1984, **80**, 4824-4831.
28. S. Boyé, A. Campos, S. Douin, C. Fellows, D. Gauyacq, N. Shafizadeh, P. Halvick and M. oggio-Pasqua, *J. Chem. Phys.*, 2002, **116**, 8843-8855.
29. D. H. Mordaunt and M. N. R. Ashfold, *J. Chem. Phys.*, 1994, **101**, 2630-2631.
30. J. C. Han, C. Ye, M. Suto and L. C. Lee, *J. Chem. Phys.*, 1989, **90**, 4000-4007.
31. J. Jiang, A. K. Muthike, T. J. Erickson and R. W. Field, *J. Mol. Spectrosc.*, 2019, **361**, 24-33.
32. T. A. Cool and P. M. Goodwin, *J. Chem. Phys.*, 1991, **94**, 6978-6988.
33. D. Duflot, J. M. Robbe and J. P. Flament, *J. Chem. Phys.*, 1994, **100**, 1236-1246.
34. M. Martin, *J. Photochem. Photobiol. A*, 1992, **66**, 263-289.
35. J. F. Babb, R. T. Smyth and B. M. McLaughlin, *Astrophys. J*, 2019, **876**, 38.
36. G. J. Vázquez, J. M. Amero, H. P. Liebermann, R. J. Buenker and H. Lefebvre-Brion, *J. Chem. Phys.*, 2007, **126**, 164302.
37. A. Hafliðason, H. Wang and Á. Kvaran, *Phys. Chem. Chem. Phys.*, 2016, **18**, 1797-1806.
38. J. Long, H. Wang and Á. Kvaran, *J. Phys. Chem. A*, 2014, **118**, 182.

4.6.1 Supporting information

Multiphoton breakdown of acetylene; Formation of organic building block fragments

Meng-Xu Jiang[1], Ioannis Giannakidis[2], Peter C. Samartzis[2]* and Ágúst Kvaran[1]*

1. *Science Institute, University of Iceland, Dunhagi 3, 107 Reykjavík, Iceland.*
2. *Institute of Electronic Structure and Laser, Foundation for Research and Technology-Hellas, Vassilika Vouton, 71110 Heraklion, Greece.*

Supplementary material

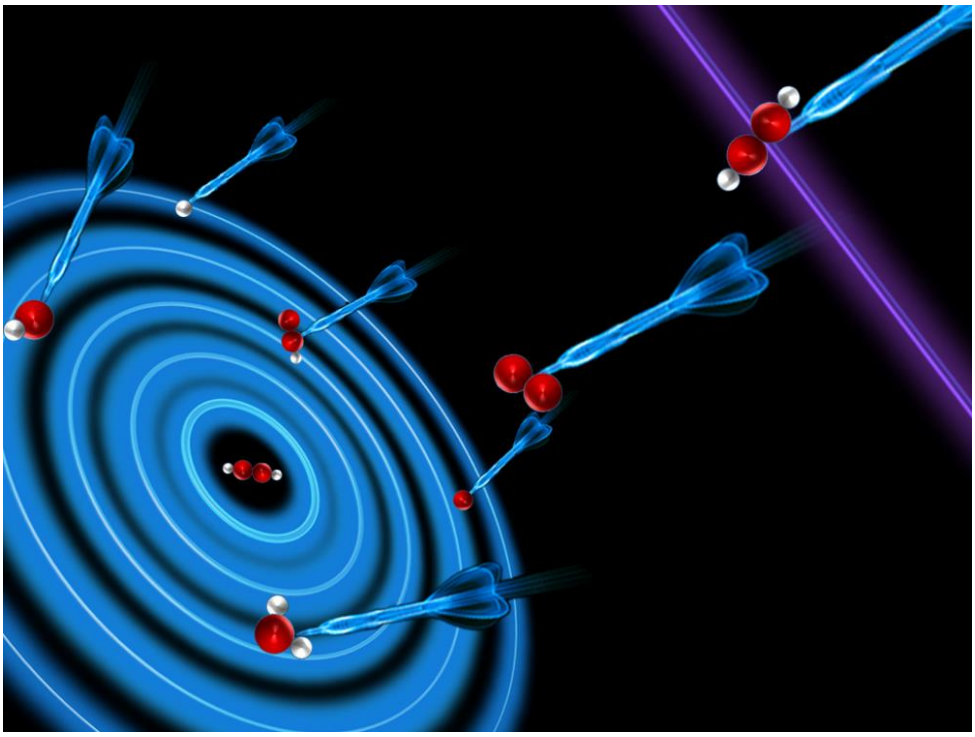

Content: pages:

Figures:

Content: **pages:**

Tables:

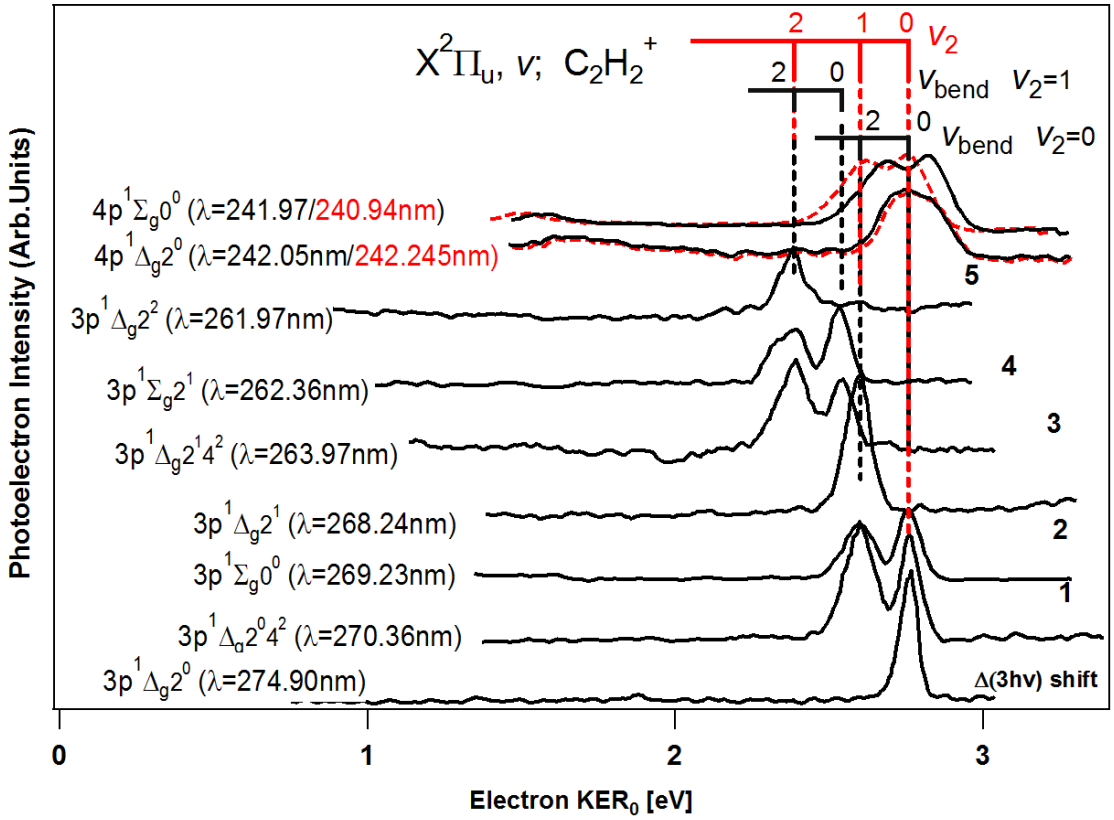

Fig. S1, Photoelectron spectra: Photoelectron spectra extracted from reference **[1]** (black) and from reference **[2]** (red) plotted as a function of the kinetic energy release (KER) for the spectrum derived by the λ = 261.97 nm excitation ("reference spectrum") shifted by three- photon energy differences, (Δ(3*hv*)) with respect to the "reference spectrum" (see main text / paper). Rydberg states and excitation wavelengths are indicated to the left. KER thresholds / assignments for ionization of fragments, according to reference **[1]** are indicated by sticks above the spectra.

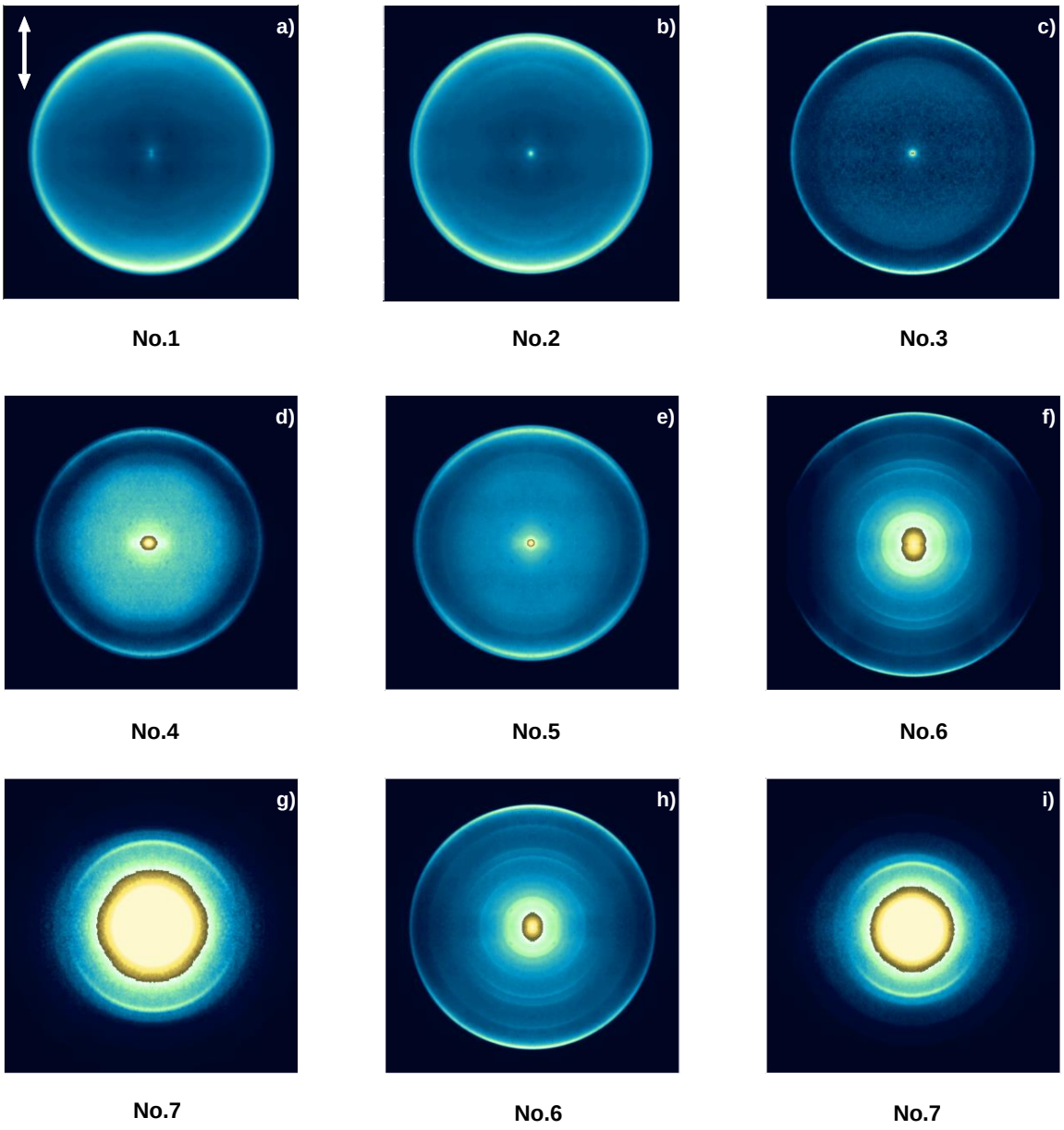

Fig. S2, photoelectron images: Photoelectron images for the excitations (no. 1 – 7) listed in **Table S1** (**Table 1** in paper). Images (a)-(g) and (h)-(i) were recorded for repeller voltages of -3kV and -5kV, respectively. The laser polarization is indicated by a double arrow in (a).

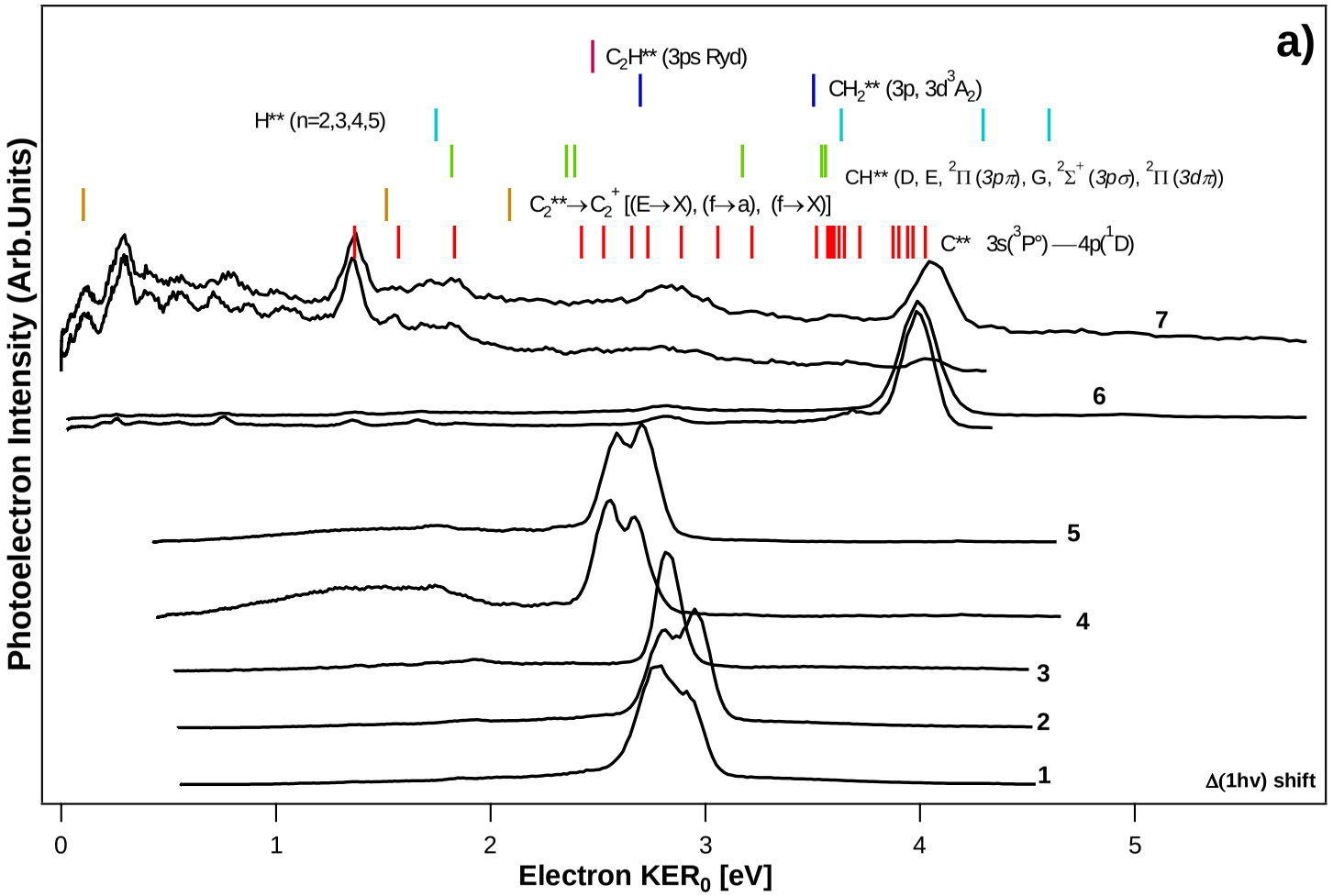

Fig. S3 (a), Electron KERs and energy thresholds: e-KERs derived from images no. 1 – 7 (**Table S1**) plotted as a function of the kinetic energy release (KER) for the no. 7 (KER_0), shifted by one-photon energy differences, ($\Delta(1h\nu)$) with respect to the "reference spectrum", no. 7 (see main text). KER thresholds for ionization of fragments, as specified, are indicated by sticks above the spectra.

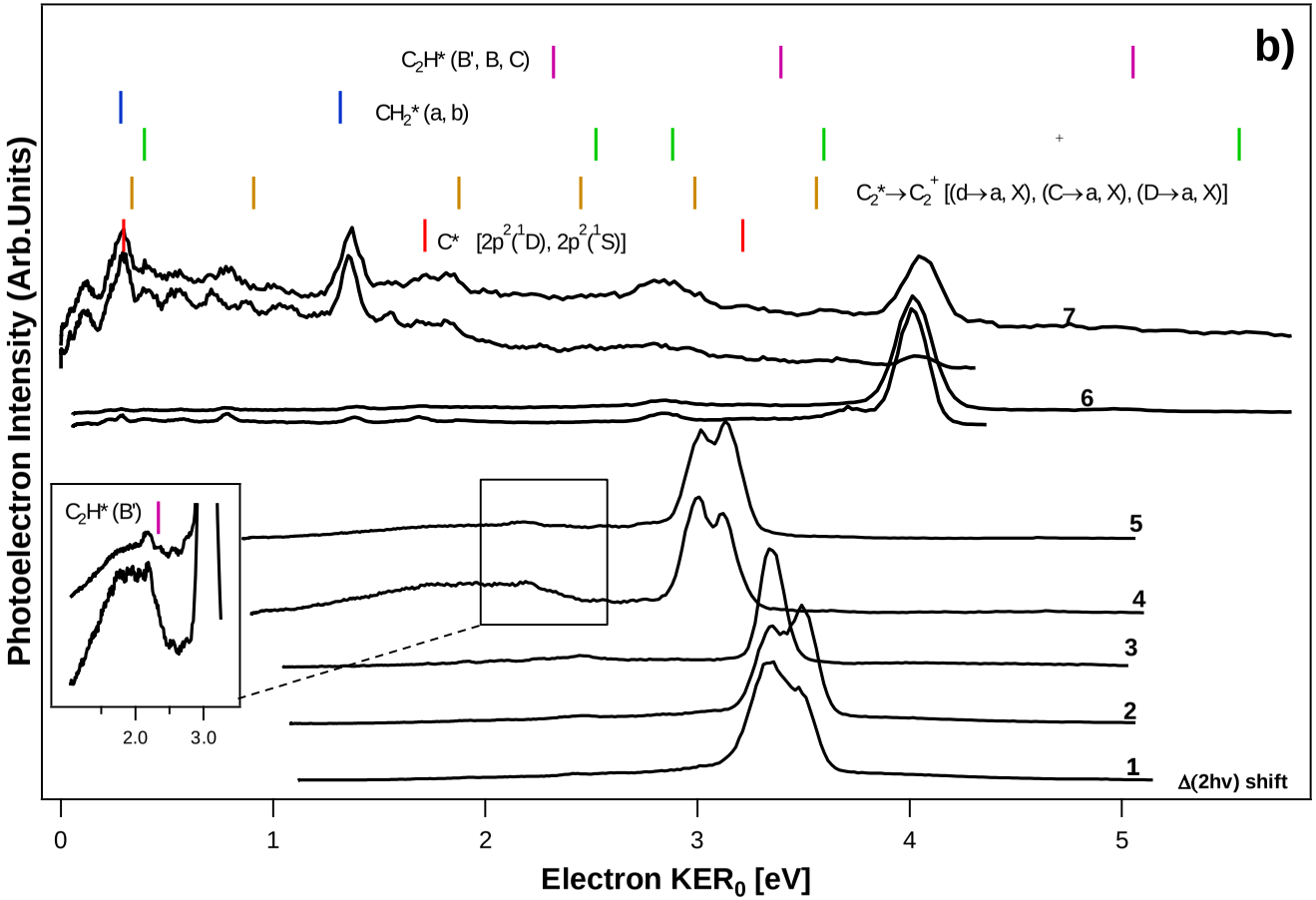

Fig. S3 (b), Electron KERs and energy thresholds: e-KERs derived from images no. 1 – 7 (**Table S1**) plotted as a function of the kinetic energy release (KER) for the no. 7 (KER_0), shifted by two-photon energy differences, ($\Delta(2h\nu)$) with respect to the "reference spectrum", no. 7 (see main text). KER thresholds for ionization of fragments, as specified, are indicated by sticks above the spectra.

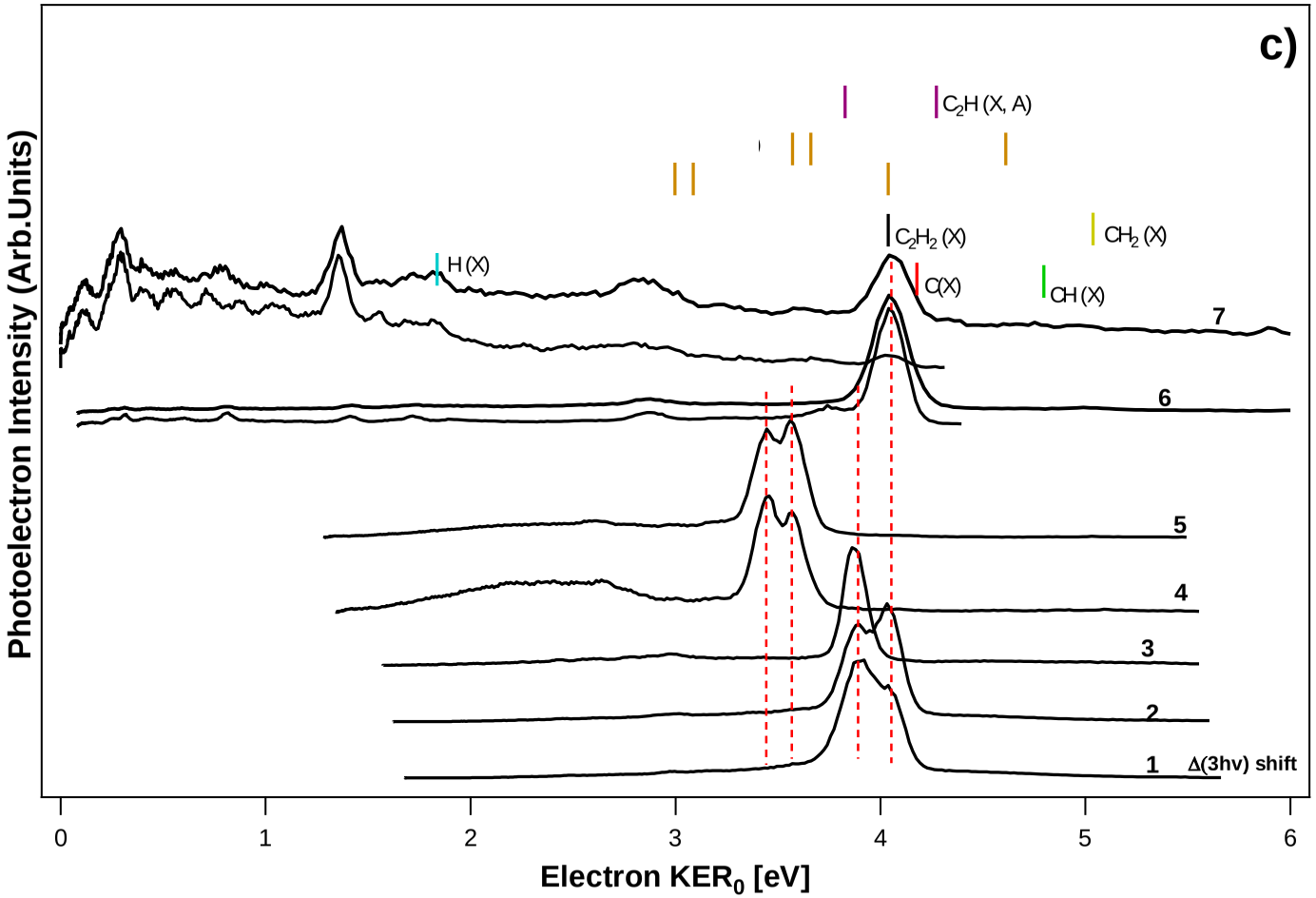

Fig. S3 (c), Electron KERs and energy thresholds: e-KERs derived from images no. 1 – 7 (**Table S1**) plotted as a function of the kinetic energy release (KER) for the no. 7 (KER_0), shifted by three-photon energy differences, ($\Delta(3h\nu)$) with respect to the "reference spectrum", no. 7 (see main text). KER thresholds for ionization of fragments, as specified, are indicated by sticks above the spectra.

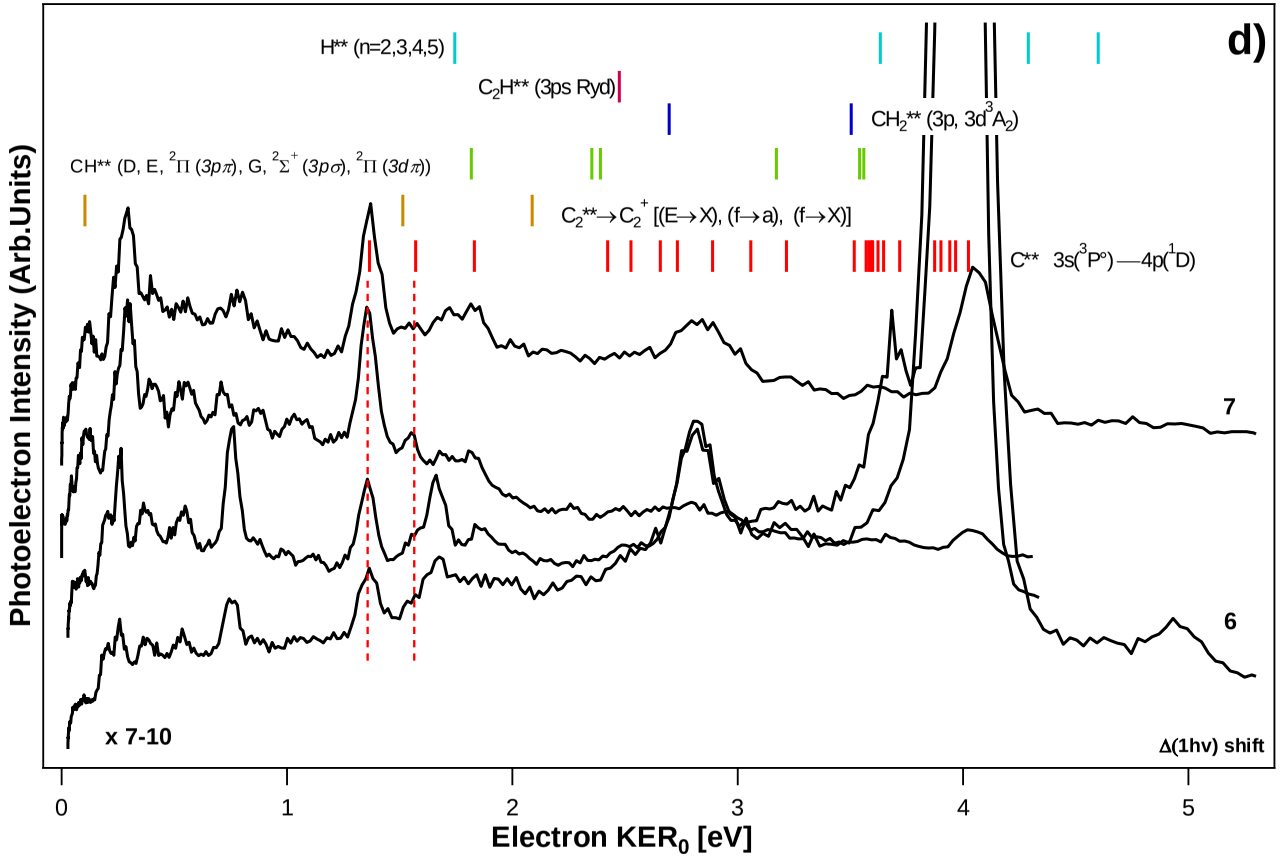

Fig. S3 (d), Electron KERs and energy thresholds: e-KERs derived from images no. 6-7 (**Table S1**) plotted as a function of the kinetic energy release (KER) for the no. 7 (KER_0), shifted by one-photon energy differences, ($\Delta(1h\nu)$) with respect to the "reference spectrum", no. 7 (see main text). KER thresholds for ionization of fragments, as specified, are indicated by sticks above the spectra. The spectrum for no.6 is magnified by factors 7-10.

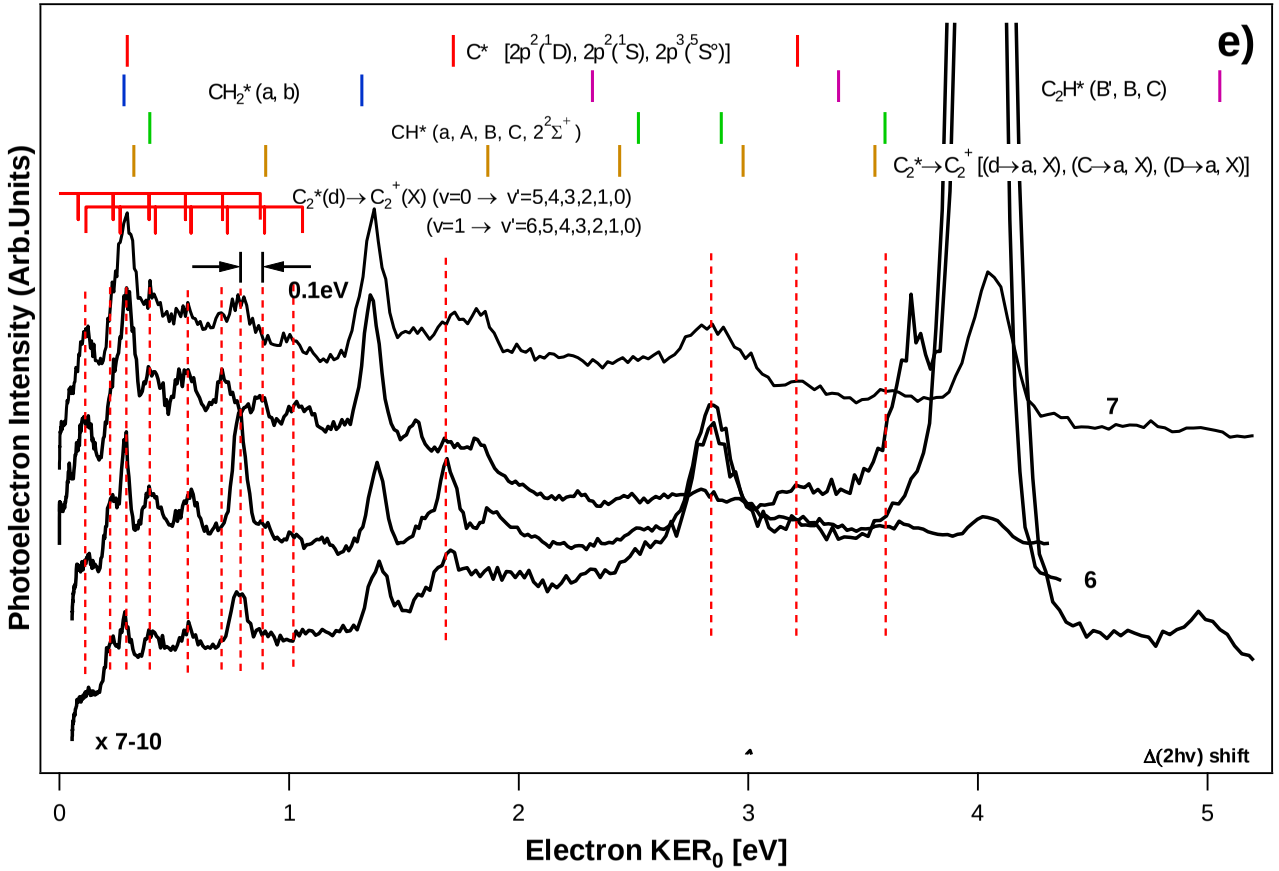

Fig. S3 (e), Electron KERs and energy thresholds: e-KERs derived from images no. 6-7 (**Table S1**) plotted as a function of the kinetic energy release (KER) for the no. 7 (KER_0), shifted by two-photon energy differences, ($\Delta(2h\nu)$) with respect to the "reference spectrum", no. 7 (see main text). KER thresholds for ionization of fragments, as specified, are indicated by sticks above the spectra. The spectrum for no.6 is magnified by factors 7-10.

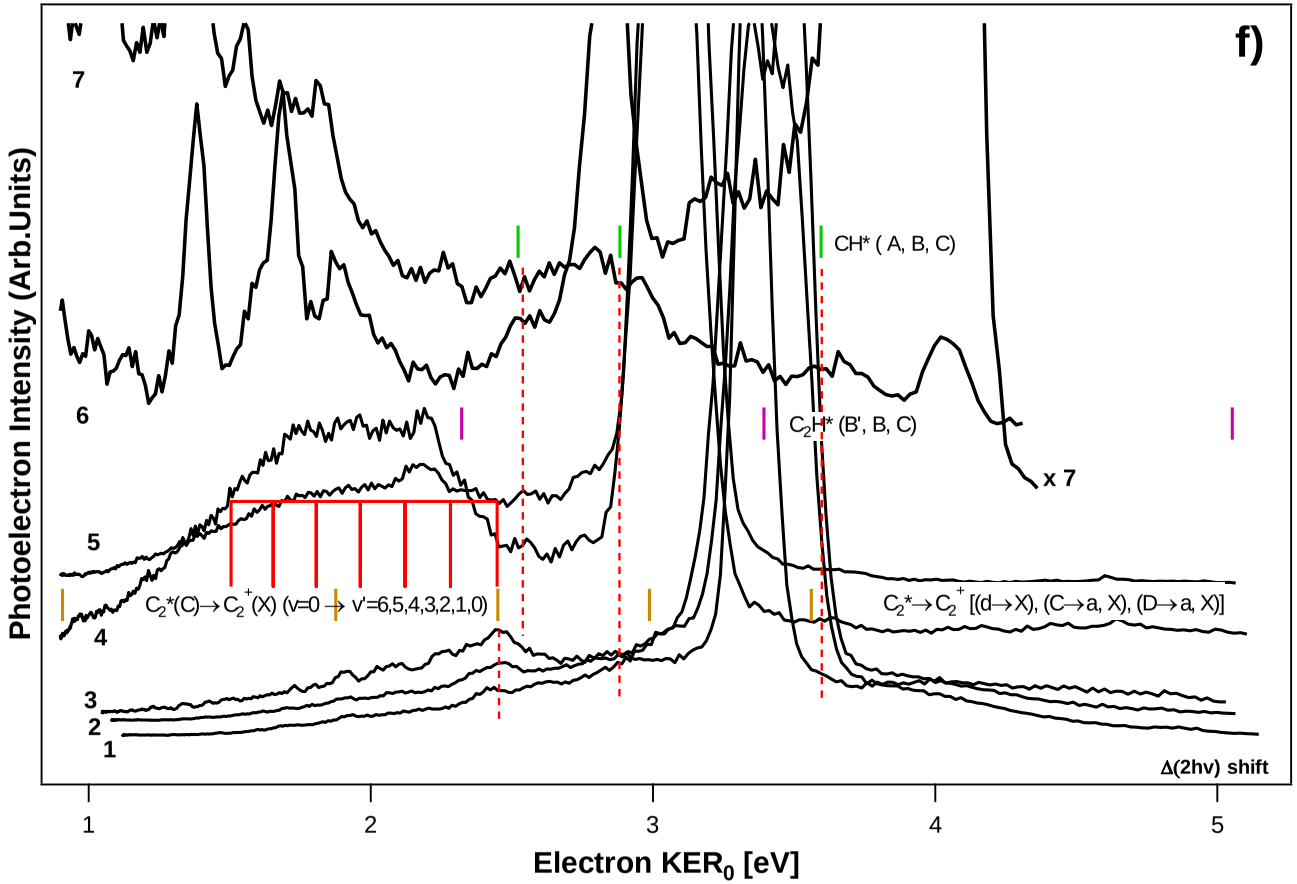

Fig. S3 (f), Electron KERs and energy thresholds: e-KERs derived from images no. 1-7 (**Table S1**) plotted as a function of the kinetic energy release (KER) for the no. 7 (KER_0), shifted by two-photon energy differences, ($\Delta(2h\nu)$) with respect to the "reference spectrum", no. 7 (see main text). KER thresholds for ionization of fragments, as specified, are indicated by sticks. The spectrum for no.1-5 is magnified.

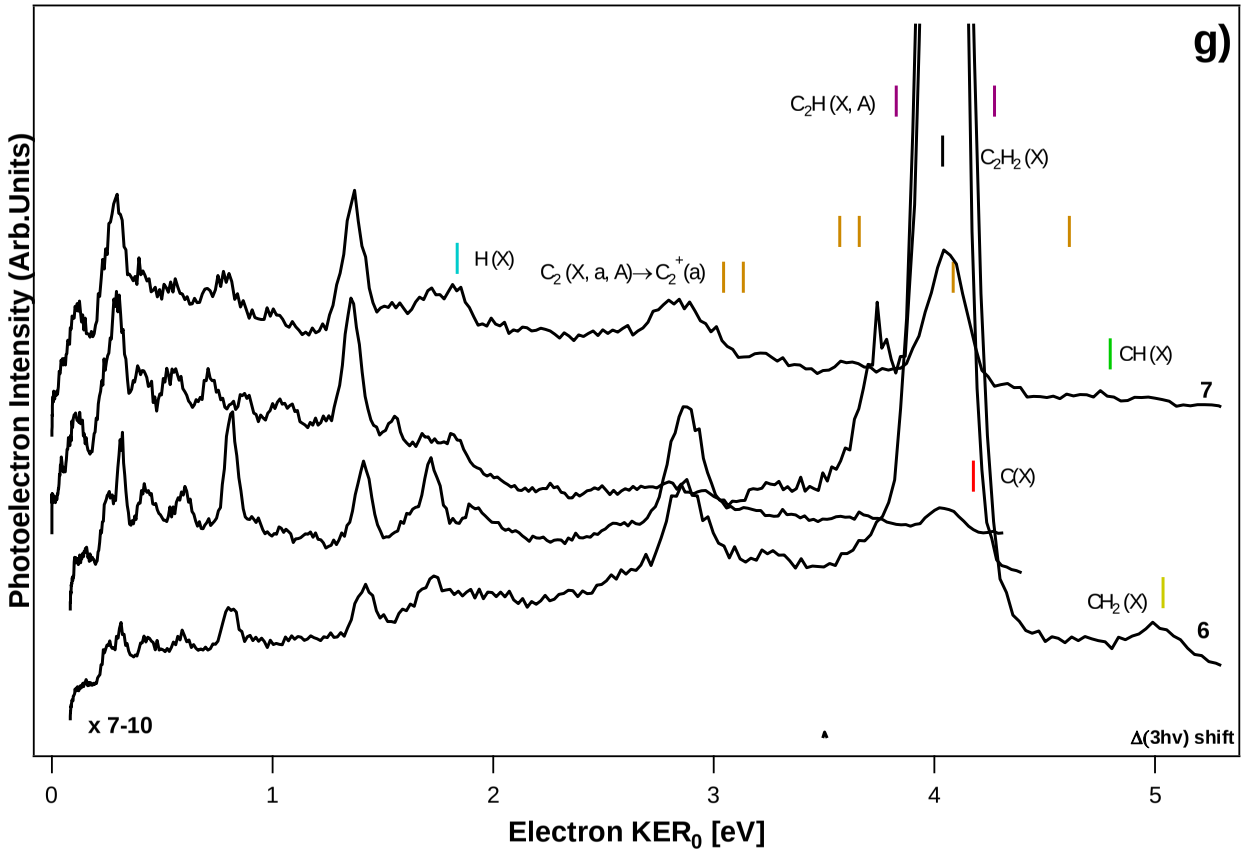

Fig. S3 (g), Electron KERs and energy thresholds: e-KERs derived from images no. 6-7 (**Table S1**) plotted as a function of the kinetic energy release (KER) for the no. 7 (KER_0), shifted by three-photon energy differences, ($\Delta(3h\nu)$) with respect to the "reference spectrum", no. 7 (see main text). KER thresholds for ionization of fragments, as specified, are indicated by sticks. The spectrum for no.6 is magnified as indicated.

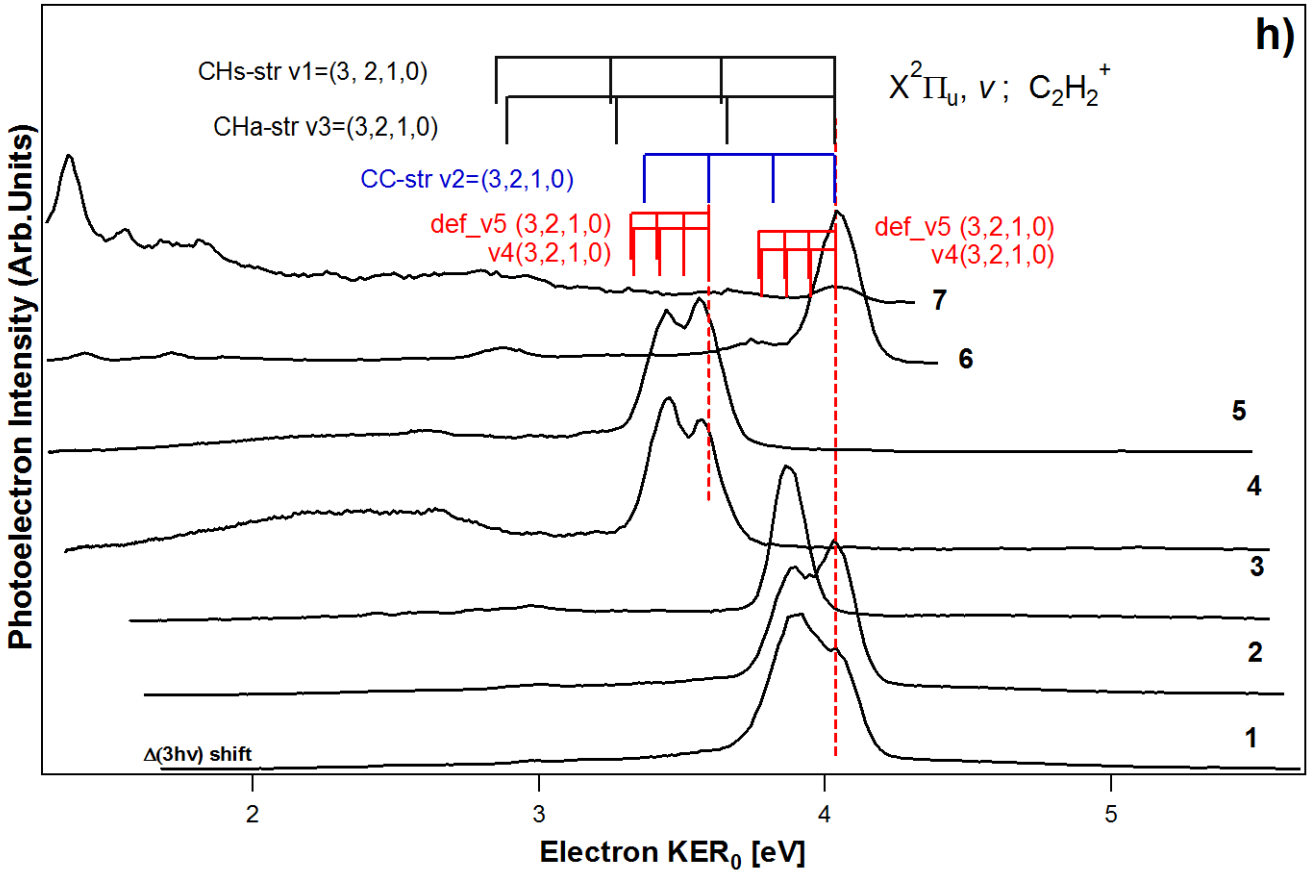

Fig. S3 (h), Electron KERs and energy thresholds: e-KERs derived from images no. 1-7 (**Table S1**) plotted as a function of the kinetic energy release (KER) for the no. 7 (KER_0), shifted by three-photon energy differences, ($\Delta(3h\nu)$) with respect to the "reference spectrum", no. 7 (see main text). KER thresholds for autoionization of superexcited C_2H_2, ($C_2H_2^{\#}$), as specified, are indicated by sticks above the spectra.

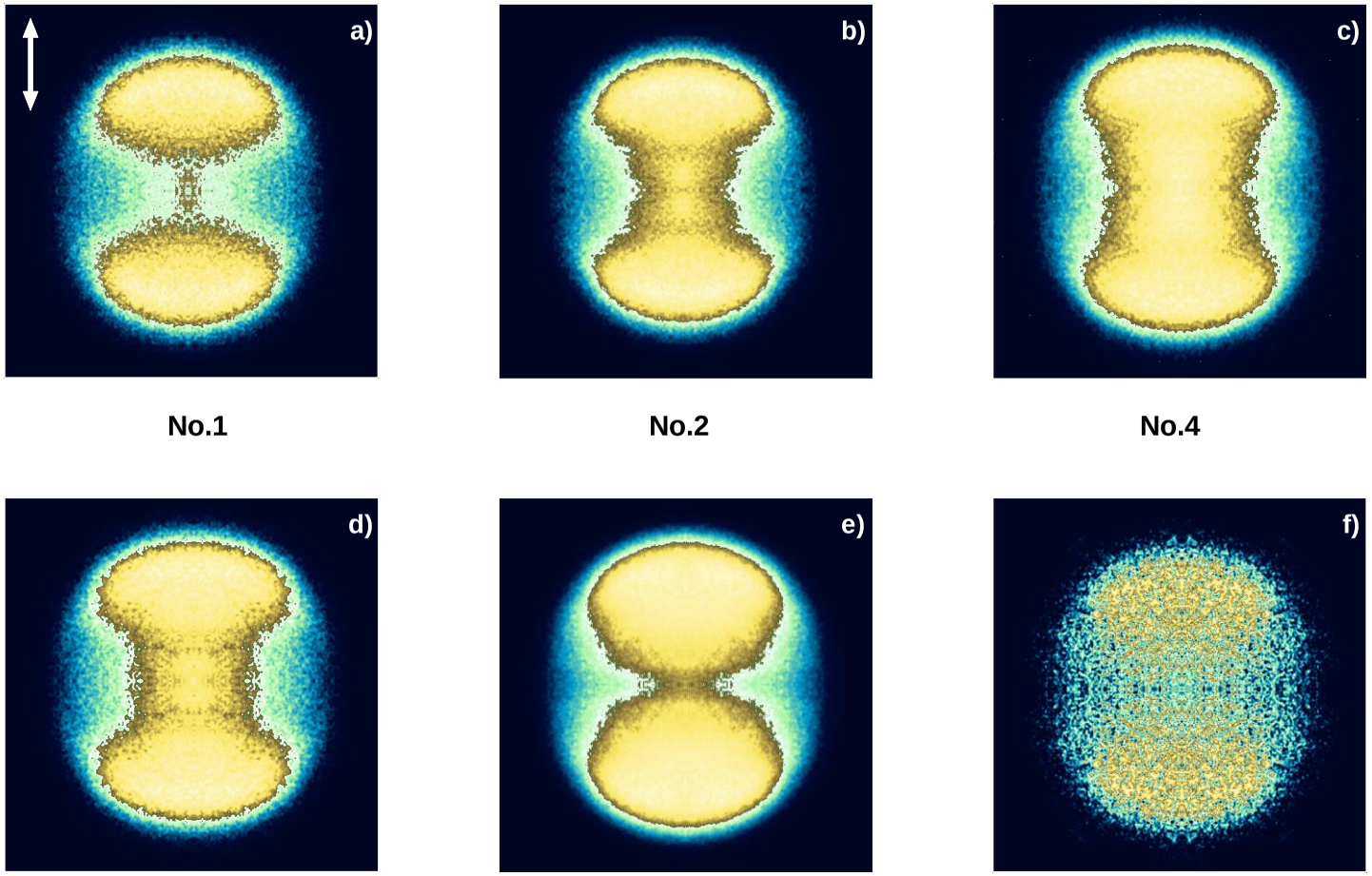

Fig. S4, H^+ ion images: Images recorded for the excitation no.1-2 and 4-7 as specified in **Table S1**. The laser polarization is indicated by a double arrow in (a).

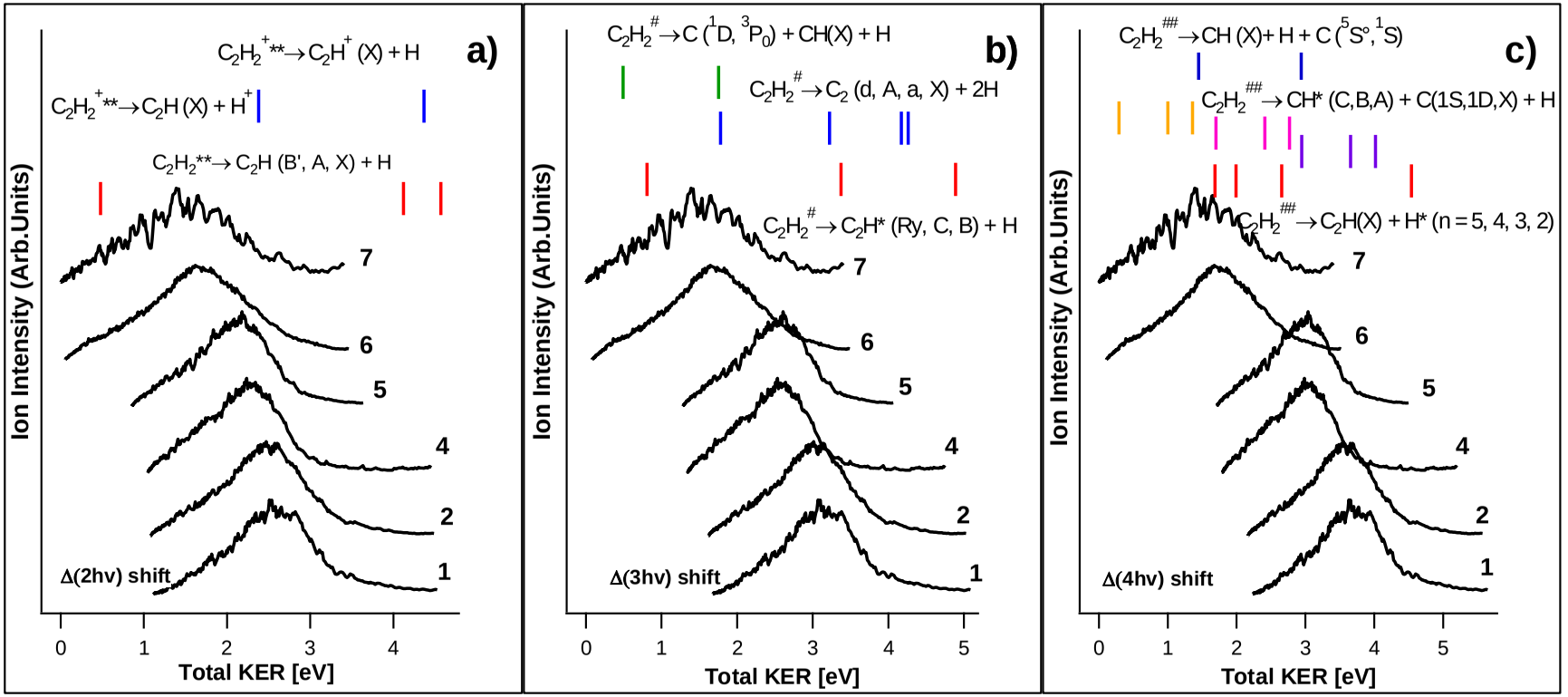

Fig. S5, H^+ kinetic energy release spectra (KERs): Ion kinetic energy release spectra (Ion-KERs) derived from the images no.1,2,4 - 7 (see **Table S1**). The spectra are plotted as a function of the total kinetic energy release for the no. 7 (Total KER_0) and shifted by n-photon energy differences (Δ(n*hν*)) with respect to the "reference spectrum", no. 7 (see main text) as, Δ(*2hν*) (a), Δ(*3hν*) (b) and Δ(*4hν*) (c). KER thresholds for fragment formations by n-photo-dissociation (n = 2, 3 and 4 for photodissociation or autoionization via the C_2H_2**, $C_2H_2^{\#}$ and $C_2H_2^{\#\#}$ intermediate species; see main text), as specified, are indicated by sticks above the spectra.

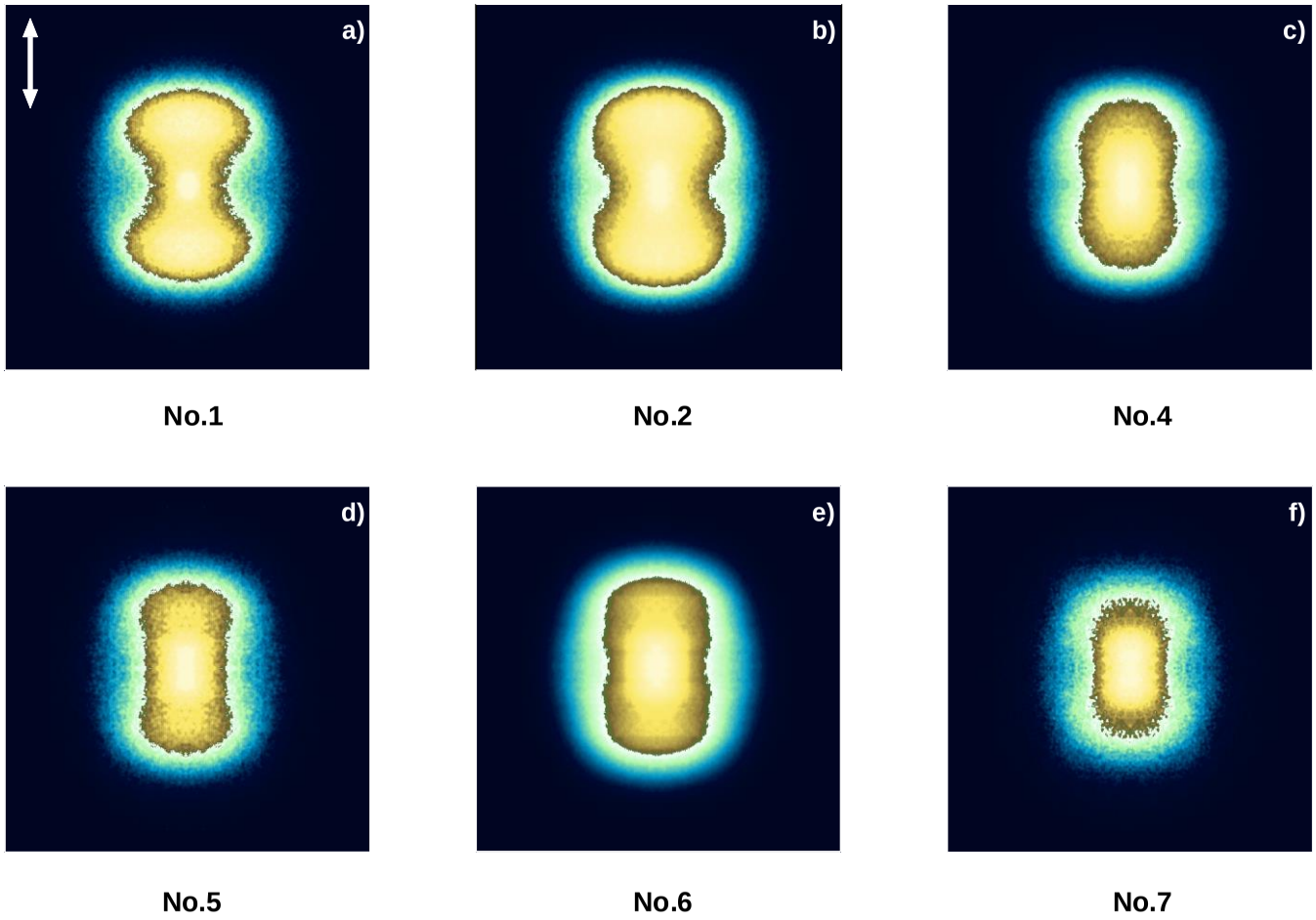

Fig. S6, C^+ ion images: Images recorded for the excitation no.1-2 and 4-7 as specified in **Table S1**. The laser polarization is indicated by a double arrow in (a).

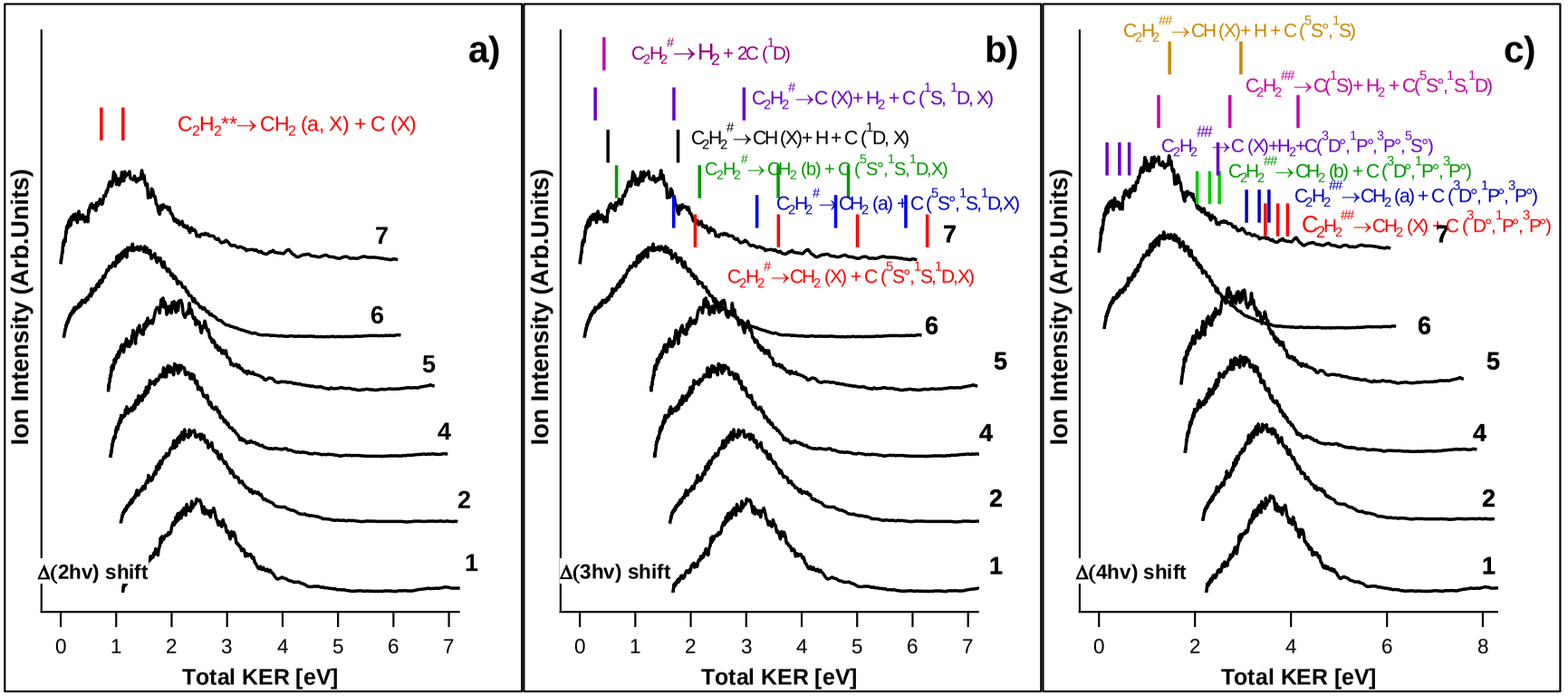

Fig. S7, C^+ kinetic energy release spectra (KERs): Ion kinetic energy release spectra (Ion-KERs) derived from the images no.1,2,4 - 7 (see **Table S1**). The spectra are plotted as a function of the total kinetic energy release for the no. 7 (Total KER_0) and shifted by n-photon energy differences ($\Delta(nhv)$) with respect to the "reference spectrum", no. 7 (see main text) as, $\Delta(2hv)$ (a), $\Delta(3hv)$ (b) and $\Delta(4hv)$ (c). KER thresholds for fragment formations by n-photo-dissociation (n = 2, 3 and 4 for photodissociation via the C_2H_2**, $C_2H_2^{\#}$ and $C_2H_2^{\#\#}$ intermediate species; see main text), as specified, are indicated by sticks above the spectra.

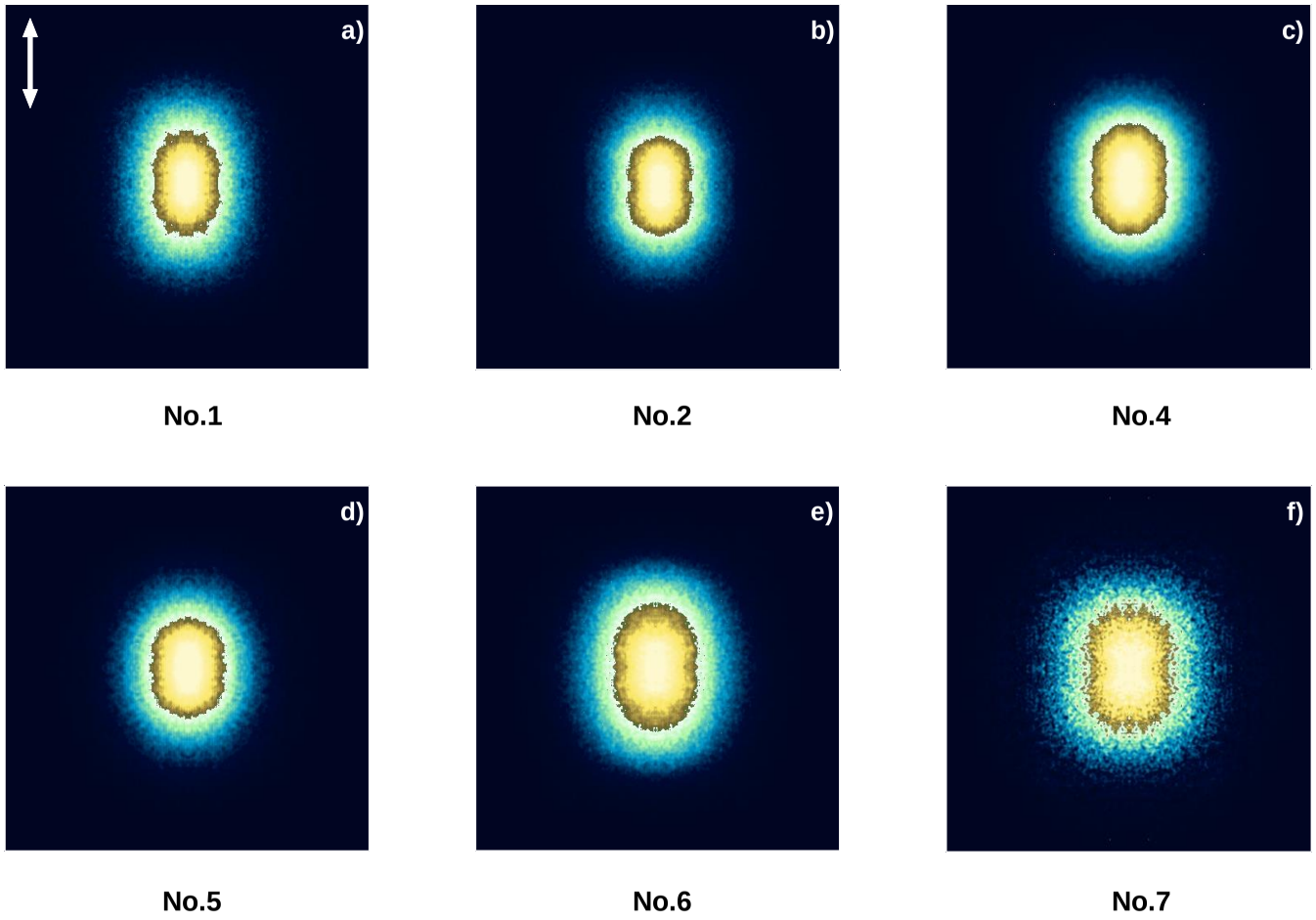

Fig. S8, CH^+ ion images: Images recorded for the excitation no.1-2 and 4-7 as specified in **Table S1**. The laser polarization is indicated by a double arrow in (a).

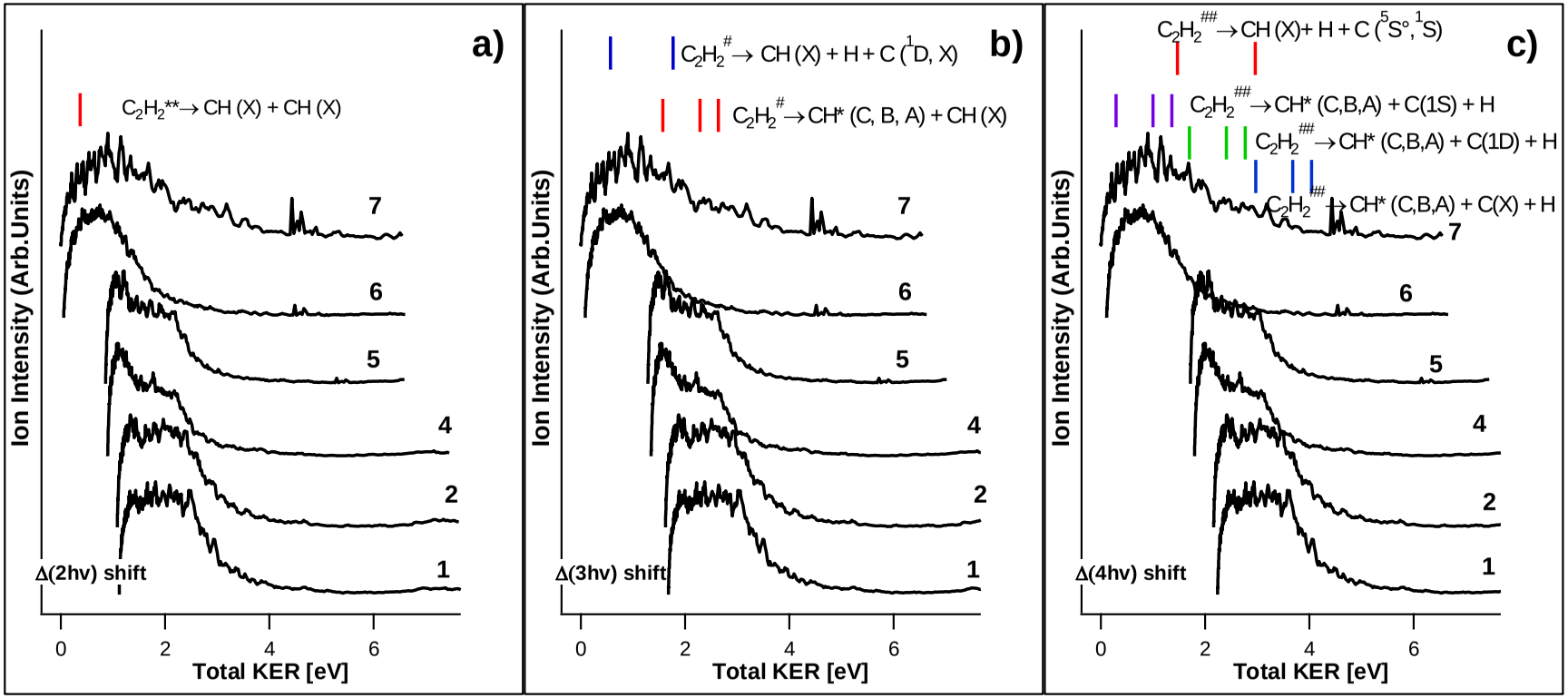

Fig. S9, CH^+ kinetic energy release spectra (KERs): Ion kinetic energy release spectra (Ion-KERs) derived from the images no.1,2,4 -7 (see **Table S1**). The spectra are plotted as a function of the total kinetic energy release for the no. 7 (Total KER_0) and shifted by n-photon energy differences ($\Delta(n\mathit{hv})$) with respect to the "reference spectrum", no. 7 (see main text) as, $\Delta(\mathit{2hv})$ (a), $\Delta(\mathit{3hv})$ (b) and $\Delta(\mathit{4hv})$ (c). KER thresholds for fragment formations by n-photo-dissociation (n = 2, 3 and 4 for photodissociation via the C_2H_2**, $C_2H_2^{\#}$ and $C_2H_2^{\#\#}$ intermediate species; see main text), as specified, are indicated by sticks above the spectra.

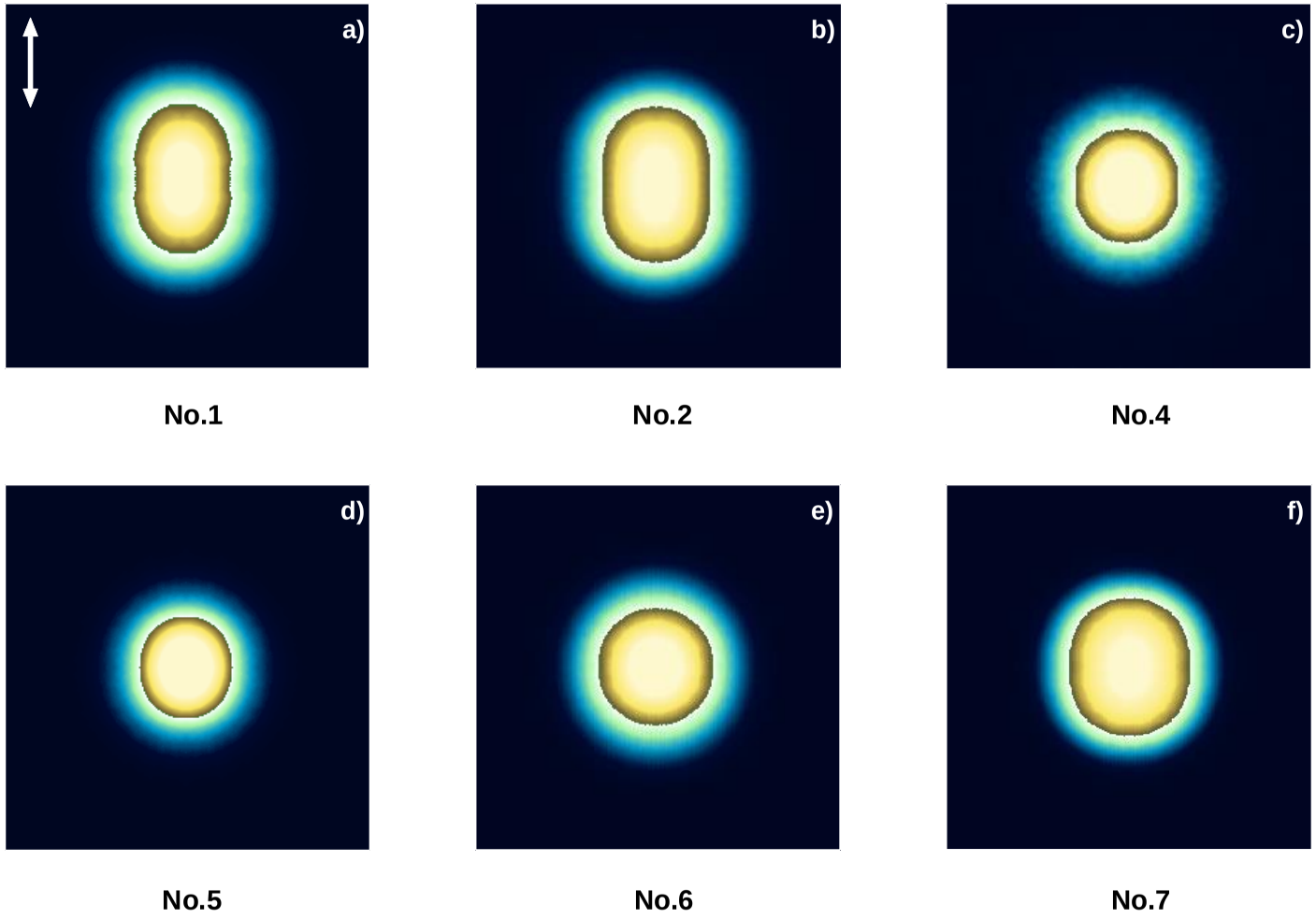

Fig. S10, C_2^+ ion images: Images recorded for the excitation no.1-2 and 4-7 as specified in **Table S1**. The laser polarization is indicated by a double arrow in (a).

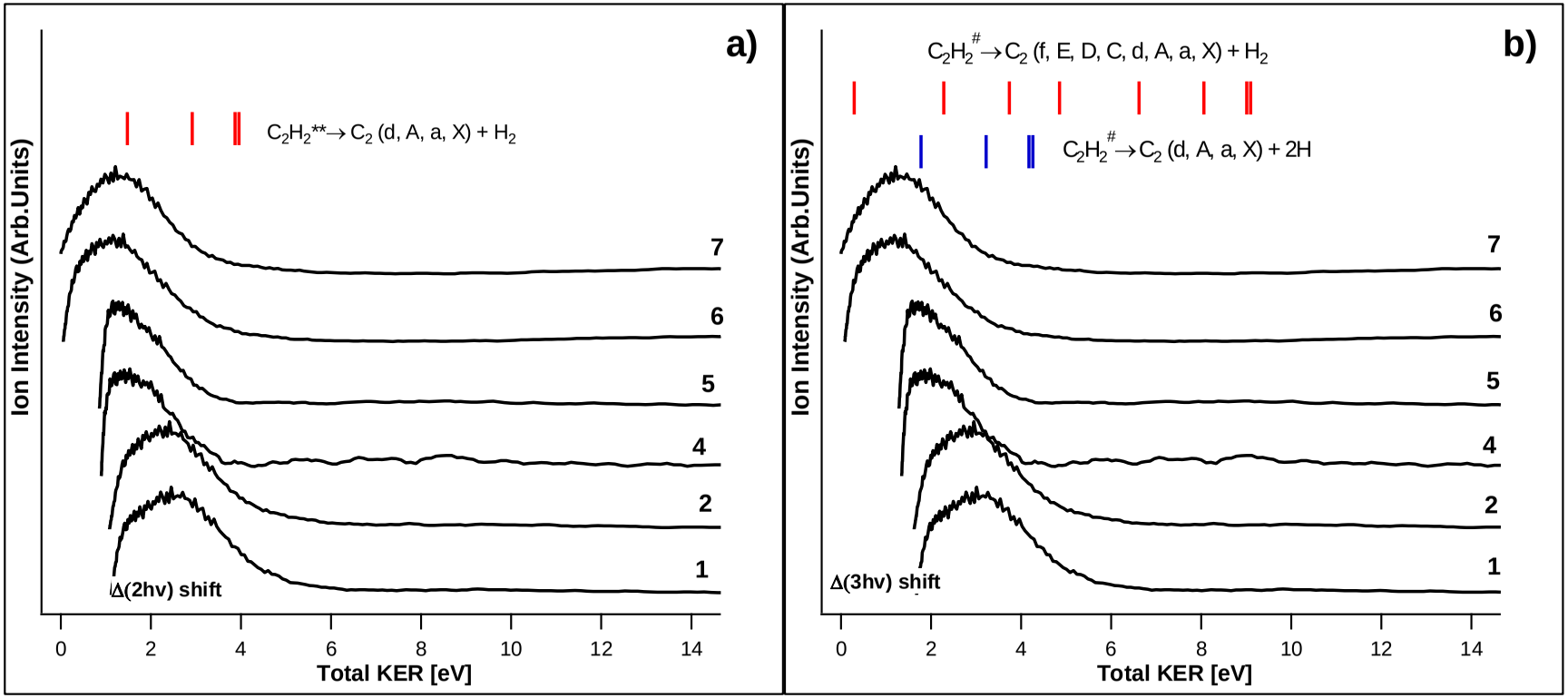

Fig. S11, C_2^+ kinetic energy release spectra (KERs): Ion kinetic energy release spectra (Ion-KERs) derived from the images no.1,2,4 -7 (see **Table S1**). The spectra are plotted as a function of the total kinetic energy release for the no. 7 (Total KER_0) and shifted by n-photon energy differences ($\Delta(n\mathit{hv})$) with respect to the "reference spectrum", no. 7 (see main text) as, $\Delta(\mathit{2hv})$ (a) and $\Delta(\mathit{3hv})$ (b). KER thresholds for fragment formations by n-photo-dissociation (n = 2 and 3 for photodissociation via the $C_2H_2^{**}$ and $C_2H_2^{\#}$ intermediate species; see main text), as specified, are indicated by sticks above the spectra.

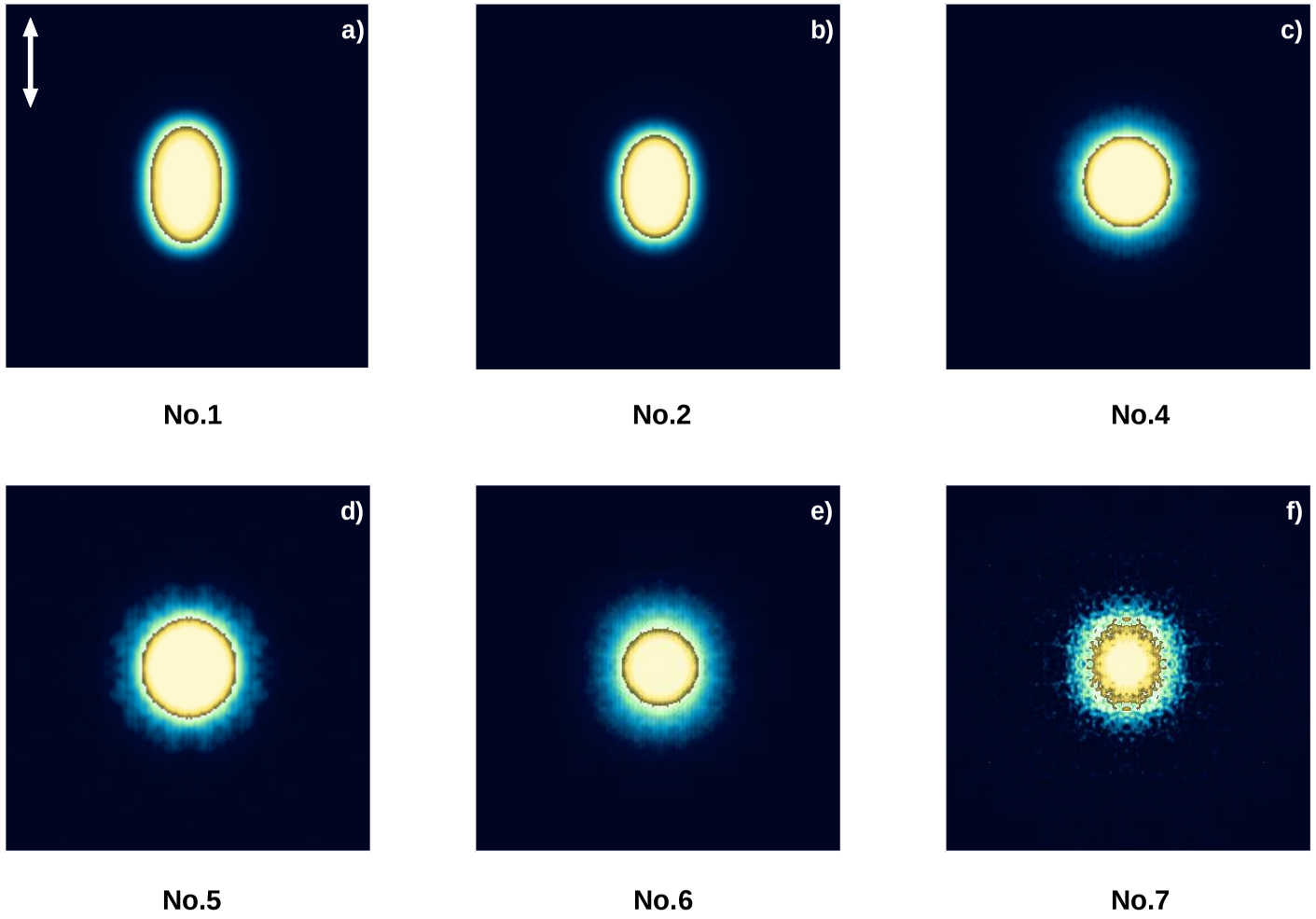

Fig. S12, C_2H^+ ion images: Images recorded for the excitation no.1-2 and 4-7 as specified in **Table S1**. The laser polarization is indicated by a double arrow in (a).

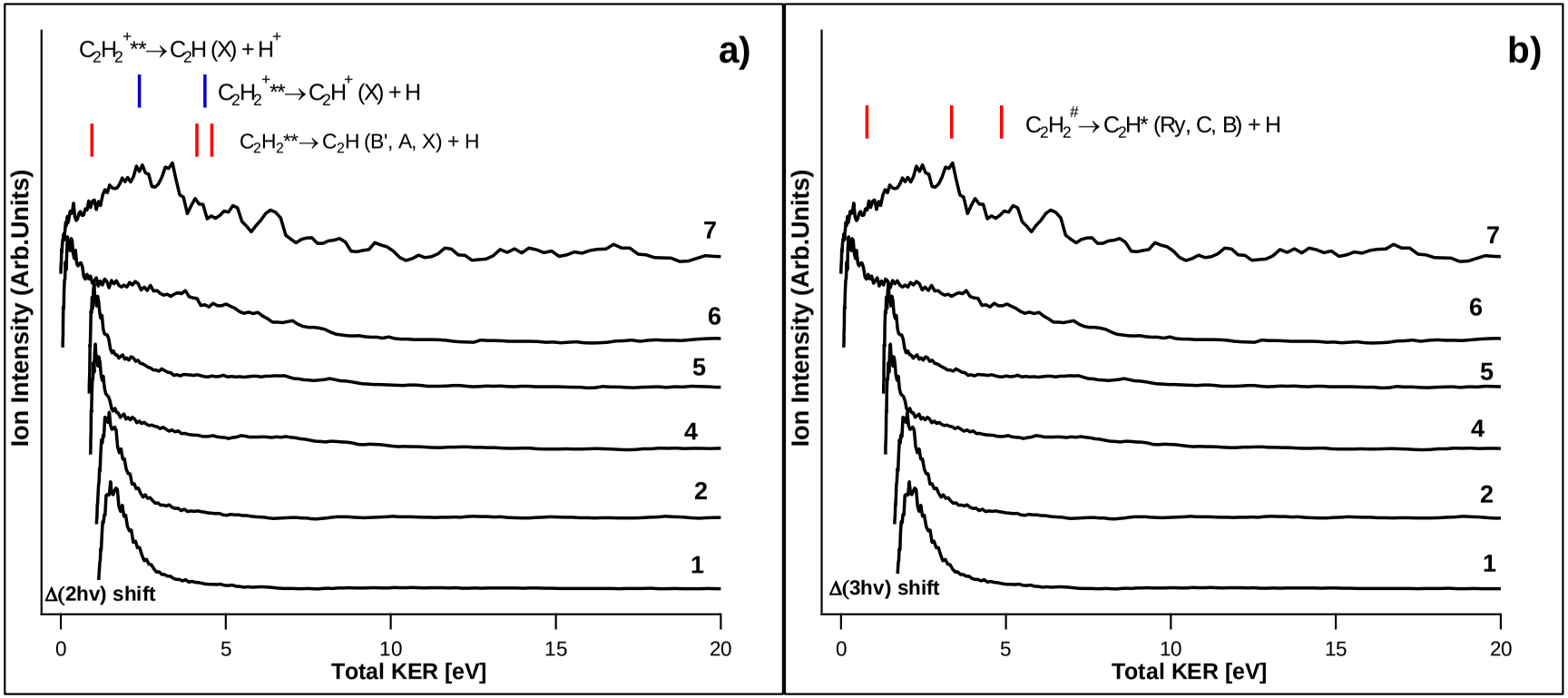

Fig. S13, C_2H^+ kinetic energy release spectra (KERs): Ion kinetic energy release spectra (Ion-KERs) derived from the images no.1,2,4 -7 (see **Table S1**). The spectra are plotted as a function of the total kinetic energy release for the no. 7 (Total KER_0) and shifted by n-photon energy differences (Δ(n*hv*)) with respect to the "reference spectrum", no. 7 (see main text) as, Δ(*2hv*) (a) and Δ(*3hv*) (b). KER thresholds for fragment formations by n-photo-dissociation (n = 2 and 3 for photodissociation via the C_2H_2** and $C_2H_2^{\#}$ intermediate species; see main text), as specified, are indicated by sticks above the spectra.

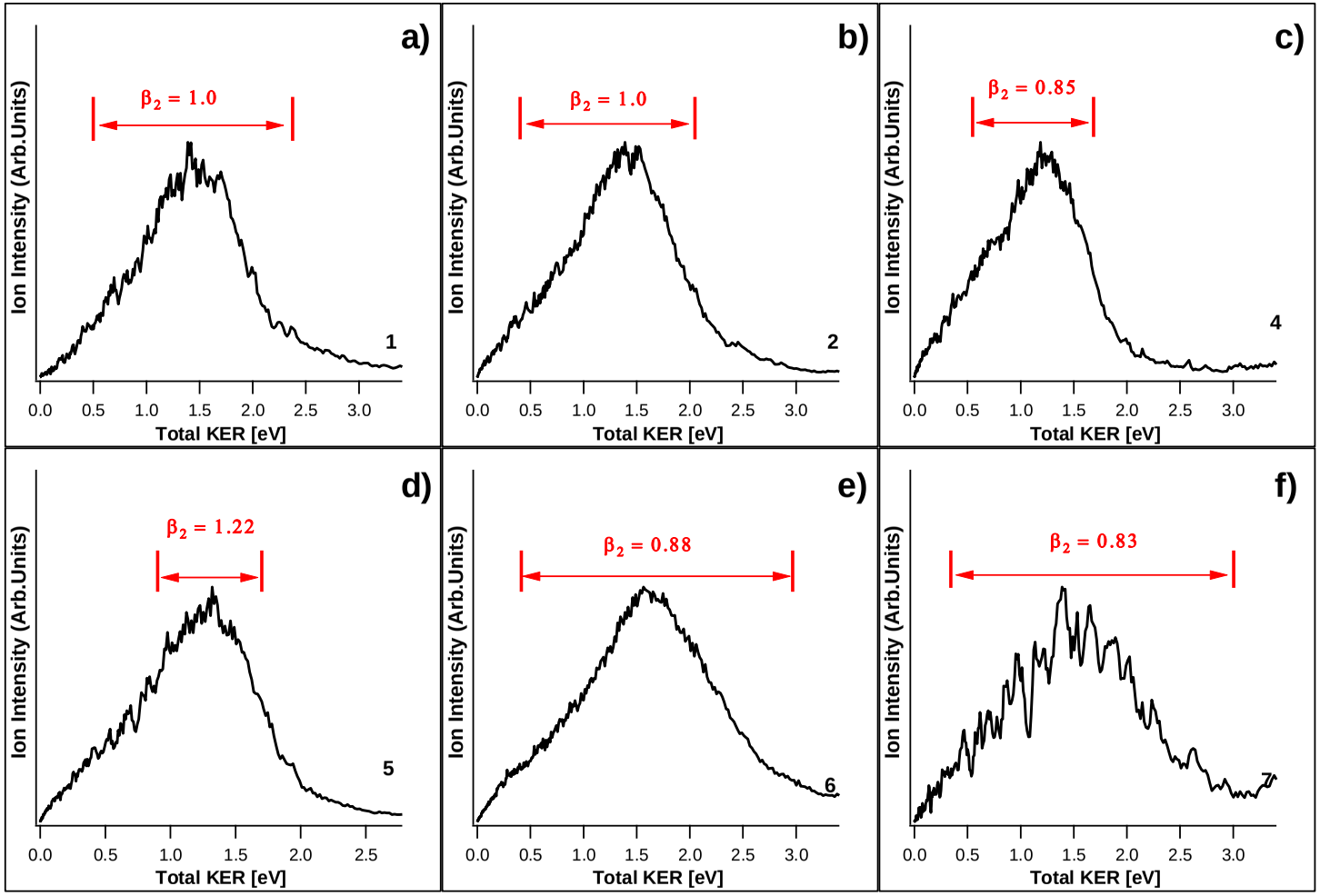

Fig. S14, H^+ angular distributions: H^+ KER spectra for images no. 1,2 and 4-7, average anisotropy / β_2 parameters (see **Table S2**) and energy ranges used for the β_2 determinations.

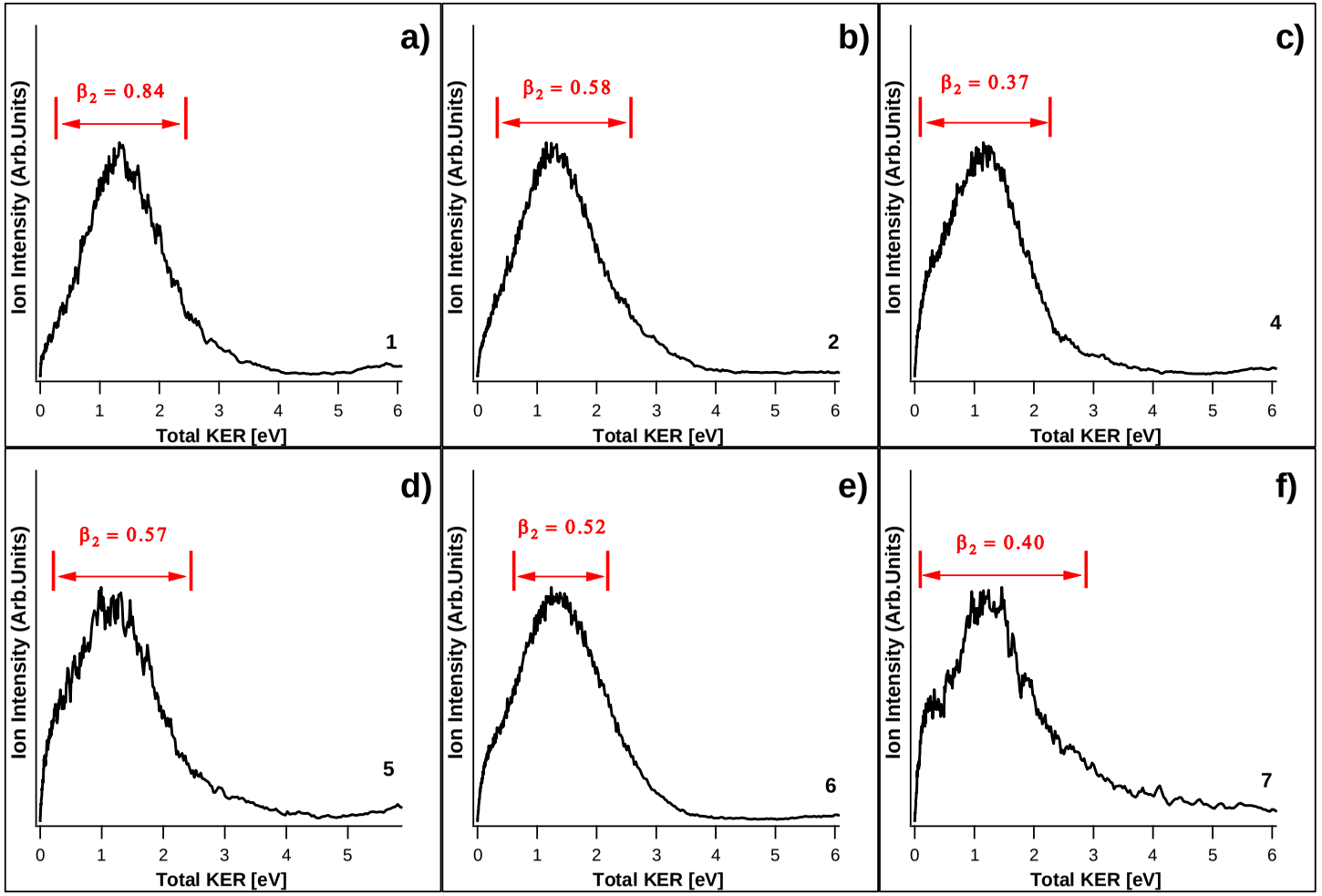

Fig. S15, C^+ angular distributions: C^+ KER spectra for images no. 1,2 and 4-7, average anisotropy / β_2 parameters (see **Table S2**) and energy ranges used for the β_2 determinations.

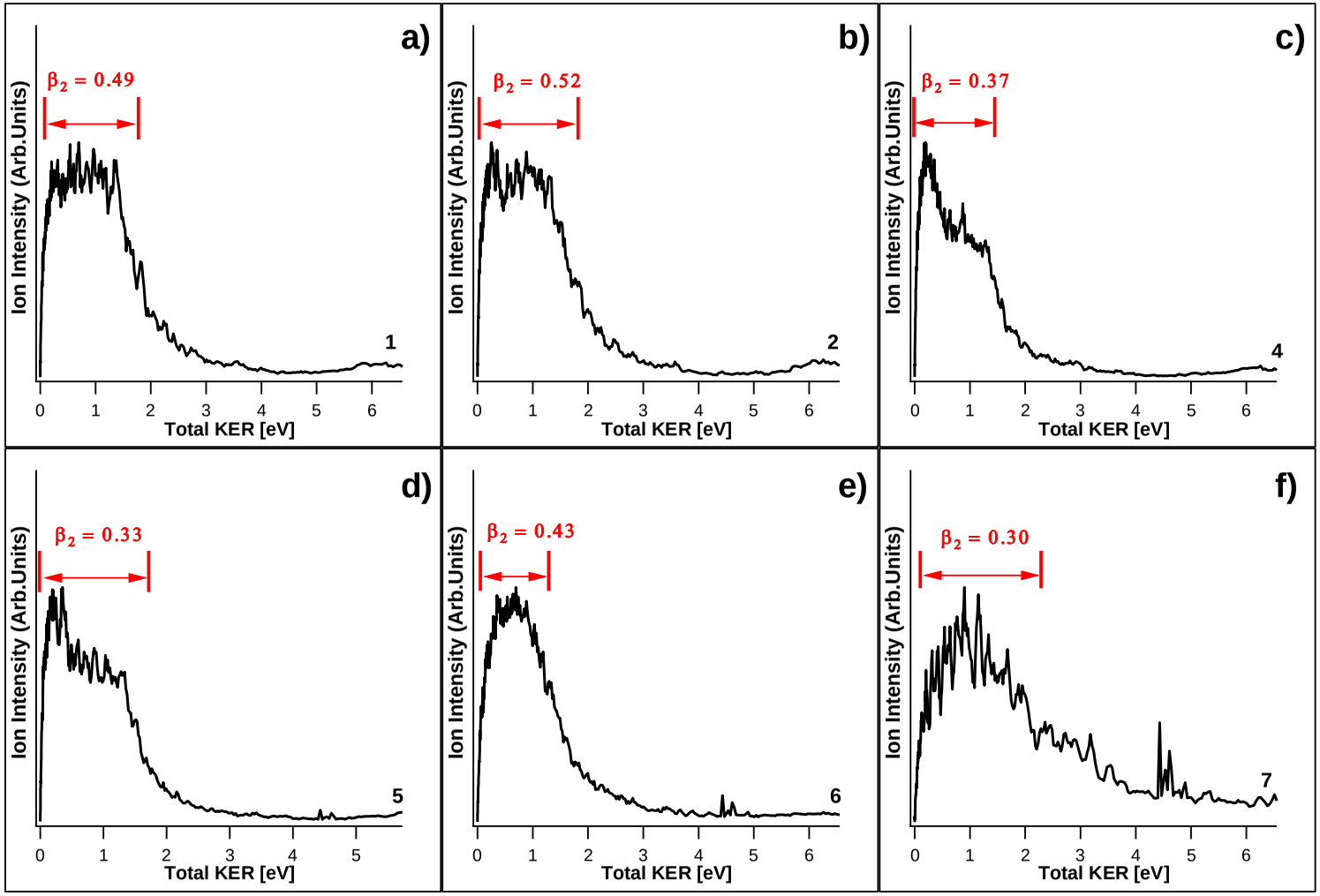

Fig. S16, CH^+ angular distributions: CH^+ KER spectra for images no. 1,2 and 4-7, average anisotropy / β_2 parameters (see **Table S2**) and energy ranges used for the β_2 determinations.

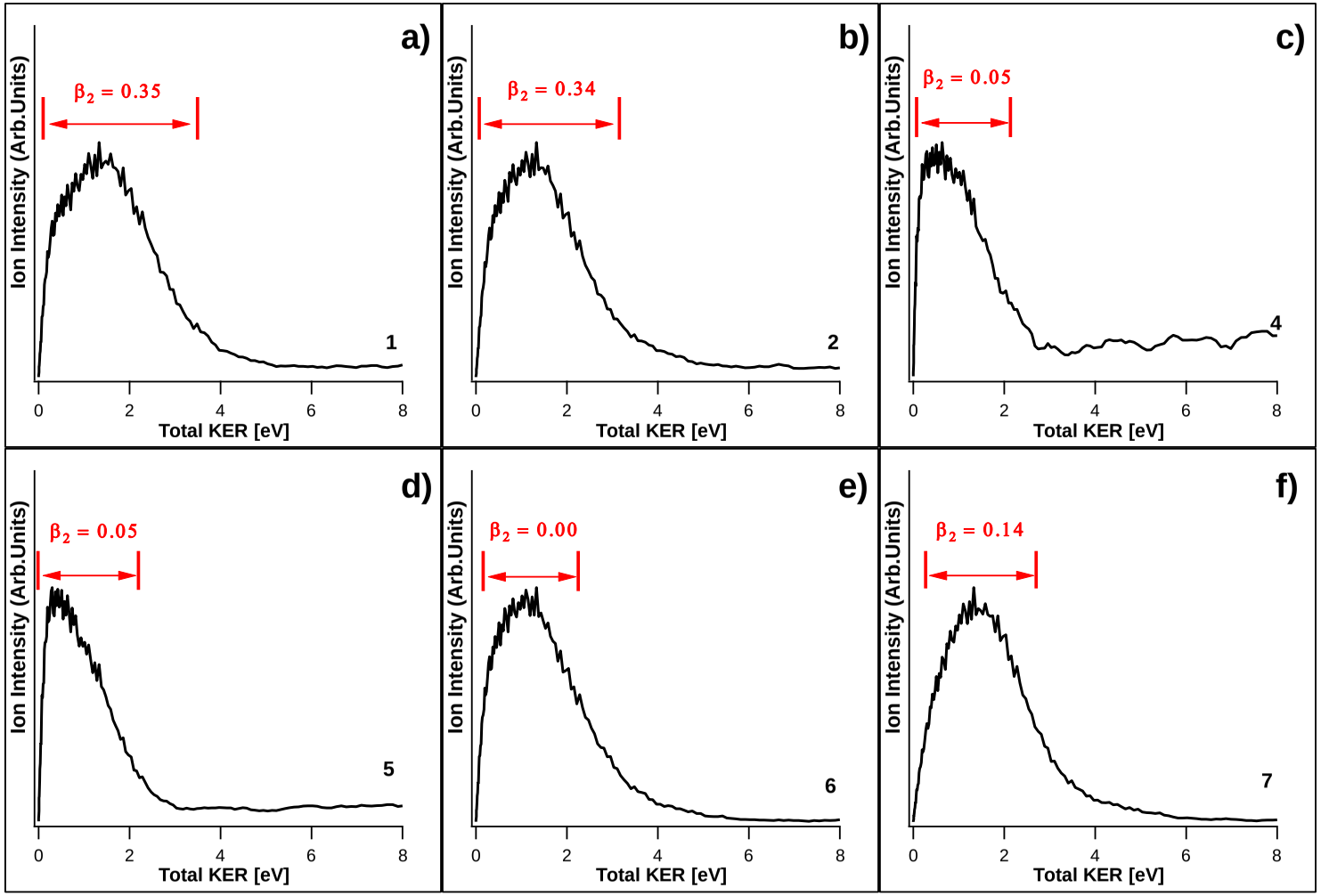

Fig. S17, C_2^+ angular distributions: C_2^+ KER spectra for images no. 1,2 and 4-7, average anisotropy / β_2 parameters (see **Table S2**) and energy ranges used for the β_2 determinations.

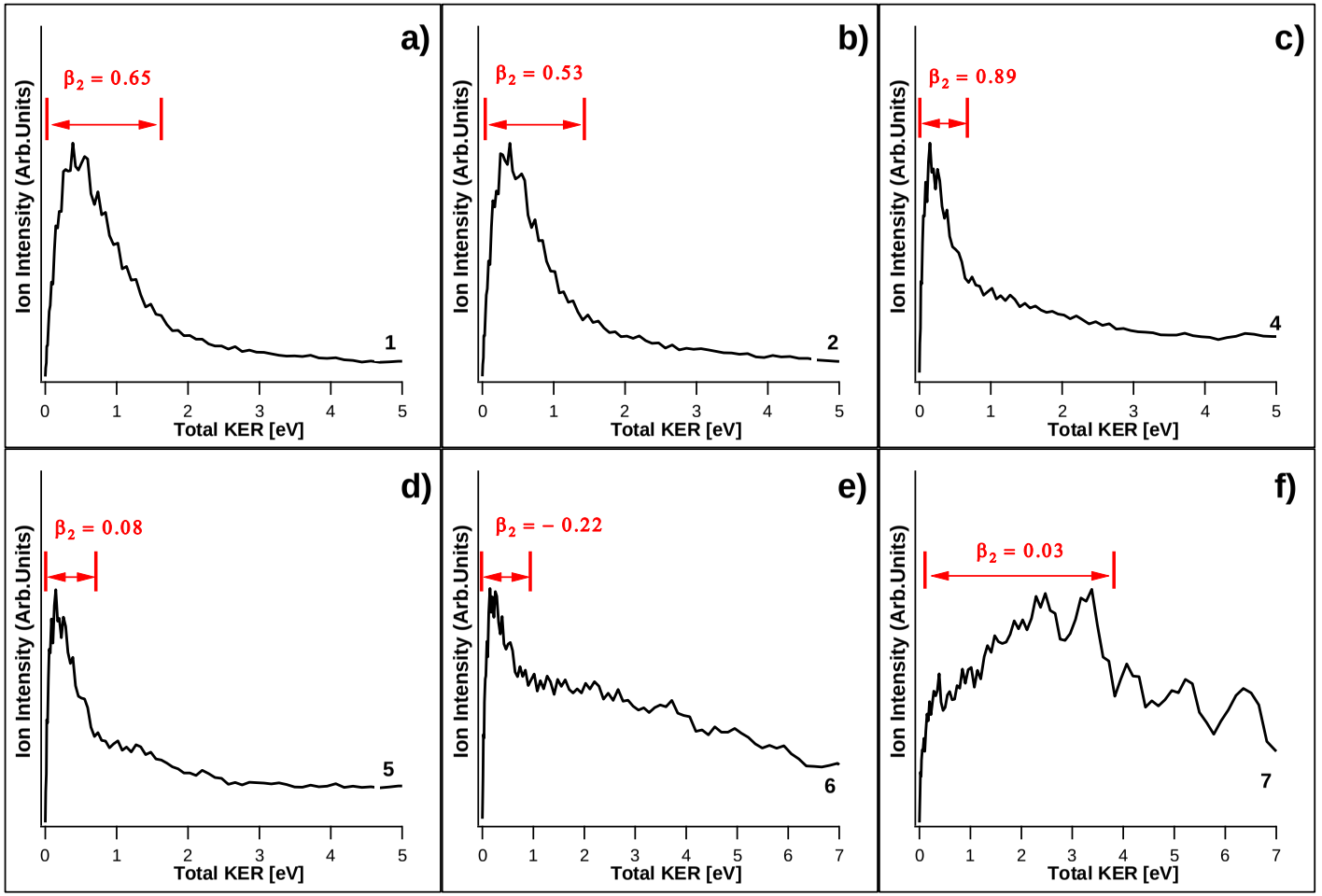

Fig. S18, C_2H^+ angular distributions: C_2H^+ KER spectra for images no. 1,2 and 4-7, average anisotropy / β_2 parameters (see **Table S2**) and energy ranges used for the β_2 determinations.

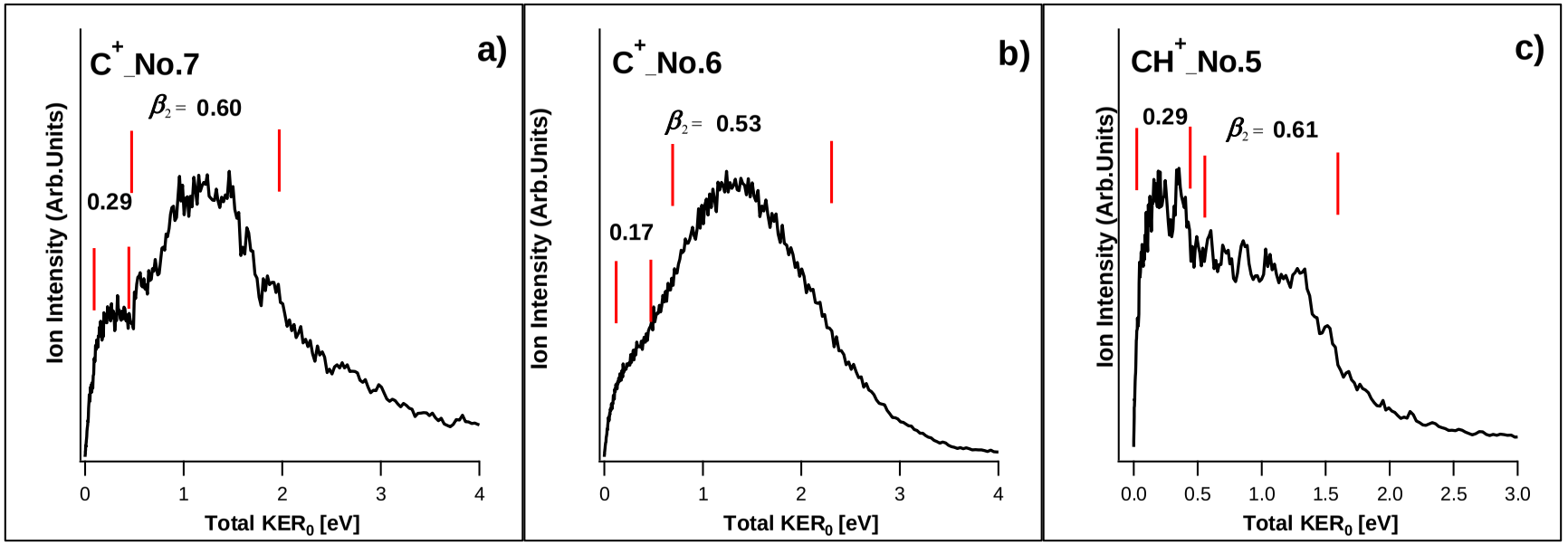

Fig. S19, Ion angular distributions: a) and b) C^+ KER spectra for images no. 7 and 6, **c)** CH^+ KER spectrum for image no.5 average anisotropy / β_2 parameters and energy ranges used for the β_2 determinations.

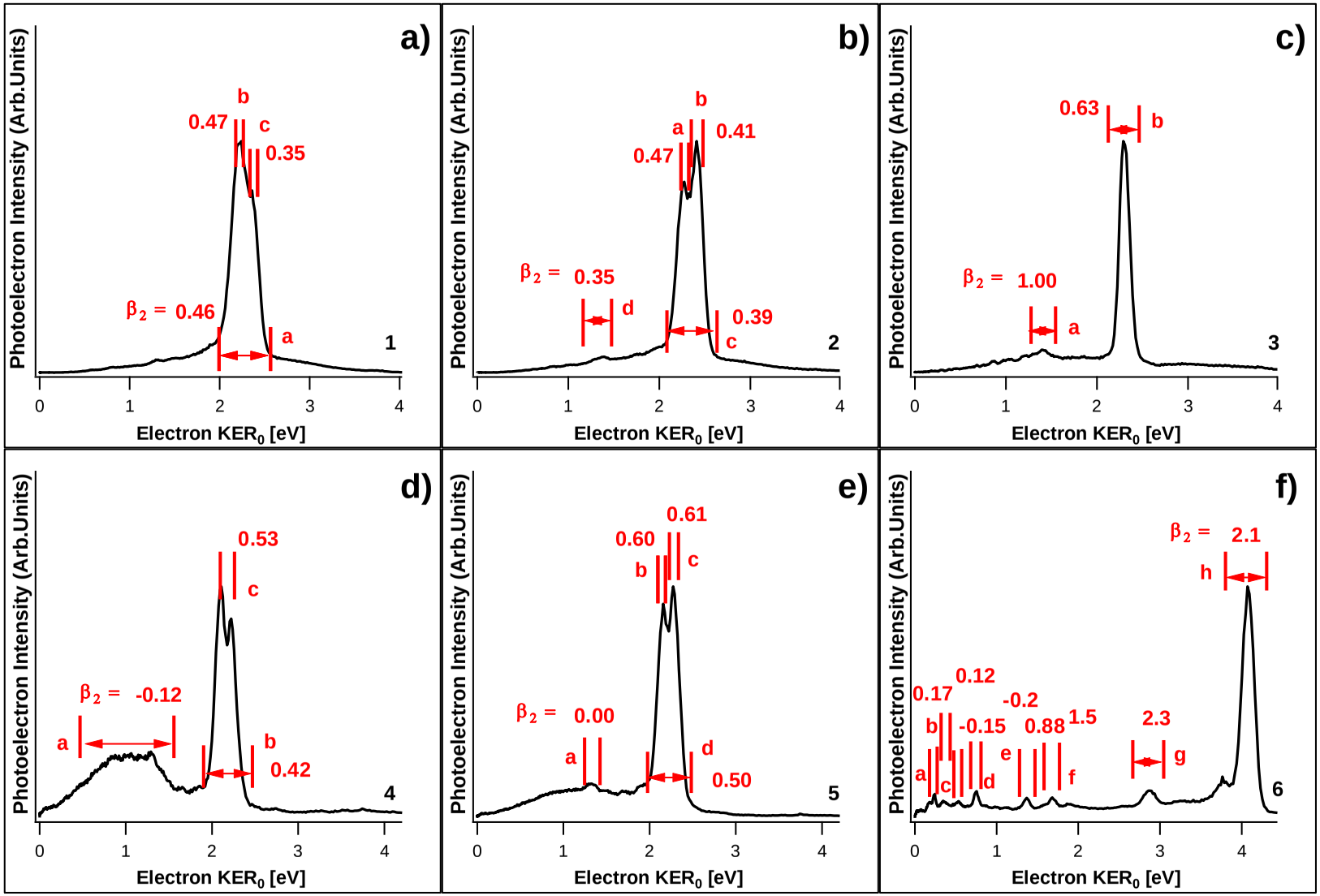
a)
Photoelectron Intensity (Arb.Units)
b
0.47
c
0.35
β2 = 0.46
a
1
Electron KER0 [eV]
b)
b
a
0.41
0.47
β2 = 0.35
d
0.39
c
2
c)
0.63
b
β2 = 1.00
a
3
d)
0.53
c
β2 = -0.12
a
b
0.42
4
e)
0.61
0.60
b
c
β2 = 0.00
a
d
0.50
5
f)
β2 = 2.1
h
0.12
0.17
-0.2
b
-0.15
0.88
1.5
2.3
e
g
a
c
d
f
6
0
1
2
3
4

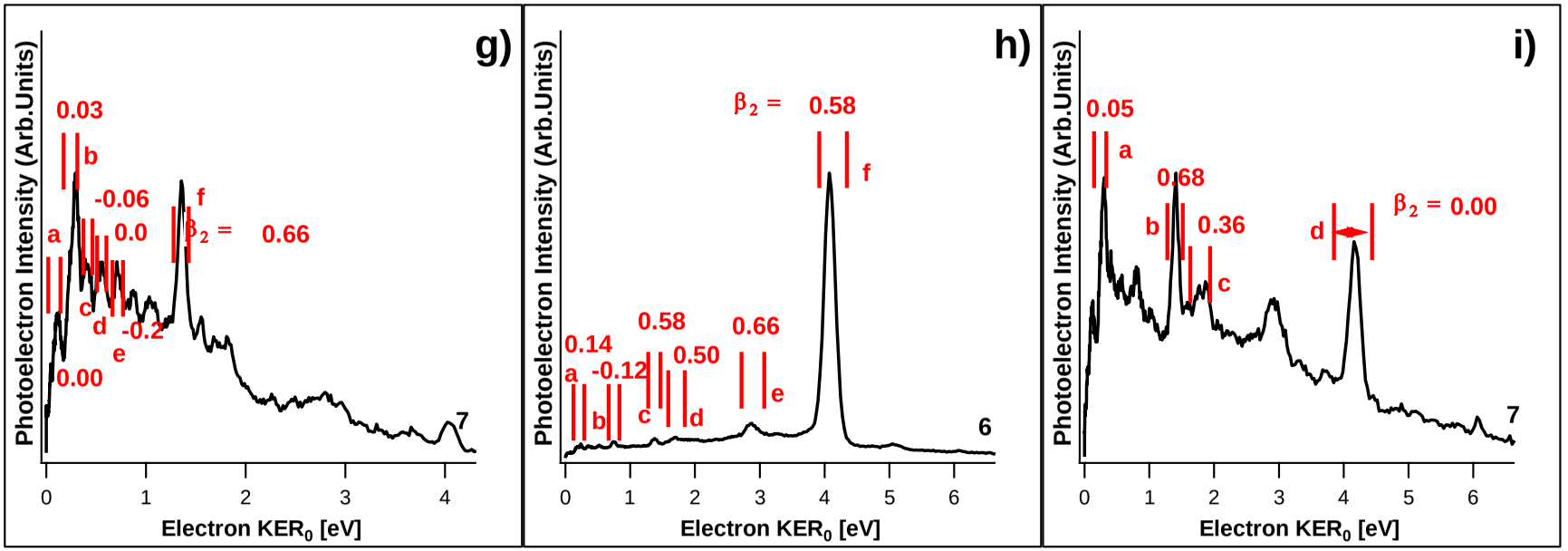

Fig. S20, photoelectron angular distributions: e-KER spectra for images no. 1-7, average anisotropy / β_2 parameters (see **Table S2**) and energy ranges used for the β_2 determinations. (f) and (h) recorded for repeller voltages of -3kV and -5kV, respectively for no.6 and (g) and (i) recorded for repeller voltages of -3kV and -5kV, respectively for no.7.

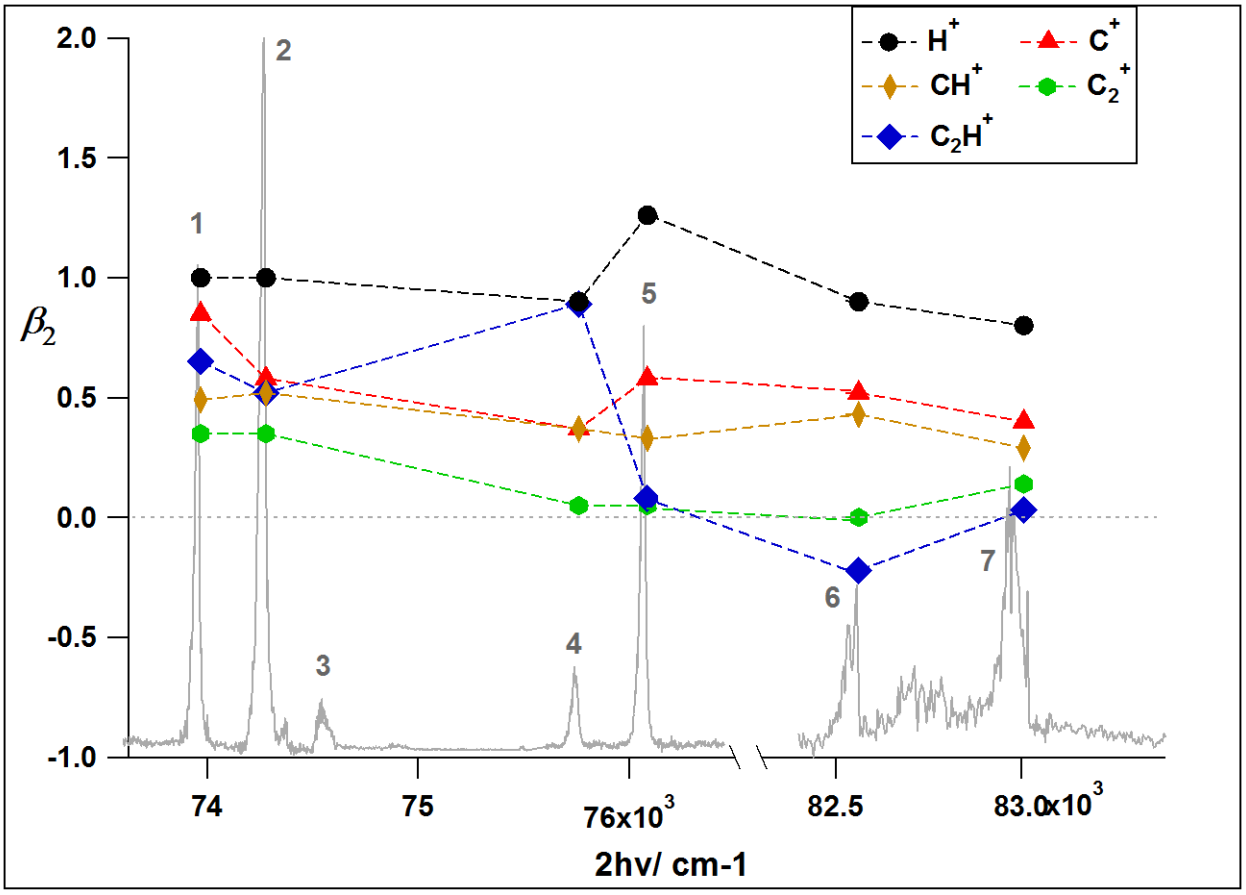

Fig. S21, β_2 parameters vs. ion images: Average β_2 parameters (**Table S2**) derived from ion images as a function of excitation**s (**no. 1,2, 4-7; **Table S1)** and ions.

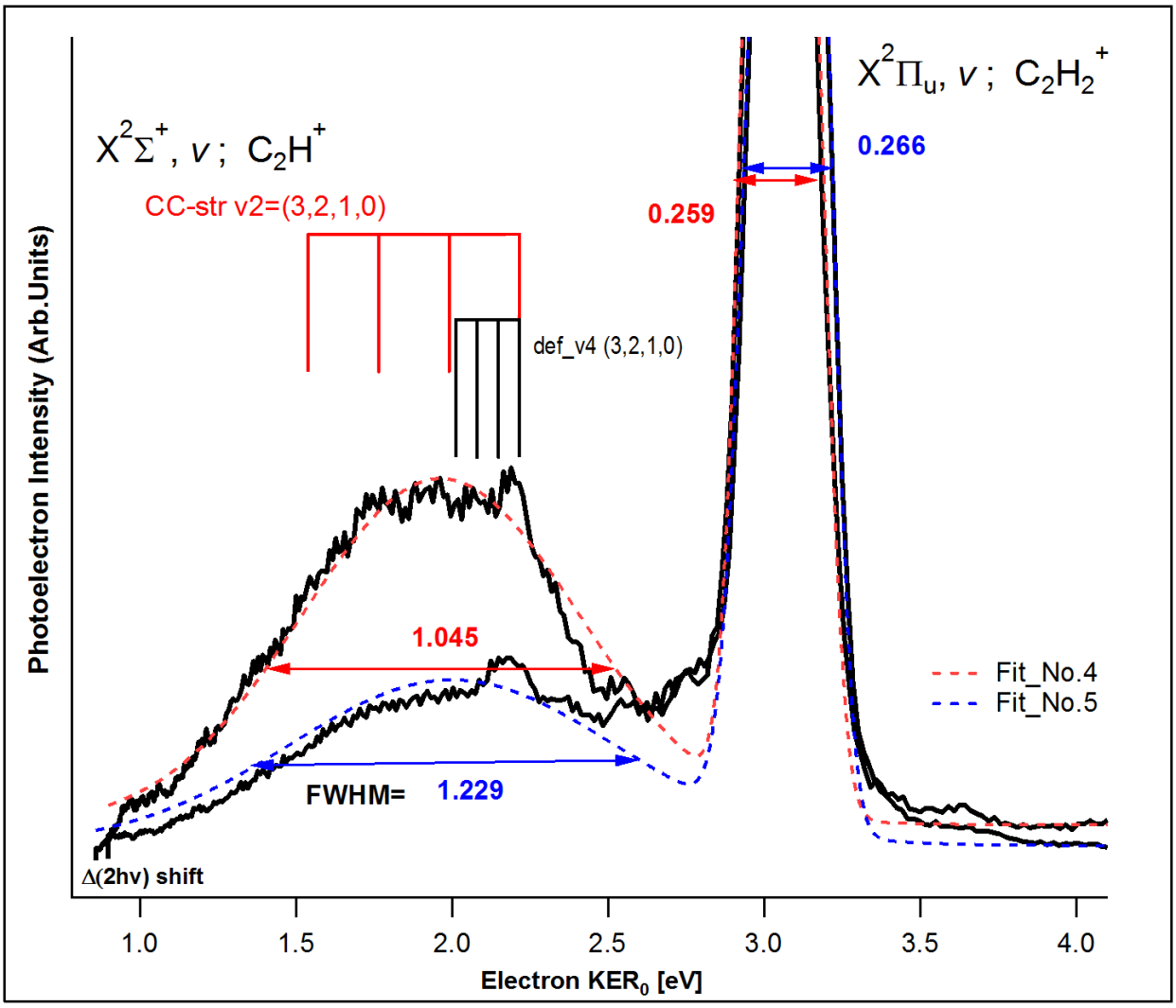

Fig. S22, electron KERs for images no. 4-5 (Table S1): e-KERs plotted as a function of the kinetic energy release (KER) for the no. 7 (KER_0), shifted by two-photon energy differences, ($\Delta(2h\nu)$) with respect to the "reference spectrum", no. 7 (see main text). Full width at half maximum (FWHM) of broad spectra were determined, as indicated. KER thresholds for $C_2H^+(X)$ vibrational mode formations, as specified, are indicated by sticks above the spectra.

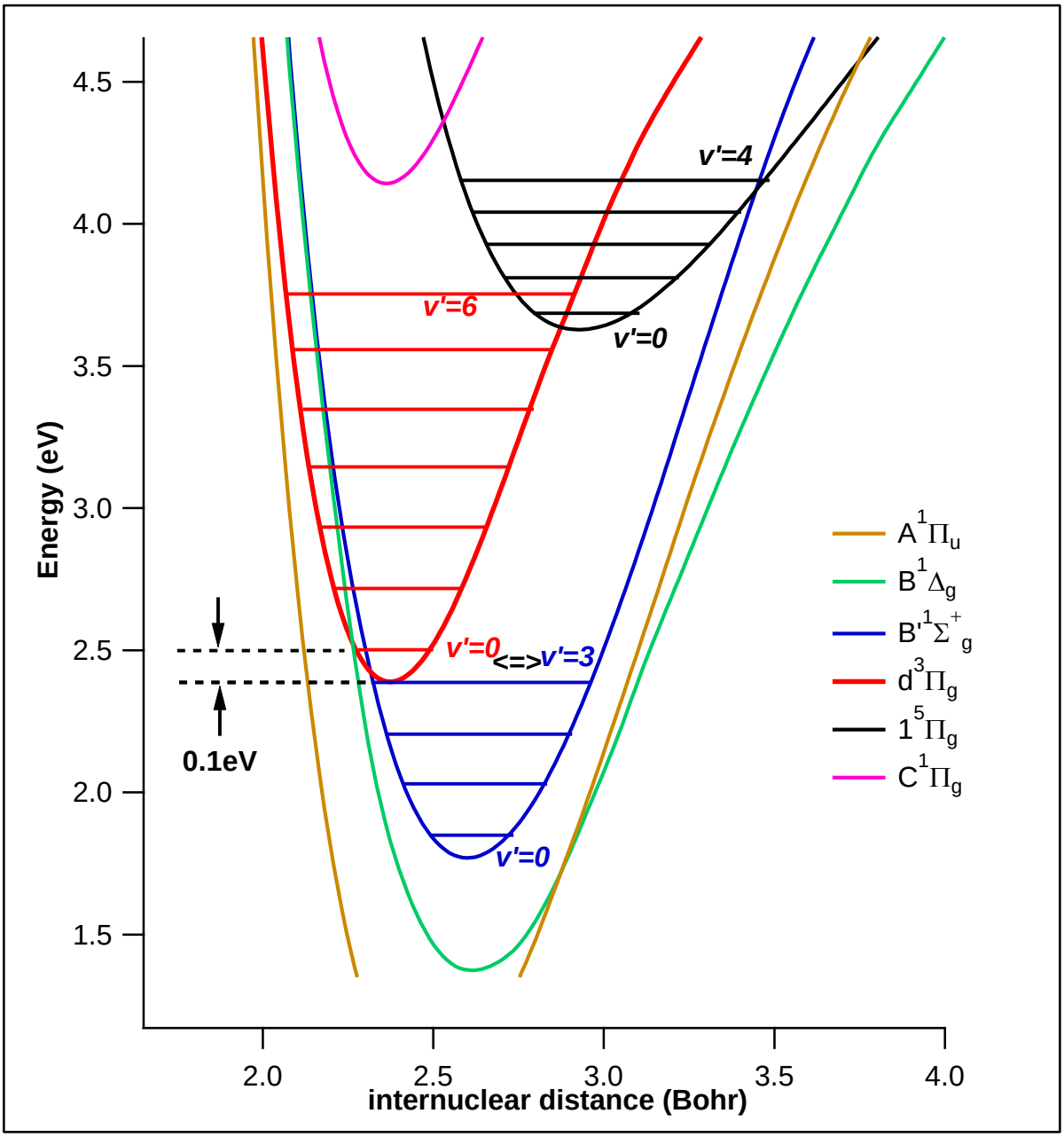

Fig. S23, Potential energy curves for excited C_2 states: Potential energy curves for C_2^{**} derived from ref. **[3]** and **[4]**). Spectroscopic constant for B′ $^1\Sigma_g^+$ state of ω_e=1424.11cm^{-1} and $\omega_e x_e$=2.57cm^{-1}were used.**[4]**

Tables S1, Images and resonant excitations.

Image no.	C_2H_2 Rydberg states; *nl*; $^1\Lambda_g$, $(v_1v_2v_3v_4v_5)$[a]	One-photon excitation/ nm	Two-photon excitation/ cm^{-1}
1	*3p*; $^1\Delta_g$, (00020)	270.364	73969
2	*3p*; $^1\Sigma_g$, (00000)	269.255	74279
3	*3p*; $^1\Sigma_g$, (01000)	268.262	74554
4	*3p*; $^1\Delta_g$, (01020)	263.992	75760
5	*3p*; $^1\Sigma_g$, (01000)	262.864	76085
6	*4p*; $^1\Delta_g$, (00000)	242.245	82561
7	*4p*; $^1\Sigma_g$, (00000)	240.947	83006

[a] n: principal quantum number for Rydberg electron. l: Rydberg electron orbital. (v_1, v_2, v_3, v_4, v_5): vibrational quantum numbers referring to vibrational modes. v_1 (C-H symmetric stretch), v_2 (C-C stretch) v_3 (C-H asymmetric stretch), v_4 and v_5 (bend)

Table S2 (a), **Anisotropy parameters for images:** Anisotropy parameters, $\beta_n = \beta_2, \beta_4$, and β_6 determined from ion images (see **Fig. S14 – S18** for energy ranges) for n = 2 / 2,4 / 2,4,6 vs. ions and excitations (no/#, 1,2, 4 – 7; see **Table S1**).

#	Ion	β_2	β_4	β_6	Ion	β_2	β_4	β_6	Ion	β_2	β_4	β_6	Ion	β_2	β_4	β_6	Ion	β_2	β_4	β_6
1	H^+	0.87			C^+	0.78			CH^+	0.51			C_2^+	0.36			CH_2^+	0.71		
		1	-0.49			0.85	-0.2			0.49	0.06			0.35	0.02			0.65	0.18	
		1	-0.46	-0.14		0.85	-0.18	-0.03		0.49	0.06	-0.01		0.35	0	0.03		0.64	0.17	0.03
2		0.86				0.49				0.52				0.32				0.6		
		1	-0.55			0.58	-0.21			0.52	0.01			0.35	-0.06			0.52	0.18	
		1.01	-0.46	-0.33		0.59	-0.17	-0.08		0.51	-0.01	0.03		0.35	-0.05	-0.01		0.52	0.16	0.04
4		0.8				0.34				0.38				0.04				0.8		
		0.89	-0.37			0.37	-0.13			0.37	-0.06			0.05	-0.01			0.89	-0.37	
		0.89	-0.3	-0.27		0.37	-0.13	0.01		0.37	-0.05	-0.03		0.05	-0.01	-0.02		0.89	-0.3	-0.27
5		1.14				0.55				0.35				0.05				0.1		
		1.26	-0.46			0.58	-0.1			0.33	0.08			0.05	0.01			0.08	0.04	
		1.27	-0.38	-0.33		0.58	-0.1	-0.03		0.33	0.08	-0.01		0.05	0.01	0.02		0.07	0.01	0.05
6		0.84				0.51				0.42				0				-0.17		
		0.9	-0.21			0.52	-0.03			0.43	-0.02			0	-0.02			-0.22	0.12	
		0.9	-0.19	-0.1		0.53	0.01	-0.1		0.43	-0.02	-0.02		0	-0.01	-0.01		-0.22	0.13	-0.01
7		0.88				0.37				0.28				0.13				0.12		
		0.79	0.33			0.4	-0.12			0.29	0.05			0.14	-0.02			0.03	0.23	
		0.79	0.26	0.28		0.4	-0.1	-0.1		0.32	0.08	0.17		0.14	-0.03	0.02		0.01	0.16	0.18

Table S2 (b), **Anisotropy parameters for images: :** Anisotropy parameters, $\beta_n = \beta_2$ and β_4, determined from photoelectron images (see **Fig. S19 (a – g)** for energy ranges a - h) for n = 2 / 2,4 vs. excitations (no/#, 1 – 7; see **Table S1**). Repeller voltage: -3 kV.

-3kV		β_2	β_4	β_2	β_4	β_2	β_4	β_2	β_4	β_2	β_4	β_2	β_4	β_2	β_4	β_2	β_4
PES	**#**	**a**	**a**	**b**	**b**	**c**	**c**	**d**	**d**	**e**	**e**	**f**	**f**	**g**	**g**	**h**	**h**
	1	0.47		0.47		0.35											
		0.45	0.06	0.47	0.03	0.35	0.01										
	2	0.48		0.42		0.34		0.39									
		0.46	0.03	0.4	0.03	0.35	-0.03	0.38	0.02								
	3	1.29		0.71													
		0.82	1.16	0.55	0.37												
	4	-0.16		0.42		0.52											
		-0.07	-0.21	0.42	0.01	0.53	-0.03										
	5	-0.07		0.62		0.65		0.49									
		0.02	-0.19	0.57	0.07	0.57	0.06	0.5	-0.02								
	6	0.17		0.12		-0.16		-0.14		0.93		1.67		2.83		2.16	
		0.17	-0.01	0.12	-0.01	-0.14	-0.26	-0.35	-0.12	0.84	0.2	1.33	0.88	2.3	1.56	2.1	0.16
	7	0.01		0.05		-0.03		0.03		-0.23		0.61					
		-0.06	0.16	0.01	0.1	-0.11	0.16	-0.03	0.14	-0.18	-0.11	0.71	-0.3				

Table S2 (c), **Anisotropy parameters for images: :** Anisotropy parameters, $\beta_n = \beta_2$ and β_4, determined from photoelectron images (see **Fig. S19 (h – i)** for energy ranges, a - f) for n = 2 / 2,4 vs. excitations (no. / #: 6 – 7; see **Table S1**). Repeller voltage: -5 kV.

-5kV		β_2	β_4	β_2	β_4	β_2	β_4	β_2	β_4	β_2	β_4	β_2	β_4
PES	**#**	**a**	**a**	**b**	**b**	**c**	**c**	**d**	**d**	**e**	**e**	**f**	**f**
	6	0.13		-0.14		0.56		0.5		0.72		0.56	
		0.14	-0.01	-0.09	-0.11	0.6	-0.09	0.5	-0.01	0.6	0.3	0.6	-0.1
	7	0.06		0.67		0.39		0.13					
		0.04	0.04	0.69	-0.03	0.33	0.12	-0.03	0.35				

Table S3, Dissociation products: Low-lying valance states of CH/CH*, correlating to H (n=1) + C ($^3P_0$, $^1D_2$, $^1S_0$, $^5S^o_2$),according to *ab initio* calculation by Vázquez et al.[5]

Molecular states	Atomic energies (eV)	Atomic states
$c^4\Sigma^-$, $(1)^6\Sigma^-$	*4.182*	C($^5S^o_2$)
$(2)^2\Sigma^+$,	*2.684*	C($^1S_0$)
$A^2\Delta$,$C^2\Sigma^+$, $(2)D^2\Pi$	*1.263*	C($^1D_2$)
$X^2\Pi$, $B^2\Sigma^-$, $a^4\Sigma^-$, $b^4\Pi$	*0.000*	C($^3P_0$)

Table S4 (a) Thresholds vs. fragment dissociation: Dissociaction energies (D_0) for fragments of C_2H_2. m(min) are the minimum number of photons required for the fragment formations in multiphoton dissociation, corresponding to excitation no. 7 (**Table S1**).

Fragment	D_0(eV)	m(min)/*hv*
H(n=1) + C_2H(X)	5.712[a]	2
H*(n=2) + C_2H(X)	15.911[b]	4
H(n=1) + C_2H*(B')	9.352[b]	2
H2 + C_2(X)	6.333[c]	2
H2 + C_2(d)	8.816[b]	2
H2 + C_2(C)	10.581[b]	3
CH_2(X)+ C($^3P_0$)	9.170[c]	2
CH_2(X)+ C*($^1D_2$)	10.433[b]	3
CH_2(X)+ C*($^1S_0$)	11.854[b]	3
CH_2(X)+ C*($^5S^o_2$)	13.352[b]	3
CH_2(X)+ C*($^3P^o_0$)	16.650[b]	4
CH_2(X)+ C*($^1P^o_1$)	16.854[b]	4
CH_2(X)+ C*($^3D^o_3$)	17.115[b]	4
CH(X)+ CH(X)	9.921[d]	2
CH(X)+ CH*(A)	12.796[b]	3
CH(X)+ CH*(B)	13.150[b]	3
CH(X)+ CH*(C)	13.864[b]	3
2H + C_2(X)	11.174[b]	3
2H + C_2*(d)	13.657[b]	3
2H + C_2*(C)	15.422[b]	4
CH(X)+H+ C($^3P_0$)	13.666[b]	3
H_2+ C($^3P_0$) +C($^3P_0$)	12.475[b]	3

a. From Mordaunt's paper (Ref. [6])

b. alculated values refers to fragment energetic in NIST (Ref. [7])

c. om Matthíasson's paper (Ref. [8])

d. From Evrin's paper (Ref. [9])

Table S4 (b), Thresholds vs. ionizations: Ionization energies (IE) for the parent molecule and fragments. m(min) are the minimum number of photons required for ionization of the species in multiphoton excitation, corresponding to excitation no. 7 (**Table S1**). E_{thr} are common thresholds for ionization of fragment species according to equation $E_{thr}(Fi/Fi^*) = n\hbar\nu - IE(Fi/Fi^*)$; n = 1,2,3 with respect to the "reference spectrum", no. 7. (see main text).

Molecule	m(min) / *hν*	IE(eV)	E_{thr}(eV)
$C_2H_2(X)$	3	11.400	4.037
Fragments	m(min) / *hν*	IE(eV)	E_{thr}(eV)
H(n=1)	3	13.598	1.837
H*(n=2)	1	13.598	1.744
$C(^3P_0)$	3	11.260	4.177
$C^*(^1D_2)$	2	11.260	0.295
$C^*(^1S_0)$	2	11.260	1.715
$C^*(^5S^o_2)$	2	11.260	3.214
$C^*(^3P^o_0)$	1	11.260	1.366
$C^*(^1P^o_1)$	1	11.260	1.570
$C^*(^3D^o_3)$	1	11.260	1.831
CH(X)	3	10.640	4.797
CH*(A)	2	10.640	2.521
CH*(B)	2	10.640	2.882
CH*(C)	2	10.640	3.595
$CH_2(X)$	3	10.640	5.037
$C_2(X)$	3	11.866	3.659
C_2*(d)	2	11.866	0.908
C_2*(C)	2	11.866	2.450
$C_2H(X)$	3	11.610	3.827
$C_2H^*(B')$	2	11.610	2.321

a. om NIST (Ref. [7])
b. From Krechkivska's paper (Ref. [10])

References:

1. M. N. R. Ashfold, B. Tutcher, B. Yang, Z. K. Jin and S. L. Anderson, *J. Chem. Phys.*, 1987, **87**, 5105-5115.
2. K. Tsuji, N. Arakawa, A. Kawai and K. Shibuya, *J. Phys. Chem. A*, 2002, **106**, 747-753.
3. J. F. Babb, R. T. Smyth and B. M. McLaughlin, *Astrophys. J*, 2019, **876**, 38.
4. M. Martin, *J. Photochem. Photobiol. A*, 1992, **66**, 263-289.
5. G. J. Vázquez, J. M. Amero, H. P. Liebermann, R. J. Buenker and H. Lefebvre-Brion, *J. Chem. Phys.*, 2007, **126**, 164302.
6. D. H. Mordaunt and M. N. R. Ashfold, *J. Chem. Phys.*, 1994, **101**, 2630-2631.
7. NIST Chemistry WebBook - (National Institute of Standards and Technology) https://webbook.nist.gov/chemistry/name-ser/
8. K. Matthíasson, H. Wang and Á. Kvaran, *Chem.Phys. L*, 2008, **458**, 58-63.
9. K. M. Ervin, S. Gronert, S. E. Barlow, M. K. Gilles, A. G. Harrison, V. M. Bierbaum, C. H. ePuy, W. C. Lineberger and G. B. Ellison, *J. Am. Chem. Soc.* , 1990, **112**, 5750-5759.
10. O. Krechkivska, G. B. Bacskay, B. A. Welsh, K. Nauta, S. H. Kable, J. F. Stanton and T. W. chmidt, *J. Chem. Phys.*, 2016, **144**, 144305.

5 Summary and conclusion

5.1 HI

One-color REMPI data of HI, in the two-photon excitation region of 72 400- 80300 cm^{-1}, were recorded to identify new Rydberg and ion-pair states. The Rydberg state spectra were assigned to state properties by considering (i)-the nature of the spectral structure concerning relative intensities of line series and appearance or absence of rotational lines, (ii)-relative and absolute ion intensities, (iii)-the magnitude of rotational constants, (iv) -perturbation effects, which show as line shifts (LI-effect) and/or intensity alterations (LI / LW-effect) in the spectra, (v)-by performing detailed quantum defect analyses of the states energetics (band origins). Five cases of state interactions, homogeneous ($\Delta\Omega = 0$) and heterogeneous ($\Delta\Omega \neq 0$) in nature, were specifically discussed for LS-, LI- and LW-effects:

(a) $g^3\Sigma^-_{0^+}[1/2]7p\pi$(v'= 0) Rydberg state $\leftrightarrow$ $V^1\Sigma^+$(v'= m + 19) ion-pair state, ($\Delta\Omega = 0$)

(b) $P^1\Delta_2\,[1/2]4f\pi$(v'= 0) Rydberg state $\leftrightarrow$ $k^3\Pi_2\,[1/2]5d\delta$(v'= *1*) Rydberg state, ($\Delta\Omega = 0$)

(c) $j^3\Sigma^-_{0^+}[1/2]5d\pi$(v'= 1) Rydberg state $\leftrightarrow$ $V^1\Sigma^+$(v'= m + 22) ion-pair state, ($\Delta\Omega = 0$)

(d) $M^1\Pi_1\,[1/2]7s\sigma$(v'= 0) Rydberg state $\leftrightarrow$ $V^1\Sigma^+$(v'= m + 29) ion-pair state, ($\Delta\Omega \neq 0$)

(e) $r^3\Pi_0\,[1/2]7p\sigma$(v'= 0) Rydberg state $\leftrightarrow$ $V^1\Sigma^+$(v'= m + 36) ion-pair state. ($\Delta\Omega = 0$)

The effect of state mixing, hence state character, on transition probabilities is evident by ion intensity borrowing vs. ion intensity giving effects clearly seen in REMPI spectra of the interacting states. The effects of state mixing/interaction on photofragmentation processes were discussed in detail. It has been proposed that ion formation in multiphoton ionization via two-photon resonant excitation to intermediate states (HI**(v') involves further third photon excitation to superexcited state(s) ($HI^{\#}$) followed by the number of fragmentation processes. Relative ion signal intensities ($I(HI^+)$ vs. $I(I^+)$ vs. $I(H^+)$) are found to be comparable for all spectra of pure Rydberg states, which experience limited mixing with the ion-pair vibrational state (i.e., $I(HI^+) > I(I^+) > I(H^+)$). For ion-pair state spectra, on the other hand, $I(I^+) > I(H^+) > I(HI^+)$ for the overall excitation region.

5.2 CH_3I

Ion and photoelectron (PE) slice images were recorded for multiphoton excitation of CH_3I involving two-photon resonant transitions to a total of eight ns, np and nd molecular Rydberg states and different vibrational states (v_1,v_2,v_3) (CH_3I**(Ry; v_1,v_2,v_3)) in the two-photon excitation region of 55 700 and 70 000 cm^{-1}. The analyses show that superexcited state(s), $CH_3I^{\#}$ are created by three-photon excitations followed by (a) -dissociation to form Rydberg state iodine atoms, I**, along with CH_3(X), followed by one-photon ionization of I** (major

channel), (b)-dissociation to form the ion pair CH_3^+ and I^- followed by one-photon electron ejection from I^-, (c)-autoionization to form CH_3I^+ (X) and further one-photon dissociation to form CH_3^+ along with I or I*(spin-orbit excited I).

5.3 $I^{\#}$

I^+ REMPI spectra were derived from mass-resolved REMPI data for CH_3I and HI for the high energy two-photon excitation region of 76 680–82 620 cm^{-1}. Several new iodine atomic lines due to two-photon resonant excitations to superexcited Rydberg states ($I^{\#}$), not previously observed, were discovered. Detailed quantum defect analysis allowed the assignment of the lines concerning the nature of the Rydberg states, specified by Rydberg electron principal quantum numbers (*n*), its orbital angular momentum quantum numbers (*l*), and ion core terms. Line widths and intensities of peaks vary dramatically depending on the ionization processes and excited states involved. The autoionization processes driven by Coulomb interaction forces (Coulomb transfer mechanism) are found to be the fastest (shortest living $I^{\#}$); however, those driven by spin-orbit or spin-spin forces (spin-flip mechanisms) are slower (longer living $I^{\#}$).

5.4 C_2H_2

Acetylene/C_2H_2: All in all, three-photon dissociation processes, via two-photon resonant excitations to Rydberg states (C_2H_2**) followed by one-photon excitation to superexcited state(s) ($C_2H_2^{\#}$) are found to play the most significant role in an overall multiphoton-fragmentation process of acetylene. While several photoexcited molecular states (Rydberg states, C_2H_2**, first superexcited state(s), $C_2H_2^{\#}$ and second superexcited state(s), $C_2H_2^{\#\#}$) are found to be involved in the multiphoton fragmentation, its involvement and importance vary depending on the photon density. The first superexcited state(s) ($C_2H_2^{\#}$), being metastable, hence short-lived, concerning both autoionization and dissociation, makes it an important gateway for fragment formation in competition with molecular autoionization. Further excitation to the second superexcited state(s) ($C_2H_2^{\#\#}$) will compete with those fast fragmentation and autoionization channels and vastly diminish with decreasing photon density. To a large extent, the resonance excitation to the Rydberg states (C_2H_2**) acts as an enhancement step for further transition to the $C_2H_2^{\#}$ state(s). Thus, in combination, it makes sense that the first superexcited state(s) ($C_2H_2^{\#}$) plays the most crucial role as a gateway toward the fragment formations prior to ionization in our experimental conditions.

5.5 CH_3Br

Two-color mass-resolved REMPI (MR-REMPI) / pump and probe experiments were successfully applied for CH_3Br. CH_3 ($3p^2A_2''$ (000)) Rydberg state spectrum recorded by use of the two-color REMPI pump and probe system for CH_3Br, indicates that valuable photofragmentation experiments and spectra analysis of fragment species can be achieved by using our two-color REMPI system. For specific qualitative analysis of photofragmentation processes, such as photodissociation dynamics, the two-color REMPI system needs more technical improvements.

References

1. R. P. Feynman, R. B. Leighton and M. Sands, The Feynman Lectrures on Physics, Addison-Wesley Publishing Company, Inc., Reading, MA, London, 2nd edn., 1964.
2. K. J. Laidler, J. H. Meiser and B. C. Sanctuary, *Physical Chemistry*, Houghton Mifflin Company, Boston, NY, 4th edn., 2003.
3. Cohen-Tannoudji, B. Diu and F. Laloe, *Quantum Mechanics*, Hermann and John Wiley & Sons. Inc., Canada, 2005.
4. S. Solomon, Reviews of Geophysics, 1999, 37, 275-316.
5. J. H. Seinfeld and S. N. Pandis, Atmospheric chemistry and physics: from air pollution to climate change John Wiley and Sons, 2006. 211.
6. M. J. Simpson, R. P. Tuckett, K. F. Dunn, C. A. Hunniford and C. J. Latimer, *J. Chem. Phys.*, 2009, 130.
7. N. Hoffmann, *Chem. Rev.*, 2008, 108, 1052.
8. F. B. Mallory and C. W. Mallory, Photocyclization of stilbenes and related molecules, Robert E. Krieger Publishing company, 1988.
9. Q. Liu, L. Wu, R. Jackstell and M. Beller, *Nat. Commun.*, 2015, 6, 5933.
10. E. Herbst, *Chem. Soc. Rev.*, 2001, 30, 168.
11. J. I. Lunine, Astrobiology, Pearson - Addison-Wesley 2005.
12. A. M. Shaw, Astrochemistry; From Astronomy to Astrobiology, Wiley 2006.
13. A. E. Douglas and F. R. Greening, *Can. J. Phys.*, 1979, 57, 1650-1661.
14. D. S. Green, G. A. Bickel and S. C. Wallace, *J. Mol. Spectrosc.*, 1991, 150, 303-353.
15. D. S. Green, G. A. Bickel and S. C. Wallace, *J. Mol. Spectrosc.*, 1991, 150, 354-387.
16. J.B. Nee, M. Suto, L.C. Lee, *J. Chem. Phys.* 1986, 85, 719.
17. M.S. Banna, B.E. Mills, D.W. Davis, and D.A. Shirley, *J. Chem. Phys.*, 1974, 61, 4780.
18. Berkowitz, J., Chupka, W.A., Guyon, P.M., Holloway, J.H., and Spohr, R., *J. Chem. Phys.*, 1971, 54, 5165.
19. A. Bodi, Á. Kvaran and B. Sztáray, *J. Phys. Chem. A*, 2009, 114, 9991.
20. K. Matthíasson, Á. Kvaran, G. A. Garcia, P. Weidner, and B. Sztáray, *Phys. Chem. Chem. Phys.*, 2021, 23, 8292.
21. S. Kauczok, C. Maul, A.I. Chichinin, K.H. Gericke, *J. Chem. Phys.*, 2010, 133, 024301.
22. R. Liyanage, P.T.A. Reilly, Y.-a. Yang, R.J. Gordon, *Chem. Phys. Lett.*, 1993, 216, 544.
23. A.J. Yencha, T. Ridley, R. Maier, R.V. Flood, K.P. Lawley, R.J. Donovan, A. Hopkirk, *J. Phys. Chem.*, 1993, 97, 4582.
24. J. Long, H. Wang, Á. Kvaran, *J. Mol. Spectrosc.*, 2012, 282, 20.
25. Á. Kvaran, H. Wang, B.G. Waage, Can. J. Phys., 2001, 79, 197.
26. S. Arepalli, N. Presser, D. Robie, and R.J. Gordon, *Chem. Phys. Lett.*, 1985. 118, 88.
27. S. Arepalli, N. Presser, D. Robie, and R.J. Gordon, *Chem. Phys. Lett.*, 1985. 117, 64.
28. D. W. Bauerle, Laser Processing and Chemistry, Springer, 2011.
29. K. Matthiasson, J. Long, H. Wang and A. Kvaran, *J. Chem. Phys.*, 2011, 134, 164302. J. Long, H. R. Hrodmarsson, H.Wang and A. Kvaran, *J. Chem. Phys*, 2012, 136, 214315.
30. J. Long, H. Wang and A. Kvaran, *J. Chem. Phys.*, 2013, 138, 044308.

31. D. Zaouris, A. Kartakoullis, P. Glodic, P. Samartzis, H. R. Hróðmarsson and Á. Kvaran, *Phys. Chem. Chem. Phys.*, 2015, 17, 10468.
32. P. Glodic, D. Zaouris, P. C. Samartzis, A. Hafliðason and Á. Kvaran, *Phys. Chem. Chem. Phys.*, 2016, 18, 26291.
33. H. R. Hróðmarsson, A. Kartakoullis, D. Zaouris, P. Glodic, H.Wang, P. C. Samartzis, and A. Kvaran, *Phys. Chem. Chem. Phys.*, 2017, 19, 11354.
34. A. Hafliðason, P. Glodic, G.Koumrianou, P. C. Samartzis and Ágúst Kvaran, *Phys. Chem. Chem. Phys.*, 2018, 20, 17423.
35. A. Hafliðason, P. Glodic, G.Koumrianou, P. C. Samartzis and Ágúst Kvaran, *Phys. Chem. Chem. Phys.*, 2019, 21, 10391.
36. "Constants of diatomic molecules", NIST Chemistry WebBook, http://webbook.nist.gov/cgi/cbook.cgi?ID=C7698057&Units=SI&Mask=1000, (accessed May 2017).
37. S.G. Tilford, M.L. Ginter, A.M. Bass, *J. Mol. Spectrosc.*, 1970, 34, 327.
38. D.S. Ginter, M.L. Ginter, S.G. Tilford, *J. Mol. Spectrosc.*, 1982, 92.
39. M.L. Ginter, S.G. Tilford, A.M. Bass, *J. Mol. Spectrosc.*, 1975, 57, 271.
40. S.A. Wright, J.D. McDonald, *J.Chem.Phys.*, 1994, 101, 238.
41. S.T. Pratt, M.L. Ginter, *J. Chem. Phys.*, 1995, 102, 1882.
42. P. M. Regan, D. Ascenzi, E. Wrede, P. A. Cook, M. N. R. Ashfold and A. J. Orr-Ewing, *Phys. Chem. Chem. Phys.*, 2000, 2, 23.
43. H. R. Hróðmarsson, H. Wang, and Á. Kvaran, *J. Mol. Spectrosc.*, 2013, 5, 290.
44. H. R. Hróðmarsson, H. Wang, and Á. Kvaran, *J. Chem. Phys.*, 2014, 140, 244304.
45. H. R. Hróðmarsson, H. Wang, and Á. Kvaran, *J. Chem. Phys.*, 2015, 142, 244312.
46. H. R. Hróðmarsson, H. Wang, and Á. Kvaran, *Phys. Chem. Chem. Phys.*, 2015, 142, 244312.
47. W. C. Price, *J. Chem. Phys.*, 1936, 4, 539.
48. A. Gedanken and M. D. Rowe, *Chem. Phys. Lett.*, 1975, 34, 39.
49. S. Felps, P. Hochmann, P. Brint and S. P. McGlynn, *J. Mol. Spectrosc.*, 1976, 59, 355.
50. S. Eden, P. Limao-Vieira, S. V. Hoffmann and N. J. Mason, *Chem. Phys.*, 2007, 331, 232.
51. R. Locht, B. Leyh, H. W. Jochims and H. Baumgartel, *Chem. Phys.*, 2009, 365, 109.
52. S. P. Sapers and D. J. Donaldson, *Chem. Phys. Lett.*, 1990, 173, 257.
53. M. R. Dobber, W. J. Buma and C. A. D. Lange, *J. Chem. Phys.*, 1993, 99, 836.
54. Z. Min, T. Ridley, K. P. Lawley and R. J. Donovan, *J. Photochem. Photobiol. A*, 1996, 100, 9.
55. N. A. Macleod, S. Wang, J. Hennessy, T. Ridley, K. P. Lawley and R. J. Donovan, *J. Chem. Soc. Faraday Trans.*, 1998, 94, 2689.
56. H. Shen, L. Q. Hua, C. J. Hu and B. Zhang, *J. Mol. Spectrosc.*, 2009, 257, 200.
57. A. Wakai, K. Tsuchida, T. Fukumura and K. Suzuki, *Chem. Phys. Lett.*, 2011, 516, 23.
58. S. J. Riley and K. R. Wilson, *Faraday Discuss. Chem. Soc.*, 1972, 53, 132.
59. R. O. Loo, G. E. Hall, H. P. Haerri and P. L. Houston, *J. Phys. Chem.*, 1988, 92, 5.
60. R. O. Loo, H. P. Haerri, G. E. Hall and P. L. Houston, *J. Chem. Phys.*, 1989, 90, 4222.
61. D. W. Chandler, J. W. T. Jr., M. H. M. Janssen and D. H. Parker, *Chem. Phys. Lett.*, 1989, 156, 151.
62. Y. J. Jung, Y. S. Kim, W. K. Kang and K.-H. Jung, *J. Chem. Phys.*, 1997, 107, 7187.

63. L. Rubio-Lago, A. Garcia-Vela, A. Arregui, G. A. Amaral and L. Banares, *J. Chem. Phys.*, 2009, 131, 174309.
64. D. Jo Scardino, M. D. McDowell, J. D. Graham and N. I. Hammer, *J. At. Mol. Sci.*, 2011, 2, 93.
65. M. G. Gonza´lez, J. D. Rodrı´guez, L. Rubio-Lago, A. Garcı´a-Vela and L. Ban˜ares, *Phys. Chem. Chem. Phys.*, 2011, 13, 16404.
66. L. Rubio-Lago, J. D. Rodrı´guez, A. Garcı´a-Vela, M. G. Gonza´lez, G. A. Amaral and L. Ban˜ares, *Phys. Chem. Chem. Phys.*, 2011, 13, 8186.
67. M. Poullain Sonia, V. Chicharro David, L. Rubio-Lago, A. Garcı´a-Vela and L. Ban˜ares, Philos. Trans. R. Soc. London, Ser. A, 2017, 375, 20160205.
68. Y. Amatatsu, S. Yabushita and K. Morokuma, *J. Chem. Phys.*, 1996, 104, 9783.
69. D. Xie, H. Guo, Y. Amatatsu and R. Kosloff, *J. Phys. Chem. A*, 2000, 104, 1009.
70. A. B. Alekseyev, H.-P. Liebermann, R. J. Buenker and S. N. Yurchenko, *J. Chem. Phys.*, 2007, 126, 234102.
71. A. B. Alekseyev, H.-P. Liebermann and R. J. Buenker, *J. Chem. Phys.*, 2007, 126, 234103.
72. D. H. Parker and R. B. Bernstein, *J. Phys. Chem.*, 1982, 86, 60.
73. N. Thire´, R. Cireasa, D. Staedter, V. Blanchet and S. T. Pratt, *Phys. Chem. Chem. Phys.*, 2011, 13, 18485.
74. M. G. Gonzalez, J. D. Rodriguez, L. Rubio-Lago and L. Banares, *J. Chem. Phys.*, 2011, 135, 021102.
75. S. Marggi Poullain, M. G. Gonza´lez, P. C. Samartzis, T. N. Kitsopoulos, L. Rubio-Lago and L. Ban˜ares, *Phys. Chem. Chem. Phys.*, 2015, 17, 29958.
76. S. Marggi Poullain, D. V. Chicharro, A. Zanchet, M. G. Gonza´lez, L. Rubio-Lago, M. L. Senent, A. Garcı´a-Vela and L. Ban˜ares, *Phys. Chem. Chem. Phys.*, 2016, 18, 17054.
77. J. Berkowitz, C.H. Batson, G.L. Goodman, *Phys. Rev. A*, 1981, 24, 149.
78. Y.J. Jung, Y.S. Kim, W.K. Kang, K.-H. Jung, *J. Chem. Phys.*, 1997, 107,7187.
79. C.J. Hu, S.X. Pei, Y.L. Chen, K.P. Liu, *J. Phys. Chem. A*, 2007, 111, 6813.
80. H. Shen, L.Q. Hua, C.J. Hu, B. Zhang, *J. Mol. Spectrosc.*, 2009, 257, 200.
81. W. C. Price, *J. Chem. Phys.*, 1936, 4, 539.
82. G. C. Causley and B. R. Russell, *J. Chem. Phys.*, 1975, 62, 848.
83. S. Felps, P. Hochmann, P. Brint, and S. P. McGlynn, *J. Mol. Spectrosc.*, 1976,59, 355.
84. R. Locht, G. Hagenow, K. Hottmann, and H. Baumgartel, *Chem.Phys.*, 1991, 151, 137.
85. L. T. Molina, M. J. Molina, and F. S. Rowland, *J. Phys. Chem.*, 1982, 86, 2672.
86. M. S. DeVries, N. J. A. VanVeen, T. Baller, and A. E. DeVries, *Chem.Phys.*, 1981, 56, 157.
87. W. P. Hess, D. W. Chandler, and J. W. Thoman, *Chem.Phys*, 1992, 163, 277.
88. T. Gougousi, P. C. Samartzis, and T. N. Kitsopoulos, *J. Chem. Phys.*, 1998, 108, 5742.
89. V. Blanchet, S. Boyé, S. Zamith, A. Campos, B. Girard, J. Liévin, and D. Gauyacq, *J. Chem. Phys.*, 2003, 119, 3751.
90. A. M. Shaw, Astrochemistry; From Astronomy to Astrobiology. 2006 (Wiley,).
91. D. D. Xu, J. H. Huang, R. J. Price, and W. M. Jackson, *J. Phys. Chem. A*, 2004, 108, 9916.
92. C. Escure, T. Leininger, and B. Lepetit, *J. Chem. Phys.*, 2009, 130, 244305.
93. A. Kvaran, H. Wang, K. Matthiasson and A. Bodi, *J. Phys. Chem. A*, 2010, 114, 9991-9998.

94. S. Boye, A. Campos, S. Douin, C. Fellows, D. Gauyacq, N. Shafizadeh, P. Halvick, and M. Boggio-Pasqua, *J. Chem. Phys.*, 2002 116, 8843.
95. S. Sorensen, O. Bjorneholm, I. Hjelte, T. Kihlgren, G. Ohrwall, S. Sundin, S. Svensson, S. Buil, D. Descamps, A. L'Huillier, J. Norin, and C. Wahlstrom, *J. Chem. Phys.*, 2000, 112, 8038.
96. A. Campos, S. Boyé, P. Brechignac, S. Douin, C. Fellows, N. Shafizadeh, and D. Gauyacq, *Chem. Phys.* L., 1999, 314, 91.
97. P. Loffler, E. Wrede, L. Schnieder, J. Halpern, W. Jackson, and K. Welge, *J. Chem. Phys.*, 1998, 109, 5231.
98. P. Loffler, D. Lacombe, A. Ross, E. Wrede, L. Schnieder, and K. Welge, *Chem. Phys.* L.,1996, 252, 304.
99. K. Tsuji, N. Arakawa, A. Kawai, and K. Shibuya, *J. Phys. Chem. A*, 2002, 106, 747.
100. M. N. R. Ashfold, B. Tutcher, B, Yang, Z. K. Jin and S. L. Anderson, *J. Chem. Phys.*, 1987, 87, 5105.
101. A. Campos, S. Boye, S. Douin, C. Fellows, J. Fillion, N. Shafizadeh, and D. Gauyacq, *J. Phys. Chem.*, 2001, 105, 9104.
102. J. C. Han, C. Ye, M. Suto and L. C. Lee, *J. Chem. Phys.*, 1989, **90**, 4000-4007.
103. V. Blanchet, S. Boyé, S. Zamith, A. Campos, B. Girard, J. Liévin and D. Gauyacq, *J. Chem. Phys.*, 2003, 119, 3751.
104. J. Jiang, A. K. Muthike, T. J. Erickson, R. W. Field, *J. Mol. Spectrosc.*, 2019, 361, 24.
105. J. Jiang, Z. Du, J. Liévin, R. W. Field, *Mol. Phys.*, 2020, 118, 15.
106. K. Matthíasson, H. Wang, A. Kvaran, *J. Mol. Spectrosc.*, 2009, 225, 1-5.
107. A. Hafliðason, PhD dissertation (2018).
108. G. Herzberg, Molecular Spectra and Molecular Structure; I. Spectra of Diatomic Molecules, Van Nostrand Reinhold Company, New York, 2nd edn., 1950.
109. R.G. Bray, and R.M. Hochstrasser, *Mol. Phys.*, 1976. 31(4), 1199.
110. J.B. Halpern, H. Zacharias, and R. Wallenstein, *J. Mol. Spectrosc.*, 1980. 79(1), 1.
111. J. D. Birks: Excimer. Rep. Prog. Phys. 1977. 38. 903.
112. C. K. Rhodes (Ed): Excimer laser. 2nd edn., *Topics Appl.Phys.*, Vol 30 (springer Berlin Heidelberg).
113. J. E. Geusic, H. M. Marcos, and L.G. Van Uitert, *Applied Physics Letters*. 1964. 4 (10) 182.
114. Y. Amnon, *Quantum Electronics* (3rd ed.). Wiley, pp. 208–11, 1989.
115. G. Pietri, *IEEE Trans.* 1975, NS-22.2084.
116. WaveMetrics, IgorPro, Technical graphing and data analysis software for scientists and engineers: https://www.wavemetrics.com/, WaveMetrics, Inc. USA, 1988-2014.
117. C. M. Western, PGOPHER, a Program for Simulating Rotational Structure, C. M. Western, University of Bristol, http://pgopher.chm.bris.ac.uk University of Bristol 9.0.116 edn., 2003-2015.

Appendix: Conference presentations

Poster

Spectroscropy and state interactions in the molecular Rydberg states region; Mass resolved REMPI of HI. The 26th Colloquium on High-Resolution Molecular Spectroscopy, Dijon, France, August 2019

Oral presentation

Multiphoton breakdown of acetylene; Formation of organic building block fragments. Stereodynamics 2022, Crete, Greece, November 2022